METHODS IN ENZYMOLOGY

Editors-in-Chief

JOHN N. ABELSON AND MELVIN I. SIMON

Division of Biology
California Institute of Technology
Pasadena, California

Founding Editors

SIDNEY P. COLOWICK AND NATHAN O. KAPLAN

Academic Press is an imprint of Elsevier
525 B Street, Suite 1900, San Diego, CA 92101-4495, USA
225 Wyman Street, Waltham, MA 02451, USA
32 Jamestown Road, London NW1 7BY, UK

First edition 2012

ISBN: 978-0-12-391860-4
ISSN: 0076-6879

Printed and bound in United States of America
12 13 14 10 9 8 7 6 5 4 3 2 1

Contributors

Cláudia Andrade
Health Sciences Research Center, Instituto Superior de Ciências da Saúde, Norte, Rua Central de Gandra, Gandra, Portugal

Fernanda Andrade
Department of Pharmaceutical Technology, Faculty of Pharmacy, University of Porto, Rua Aníbal Cunha, Porto, Portugal

Francisca Araújo
Health Sciences Research Center, Instituto Superior de Ciências da Saúde, Norte, Rua Central de Gandra, Gandra, Portugal

José L. Arias
Department of Pharmacy and Pharmaceutical Technology, Faculty of Pharmacy, University of Granada, Granada, Spain

Moungi G. Bawendi
Department of Chemistry, Massachusetts Institute of Technology, Cambridge, Massachusetts, USA

Ebru Bodur
Department of Medical Biochemistry, Faculty of Medicine, Hacettepe University, Ankara, Turkey

Maria Luisa Bondì
Istituto per lo Studio dei Materiali Nanostrutturati (ISMN), Consiglio Nazionale delle Ricerche, Palermo, Italy

Seçil Caban
Department of Pharmaceutical Technology, Faculty of Pharmacy, Hacettepe University, Ankara, Turkey

Claudia Calcagno
Translational and Molecular Imaging Institute, Mount Sinai School of Medicine, New York, USA

Yılmaz Çapan
Department of Pharmaceutical Technology, Faculty of Pharmacy, Hacettepe University, Ankara, Turkey

Eric T. Christenson
Cell Biology and Physiology, Washington University School of Medicine, St Louis, Missouri, USA

Emanuela Fabiola Craparo
Dipartimento di Scienze e Tecnologie Molecolari e Biomolecolari (STEMBIO), Università di Palermo, Palermo, Italy

Turgay Dalkara
Institute of Neurological Sciences and Psychiatry and, Department of Neurology, Faculty of Medicine, Hacettepe University, Ankara, Turkey

Christiane Damgé
EA 3452, University Henri Poincaré, Faculty of Pharmacy, Nancy, France

Fabienne Danhier
Louvain Drug Research Institute, Pharmaceutics and Drug Delivery, Université Catholique de Louvain, Brussels, Belgium

Anne L. van de Ven
Department of Nanomedicine, The Methodist Hospital Research Institute, Houston, Texas, USA

Roberto Di Gesù
Dipartimento di Scienze e Tecnologie Molecolari e Biomolecolari (STEMBIO), Università di Palermo, Palermo, Italy

Kenneth Dunner Jr.
High Resolution Microscopy Imaging Facility, MD Anderson Cancer Center, Houston, Texas, USA

S. Sibel Erdem
Center for Systems Biology, Harvard Medical School and Massachusetts General Hospital, Charlestown, Massachusetts, USA

I-Ju Fang
Department of Chemistry, Iowa State University, Ames, Iowa, USA

Zahi A. Fayad
Translational and Molecular Imaging Institute, Mount Sinai School of Medicine, New York, USA

Olivier Feron
Institute of Experimental and Clinical Research, Pole of Pharmacology, Université Catholique de Louvain, Brussels, Belgium

Mauro Ferrari
Department of Nanomedicine, The Methodist Hospital Research Institute, Houston, Texas, USA

Pedro Fonte
Health Sciences Research Center, Instituto Superior de Ciências da Saúde, Norte, Rua Central de Gandra, Gandra, Portugal

Dai Fukumura
Edwin L. Steele Laboratory, Massachusetts General Hospital and Harvard Medical School, Boston, Massachusetts, USA

Visitación Gallardo
Department of Pharmacy and Pharmaceutical Technology, Faculty of Pharmacy, University of Granada, Granada, Spain

Yasemin Gürsoy-Özdemir
Institute of Neurological Sciences and Psychiatry and, Department of Neurology, Faculty of Medicine, Hacettepe University, Ankara, Turkey

Tetsuya Hara
Cardiology Division, Cardiovascular Research Center, Harvard Medical School and Massachusetts General Hospital, Boston, Massachusetts, USA

Olena Ivashyna
Cell Biology and Physiology, Washington University School of Medicine, St Louis, Missouri, USA

Christine Jérôme
Centre d'Etude et de Recherche sur les Macromolécules, Université de Liège, Liège, Belgium

Farouc A. Jaffer
Cardiology Division, Cardiovascular Research Center, Harvard Medical School and Massachusetts General Hospital, Boston, Massachusetts, USA

Rakesh K. Jain
Edwin L. Steele Laboratory, Massachusetts General Hospital and Harvard Medical School, Boston, Massachusetts, USA

Mark Kester
Penn State Hershey Cancer Institute, and Department of Pharmacology, Pennsylvania State College of Medicine, Hershey, Pennsylvania, USA

Fatima A. Khaja
Department of Biopharmaceutical Sciences, College of Pharmacy, University of Illinois at Chicago, Chicago, Illinois, USA

Otilia M.Y. Koo
Department of Biopharmaceutical Sciences, College of Pharmacy, University of Illinois at Chicago, Chicago, Illinois, and Drug Product Science and Technology, Bristol-Myers Squibb Company, New Brunswick, New Jersey, USA

Alf Lamprecht
Laboratory of Pharmaceutical Technology and Biopharmaceutics, University of Bonn, Bonn, Germany, and Laboratory of Pharmaceutical Engineering, University of Franche-Comté, Besançon, France

Gregory M. Lanza
Department of Medicine; Cell Biology and Physiology, and Biomedical Engineering, Washington University School of Medicine, St Louis, Missouri, USA

Gilberto Ka Kit Leung
Li Ka Shing Faculty of Medicine, Department of Surgery, The University of Hong Kong, Hong Kong SAR, China

Xin Liu
Penn State Hershey Cancer Institute, Pennsylvania State College of Medicine, Hershey, Pennsylvania, USA

Mark E. Lobatto
Translational and Molecular Imaging Institute, Mount Sinai School of Medicine, New York, USA, and Department of Vascular Medicine, Academic Medical Center, Amsterdam, The Netherlands

Thomas P. Loughran Jr.
Penn State Hershey Cancer Institute, Pennsylvania State College of Medicine, Hershey, Pennsylvania, USA

Aaron Mack
Department of Nanomedicine, The Methodist Hospital Research Institute, Houston, Texas, USA

Jacqueline Marchand-Brynaert
Institute of Condensed Matter and Nanosciences, Organic and Medicinal Chemistry, Université Catholique de Louvain, Louvain-la-Neuve, Belgium

Jon N. Marsh
Department of Medicine, Washington University School of Medicine, St Louis, Missouri, USA

Jason R. McCarthy
Center for Systems Biology, Harvard Medical School and Massachusetts General Hospital, Charlestown, Massachusetts, USA

Josbert M. Metselaar
Utrecht Institute for Pharmaceutical Sciences, Utrecht University, Utrecht, The Netherlands

W. Mosgoeller
Institut für Krebsforschung, Borschkegasse 8a, Klinik für Innere Medizin I, Medical University Vienna, Vienna, Austria

Willem J.M. Mulder
Translational and Molecular Imaging Institute, Mount Sinai School of Medicine, New York, USA, and Department of Vascular Medicine, Academic Medical Center, Amsterdam, The Netherlands

José das Neves
Department of Pharmaceutical Technology, Faculty of Pharmacy, University of Porto, Rua Aníbal Cunha, Porto, Portugal

Hayat Önyüksel
Department of Biopharmaceutical Sciences, College of Pharmacy, University of Illinois at Chicago, Chicago, Illinois, USA

Hua Pan
Department of Medicine, Washington University School of Medicine, St Louis, Missouri, USA

Vincent Pourcelle
Institute of Condensed Matter and Nanosciences, Organic and Medicinal Chemistry, Université Catholique de Louvain, Louvain-la-Neuve, Belgium

R. Prassl
Institute of Biophysics and Nanosystems Research, Austrian Academy of Sciences and Ludwig Boltzmann Institute for Lung Vascular Research, Graz, Austria

Véronique Préat
Louvain Drug Research Institute, Pharmaceutics and Drug Delivery, Université Catholique de Louvain, Brussels, Belgium

Catarina Pinto Reis
CBIOS-LNBN (Laboratory of Nanoscience and Biomedical Nanotechnology) and Faculty of Sciences and Health Technologies, Lusophone University of Humanities and Technologies, Lisbon, Portugal

M. Adolfina Ruiz
Department of Pharmacy and Pharmaceutical Technology, Faculty of Pharmacy, University of Granada, Granada, Spain

Ruxana T. Sadikot
Jesse Brown VA Medical Center, Section of Pulmonary, Critical Care Medicine, University of Illinois at Chicago, Chicago, Illinois, USA

Bruno Sarmento
Health Sciences Research Center, Instituto Superior de Ciências da Saúde, Norte, Rua Central de Gandra, Gandra, and Department of Pharmaceutical Technology, Faculty of Pharmacy, University of Porto, Rua Aníbal Cunha, Porto, Portugal

Irina Y. Sazonova
Section of Cardiology, Department of Medicine, Medical College of Georgia, Georgia Health Sciences University, Augusta, Georgia, USA

Paul H. Schlesinger
Cell Biology and Physiology, Washington University School of Medicine, St Louis, Missouri, USA

Rita E. Serda
Department of Nanomedicine, The Methodist Hospital Research Institute, Houston, Texas, USA

Neelesh R. Soman
Biomedical Engineering, Washington University School of Medicine, St Louis, Missouri, USA

Gert Storm
Utrecht Institute for Pharmaceutical Sciences, Utrecht University, Utrecht, The Netherlands

Erik S.G. Stroes
Department of Vascular Medicine, Academic Medical Center, Amsterdam, The Netherlands

Triantafyllos Stylianopoulos
Department of Mechanical and Manufacturing Engineering, University of Cyprus, Nicosia, Cyprus

Melissa A. Tran
Department of Pharmacology, Pennsylvania State College of Medicine, Hershey, Pennsylvania, USA

Brian G. Trewyn
Department of Chemistry, Iowa State University, Ames, Iowa, USA

Philip Wachsmann
Laboratory of Pharmaceutical Technology and Biopharmaceutics, University of Bonn, Bonn, Germany

Yue Chun Wang
Li Ka Shing Faculty of Medicine, Department of Surgery, The University of Hong Kong, Hong Kong SAR, and Department of Physiology, School of Medicine, Ji Nan University of China, Guangzhou, China

Rebecca J. Watters
Penn State Hershey Cancer Institute, Pennsylvania State College of Medicine, Hershey, Pennsylvania, USA

Volkmar Weissig
Midwestern University College of Pharmacy Glendale, Glendale, Arizona, USA

Samuel A. Wickline
Department of Medicine; Cell Biology and Physiology, and Biomedical Engineering, Washington University School of Medicine, St Louis, Missouri, USA

Cliff Wong
Department of Chemistry, Massachusetts Institute of Technology, Cambridge, Massachusetts, USA

Wutian Wu
Department of Anatomy; State Key Laboratory of Brain and Cognitive Sciences; Li Ka Shing Faculty of Medicine, Research Center of Reproduction, Development and Growth, The University of Hong Kong, Hong Kong SAR, China, and Joint Laboratory for Brain Function and Health (BFAH), Jinan University and The University of Hong Kong, Guangzhou, China

Müge Yemişci
Institute of Neurological Sciences and Psychiatry and, Department of Neurology, Faculty of Medicine, Hacettepe University, Ankara, Turkey

A. Zimmer
Institute of Pharmaceutical Sciences, Department of Pharmaceutical Technology, Karl-Franzens-University of Graz, Graz, Austria

PREFACE

This volume of *Methods in Enzymology* introduces the applications and methods of nanomedicine, a field that has been emerging in the past decade, in conjunction with advances in nanotechnology and bionanoscience.

In Chapter 1, Rita E. Serda and colleagues describe the fabrication of porous silicon-based logic-embedded vectors and their optimization to reach nonendosomal targets. Samuel A. Wickline and collaborators, in Chapter 2, describe methods for the postformulation insertion of peptide drugs into lipidic nanostructures and the evaluation of their therapeutic effectiveness both *in vitro* and *in vivo*. The synthesis of several different mesoporous silica nanoparticle materials used for the transport of drug molecules, neurotransmitters, and macromolecules across cell membranes, and the cell wall of plant cells, are outlined by I.-Ju. Fang and Brian G. Trewyn in Chapter 3.

The next set of chapters describes cancer nanomedicines. José L. Arias et al., in Chapter 4, describe the formulation of magnetically responsive nanopolymers that may be used for efficient multifunctional anticancer therapy. Integration of C_6-ceramide into sterically stabilized nanoliposomes has led to the development of a promising therapeutic either on its own or in combination with other agents for the treatment of cancer in preclinical studies. The methods used for these studies are described by Xin Liu and colleagues in Chapter 5. Dai Fukumura and colleagues, in Chapter 6, have developed a multistage nanoparticle delivery system as a potential means to improve the efficacy of anticancer therapy and describe a formulation that shrinks in size once it enters the tumor interstitial space to optimize the delivery to tumors and within tumors. Mitochondria play a key role in apoptosis and several drugs are known to trigger apoptosis by interacting with mitochondria. The methods for the preparation of mitochondria-targeted nanocarriers and protocols for their *in vitro* and *in vivo* assessment are provided in Chapter 7 by Volkmar Weissig. Arginine–glycine–aspartate-grafted nanoparticles can target $\alpha_v\beta_3$ integrin overexpressed by the tumor endothelium, and extravasate more efficiently and enter the tumor via the enhanced permeability and retention effect. In Chapter 8, Véronique Préat and collaborators delineate the methods used for the preparation of the nanoparticles, for the validation of their potential to target tumor endothelium *in vitro* and *vivo*, and for tumor delivery of poorly soluble and/or highly cytotoxic drugs.

Wutian Wu and colleagues, in Chapter 9, describe the use of a self-assembling peptide nanofiber scaffold for the reconstruction of injured brain tissue in a rodent model of surgical brain injury.

The section on cardiac nanomedicines includes contributions by Jason R. McCarthy and Willem J.M. Mulder and colleagues (Chapters 10 and 11, respectively). In the first, the methodology associated with the synthesis of a novel thrombus-targeted fibrinolytic nanoagent and the effect of the conjugation of tissue plasminogen activator to the nanoparticle surface on the activity of nanoagents are described. In the second, the authors illustrate the methods for inducing atherosclerosis in a rabbit model, the preparation of anti-inflammatory liposomes, and monitoring the therapeutic efficacy of experimental therapeutics with noninvasive imaging techniques.

Maria Luisa Bondì and Turgay Dalkara and collaborators (Chapters 12 and 13, respectively) have contributed chapters on the application of nanomedicines to central nervous system diseases. Bondì et al., in Chapter 12, outline the main production methods of lipid nanostructures such as solid lipid nanoparticles and nanostructured lipid carriers, particularly for overcoming the blood–brain barrier for the treatment of several brain diseases. In Chapter 13, Dalkara and colleagues introduce a nanomedicine made of pegylated chitosan nanoparticles with conjugated anti-transferrin receptor antibodies that can transport a blood–brain-barrier-impermeable caspase inhibitor to the brain.

In the section on diabetes nanomedicines, Catarina Pinto Reis and Christiane Damgé review alternative and more convenient methods for insulin delivery using nanotechnology (Chapter 14). Bruno Sarmento and colleagues describe, in Chapter 15, the preparation of solid lipid nanoparticles coated with the mucoadhesive polymer chitosan for intestinal absorption of insulin. They also describe methods to determine the *in vitro* intestinal permeability of insulin by means of these nanoparticles and *in vivo* models to evaluate their hypoglycemic effect in diabetic animals.

In Chapter 16, Ruxana T. Sadikot addresses the targeted delivery of drugs for the treatment of acute lung injury and acute respiratory distress syndrome, using long-acting biocompatible and biodegradable phospholipid micelles. Chapter 17, by Andreas Zimmer and colleagues, describes the use of nanocrystalline solid dispersions, PEG-PLGA nanoparticles, proticles, nanoparticle precipitates, and liposomes for the treatment of pulmonary arterial hypertension.

In the section on nanomedicines for inflammatory diseases, Hayat Önyüksel and colleagues discuss lipid-based and polymeric nanomedicines for the treatment of rheumatoid arthritis, ocular inflammation, and inflammatory bowel disease, including the animal models for these diseases (Chapter 18). In the final chapter of the volume, Philip Wachsmann and Alf Lamprecht describe the preparation, characterization, and use of polymeric nanoparticles in the therapy of murine experimental colitis (Chapter 19).

I would like to thank Zoe Kruze and Shaun Gamble of Elsevier London, and Priya Kumaraguruparan of Elsevier Chennai for all their help in preparing the volume. I would also like to thank my family for their support during the editing of this volume.

I dedicate this volume to the memories of my aunt, Sevim Uygurer, who always supported me since my childhood, and my cousin, Dr. Ferruh Ertürk, a professor of environmental engineering at Yıldız University in Istanbul, with whom I used to spend hours playing as a child.

Nejat Düzgüneş

METHODS IN ENZYMOLOGY

VOLUME I. Preparation and Assay of Enzymes
Edited by SIDNEY P. COLOWICK AND NATHAN O. KAPLAN

VOLUME II. Preparation and Assay of Enzymes
Edited by SIDNEY P. COLOWICK AND NATHAN O. KAPLAN

VOLUME III. Preparation and Assay of Substrates
Edited by SIDNEY P. COLOWICK AND NATHAN O. KAPLAN

VOLUME IV. Special Techniques for the Enzymologist
Edited by SIDNEY P. COLOWICK AND NATHAN O. KAPLAN

VOLUME V. Preparation and Assay of Enzymes
Edited by SIDNEY P. COLOWICK AND NATHAN O. KAPLAN

VOLUME VI. Preparation and Assay of Enzymes *(Continued)*
Preparation and Assay of Substrates
Special Techniques
Edited by SIDNEY P. COLOWICK AND NATHAN O. KAPLAN

VOLUME VII. Cumulative Subject Index
Edited by SIDNEY P. COLOWICK AND NATHAN O. KAPLAN

VOLUME VIII. Complex Carbohydrates
Edited by ELIZABETH F. NEUFELD AND VICTOR GINSBURG

VOLUME IX. Carbohydrate Metabolism
Edited by WILLIS A. WOOD

VOLUME X. Oxidation and Phosphorylation
Edited by RONALD W. ESTABROOK AND MAYNARD E. PULLMAN

VOLUME XI. Enzyme Structure
Edited by C. H. W. HIRS

VOLUME XII. Nucleic Acids (Parts A and B)
Edited by LAWRENCE GROSSMAN AND KIVIE MOLDAVE

VOLUME XIII. Citric Acid Cycle
Edited by J. M. LOWENSTEIN

VOLUME XIV. Lipids
Edited by J. M. LOWENSTEIN

VOLUME XV. Steroids and Terpenoids
Edited by RAYMOND B. CLAYTON

Volume XVI. Fast Reactions
Edited by Kenneth Kustin

Volume XVII. Metabolism of Amino Acids and Amines (Parts A and B)
Edited by Herbert Tabor and Celia White Tabor

Volume XVIII. Vitamins and Coenzymes (Parts A, B, and C)
Edited by Donald B. McCormick and Lemuel D. Wright

Volume XIX. Proteolytic Enzymes
Edited by Gertrude E. Perlmann and Laszlo Lorand

Volume XX. Nucleic Acids and Protein Synthesis (Part C)
Edited by Kivie Moldave and Lawrence Grossman

Volume XXI. Nucleic Acids (Part D)
Edited by Lawrence Grossman and Kivie Moldave

Volume XXII. Enzyme Purification and Related Techniques
Edited by William B. Jakoby

Volume XXIII. Photosynthesis (Part A)
Edited by Anthony San Pietro

Volume XXIV. Photosynthesis and Nitrogen Fixation (Part B)
Edited by Anthony San Pietro

Volume XXV. Enzyme Structure (Part B)
Edited by C. H. W. Hirs and Serge N. Timasheff

Volume XXVI. Enzyme Structure (Part C)
Edited by C. H. W. Hirs and Serge N. Timasheff

Volume XXVII. Enzyme Structure (Part D)
Edited by C. H. W. Hirs and Serge N. Timasheff

Volume XXVIII. Complex Carbohydrates (Part B)
Edited by Victor Ginsburg

Volume XXIX. Nucleic Acids and Protein Synthesis (Part E)
Edited by Lawrence Grossman and Kivie Moldave

Volume XXX. Nucleic Acids and Protein Synthesis (Part F)
Edited by Kivie Moldave and Lawrence Grossman

Volume XXXI. Biomembranes (Part A)
Edited by Sidney Fleischer and Lester Packer

Volume XXXII. Biomembranes (Part B)
Edited by Sidney Fleischer and Lester Packer

Volume XXXIII. Cumulative Subject Index Volumes I-XXX
Edited by Martha G. Dennis and Edward A. Dennis

Volume XXXIV. Affinity Techniques (Enzyme Purification: Part B)
Edited by William B. Jakoby and Meir Wilchek

VOLUME XXXV. Lipids (Part B)
Edited by JOHN M. LOWENSTEIN

VOLUME XXXVI. Hormone Action (Part A: Steroid Hormones)
Edited by BERT W. O'MALLEY AND JOEL G. HARDMAN

VOLUME XXXVII. Hormone Action (Part B: Peptide Hormones)
Edited by BERT W. O'MALLEY AND JOEL G. HARDMAN

VOLUME XXXVIII. Hormone Action (Part C: Cyclic Nucleotides)
Edited by JOEL G. HARDMAN AND BERT W. O'MALLEY

VOLUME XXXIX. Hormone Action (Part D: Isolated Cells, Tissues, and Organ Systems)
Edited by JOEL G. HARDMAN AND BERT W. O'MALLEY

VOLUME XL. Hormone Action (Part E: Nuclear Structure and Function)
Edited by BERT W. O'MALLEY AND JOEL G. HARDMAN

VOLUME XLI. Carbohydrate Metabolism (Part B)
Edited by W. A. WOOD

VOLUME XLII. Carbohydrate Metabolism (Part C)
Edited by W. A. WOOD

VOLUME XLIII. Antibiotics
Edited by JOHN H. HASH

VOLUME XLIV. Immobilized Enzymes
Edited by KLAUS MOSBACH

VOLUME XLV. Proteolytic Enzymes (Part B)
Edited by LASZLO LORAND

VOLUME XLVI. Affinity Labeling
Edited by WILLIAM B. JAKOBY AND MEIR WILCHEK

VOLUME XLVII. Enzyme Structure (Part E)
Edited by C. H. W. HIRS AND SERGE N. TIMASHEFF

VOLUME XLVIII. Enzyme Structure (Part F)
Edited by C. H. W. HIRS AND SERGE N. TIMASHEFF

VOLUME XLIX. Enzyme Structure (Part G)
Edited by C. H. W. HIRS AND SERGE N. TIMASHEFF

VOLUME L. Complex Carbohydrates (Part C)
Edited by VICTOR GINSBURG

VOLUME LI. Purine and Pyrimidine Nucleotide Metabolism
Edited by PATRICIA A. HOFFEE AND MARY ELLEN JONES

VOLUME LII. Biomembranes (Part C: Biological Oxidations)
Edited by SIDNEY FLEISCHER AND LESTER PACKER

Volume LIII. Biomembranes (Part D: Biological Oxidations)
Edited by Sidney Fleischer and Lester Packer

Volume LIV. Biomembranes (Part E: Biological Oxidations)
Edited by Sidney Fleischer and Lester Packer

Volume LV. Biomembranes (Part F: Bioenergetics)
Edited by Sidney Fleischer and Lester Packer

Volume LVI. Biomembranes (Part G: Bioenergetics)
Edited by Sidney Fleischer and Lester Packer

Volume LVII. Bioluminescence and Chemiluminescence
Edited by Marlene A. DeLuca

Volume LVIII. Cell Culture
Edited by William B. Jakoby and Ira Pastan

Volume LIX. Nucleic Acids and Protein Synthesis (Part G)
Edited by Kivie Moldave and Lawrence Grossman

Volume LX. Nucleic Acids and Protein Synthesis (Part H)
Edited by Kivie Moldave and Lawrence Grossman

Volume 61. Enzyme Structure (Part H)
Edited by C. H. W. Hirs and Serge N. Timasheff

Volume 62. Vitamins and Coenzymes (Part D)
Edited by Donald B. McCormick and Lemuel D. Wright

Volume 63. Enzyme Kinetics and Mechanism (Part A: Initial Rate and Inhibitor Methods)
Edited by Daniel L. Purich

Volume 64. Enzyme Kinetics and Mechanism
(Part B: Isotopic Probes and Complex Enzyme Systems)
Edited by Daniel L. Purich

Volume 65. Nucleic Acids (Part I)
Edited by Lawrence Grossman and Kivie Moldave

Volume 66. Vitamins and Coenzymes (Part E)
Edited by Donald B. McCormick and Lemuel D. Wright

Volume 67. Vitamins and Coenzymes (Part F)
Edited by Donald B. McCormick and Lemuel D. Wright

Volume 68. Recombinant DNA
Edited by Ray Wu

Volume 69. Photosynthesis and Nitrogen Fixation (Part C)
Edited by Anthony San Pietro

Volume 70. Immunochemical Techniques (Part A)
Edited by Helen Van Vunakis and John J. Langone

Volume 71. Lipids (Part C)
Edited by John M. Lowenstein

Volume 72. Lipids (Part D)
Edited by John M. Lowenstein

Volume 73. Immunochemical Techniques (Part B)
Edited by John J. Langone and Helen Van Vunakis

Volume 74. Immunochemical Techniques (Part C)
Edited by John J. Langone and Helen Van Vunakis

Volume 75. Cumulative Subject Index Volumes XXXI, XXXII, XXXIV–LX
Edited by Edward A. Dennis and Martha G. Dennis

Volume 76. Hemoglobins
Edited by Eraldo Antonini, Luigi Rossi-Bernardi, and Emilia Chiancone

Volume 77. Detoxication and Drug Metabolism
Edited by William B. Jakoby

Volume 78. Interferons (Part A)
Edited by Sidney Pestka

Volume 79. Interferons (Part B)
Edited by Sidney Pestka

Volume 80. Proteolytic Enzymes (Part C)
Edited by Laszlo Lorand

Volume 81. Biomembranes (Part H: Visual Pigments and Purple Membranes, I)
Edited by Lester Packer

Volume 82. Structural and Contractile Proteins (Part A: Extracellular Matrix)
Edited by Leon W. Cunningham and Dixie W. Frederiksen

Volume 83. Complex Carbohydrates (Part D)
Edited by Victor Ginsburg

Volume 84. Immunochemical Techniques (Part D: Selected Immunoassays)
Edited by John J. Langone and Helen Van Vunakis

Volume 85. Structural and Contractile Proteins (Part B: The Contractile Apparatus and the Cytoskeleton)
Edited by Dixie W. Frederiksen and Leon W. Cunningham

Volume 86. Prostaglandins and Arachidonate Metabolites
Edited by William E. M. Lands and William L. Smith

Volume 87. Enzyme Kinetics and Mechanism (Part C: Intermediates, Stereo-chemistry, and Rate Studies)
Edited by Daniel L. Purich

Volume 88. Biomembranes (Part I: Visual Pigments and Purple Membranes, II)
Edited by Lester Packer

Volume 89. Carbohydrate Metabolism (Part D)
Edited by Willis A. Wood

Volume 90. Carbohydrate Metabolism (Part E)
Edited by Willis A. Wood

Volume 91. Enzyme Structure (Part I)
Edited by C. H. W. Hirs and Serge N. Timasheff

Volume 92. Immunochemical Techniques (Part E: Monoclonal Antibodies and General Immunoassay Methods)
Edited by John J. Langone and Helen Van Vunakis

Volume 93. Immunochemical Techniques (Part F: Conventional Antibodies, Fc Receptors, and Cytotoxicity)
Edited by John J. Langone and Helen Van Vunakis

Volume 94. Polyamines
Edited by Herbert Tabor and Celia White Tabor

Volume 95. Cumulative Subject Index Volumes 61–74, 76–80
Edited by Edward A. Dennis and Martha G. Dennis

Volume 96. Biomembranes [Part J: Membrane Biogenesis: Assembly and Targeting (General Methods; Eukaryotes)]
Edited by Sidney Fleischer and Becca Fleischer

Volume 97. Biomembranes [Part K: Membrane Biogenesis: Assembly and Targeting (Prokaryotes, Mitochondria, and Chloroplasts)]
Edited by Sidney Fleischer and Becca Fleischer

Volume 98. Biomembranes (Part L: Membrane Biogenesis: Processing and Recycling)
Edited by Sidney Fleischer and Becca Fleischer

Volume 99. Hormone Action (Part F: Protein Kinases)
Edited by Jackie D. Corbin and Joel G. Hardman

Volume 100. Recombinant DNA (Part B)
Edited by Ray Wu, Lawrence Grossman, and Kivie Moldave

Volume 101. Recombinant DNA (Part C)
Edited by Ray Wu, Lawrence Grossman, and Kivie Moldave

Volume 102. Hormone Action (Part G: Calmodulin and Calcium-Binding Proteins)
Edited by Anthony R. Means and Bert W. O'Malley

Volume 103. Hormone Action (Part H: Neuroendocrine Peptides)
Edited by P. Michael Conn

Volume 104. Enzyme Purification and Related Techniques (Part C)
Edited by William B. Jakoby

Volume 105. Oxygen Radicals in Biological Systems
Edited by Lester Packer

Volume 106. Posttranslational Modifications (Part A)
Edited by Finn Wold and Kivie Moldave

Volume 107. Posttranslational Modifications (Part B)
Edited by Finn Wold and Kivie Moldave

Volume 108. Immunochemical Techniques (Part G: Separation and Characterization of Lymphoid Cells)
Edited by Giovanni Di Sabato, John J. Langone, and Helen Van Vunakis

Volume 109. Hormone Action (Part I: Peptide Hormones)
Edited by Lutz Birnbaumer and Bert W. O'Malley

Volume 110. Steroids and Isoprenoids (Part A)
Edited by John H. Law and Hans C. Rilling

Volume 111. Steroids and Isoprenoids (Part B)
Edited by John H. Law and Hans C. Rilling

Volume 112. Drug and Enzyme Targeting (Part A)
Edited by Kenneth J. Widder and Ralph Green

Volume 113. Glutamate, Glutamine, Glutathione, and Related Compounds
Edited by Alton Meister

Volume 114. Diffraction Methods for Biological Macromolecules (Part A)
Edited by Harold W. Wyckoff, C. H. W. Hirs, and Serge N. Timasheff

Volume 115. Diffraction Methods for Biological Macromolecules (Part B)
Edited by Harold W. Wyckoff, C. H. W. Hirs, and Serge N. Timasheff

Volume 116. Immunochemical Techniques
(Part H: Effectors and Mediators of Lymphoid Cell Functions)
Edited by Giovanni Di Sabato, John J. Langone, and Helen Van Vunakis

Volume 117. Enzyme Structure (Part J)
Edited by C. H. W. Hirs and Serge N. Timasheff

Volume 118. Plant Molecular Biology
Edited by Arthur Weissbach and Herbert Weissbach

Volume 119. Interferons (Part C)
Edited by Sidney Pestka

Volume 120. Cumulative Subject Index Volumes 81–94, 96–101

Volume 121. Immunochemical Techniques (Part I: Hybridoma Technology and Monoclonal Antibodies)
Edited by John J. Langone and Helen Van Vunakis

Volume 122. Vitamins and Coenzymes (Part G)
Edited by Frank Chytil and Donald B. McCormick

Volume 123. Vitamins and Coenzymes (Part H)
Edited by Frank Chytil and Donald B. McCormick

Volume 124. Hormone Action (Part J: Neuroendocrine Peptides)
Edited by P. Michael Conn

Volume 125. Biomembranes (Part M: Transport in Bacteria, Mitochondria, and Chloroplasts: General Approaches and Transport Systems)
Edited by Sidney Fleischer and Becca Fleischer

Volume 126. Biomembranes (Part N: Transport in Bacteria, Mitochondria, and Chloroplasts: Protonmotive Force)
Edited by Sidney Fleischer and Becca Fleischer

Volume 127. Biomembranes (Part O: Protons and Water: Structure and Translocation)
Edited by Lester Packer

Volume 128. Plasma Lipoproteins (Part A: Preparation, Structure, and Molecular Biology)
Edited by Jere P. Segrest and John J. Albers

Volume 129. Plasma Lipoproteins (Part B: Characterization, Cell Biology, and Metabolism)
Edited by John J. Albers and Jere P. Segrest

Volume 130. Enzyme Structure (Part K)
Edited by C. H. W. Hirs and Serge N. Timasheff

Volume 131. Enzyme Structure (Part L)
Edited by C. H. W. Hirs and Serge N. Timasheff

Volume 132. Immunochemical Techniques (Part J: Phagocytosis and Cell-Mediated Cytotoxicity)
Edited by Giovanni Di Sabato and Johannes Everse

Volume 133. Bioluminescence and Chemiluminescence (Part B)
Edited by Marlene DeLuca and William D. McElroy

Volume 134. Structural and Contractile Proteins (Part C: The Contractile Apparatus and the Cytoskeleton)
Edited by Richard B. Vallee

Volume 135. Immobilized Enzymes and Cells (Part B)
Edited by Klaus Mosbach

Volume 136. Immobilized Enzymes and Cells (Part C)
Edited by Klaus Mosbach

Volume 137. Immobilized Enzymes and Cells (Part D)
Edited by Klaus Mosbach

Volume 138. Complex Carbohydrates (Part E)
Edited by Victor Ginsburg

Volume 139. Cellular Regulators (Part A: Calcium- and Calmodulin-Binding Proteins)
Edited by Anthony R. Means and P. Michael Conn

Volume 140. Cumulative Subject Index Volumes 102–119, 121–134

Volume 141. Cellular Regulators (Part B: Calcium and Lipids)
Edited by P. Michael Conn and Anthony R. Means

Volume 142. Metabolism of Aromatic Amino Acids and Amines
Edited by Seymour Kaufman

Volume 143. Sulfur and Sulfur Amino Acids
Edited by William B. Jakoby and Owen Griffith

Volume 144. Structural and Contractile Proteins (Part D: Extracellular Matrix)
Edited by Leon W. Cunningham

Volume 145. Structural and Contractile Proteins (Part E: Extracellular Matrix)
Edited by Leon W. Cunningham

Volume 146. Peptide Growth Factors (Part A)
Edited by David Barnes and David A. Sirbasku

Volume 147. Peptide Growth Factors (Part B)
Edited by David Barnes and David A. Sirbasku

Volume 148. Plant Cell Membranes
Edited by Lester Packer and Roland Douce

Volume 149. Drug and Enzyme Targeting (Part B)
Edited by Ralph Green and Kenneth J. Widder

Volume 150. Immunochemical Techniques (Part K: *In Vitro* Models of B and T Cell Functions and Lymphoid Cell Receptors)
Edited by Giovanni Di Sabato

Volume 151. Molecular Genetics of Mammalian Cells
Edited by Michael M. Gottesman

Volume 152. Guide to Molecular Cloning Techniques
Edited by Shelby L. Berger and Alan R. Kimmel

Volume 153. Recombinant DNA (Part D)
Edited by Ray Wu and Lawrence Grossman

Volume 154. Recombinant DNA (Part E)
Edited by Ray Wu and Lawrence Grossman

Volume 155. Recombinant DNA (Part F)
Edited by Ray Wu

Volume 156. Biomembranes (Part P: ATP-Driven Pumps and Related Transport: The Na, K-Pump)
Edited by Sidney Fleischer and Becca Fleischer

Volume 157. Biomembranes (Part Q: ATP-Driven Pumps and Related Transport: Calcium, Proton, and Potassium Pumps)
Edited by Sidney Fleischer and Becca Fleischer

Volume 158. Metalloproteins (Part A)
Edited by James F. Riordan and Bert L. Vallee

Volume 159. Initiation and Termination of Cyclic Nucleotide Action
Edited by Jackie D. Corbin and Roger A. Johnson

Volume 160. Biomass (Part A: Cellulose and Hemicellulose)
Edited by Willis A. Wood and Scott T. Kellogg

Volume 161. Biomass (Part B: Lignin, Pectin, and Chitin)
Edited by Willis A. Wood and Scott T. Kellogg

Volume 162. Immunochemical Techniques (Part L: Chemotaxis and Inflammation)
Edited by Giovanni Di Sabato

Volume 163. Immunochemical Techniques (Part M: Chemotaxis and Inflammation)
Edited by Giovanni Di Sabato

Volume 164. Ribosomes
Edited by Harry F. Noller, Jr., and Kivie Moldave

Volume 165. Microbial Toxins: Tools for Enzymology
Edited by Sidney Harshman

Volume 166. Branched-Chain Amino Acids
Edited by Robert Harris and John R. Sokatch

Volume 167. Cyanobacteria
Edited by Lester Packer and Alexander N. Glazer

Volume 168. Hormone Action (Part K: Neuroendocrine Peptides)
Edited by P. Michael Conn

Volume 169. Platelets: Receptors, Adhesion, Secretion (Part A)
Edited by Jacek Hawiger

Volume 170. Nucleosomes
Edited by Paul M. Wassarman and Roger D. Kornberg

Volume 171. Biomembranes (Part R: Transport Theory: Cells and Model Membranes)
Edited by Sidney Fleischer and Becca Fleischer

Volume 172. Biomembranes (Part S: Transport: Membrane Isolation and Characterization)
Edited by Sidney Fleischer and Becca Fleischer

VOLUME 173. Biomembranes [Part T: Cellular and Subcellular Transport: Eukaryotic (Nonepithelial) Cells]
Edited by SIDNEY FLEISCHER AND BECCA FLEISCHER

VOLUME 174. Biomembranes [Part U: Cellular and Subcellular Transport: Eukaryotic (Nonepithelial) Cells]
Edited by SIDNEY FLEISCHER AND BECCA FLEISCHER

VOLUME 175. Cumulative Subject Index Volumes 135–139, 141–167

VOLUME 176. Nuclear Magnetic Resonance (Part A: Spectral Techniques and Dynamics)
Edited by NORMAN J. OPPENHEIMER AND THOMAS L. JAMES

VOLUME 177. Nuclear Magnetic Resonance (Part B: Structure and Mechanism)
Edited by NORMAN J. OPPENHEIMER AND THOMAS L. JAMES

VOLUME 178. Antibodies, Antigens, and Molecular Mimicry
Edited by JOHN J. LANGONE

VOLUME 179. Complex Carbohydrates (Part F)
Edited by VICTOR GINSBURG

VOLUME 180. RNA Processing (Part A: General Methods)
Edited by JAMES E. DAHLBERG AND JOHN N. ABELSON

VOLUME 181. RNA Processing (Part B: Specific Methods)
Edited by JAMES E. DAHLBERG AND JOHN N. ABELSON

VOLUME 182. Guide to Protein Purification
Edited by MURRAY P. DEUTSCHER

VOLUME 183. Molecular Evolution: Computer Analysis of Protein and Nucleic Acid Sequences
Edited by RUSSELL F. DOOLITTLE

VOLUME 184. Avidin-Biotin Technology
Edited by MEIR WILCHEK AND EDWARD A. BAYER

VOLUME 185. Gene Expression Technology
Edited by DAVID V. GOEDDEL

VOLUME 186. Oxygen Radicals in Biological Systems (Part B: Oxygen Radicals and Antioxidants)
Edited by LESTER PACKER AND ALEXANDER N. GLAZER

VOLUME 187. Arachidonate Related Lipid Mediators
Edited by ROBERT C. MURPHY AND FRANK A. FITZPATRICK

VOLUME 188. Hydrocarbons and Methylotrophy
Edited by MARY E. LIDSTROM

VOLUME 189. Retinoids (Part A: Molecular and Metabolic Aspects)
Edited by LESTER PACKER

Volume 190. Retinoids (Part B: Cell Differentiation and Clinical Applications)
Edited by Lester Packer

Volume 191. Biomembranes (Part V: Cellular and Subcellular Transport: Epithelial Cells)
Edited by Sidney Fleischer and Becca Fleischer

Volume 192. Biomembranes (Part W: Cellular and Subcellular Transport: Epithelial Cells)
Edited by Sidney Fleischer and Becca Fleischer

Volume 193. Mass Spectrometry
Edited by James A. McCloskey

Volume 194. Guide to Yeast Genetics and Molecular Biology
Edited by Christine Guthrie and Gerald R. Fink

Volume 195. Adenylyl Cyclase, G Proteins, and Guanylyl Cyclase
Edited by Roger A. Johnson and Jackie D. Corbin

Volume 196. Molecular Motors and the Cytoskeleton
Edited by Richard B. Vallee

Volume 197. Phospholipases
Edited by Edward A. Dennis

Volume 198. Peptide Growth Factors (Part C)
Edited by David Barnes, J. P. Mather, and Gordon H. Sato

Volume 199. Cumulative Subject Index Volumes 168–174, 176–194

Volume 200. Protein Phosphorylation (Part A: Protein Kinases: Assays, Purification, Antibodies, Functional Analysis, Cloning, and Expression)
Edited by Tony Hunter and Bartholomew M. Sefton

Volume 201. Protein Phosphorylation (Part B: Analysis of Protein Phosphorylation, Protein Kinase Inhibitors, and Protein Phosphatases)
Edited by Tony Hunter and Bartholomew M. Sefton

Volume 202. Molecular Design and Modeling: Concepts and Applications (Part A: Proteins, Peptides, and Enzymes)
Edited by John J. Langone

Volume 203. Molecular Design and Modeling: Concepts and Applications (Part B: Antibodies and Antigens, Nucleic Acids, Polysaccharides, and Drugs)
Edited by John J. Langone

Volume 204. Bacterial Genetic Systems
Edited by Jeffrey H. Miller

Volume 205. Metallobiochemistry (Part B: Metallothionein and Related Molecules)
Edited by James F. Riordan and Bert L. Vallee

Volume 206. Cytochrome P450
Edited by Michael R. Waterman and Eric F. Johnson

Volume 207. Ion Channels
Edited by Bernardo Rudy and Linda E. Iverson

Volume 208. Protein–DNA Interactions
Edited by Robert T. Sauer

Volume 209. Phospholipid Biosynthesis
Edited by Edward A. Dennis and Dennis E. Vance

Volume 210. Numerical Computer Methods
Edited by Ludwig Brand and Michael L. Johnson

Volume 211. DNA Structures (Part A: Synthesis and Physical Analysis of DNA)
Edited by David M. J. Lilley and James E. Dahlberg

Volume 212. DNA Structures (Part B: Chemical and Electrophoretic Analysis of DNA)
Edited by David M. J. Lilley and James E. Dahlberg

Volume 213. Carotenoids (Part A: Chemistry, Separation, Quantitation, and Antioxidation)
Edited by Lester Packer

Volume 214. Carotenoids (Part B: Metabolism, Genetics, and Biosynthesis)
Edited by Lester Packer

Volume 215. Platelets: Receptors, Adhesion, Secretion (Part B)
Edited by Jacek J. Hawiger

Volume 216. Recombinant DNA (Part G)
Edited by Ray Wu

Volume 217. Recombinant DNA (Part H)
Edited by Ray Wu

Volume 218. Recombinant DNA (Part I)
Edited by Ray Wu

Volume 219. Reconstitution of Intracellular Transport
Edited by James E. Rothman

Volume 220. Membrane Fusion Techniques (Part A)
Edited by Nejat Düzgüneş

Volume 221. Membrane Fusion Techniques (Part B)
Edited by Nejat Düzgüneş

Volume 222. Proteolytic Enzymes in Coagulation, Fibrinolysis, and Complement Activation (Part A: Mammalian Blood Coagulation Factors and Inhibitors)
Edited by Laszlo Lorand and Kenneth G. Mann

Volume 223. Proteolytic Enzymes in Coagulation, Fibrinolysis, and Complement Activation (Part B: Complement Activation, Fibrinolysis, and Nonmammalian Blood Coagulation Factors)
Edited by Laszlo Lorand and Kenneth G. Mann

Volume 224. Molecular Evolution: Producing the Biochemical Data
Edited by Elizabeth Anne Zimmer, Thomas J. White, Rebecca L. Cann, and Allan C. Wilson

Volume 225. Guide to Techniques in Mouse Development
Edited by Paul M. Wassarman and Melvin L. DePamphilis

Volume 226. Metallobiochemistry (Part C: Spectroscopic and Physical Methods for Probing Metal Ion Environments in Metalloenzymes and Metalloproteins)
Edited by James F. Riordan and Bert L. Vallee

Volume 227. Metallobiochemistry (Part D: Physical and Spectroscopic Methods for Probing Metal Ion Environments in Metalloproteins)
Edited by James F. Riordan and Bert L. Vallee

Volume 228. Aqueous Two-Phase Systems
Edited by Harry Walter and Göte Johansson

Volume 229. Cumulative Subject Index Volumes 195–198, 200–227

Volume 230. Guide to Techniques in Glycobiology
Edited by William J. Lennarz and Gerald W. Hart

Volume 231. Hemoglobins (Part B: Biochemical and Analytical Methods)
Edited by Johannes Everse, Kim D. Vandegriff, and Robert M. Winslow

Volume 232. Hemoglobins (Part C: Biophysical Methods)
Edited by Johannes Everse, Kim D. Vandegriff, and Robert M. Winslow

Volume 233. Oxygen Radicals in Biological Systems (Part C)
Edited by Lester Packer

Volume 234. Oxygen Radicals in Biological Systems (Part D)
Edited by Lester Packer

Volume 235. Bacterial Pathogenesis (Part A: Identification and Regulation of Virulence Factors)
Edited by Virginia L. Clark and Patrik M. Bavoil

Volume 236. Bacterial Pathogenesis (Part B: Integration of Pathogenic Bacteria with Host Cells)
Edited by Virginia L. Clark and Patrik M. Bavoil

Volume 237. Heterotrimeric G Proteins
Edited by Ravi Iyengar

Volume 238. Heterotrimeric G-Protein Effectors
Edited by Ravi Iyengar

Volume 239. Nuclear Magnetic Resonance (Part C)
Edited by Thomas L. James and Norman J. Oppenheimer

Volume 240. Numerical Computer Methods (Part B)
Edited by Michael L. Johnson and Ludwig Brand

Volume 241. Retroviral Proteases
Edited by Lawrence C. Kuo and Jules A. Shafer

Volume 242. Neoglycoconjugates (Part A)
Edited by Y. C. Lee and Reiko T. Lee

Volume 243. Inorganic Microbial Sulfur Metabolism
Edited by Harry D. Peck, Jr., and Jean LeGall

Volume 244. Proteolytic Enzymes: Serine and Cysteine Peptidases
Edited by Alan J. Barrett

Volume 245. Extracellular Matrix Components
Edited by E. Ruoslahti and E. Engvall

Volume 246. Biochemical Spectroscopy
Edited by Kenneth Sauer

Volume 247. Neoglycoconjugates (Part B: Biomedical Applications)
Edited by Y. C. Lee and Reiko T. Lee

Volume 248. Proteolytic Enzymes: Aspartic and Metallo Peptidases
Edited by Alan J. Barrett

Volume 249. Enzyme Kinetics and Mechanism (Part D: Developments in Enzyme Dynamics)
Edited by Daniel L. Purich

Volume 250. Lipid Modifications of Proteins
Edited by Patrick J. Casey and Janice E. Buss

Volume 251. Biothiols (Part A: Monothiols and Dithiols, Protein Thiols, and Thiyl Radicals)
Edited by Lester Packer

Volume 252. Biothiols (Part B: Glutathione and Thioredoxin; Thiols in Signal Transduction and Gene Regulation)
Edited by Lester Packer

Volume 253. Adhesion of Microbial Pathogens
Edited by Ron J. Doyle and Itzhak Ofek

Volume 254. Oncogene Techniques
Edited by Peter K. Vogt and Inder M. Verma

Volume 255. Small GTPases and Their Regulators (Part A: Ras Family)
Edited by W. E. Balch, Channing J. Der, and Alan Hall

Volume 256. Small GTPases and Their Regulators (Part B: Rho Family)
Edited by W. E. Balch, Channing J. Der, and Alan Hall

Volume 257. Small GTPases and Their Regulators (Part C: Proteins Involved in Transport)
Edited by W. E. Balch, Channing J. Der, and Alan Hall

Volume 258. Redox-Active Amino Acids in Biology
Edited by Judith P. Klinman

Volume 259. Energetics of Biological Macromolecules
Edited by Michael L. Johnson and Gary K. Ackers

Volume 260. Mitochondrial Biogenesis and Genetics (Part A)
Edited by Giuseppe M. Attardi and Anne Chomyn

Volume 261. Nuclear Magnetic Resonance and Nucleic Acids
Edited by Thomas L. James

Volume 262. DNA Replication
Edited by Judith L. Campbell

Volume 263. Plasma Lipoproteins (Part C: Quantitation)
Edited by William A. Bradley, Sandra H. Gianturco, and Jere P. Segrest

Volume 264. Mitochondrial Biogenesis and Genetics (Part B)
Edited by Giuseppe M. Attardi and Anne Chomyn

Volume 265. Cumulative Subject Index Volumes 228, 230–262

Volume 266. Computer Methods for Macromolecular Sequence Analysis
Edited by Russell F. Doolittle

Volume 267. Combinatorial Chemistry
Edited by John N. Abelson

Volume 268. Nitric Oxide (Part A: Sources and Detection of NO; NO Synthase)
Edited by Lester Packer

Volume 269. Nitric Oxide (Part B: Physiological and Pathological Processes)
Edited by Lester Packer

Volume 270. High Resolution Separation and Analysis of Biological Macromolecules (Part A: Fundamentals)
Edited by Barry L. Karger and William S. Hancock

Volume 271. High Resolution Separation and Analysis of Biological Macromolecules (Part B: Applications)
Edited by Barry L. Karger and William S. Hancock

Volume 272. Cytochrome P450 (Part B)
Edited by Eric F. Johnson and Michael R. Waterman

Volume 273. RNA Polymerase and Associated Factors (Part A)
Edited by Sankar Adhya

Volume 274. RNA Polymerase and Associated Factors (Part B)
Edited by Sankar Adhya

Volume 275. Viral Polymerases and Related Proteins
Edited by Lawrence C. Kuo, David B. Olsen, and Steven S. Carroll

Volume 276. Macromolecular Crystallography (Part A)
Edited by Charles W. Carter, Jr., and Robert M. Sweet

Volume 277. Macromolecular Crystallography (Part B)
Edited by Charles W. Carter, Jr., and Robert M. Sweet

Volume 278. Fluorescence Spectroscopy
Edited by Ludwig Brand and Michael L. Johnson

Volume 279. Vitamins and Coenzymes (Part I)
Edited by Donald B. McCormick, John W. Suttie, and Conrad Wagner

Volume 280. Vitamins and Coenzymes (Part J)
Edited by Donald B. McCormick, John W. Suttie, and Conrad Wagner

Volume 281. Vitamins and Coenzymes (Part K)
Edited by Donald B. McCormick, John W. Suttie, and Conrad Wagner

Volume 282. Vitamins and Coenzymes (Part L)
Edited by Donald B. McCormick, John W. Suttie, and Conrad Wagner

Volume 283. Cell Cycle Control
Edited by William G. Dunphy

Volume 284. Lipases (Part A: Biotechnology)
Edited by Byron Rubin and Edward A. Dennis

Volume 285. Cumulative Subject Index Volumes 263, 264, 266–284, 286–289

Volume 286. Lipases (Part B: Enzyme Characterization and Utilization)
Edited by Byron Rubin and Edward A. Dennis

Volume 287. Chemokines
Edited by Richard Horuk

Volume 288. Chemokine Receptors
Edited by Richard Horuk

Volume 289. Solid Phase Peptide Synthesis
Edited by Gregg B. Fields

Volume 290. Molecular Chaperones
Edited by George H. Lorimer and Thomas Baldwin

Volume 291. Caged Compounds
Edited by Gerard Marriott

Volume 292. ABC Transporters: Biochemical, Cellular, and Molecular Aspects
Edited by Suresh V. Ambudkar and Michael M. Gottesman

Volume 293. Ion Channels (Part B)
Edited by P. Michael Conn

Volume 294. Ion Channels (Part C)
Edited by P. Michael Conn

Volume 295. Energetics of Biological Macromolecules (Part B)
Edited by Gary K. Ackers and Michael L. Johnson

Volume 296. Neurotransmitter Transporters
Edited by Susan G. Amara

Volume 297. Photosynthesis: Molecular Biology of Energy Capture
Edited by Lee McIntosh

Volume 298. Molecular Motors and the Cytoskeleton (Part B)
Edited by Richard B. Vallee

Volume 299. Oxidants and Antioxidants (Part A)
Edited by Lester Packer

Volume 300. Oxidants and Antioxidants (Part B)
Edited by Lester Packer

Volume 301. Nitric Oxide: Biological and Antioxidant Activities (Part C)
Edited by Lester Packer

Volume 302. Green Fluorescent Protein
Edited by P. Michael Conn

Volume 303. cDNA Preparation and Display
Edited by Sherman M. Weissman

Volume 304. Chromatin
Edited by Paul M. Wassarman and Alan P. Wolffe

Volume 305. Bioluminescence and Chemiluminescence (Part C)
Edited by Thomas O. Baldwin and Miriam M. Ziegler

Volume 306. Expression of Recombinant Genes in Eukaryotic Systems
Edited by Joseph C. Glorioso and Martin C. Schmidt

Volume 307. Confocal Microscopy
Edited by P. Michael Conn

Volume 308. Enzyme Kinetics and Mechanism (Part E: Energetics of Enzyme Catalysis)
Edited by Daniel L. Purich and Vern L. Schramm

Volume 309. Amyloid, Prions, and Other Protein Aggregates
Edited by Ronald Wetzel

Volume 310. Biofilms
Edited by Ron J. Doyle

VOLUME 311. Sphingolipid Metabolism and Cell Signaling (Part A)
Edited by ALFRED H. MERRILL, JR., AND YUSUF A. HANNUN

VOLUME 312. Sphingolipid Metabolism and Cell Signaling (Part B)
Edited by ALFRED H. MERRILL, JR., AND YUSUF A. HANNUN

VOLUME 313. Antisense Technology
(Part A: General Methods, Methods of Delivery, and RNA Studies)
Edited by M. IAN PHILLIPS

VOLUME 314. Antisense Technology (Part B: Applications)
Edited by M. IAN PHILLIPS

VOLUME 315. Vertebrate Phototransduction and the Visual Cycle (Part A)
Edited by KRZYSZTOF PALCZEWSKI

VOLUME 316. Vertebrate Phototransduction and the Visual Cycle (Part B)
Edited by KRZYSZTOF PALCZEWSKI

VOLUME 317. RNA–Ligand Interactions (Part A: Structural Biology Methods)
Edited by DANIEL W. CELANDER AND JOHN N. ABELSON

VOLUME 318. RNA–Ligand Interactions (Part B: Molecular Biology Methods)
Edited by DANIEL W. CELANDER AND JOHN N. ABELSON

VOLUME 319. Singlet Oxygen, UV-A, and Ozone
Edited by LESTER PACKER AND HELMUT SIES

VOLUME 320. Cumulative Subject Index Volumes 290–319

VOLUME 321. Numerical Computer Methods (Part C)
Edited by MICHAEL L. JOHNSON AND LUDWIG BRAND

VOLUME 322. Apoptosis
Edited by JOHN C. REED

VOLUME 323. Energetics of Biological Macromolecules (Part C)
Edited by MICHAEL L. JOHNSON AND GARY K. ACKERS

VOLUME 324. Branched-Chain Amino Acids (Part B)
Edited by ROBERT A. HARRIS AND JOHN R. SOKATCH

VOLUME 325. Regulators and Effectors of Small GTPases
(Part D: Rho Family)
Edited by W. E. BALCH, CHANNING J. DER, AND ALAN HALL

VOLUME 326. Applications of Chimeric Genes and Hybrid Proteins
(Part A: Gene Expression and Protein Purification)
Edited by JEREMY THORNER, SCOTT D. EMR, AND JOHN N. ABELSON

VOLUME 327. Applications of Chimeric Genes and Hybrid Proteins
(Part B: Cell Biology and Physiology)
Edited by JEREMY THORNER, SCOTT D. EMR, AND JOHN N. ABELSON

Volume 328. Applications of Chimeric Genes and Hybrid Proteins (Part C: Protein–Protein Interactions and Genomics)
Edited by Jeremy Thorner, Scott D. Emr, and John N. Abelson

Volume 329. Regulators and Effectors of Small GTPases (Part E: GTPases Involved in Vesicular Traffic)
Edited by W. E. Balch, Channing J. Der, and Alan Hall

Volume 330. Hyperthermophilic Enzymes (Part A)
Edited by Michael W. W. Adams and Robert M. Kelly

Volume 331. Hyperthermophilic Enzymes (Part B)
Edited by Michael W. W. Adams and Robert M. Kelly

Volume 332. Regulators and Effectors of Small GTPases (Part F: Ras Family I)
Edited by W. E. Balch, Channing J. Der, and Alan Hall

Volume 333. Regulators and Effectors of Small GTPases (Part G: Ras Family II)
Edited by W. E. Balch, Channing J. Der, and Alan Hall

Volume 334. Hyperthermophilic Enzymes (Part C)
Edited by Michael W. W. Adams and Robert M. Kelly

Volume 335. Flavonoids and Other Polyphenols
Edited by Lester Packer

Volume 336. Microbial Growth in Biofilms (Part A: Developmental and Molecular Biological Aspects)
Edited by Ron J. Doyle

Volume 337. Microbial Growth in Biofilms (Part B: Special Environments and Physicochemical Aspects)
Edited by Ron J. Doyle

Volume 338. Nuclear Magnetic Resonance of Biological Macromolecules (Part A)
Edited by Thomas L. James, Volker Dötsch, and Uli Schmitz

Volume 339. Nuclear Magnetic Resonance of Biological Macromolecules (Part B)
Edited by Thomas L. James, Volker Dötsch, and Uli Schmitz

Volume 340. Drug–Nucleic Acid Interactions
Edited by Jonathan B. Chaires and Michael J. Waring

Volume 341. Ribonucleases (Part A)
Edited by Allen W. Nicholson

Volume 342. Ribonucleases (Part B)
Edited by Allen W. Nicholson

Volume 343. G Protein Pathways (Part A: Receptors)
Edited by Ravi Iyengar and John D. Hildebrandt

Volume 344. G Protein Pathways (Part B: G Proteins and Their Regulators)
Edited by Ravi Iyengar and John D. Hildebrandt

Volume 345. G Protein Pathways (Part C: Effector Mechanisms)
Edited by Ravi Iyengar and John D. Hildebrandt

Volume 346. Gene Therapy Methods
Edited by M. Ian Phillips

Volume 347. Protein Sensors and Reactive Oxygen Species (Part A: Selenoproteins and Thioredoxin)
Edited by Helmut Sies and Lester Packer

Volume 348. Protein Sensors and Reactive Oxygen Species (Part B: Thiol Enzymes and Proteins)
Edited by Helmut Sies and Lester Packer

Volume 349. Superoxide Dismutase
Edited by Lester Packer

Volume 350. Guide to Yeast Genetics and Molecular and Cell Biology (Part B)
Edited by Christine Guthrie and Gerald R. Fink

Volume 351. Guide to Yeast Genetics and Molecular and Cell Biology (Part C)
Edited by Christine Guthrie and Gerald R. Fink

Volume 352. Redox Cell Biology and Genetics (Part A)
Edited by Chandan K. Sen and Lester Packer

Volume 353. Redox Cell Biology and Genetics (Part B)
Edited by Chandan K. Sen and Lester Packer

Volume 354. Enzyme Kinetics and Mechanisms (Part F: Detection and Characterization of Enzyme Reaction Intermediates)
Edited by Daniel L. Purich

Volume 355. Cumulative Subject Index Volumes 321–354

Volume 356. Laser Capture Microscopy and Microdissection
Edited by P. Michael Conn

Volume 357. Cytochrome P450, Part C
Edited by Eric F. Johnson and Michael R. Waterman

Volume 358. Bacterial Pathogenesis (Part C: Identification, Regulation, and Function of Virulence Factors)
Edited by Virginia L. Clark and Patrik M. Bavoil

Volume 359. Nitric Oxide (Part D)
Edited by Enrique Cadenas and Lester Packer

Volume 360. Biophotonics (Part A)
Edited by Gerard Marriott and Ian Parker

Volume 361. Biophotonics (Part B)
Edited by Gerard Marriott and Ian Parker

Volume 362. Recognition of Carbohydrates in Biological Systems (Part A)
Edited by Yuan C. Lee and Reiko T. Lee

Volume 363. Recognition of Carbohydrates in Biological Systems (Part B)
Edited by Yuan C. Lee and Reiko T. Lee

Volume 364. Nuclear Receptors
Edited by David W. Russell and David J. Mangelsdorf

Volume 365. Differentiation of Embryonic Stem Cells
Edited by Paul M. Wassauman and Gordon M. Keller

Volume 366. Protein Phosphatases
Edited by Susanne Klumpp and Josef Krieglstein

Volume 367. Liposomes (Part A)
Edited by Nejat Düzgüneş

Volume 368. Macromolecular Crystallography (Part C)
Edited by Charles W. Carter, Jr., and Robert M. Sweet

Volume 369. Combinational Chemistry (Part B)
Edited by Guillermo A. Morales and Barry A. Bunin

Volume 370. RNA Polymerases and Associated Factors (Part C)
Edited by Sankar L. Adhya and Susan Garges

Volume 371. RNA Polymerases and Associated Factors (Part D)
Edited by Sankar L. Adhya and Susan Garges

Volume 372. Liposomes (Part B)
Edited by Nejat Düzgüneş

Volume 373. Liposomes (Part C)
Edited by Nejat Düzgüneş

Volume 374. Macromolecular Crystallography (Part D)
Edited by Charles W. Carter, Jr., and Robert W. Sweet

Volume 375. Chromatin and Chromatin Remodeling Enzymes (Part A)
Edited by C. David Allis and Carl Wu

Volume 376. Chromatin and Chromatin Remodeling Enzymes (Part B)
Edited by C. David Allis and Carl Wu

Volume 377. Chromatin and Chromatin Remodeling Enzymes (Part C)
Edited by C. David Allis and Carl Wu

Volume 378. Quinones and Quinone Enzymes (Part A)
Edited by Helmut Sies and Lester Packer

Volume 379. Energetics of Biological Macromolecules (Part D)
Edited by Jo M. Holt, Michael L. Johnson, and Gary K. Ackers

Volume 380. Energetics of Biological Macromolecules (Part E)
Edited by Jo M. Holt, Michael L. Johnson, and Gary K. Ackers

Volume 381. Oxygen Sensing
Edited by Chandan K. Sen and Gregg L. Semenza

Volume 382. Quinones and Quinone Enzymes (Part B)
Edited by Helmut Sies and Lester Packer

Volume 383. Numerical Computer Methods (Part D)
Edited by Ludwig Brand and Michael L. Johnson

Volume 384. Numerical Computer Methods (Part E)
Edited by Ludwig Brand and Michael L. Johnson

Volume 385. Imaging in Biological Research (Part A)
Edited by P. Michael Conn

Volume 386. Imaging in Biological Research (Part B)
Edited by P. Michael Conn

Volume 387. Liposomes (Part D)
Edited by Nejat Düzgüneş

Volume 388. Protein Engineering
Edited by Dan E. Robertson and Joseph P. Noel

Volume 389. Regulators of G-Protein Signaling (Part A)
Edited by David P. Siderovski

Volume 390. Regulators of G-Protein Signaling (Part B)
Edited by David P. Siderovski

Volume 391. Liposomes (Part E)
Edited by Nejat Düzgüneş

Volume 392. RNA Interference
Edited by Engelke Rossi

Volume 393. Circadian Rhythms
Edited by Michael W. Young

Volume 394. Nuclear Magnetic Resonance of Biological Macromolecules (Part C)
Edited by Thomas L. James

Volume 395. Producing the Biochemical Data (Part B)
Edited by Elizabeth A. Zimmer and Eric H. Roalson

Volume 396. Nitric Oxide (Part E)
Edited by Lester Packer and Enrique Cadenas

Volume 397. Environmental Microbiology
Edited by Jared R. Leadbetter

Volume 398. Ubiquitin and Protein Degradation (Part A)
Edited by Raymond J. Deshaies

Volume 399. Ubiquitin and Protein Degradation (Part B)
Edited by Raymond J. Deshaies

Volume 400. Phase II Conjugation Enzymes and Transport Systems
Edited by Helmut Sies and Lester Packer

Volume 401. Glutathione Transferases and Gamma Glutamyl Transpeptidases
Edited by Helmut Sies and Lester Packer

Volume 402. Biological Mass Spectrometry
Edited by A. L. Burlingame

Volume 403. GTPases Regulating Membrane Targeting and Fusion
Edited by William E. Balch, Channing J. Der, and Alan Hall

Volume 404. GTPases Regulating Membrane Dynamics
Edited by William E. Balch, Channing J. Der, and Alan Hall

Volume 405. Mass Spectrometry: Modified Proteins and Glycoconjugates
Edited by A. L. Burlingame

Volume 406. Regulators and Effectors of Small GTPases: Rho Family
Edited by William E. Balch, Channing J. Der, and Alan Hall

Volume 407. Regulators and Effectors of Small GTPases: Ras Family
Edited by William E. Balch, Channing J. Der, and Alan Hall

Volume 408. DNA Repair (Part A)
Edited by Judith L. Campbell and Paul Modrich

Volume 409. DNA Repair (Part B)
Edited by Judith L. Campbell and Paul Modrich

Volume 410. DNA Microarrays (Part A: Array Platforms and Web-Bench Protocols)
Edited by Alan Kimmel and Brian Oliver

Volume 411. DNA Microarrays (Part B: Databases and Statistics)
Edited by Alan Kimmel and Brian Oliver

Volume 412. Amyloid, Prions, and Other Protein Aggregates (Part B)
Edited by Indu Kheterpal and Ronald Wetzel

Volume 413. Amyloid, Prions, and Other Protein Aggregates (Part C)
Edited by Indu Kheterpal and Ronald Wetzel

Volume 414. Measuring Biological Responses with Automated Microscopy
Edited by James Inglese

Volume 415. Glycobiology
Edited by Minoru Fukuda

Volume 416. Glycomics
Edited by Minoru Fukuda

Volume 417. Functional Glycomics
Edited by Minoru Fukuda

Volume 418. Embryonic Stem Cells
Edited by Irina Klimanskaya and Robert Lanza

Volume 419. Adult Stem Cells
Edited by Irina Klimanskaya and Robert Lanza

Volume 420. Stem Cell Tools and Other Experimental Protocols
Edited by Irina Klimanskaya and Robert Lanza

Volume 421. Advanced Bacterial Genetics: Use of Transposons and Phage for Genomic Engineering
Edited by Kelly T. Hughes

Volume 422. Two-Component Signaling Systems, Part A
Edited by Melvin I. Simon, Brian R. Crane, and Alexandrine Crane

Volume 423. Two-Component Signaling Systems, Part B
Edited by Melvin I. Simon, Brian R. Crane, and Alexandrine Crane

Volume 424. RNA Editing
Edited by Jonatha M. Gott

Volume 425. RNA Modification
Edited by Jonatha M. Gott

Volume 426. Integrins
Edited by David Cheresh

Volume 427. MicroRNA Methods
Edited by John J. Rossi

Volume 428. Osmosensing and Osmosignaling
Edited by Helmut Sies and Dieter Haussinger

Volume 429. Translation Initiation: Extract Systems and Molecular Genetics
Edited by Jon Lorsch

Volume 430. Translation Initiation: Reconstituted Systems and Biophysical Methods
Edited by Jon Lorsch

Volume 431. Translation Initiation: Cell Biology, High-Throughput and Chemical-Based Approaches
Edited by Jon Lorsch

Volume 432. Lipidomics and Bioactive Lipids: Mass-Spectrometry–Based Lipid Analysis
Edited by H. Alex Brown

Volume 433. Lipidomics and Bioactive Lipids: Specialized Analytical Methods and Lipids in Disease
Edited by H. Alex Brown

Volume 434. Lipidomics and Bioactive Lipids: Lipids and Cell Signaling
Edited by H. Alex Brown

Volume 435. Oxygen Biology and Hypoxia
Edited by Helmut Sies and Bernhard Brüne

Volume 436. Globins and Other Nitric Oxide-Reactive Protiens (Part A)
Edited by Robert K. Poole

Volume 437. Globins and Other Nitric Oxide-Reactive Protiens (Part B)
Edited by Robert K. Poole

Volume 438. Small GTPases in Disease (Part A)
Edited by William E. Balch, Channing J. Der, and Alan Hall

Volume 439. Small GTPases in Disease (Part B)
Edited by William E. Balch, Channing J. Der, and Alan Hall

Volume 440. Nitric Oxide, Part F Oxidative and Nitrosative Stress in Redox Regulation of Cell Signaling
Edited by Enrique Cadenas and Lester Packer

Volume 441. Nitric Oxide, Part G Oxidative and Nitrosative Stress in Redox Regulation of Cell Signaling
Edited by Enrique Cadenas and Lester Packer

Volume 442. Programmed Cell Death, General Principles for Studying Cell Death (Part A)
Edited by Roya Khosravi-Far, Zahra Zakeri, Richard A. Lockshin, and Mauro Piacentini

Volume 443. Angiogenesis: *In Vitro* Systems
Edited by David A. Cheresh

Volume 444. Angiogenesis: *In Vivo* Systems (Part A)
Edited by David A. Cheresh

Volume 445. Angiogenesis: *In Vivo* Systems (Part B)
Edited by David A. Cheresh

Volume 446. Programmed Cell Death, The Biology and Therapeutic Implications of Cell Death (Part B)
Edited by Roya Khosravi-Far, Zahra Zakeri, Richard A. Lockshin, and Mauro Piacentini

Volume 447. RNA Turnover in Bacteria, Archaea and Organelles
Edited by Lynne E. Maquat and Cecilia M. Arraiano

Volume 448. RNA Turnover in Eukaryotes: Nucleases, Pathways and Analysis of mRNA Decay
Edited by Lynne E. Maquat and Megerditch Kiledjian

Volume 449. RNA Turnover in Eukaryotes: Analysis of Specialized and Quality Control RNA Decay Pathways
Edited by Lynne E. Maquat and Megerditch Kiledjian

Volume 450. Fluorescence Spectroscopy
Edited by Ludwig Brand and Michael L. Johnson

Volume 451. Autophagy: Lower Eukaryotes and Non-Mammalian Systems (Part A)
Edited by Daniel J. Klionsky

Volume 452. Autophagy in Mammalian Systems (Part B)
Edited by Daniel J. Klionsky

Volume 453. Autophagy in Disease and Clinical Applications (Part C)
Edited by Daniel J. Klionsky

Volume 454. Computer Methods (Part A)
Edited by Michael L. Johnson and Ludwig Brand

Volume 455. Biothermodynamics (Part A)
Edited by Michael L. Johnson, Jo M. Holt, and Gary K. Ackers (Retired)

Volume 456. Mitochondrial Function, Part A: Mitochondrial Electron Transport Complexes and Reactive Oxygen Species
Edited by William S. Allison and Immo E. Scheffler

Volume 457. Mitochondrial Function, Part B: Mitochondrial Protein Kinases, Protein Phosphatases and Mitochondrial Diseases
Edited by William S. Allison and Anne N. Murphy

Volume 458. Complex Enzymes in Microbial Natural Product Biosynthesis, Part A: Overview Articles and Peptides
Edited by David A. Hopwood

Volume 459. Complex Enzymes in Microbial Natural Product Biosynthesis, Part B: Polyketides, Aminocoumarins and Carbohydrates
Edited by David A. Hopwood

Volume 460. Chemokines, Part A
Edited by Tracy M. Handel and Damon J. Hamel

Volume 461. Chemokines, Part B
Edited by Tracy M. Handel and Damon J. Hamel

Volume 462. Non-Natural Amino Acids
Edited by Tom W. Muir and John N. Abelson

Volume 463. Guide to Protein Purification, 2nd Edition
Edited by Richard R. Burgess and Murray P. Deutscher

Volume 464. Liposomes, Part F
Edited by Nejat Düzgüneş

Volume 465. Liposomes, Part G
Edited by Nejat Düzgüneş

Volume 466. Biothermodynamics, Part B
Edited by Michael L. Johnson, Gary K. Ackers, and Jo M. Holt

Volume 467. Computer Methods Part B
Edited by Michael L. Johnson and Ludwig Brand

Volume 468. Biophysical, Chemical, and Functional Probes of RNA Structure, Interactions and Folding: Part A
Edited by Daniel Herschlag

Volume 469. Biophysical, Chemical, and Functional Probes of RNA Structure, Interactions and Folding: Part B
Edited by Daniel Herschlag

Volume 470. Guide to Yeast Genetics: Functional Genomics, Proteomics, and Other Systems Analysis, 2nd Edition
Edited by Gerald Fink, Jonathan Weissman, and Christine Guthrie

Volume 471. Two-Component Signaling Systems, Part C
Edited by Melvin I. Simon, Brian R. Crane, and Alexandrine Crane

Volume 472. Single Molecule Tools, Part A: Fluorescence Based Approaches
Edited by Nils G. Walter

Volume 473. Thiol Redox Transitions in Cell Signaling, Part A Chemistry and Biochemistry of Low Molecular Weight and Protein Thiols
Edited by Enrique Cadenas and Lester Packer

Volume 474. Thiol Redox Transitions in Cell Signaling, Part B Cellular Localization and Signaling
Edited by Enrique Cadenas and Lester Packer

Volume 475. Single Molecule Tools, Part B: Super-Resolution, Particle Tracking, Multiparameter, and Force Based Methods
Edited by Nils G. Walter

Volume 476. Guide to Techniques in Mouse Development, Part A Mice, Embryos, and Cells, 2nd Edition
Edited by Paul M. Wassarman and Philippe M. Soriano

Volume 477. Guide to Techniques in Mouse Development, Part B Mouse Molecular Genetics, 2nd Edition
Edited by Paul M. Wassarman and Philippe M. Soriano

Volume 478. Glycomics
Edited by Minoru Fukuda

VOLUME 479. Functional Glycomics
Edited by MINORU FUKUDA

VOLUME 480. Glycobiology
Edited by MINORU FUKUDA

VOLUME 481. Cryo-EM, Part A: Sample Preparation and Data Collection
Edited by GRANT J. JENSEN

VOLUME 482. Cryo-EM, Part B: 3-D Reconstruction
Edited by GRANT J. JENSEN

VOLUME 483. Cryo-EM, Part C: Analyses, Interpretation, and Case Studies
Edited by GRANT J. JENSEN

VOLUME 484. Constitutive Activity in Receptors and Other Proteins, Part A
Edited by P. MICHAEL CONN

VOLUME 485. Constitutive Activity in Receptors and Other Proteins, Part B
Edited by P. MICHAEL CONN

VOLUME 486. Research on Nitrification and Related Processes, Part A
Edited by MARTIN G. KLOTZ

VOLUME 487. Computer Methods, Part C
Edited by MICHAEL L. JOHNSON AND LUDWIG BRAND

VOLUME 488. Biothermodynamics, Part C
Edited by MICHAEL L. JOHNSON, JO M. HOLT, AND GARY K. ACKERS

VOLUME 489. The Unfolded Protein Response and Cellular Stress, Part A
Edited by P. MICHAEL CONN

VOLUME 490. The Unfolded Protein Response and Cellular Stress, Part B
Edited by P. MICHAEL CONN

VOLUME 491. The Unfolded Protein Response and Cellular Stress, Part C
Edited by P. MICHAEL CONN

VOLUME 492. Biothermodynamics, Part D
Edited by MICHAEL L. JOHNSON, JO M. HOLT, AND GARY K. ACKERS

VOLUME 493. Fragment-Based Drug Design
Tools, Practical Approaches, and Examples
Edited by LAWRENCE C. KUO

VOLUME 494. Methods in Methane Metabolism, Part A
Methanogenesis
Edited by AMY C. ROSENZWEIG AND STEPHEN W. RAGSDALE

VOLUME 495. Methods in Methane Metabolism, Part B
Methanotrophy
Edited by AMY C. ROSENZWEIG AND STEPHEN W. RAGSDALE

Volume 496. Research on Nitrification and Related Processes, Part B
Edited by Martin G. Klotz and Lisa Y. Stein

Volume 497. Synthetic Biology, Part A
Methods for Part/Device Characterization and Chassis Engineering
Edited by Christopher Voigt

Volume 498. Synthetic Biology, Part B
Computer Aided Design and DNA Assembly
Edited by Christopher Voigt

Volume 499. Biology of Serpins
Edited by James C. Whisstock and Phillip I. Bird

Volume 500. Methods in Systems Biology
Edited by Daniel Jameson, Malkhey Verma, and Hans V. Westerhoff

Volume 501. Serpin Structure and Evolution
Edited by James C. Whisstock and Phillip I. Bird

Volume 502. Protein Engineering for Therapeutics, Part A
Edited by K. Dane Wittrup and Gregory L. Verdine

Volume 503. Protein Engineering for Therapeutics, Part B
Edited by K. Dane Wittrup and Gregory L. Verdine

Volume 504. Imaging and Spectroscopic Analysis of Living Cells
Optical and Spectroscopic Techniques
Edited by P. Michael Conn

Volume 505. Imaging and Spectroscopic Analysis of Living Cells
Live Cell Imaging of Cellular Elements and Functions
Edited by P. Michael Conn

Volume 506. Imaging and Spectroscopic Analysis of Living Cells
Imaging Live Cells in Health and Disease
Edited by P. Michael Conn

Volume 507. Gene Transfer Vectors for Clinical Application
Edited by Theodore Friedmann

Volume 508. Nanomedicine
Cancer, Diabetes, and Cardiovascular, Central Nervous System, Pulmonary and Inflammatory Diseases
Edited by Nejat Düzgüneş

CHAPTER ONE

Preparation, Characterization, and Cellular Associations of Silicon Logic-Embedded Vectors

Anne L. van de Ven,* Aaron Mack,* Kenneth Dunner Jr.,† Mauro Ferrari,* *and* Rita E. Serda*

Contents

* Department of Nanomedicine, The Methodist Hospital Research Institute, Houston, Texas, USA
† High Resolution Microscopy Imaging Facility, MD Anderson Cancer Center, Houston, Texas, USA

Methods in Enzymology, Volume 508
ISSN 0076-6879, DOI: 10.1016/B978-0-12-391860-4.00001-X

Abstract

Logic-embedded vectors (LEVs) have been introduced as a means to overcome sequential, biological barriers that prevent particle-based drug delivery systems from reaching their targets. In this chapter, we address the challenge of fabricating and optimizing LEVs to reach non-endosomal targets. We describe the general preparation, characterization, and cellular association of porous silicon-based LEVs. A specific example of LEV fabrication from start to finish, along with optimization and troubleshooting information, is presented to serve as a template for future designs.

1. Introduction

Particle-based drug delivery systems are subject to sequential physical and biological barriers that prevent them from reaching their site of activity. Logic-embedded vectors (LEVs), whose size, shape, surface, and cargo properties can be modulated for specific applications, have been proposed as a means to overcome these barriers. This concept was first introduced by Ferrari (2010) and validated by Serda *et al.* (2010a). By definition, LEVs require the use of multiple, discrete components to achieve multiple, specific, sequential functions. This has led to the fabrication of nested LEVs, in which small, surface-tailored components are encapsulated within a porous carrier until triggered to release. The carrier may also be programmed to have specific functions, such as long circulation time (Godin *et al.*, 2008), intravascular margination behavior (Decuzzi and Ferrari, 2008; Decuzzi *et al.*, 2009), and controlled release of cargo including nanoparticles (NPs), bioactive molecules, imaging agents, and their combinations (Tasciotti *et al.*, 2008). By appropriately functionalizing the carrier surface, particles can be programmed for cell uptake (Serda *et al.*, 2009a,b, 2010a,b, 2011a) and intracellular drug release (Tanaka *et al.*, 2010). These carriers and their cargo, however, generally remain trapped within the endosomal pathway when using conventional approaches.

In this chapter, we address the challenge of fabricating and optimizing LEVs to reach targets outside of the endosomal degradation pathway. Using porous silicon (pSi) particles as a platform technology, we describe frequently used techniques for LEV preparation, characterization, and cell association. These techniques are followed by a specific example of LEV construction using pSi particles and surface-tailored iron oxide (IO) NPs to achieve differential partitioning into unique cellular destinations. The procedure is described step-by-step, along with optimization and troubleshooting information.

2. Preparation of pSi Carrier Particles

2.1. Fabrication

pSi is generally produced by electrochemical etching, which uses hydrofluoric acid and strong electrical currents to etch pores of defined sizes into silicon substrates (Chiappini *et al.*, 2010; Xue *et al.*, 2011). Particles are created by lithography of the pSi. Quality control to produce particles of uniform size, shape, and porosity is important from a drug delivery perspective so that particle degradation and drug release can be more easily predicted (Bimbo *et al.*, 2010; Chiappini *et al.*, 2010; Serda *et al.*, 2010a,b). Detailed fabrication protocols may be found in the papers referenced here.

2.2. Surface preparation

Silicon particles for biological applications are generally oxidized to improve their hydrophilicity and facilitate the attachment of bioactive molecules. In our laboratory, pSi particles are oxidized using Piranha etch solution to achieve a uniformly oxidized surface and remove trace organic substances. This etch solution is composed of two parts 18 *M* sulfuric acid (H_2SO_4) and one part 30% hydrogen peroxide (H_2O_2). Typically, we disperse the dried particles (contained in a glass vial) in H_2O_2 using sonication, then add a teflon stir bar and H_2SO_4. The solution is reacted for 2 h at 100 °C using a heated stir plate, after which the particles are pelleted at 4200 rpm, washed twice with Millipore water, and then resuspended in 10% nitric acid to increase the number of surface hydroxyl groups (Guhathakurta and Subramanian, 2007; Serda *et al.*, 2011a). After 30 min, the particles are pelleted, washed twice with Millipore water, once with 50% 2-propanol (IPA), then resuspended in 100% IPA. At this point, Fourier transform infrared spectroscopy (FTIR) and zeta potential measurements (described in further detail below) are performed for quality control purposes. The pSi concentration is assessed using a Beckman Coulter Multisizer. Particles that will be directly loaded using the incipient wetness method (described further below) are aliquoted (10^8–10^9 particles/tube), pelleted, and dried overnight in a vacuum desiccator.

2.3. Surface functionalization

Oxidized particles may be functionalized with different molecules to achieve specific functions *in vitro* and *in vivo*. For pSi particles, this is generally done via silanization or esterification. We use a variety of silianes with different terminal groups, including 3-(aminopropyl)triethoxysilane (APTES; Sigma-Aldrich, St. Louis, MO) and 2-(carbomethoxy)ethyltrimethoxysilane

(CETES), which feature terminal amine and carboxyl groups, respectively. To modify oxidized pSi, silanes are diluted to a concentration of 0.5–2.0% in 95% IPA (made freshly by adding 5% water to 100% IPA). Particles are suspended in the silane solution by sonication, and allowed to react for 0.5–2.0 h at 35 °C, while vortexing at 1400 rpm using a Thermomixer. The silane concentration and reaction time are chosen based upon the desired amount of silanization, with higher concentrations and longer reaction times yielding a more highly polymerized layer (Moon *et al.*, 1996). An advantage of silane-based surface modification is that it can be performed before or after loading of the particle pores and it is useful for NP entrapment and as a barrier to NP release (Serda *et al.*, 2010a,b). After silanization, particles are centrifuged at 4200 rpm, washed three times with 100% IPA, pelleted, and dried overnight in a vacuum desiccator to induce silane cross-linking.

Nonpolymerizing functional groups may be used to minimize blockage of the nanoporous substrate. Molecules such as 3-(aminopropyl)(ethoxy) dimethylsilane and ethanolamine yield a monolayer of surface modification. This approach is useful when one would like to load negatively charged cargo into the pores after surface modification. Both molecules feature a terminal amine group for further functionalization, but unlike APTES, cause little to no clogging of the nanoporous substrate (Moon *et al.*, 1996).

Bioactive ligands, such as antibodies and peptides, may be covalently linked to modified pSi surfaces using standard *N*-(3-dimethylaminopropyl)-*N*′-ethylcarbodiimide hydrochloride (EDC) chemistry. Briefly, carboxyl groups on the ligand surface are activated by the addition of a 10 m*M* MES solution (pH 6.0) containing freshly dissolved 0.4 mg/ml EDC and 1.1 mg/ml *N*-hydroxysulfosuccinimide ester (Sulfo-NHS). Ligands are reacted for 15 min and then purified using a Zeba desalting column. To raise the ligand pH to 7.2 for the next chemical reaction, the Zeba column is primed with 10 m*M* phosphate buffer (PB, pH 7.2) prior to use. The activated ligand solution is added to APTES-modified pSi, sonicated, and allowed to react for up to 2 h at room temperature with intermittent vortexing. After functionalization, the particles are washed twice with 10 m*M* PB and used immediately or lyophilized after pelleting for long-term storage. Detailed protocols for this and other common cross-linking reactions may be found in Hermanson (2008).

2.4. Surface characterization

FTIR is the primary method used to verify surface functionalization (Ferraro and Basile, 1985; Teo *et al.*, 1997). FTIR measures infrared absorption resulting from vibration of the bonds between atoms. The technique uses an interferometer to isolate infrared wavelengths based on destructive interference, and then a Fourier transform is applied at each wavelength to produce an absorbance spectrum. Individual spectral peaks

correlate with the presence of specific bonds and can be used to identify material composition. Peak height can be used to quantify the amount of material present. Chemical modification of a particle surface (via either covalent conjugation or electrostatic interactions) is generally verified by looking for a reduction or shift in one or more absorbance peaks compared to an unmodified control. This technique uses very little sample ($\sim 10^6$–10^7 particles per test) and does not require any chemical dissociation.

Dynamic light scattering (DLS) measurements are used to determine particle size in solution (Goldburg, 1999). This technique relies on photon correlation spectroscopy and is suitable for spherical particles 10 nm–3 μm in size. When a laser is passed through a dilute solution of particles, Brownian motion of the particles causes a Doppler shift in the laser scattering. This wavelength shift directly correlates with particle size. DLS can distinguish between particles of different sizes within a single sample and is therefore useful for assessing particle dispersity and aggregation. Since DLS is easy and requires little sample ($\sim 10^6$ particles per test), we use it for both particle optimization and quality control.

Zeta potential measurements can be used to collect information about the surface charge of particles in solution (Serda *et al.*, 2011b). Like DLS, zeta potential measurements rely on light scattering detection of particle movement and electron field analysis. Devices such as the Brookhaven Instrument Corporation (Holtsville, NY) Zeta-PALS instrument have both functionalities and thus allow a single sample to be used for both assays. Zeta potential is measured by applying an electric field through a dilute particle solution and measuring the resultant particle migration velocity. We typically suspend a small amount of particles ($< 10^6$ particles per test) in 10 m*M* PB for analysis. This solution mimics physiological pH while allowing electrical conductance across the solution. PB can be easily titrated to a variety of pHs by mixing 10 m*M* sodium phosphate monobasic buffer (pH 4.8) and 10 m*M* sodium phosphate dibasic buffer (pH 9.3). It should be noted that zeta potential is an average bulk measurement and thus cannot distinguish between particles of different surface charges within a single sample.

A variety of colorimetric assays may be used to measure for the presence of specific functional groups on the pSi surface. This is particularly useful when optimizing or troubleshooting multistep conjugation reactions, such as the covalent attachment of ligands via a silane intermediary. Our group favors the use of APTES for ligand addition, thus we commonly use a nitrobenzaldehyde assay to quantify the presence of amine groups (Moon *et al.*, 1996, 1997; Xiao *et al.*, 1998). Briefly, particles are washed once in 99.2% ethanol mixed with 0.8% glacial acetic acid (hereafter called the coupling solution), pelleted at 4500 × *g*, and then resuspended in coupling solution containing 0.7 mg/ml 4-nitrobenzaldehyde (4-NBZ; Sigma-Aldrich).

The 4-NBZ is allowed to react with the terminal amine groups for 3 h at 50 °C while mixing at 900 rpm. Particles are then pelleted, washed three times in coupling solution, and then resuspended in a hydrolysis solution containing 0.133% glacial acetic acid, 49.933% ethanol, and 49.933% Millipore water. This step cleaves the bound 4-NBZ, which absorbs light at 268 nm. After pelleting the hydrolyzed particles, the supernatant is transferred to a UV-transparent 96-well plate, measured on a spectrophotometer, and compared to the titration curve of known 4-NBZ concentrations. Similar protocols are available in the literature for measuring other reactive terminal groups commonly used for protein conjugation including carboxyl groups (Everaerts *et al.*, 2007). Generally, it is important to select an assay that is highly sensitive and quantitative, allowing the same assay to be used for both optimization and quality control purposes.

3. LEV Assembly

3.1. Loading via the incipient wetness method

To load NPs into pSi carriers, in our laboratories, we use a technique termed the incipient wetness loading (Serda *et al.*, 2010b). Here, dried pSi particles are treated with a high concentration (1.0–5.0 mg/ml) of NPs contained within an aqueous or organic solution. Bath sonication is initially used to disperse the mixture and repeated several times over the course of 20–30 min. To separate the pSi from the unloaded NPs, it is important to centrifuge the mixture at a speed and time that selectively pellets only the pSi. The supernatant is removed and the pSi particles are washed two or three times in the buffer of choice.

To increase the carrying capacity of LEVs, charge-based loading methods may be employed alongside incipient wetness loading (Serda *et al.*, 2010a; Serda *et al.,* 2010b; Tasciotti *et al.*, 2008). Particle charge plays an important role in the retention of NPs within porous structures. Oxidized pSi is highly negatively charged ($pK_a \sim 2.2$) as a result of the hydroxyl groups present on the particle surface. For efficient loading, one should choose a cargo of sufficiently different pK_a and loading buffer with a pH between that of the pSi and NPs. For samples of unknown pK_a, this value can be determined experimentally by measuring the particle zeta potential across a range of pH. To load aminated IO NPs ($pK_a \sim 8$), for example, a borate buffer at pH 5.0 is used. When the pK_a of the NPs is too close to that of the pSi, such as for carboxylated IO NPs ($pK_a \sim 4$), NP retention can be improved by modifying the NPs with positively charged molecules like chitosan ($pK_a \sim 12$, described in further detail below).

3.2. Loading characterization

Scanning electron microscopy (SEM) can be used to characterize LEVs after loading. This technique uses a narrow electron beam to collect high-resolution, high-magnification images of backscattered electrons emitted from sample surfaces. Due to the narrowness of the excitation beam, the resultant images have a high depth-of-field that can be used to understand particle topography. Since an SEM of sufficient resolution can distinguish individual NPs within the pores of pSi particles, we use SEM on a regular basis to confirm pSi loading, evaluate the nature of NP loading, and qualitatively determine loading efficiency. Sample preparation is simple and requires only a small amount of LEVs ($\sim 10^6$) to be dried on a SEM stub and generally uses much less sample than destructive, time-consuming, chemical-based assays.

4. LEV Uptake and Trafficking by Cells

4.1. Transmission electron microscopy

The gold standard for investigating the intracellular uptake and localization of NPs, including LEVs, is transmission electron microscopy (TEM). TEM uses an electron beam to shine through ultrathin sample preparations and produce an image with nanometer or subnanometer resolution. Cellular structures including lipid membranes, organelles, and chromatin can be imaged in cross section when samples are sliced appropriately thin (< 100 nm). This technique is especially useful for visualizing individual LEV components that are beyond the resolution limit of optical microscopes. An additional advantage of this approach is that LEV components are not required to have intrinsic optical properties. We use this technique to analyze the subcellular localization of LEV formulations at different time-points after internalization by cells. The association of LEV components with specific organelles can give insights into the mechanisms that regulate LEV uptake and trafficking, as well as their influence on cell structure and function.

5. Case Study: Fabrication and Characterization of Chitosan-Coated IO LEVs

LEVs capable of releasing nanoscale cargo from the endosome may be fabricated using chitosan as a permeation enhancer. Chitosan is a biocompatible, biodegradable, cationic polysaccharide comprised of repeating units of

glucosamine and *N*-acetyl glucosamine. The cationic properties of this polymer make it uniquely suited for enhancing NP transport through tissues (Ghosn *et al.*, 2009) and cells (Serda *et al.*, 2010a). Below, we describe how chitosan can be electrostatically wrapped around anionic NPs and then loaded into pSi particles to protect its bioactivity. For each step, optimization and troubleshooting information is provided.

5.1. Step 1: Chitosan preparation

Chitosan may be purchased in a variety of molecular weights and with different amounts of deacetylation. Varying these parameters affects the polymer packing density, charge, and toxicity. Chitosan with a molecular weight of 130 kDa and 86% deacetylation (Protasan, UP CL 113; Novamatrix, Norway) works well with silicon LEVs, being sufficiently small and positively charged while demonstrating minimal toxicity. Since chitosan is not soluble at physiological pH, it must be dissolved in an acidic solution. We dissolve chitosan at 30 mg/ml in 50 m*M* borate buffer (pH 5.0, Sigma-Aldrich).

5.2. Step 2: Chitosan coating of anionic IO

Chitosan readily coats NPs with a negative surface charge, such as carboxylated superparamagnetic IO NPs (SPIONs; Ocean NanoTech, Springdale, AZ), via electrostatic interactions. For SPIONs of 30 nm diameter, chitosan is added at a ratio of 1:0.6 (w/w) at room temperature for 1 h. The ideal ratio is dependent on SPION size: if too little chitosan is added, the SPIONs cross-link and aggregate; if too much chitosan is added, it becomes difficult to remove the excess chitosan. To find the ideal ratio for specific SPIONs, the mean zeta potential and DLS diameter should be monitored across multiple ratiometric dilutions. Note that NPs should be purified (Step 3) prior to analysis to avoid interference from unbound chitosan. The reaction also requires a sufficient volume to coat uniformly the NPs without cross-linking them; thus, it is recommended that the stock NPs be suspended at the concentration of 0.1% (w/v).

5.3. Step 3: Removal of unbound chitosan

To remove unbound chitosan, purification columns may be used. For SPIONs, we can take advantage of their magnetic properties to hold the NPs in place while washing away free chitosan. Unbound chitosan is removed using a MACS magnetic purification column (Miltenyi Biotec, Inc., Auburn, CA) and washing twice with 1.0 ml of borate buffer (pH 5.0) while the sample is held next to the magnet. The sample is then removed from the magnet and released into a fresh tube using an additional 0.2 ml

borate buffer. Alternatively, a SuperMag Multitube Separator (Ocean NanoTech) with two 0.5 ml washes may be used.

5.4. Step 4: Confirming the presence of chitosan coating

Several assays are useful for confirming and optimizing the chitosan coating procedure. Chitosan-coated SPIONs have several unique spectral peaks that can be detected by FTIR (Fig. 1.1). Twenty microliter samples (~5 μg) are dried on a glass slide in a vacuum desiccator, mixed with potassium bromide (KBr) (Sigma-Aldrich), and pressed into pellets for analysis on a Nicolet FTIR Spectrophotometer (Thermo Scientific, Pittsburgh, PA). The infrared peaks contributed by the chitosan become more distinctive as the

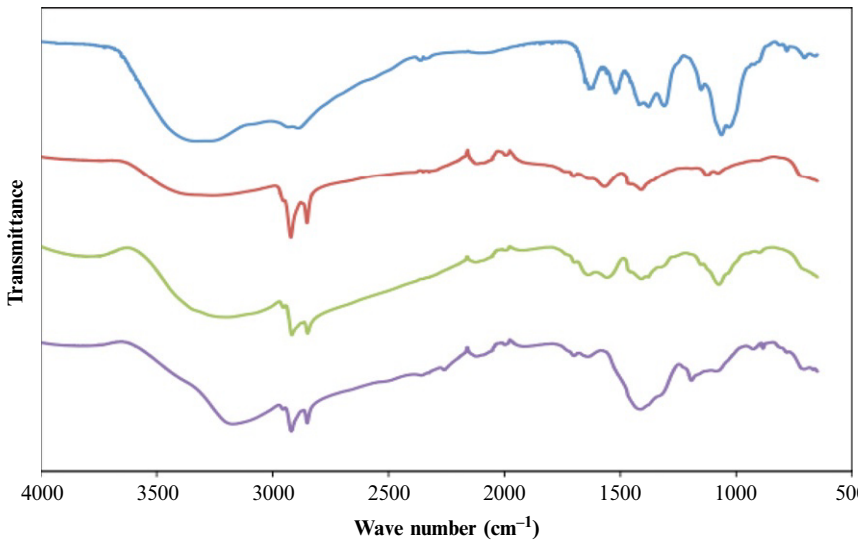

	vO–H, vN–H	vC–H	vC–C	δN–H	δN–H	δC–H	vC–O	vC–O
Chitosan	3325		2889	1626	1520	1378	1151	1063
IO	3260	2921	2852		1567	1409	1125	
IO-chitosan (pre-filter)	3197	2917	2849		1557	1408		1074
IO-chitosan (post-filter)	3173	2919	2850	1641		1412	1193	

Figure 1.1 FTIR spectra of chitosan, iron oxide (IO), and IO-chitosan before and after filtering. Successful chitosan coating is characterized by the presence of distinctive peaks.

chitosan concentration is increased; therefore, this approach may be used to quantify chitosan binding.

The number of chitosan molecules per SPION can be quantified directly using a colorimetric assay adapted from Genta *et al.* (1999). Aliquots of purified samples (20 μl, ~5 μg) are raised to 150 μl using a glycine–HCl buffer (980 m*M* glycine, 80 m*M* NaCl, and 20 m*M* HCl) and then diluted 1:1 using freshly prepared 0.3% (w/v) Congo red dye in water. Chitosan-coated SPIONs have a distinctive absorbance peak centered at 520 nm, whereas uncoated SPIONs peak at ~560 nm. The height of the 520 nm peak can be measured and compared to chitosan standards (spiked with SPIONs) to quantify the chitosan coating.

DLS and zeta potential analysis can be used to measure the mean particle diameter and surface charge, respectively. An acidic buffer, such as borate buffer, pH 5.0, should be used rather than physiological buffers to avoid chitosan precipitation. It is important that the samples appear monodisperse (i.e., only showing one peak when using DLS) and have a negative surface charge prior to loading.

5.5. Step 5: Loading of SPIONs

Oxidized pSi particles (5×10^6) are dried overnight in a vacuum desiccator. SPIONs are added to oxidized pSi at high concentration (0.5–1.0 mg/ml) and loaded via the incipient wetness method for 30 min at room temperature. Samples are centrifuged at $1000 \times g$ to pellet selectively the loaded pSi, washed twice in borate buffer, and suspended in fresh borate buffer (for storage) or serum-free cell culture media (for immediate use). One advantage of this loading approach is that it preferentially selects for chitosan-coated particles. At pH 5.0, adequately coated SPIONs have a positive zeta potential (+26 mV), whereas uncoated SPIONs have a negative zeta potential (−27 mV); thus, only the coated particles load into oxidized silicon particles (−23 mV). It should be noted that chitosan removal (Step 3) is critical for successful loading, since free chitosan (+71 mV) will compete with coated SPIONs for entry into the pores (Fig. 1.2). Loading works best with freshly purified solutions, since the chitosan-coated SPIONs tend to aggregate with storage.

5.6. Step 6: Verification of LEV assembly

A small aliquot of assembled LEVs is dried overnight on a SEM stub in a vacuum desiccator. Images of LEV surface topography are collected using an SEM, such as a Hitachi S-5500, under high vacuum at 20–30 kV with a spot size of 3.0–5.0. Figure 1.3 shows examples of LEVs loaded with aminated SPIONs (+21 mV) and chitosan-coated SPIONs (+26 mV) at multiple magnifications.

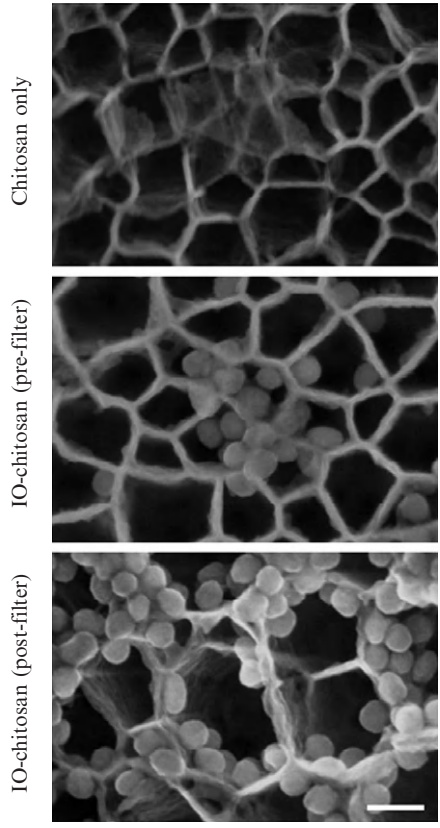

Figure 1.2 SEM images of pSi loading with IO-chitosan. The importance of removing excess chitosan is highlighted here: Free chitosan competes with IO and results in poor IO loading. Scale bar is 50 nm.

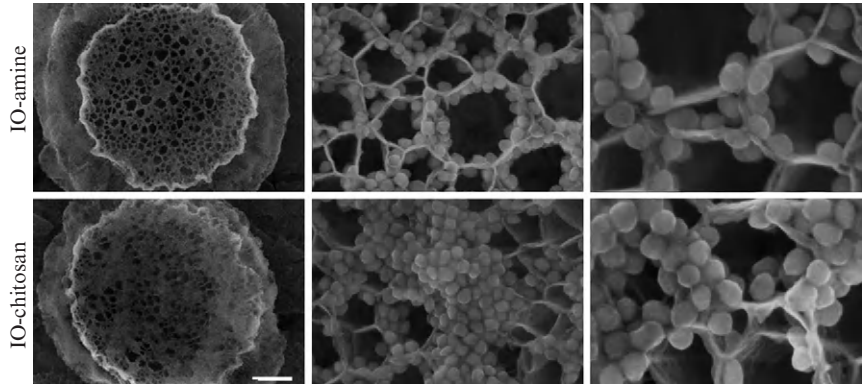

Figure 1.3 SEM images of pSi loaded with IO-amine and IO-chitosan via the incipient wetness method. The positively charged NPs appear to preferentially line the walls of the pores. The IO-chitosan shows some minor aggregation on the particle surface. Scale bars are 500, 80, and 40 nm.

5.7. Step 7: Incubation of LEVs with live cells

Cells are seeded at a concentration of 1×10^5 cells per well in 6-well plates. Twenty-four hours after seeding, 10–20 LEVs per cell (normalized to the number of seeded cells) are added directly to the cell culture media. Particles are sonicated immediately before addition to ensure that they are monodisperse. Cells and LEVs are co-incubated at 37 °C for 2–24 h, after which the cells are washed twice with phosphate buffered saline to remove non-internalized LEVs.

5.8. Step 8: TEM preparation

Cells are fixed for 1 h using freshly prepared 0.1 *M* cacodylate buffer (pH 7.3) containing 3% glutaraldehyde and 2% paraformaldehyde. After fixation, the samples are washed three times, treated with 0.1% tannic acid (in 0.1 *M*cacodylate buffer) for 15 min, washed three times, and postfixed with 1% osmium tetroxide (in 0.1 *M* cacodylate buffer) for 30 min. All washing steps up to the osmium tetroxide step use 0.1 *M* cacodylate buffer; thereafter, the samples are washed three times in distilled water. After washing, the samples are stained en bloc with 1% uranyl acetate for 30 min and then dehydrated in increasing concentrations of ethanol (50%, 70%, 80%, 90%, 95%, 100%, 100%, 100%) for 5 min each. Polymer infiltration is performed by the sequential addition of 2 ml of a 1:1 mixture of LX-112 resin and ethanol for 1 h, followed by a 2:1 LX-112:ethanol mixture for 1 h, and followed by 100% LX-112 applied twice for 1 h each. The samples are then embedded in 1.0 ml of 100% LX-112 resin and allowed to polymerize for 48 h at 70 °C. After polymerization, the resin is released from the 6-well plate using liquid nitrogen. Areas of interest are cut out using a jeweler's saw and trimmed with a razor blade. Ultrathin sections (~70 nm) are cut from trimmed blocks using a microtome, such as the Leica Ultracut (Leica, Deerfield, IL). Sections are floated onto TEM grids and counterstained using a Leica EM stainer. Samples are sequentially treated with 1% uranyl acetate for 4 min, a water wash, and 1% lead citrate for 1 min. Samples are then examined using a TEM, such as the JEM 1010 (JEOL, USA, Inc., Peabody, MA) with an accelerating voltage of 80 kV. Digital images are obtained using the AMT Imaging System (Advanced Microscopy Techniques Corp, Danvers, MA).

5.9. Step 9: Evaluation of cell-particle associations

TEM images of early LEV uptake provide insights into the mechanisms of particle uptake. Figure 1.4 shows cells 2 h after co-incubation with IO-chitosan or IO-chitosan-loaded LEVs. Ruffles in the cell membrane

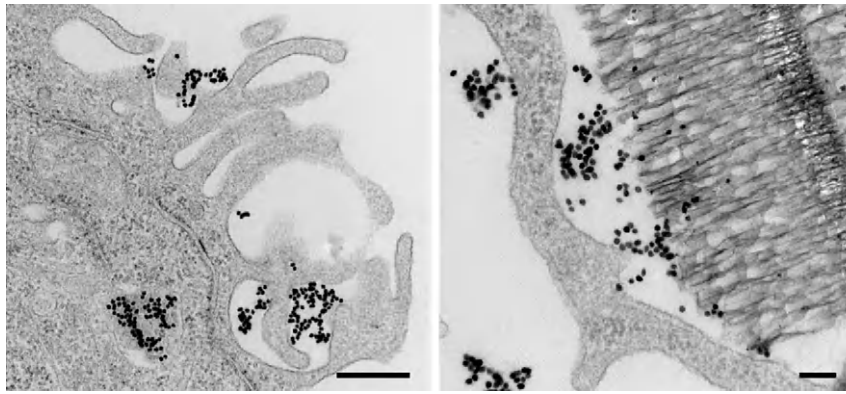

IO-Chitosan IO-Chitosan LEV

Figure 1.4 TEM images of IO-chitosan (left) and LEVs loaded with IO-chitosan (right) 2 h after coincubation with cells. IO nanoparticles appear as dark dots while pSi appears as porous sponge-like structure. At this time-point, internalized IO and LEVs are surrounded by a well-defined endosomal membrane. This membrane is relatively loose, allowing for the unloading of pSi cargo. Scale bar is 500 nm.

appear to fold-over, loosely capturing IO-chitosan and pSi via what is probably pinocytosis. Internalized LEVs appear in large vacuoles. At 2 h, the endosomal membrane is loosely associated with the LEVs, providing plenty of space for unloading of the SPIONs.

The trafficking of individual LEV components may be monitored using TEM. Figure 1.5 shows the cells 24 h after coincubation with empty pSi (left), IO-chitosan (middle), or IO-chitosan loaded LEVs (right). We find that pSi particles are retained within the endo-lysosomal pathway, even when their cargo trafficks to other intracellular destinations. Freely administered IO-chitosan appears to remain trapped in the endosomes. By contrast, IO-chitosan that was previously protected within pSi particles is now seen free in the cytoplasm, in close proximity to mitochondria. It is known that protonation of the chitosan backbone during endosome maturation leads to localized membrane destabilization (Bowman and Leong, 2006), which in turn may facilitate IO escape. Differential trafficking is observed for IO-amine of similar surface charge (Serda *et al.*, 2010a). When released from the pSi after endosomal uptake, these cationic particles accumulate in multivesicular bodies and are exported out of the cell. The differential trafficking of IO-amine and IO-chitosan LEVs suggests that: (i) endosomal escape of IO is mediated directly by the presence of chitosan and (ii) loaded IO-chitosan is protected from exposure to physiological pH and thereby better retains its bioactivity than freely administered IO-chitosan.

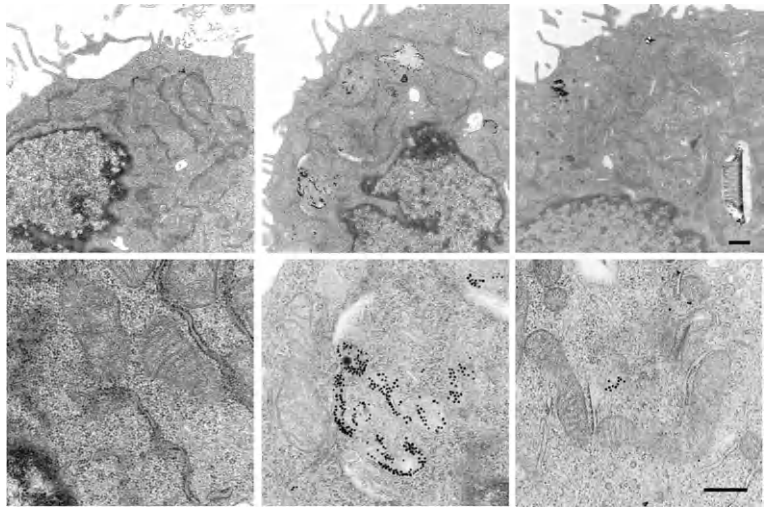

Figure 1.5 **TEM images of cells treated for 24 h. Freely administered IO-chitosan appears in multivesicular bodies, whereas protected IO-chitosan freely associates with mitochondria. An ultrastructural analysis reveals no associated cell toxicity. Indicators of healthy cell function include the presence of an intact cell membrane and the absence of nuclear condensation, membrane blebbing, and vacuoles. Scale bars are 500 nm.**

6. Conclusions

A major advantage of LEVs is their ability to deliver components to multiple intracellular sites, creating an opportunity for simultaneously targeting independent or synergistic pathways. In this chapter, we provide an example of how pSi carriers may be fabricated, loaded with bioactive particles, and differentially partitioned upon cellular uptake. Examples of characterization techniques are presented together with optimization and troubleshooting information, in order to serve as a template for the design and fabrication of new LEVs. It is exciting to speculate that future designs will be programmed to perform coordinated and synergistic modulation of intracellular functions.

ACKNOWLEDGMENTS

We thank Hitachi for training and use of the S-5500 high-resolution scanning electron microscope. This research was supported by the Department of Defense grants DODW81XWH-07–1-0596 and DODW81XWH-09–1-0212; NASA NNJ06HE06A; NIH RO1CA128797, U54CA143837, MH58920, and RC2GM092599; MDACC Institutional Core Grant CA016672; and The State of Texas, Emerging Technology Fund.

REFERENCES

Bimbo, L. M., Sarparanta, M., Santos, H. A., Airaksinen, A. J., Makila, E., Laaksonen, T., Peltonen, L., Lehto, V.-P., Hirvonen, J., and Salonen, J. (2010). Biocompatibility of thermally hydrocarbonized porous silicon nanoparticles and their biodistribution in rats. *ACS Nano* **4,** 3023–3032.

Bowman, K., and Leong, K. W. (2006). Chitosan nanoparticles for oral drug and gene delivery. *Int. J. Nanomedicine* **1,** 117–128.

Chiappini, C., Tasciotti, E., Fakhoury, J. R., Fine, D., Pullan, L., Wang, Y. C., Fu, L., Liu, X., and Ferrari, M. (2010). Tailored porous silicon microparticles: Fabrication and properties. *Chemphyschem* **11,** 1029–1035.

Decuzzi, P., and Ferrari, M. (2008). Design maps for nanoparticles targeting the diseased microvasculature. *Biomaterials* **29,** 377–384.

Decuzzi, P., Pasqualini, R., Arap, W., and Ferrari, M. (2009). Intravascular delivery of particulate systems: Does geometry really matter? *Pharm. Res.* **26,** 235–243.

Everaerts, F., Torrianni, M., Hendriks, M., and Feijen, J. (2007). Quantification of carboxyl groups in carbodiimide cross-linked collagen sponges. *J. Biomed. Mater. Res. A* **83,** 1176–1183.

Ferrari, M. (2010). Frontiers in cancer nanomedicine: Directing mass transport through biological barriers. *Trends Biotechnol.* **28,** 181–188.

Ferraro, J. R., and Basile, L. J. (eds.), (1985). Fourier Transform Infrared Spectroscopy: Applications to Chemical Systems. Academic Press, New York, FL. Vol. 4, p. 61.

Genta, I., Perugini, P., Pavanetto, F., Modena, T., Conti, B., and Muzzarelli, R. A. (1999). Microparticulate drug delivery systems. *EXS* **87,** 305–313.

Ghosn, B., van de Ven, A. L., Tam, J., Gillenwater, A., Sokolov, K. V., Richards-Kortum, R., and Roy, R. J. (2010). Efficient mucosal delivery of optical contrast agents using imidazole-modified chitosan. *Biomed. Opt.* **15**(1), 015003-1–015003-11.

Godin, B., Gu, J., Serda, R. E., Ferrati, S., and Liu, X. (2008). Multistage mesoporous silicon-based nanocarriers: Biocompatibility and controlled degradation in physiological fluids. 35th Annual Meeting & Exposition of the Controlled Release Society 575.

Goldburg, W. I. (1999). Dynamic Light Scatter. *Am. J. Physics* **67,** 1152–1160.

Guhathakurta, S., and Subramanian, A. (2007). Effect of hydrofluoric acid in oxidizing acid mixtures on the hydroxylation of silicon surface. *J. Electrochem. Soc.* **154,** P136–P146.

Hermanson, G. T. (2008). Bioconjugate Techniques. Academic Press, San Diego, CA.

Moon, J. H., Shin, J. W., Kim, S. Y., and Park, J. W. (1996). Formation of uniform aminosilane thin layers: An imine formation to measure relative surface density of the amine group. *Langmuir* **12,** 4621–4624.

Moon, J. H., Kim, J. H., Kim, K.-J., Kang, T.-H., Kim, B., Kim, C.-H., Hahn, J. H., and Park, J. W. (1997). Absolute surface density of the amine group of the aminosilylated thin layers: Ultraviolet visible spectroscopy, second harmonic generation, and synchrotron-radiation photoelectron spectroscopy study. *Langmuir* **13,** 4305–4310.

Serda, R. E., Gu, J., Bhavane, R. C., Liu, X., Chiappini, C., Decuzzi, P., and Ferrari, M. (2009a). The association of silicon microparticles with endothelial cells in drug delivery to the vasculature. *Biomaterials* **30,** 2440–2448.

Serda, R. E., Gu, J., Burks, J. K., Ferrari, K., Ferrari, C., and Ferrari, M. (2009b). Quantitative mechanics of endothelial phagocytosis of silicon microparticles. *Cytometry A* **75,** 752–760.

Serda, R. E., Mack, A., van de Ven, A. L., Ferrati, S., Dunner, K., Jr., Godin, B., Chiappini, C., Landry, M., Brousseau, L., Liu, X., Bean, A. J., and Ferrari, M. (2010a). Logic-embedded vectors for intracellular partitioning, endosomal escape, and exocytosis of nanoparticles. *Small* **6,** 2691–2700.

Serda, R. E., Mack, A., Pulikkathara, M., Zaske, A. M., Chiappini, C., Fakhoury, J., Webb, D., Godin, B., Conyers, J. L., Liu, X. W., Bankson, J. A., and Ferrari, M. (2010b). Cellular association and assembly of a multistage delivery system. *Small* **6,** 1329–1340.

Serda, R. E., Blanco, E., Mack, A., Stafford, S. J., Amra, S., Li, Q., van de Ven, A., Tanaka, T., Torchilin, V. P., Wiktorowicz, J. E., and Ferrari, M. (2011a). Proteomic analysis of serum opsonins impacting biodistribution and cellular association of porous silicon microparticles. *Mol. Imaging* **10,** 43–55.

Serda, R. E., Godin, B., Blanco, E., Chiappini, C., and Ferrari, M. (2011b). Multi-stage delivery nano-particle systems for therapeutic applications. *Biochim. Biophys. Acta* **1810,** 317–329.

Tanaka, T., Mangala, L. S., Vivas-Mejia, P. E., Nieves-Alicea, R., Mann, A. P., Mora, E., Han, H. D., Shahzad, M. M., Liu, X., Bhavane, R., Gu, J., Fakhoury, J. R., *et al.* (2010). Sustained small interfering RNA delivery by mesoporous silicon particles. *Cancer Res.* **70,** 3687–3696.

Tasciotti, E., Liu, X., Bhavane, R., Plant, K., Leonard, A. D., Price, B. K., Cheng, M. M., Decuzzi, P., Tour, J. M., Robertson, F., and Ferrari, M. (2008). Mesoporous silicon particles as a multistage delivery system for imaging and therapeutic applications. *Nat. Nanotechnol.* **3,** 151–157.

Teo, L.-S., Chen, C.-Y., and Kuo, J.-F. (1997). Fourier transform infrared spectroscopy study on effects of temperature on "Hydrogen-bonding properties of segmented polyether poly(urethane urea) copolymer" *Macromolecules* **30,** 1793–1799.

Xiao, S.-J., Textor, M., Spencer, N. D., and Sigrist, H. (1998). Covalent attachment of cell-adhesive, (Arg-Gly-Asp)-containing peptides to titanium surfaces. *Langmuir* **14,** 5507–5516.

Xue, M., Zhong, X., Shaposhnik, Z., Qu, Y., Tamanoi, F., Duan, X., and Zink, J. I. (2011). pH-Operated mechanized porous silicon nanoparticles. *J. Am. Chem. Soc.* **133,** 8798–8801.

CHAPTER TWO

Postformulation Peptide Drug Loading of Nanostructures

Hua Pan,[*] Jon N. Marsh,[*] Eric T. Christenson,[†] Neelesh R. Soman,[‡] Olena Ivashyna,[†] Gregory M. Lanza,[*,†,‡] Paul H. Schlesinger,[†] *and* Samuel A. Wickline[*,†,‡]

Contents

[*] Department of Medicine, Washington University School of Medicine, St Louis, Missouri, USA
[†] Cell Biology and Physiology, Washington University School of Medicine, St Louis, Missouri, USA
[‡] Biomedical Engineering, Washington University School of Medicine, St Louis, Missouri, USA

Methods in Enzymology, Volume 508
ISSN 0076-6879, DOI: 10.1016/B978-0-12-391860-4.00002-1

Abstract

Cytolytic peptides have commanded attention for their anticancer potential because the membrane-disrupting function that produces cell death is less likely to be overcome by resistant mutations. Congruently, peptides that are involved in molecular recognition and biological activities become attractive therapeutic candidates because of their high specificity, better affinity, reduced immunogenicity, and reduced off target toxicity. However, problems of inadequate delivery, rapid deactivation *in vivo*, and poor bioavailability have limited clinical application. Therefore, peptide drug development for clinical use requires an appropriate combination of an effective therapeutic peptide and a robust delivery methodology. In this chapter, we describe methods for the *postformulation* insertion of peptide drugs into lipidic nanostructures, the physical characterization of peptide–nanostructure complexes, and the evaluation of their therapeutic effectiveness both *in vitro* and *in vivo*.

1. Introduction

Cytolytic peptides are an attractive class of candidates for anticancer treatment because of their broad spectrum lytic properties (Giuliani *et al.*, 2007; Hancock and Sahl, 2006; Papo and Shai, 2005). They rapidly associate with and integrate into cellular membranes, forming pores that disrupt the membrane. After cellular uptake, they may also attack internal organelles in the same manner to induce cell death. Because of the unlikely development of even multistep cancer cell resistance to this attack on diverse cellular membranes by pore-forming agents, cytolytic peptides have been long recognized as promising candidate agents for cancer therapy. However, the very attributes of nonspecific membrane disruption, in addition to rapid enzymatic degradation *in vivo* unless protected, has limited their clinical application. Unfortunately, cytolytic peptides manifest profound membrane disruption on traditional lipid bilayer delivery systems, such as liposomes, which also has stymied their use *in vivo*.

In this chapter, we discuss how this problem of carrier disruption might be avoided with the use of a stable perfluorocarbon (PFC) nanoparticle system for delivery (Soman *et al.*, 2008, 2009). PFC nanoparticles consist of a hydrophobic and lipophobic PFC core surrounded by a lipid surfactant monolayer for stabilization. We have designed a postformulation self-assembling process

for peptide insertion, whereby preformulated PFC nanoparticles can accommodate cytolytic peptides in their lipid monolayer without losing their structural integrity (Soman *et al.*, 2008). We discuss the use of melittin, a 26-amino acid, cationic, amphipathic cytolytic peptide to exemplify the methods for postformulation peptide drug loading into PFC nanoparticles. We also discuss methods for evaluating the therapeutic utility of melittin-loaded nanoparticles *in vitro* and *in vivo*.

A variety of biologically active peptides might serve as potential activators or inhibitors of important cellular processes if they could be delivered specifically and safely to the correct cellular location. For example, peptide inhibitors that suppress the activation of the NF-κB signaling pathway could be used for anti-inflammatory applications (May *et al.*, 2000), to block DNA replication for anticancer therapy (Warbrick *et al.*, 1995), or to prevent HIV-1 assembly for potential anti-HIV treatment (Sticht *et al.*, 2005). The effective use of such peptides faces the challenge of the rapid protease degradation and limited bioavailability, in large part due to their inability to pass the cell membrane barrier.

Herein, we demonstrate an approach for loading peptide drugs onto a nanostructure based on their fusion to a linker peptide that is modified from the well-studied membrane active peptide, melittin (Dathe and Wieprecht, 1999; DeGrado *et al.*, 1982; Gevod and Birdi, 1984; Werkmeister *et al.*, 1993). We have shown that altering the amino acid sequence of melittin to produce structural changes that reduce the lytic activity from the native melittin allows it to be delivered to cells at much increased concentrations, as compared with melittin, without producing cell death (Pan *et al.*, 2010). Further by separating melittin's lytic activity from its membrane binding and insertion, we generated a useful "linker peptide," VLTTGLPALIS-WIKRKRQQ, which retains the property of stable ability of insertion into a lipid mono- or bilayered membrane through a self-assembly process (Pan *et al.*, 2010).

As a demonstration of the potential of this linker strategy, we have conjugated a known peptide that inhibits the NF-κB signaling pathway by interacting with the Nemo-binding domain (NBD) (May *et al.*, 2000), to the N-terminus of the linker peptide. Under normal conditions, NF-κB is sequestered in the cytoplasm as an inactive complex with the inhibitory protein IκB. Upon internal or external stimulation, IκB is phosphorylated by the activated IKK complex, resulting in ubiquitination and degradation of IκB. Consequently, NF-κB becomes free to translocate to the nucleus where it initiates the expression of NF-κB-dependent genes. The NBD inhibitory peptide prevents the activation of the IKK complex; this, in turn, inhibits IκB phosphorylation and subsequently inhibits the nuclear translocation of NF-κB and its dependent gene expression. In this chapter, we describe the methods for generating and characterizing NF-κB inhibitory PFC nanoparticles and experimental procedures for *in vitro* evaluation.

2. Lipidic Nanostructure Preparation

2.1. Liposome preparation

Liposomes are synthesized using standard protocols. Lipid components themselves are available from a variety of commercial sources and can be mixed to suit specific experimental needs. For liposome preparation, we typically mix chloroform-dissolved lipids to the desired molar ratio and aliquot 10 mg (12–15 μmol) total lipid into glass test tubes. The tubes are then insulated by shallow immersion in a room temperature water bath and organic solvent evaporated under a nitrogen stream. The lipids will then have a glassy appearance on the bottom of the tube. Placing the tubes in a vacuum desiccator for 2 h will remove residual solvent, and the lipid films will no longer appear wet. For storage, lipid tubes can then be flushed with argon, sealed with parafilm, and placed at −20 °C. Dried lipids, however, are much more susceptible to oxidation and should not be stored for more than a few weeks.

To rehydrate dried lipid films and generate multilamellar vesicles (MLVs), 1 ml of a buffered solution is added to the film, and the mixture is vortex mixed vigorously or bath sonicated. Sixty to 120 s should fully resuspend the film and the resulting lipid slurry will have a cloudy appearance. If there are discernable lipid particulates or film remaining on the glass, the vortexing and sonication should be repeated. Next, the suspension is transferred to a plastic microcentrifuge tube, and the tube is first frozen in liquid nitrogen and then thawed in a water bath. Note that each of the nonfreezing vesicle synthesis steps should be above the phase transition of the lipids; in most cases, room temperature will suffice but is nevertheless a parameter to be considered. The freezing and thawing cycle is repeated 10–15 cycles to equilibrate the intravesicular buffer solute with that of the bulk solution. If desired, a portion of the MLV suspension can be left frozen and stored at −80 °C, and preserved for use within 1 month.

Unilamellar vesicles, from 50 to 200 nm in diameter, can then be generated by extrusion of MLVs through appropriate polycarbonate membranes. Nine to 11 passages through the membrane are sufficient to produce a liposome suspension with low polydispersity. Vesicles are stable for 3–4 weeks when stored at 4 °C. Vesicular phospholipid yield can be readily assessed using various methods (Düzgüneş, 2003a; Stewart, 1980).

Liposomes encapsulating fluorescent dyes are standard tools in the investigation of membrane-disrupting compounds. The freeze/thaw vesicle preparation method easily incorporates such an addition simply by adding the fluorophore of choice to the lipid rehydration buffer (Dalla and Menestrina, 2003; Düzgüneş, 2003b). Removal of nonincorporated dye is accomplished via gel filtration chromatography. Small dyes like carboxyfluorescein or

calcein can be separated from liposomes by gravity flow columns packed with Sephadex G-25; Sepharose CL-2B can eliminate larger dyes like FITC-conjugated dextran. The useful life span of dye-filled liposomes is 1–2 weeks when stored at 4 °C.

For liposomes to be employed for surface plasmon resonance (SPR) spectroscopy, the rehydration buffer should be identical to the experimental running buffer. This allows more accurate determination of sensor chip-bound lipid mass because the intra- and extravesicular solutions will exhibit the same refractive index. Maintaining identical solutions inside and outside the bound vesicles is especially important when studying compounds that permeabilize bilayers, because vesicle leakage can introduce substantial confounding artifacts to the assay measurements. Liposome size is another parameter that should not be overlooked as some proteins and peptides are responsive to intrinsic bilayer curvature. With regards to SPR, 50 nm small unilamellar vesicles (vs. 100 or 200 nm large unilamellar vesicles) accommodate much greater lipid per unit volume, thus membranous surface binding area within the detection field is maximized. This seeming advantage may be detrimental, however, if the analyte is sensitive to the comparatively large local curvature of 50 nm liposomes.

2.2. Preparation of PFC nanoparticles

PFC nanoparticles consist of a hydrophobic PFC core surrounded by a lipid surfactant monolayer (Lanza *et al.*, 1996). To make PFC nanoparticles, typically, 600 mg lipid/surfactant comixture of phosphatidylcholine (98 mol%) and dipalmitoyl-phosphatidylethanolamine (2 mol%) is used for making 30 ml PFC nanoparticles. However, other lipid components can be added to suit specific experimental needs. The lipid/surfactant mixture is dissolved in chloroform, evaporated under reduced pressure, and dried in a 50 °C vacuum oven overnight, before being dispersed into water by sonication to result in a liposome suspension. After combining with PFC (20%, v/v) and distilled deionized water, the suspension is emulsified for 30–60 s by sonification. The emulsified mixture is then transferred to an S110 Microfluidics emulsifier and continuously processed at 20,000 lbf/in.^{2} for 4 min in an ice bath. The procedure is sufficient to produce 250 nm hydrodynamic diameter PFC nanoparticles with low-size polydispersity. The PFC nanoparticles are stable for at least 3 months, when stored at 4 °C in stopper crimp-sealed vials (Sigma, St. Louis, MO) and blanketed with nitrogen. To generate functionalized PFC nanoparticles during their formulation, the functional entities, such as imaging agents, drugs, or targeting ligands, first can be conjugated to the lipids with conventional conjugation chemistry to obtain functionalized lipids. Then the desired amount of functionalized lipids can be added into the lipid/surfactant comixture to formulate functionalized PFC nanoparticles.

2.3. Incorporation of peptide drugs into the lipidic nanostructures

In this section, postformulation incorporation of peptide drugs onto lipidic nanostructure PFC nanoparticles or liposomes is outlined. Because of the nonspecific lipid membrane destructive nature of cytolytic peptide agents such as melittin, stable PFC nanoparticles represent a promising carrier for them (Soman *et al.*, 2009, 2008). Melittin-loaded PFC nanoparticles with maximized melittin loading are prepared by mixing 40 μl of 1 m*M* melittin in the buffer (100 m*M* KCl in 10 m*M* HEPES, pH 7) with 50 μl of PFC nanoparticles diluted in 1 ml PBS or 1 ml saline for *in vitro* or *in vivo* studies, respectively. The mixture is incubated at room temperature for 10 min. After the incubation, the mixture is washed twice by centrifugation at 100 g for 10 min to remove free melittin in the supernatant.

For peptide drugs that cannot pass through the cell membrane, such as the NF-κB signaling pathway inhibitory peptide, NBD inhibitory peptide (May *et al.*, 2000), they need first to be conjugated onto the linker peptide with an intervening spacer, such as two glycines between linker peptide and peptide drug, which could be done by using solid-phase peptide synthesis. To deliver NBD inhibitory peptides with nanoparticles, we conjugated the NBD inhibitory peptide onto the N-terminus of the peptide linker with two glycines interposed as a spacer (Pan *et al.*, 2011). Customized peptides can be ordered from commercial sources, or synthesized in house by using a peptide synthesizer (Model: CS136, CS Bio Co, Menlo Park, CA) through solid-phase peptide synthesis. To generate NF-κB inhibitory PFC nanoparticles with different amounts of drug loading, 0.5–45 μl of 2 m*M* NBD–linker, prepared in MilliQ H_2O, is mixed with 30 μl of PFC nanoparticles. The mixture is incubated at 4 °C overnight, before washing twice and centrifuging at 100 × *g* for 10 min to remove free peptides. For incorporation of the peptide drug complexes into liposomes using the peptide linker strategy, the suggested maximum peptide: lipid ratio is 1:40. At this ratio, the engineered linker peptide produces no liposome bilayer disruption and liposome contents are retained encapsulated. After overnight incubation at 4 °C, any free peptide can be separated from peptide drug-loaded liposomes by gravity flow columns packed with Sephadex G-25.

It is important to note that this postformulation loading of peptide drugs on the lipidic nanostructures is governed by the interaction between an amphipathic cationic peptide and the lipid membrane. Therefore, several parameters, such as the lipid composition, size of the nanostructure, the concentration of the peptide drug, the ionic strength of the mixture, and incubation temperature and duration, should be optimized for each specific application.

3. Physical Characterization of the Peptide Drug-Loaded Nanostructure

3.1. Particle size measurements

The hydrodynamic size distribution of the peptide drug-loaded nanostructures can be analyzed with dynamic light scattering (DLS). DLS is also referred to as Quasi-Elastic Light Scattering or Photon Correlation Spectroscopy. This analysis is typically performed at room temperature by diluting samples (1–2.5%, v/v) in the filtered buffer that is used for making the base nanostructures. The filter pore size is 0.2 μm. Nanoparticles in dispersions undergo constant Brownian motion, which results in time-dependent fluctuation of scattered light intensity. DLS instruments calculate the autocorrelation of the scattering fluctuations for monodisperse samples by using Eq. (2.1):

$$G(\tau) = A\left(1 + B\ \exp\left(-2Dq^2\tau\right)\right) \tag{2.1}$$

where G is the correlation function, A is the baseline, B is the intercept, D is the translational diffusion coefficient, which represents the particle size, τ is the delay time, and q is described in Eq. (2.2),

$$q = (4\pi n/\lambda_0)\sin(\theta/2) \tag{2.2}$$

where n is the dispersant refractive index, λ_0 is the laser wavelength, and θ is the scattering angle.

For polydisperse samples, the calculation is done by using Eq. (2.3)

$$G(\tau) = A\left(1+Bg(\tau)^2\right) \tag{2.3}$$

where $g(\tau)$ is the sum of all the exponential components in the autocorrelation function.

For single scattering species, autocorrelation of the scattered light intensity is determined by the particle size. The smaller the particles, the faster the Brownian motion is. Therefore, the autocorrelation of small particles displays a shorter lag time. The correlogram generated by the DLS instrument is used in combination with medium ionic strength, temperature, viscosity, refractive index, and particle geometry to calculate the mean hydrodynamic size or the size distribution. For postformulation modification of lipidic particles, DLS can be used to monitor particle size or particle disruption which would indicate important changes in size distribution or disruption of the lipidic carrier platform. Our DLS hydrodynamic size measurements of

the particles are acquired using a Brookhaven Instruments PALS Zeta Potential Analyzer (Brookhaven Instruments Corp., Holtsville, NY).

3.2. Zeta potential measurements

Zeta potential represents the surface charge of nanoparticles and reflects their long-term stability. Based on DVLO theory, developed by Derjaguin, Verwey, Landau, and Overbeek in the 1940s, the stability of particles in suspension depends on the total potential energy function V_T as described in Eq. (2.4):

$$V_{\mathrm{T}} = V_{\mathrm{A}} + V_{\mathrm{R}} + V_{\mathrm{S}} \tag{2.4}$$

where V_{A} is the attractive energy from van der Waals interactions, V_{R} is the repulsive force from the electrical double layer of particles, when they are brought close by Brownian motion, respectively, and V_{S} stands for the potential energy from the solvent. V_{A} and V_{R}, described in Eqs. (2.5) and (2.6), respectively, play much more important roles than V_{S}.

$$V_{\mathrm{A}} = -A/(12\pi D^2) \tag{2.5}$$

where A is the Hamaker constant and D is the distance between particles.

$$V_{\mathrm{R}} = 2\pi\varepsilon a\zeta^2 \exp(-\kappa D) \tag{2.6}$$

Where ε is the dielectric constant, a is the radius of the particle, π is the solvent permeability, ζ is the zeta potential, and κ represents the ionic composition.

Therefore, the larger the zeta potential, the greater the repulsive force and the more stable the particle suspension system. The zeta potential measurement is acquired by using a Brookhaven Instruments PALS Zeta Potential Analyzer (Brookhaven Instruments Corp.). Zeta potential data are collected in the phase-analysis light scattering (PALS) mode, in which a laser light illuminates the particles in an electric field, and the scattered light is compared with a reference laser light for phase difference. This technique analyzes the scattered light phase shift from particle movements. The phase shift then can be used to determine electrophoretic mobility. The Smoluchowski approximation is used to calculate the zeta potential (ζ) from the measured electrophoretic mobility (μ) of the samples by using Eq. (2.7):

$$\mu = \varepsilon\zeta(1.5)/\eta \tag{2.7}$$

where ε is the dielectric constant and η is the absolute viscosity of the medium.

For all our measurements, the temperature of the diluted nanoparticle sample is equilibrated at 25 °C and the measurement pH is 7.

3.3. Morphology and integrity of the peptide drug-loaded nanostructure by electron microscopy

The morphology and integrity of the peptide drug-loaded nanostructure can be visualized by electron microscopy (Pan *et al.*, 2010; Soman *et al.*, 2008). For peptide-loaded PFC nanoparticles, fixation in 2.5% glutaraldehyde in PBS for 30 min on ice is carried out followed by spinning at top speed in a microcentrifuge for 15 min to obtain a pellet. After rinsing once in PBS and twice in 0.1 *M* sodium cacodylate, the particles are sequentially stained in 1.25% osmium tetroxide, 2% tannic acid, and 4% uranyl acetate for 1 h each at room temperature. In between the osmium tetroxide and tannic acid, samples are rinsed with the sodium cacodylate buffer three times. In between the tannic acid and the uranyl acetate, the samples are rinsed twice in sodium cacodylate and once in 15% ethanol. After the staining, tissue is dehydrated through 50%, 75%, and 95% ethanol for 5 min each, followed by 100% ethanol four times, 5 min each. The sample is then rinsed twice in propylene oxide 15 min each and left in propylene oxide/Polybed 812 1:1 overnight while rotating on a tube rotator. Samples are transferred into pure Polybed 812 (Polysciences Inc., Warrington, PA), placed in a desiccator for 24 h and baked for 48 h at 60 °C. The embedded tissue is thin-sectioned by an ultramicrotome, poststained in uranyl acetate and lead citrate, viewed on a transmission electron microscope, and images are recorded with a high-resolution digital camera.

For the liposome samples, negative staining can be applied. Nickel mesh grids that are formvar and carbon coated are rendered hydrophilic by glow discharging. Liposomes mixed with peptide drug are incubated with the grids for 1 min, gently blotted on filter paper, rinsed twice in distilled water, blotted again, and then stained with 1% uranyl acetate for 1 min. After the grids are blotted and air dried, the samples are ready to be viewed by transmission electron microscopy.

3.4. Quantifying peptide drug loading

When the peptide or protein contains aromatic residues, such as tryptophan, tyrosine, or phenylalanine, they will exhibit detectable intrinsic fluorescence. In the linear range, the fluorescence intensity reflects the peptide concentration. Melittin and linker peptides have such a tryptophan residue. Therefore, quantification of peptide drug loading can be performed by measuring the tryptophan fluorescence intensity. To determine peptide drug loading, we measure the amount of unloaded peptide, which remains in the supernatant from each centrifugation. A fluorescent spectrofluorometer (Varian, Inc., Palo

Alto, CA) is used to measure the tryptophan fluorescence emission at 350 nm after being excited at 280 nm. The measured fluorescence intensity is converted to the amount of peptide by utilizing a standard curve, which is generated by preparing peptide aliquots of known concentrations. Therefore, the amount of loaded peptide is calculated in Eq. (2.8):

$$P_l = P_t - P_u \tag{2.8}$$

where P_l represents the amount of peptide loaded, P_t represents the total amount of peptide used for loading, and P_u represents the amount of unloaded peptide remaining.

Peptide drug quantification is also routinely performed by analytic HPLC. To quantify the amount of peptide drug loaded onto PFC nanoparticles by analytic HPLC, we crack the PFC nanoparticles by adding a 2× volume of isopropyl alcohol (IPA) followed with vigorous mixing. After mixing, a PFC droplet can be observed on the bottom of the tube, which confirms the separation of the nanoparticle components. The tube is then placed in a 40 °C water bath and dried under a N_2 stream. The drying time depends on the starting volume. After the sample is dried completely, a desired volume of IPA/H_2O (1:1) is added into the tube followed with vigorously vortexing. The samples, along with standards, are then transferred to autosampler vials and loaded into the analytic HPLC system.

Analytic HPLC methods can be designed based on preparative HPLC methods. To develop a robust analytic HPLC method, it is useful to start with an aged HPLC column for initial HPLC method development, especially when there are more than one peptide drugs in the sample, because it is more difficult to achieve the desired resolution with aged columns than with newer ones. Aged columns are ones that have experienced more than 200 injections. With a robust analytic HPLC method, the peptide drugs in the samples are quantified by comparison against a standard curve. The concentration of the samples should be in the linear region of the standard curve. For a peptide drug that manifests intrinsic fluorescence (e.g., tryptophan), the fluorescence detection option can be used to increase HPLC sensitivity.

3.5. Analysis of peptide drug loading into lipidic nanostructures by fluorescence correlation spectroscopy

Fluorescence correlation spectroscopy (FCS) is a quantitative technique that reports fluctuations of fluorescence intensity as fluorescent molecules pass through a small observation volume (< 1 femtoliter) (Bacia and Schwille, 2007). Statistical analysis of the temporal fluctuations of fluorescence intensity allows for the simultaneous determination of the mobility and the

number of fluorescent species in the observation volume. After loading of the fluorescently labeled peptide drug onto the nanostructure, the mobility of the fluorescently labeled peptide drug will decrease, because the nanoparticles to which it is now attached move slower than the free fluorescent molecules (Pan *et al.*, 2011). This decrease in mobility of free and bound to the nanoparticles fluorescently labeled peptides together with their particle numbers is used to determine the apparent binding constant of peptide to nanoparticles.

Equipment for FCS measurements comprises an LSM 510 ConFocor 2 system and a Zeiss Axiovert 200 *M* inverted microscope (Zeiss, Germany). A water immersion C-Apochromat 40× objective (Zeiss) is employed to focus the excitation light to a diffraction-limited spot. An LP530-nm filter is placed in front of the detector. The pinhole size is set at 70 μm for a 25-mW 488 nm excitation laser light, which is set at 1% of the acousto-optical tunable transmission. The sample is placed in a Lab-Tek observation chamber (Fisher Scientific, Pittsburgh, PA) for the FCS measurements. Each sample is measured for 50 s at least nine times for data analysis. Free Alexa Fluor-488 in solution is used to calibrate the detection volume, which is defined by the focal volume of a laser scanning microscope, and the autocorrelation of the fluorescence intensity is calculated using Eq. (2.9):

$$G(\tau) = \frac{\langle \delta F(t) \delta F(t+\tau) \rangle}{\langle F(t) \rangle^2} \tag{2.9}$$

where G is the autocorrelation function, F is the time dependence of the fluorescence intensity, τ is the correlation time and the angular brackets refer to time averaging, and $\delta F(t) = F(t) - \langle F(t) \rangle$

The correlation curve obtained from the experiment is fitted with Eq. (2.10) that describes the fluorescence intensity fluctuations due to the Brownian diffusion of the fluorescent molecules in the observation volume and also accounts for the photophysical characteristics of the fluorescent molecules:

$$G_{3D}(\tau) = \frac{1}{N}\left[1 + T(1-T)^{-1}\exp\left(\frac{\tau}{\tau_T}\right)\right]\left(1 + \frac{\tau}{\tau_D}\right)^{-1}\left(1 + \frac{\tau}{\tau_D S^2}\right)^{-1/2} \tag{2.10}$$

where N is the average number of fluorescent particles in the observation volume, T is the fraction of fluorophores in the triplet state, τ_T is the lifetime of the triplet state of the fluorophore, τ_D is the characteristic diffusion time of the fluorophore, and ω_0 is the waist radius of the laser focus. The structural parameter $S = \omega_z/\omega_0$ measures the aspect ratio of the observation

volume, which is assumed to have a Gaussian shape. The diffusion time τ_D is related to the diffusion coefficient D through the expression described in Eq. (2.11):

$$\tau_D = \frac{\omega_0^2}{4D} \tag{2.11}$$

The waist of the focus ω_0 is determined by fitting the autocorrelation curve obtained from free Alexa Fluor 488 measured under the same experimental parameters. Parenthetically, the evaluation of binding of fluorescently labeled peptides to nanoparticles studied by FCS is especially interesting, because it does not require the separation of the bound and free fluorescent peptide species due to the marked differences in their mobility measured directly and noninvasively by FCS. Therefore, FCS can be used to directly evaluate the equilibrium binding of the fluorescently labeled peptide to lipidic particles as well as equilibrium binding of these fluorescent particles to the membranes of giant unilamellar vesicles, and possibly live cells.

3.6. Evaluation of peptide drug-nanostructure insertion by SPR

The insertion of the peptide drug into the lipid membrane of the nanostructures can be studied by using SPR, which detects changes in the reflective index of a surface (Pan *et al.*, 2011; Soman *et al.*, 2008). The Biacore-X 100 and a carboxymethylated dextran chip L1 (Biacore Inc., Piscataway, NJ) are used to study the insertion. The L1 sensor chip is designed to capture lipidic vesicles. On the L1 sensor chip, there are no anchoring molecules and the structure of the lipidic vesicle is maintained. Prior to the experiments, the L1 sensor chip needs to be equilibrated by priming the system 3–4 times with running buffer, which needs to be prefiltered through a 0.22-μm filter before use. PFC nanoparticles at a concentration of 3 m*M*, or liposomes at a phospholipid concentration of 0.6 mg/ml are injected at 3 μl/min for 30 min or 12 min, respectively. Loosely deposited nanoparticles or liposomes should be removed by performing extra washing at 100 μl/min for 30 s after immobilization to ensure a stable baseline. Complete coverage of the sensor chip by the nanostructures can be confirmed by injecting bovine serum albumin (1 mg/ml in running buffer) at 15 μl/min for 2 min. Different peptides in selected concentrations are then injected at a flow rate of 30 μl/min for 1 min, followed by washing for 1–24 h. At the end of each experiment, the L1 sensor chip will be regenerated by two consecutive injections of 3-[(3-cholamidopropyl)dimethylammonio]-1-propanesulfonate, CHAPS, at a flow rate of 100 μl/min for 30 s. The data can be analyzed with BiaEvaluation software (Biacore Inc.,). A two-state model, described in Eq. (2.12), is used for curve fitting.

$$P + L \underset{k_{d1}}{\overset{k_{a1}}{\rightleftarrows}} \mathrm{PL} \underset{k_{d2}}{\overset{k_{a2}}{\rightleftharpoons}} \mathrm{PL}^{*} \tag{2.12}$$

where P and L represent the peptide and lipid membrane of lipidic nanostructures, respectively; and PL and PL* represent the electrostatic and the hydrophobic interaction between the peptide and lipid membrane, respectively. In this model, the rate constant k_{a1} has the unit 1/M s, as it represents a second-order reaction; the rate constants k_{d1}, k_{a2}, k_{d2} have the units 1/s, being first-order reactions (M, molarity or mol/l; s, seconds). The SPR can directly evaluate the dissociation of the peptide from the immobilized lipidic structure, which provides an estimate of its stability. In addition, the SPR is configured as a high-throughput assay and can speed development when a larger variety of peptides are of interest.

3.7. Verification of peptide drug-nanostructure integration by circular dichroism spectroscopy

Circular dichroism (CD) is commonly used to investigate the secondary structure of proteins and peptides. The CD spectra of peptides with unordered structure/random coil exhibit a strong negative peak just below 200 nm and a positive peak, or a negative shoulder, between 220 and 230 nm. The CD spectra of an α-helical secondary structure exhibits a positive peak near 190 nm and two negative peaks around 205 and 222 nm. For β-sheet structures, CD spectra exhibit one negative peak around 215 nm and a positive peak near 198 nm (Fasman, 1996). When melittin or the peptide linker–drug complex insert into the lipid membrane of the nanostructure, they form α-helical secondary structures that can be detected by using CD spectroscopy (Pan *et al.*, 2011; Soman *et al.*, 2008).

CD spectra are measured using a Jasco J-810 spectropolarimeter (Jasco Inc., Eastern, MD). Before turning on the lamp, the instrument is flushed with N_2 at a flow rate of 20 for 5 min. A 1 mm path length, quartz cuvette is used to hold the samples. In our case, samples are diluted in 10 mM potassium phosphate buffer (pH 7.0) with a dilution factor of 1:30. When inserting the cuvette into the sample chamber, the door is opened as little as possible. The system should always be flushed with N_2 for 2 min before the measurements. Spectra are scanned under continuous scanning mode at a scan rate of 100 nm/min across the wavelength range from 190 to 260 nm. About 10–20 scans are used (Pan *et al.*, 2011; Soman *et al.*, 2008). Besides the CD signal, the Photomultiplier tube (PMT) voltage should always be monitored. If the voltage is great or equal to 800 V, the corresponding spectrum will become unreliable. There are several ways to lower the PMT voltage, such as increasing the N_2 flow rate, diluting the sample further, and using a cuvette with a shorter path length.

4. Assessment of Cellular Delivery and Bioactivity *In Vitro*

4.1. Carboxyfluorescein dequenching assay to illustrate cellular delivery by using lipid bilayer model system

Carboxyfluorescein encapsulating liposomes can be used as a model system to evaluate the pore-forming activity of melittin in cells. Encapsulated carboxyfluorescein exhibits fluorescence self-quenching. Upon the release from the liposomes, the fluorescence intensity will increase. Therefore, the kinetics of melittin membrane pore formation can be assessed by measuring the changes in carboxyfluorescein fluorescence intensity, by using a Cary Eclipse spectrofluorometer (Varian, Inc.). The excitation and emission wavelengths are 497 and 520 nm, respectively. Carboxyfluorescein fluorescence dequenching as function of time is described in Eq. (2.13) (Rex and Schwarz, 1998).

$$F_{520,\,t} = F_0 A_1 \left(1 - e^{-(t/\tau)}\right) + mt \tag{2.13}$$

where $F_{520,\,t}$ represents the fluorescence intensity measured at 520 nm at time point, t, F_0 represents the fluorescence intensity measured at time zero, A_1 is the amplitude of the exponential component, τ represents the dequenching time constant, and m represents the slope of the linear component.

A baseline fluorescence reading of carboxyfluorescein encapsulated in liposomes is measured before adding melittin-loaded PFC nanoparticles at various concentrations. Addition of Triton X is used to confirm complete carboxyfluorescein release. Melittin pore-forming kinetics are defined by τ and A_1, which are determined by applying the Levenberg–Marquardt algorithm for nonlinear least squares analysis on fitting the acquired fluorescent intensity changes overtime (Soman *et al.*, 2008). Activity of nanoparticle-loaded melittin on liposomes is illustrated in Fig. 2.1.

4.2. Confocal microscopy to visualize cellular uptake of peptide drug delivered by nanostructures

To visualize cellular delivery of the peptide drug melittin, we label melittin with the fluorescent molecule, fluorescein isothiocyanate (FITC). The fluorescence-labeled peptide can be prepared with a FluoroTag FITC Kit (Sigma-Aldrich, St. Louis, MO) (Soman *et al.*, 2009). Cells are cultured on the 0.17 mm Delta TPG Dish (Bioptechs Inc., Butler, PA) with 1 ml of cell culture medium. FITC-melittin-loaded $\alpha_\gamma\beta_3$-integrin targeted or nontargeted PFC nanoparticles (1 μl) are incubated with C32 cells for 1 h at 37 °C.

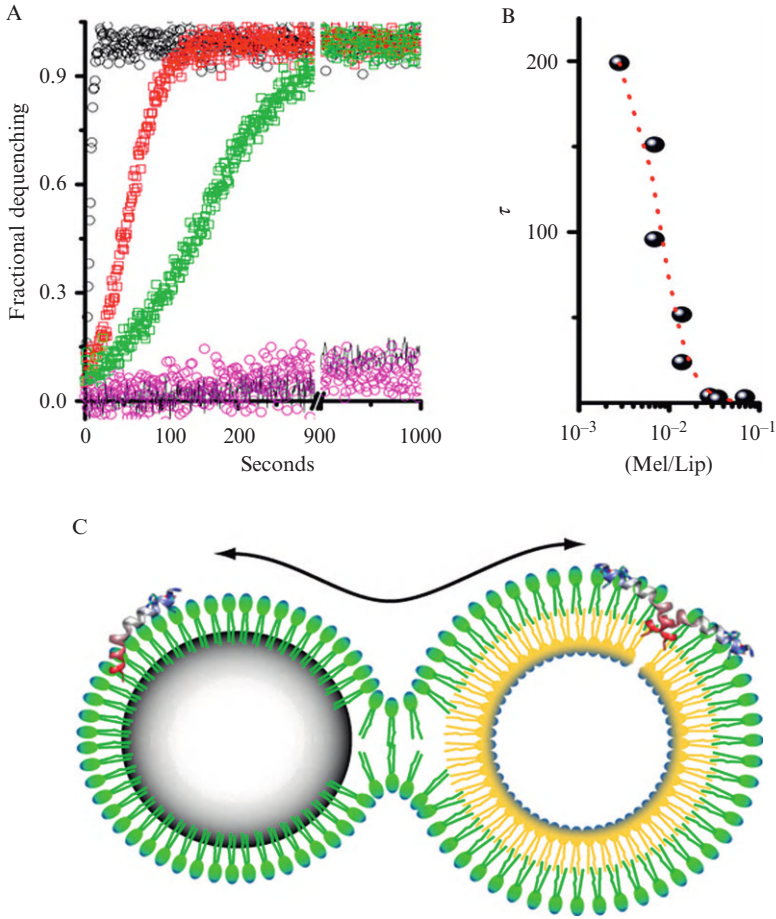

Figure 2.1 Activity of nanoparticle-bound melittin on liposomes. (A) A comparison of pore activation by melittin transferred to liposomes from solution or from the surface of nanoparticles measured by dequenching times due to release of carboxyfluorescein from liposome core. Black circles are pore activation from 200 n*M* free melittin, $t_{1/2}$ 2.8 s. Red squares are pore activation from the 200 n*M* melittin bound to 40 mg of nanoparticles, $t_{1/2}$ 21 s. Green squares are pore activation by melittin transferred to liposomes from 20 mg nanoparticles with 200 n*M* melittin, $t_{1/2}$ 58 s. Also shown is the fluorescence dequenching in the presence of the nanoparticles without melittin (pink) and the dequenching of incubated liposomes (black line). See text for the interpretation of the melittin kinetics. (B) The concentration dependence of melittin as a function of the ratio of melittin to lipid versus the halftime for dequenching. (C) Schematic of the proposed hemifusion model between a nanoparticle and a liposome. The continuity of the emulsion monolayer and the outer leaflet of the liposome permit the transfer of cargo from the PFC nanoparticle to the bilayer membrane leading to formation of a pore and subsequent release of carboxyfluorescein from the liposome core. (Reprinted with permission from Soman *et al.*, 2008.)

After the incubation, to remove unbound nanoparticles, cells are washed five times with PBS, by shaking at 200 rpm on a shaker for 5 min each. Then, the cells are fixed in 1 ml of 4% paraformaldehyde by incubating at 37 °C for 5 min, followed by five times washing with PBS. Cells should be protected from direct light before visualization with a confocal microscope (Zeiss Meta 510, Thornwood, NY) with the use of standard filter sets. Concomitant differential interference contrast imaging is used to define the cell outlines. To spatially delineate melittin cellular uptake in 3D, Z-stack images are acquired. The T3D package in NOEsys (Research Systems, Inc., Boulder, CO) is used for image reconstruction.

4.3. Hemolysis assay to evaluate biosafety *in vitro*

The off target side effects of melittin-loaded PFC nanoparticles can be evaluated by using red blood cells (RBCs), because it is known that free melittin rapidly induces hemolysis (Soman *et al.*, 2009). The RBCscan be separated from the blood by using Ficoll-Paque™ PREMIUM (GE Healthcare, Piscataway, NJ). The blood supplemented with anticoagulants should be used within 8 h. The blood is diluted two- to fourfold with saline and is carefully layered on top of Ficoll. The volume ratio of diluted blood and Ficoll is 7:5. The mixture is centrifuged at 400 × *g* for 30 min at 4 °C in a swinging bucket. After the centrifugation, RBCs come to rest at the bottom of the tube. Isolated RBCs are then washed three times in saline by centrifugation at 400 × *g* for 30 min and resuspended in saline to obtain an approximately constant 5×10^5 cells for each test. For negative and positive controls, RBCs in PBS (A_{blank}) and in 0.1% Triton X-100 (A_{triton}) are used, respectively. Treatments are performed incubating RBCs with various amounts of melittin-loaded PFC nanoparticles at 37 °C for 3 h (Soman *et al.*, 2009). After the treatment, samples are centrifuged at 100 × *g* for 10 min. The supernatants are loaded into a 96-well plate with 100 µl/well for absorbance measurements at 540 nm using a microplate reader (Bio-Rad, Hercules, CA). The percentage of hemolysis is calculated according to Eq. (2.14):

$$\%\text{hemolysis} = 100 \times \frac{A_{\text{sample}} - A_{\text{blank}}}{A_{\text{triton}} - A_{\text{blank}}} \tag{2.14}$$

4.4. Transcription factor assay to evaluate the inhibition of nuclear translocation of NF-κB protein

Under normal conditions, NF-κB is sequestered in the cytoplasm as an inactive complex with the inhibitory protein IκB. Activation of the IKK complex leads to IκB phosphorylation, which causes ubiquitination and

degradation of IκB. Consequently, NF-κB proteins are free to translocate to the nucleus to initiate the expression of NF-κB-dependent genes. The NBD inhibitory peptide prevents the activation of the IKK complex, which then inhibits IκB phosphorylation and sequentially inhibits NF-κB nuclear translocation and NF-κB-dependent gene expression (May *et al.*, 2000). To evaluate the inhibition of NF-κB protein nuclear translocation, as an example, we treat F8 cells with NF-κB inhibitory PFC nanoparticles produced by the incorporation of a NBD–linker peptide complex into the PFC nanoparticles as described in Section 2.3. The F8 cells, a leukemia/lymphoma cell line, are generated from a large granular lymphocytic leukemia transgenic mice model (Grossman *et al.*, 1995) and manifest constitutive NF-κB activation (Bernal-Mizrachi *et al.*, 2006). F8 cells are seeded in T-25 flasks at 2×10^6 per flask and incubated overnight in a humidified atmosphere of 95% air and 5% CO_2 in cell culture medium: RPMI, 10% FBS, 4 m*M* glutamine, and 100 U penicillin/100 μg/ml streptomycin. The cells are then treated with NF-κB inhibitory PFC nanoparticles or control PFC nanoparticles at various concentrations for 8 h before the extraction of the nuclear protein fraction. Control PFC nanoparticles are generated by loading a mutated version of the NBD peptide onto the PFC nanoparticles using the same postformulation method. The nuclear protein fraction can be extracted with a nuclear extract kit (Active Motif, Carlsbad, CA). To prevent protein degradation, all procedures should be performed at 4 °C or on ice, and all the tubes should be prechilled on ice. To ensure the complete suspension of the nuclear pellet in complete lysis buffer, we employ sonication in an ice bath. After the protein extraction, the protein concentration is measured with a Pierce® BCA Protein Assay Kit (Pierce Biotechnology, Rockford, IL). Normally, 1:10 diluted protein fraction is used for the concentration measurement.

Four methods could be used to assess NF-κB activation: Western blot, electrophoretic mobility shift assay, reporter gene assays (e.g., luciferase), and ELISA. Here, we use the ELISA assay to directly evaluate nuclear p65. Normally, 2–20 μg of the total nuclear protein fraction is used to measure nuclear NF-κB proteins. For F8 cells, 10 μg of the total nuclear protein fraction is used to evaluate the nuclear NF-κB protein, p65, by using the TransAM™ NF-κB p65 Transcription Fact Assay Kit (Active Motif) (Pan *et al.*, 2011). A standard curve can be generated from recombinant p65 proteins with known concentrations and used for quantification. At least two wells each need to be prepared for positive and negative controls. The positive control is the Jurkat cell nuclear extract, which is important for troubleshooting when there is a weak or no signal. The negative control is the complete lysis buffer, which will provide information such as whether the antibody needs to be further diluted or if wells are washed thoroughly.

Positive controls, negative controls, and samples are first incubated with DNA that contains an NF-κB consensus sequence. This incubation can be

done at room temperature with agitation for 1 h or at 4 °C overnight without agitation. After three washes, primary antibody (1:1000 dilution) is added into each testing well (100 μl/well), followed by incubation at room temperature for 1 h without agitation. The wells are washed three times again, before addition of secondary antibody (1:1000 dilution; 100 μl/well). The developing solution is brought to room temperature, and the 1 h secondary antibody incubation is started. After the secondary antibody incubation, the plate is washed four times before adding the developing solution (100 μl/well). Between each wash, the plate is blotted gently on absorption tissue. The development is observed closely, and the reaction is stopped by adding the stop solution (100 μl/well) when the color turns from medium blue to dark blue. The inhibition of p65 translocation by NF-κB inhibitory PFC nanoparticles occurs in a dose-dependent manner, which is presented in Fig. 2.2.

4.5. Flow cytometry to define the expression of the NF-κB-dependent gene, ICAM-1

Flow cytometry measures the physical properties of individual particles or cells ranging from 500 nm to 40 μm in diameter by analyzing the light scattered and/or emitted from the particles or cells when they pass through a laser beam. In the flow cytometer, the hydrodynamic force from sheath

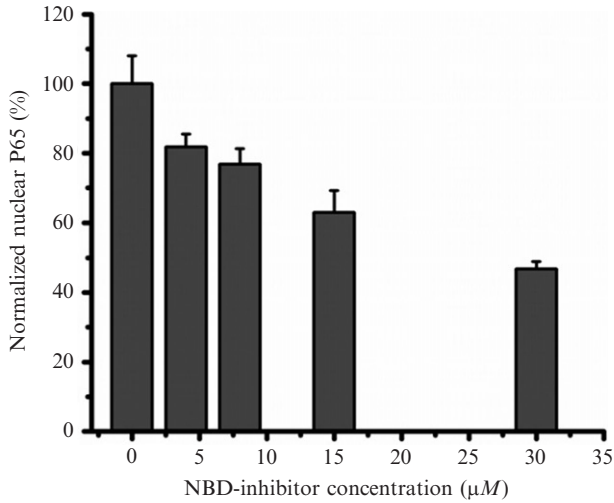

Figure 2.2 Inhibition of NF-κB signaling pathway by NBD–linker incorporated PFC nanoparticles (NF-κB inhibitory PFC NPs). NF-κB inhibitory PFC NPs inhibit NF-κB protein (P65) translocation into the nucleus in a dose-dependent fashion. Data presented as mean ± SD ($n = 3$). (Reprinted with permission from Pan *et al.*, 2011.)

flow centers the cells in a thin stream and passes one cell at a time through the laser beam at a flow rate of thousands of cells per minute. Therefore, the fluorescence from a single cell can be evaluated. Forward scatter (FSc) provides information on the cell size. Side scatter (SSc), also known as orthogonal scatter, represents the cell "complexity/granularity." Both FSc and SSc are used typically to identify cells for their fluorescence signature measurements.

To exemplify NF-κB-dependent gene (ICAM-1) expression, cells with or without NF-κB inhibitory PFC nanoparticle treatments for 9.5 h are stained with FITC-conjugated hamster antimouse CD54 (i.e., ICAM antibody) (BD Pharmingen, San Jose, CA) for flow cytometry analysis. For staining, 1×10^6 cells are used in each sample. Cells are washed three times in 3 ml incubation buffer, HBSS, 2% FBS, and 1 m*M* EDTA, by centrifugation at 1000 rpm for 5 min in a countertop centrifuge. After the third wash, cells are resuspended in 100 μl incubation buffer for 10 min and then incubated with FITC-labeled hamster antimouse CD54 antibody for 1 h on ice and protected from light. FITC hamster IgG1 κ isotype (BD Pharmingen) (1:1000 dilution) is used as a control. After staining, cells are washed five times and resuspended in incubation buffer before flow cytometry analysis, using a CyAn™ ADP analyzer (Beckman Coulter, Carpinteria, CA). Cells are gated by FSc and SSc from a total of 50,000 recorded events. Summit™ Software provided with the instrument is used for data analysis.

5. Assessment of Therapeutic Intervention *In Vivo*

Therapeutic intervention with peptide drugs packaged in the nanodelivery system can also be verified *in vivo*. The methods for evaluating therapeutic intervention will be specific for each application. One commonly used approach is to visualize the changes in the tissue of interest by histological and immunohistochemical assessment. We suggest reviewing the comprehensive text, Histological and Histochemical Methods: Theory and Practice (Kiernan, 2008), for detailed methods and techniques.

For investigating the therapeutic efficacy of anticancer treatments, tumor growth inhibition is one of the most important readouts. In Fig. 2.3, the anticancer effect of melittin-loaded PFC nanoparticles is verified by histology/immunohistochemistry and with tumor growth inhibition readouts. The tumor growth inhibition is evaluated by noninvasive ultrasound measurements for monitoring tumor growth *in vivo*. The methods for ultrasound measurement are described below.

Tumor growth can be noninvasively monitored *in vivo* by transcutaneous imaging with commercially available high-frequency ultrasound systems.

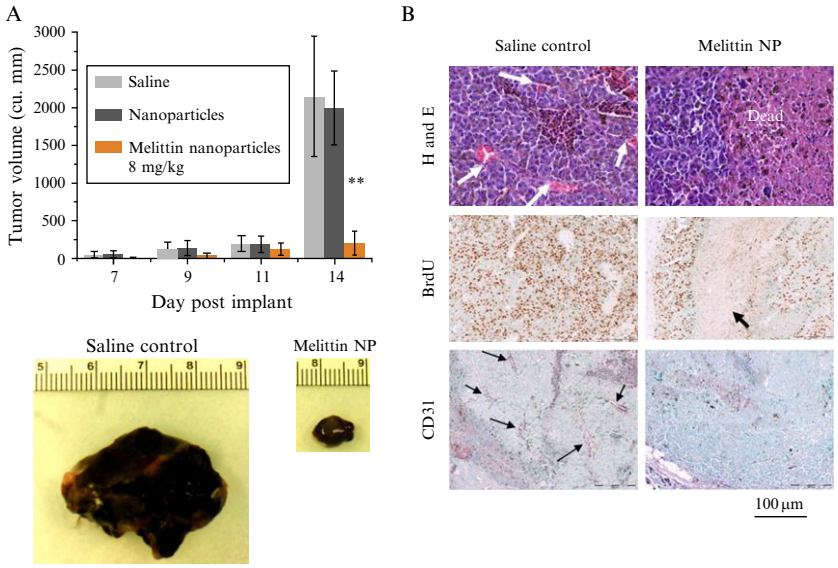

Figure 2.3 Therapeutic efficacy of melittin-loaded nanoparticles in syngeneic B16F10 mouse melanoma tumors. (A) Graph showing the increase in tumor volume of B16F10 melanoma tumors during the course of treatment with melittin-loaded nanoparticles (8.5 mg/kg) or controls (saline or nanoparticles alone; $n = 5$ each group). Note the dramatic difference in tumor volume at day 14 after four doses of melittin-loaded nanoparticles. Data are represented as mean ± SD. $^{**}P < 0.01$. (B) Histological assessment of B16F10 melanoma tumors excised at day 14. Note the extensive nonproliferating dead areas in the treated tumors along with the markedly decreased vascularity. Arrows indicate blood vessels in the H&E and CD31 photographs and dead areas in the BrdU photographs. (Reprinted with permission from Soman *et al.*, 2009.)

Depending on tumor size, at least two ultrasound systems are applicable. Each has a specific tumor size range over which imaging is optimal. For tumors less than approximately 1 cm in diameter, a high-frequency, mechanically scanned, single-element imaging system is employed (Vevo 660, VisualSonics, Toronto, Ontario, Canada); a less expensive but effective linear array system (Spark High-Frequency Imaging System, Ardent Sound, Mesa, AZ) can be used to image somewhat larger tumors. Probes used for the Vevo system are RMV-703 (35 MHz, 10 mm focus, 4 mm diameter) and RMV-704 (40 MHz, 6 mm focus, 3 mm diameter). The Spark system is paired with a high-frequency (nominal 14–23 MHz, 128-element, 0.205 mm pitch) linear array with user-selectable focal zone placement. Both systems are modified to output analog radiofrequency (RF) data (beamformed A-lines for the Spark system) and associated trigger signals, to permit digitization of the raw RF waveforms to acquire backscatter data from the

mouse tumors. Waveforms from the Vevo system are digitized at 400 MHz with a 12-bit digitizer (Compuscope 12400, Gage Applied Technologies, Lockport, IL) and stored for offline analysis. Waveforms from the Spark system are similarly acquired but digitized at the system's internal clock rate of 66.667 MHz. Although RF data have been recorded and used in our analyses, the image data itself displayed by either device can also be used to map the tumor locations and dimensions.

Prior to scanning, each animal is anesthetized and the area around the tumor is shaved and depilated. The transducer probes are affixed to a motorized gantry under computer control to enable automated scanning of the probe across the length of the tumor. Each anesthetized animal is placed on its back on a heated platform beneath the probe, and a small amount of ultrasound coupling gel is applied to the area proximal to the tumor. The probe is positioned so that the central area of the tumor is situated in the focal region of the transducer. RF data corresponding to cross-sectional views of the tumor are acquired at multiple sites along the length of the tumor so that the entire tumor volume is interrogated. The probe is translated laterally (perpendicular to the transducer's imaging plane) in 100-μm steps between each scan plane acquisition. Subsequent to acquisition, the backscattered energy of each RF waveform (defined as the sum of the squared digitized voltage values in a center-weighted sliding window) is computed and used to create gray-scale images. As mentioned above, the direct image output from the device can also be used analogously for processing. All computation, image reconstruction, and image analysis are performed using custom Java plugins written for the open-source image analysis package ImageJ (W. S. Rasband, U. S. National Institutes of Health, Bethesda, MD, imagej.nih.gov/ij/, 1997–2011). User-specified regions of interest (ROI's) are drawn on each image frame, and the area of the ROI measured. The areas of the ROI's are multiplied by the distance between scan planes to yield subvolumes, which are summed to compute the entire tumor volume. Figure 2.4 shows a representative ultrasound *in vivo* image of a B16F10 melanoma tumor in the mouse inguinal region.

6. Conclusions

The advantages and potential of peptide drugs have long been recognized. However, rapid enzymatic degradation *in vivo*, poor bioavailability, and potential off target effects of free agents have limited their clinical application. To overcome these hurdles, development of effective packaging/delivery systems is highlighted in this methodological chapter of peptide drug formulation. A major challenge in formulating such peptide drugs into delivery systems is the preservation of drug activity throughout the

Figure 2.4 Representative ultrasound *in vivo* visualization of B16F10 subcutaneous melanoma tumor in mouse inguinal region illustrating complex internal architecture of growing tumor mass. (Reprinted with permission from Pan *et al.*, 2010.)

formulation procedures. The postformulation peptide drug loading strategy described herein enables the addition of therapeutic peptides into the nanostructures after their formulation. Thus, peptide drug(s) may be loaded onto nanostructures in a simple mixing step to avoid harsh formulation steps, which should also facilitate sterile preparation of such compounds. These peptide postformulation strategies, in conjunction with targeted lipidic nanostructure delivery systems, exemplify a promising method for peptide drug deployment.

REFERENCES

Bacia, K., and Schwille, P. (2007). Fluorescence correlation spectroscopy. *Methods Mol. Biol.* **398,** 73–84.

Bernal-Mizrachi, L., Lovly, C. M., and Ratner, L. (2006). The role of NF-κB-1 and NF-κB-2-mediated resistance to apoptosis in lymphomas. *Proc. Natl. Acad. Sci. USA* **103,** 9220–9225.

Dalla Serra, M., and Menestrina, G. (2003). Liposomes in the study of pore-forming toxins. *Methods Enzymol.* **372,** 99–133.

Dathe, M., and Wieprecht, T. (1999). Structural features of helical antimicrobial peptides: Their potential to modulate activity on model membranes and biological cells. *Biochim. Biophys. Acta* **1462,** 71–87.

DeGrado, W. F., Musso, G. F., Lieber, M., Kaiser, E. T., and Kezdy, F. J. (1982). Kinetics and mechanism of hemolysis induced by melittin and by a synthetic melittin analogue. *Biophys. J.* **37,** 329–338.

Düzgüneş, N. (2003a). Preparation and quantitation of small unilamellar liposomes and large unilamellar reverse-phase evaporation liposomes. *Methods Enzymol.* **367,** 23–27.

Düzgüneş, N. (2003b). Fluorescence assays for liposome fusion. *Methods Enzymol.* **372,** 260–274.

Fasman, G. D. (ed.) (1996). Circular Dichroism and the Conformational Analysis of Biomolecules, Plenum Press, New York, London.

Gevod, V. S., and Birdi, K. S. (1984). Melittin and the 8-26 fragment. Differences in ionophoric properties as measured by monolayer method. *Biophys. J.* **45,** 1079–1083.

Giuliani, A., Pirri, G., and Nicoletto, S. (2007). Antimicrobial peptides: An overview of a promising class of therapeutics. *Cent. Eur. J. Biol.* **2,** 1–33.

Grossman, W. J., Kimata, J. T., Wong, F. H., Zutter, M., Ley, T. J., and Ratner, L. (1995). Development of leukemia in mice transgenic for the tax gene of human T-cell leukemia virus type I. *Proc. Natl. Acad. Sci. USA* **92,** 1057–1061.

Hancock, R. E., and Sahl, H. G. (2006). Antimicrobial and host-defense peptides as new anti-infective therapeutic strategies. *Nat. Biotechnol.* **24,** 1551–1557.

Kiernan, J. (2008). Histological and Histochemical Methods: Theory and Practice. Scion, Bloxham, UK.

Lanza, G. M., Wallace, K. D., Scott, M. J., Cacheris, W. P., Abendschein, D. R., Christy, D. H., Sharkey, A. M., Miller, J. G., Gaffney, P. J., and Wickline, S. A. (1996). A novel site-targeted ultrasonic contrast agent with broad biomedical application. *Circulation* **94,** 3334–3340.

May, M. J., D'Acquisto, F., Madge, L. A., Glockner, J., Pober, J. S., and Ghosh, S. (2000). Selective inhibition of NF-kappaB activation by a peptide that blocks the interaction of NEMO with the IkappaB kinase complex. *Science* **289,** 1550–1554.

Pan, H., Myerson, J. W., Ivashyna, O., Soman, N. R., Marsh, J. N., Hood, J. L., Lanza, G. M., Schlesinger, P. H., and Wickline, S. A. (2010). Lipid membrane editing with peptide cargo linkers in cells and synthetic nanostructures. *FASEB J.* **24,** 2928–2937.

Pan, H., Ivashyna, O., Sinha, B., Lanza, G. M., Ratner, L., Schlesinger, P. H., and Wickline, S. A. (2011). Post-formulation peptide drug loading of nanostructures for metered control of NF-kappaB signaling. *Biomaterials* **32,** 231–238.

Papo, N., and Shai, Y. (2005). Host defense peptides as new weapons in cancer treatment. *Cell. Mol. Life Sci.* **62,** 784–790.

Rex, S., and Schwarz, G. (1998). Quantitative studies on the melittin-induced leakage mechanism of lipid vesicles. *Biochemistry* **37,** 2336–2345.

Soman, N. R., Lanza, G. M., Heuser, J. M., Schlesinger, P. H., and Wickline, S. A. (2008). Synthesis and characterization of stable fluorocarbon nanostructures as drug delivery vehicles for cytolytic peptides. *Nano Lett.* **8,** 1131–1136.

Soman, N. R., Baldwin, S. L., Hu, G., Marsh, J. N., Lanza, G. M., Heuser, J. E., Arbeit, J. M., Wickline, S. A., and Schlesinger, P. H. (2009). Molecularly targeted nanocarriers deliver the cytolytic peptide melittin specifically to tumor cells in mice, reducing tumor growth. *J. Clin. Invest.* **119,** 2830–2842.

Stewart, J. C. (1980). Colorimetric determination of phospholipids with ammonium ferrothiocyanate. *Anal. Biochem.* **104,** 10–14.

Sticht, J., Humbert, M., Findlow, S., Bodem, J., Muller, B., Dietrich, U., Werner, J., and Krausslich, H. G. (2005). A peptide inhibitor of HIV-1 assembly in vitro. *Nat. Struct. Mol. Biol.* **12,** 671–677.

Warbrick, E., Lane, D. P., Glover, D. M., and Cox, L. S. (1995). A small peptide inhibitor of DNA replication defines the site of interaction between the cyclin-dependent kinase inhibitor p21WAF1 and proliferating cell nuclear antigen. *Curr. Biol.* **5,** 275–282.

Werkmeister, J. A., Kirkpatrick, A., McKenzie, J. A., and Rivett, D. E. (1993). The effect of sequence variations and structure on the cytolytic activity of melittin peptides. *Biochim. Biophys. Acta* **1157,** 50–54.

CHAPTER THREE

Application of Mesoporous Silica Nanoparticles in Intracellular Delivery of Molecules and Proteins

I-Ju Fang *and* Brian G. Trewyn

Contents

Abstract

Delivery of drugs and molecules to eukaryote animal and plant cells can be enhanced when mediated by mesoporous silica nanoparticle (MSN) materials. This chapter describes, in detail, the synthesis of several different MSN materials used for the transport of various hydrophilic and hydrophobic drug molecules, neurotransmitters, and macromolecules across the cell membrane, and in some cases, the cell wall of plant cells. In addition, the utility of MSN for mediating the delivery of cell-impermeable proteins is described in detail. Though the experimental descriptions are specifically detailed to research that has been completed, the procedures are applicable to additional drug and protein delivery experiments. Also summarized are several considerations that need to be addressed when utilizing MSN materials with biological systems to avoid complicating experiments.

Department of Chemistry, Iowa State University, Ames, Iowa, USA

Methods in Enzymology, Volume 508
ISSN 0076-6879, DOI: 10.1016/B978-0-12-391860-4.00003-3

1. Introduction

Transporting drugs and molecules through cell membranes have recently been the topic of a significant amount of research in the area of drug delivery and controlled release (Amar-Yuli *et al.*, 2010; Fredenberg *et al.*, 2011; Jiang *et al.*, 2011; Liversidge, 2011). Several different types of drug carriers or "vehicles" have been developed for this task including polymers, liposomes, dendrimers, and inorganic nanoparticles (Düzgünes *et al.*, 2005; Liechty *et al.*, 2010; Paleos *et al.*, 2010; Salem *et al.*, 2005; Trewyn *et al.*, 2007). Utilizing these vehicles has several advantages over conventional dosage methods, including decreased drug inactivation, increased efficacy, and reduced nonspecific interactions, to name just a few. One type of inorganic nanoparticle that has been successfully applied as a controlled-release drug delivery system is mesoporous silica nanoparticle (MSN) materials (Ambrogio *et al.*, 2011; He and Shi, 2011; Lee *et al.*, 2011; Popat *et al.*, 2011; Rosenholm *et al.*, 2011; Vivero-Escoto *et al.*, 2010). In the early 1990s, mesoporous silica materials were discovered independently by researchers at the Mobil Oil Corporation in the United States and by researchers at Waseda University in Japan. (Beck *et al.*, 1992; Inagaki *et al.*, 1993; Kresge *et al.*, 1992) The unique characteristics of MSN material make it ideal for applications in catalysis, separations, sensors, and drug delivery (Linares *et al.*, 2011; Slowing *et al.*, 2010; Zhao *et al.*, 2010).

The delivery of small molecules (neurotransmitters and anticancer drugs) and large biomolecules (proteins and DNA) into animal and plant cells has been demonstrated by utilizing MSN material as the transport vehicle, and by taking advantage of the endocytotic character of MSN materials. Because of the unique system of parallel, individual pores, the MSN nanocarrier system has demonstrated "zero release" of drugs prior to the MSN carriers reaching the targeted cells (Fig. 3.1; Slowing *et al.*, 2007a). In certain instances, MSN-based drug delivery systems are triggered by external stimuli, and release their cargo at the desired destination. Because of the nature of the cargo, the interior and exterior surfaces of the MSN need to be specifically functionalized for the purpose of drug delivery. The key points and related syntheses are discussed in detail below. All chemicals discussed and used are purchased from Sigma-Aldrich Co and used in the state they arrived unless otherwise stated.

2. Intracellular Delivery into Animal Cells Utilizing MSN

Several reports have demonstrated the uptake of MSN material by eukaryotic cells through endocytosis processes. The process of MSN internalization makes it possible to utilize this unique delivery vehicle to

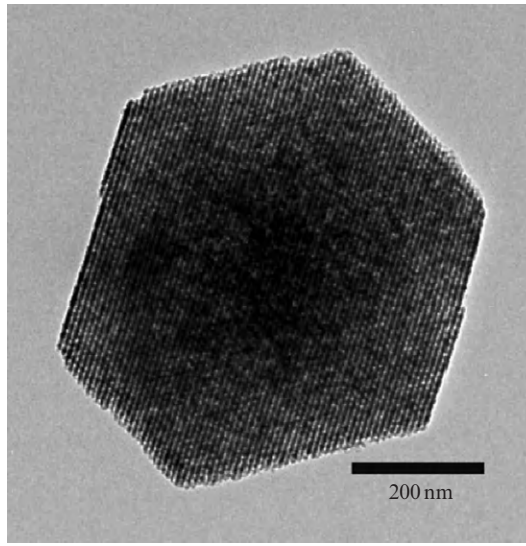

Figure 3.1 Transmission electron micrograph of a mesoporous silica nanoparticle.

efficiently deliver many different types of molecules. One particular area of interest is in the uptake of cell membrane impermeable molecules that cannot be internalized by cells directly through standard dosage means. With the help of MSN materials, procedures have been developed to increase the efficiency of animal and plant cell uptake of various molecules.

2.1. Delivery of drugs

The regular pore MCM-41-type MSN material has several characteristics as drug and molecule delivery and controlled-release devices that distinguish it from other systems. These include a high surface area (>800 m^2 g^{-1}), an easily tunable pore size (2–10 nm), and unique functional surface chemistry (Kresge *et al.*, 1992). These MSN structure properties make it a desirable material for loading, delivering, and releasing drugs in a controlled manner. The drugs that are loaded and released are unique and require specific MSN properties. One such example of molecular properties that need to be addressed with utilizing MSN materials for drug delivery is the hydrophilic or hydrophobic nature of the drug/molecule. Different strategies for the synthesis of MSN, the drug loading, and the drug release are adapted to optimize the utility of MSN.

For *hydrophilic* drugs, the delivery of a neurotransmitter (ATP) and an antibiotic (vancomycin) to astrocyte cells by pore-capped MSN materials has been demonstrated (Lai *et al.*, 2003). The procedures for the synthesis of drug loaded, cadmium sulfide nanoparticle (CdS) capped MSN are as

follows: 2-(propyldisulfanyl) ethylamine-functionalized mesoporous silica nanospheres (linker-MSN) are synthesized as the core MSN support with a disulfide reducible ligand. The CdS nanoparticles are ligated with mercaptoacetic acid to produce acid-CdS nanoparticles, whose monodisperse size is compatible with the regular pore size of MSNs through an amidation reaction (Fig. 3.2). The most important aspect of this type of nanoparticle-based controlled release system is the cleavable disulfide bond triggered by dithiothreitol (DTT) and mercaptoethanol (ME). As a result of this complete capping, no drug leakage occurs until the MSN material is exposed to a disulfide reducing agent. The linker-MSN (100 mg) is dispersed in a phosphate-buffered saline (PBS) solution (pH 7.4) of ATP or vancomycin at a concentration of 5 m*M* for 24 h. The mercaptoacetic acid-functionalized CdS nanoparticles (0.15 mmol) are dissolved in 2 ml of PBS with a constant concentration of vancomycin or ATP to prevent drug diffusion from MSN pores. The amide linking agent, 1-[3-(dimethylamino)propyl]-3-ethylcarbodiimide hydrochloride (EDC) (57.5 mg), is introduced to the CdS/drug mixture solution. The reaction mixture is stirred for 24 h, followed by centrifugation for 3 min 12,000 × *g*. The resulting products obtained are ATP- or vancomycin-loaded, CdS-capped MSN with loading densities of 83.9 and 30.3 mol% for vancomycin and ATP, respectively. This system successfully released neurotransmitters triggered by perfusion of ME in the presence of astrocytes, causing an increase in the concentration of intracellular Ca^{2+}. In addition to the CdS nanoparticle caps, we have developed iron oxide nanoparticle-capped MSN (magnet-MSN) as nanocarriers, that made the entire system magnetic, and, after cellular internalization, the cells could be moved under the control of a magnetic field (Giri *et al.*, 2005).

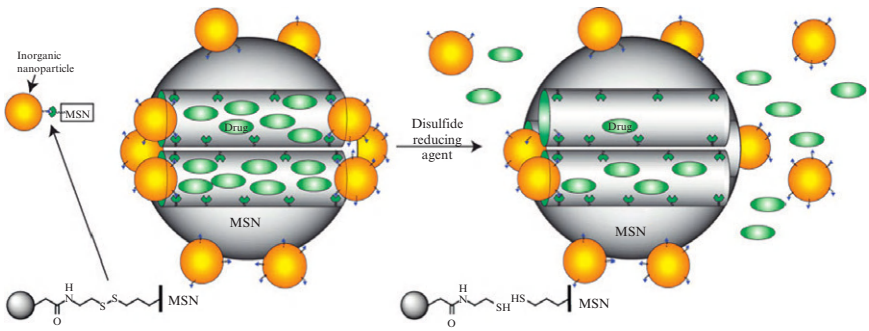

Figure 3.2 Schematic representation of the designed stimuli-responsive drug loading, capping, and release system mediated by mesoporous silica nanoparticle materials. Examples of inorganic nanoparticles that have been successfully employed as pore caps include cadmium sulfide, iron oxide, and gold.

In another system, MSN-mediated intracellular delivery of cysteine (Cys) was demonstrated (Mortera *et al.*, 2009). Cysteine is toxic and not stable in the extracellular matrix; so the cargo, Cys, is covalently bound to the interior of thiol-functionalized MSN through a disulfide bond bridge (Cys-MSN). This disulfide bond between Cys and MSN material is reduced by the intracellular antioxidants, including nicotinamide adenine dinucleotide hydride (NADH), dihydrolipoic acid (DHLA), and glutathione. Cysteine molecules are released from MSN material into the cytoplasm. Potentially, Cys-MSN can be applied to several chronic inflammation disorders caused by low intracellular concentrations of glutathione.

Because the silanol-based surface of MSN material is very hydrophilic, there is low affinity for the adsorption of *hydrophobic* drugs that are only slightly water-soluble. This hydrophobic characteristic is common among most anticancer drugs and adds complications to their use. Anionic surfactant-templated MSNs were designed for the delivery of some of these *hydrophobic* drugs (Tsai *et al.*, 2011). The anticancer drug resveratrol is used as the guest molecule to demonstrate the potential delivery system. The anionic surfactant is used as a template to form the pore framework to create a hydrophobic environment inside the MSN pores with a high affinity for resveratrol. The release of resveratrol is surfactant-assisted, the surfactant template diffuses from the pores with the resveratrol cargo when MSN material is dispersed in dilute PBS solution (Fig. 3.3).

For the synthesis of the anionic surfactant-templated MSN material, the structure directing agent, undec-1-en-11-yltetra(ethylene glycol) phosphate monoester surfactant (PMES, 0.5 mmol) is dissolved in 100 ml of nanopure water and stirred vigorously at 80 °C for 1 h. Then, pure aminopropyltrimethoxysilane (APTMS) is injected dropwise into the solution (1.0 mmol), followed by the addition of tetraethylorthosilicate (TEOS, 4.5 mmol) at the rate of 20 ml h^{-1}. The reaction solution is stirred vigorously

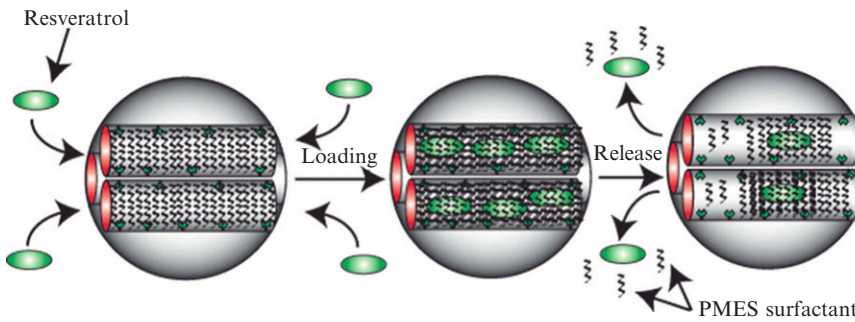

Figure 3.3 Schematic representing the process of loading resveratrol in to PMES-MSN, and the release of the drug along with PMES surfactant.

at 80 °C for 10 min and then aged at 80 °C for 24 h. The as-made product, PMES-MSN, is isolated by filtration, washed with nanopure water and methanol, and dried under vacuum at room temperature overnight. Loading resveratrol follows the synthesis and characterization of PMES-MSN by dissolving 0.05 mmol resveratrol in 100 ml of 10% ethanol in water. PMES-MSN (300 mg) is added to 30 ml of this solution and stirred for 24 h at room temperature. To avoid the photoisomerization of resveratrol under UV light, the material is protected from light. Resveratrol is released from the pores of PMES-MSN when dispersed in dilute PBS and stirred at room temperature.

2.2. Double delivery of drugs

One unique advantage of MSN material is the intrinsic nanoparticle morphology of two independent surfaces. MSN materials have an interior pore surface and an exterior surface that can be functionalized selectively and independently. Thus, MSN material can co-deliver chemical, protein and genomic material, utilizing these surfaces of the MSN. For example, the pores of MSN can be loaded with cyclic adenosine monophosphate (cAMP) and capped with a sugar derivative of insulin protein (Fig. 3.4A; Zhao *et al.*, 2009). The unique

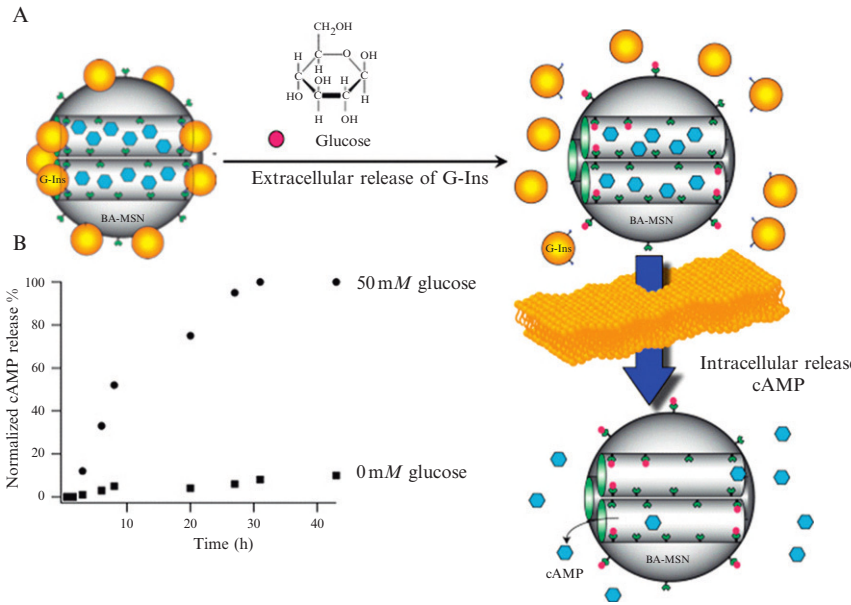

Figure 3.4 (A) Schematic representation of the [glucose]-dependent extracellular release of G-Ins and the intracellular release of cAMP and (B) a quantitative display of the [glucose]-dependant release of cAMP.

mechanism that was designed for this co-delivery system allows for both the insulin and cAMP to be released dependent upon the concentration of extracellular glucose. Using this insulin bonding scheme, the concentration of glucose manipulates the release kinetics of insulin and cyclic AMP. The insulin is covalently bound to the MSN surface by the binding between the phenylboronic acid of MSN exterior and the vicinal diols of insulin. This type of binding is reversible in high concentrations of glucose. The insulin-capped, cAMP-loaded MSNs are an efficient self-regulated device regulated by the concentration of glucose.

To synthesize the phenylboronic acid-functionalized MSNs (BA-MSNs), aminopropyl functionalized MSN (AP-MSN) is used as the precursor for the further derivativization of the boric acid group on the MSN surface. The AP-MSN (400 mg) is dispersed in 20 ml DMSO and 0.9 mmol 4-carboxyphenylboronic acid (CBA) is activated with 0.9 mmol *N*-hydroxysuccinimide (NHS) and 1 mmol EDC in 5 ml DMSO, stirring at room temperature for at least 15 min before adding it to the AP-MSN suspension. The mixture is stirred at room temperature overnight, followed by filtration and washing with DMSO, water and methanol to remove excess CBA.

Insulin is gluconic acid-functionalized according to the literature (G-Ins) and is further labeled with fluorescein dye (fluorescein isothiocyanate, FITC) for *in vitro* controlled-release studies (Shino *et al.*, 1994). G-Ins (200 mg) is dissolved in 50 ml sodium carbonate buffer (0.1 *M*, pH 9) and then reacted with 2.5 ml FITC in DMSO at 1 mg ml^{-1} is added while the G-Ins solution is stirred in the dark to avoid fluorephore photobleaching. The reaction is stirred for another 2 h at room temperature, and then 1 *M* NH_4Cl was added to quench excess FITC. After stirring for 1 h, the solution is dialyzed in PBS and freeze-dried to obtain FITC-labeled G-Ins (FITC-G-Ins). The ratio of FITC to G-Ins is estimated by measuring the ratio of the absorbance at 495 and 280 nm, corresponding to the absorption bands for fluorescein and G-Ins, respectively.

To load cAMP into the mesopores and cap with G-Ins, the BA-MSN (100 mg) is stirred in a 1 m*M* cAMP solution (10 ml PBS, 154 m*M* NaCl, pH 7.4) for 24 h in the dark. Then, FITC-G-Ins (200 mg) is added to the suspension, and the mixture is stirred in the dark overnight, followed by filtration and extensive washing with PBS to remove physically adsorbed cAMP and nonassociated FITC-G-Ins from the exterior surface of the MSN material. The resulting precipitate is isolated and dried under high vacuum. The loading of cAMP and FITC-G-Ins is calculated by subtracting the amount of cAMP/FITC-G-Ins remaining in the supernatant from the amount of cAMP/FITC-G-Ins originally in the reaction mixture.

Cyclic AMP-loaded FITC-G-Ins-MSN (6 mg) is dispersed in 3 ml of PBS with the introduction of different concentrations of glucose triggers. Aliquots (1.5 ml) are removed after stirring for 2 days in the dark at room temperature, followed by separation by centrifugation. To measure the

kinetics of release, cAMP-loaded FITC-G-Ins-MSN (30 mg) is dispersed in 15 ml of PBS with 50 m*M* glucose (Fig. 3.4B). Aliquots (1.2 ml) are removed at the specific time intervals from the suspension, followed by centrifugation. The release kinetics of FITC-G-Ins and cAMP are monitored by fluorescence emission spectroscopy and HPLC, respectively.

2.3. Delivery of cell membrane impermeable macromolecules

Most macromolecules cannot penetrate cell membranes through an endocytotic pathway because of their size and/or charge. However, MSN materials can be used as carriers to promote the cellular internalization of macromolecules. Cell membrane impermeable proteins and polysaccharides have been delivered into cells by the aid of MSN materials utilizing recently developed large pore MSN synthesis techniques that contain these macromolecules in the mesopore framework. There are two types of large pore MSN materials: one is the MCM-41 type and the other is the SBA-15 type (Kresge *et al.*, 1992; Zhao *et al.*, 1998).

MCM-41-type MSN with large pore diameter (5.4 nm) is synthesized for the intracellular delivery of cell membrane impermeable protein cytochrome *c* by employing mesitylene, a pore-expanding agent, used in conjunction with the traditional MCM-41 surfactant template (Slowing *et al.*, 2007b). The activity of the released cytochrome *c* remained after loading and releasing from the pores of the MSN.

To synthesize MCM-41-type large pore MSN, cetyltrimethylammonium bromide (CTAB, 2.7 mmol) is dissolved in a solution of 480 ml water and 3.5 ml of 2 *M* NaOH, followed by the addition of mesitylene (48.8 mmol) to the solution. The mixture is stirred vigorously until the solution is stable at 80 °C. Tetraethyl orthosilicate (21.9 mmol) is then introduced to the solution dropwise at a rate of 1 ml min^{-1}. The reaction mixture is stirred at 80 °C for 2 h. The resulting white precipitate (as-made MSN) is isolated by filtration, washed with methanol, and dried under vacuum at high temperature (100 °C) for 12 h. The structure-template surfactant, CTAB, and mesitylene are removed from the pores of the as-made MSN by acid extraction. A suspension of 1.0 g of the as-made MSN material is stirred for 6 h at 50 °C in a 100 ml methanol with 0.75 ml concentrated HCl. The template-free solid product is then isolated via filtration and dried under vacuum at room temperature for 12 h. For loading of FITC-labeled cytochrome *c* into the pores of the MSN, 5 ml of the protein solution ranging from 0.4 to 8 mg ml^{-1} in PBS are stirred for 6 h at room temperature with 20 mg of MSN. The suspensions are centrifuged and the loading is determined by measuring the difference in absorption of the Soret band of cytochrome *c* at 410 nm in the supernatant before and after loading. The isolated protein-MSN composites are dried under vacuum in the dark at room temperature to avoid fluorophore photobleaching for 12 h.

Suspensions of the FITC-cytochrome *c*-loaded MSN in PBS are prepared at a concentration of 100 μg ml^{-1}. The release of FITC-cytochrome *c* from MSN materials is monitored by UV–vis spectrophotometry.

Large pore MSN can accommodate the loading of several large macromolecules that are too large for standard MCM-41 type MSN. Dextran is a polysaccharide complex that has a dynamic diameter of approximately 8 nm. Mesoporous polymer-silica hybrid nanoparticles are synthesized for the delivery of macromolecules like dextran into cells (Kim *et al.*, 2011). A uniform, thin polymer layer is formed on the MSN surface upon the addition and heat treatment of the polymer monomer (methacrylic acid, MAA). When dextran is loaded into polymethacrylic acid-coated MSN (PMAA-MSN) at low pH (<5), a stable complex between PMAA-MSN and dextran is formed because of the hydrogen bonding interactions between carboxylic acid groups on the PMAA and the hydroxyl group of dextran. However, the hydrogen bond would be diminished when the MAA becomes deprotonated at pH levels greater than the pK_a of polymethacrylic acid ($pK_a = 4.85$). Polymer–silica nanoparticles are biocompatible and are engulfed efficiently by cells. As a result, the PMAA layer on MSN plays an important role in controlling the loading and release of dextran. At low pH, dextran is loaded into PMAA-MSNs and then released in higher pH, such as intracellular pH.

For the synthesis details, the large pore SBA-15 type MSN materials are synthesized as follows. First, a triblock copolymer Pluronic P104 ($EO_{27}PO_{61}EO_{27}$; 7 g) is dissolved in a 1.6 *M* HCl aqueous solution (270 g), the temperature is stabilized at 56 °C and tetramethyl orthosilicate (10.6 g) is added quickly into the solution. Unique to this MSN material, temperature is an important parameter in controlling the particle and pore morphology. After stirring for 24 h, the reaction solution is transferred to a Teflon-lined high-pressure autoclave for hydrothermal treatment at 150 °C for 24 h. The resulting large pore MSN product is isolated by filtration, washed with water and methanol, and dried under high temperature. The template removal of MSN is conducted through a high-temperature calcination process at 550 °C. To form a uniform polymer layer on the interior surface of MSN material, the methacrylic acid monomer (MAA; 0.190 g), ethylene dimethacrylate cross-linker (EDMA; 0.11 g), and the radical initiator α,α′-azoisobutyronitrile (AIBN; 16 mg) are dissolved in 1.25 ml of dichloromethane. The monomer diffuses into the mesopores of the large pore MSN (1 g) via a wet impregnation method. After 2 h of drying at 40 °C to remove the dichloromethane, the mixture is transferred into a Schlenk reactor and subjected to freeze-vacuum-thaw cycles three times with liquid nitrogen. The mixture is kept at 35 °C for 6 h under vacuum, and the polymerization of MAA is performed at 60 °C for 6 h, 100 °C for 1 h, and 120 °C for 1 h. The product, PMAA-MSN, is washed with chloroform and ethanol several times and dried at 80 °C under vacuum. The PMAA-MSN hybrid materials are directly

loaded with FITC-Dextran (40 kDa) prepared in pH 3 buffer by mixing PMAA-MSN (3.2 mg) with 5 ml of the FITC-Dextran solution. After the suspension was stirred for 24 h, the final product was centrifuged and washed with a buffer solution three times. The amount of FITC-Dextran loaded on the PMAA-MSN was determined by UV–vis spectroscopy. The supernatant solution was analyzed at 451 nm. The sample was dried under vacuum at room temperature.

The release profile of 40 kDa FITC-Dextran from the PMAA-MSNs in a pH 7 solution was measured at room temperature using the FITC-Dextran-loaded PMAA-MSN at pH 3. PMAA-MSN successfully delivered the dextran cargo into eukaryote cells.

2.4. MSN-mediated delivery of DNA

Polyamidoamine (PAMAM) dendrimer has proven to be an efficient gene transfection reagent. Second generation PAMAM (G2-PAMAM) is used to complex DNA onto the exterior surface of MSN material (Radu *et al.*, 2004). In detail, G2-PAMAM (0.11 mmol) in ethanol is added to an isocyanatopropyl-functionalized MSN (ICP-MSN) suspension and stirred for 20 h to form covalent urea bonds between the primary amines of the PAMAM and the ICP groups of the MSN.

The results demonstrate that the G2-PAMAM-MSN forms a complex with plasmid DNA at weight ratios larger than 1:5. Also, the G2-PAMAM-MSN-DNA complex protects DNA from digestion by nuclease enzymes because of the shielding of PAMAM-MSN complex. Significant GFP expression is observed in the cytoplasm after G2-PAMAM-MSN-DNA complexes are internalized by cells. Once the complexes are internalized, the DNA is released from the surface of the PAMAM-MSN and diffuse into the cell cytoplasm.

2.5. Delivery into plant cells utilizing MSN

As previously mentioned, surface functionalized MSN is often used as vehicles to transport guest molecules into animal cells; however, utilizing MSN to carry guest molecules into plant cells is a much more challenging task. Compared to animal cells, the internalization of MSN into plant cells is limited because plant cells have a thick cellulose cell wall to give structure support and protection from environment stress. To further investigate the endocytosis of MSN materials by plant cells, Lin, Wang, and coworkers developed a MSN technology to study the endocytosis of MSN and delivery of genomic material into plant cells and plant protoplasts (cells with the cell wall enzymatically removed) (Torney *et al.*, 2007). For plant cells without cell walls, MSN are directly internalize into the cytoplasm and deliver and release DNA, which is subsequently expressed. For plant cells

containing cell walls, a gene gun bombardment technique is necessary to get the MSN through the cell wall and into plant cells (Fig. 3.5A). Basic ideas for the development MSN delivery systems for plant cells, how to apply MSN to plant science, and how to successfully deliver small drug molecules to plant cells in a controlled fashion are introduced here.

2.5.1. The study of endocytosis of MSN by plant protoplasts

Surface functionality of MSN material plays an instrumental role in the endocytosis of MSN by protoplast cells. Tagging the MSN material with FITC dye in a manner similar to that stated above allows for the observation of the dynamic distribution of MSN materials in plant cells. Protoplasts failed to internalize MSN materials that were not surface functionalized. However, a triethylene glycol (TEG) functional group covalently attached to the MSN surface makes it possible for protoplasts to uptake MSN.

The MSN material (200 nm in diameter) is covalently doped with fluorescein as described above to visualize the internalization of MSN by plant cells and protoplasts. To limit the diffusion of the TEG ligand into the pores, the exterior surface of the MSN is covalently coated with TEG by a

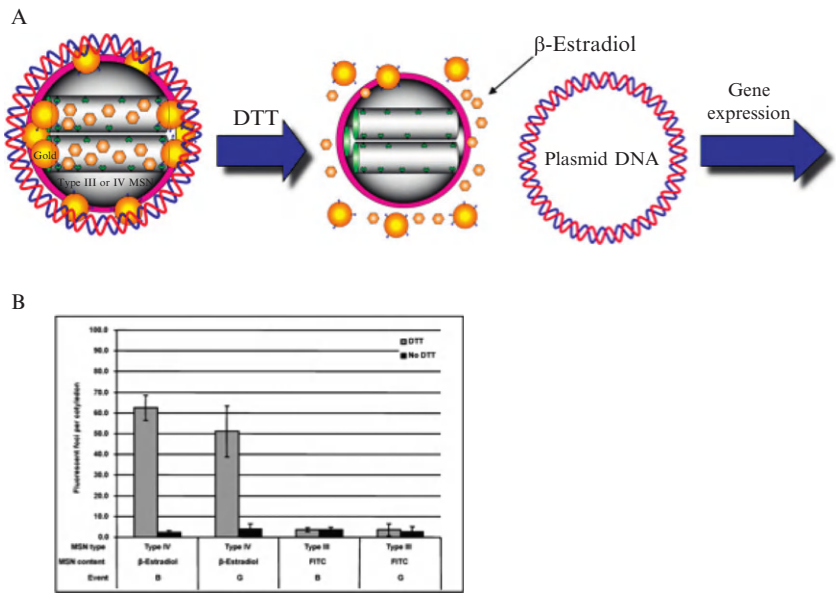

Figure 3.5 (A) Illustration of the disulfide reducer controlled uncapping of MSN pores and the subsequent release of β-oestradiol (A) and (B) the fluorescent foci per transgenic cotyledon grown in the presence (gray bars) and absence (black bars) of DTT.

postsynthesis grafting method prior to acid extraction of the surfactant template. The synthesis of the TEG ligand is achieved by reacting the TEG precursor 1-[2-(2-bromo-ethoxy)-ethoxy]-2-methoxy-ethane with 3-APTMS overnight in refluxing ethanol. The surfactant template is removed by acid extraction following successful attachment of the TEG ligand. The product of this reaction is directly available for endocytosis experiments.

2.5.1.1. Endocytosis experiments Protoplasts (10^6 cells ml^{-1}) are incubated with 10 μg TEG-coated FITC-labeled MSN (TEG-FITC-MSN) in media overnight. To remove physically adsorbed TEG-FITC-MSN that had not been internalized by the protoplasts, the mixtures are incubated with K4 medium and centrifuged for 10 min at $100 \times g$ at room temperature. Only protoplasts at the interphase are collected for analysis.

Although protoplasts could directly internalize TEG-FITC-MSN, the delivery of MSN materials to intact plant cells is more attractive and practical for plant research. For this reason, the synthesis and functionalization of MSN is modified to co-deliver bioactive agents through the common gene gun bombardment method often used in the field.

2.5.2. Gene gun bombardment

Gene gun bombardment is a method for the physical introduction of DNA into plant cells containing cell walls. The gene gun is utilized to bombard the plant cell wall with many DNA coated metal particles by using compressed helium as the propellant. The metal particles commonly used for gene gun bombardment include gold, tungsten, palladium, rhodium, platinum, and iridium. They are coated with DNA, accelerated by helium gas, and bombard the plant cells. The metal particles (0.45–1.5 μm in diameter) punch holes in and pass through the cell wall and enter the plant cells, leaving the DNA cargo inside the cells. The DNA coated metal particles randomly bombard the cells, no targeting is currently possible with this method. For example, the metal particles are localized everywhere in the cell including the nucleus and cytoplasm. Once the DNA cargo diffuses from the surface of the metal carrier, it has the opportunity to influence the intracellular genetic process.

Density is an important property of the metals used for this process, pure silica particles cannot gain enough momentum with helium propellant to break through the cell wall. To combine the advantageous properties of gold particles (density, biocompatibility, and DNA affinity) with the highly porous framework of MSN, a new gold nanoparticle-capped MSN system was designed and synthesized. To synthesize acid-functionalized gold nanoparticles, hydrogen tetrachloroaurate (III) hydrate (7.63×10^{-4} mol) is dissolved in 15 ml methanol, followed by the quick introduction of 1.8×10^{-3} mol 11-mercaptoundecanoic acid and 3 ml acetic acid. Under vigorous

stirring, 0.4 *M* sodium borohydride in 30 ml water is added dropwise. The desired 10–15 nm acid-functionalized gold nanoparticles are washed with methanol, ethyl ether, and water and dried under vacuum. These acidic gold nanoparticles are coupled to amino groups on the MSN surface by standard amidation linker chemistry. To coat the gene gun microcarrier with DNA, gold capped-MSN material is dispersed in ethanol with the DNA of interest, and the tube is vortexed. Once the gene gun microcarrier is loaded with DNA, it is immersed into liquid nitrogen immediately to avoid agglomeration of DNA-bound MSN material and freeze dry the sample before bombarding into the plant cells.

The unique porous structure of MSN makes it possible for the dual delivery of bioactive agents: chemicals and proteins in the porous framework and genomic material adsorbed to the gold nanoparticle-coated exterior. For example, the interior of the MSN can be loaded with a chemical promoter to increase the efficiency of gene expression and the exterior surface of MSN can be coated with plasmid DNA for the desired gene expression. In the past, only nucleic acids could be carried by the nonporous gold particles. The development of MSNs technology in plant cells opened the door for co-delivery of DNA and its corresponding inducer. Furthermore, MSN material is capped with gold nanoparticles by a cleavable disulfide bond linked amide bond and the intracellular delivery is precisely controlled by the addition of DTT.

2.5.3. Co-delivery of genetic material and its activator into plant cells

Co-delivery of chemicals and DNA is great step forward in the area of plant science genomic research. It opens the door for scientists to look into methods for control in plant gene transfection. The transformation process is used to deliver genetic components into plant cells by using DNA-bound gold nanoparticle-capped drug-loaded MSN.

2.5.3.1. The design of the DNA delivery system MSN material is used as a vehicle to carry GFP plasmid DNA and its inducer β-oestradiol into plant cells. To retain the β-oestradiol in the pores, the MSN pores are capped with gold nanoparticles, the synthesis of which is outlined above. To dictate the release of the β-oestradiol the gold nanoparticles are covalently linked to the MSN material by disulfide linkers that are reduced in the presence of disulfide reducing agents. Only DNA-bound gold nanoparticles capped β-oestradiol loaded MSNs treated with DTT show the GFP expression in the cytoplasm. Prior to DTT treatment, loaded drugs (gene inducer) are trapped inside the pores and do not influence gene expression.

The MSN material with primary amine linkers containing a cleavable disulfide bond (linker-MSN) is synthesized as the MSN precursor for plant cell delivery. To load the pores with the plasmid activator, linker-MSN

(100 mg) is mixed with 5.0×10^{-2} *M* β-oestradiol at room temperature for 24 h. To covalently cap the linker-MSN, the gold nanoparticles are functionalized with 11-mercaptoundecanoic acid. These gold nanoparticles are introduced into the MSN material suspension with the same concentration of the cargo molecules with the amide coupling reagent (80 mg) for another 24 h. Gold capped β-oestradiol loaded MSN material is isolated by washing and centrifuging prior to DNA coating.

2.5.3.2. DNA/MSN coating To adsorb plasmid DNA to the surface of gold (Au) capped β-oestradiol loaded MSN material, plasmid DNA (1 μg) is mixed with 10 μg the MSN complex in 50 μl water for 2 h at 23 °C, the optimal ratio of DNA to MSN material is 1:10.

In summary, the co-delivery of genes and inducers is successfully achieved by combining functionalized MSN technology with gene gun bombardment. The drug release was precisely controlled with DTT treatment and the GFP plasmid DNA is highly expressed in the plant cells (Fig. 3.5B). This demonstrates a successful application of MSN-based delivery systems to genetic engineering research in plant science.

2.6. Testing biological interactions of MSN on animal cells

To investigate biological interactions of MSN material on cells, some factors outlined and discussed below need to be considered.

2.6.1. Issues with serum and serum-free media on the uptake and cell interaction with MSNs

Cells usually are cultured in media containing either horse or fetal bovine serum for proliferation. Cells take up essential nutrients from media including serum proteins. When cells are treated with MSN material, serum in the media affect the cellular behavior. Serum-free media is utilized during experiments with cells and MSN material to avoid this effect that occurs when serum is present. It is not entirely clear what causes this effect in the presence of serum but one hypothesis is that serum adsorbs to the surface of the MSN material, and interferes with the MSN/cell interaction or causes the MSN material to aggregate. What is known for certain is that, serum in the media decreases the uptake efficiency of MSN by all cell lines tested. The degree of nanoparticle aggregation in serum containing media influences both the endocytosis efficiency and kinetics. In summary, cells engulf MSN materials more efficiently and at a faster rate in serum-free media than in the standard 10% serum media.

2.6.2. The difference between proliferation and viability

Cell proliferation and viability are important parameters for the biological study of MSN material. Cell proliferation is defined as the cellular growth rate or as the quantified value for the daughter cell population (Gratzner, 1982). Cell viability is the quantification of the number of live cells and is usually expressed as a percentage of the control (King, 2000; Kroemer *et al.*, 2009). Viability assays are important when initially seeding the cells onto a plate and to estimate the cytotoxicity of nanoparticles. For example, by measuring the viability, we determine the cell density that needs to be seeded in the plate to form a monolayer for further experiments at a desired time. Information on the cytotoxicity of nanoparticles or the release efficiency of MSN-based anticancer drug delivery systems is gained by viability assays. Many reagents are used to monitor or estimate the viability and proliferation of cells. For proliferation assays, changes in nucleic acid content are most commonly measured; but for viability assays, dye reagents are employed that can distinguish the live cells from non-cell species and cell membrane integrity. For example, the Guava ViaCount assay employees two dyes to determine cell status. The first dye enters all cells (live and dead) and bind to intracellular DNA. The second dye enters only dead cells, live cells exclude this dye because of the presence of an intact cell membrane. As a result, dead cells, viable cells, and non-cell species are distinguished by this fluorescent dye system.

Cell viability with MSN treatments is also an interesting property to investigate. Cell viability tests are run to understand the conditions and limits that are associated with MSN biocompatibility. Many controls are needed to evaluate the cytotoxicity of nanoparticles versus the cytotoxicity of molecules that are carried by the nanoparticles.

2.6.3. The purpose of the trypan blue

Trypan blue is a stain used to quantify live cells by labeling dead cells exclusively. Because live cells have an intact cell membrane, trypan blue cannot penetrate the cell membrane of live cells and enter the cytoplasm. In a dead cell, trypan blue passes through the porous cell membrane and enters the cytoplasm. Under light microscopy analysis, only dead cells have a blue color. Trypan blue is also used to eliminate false positives from occurring during cell counting by flow cytometry (Radu *et al.*, 2004; Slowing *et al.*, 2006; Trewyn *et al.*, 2008). Fluorescein labeled MSN can be either internalized by cells or they can physically adsorb to the exterior of the cell membrane. When these two events occur, it is often difficult to distinguish between them by flow cytometry. By adding trypan blue to the solution, the extracellular FITC-MSN material is quenched, excluding them from the quantification. Only live cells that have internalized the FITC-MSN

report a positive result. Trypan blue cannot penetrate the membrane of live cells, it will quench all the fluorescence from the physically adsorbed MSN on cell membrane. Thus, when Trypan blue is utilized, the fluorescence detected by flow cytometry is from the cells with internalized fluorescent MSN or cell autofluorescence. The concentration of the trypan blue solution used is typically 0.4% (w/w).

2.6.4. Fluorescently labeling MSN (covalently) for endocytosis experiments

The endocytotic behavior of MSN material has drawn a considerable amount of attention in recent years. The endocytosis efficiency is commonly determined by measuring the percentage of cells displaying fluorescence above the intensity of cell autofluorescence. Generally, MSN materials are covalently labeled with a fluorescent dye, FITC is the amine reactive derivative of fluorescein commonly the fluorophore employed. For the synthesis of FITC-labeled MSN, FITC is reacted with a primary amino group derivatized silane coupling reagent (e.g., aminopropyl trialkoxysilane coupling reagent).

For a standard synthesis, 10 mg of aminopropyl trimethoxysilane (APTMS) reagent is mixed with FITC for 2 h in anhydrous DMSO or DMF followed by a grafting step with pristine MSN material. The FITC forms a covalent bond with the amino group of APTMS. As a result, FITC is well distributed on the surface of the silica framework. Once FITC-labeled MSN are internalized by cells they display a green fluorescence stronger than the cell autofluorescence. The endocytotic efficiency of MSN by cells is determined and the cellular dynamic distribution of FITC doped MSN is monitored by measuring the percent of cells displaying fluorescence.

2.6.5. Utilizing confocal fluorescence microscopy versus traditional fluorescence microscopy

Fluorescence is an important contrasting method in microscopy, nanoparticles are visualized when labeled with a fluorophore. Both confocal fluorescence microscopy and traditional fluorescence microscopy are used to study the cell interactions with fluorescent MSN. Fluorescence is used to generate the image of the cells with endocytosed fluorescent MSN. Although traditional fluorescence microscopy can identify if the cells are associated with fluorescent MSN, it cannot distinguish the physically adsorbed MSN from the internalized MSN for cells. Only confocal microscopy can restrict the depth of field and eliminate most out of focus light to increase the contrast and resolution of the images. Only the fluorescence very close to the focal plane is detected. Furthermore, fragment scanning is possible with confocal microscopy in the direction of sample depth. Thus, multiscanning images (z-axis scanning) for one cell at different depths is

often used to verify cell internalization of the MSN. By comparing the images obtained at the different cell depths, the location of MSN materials, either physically adsorbed on cell membrane or endocytosed into the cytoplasm can be concluded. The cells are seeded in prewashed cover slips (22 mm^2) and placed in the wells of 6-well plates at a concentration of 10^5 cells ml^{-1} for 30 h. After 30 h incubation, the cell media was replaced with MSN suspension and incubated for an additional 12 h. After the removal of the MSN suspension, the cells are washed with PBS buffer three times and stained with 57.0 m*M* nucleus dye for 30 min. These coverslips were removed from plates and fixed to glass slides with liquid adhesive.

To clarify the interaction between cells and MSN, the issues discussed above are essential and need to be well controlled to accurately study of cellular behavior of MSN.

3. Conclusions

The detailed methods and studies described in this chapter outline procedures for the synthesis of MSN materials, loading the pores and external surface with various drug molecules, neurotransmitters, macromolecules and genomic material. The procedures to utilize these delivery devices in eukaryote and plant cells are substantially outlined. Finally, several factors are identified and reported that scientists and researchers need to be aware of when investigating MSN-based delivery devices. Identifying new strategies for releasing substances from the pores and surface of MSN materials will dictate the continued success of MSN-based delivery systems. In addition, new functional groups such as magnetic nanoparticles and surface bound polymers may lead to the new development of novel MSN-based delivery devices.

REFERENCES

Amar-Yuli, I., Aserin, A., and Garti, N. (2010). Controlled release and delivery technology of biologically active proteins and peptides. *In* "Bioactive Proteins and Peptides as Functional Foods and Nutraceuticals," (Y. Mine, Y. Li-Chan, and B. Jiang, eds.), pp. 359–382. Blackwell Publishing and Institute of Food Technologies, Malden, MA.

Ambrogio, M. W., Thomas, C. R., Zhao, Y.-L., Zink, J. I., and Stoddart, J. F. (2011). Mechanized silica nanoparticles: A new frontier in theranostic nanomedicine. *Acc. Chem. Res.* **44,** 903–913.

Beck, J. S., Vartuli, J. C., Roth, W. J., Leonowicz, M. E., Kresge, C. T., Schmitt, K. D., Chu, C. T. W., Olson, D. H., and Sheppard, E. W. (1992). A new family of mesoporous molecular sieves prepared with liquid crystal templates. *J. Am. Chem. Soc.* **114,** 10834–10843.

Düzgünes, N., Simões, S., Slepushkin, V., Pretzer, E., Flasher, D., Salem, I. I., Steffan, G., Konopka, K., and Pedroso de Lima, M. C. (2005). Delivery of antiviral agents in liposomes. *Methods Enzymol.* **391,** 351–373.

Fredenberg, S., Wahlgren, M., Reslow, M., and Axelsson, A. (2011). The mechanisms of drug release in poly(lactic-co-glycolic acid)-based drug delivery systems—A review. *Int. J. Pharm.* **415,** 34–52.

Giri, S., Trewyn, B. G., Stellmaker, M. P., and Lin, V. S. Y. (2005). Stimuli-responsive controlled-release delivery system based on mesoporous silica nanorods capped with magnetic nanoparticles. *Angew. Chem. Int. Ed.* **44,** 5038–5044.

Gratzner, H. G. (1982). Monoclonal antibody to 5-bromo- and 5-iododeoxyuridine: A new reagent for detection of DNA replication. *Science* **218,** 474–475(Washington, DC, 1883).

He, Q., and Shi, J. (2011). Mesoporous silica nanoparticle based nano drug delivery systems: Synthesis, controlled drug release and delivery, pharmacokinetics and biocompatibility. *J. Mater. Chem.* **21,** 5845–5855.

Inagaki, S., Fukushima, Y., and Kuroda, K. (1993). Synthesis of highly ordered mesoporous materials from a layered polysilicate. *J. Chem. Soc., Chem. Commun.* **8,** 680–682.

Jiang, X., Cheng, Y.-S., and Smyth, H. D. C. (2011). Nanostructured aerosol particles: Fabrication, pulmonary drug delivery, and controlled release. *J. Nanomater.* (198792), 2, http://www.hindawi.com/journals/jnm/2011/198792/cta/.

Kim, T.-W., Slowing, I. I., Chung, P.-W., and Lin, V. S.-Y. (2011). Ordered mesoporous polymer-silica hybrid nanoparticles as vehicles for the intracellular controlled release of macromolecules. *ACS Nano* **5,** 360–366.

King, M. A. (2000). Detection of dead cells and measurement of cell killing by flow cytometry. *J. Immunol. Methods* **243,** 155–166.

Kresge, C. T., Leonowicz, M. E., Roth, W. J., Vartuli, J. C., and Beck, J. S. (1992). Ordered mesoporous molecular sieves synthesized by a liquid-crystal template mechanism. *Nature* **359,** 710–712(London, UK).

Kroemer, G., Galluzzi, L., Vandenabeele, P., Abrams, J., Alnemri, E. S., Baehrecke, E. H., Blagosklonny, M. V., El-Deiry, W. S., Golstein, P., Green, D. R., Hengartner, M., Knight, R. A., *et al.* (2009). Classification of cell death: Recommendations of the Nomenclature Committee on Cell Death 2009. *Cell Death Differ.* **16,** 3–11.

Lai, C.-Y., Trewyn, B. G., Jeftinija, D. M., Jeftinija, K., Xu, S., Jeftinija, S., and Lin, V. S. Y. (2003). A mesoporous silica nanosphere-based carrier system with chemically removable CdS nanoparticle caps for stimuli-responsive controlled release of neurotransmitters and drug molecules. *J. Am. Chem. Soc.* **125,** 4451–4459.

Lee, J. E., Lee, N., Kim, T., Kim, J., and Hyeon, T. (2011). Multifunctional mesoporous silica nanocomposite nanoparticles for theranostic applications. *Acc. Chem. Res.* **44,** 893–902.

Liechty, W. B., Kryscio, D. R., Slaughter, B. V., and Peppas, N. A. (2010). Polymers for drug delivery systems. *Annu. Rev. Chem. Biomol. Eng.* **1,** 149–173.

Linares, N., Serrano, E., Rico, M., Mariana Balu, A., Losada, E., Luque, R., and Garcia-Martinez, J. (2011). Incorporation of chemical functionalities in the framework of mesoporous silica. *Chem. Commun. (Cambridge, UK)* **47,** 9024–9035.

Liversidge, G. (2011). Controlled release & nanotechnologies: Recent advances & future opportunities. *Drug Dev. Deliv.* **11**(42), 44–46.

Mortera, R., Vivero-Escoto, J., Slowing, I. I., Garrone, E., Onida, B., and Lin, V. S. Y. (2009). Cell-induced intracellular controlled release of membrane impermeable cysteine from a mesoporous silica nanoparticle-based drug delivery system. *Chem. Commun. (Cambridge, UK)* 3219–3221.

Paleos, C. M., Tsiourvas, D., Sideratou, Z., and Tziveleka, L.-A. (2010). Drug delivery using multifunctional dendrimers and hyperbranched polymers. *Expert Opin. Drug Deliv.* **7,** 1387–1398.

Popat, A., Hartono, S. B., Stahr, F., Liu, J., Qiao, S. Z., and Lu, G. Q. (2011). Mesoporous silica nanoparticles for bioadsorption, enzyme immobilisation, and delivery carriers. *Nanoscale* **3,** 2801–2818.

Radu, D. R., Lai, C.-Y., Jeftinija, K., Rowe, E. W., Jeftinija, S., and Lin, V. S. Y. (2004). A polyamidoamine dendrimer-capped mesoporous silica nanosphere-based gene transfection reagent. *J. Am. Chem. Soc.* **126,** 13216–13217.

Rosenholm, J. M., Sahlgren, C., and Linden, M. (2011). Multifunctional mesoporous silica nanoparticles for combined therapeutic, diagnostic and targeted action in cancer treatment. *Curr. Drug Targets* **12,** 1166–1186.

Salem, I. I., Flasher, D. L., and Düzgünes, N. (2005). Liposome-encapsulated antibiotics. *Methods Enzymol.* **391,** 261–291.

Shino, D., Kataoka, K., Koyamo, Y., Yokoyama, M., Okano, T., and Sakurai, Y. (1994). A self-regulated insulin delivery system using boronic acid gel. *J. Intell. Mater. Syst. Struct.* **5,** 311–314.

Slowing, I., Trewyn, B. G., and Lin, V. S. Y. (2006). Effect of surface functionalization of MCM-41-type mesoporous silica nanoparticles on the endocytosis by human cancer cells. *J. Am. Chem. Soc.* **128,** 14792–14793.

Slowing, I. I., Trewyn, B. G., Giri, S., and Lin, V. S. Y. (2007a). Mesoporous silica nanoparticles for drug delivery and biosensing applications. *Adv. Funct. Mater.* **17,** 1225–1236.

Slowing, I. I., Trewyn, B. G., and Lin, V. S.-Y. (2007b). Mesoporous silica nanoparticles for intracellular delivery of membrane-impermeable proteins. *J. Am. Chem. Soc.* **129,** 8845–8849.

Slowing, I. I., Vivero-Escoto, J. L., Trewyn, B. G., and Lin, V. S. Y. (2010). Mesoporous silica nanoparticles: Structural design and applications. *J. Mater. Chem.* **20,** 7924–7937.

Torney, F., Trewyn, B. G., Lin, V. S. Y., and Wang, K. (2007). Mesoporous silica nanoparticles deliver DNA and chemicals into plants. *Nat. Nanotechnol.* **2,** 295–300.

Trewyn, B. G., Giri, S., Slowing, I. I., and Lin, V. S. Y. (2007). Mesoporous silica nanoparticle based controlled release, drug delivery, and biosensor systems. *Chem. Commun. (Cambridge, UK)* 3236–3245.

Trewyn, B. G., Nieweg, J. A., Zhao, Y., and Lin, V. S. Y. (2008). Biocompatible mesoporous silica nanoparticles with different morphologies for animal cell membrane penetration. *Chem. Eng. J. (Amsterdam, Neth.)* **137,** 23–29.

Tsai, C.-H., Vivero-Escoto, J. L., Slowing, I. I., Fang, I. J., Trewyn, B. G., and Lin, V. S. Y. (2011). Surfactant-assisted controlled release of hydrophobic drugs using anionic surfactant templated mesoporous silica nanoparticles. *Biomaterials* **32,** 6234–6244.

Vivero-Escoto, J. L., Slowing, I. I., Trewyn, B. G., and Lin, V. S. Y. (2010). Mesoporous silica nanoparticles for intracellular controlled drug delivery. *Small* **6,** 1952–1967.

Zhao, D., Feng, J., Huo, Q., Melosh, N., Frederickson, G. H., Chmelka, B. F., and Stucky, G. D. (1998). Triblock copolymer syntheses of mesoporous silica with periodic 50 to 300 angstrom pores. *Science (Washington, DC)* **279,** 548–552.

Zhao, Y., Trewyn, B. G., Slowing, I. I., and Lin, V. S. Y. (2009). Mesoporous silica nanoparticle-based double drug delivery system for glucose-responsive controlled release of insulin and cyclic AMP. *J. Am. Chem. Soc.* **131,** 8398–8400.

Zhao, Y., Vivero-Escoto, J. L., Slowing, I. I., Trewyn, B. G., and Lin, V. S. Y. (2010). Capped mesoporous silica nanoparticles as stimuli-responsive controlled release systems for intracellular drug/gene delivery. *Expert Opin. Drug Deliv.* **7,** 1013–1029.

CHAPTER FOUR

Multifunctional Anticancer Nanomedicine Based on a Magnetically Responsive Cyanoacrylate Polymer

José L. Arias, Visitación Gallardo, *and* M. Adolfina Ruiz

Contents

Department of Pharmacy and Pharmaceutical Technology, Faculty of Pharmacy, University of Granada, Granada, Spain

Methods in Enzymology, Volume 508
ISSN 0076-6879, DOI: 10.1016/B978-0-12-391860-4.00004-5

Abstract

The therapeutic effect of antitumor molecules (efficacy and safety) is severely limited by their poor pharmacokinetic characteristics. Recently, the use of colloids has been proposed for the delivery of anticancer drugs to tumor cells, thereby providing a significant advance toward new treatments with improved specificity. In this respect, magnetically responsive nanopolymers are probably one of the most promising materials. In this contribution, we describe the basic steps to be followed in the development of such composite nanoplatforms. Starting from the formulation procedure, we detail the physicochemical engineering of these nanomedicines for combined antitumor activities (anticancer drug delivery *plus* hyperthermia effect). The key features determining drug incorporation to the nanomaterial are analyzed. Such stimuli-sensitive nanoparticles have promising properties (e.g., blood compatibility, hyperthermia, magnetic targeting capabilities, high drug loading, and little burst drug release), which could be used for efficient multifunctional anticancer therapy.

1. Introduction

Antitumor molecules are currently used as part of multiple drug regimens with limited activity, even in the most sensitive malignancies (i.e., breast cancer) (Reddy and Couvreur, 2008). Chemotherapy failure is thought to be the result of (i) an extensive biodistribution and rapid plasma clearance of the anticancer molecule which lead to ineffective drug concentrations in the tumor site and (ii) multidrug resistance exhibited by cancer cells (Arias, 2011; Zhang *et al.*, 2008). With the purpose of overcoming the problem, nanoparticulate-based drug delivery systems have been developed to enhance the concentration of chemotherapy agents in the malignant mass, thus facilitating an efficient antitumor activity while minimizing the associated severe toxicity. Hence, the engineered nanoplatform is expected to control drug biodistribution and, if possible, to beat multidrug resistance mechanisms (Arias *et al.*, 2011; Holgado *et al.*, 2011).

In this regard, probably the most promising results are achieved with nanoparticulate drug carriers that can alter their physical properties under exposure to a magnetic gradient, thus leading to the controlled release of the dose of chemotherapy agent inside the tumor tissue (Durán *et al.*, 2008; Maeng *et al.*, 2010; Zhang *et al.*, 2007). This chapter is devoted to the analysis of the most significant physicochemical aspects related to the formulation of a magnetic colloid for combined anticancer activities (antitumor drug delivery and hyperthermia effect). This is exemplified in a maghemite (γ-Fe_2O_3)/poly(octylcyanoacrylate) (POCA) (core/shell) nanoparticulate material loaded with methotrexate.

2. Formulation of the Magnetic Nanoplatform

2.1. The magnetic core (maghemite, γ-Fe_2O_3)

Magnetically responsive colloids for drug delivery applications should consist of an iron oxide (responsible for the magnetic responsiveness) embedded into a biodegradable matrix (either lipidic or polymeric, to allow the vehiculization of the proper dose of the active agent) (Durán *et al.*, 2008). Numerous investigations have emphasized the importance of employing ultrasmall iron oxide cores (Laurent *et al.*, 2008; Shubayev *et al.*, 2009). These nanomaterials generally consist of magnetite or maghemite cores with an average diameter of $\sim$10 nm which, along with their crystalline structure, determines their superparamagnetic character. Thanks to this property, the colloid will exhibit an excellent response toward magnetic gradients, which can be used advantageously to control the biological fate of the nanoparticle, allowing the accumulation of the drug dose into the diseased site. In addition, the oscillation of the magnetic moment of such nanomaterials under exposure to an alternating electromagnetic gradient has been described. As a consequence of this effect, the nanocores will transform into heaters that can provoke a hyperthermia effect, which could be used to kill tumor cells (Gonzales and Krishnan, 2005; Huber, 2005; Lao and Ramanujan, 2004). The interest in using superparamagnetic iron oxides further relies on their $T_2^{\star}$ property, allowing an excellent sensitivity in $T_2^{\star}$ and T_2 weighted magnetic resonance images (Shubayev *et al.*, 2009; Terreno *et al.*, 2010).

Superparamagnetic γ-Fe_2O_3 nanoparticles are synthesized frequently by oxidation of ultrasmall magnetite (Bee *et al.*, 1995). In detail, a chemical coprecipitation method is followed to prepare colloidal magnetite (Massart, 1981). First, 10 ml of a 2 *M* $FeCl_2$ solution (in 2 *M* HCl) and 40 ml of a 1 *M* $FeCl_3$ solution are added under stirring, at room temperature, to 500 ml of a 0.7 *M* ammonia solution. Immediately upon mixing of these aqueous solutions, magnetite nanoparticles are obtained. Very importantly, long-term stability of these superparamagnetic iron oxide particles can be assured only if they are kept in contact with a 2 *M* perchloric acid solution over a period of 12 h. This acidic solution is prepared carefully at room temperature in a laminar air flow hood and, very importantly, wearing protective clothing. Finally, cleaning of the nanoparticles can be achieved readily by repeated cycles of centrifugation (e.g., 1 h at 268,800 $\times$ *g*) and redispersion in deionized and filtered water, until the conductivity of the supernatant is less than 10 μS/cm. The oxidation step of magnetite into γ-Fe_2O_3 is generally carried out with ferric nitrate (600 ml; 0.34 *M*) at 90 °C for 30 min (Bee *et al.*, 1995). All chemicals used in the synthesis procedure are of analytical quality (Panreac, Spain).

Superparamagnetic γ-Fe_2O_3 particles are considered nontoxic and biodegradable (Weissleder *et al.*, 1995). In fact, it has been described that this nanomaterial could be taken up easily by macrophages, probably being metabolized in their lysosomes. Finally, the released free iron is hypothesized to be incorporated into the iron stores of the body but could be alternatively eliminated via the fecal route (Elias and Tsourkas, 2009; Schulze *et al.*, 1995).

2.2. The magnetic core/shell nanocomposite (γ-Fe_2O_3/POCA)

Drug vectors based exclusively on superparamagnetic iron oxides are characterized by a very low drug-loading capacity, and drug release properties that are difficult to control (Durán *et al.*, 2008; Maver *et al.*, 2009). This is the consequence of the frequently occurring unfavorable interactions between the adsorbed drug molecules and the iron oxide surface. For instance, drug release is usually completed in less than 1 h, which yields drug biodistribution profiles almost identical to that of conventional drug solutions. This excessively rapid drug release results in pharmacological effects undistinguishable from that of free chemotherapeutic agents. To solve the problem, iron oxide nanocores are generally entrapped into an organic or inorganic matrix with adequate drug delivery properties (Durán *et al.*, 2008).

Poly(alkylcyanoacrylates) have been investigated extensively for the delivery of cancer chemotherapy molecules (Vauthier *et al.*, 2003). Results from clinical trials have revealed the good tolerance of these polymers (Merle *et al.*, 2006), thus being postulated as an adequate shell for iron oxide cores in drug delivery (Arias *et al.*, 2008).

Classically, the formulation of iron oxide nanoparticles surface-coated by a poly(alkylcyanoacrylate) shell is based on an emulsion/polymerization method (Arias *et al.*, 2008). The mechanism of the reaction of the cyanoacrylate monomer onto the iron oxide core is an anionic process initiated by covalent bases present in the medium (e.g., OH^- ions deriving from water dissociation). The polymerization is terminated by the addition of cations that neutralize the alkylcyanoacrylate growing chains. The disposition of the polymer onto the magnetic core has been described to be the consequence of (Arias *et al.*, 2001): (i) an attractive electrostatic interaction between the positively charged iron oxides and the negatively charged alkylcyanoacrylate carbanions and (ii) the neatly attractive van der Waals and acid–base interactions between iron oxide and the polymer.

The synthesis of γ-Fe_2O_3/POCA nanocomposites starts by the dropwise addition of the octyl cyanoacrylate monomer (1%, w/v) under mechanical stirring to 50 ml of an aqueous γ-Fe_2O_3 suspension (0.75%, w/v), containing 0.1 m*M* HCl and 1% (w/v) of stabilizing agent (i.e., dextran, polyethylene glycol, or Pluronic® F-68). The acidic conditions and the surfactant

agent concentration have been found to assure the formation of spherical, very small, and moderately monodisperse nanocomposites suitable for the parenteral route of administration (Arias *et al.*, 2001, 2008). Then, mechanical stirring is maintained for at least 3 h, and the polymerization reaction is terminated by adding 1 ml of a 10^{-1} N KOH solution. The cleaning of the colloid can be easily accomplished by repeated magnetic separation and redispersion in water, until the supernatants are transparent and their conductivity (<1 μS cm^{-1}) indicates that the suspension is clean of both unreacted chemicals and nonmagnetic polymeric particles. All chemicals used in the preparation method are of analytical quality from Panreac, except for the octyl cyanoacrylate monomer (gift from Henkel Loctite, Ireland) and Pluronic® F-68 (Sigma-Aldrich, Germany).

3. Basic Characterization Procedures

The development of a drug-loaded nanocomposite against cancer involves a proper elucidation of the most significant aspects of its chemistry, physics, and physical chemistry. The main aim of this extensive characterization is not only to demonstrate that the best synthesis procedure has been followed (e.g., Arias *et al.*, 2001) but also to ensure that the important characteristics that will establish the biological fate and activity of the colloid have been achieved. In fact, it has been hypothesized that nanoparticulate platforms for drug delivery purposes with high surface electrical charge, hydrophobicity, and/or size will be characterized by the adsorption of plasma proteins (opsonins) onto their surface. As a consequence, a very rapid recognition and plasma clearance by Küpffer cells and other tissue macrophages will take place (Armstrong *et al.*, 1997; Borchard and Kreuter, 1996).

3.1. Geometry

The size and shape of a magnetic nanoparticle will determine its physical characteristics, such as magnetism and thus the magnetically responsive behavior, and its biodistribution once it is administered to a patient. In fact, it is accepted that the larger the size of a particle, the shorter its plasma half-life thanks to an enhanced activity of phagocytic cells (Decuzzi *et al.*, 2009; Maaßen *et al.*, 1993). In addition, particle shapes different from the spherical one will also facilitate the opsonization process, and consequently the nanoparticle clearance (Decuzzi *et al.*, 2009). Taking into account all this information, it can be concluded easily that there is a need for an adequate characterization of the geometry of a magnetic nanoplatform.

To that aim, size measurements are generally carried out by quasi-electric light scattering, or by photon correlation spectroscopy. These

determinations are undertaken in triplicate and at room temperature, by establishing the scattering angle within the range of 60–90°, and after suitable dilution of the aqueous nanoparticle suspensions (~0.1%, w/v). Both techniques can be used further to evaluate the stability of the magnetic colloid by measuring changes in particle size (i.e., after 2 weeks of storage at 4.0 ± 0.5 °C in water). In our case, the particle size of the γ-Fe_2O_3/POCA nanocomposites has been found to be adequate for the parenteral route of administration. The emulsion/polymerization method has resulted in the formation of well-stabilized spherical nanocomposites with an average diameter of 110 ± 15 nm, and a narrow size distribution (polydispersity index: 0.092). The size of the superparamagnetic γ-Fe_2O_3 cores is found to be 8 ± 2 nm. Finally, no nanoparticle aggregation and no appreciable change in the size of the magnetic colloid are detected after 2 weeks of storage at 4.0 ± 0.5 °C in water.

To confirm the size measurements and to ascertain particle shape, the magnetic nanoparticle aqueous suspensions can be easily checked through analysis by high-resolution transmission electron microscopy, and scanning electron microscopy (SEM). Prior to observation, dilute aqueous suspensions (~0.1%, w/v) are sonicated and drops are placed on copper grids with formvar film. The grids are then dried at room temperature in a convection oven. SEM images are analyzed to identify the cubic and spherical shapes of the magnetic core and composite particles, respectively (Fig. 4.1A and C). Additionally, both microscope techniques have confirmed the size of the γ-Fe_2O_3 cores and composite particles and have shown that the methodology for the preparation of core/shell nanoparticles enables the complete coverage of the magnetic nucleus by the polymeric shell (Fig. 4.1D).

3.2. Chemistry and internal structure

Chemical characterization of any given nanomaterial can be easily accomplished by the analysis of the corresponding Fourier transform infrared (FTIR) spectrometry data. The most significant transmittance (or absorbance) bands of the infrared spectra of the colloid (in the form of a powder prepared in a convection oven at 40 °C) should be obtained with a resolution of at least 2 cm^{-1}. Then, the bands are typically identified by comparison with previously published data (Silverstein and Webster, 1998). However, it must be kept in mind that the complete characterization of the chemical structure of the drug nanocarrier is only possible if this information is combined with that obtained from ^{1}H- and ^{13}C-nuclear magnetic resonance (NMR), and mass spectrometry experiments.

In any case, when a core/shell nanoplatform is synthesized, FTIR spectrometry can become a qualitative tool to prove the efficiency of the preparation methodology (Arias *et al.*, 2001). For example, Fig. 4.2A shows the infrared spectra of the γ-Fe_2O_3/POCA nanocomposites. The main

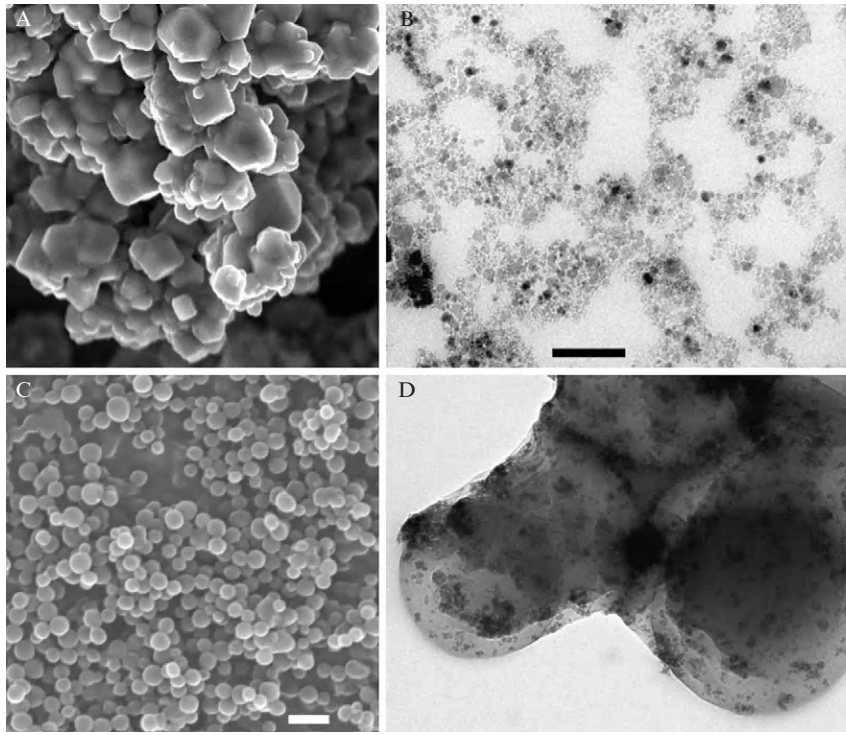

Figure 4.1 Scanning electron microscope pictures of γ-Fe_2O_3 nanoparticles (A), and γ-Fe_2O_3/POCA nanocomposites (C). High-resolution transmission electron microscopy images of γ-Fe_2O_3 (B), and γ-Fe_2O_3/POCA (core/shell) nanoparticles (D). Bar lengths: 100 nm (B), and 300 nm (C).

feature of the figure is the presence of all the bands of the polymer in the spectrum of the core/shell nanoparticles; this clearly demonstrates that the shell observed in Fig. 4.1D is indeed POCA coating. Interestingly, the 581 cm^{-1} band (not displayed by the pure polymeric nanomaterial) is characteristic of iron oxides (Arias *et al.*, 2001; Lyon, 1967). Finally, FTIR spectrometry could also be used to investigate qualitatively drug loading to a magnetic nanoplatform. However, this will only be possible if the bands of the drug molecule are observed in the infrared spectra of the magnetic nanocarrier.

The importance of the characterization of the internal structure of the magnetic core/shell nanocarrier relies on the dependence of its magnetic character on the crystalline state of the iron oxide core. The synthesis procedure must assure that such property remains even after the cores are embedded within the polymeric matrix. The elucidation of the internal structure of such nanoparticles can be performed by X-ray diffractometry

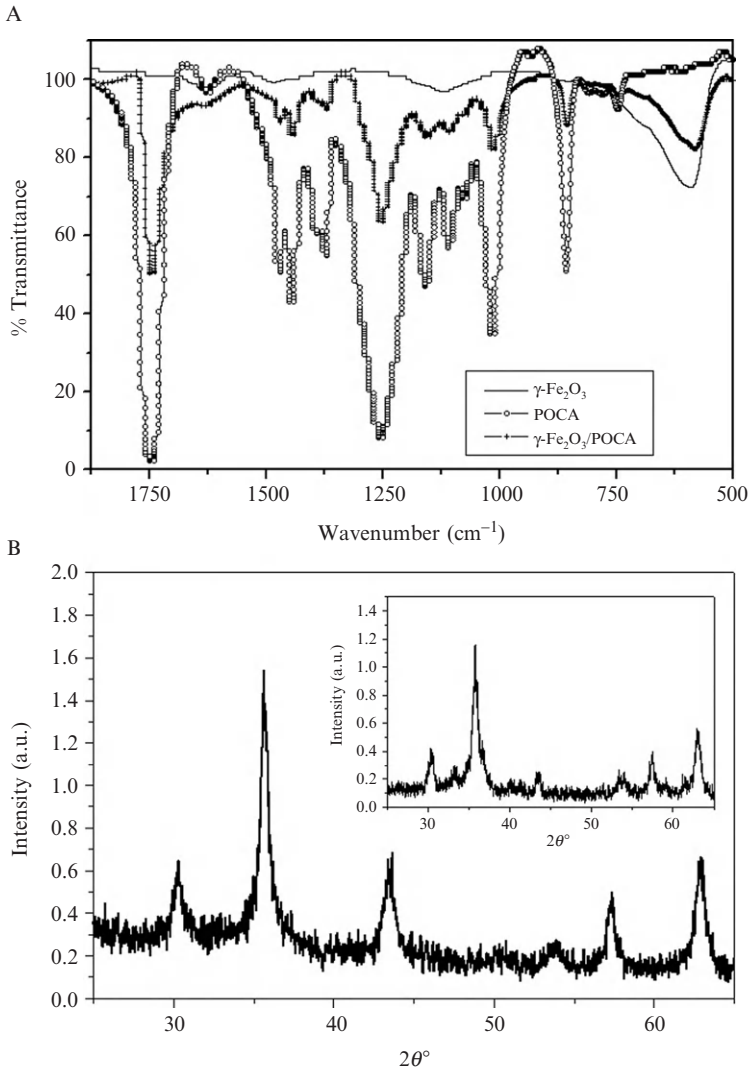

Figure 4.2 (A) Infrared spectra of γ-Fe_2O_3 (−), POCA (○), and γ-Fe_2O_3/POCA (+) nanomaterials. (B) X-ray diffractogram of γ-Fe_2O_3/POCA (core/shell) nanoparticles (inset: X-ray diffractogram of γ-Fe_2O_3). The intensity is expressed in arbitrary units.

using the Debye–Scherrer method with Cu K_α radiation. Figure 4.2B shows the X-ray diffraction patterns of γ-Fe_2O_3, and γ-Fe_2O_3/POCA nanoparticles. Interestingly, the comparison of the diffractogram of the nanocomposites with that of the pure iron oxide core (inset of the figure; see also, Depeyrot *et al.*, 2002; Santos *et al.*, 2007) confirms the

mineralogical purity of the synthesized γ-Fe_2O_3 and its high crystallinity, even upon complete coating by the polymer.

3.3. Surface electrical properties

Solid nanoparticles commonly acquire a surface charge at the moment of contact with an aqueous electrolyte solution (e.g., blood). Under these conditions, only the hydrophilic character of the nanoplatform and the repulsive (electrostatic) interactions between nanoparticles will assure kinetic stability against aggregation (flocculation). Unfortunately, magnetic attraction becomes a cause of instability if the nanoparticle has some remnant magnetization (Durán *et al.*, 2008).

Hence, it is accepted that the surface charge will play a critical role in the biological fate of a magnetic nanoparticle. This quantity is related to the zeta potential (ζ), the electrical potential at the shear plane of the double layer, which can be calculated experimentally from the electrophoretic mobility (u_e, measured by electrokinetic/electrophoretic determinations). Numerous investigations have concluded that a nanoparticle will undergo aggregation (flocculation) if the surface charge (ζ) is lower than a critical value (Durán *et al.*, 2008). Regarding the endocytosis of the nanomaterial by macrophages (and thus plasma clearance), as the surface charge is increased independently of the sign, endocytosis will be stronger (Corot *et al.*, 2006).

Considering the engineering aspects of a core/shell nanoparticle, an electrokinetic characterization of its surface could be of great help. In fact, this technique can permit to electrically differentiate the surfaces of the materials involved in its formulation, and thus the efficacy of the polymeric coating onto the magnetic core (Arias *et al.*, 2001, 2008). The surface electrical properties of the nanomaterials are commonly analyzed by electrophoresis measurements as a function of both pH and ionic strength (i.e., KNO_3 concentration) (Arias *et al.*, 2006). In detail, the determinations are done habitually in ~0.1% (w/v) nanoparticle aqueous suspensions (Malvern Zetasizer 2000 electrophoresis device, Malvern Instruments Ltd., UK) at 25.0 ± 0.5 °C, after 24 h of contact at this temperature under mechanical stirring (i.e., 50 rpm). The theory of O'Brien and White (1978) is generally used to convert u_e into ζ values. Figure 4.3A shows the ζ values for γ-Fe_2O_3, POCA, and γ-Fe_2O_3/POCA nanoparticles as a function of pH in the presence of 10^{-3} *M* KNO_3 (Panreac). Note that γ-Fe_2O_3 cores show a well-defined isoelectric point (pH_{iep} or pH of zero potential) at pH ~5.3. Interestingly, such behavior is not found in POCA nanoparticles, which have a negative surface charge for the entire pH range studied. Because of such large differences between the electrophoresis of iron oxide and polymer, electrophoresis is a very useful tool for qualitatively checking the efficiency of the polymeric coating. In fact, the figure shows clearly that the ζ–pH trend of the nanocomposites is almost undistinguishable from that

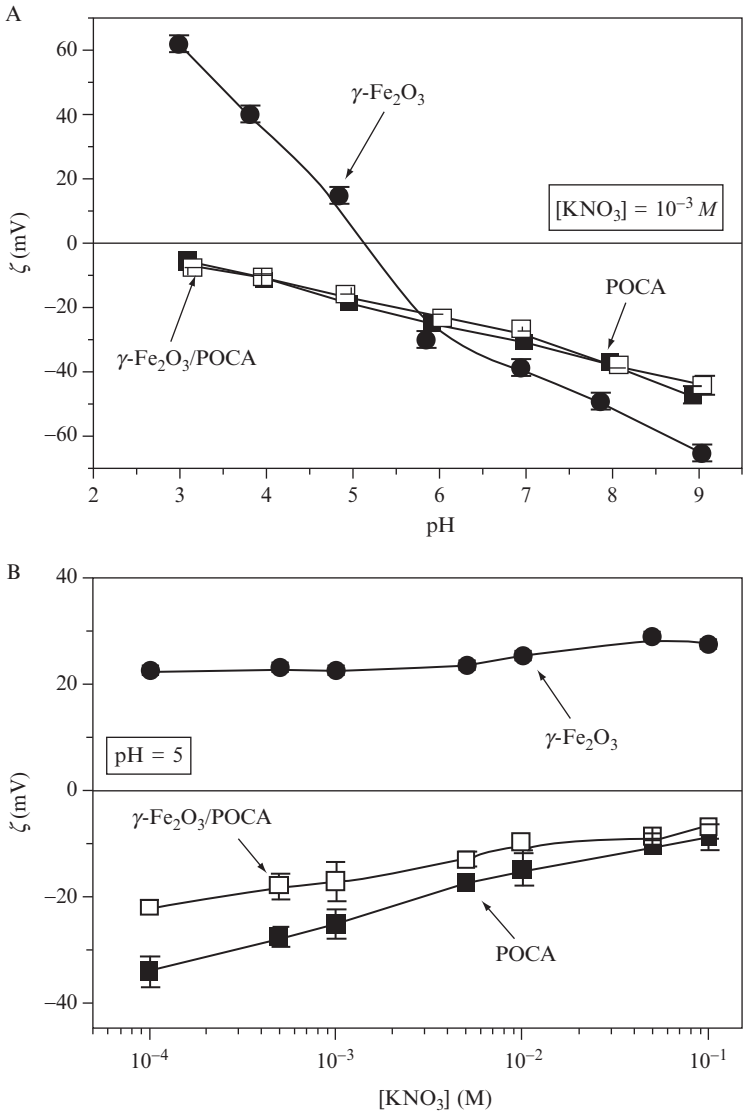

Figure 4.3 Zeta potential (ζ, mV) of γ-Fe_2O_3 (●), POCA (■), and γ-Fe_2O_3/POCA (□) nanoparticles as a function of pH in the presence of 1 m*M* KNO_3 (A), and as a function of the KNO_3 concentration at pH = 5 (B).

of the pure polymer. Thus, it can be concluded readily that the γ-Fe_2O_3 cores are very efficiently embedded within a POCA matrix, leading to core/shell nanoparticles, which are electrokinetically indistinguishable from POCA. These results can be confirmed by the determination of the

ζ–ionic strength trend. Figure 4.3B shows how similar the electrokinetics of polymer and core/shell particles are, and how different they are from that of γ-Fe_2O_3.

More interestingly, the information described about the electrophoretic properties of the nanomaterials could be further used to establish some arguments concerning the mechanism through which the POCA layer is formed onto the γ-Fe_2O_3 surface. It is clear that an attractive electrostatic interaction will exist between the positively charged γ-Fe_2O_3 particles (see Fig. 4.3A; note that in the acid conditions in which the synthesis is performed, the iron oxide cores are positively charged) and the negatively charged carbanions (coming from the polymerization of the cyanoacrylate monomer). Thanks to this attraction, the vicinity of the γ-Fe_2O_3 surface will be enriched in polymeric moieties.

Finally, we should note that the surface charge of a magnetic nanoplatform will also determine the electrostatic interactions between the carrier and the drug to be loaded. It has been determined that when the drug molecule and the particle display electrical charges of opposite sign, drug adsorption onto the nanoplatform surface will be favored electrostatically. The determination of ζ can be of great help in the qualitative estimation of drug adsorption onto the nanoparticle surface (Arias *et al.*, 2008). This is because of the sensitivity of electrophoresis to very small changes in the surface concentration of species responsible for charge generation.

3.4. Surface thermodynamics

When a magnetic nanoparticle enters the bloodstream, it interacts instantly with plasma proteins (i.e., opsonins). Nanoparticle opsonization is significantly enhanced as the hydrophobic character of the particle surface increases. Opsonization enhances the ability of the cells of the reticuloendothelial system to phagocytose the nanoparticle, and, consequently, plasma clearance of the colloid will occur. Hydrophobic surfaces will further determine the tendency of the nanoparticles to aggregate, reducing their interfacial surface area with (the aqueous) plasma. By contrast, hydrophilicity is associated with a much better retention of stability (Durán *et al.*, 2008). Hence, assessing the wettability of the nanoparticles is very important not only with respect to their dispersibility in aqueous media but also considering the effect of the hydrophilic/hydrophobic character on the interaction between the drug molecule and the nanoparticulate system, and on the capture of the nanoplatform by macrophages. These reasons determined the need for such evaluation of the γ-Fe_2O_3/POCA nanoplatform. The first step in this investigation must always be the proper determination of which surface thermodynamic model will be used to characterize the hydrophobicity/hydrophilicity of the nanoparticle. The model proposed by van Oss (2006) easily allows this evaluation by a physical quantity like the surface

tension or the surface free energy (γ_S) of the nanoparticulate solid. The model starts from the separation of γ_S into two components, γ_S^{LW} and γ_S^{AB}, accounting for the van der Waals (LW) and acid/base (AB) interfacial interactions:

$$\gamma_S = \gamma_S^{LW} + \gamma_S^{AB}. \tag{4.1}$$

The acid/base component is, in turn, considered as a harmonic mean of two additional quantities, γ_S^- and γ_S^+, known, respectively, as electron donor and electron acceptor components. Thus, the polar contribution to the surface free energy is controlled by the tendency of the solid to accept or give electrons:

$$\gamma_S^{AB} = 2\sqrt{\gamma_S^+\gamma_S^-}. \tag{4.2}$$

The same applies to the liquid (or any other) phase present in the suspension, and, most importantly to the solid/liquid interfacial free energy:

$$\begin{aligned}
\gamma_{SL} &= \gamma_{SL}^{LW} + \gamma_{SL}^{AB} \\
\gamma_{SL}^{LW} &= \left(\sqrt{\gamma_S^{LW}} - \sqrt{\gamma_L^{LW}}\right)^2 = \gamma_S^{LW} + \gamma_L^{LW} - 2\sqrt{\gamma_S^{LW}\gamma_L^{LW}} \\
\gamma_{SL}^{AB} &= 2\left(\sqrt{\gamma_S^+\gamma_S^-} + \sqrt{\gamma_L^+\gamma_L^-} - \sqrt{\gamma_S^+\gamma_L^-} - \sqrt{\gamma_S^-\gamma_L^+}\right) \\
&= 2\left(\sqrt{\gamma_S^+} - \sqrt{\gamma_L^+}\right)\left(\sqrt{\gamma_S^-} - \sqrt{\gamma_L^-}\right).
\end{aligned} \tag{4.3}$$

If we now imagine a drop of liquid in equilibrium on a molecularly flat solid surface, the contact angle θ can be related to the LW and AB components of γ_S and γ_L (Adamson and Gast, 1997; van Oss, 2006), through Young's equation:

$$2\sqrt{\gamma_S^{LW}\gamma_L^{LW}} + 2\sqrt{\gamma_S^+\gamma_L^-} + 2\sqrt{\gamma_S^-\gamma_L^+} = \gamma_L(1 + \cos\theta). \tag{4.4}$$

Note that if γ_L^{LW}, γ_L^+, and γ_L^- are known for three probe liquids, and if their corresponding contact angles are measured, a system of three equations, like Eq. (4.4), can be designed, the solution of which yields the unknowns γ_S^{LW}, γ_S^+, and γ_S^-. For instance, the liquids chosen can be water ($\gamma_L^{LW} = 21.8$ mJ/m^2, $\gamma_L^+ = \gamma_L^- = 25.5$ mJ/m^2), formamide ($\gamma_L^{LW} = 39.0$ mJ/m^2, $\gamma_L^+ = 2.28$ mJ/m^2, $\gamma_L^- = 39.6$ mJ/m^2), and diiodomethane ($\gamma_L^{LW} = 50.8$, $\gamma_L^+ = \gamma_L^- = 0$ mJ/m^2) (van Oss, 2006). All chemicals used in the characterization method are of analytical quality from Panreac, except for the formamide (Sigma-Aldrich). The contact angles of these liquids onto pellets made of the nanoparticles can be determined at room temperature using a goniometer. Pellets (radius $\sim$ 1.5 cm) of the powdered dry nanomaterials can be prepared easily by compression in a hydraulic press set to 7 ton for 3 min.

The analysis of the surface thermodynamics of the iron oxide core (γ-Fe_2O_3), the polymeric matrix (POCA), and the core/shell (γ-Fe_2O_3/POCA) nanoparticles is of great help in the determination of the nature of the polymeric coating. The contact angle data of the three probe liquids on dry nanoparticle pellets suggest important differences among the three nanomaterials (Fig. 4.4A). This is further confirmed by the evaluation of the surface free energy components that provides a better elucidation of the particle surface thermodynamics (Fig. 4.4B). It is clear that whatever the component considered, its value for the γ-Fe_2O_3/POCA nanocomposites coincides almost exactly with that of the bare polymer. Thus, the thermodynamic analysis agrees with the electrokinetic one in suggesting that an adequate coverage of γ-Fe_2O_3 nuclei has been obtained.

Furthermore, these surface free energy changes manifest themselves in the hydrophobic/hydrophilic character of the nanoplatforms. Thus, the evaluation of the free energy of interaction, not considering the electrostatic component, between the solid phases immersed in the liquid (ΔG_{SLS}^{TOT}) can be used to check the thermodynamic nature of the nanoparticle (Arias *et al.*, 2009; van Oss, 2006). This quantity is negative for hydrophobic materials, where interfacial interactions will favor the attraction of the nanoplatforms to each other. By contrast, hydrophilicity will be associated correspondingly to positive values of ΔG_{SLS}^{TOT}. In our case, the hydrophilic nature of γ-Fe_2O_3 is modified and becomes hydrophobic (like the polymer) when covered by POCA (Fig. 4.4C).

A complementary explanation of the mechanism by which the POCA layer is deposited onto the γ-Fe_2O_3 surface could also come from this thermodynamic analysis. By using the γ_S data, the free energy of interaction between γ-Fe_2O_3 (M) and POCA (P) in the aqueous medium (A), ΔG_{MAP}, can be calculated using the Dupré equation (van Oss, 2006):

$$\Delta G_{MAP} = \gamma_{MP} - \gamma_{MA} - \gamma_{PA}. \tag{4.5}$$

The result of the calculation is -7.6 ± 0.8 mJ/m^2. This means that the van der Waals and acid–base interactions between the iron oxide core and the POCA matrix are neatly attractive. As a result, it is thermodynamically favorable for the polymer to remain adsorbed onto the γ-Fe_2O_3 core rather than as an isolated entity in water.

4. Incorporation of the Antitumor Molecule to the Core/Shell Nanocomposite

4.1. The analytical evaluation: UV–Vis spectrophotometry

Numerous analytical techniques have been used to evaluate drug loading to a magnetic nanoplatform: qualitative methodologies, for example, electrophoresis, and quantitative determinations, for example, high-performance

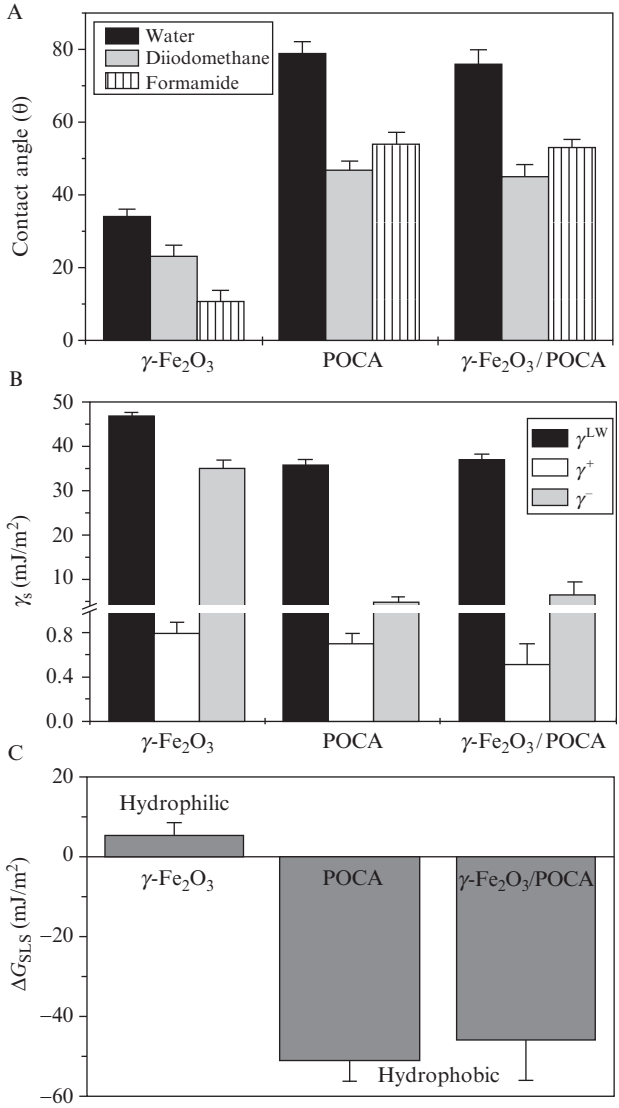

Figure 4.4 (A) Contact angle θ (degrees) of the liquids indicated on γ-Fe_2O_3, POCA, and γ-Fe_2O_3/POCA nanoparticles. (B) Surface free energy components (mJ/m^2) of the nanomaterials. γ_S^{LW} is the Lifshitz–van der Waals component; γ_S^+ (γ_S^-) is the electron acceptor (electron donor) component. (C) Solid–liquid interfacial energy of interaction values (ΔG_{SLS}, mJ/m^2) and hydrophobic/hydrophilic character of the three types of nanoparticles.

liquid chromatography (HPLC), UV–Vis spectrophotometry, NMR, and/or FTIR. Very importantly, these techniques must be previously validated and verified for accuracy, precision, and linearity under all the conditions

tested. In our case, the quantification of the loading of methotrexate to the γ-Fe_2O_3/POCA nanoparticles is done by UV–Vis absorption measurements at the maximum absorbance wavelength of the drug molecule (304 nm).

Drug loading to magnetic nanocomposites can be achieved by two different procedures, surface adsorption onto the nanoparticle surface and drug absorption within the particle matrix. In both cases, the determination of the amount of methotrexate (Sigma-Aldrich) loaded to the core/shell nanoplatform is performed in triplicate by spectrophotometric measurements of the drug remaining in the supernatant (after adequate nanoparticle centrifugation, e.g., 30 min at 100,800 × *g*), which is deduced from the total amount of methotrexate in the nanocomposite aqueous suspension. For the method to be accurate, the contribution to the absorbance of sources other than variations in drug concentration (i.e., the surfactant agent, H^+/OH^- ions balance) must be considered, by subtracting the absorbance of the supernatant produced in the same conditions but without the chemotherapy molecule. Finally, drug incorporation into the nanoparticles is commonly expressed in terms of drug loading (DL, %) and drug entrapment efficiency (EE, %):

$$\mathrm{DL} = \frac{\text{Encapsulated methotrexate (mg)}}{\text{Nanocomposite (mg)}} \times 100. \tag{4.6}$$

$$\mathrm{EE} = \frac{\text{Encapsulated methotrexate (mg)}}{\text{Total methotrexate in the core/shell nanoparticle suspension (mg)}} \times 100. \tag{4.7}$$

4.2. The adsorption procedure

Drug incorporation onto the surface of a nanoparticulate carrier has been classically analyzed by HPLC and/or UV–Vis spectrophotometry. In addition, a qualitative follow-up of the drug adsorption process can be achieved by electrokinetic measurements (Arias *et al.*, 2008). The experiment involves basically methotrexate surface adsorption onto the preformed γ-Fe_2O_3/POCA nanocomposites. In detail, the core/shell nanoparticles (∼1%, w/v) are incubated for 1 day (at room temperature, and under mechanical stirring) in an aqueous suspension containing the methotrexate molecules (i.e., up to 10 m*M*).

One of the most important parameters obviously determining the adsorption of a drug molecule is its own concentration in the incubation medium. Classically, surface incorporation of any given antitumor agent will be greater as the drug concentration in the aqueous medium is increased. In our case, methotrexate EE (%) is increased as the concentration of this anticancer molecule in the incubation medium is augmented (from

1.3 ± 0.1 to 7.4 ± 1.1% for methotrexate concentrations ranging from 0.1 to 10 m*M*). Nevertheless, maximum drug loading can be considered low (1.2 ± 0.1%), which can be explained by the unfavorable thermodynamic interaction between the hydrophobic polymeric matrix (in which the γ-Fe_2O_3 nuclei are embedded) and this hydrophilic chemotherapy molecule. In fact, other important factors must also be taken into account, for example, the surface thermodynamics of the nanocarrier. Hydrophilic nanoparticulate platforms will develop a positive interaction with polar drugs, and the adsorption of such molecules will be facilitated. By contrast, the adsorption of polar molecules onto hydrophilic surfaces will not be favored. The opposite will be true for hydrophobic nanocarriers. Another key parameter that determines drug adsorption is the electrostatic interaction between electrically charged drug molecules and surface charged nanoparticles. In this case, drug incorporation onto the surface of the nanomaterial will be favored only if this molecule and the nanoplatform exhibit opposite electrical charges.

4.3. The absorption procedure

The entrapment method for loading methotrexate onto γ-Fe_2O_3/POCA nanoparticles is typically similar to that described above for the synthesis of the magnetic nanocomposites, except that the aqueous phase also contains anticancer molecules. Methotrexate loading into the polymeric matrix is determined by the preparation (polymerization) conditions of the magnetic nanocarrier. The production performance (PP, %) under all the formulation conditions can be determined by the following equation:

$$\mathrm{PP} = \frac{\text{Methotrexate} - \text{loaded nanocomposites obtained (mg)}}{\sum\text{materials used in the elaboration of nanocomposites (mg)}} \times 100. \tag{4.8}$$

4.3.1. The effect of the polymerization conditions

With respect to the kinetics of the synthesis procedure, both the moment of drug addition to the aqueous phase and the length of the polymerization determine methotrexate loading to the magnetic nanocomposites. Drug absorption is independent of the polymerization duration only if this process is allowed to continue for at least 3 h. Concerning the moment of methotrexate addition to the aqueous phase, it does influence the loading to the nanocomposites, because of the rapid polymerization kinetics of the octyl cyanoacrylate monomer onto the magnetic cores. Methotrexate must be added to the aqueous polymerization medium preferably before the incorporation of the monomer to achieve the highest drug-loading values. For

instance, it is found that methotrexate loading falls to negligible values if it is added to the aqueous phase after the first 30 min of polymerization.

Table 4.1 shows the amount of chemotherapy molecules absorbed into the magnetic nanoparticles as a function of the drug concentration. It is clear that, compared to the surface adsorption methodology, both the EE (%) and the DL (%) are significantly increased regardless of the drug concentration. For instance, when the methotrexate concentration in the adsorption/absorption medium is 0.1 m*M*, these parameters rise from ~7.4% and ~1.2% (after drug adsorption onto the nanocomposite surface) to ~37.2% and ~6.1% (when the antitumor molecules are absorbed into the nanoparticle matrix), respectively. Furthermore, a positive effect of the increment in drug concentration on the methotrexate loading to γ-Fe_2O_3/POCA nanoparticles is observed. Finally, the size of the nanocomposites and the quality of the suspensions do not vary significantly when the nanoparticles are loaded with different amounts of methotrexate.

The influence of the concentration of monomer and surfactant agent on methotrexate loading to γ-Fe_2O_3/POCA nanocomposites can be investigated by varying the octyl cyanoacrylate concentration between 4 and 20 mg/ml, and the stabilizing agent concentration between 0% and 2% (w/v). Table 4.2 shows the dependence of methotrexate loading into the nanocomposite matrix on the quantity of Pluronic® F-68 (Sigma-Aldrich), and octyl cyanoacrylate monomer (gift from Henkel Loctite).

The addition of Pluronic® F-68 to the aqueous phase yields homogeneous distributions of core/shell nanoparticles with reduced size and good uniformity, without influencing drug loading. Interestingly, the production performance of methotrexate-loaded magnetic nanocomposites is always greater than 94% in all the formulation conditions tested, and only falls to less than 8% when no surfactant agent is added to the aqueous phase. Concerning the effect of the monomer concentration, no significant influence on methotrexate loading has been determined. In fact, the methotrexate EE is essentially independent of the amount of monomer added, staying constant at ~37%.

Table 4.1 EE (%) and DL (%) values of γ-Fe_2O_3/POCA nanocomposites prepared by the methotrexate absorption (entrapment) procedure, as a function of the drug concentration

[Methotrexate] (*M*)	EE (%)	DL (%)	Size (nm)
10^{-4}	12.3 ± 1.3	2.1 ± 0.2	110 ± 15
5×10^{-4}	19.6 ± 2.4	3.3 ± 0.3	120 ± 10
10^{-3}	24.5 ± 2.6	4.1 ± 0.3	125 ± 20
5×10^{-3}	32.6 ± 1.9	5.4 ± 0.3	115 ± 15
10^{-2}	37.2 ± 1.8	6.1 ± 0.2	115 ± 10

Table 4.2 Dependence of methotrexate loading values into γ-Fe_2O_3/POCA nanocomposites on the surfactant and octyl cyanoacrylate monomer concentrations

[Monomer] (%, w/v)	[Pluronic® F-68] (%, w/v)	Methotrexate EE (%)	Size (nm)
0.5	1	36.1 ± 2.3	120 ± 20
1	1	37.2 ± 1.8	110 ± 15
2	1	35.6 ± 2.4	115 ± 10
1	0	6.8 ± 2.9	2325 ± 565
1	0.5	34.2 ± 1.5	105 ± 10
1	2	36.4 ± 3.1	125 ± 15

The pH of the aqueous phase is an important parameter determining methotrexate loading. The kinetic of the octyl cyanoacrylate polymerization onto the magnetic cores is governed by the relative amounts of the alcoholic —OH groups of the surfactant used, and the OH^- ions from water dissociation. As the acidity of the medium increases, the polymerization rate decreases. Consequently, $[H^+]$ determines the polymerization rate and, thus, methotrexate absorption. A fast polymerization of the monomer is expected to mechanically entrap as much chemotherapy agent as possible. However, a very fast polymerization generates polymeric solids or macroaggregates. Our results indicate that methotrexate absorption is largest at $[H^+] \sim 1$ m*M* and, although a higher drug loading is expected in more basic solutions, these synthesis conditions yield nanocomposites unsuitable for parenteral administration.

4.4. *In vitro* evaluation of the drug release characteristics

Drug release determinations are generally performed *in vitro* following the dialysis bag method. The dialysis bag (i.e., cut-off of 2000 Da, Spectrum® Spectra/Por® 6 dialysis membrane tubing, USA) must retain the magnetic nanocomposites but allows the free drug to diffuse into the release medium. This experiment involves the use of phosphate buffered saline (PBS, pH = 7.4 ± 0.1) or a HCl solution (pH = 4) as the release medium. The bags are soaked in water at room temperature for 12 h before use. Then, the magnetic nanocomposite suspension (e.g., 2 ml containing 3 mg/ml of methotrexate) is placed into the dialysis bag with the two ends fixed by clamps. The bags are then placed in a glass beaker containing 100 ml of release medium kept at 37.0 ± 0.5 °C during the experiment and mechanically stirred (200 rpm). At prefixed time intervals, 1 ml of the medium is withdrawn to determine drug content using UV–Vis spectrophotometry (at 304 nm). An equal volume of release medium, maintained at the same temperature, is subsequently added after sample withdrawal to ensure the

sink conditions. This investigation is carried out in triplicate with the magnetic nanocomposites prepared following the best methotrexate loading conditions: 1 m*M* drug concentration in the adsorption/absorption process. All chemicals used in these determinations are of analytical quality (Panreac).

4.4.1. Influence of the formulation conditions

When the methotrexate-loaded γ-Fe_2O_3/POCA nanocomposites are synthesized by the absorption methodology, drug release at pH 7.4 takes place as a biphasic process: first, an early rapid release occurs, while the remaining drug is slowly liberated during a longer second phase. Such a drug release profile is illustrated in Fig. 4.5A: an initial fast (burst) drug release (up to ∼58% in ∼1 h), the remaining methotrexate being released in a sustained manner during ∼23 h (∼1 day). The burst drug release is presumably the consequence of the leakage of the surface-associated and/or poorly entrapped antitumor agent (adsorbed more deeply into the surface pores). Then, the rate of methotrexate release falls as the dominant release mechanism is changed to particle disintegration by surface erosion, drug diffusion through the polymeric network, or both. Another typical feature is that methotrexate release is enhanced slightly by an increase in drug loading.

Regarding the release at pH 7.4 of methotrexate adsorbed onto the surface of the nanocomposites, this is a physicochemical process that takes place rapidly. In fact (Fig. 4.5A), methotrexate release complete after 1 h, thanks to a single and rapid desorption process from the nanoparticle surface. An increase in the drug loaded can also enhance the cumulative methotrexate release from the nanoparticle surface.

4.4.2. Influence of the pH of the release medium

If the pH of the release medium is adjusted to 4 (Fig. 4.5B), the release profiles of methotrexate are similar to those obtained at pH 7.4 (Fig. 4.5A), except that a slower release rate is observed: ∼27% of the total methotrexate release is achieved after 1 h, and the remaining 73% is then slowly liberated within the following 95 h. The key role played by the OH^- ions on the hydrolysis of both the alkyl side chain and the ester group determines the acceleration of the surface erosion rate as the pH rises: an increase in [OH^-] induces a higher hydrolytic degradation, provoking both random scission of the polymer C—C bonds producing formaldehyde, and ester hydrolysis with formation of acidic moieties and alcohols. Through these mechanisms, it is expected that a rise in pH leads to a faster degradation and, as a result, to a more rapid methotrexate release (exemplified in Fig. 4.5A). All other characteristics of this biphasic process, pointed out before in relation to data at pH 7.4, remain essentially unchanged. Even more, the release of methotrexate from the γ-Fe_2O_3/POCA nanoparticles loaded by an adsorption process is slower, and in fact can be considered complete after ∼2 h.

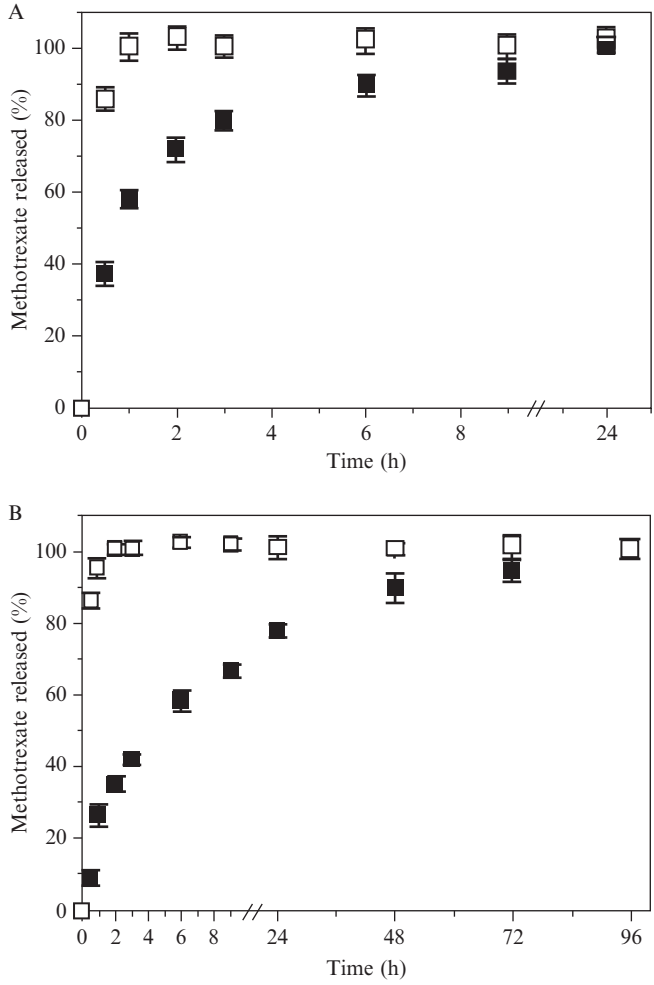

Figure 4.5 Release of methotrexate adsorbed (□) or absorbed (■) from γ-Fe_2O_3/POCA (core/shell) nanocomposites, as a function of the incubation time at 37.0 ± 0.5 °C in: (A) PBS (pH = 7.4 ± 0.1) and (B) HCl solution (pH = 4.0 ± 0.1).

5. Blood Compatibility of the Anticancer Nanomedicine

An important challenge in the development of the methotrexate-loaded γ-Fe_2O_3/POCA nanoparticles is to assure an adequate biocompatibility. Thus, the interaction of the nanocomposites with blood components is investigated to clarify the use of the magnetic nanoplatform to systemically

deliver methotrexate to tumors or cancer cells. With that aim, blood samples (5 ml) are obtained from healthy adults, and poured into flasks containing sodium citrate (used in the complement system activation and plasma clotting time experiments), or ethylenediaminetetraacetic acid (EDTA; used in the hemolysis and platelet activation experiments). Following a well-defined methodology (Dash *et al.*, 2010), the magnetic nanocomposites are kept in contact with blood aliquots to evaluate their effect on erythrocytes, coagulation, and complement system. Such techniques must be validated and verified for accuracy, precision, and linearity. All chemicals used in these experiments are of analytical quality (Panreac).

The *in vitro* effect of the methotrexate-loaded nanoparticles on erythrocyte lysis (hemolysis) can be evaluated easily by using Triton® X-100 (1%, w/v) as a positive control (100% lysis), and PBS as a negative control (0% lysis) of hemolysis. Briefly, EDTA-anticoagulated blood is centrifuged at 13,440 $\times$ *g* for 15 min. The serum fraction is then removed and the original volume is replaced with 150 m*M* NaCl. Upon repetition of this step, the final suspension is diluted 1:10 with 100 m*M* PBS. Red blood cells (10^8/ml) are incubated with the drug-loaded nanocomposites (0.05%, w/v) for 2 h at 37.0 $\pm$ 0.5 °C under mechanical stirring. The samples are then centrifuged at 13,440 $\times$ *g* (15 min). Hemoglobin release is evaluated by measuring the absorbance of the supernatant at 545 nm. Hemolysis (%) is finally determined as:

$$\text{Hemolysis} = \frac{\text{Absorbance of test samples} - \text{absorbance of control}}{\text{Highest absorbance of positive control}} \times 100. \tag{4.9}$$

Platelet activation (and aggregation) upon interaction with methotrexate-loaded nanocomposites further indicates blood incompatibility as it can lead to thrombotic complications. Platelet activation is typically quantified by the enzyme-linked immunosorbent assay (ELISA) in terms of the release of soluble P-selectin (sP-selectin) after incubation of the drug-loaded nanoparticles with blood samples. For this assay, blood is centrifuged at 6384 $\times$ *g* (20 min) to remove platelet-rich supernatant. Then, the blood is again centrifuged at 8400 $\times$ *g* (15 min), and is then combined with previously extracted plasma to obtain platelet-rich plasma (PRP). Platelet-poor plasma (PPP) is obtained by centrifuging the remaining blood at 20,160 $\times$ *g* (10 min). The PRP is then diluted 1:100 with 1% ammonium oxalate and is adjusted to a final platelet concentration of $\sim 5 \times 10^8$/ml. Three hundred milliliters of PRP are incubated with 40 mg of the methotrexate-loaded nanocomposites for 1 h at 37.0 $\pm$ 0.5 °C. The supernatant is finally centrifuged at 31,584 $\times$ *g* (15 min). Both PPP and PRP are used as controls, and PBS is used as a negative control.

Activation of the complement system can produce anaphylatoxins and, as a result, activation of the immune system. Nanocomposite opsonization with complement components (i.e., C3a and C5a) is expected to induce their blood clearance by the reticuloendothelial system. Complement activation is determined easily by quantifying C3a release upon incubation of the methotrexate-loaded nanoparticles with pooled citrated plasma (obtained by blood centrifugation). Briefly, C3 cleavage is monitored by measuring the formation of its activation peptide (C3a desArg), using a C3a enzyme immunoassay kit (Sigma-Aldrich). Equal volumes of plasma and drug-loaded nanocomposites in saline are incubated for 1 h at 37.0 ± 0.5 °C. Samples are properly diluted and incubated in a microtiter plate coated with a monoclonal antibody specific for human C3a desArg (1 h, room temperature). Subsequently, the plates are washed and incubated with peroxidase-conjugated rabbit anti-C3a for 15 min. Finally, a chromogenic substrate is added to detect the bound C3a, and absorbance is measured at 450 nm. PBS is used as a negative control.

Plasma clotting is based on intrinsic and extrinsic pathways that finally lead to clot formation. The former pathway is initiated when blood comes into contact with the nanocomposite surface, while the latter pathway is initiated upon vascular injury, leading to exposure of tissue factor. Plasma recalcification profiles are used to mimic *in vitro* the intrinsic coagulation system. Howell's method is followed to determine the plasma recalcification time, and $t_{1/2\max}$ is calculated as the time at which half the saturated (maximum) absorbance value is reached (Dash *et al.*, 2010; Sagnella and Mai-Ngam, 2005). PBS is used as a negative control. In detail, blood is centrifuged at 20,160 × *g* (8.0 ± 0.5 °C, 20 min) to obtain the PPP. Drug-loaded nanocomposites (40 mg in 1 ml of PBS) and 0.1 ml of PPP are incubated at 37.0 ± 0.5 °C for 5 min in a 96-well plate. A $CaCl_2$ solution (0.1 ml of a 25 m*M* solution) is then added, and the plasma solution is monitored for clotting by manually dipping a silicone-coated stainless-steel wire hook into the solution to detect fibrin threads. Clotting times are estimated easily as the time at which the first fibrin strand is formed on the hook.

Results from blood compatibility tests of the methotrexate-loaded γ-Fe_2O_3/POCA nanoparticles are presented in Table 4.3. The experimental data suggest that the nanomedicine exhibits a negligible effect on hemolysis, thus indicating a potentially wide safety margin *in vivo*, and suitability for intravenous administration. Regarding platelet activation, sP-selectin levels are not influenced significantly by the nanoparticles. Similar conclusions can be obtained upon analysis of complement system activation by the magnetic nanocomposite. Finally, the plasma clotting times are slightly shorter when compared to controls.

Table 4.3 Blood compatibility of methotrexate-loaded γ-Fe_2O_3/POCA (core/shell) nanoparticles in terms of hemolysis (%), platelet activation (sP-selectin release, ng/ml), complement activation (C3a release: C3a desArg, ng/ml), and plasma recalcification time ($t_{1/2max}$, min)

Sample	Hemolysis (%)	sP-selectin release (ng/ml)	C3a desArg (ng/ml)	$t_{1/2max}$ (min)
Methotrexate-loaded γ-Fe_2O_3/POCA	1.7 ± 0.2	76 ± 3	293 ± 6	10.2 ± 0.4
Control (PBS solution)	0	112 ± 5	287 ± 9	11.3 ± 0.5

Data are indicated as mean value ± standard deviation ($n = 6$).

6. Magnetic Responsive Behavior of the Anticancer Nanomedicine

6.1. Hysteresis cycle

The soft magnetic character and magnetic properties of the methotrexate nanomedicine at room temperature are completely defined by its hysteresis cycle (Fig. 4.6A). Such characterization is generally done with a vibrating magnetometer. From the linear portions (low field) of the curves in Fig. 4.6A, the saturation magnetization and initial susceptibility (χ_i) of the drug-loaded nanocomposites are estimated: 82.9 ± 2.1 kA/m and 0.79 ± 0.08, respectively. These data confirm that the core/shell nanoparticles meet the pursued requirement of being magnetizable; so, they constitute an ideal carrier for methotrexate delivery.

6.2. Optical microscope visualization

The response of the nanomedicine at room temperature to a permanent magnet of 400 mT is evaluated by optical microscopy inspection of a 1% (w/v) aqueous suspension. Interestingly, the initially homogeneous distribution of methotrexate-loaded nanoparticles in the magnetofluid (Fig. 4.6B) is strongly modified, and formation of chain-like aggregates parallel to the gradient lines occurs readily (Fig. 4.6C). This is the consequence of the significant contribution of the magnetic interaction between nanoparticles over the DLVO colloidal interactions (electrostatic van der Waals and hydration or acid–base).

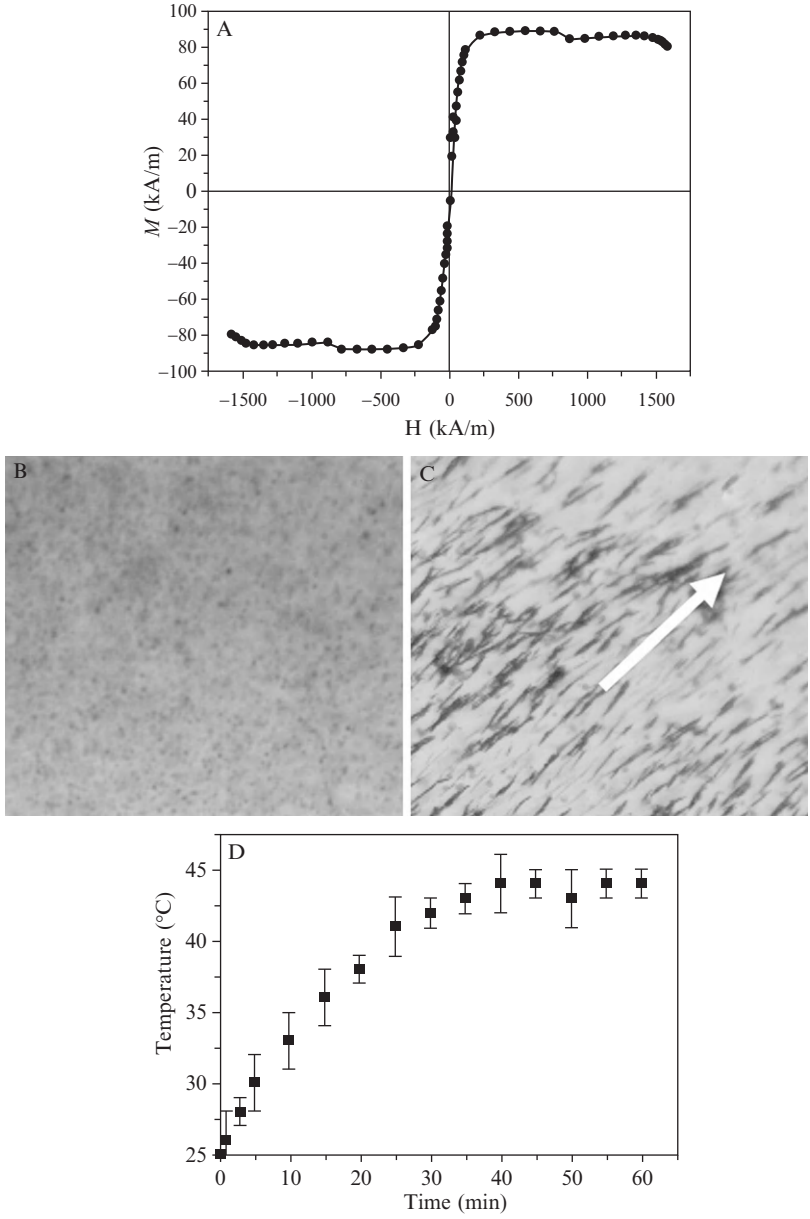

Figure 4.6 (A) Hysteresis cycle of methotrexate-loaded γ-Fe_2O_3/POCA (core/shell) nanoparticles. Optical microscope photographs (magnification: 63 ×) of an aqueous suspension of the nanomedicine without (B), and under the influence (C) of an external magnetic gradient, $B = 400$ mT, in the direction of the arrow. (D) Heating curve of a methotrexate-loaded γ-Fe_2O_3/POCA magnetofluid (8 mg/ml) exposed to a high-frequency alternating electromagnetic gradient (frequency and intensity: 250 kHz and 4 kA/m, respectively).

6.3. *In vitro* heating behavior in an alternating magnetic gradient

The *in vitro* heating behavior of the methotrexate-loaded γ-Fe_2O_3/POCA nanoparticles in a high-frequency alternating electromagnetic gradient is normally analyzed (in triplicate) at room temperature. To that aim, 5 ml of an aqueous suspension of the nanomedicine (8 mg/ml) is previously sonicated. Magnetic gradient frequency and intensity can be fixed to 250 kHz and 4 kA/m, respectively. Figure 4.6D shows the *in vitro* heating behavior of methotrexate-loaded γ-Fe_2O_3/POCA magnetofluid. Under the experimental conditions, the oscillation of the magnetic moment of the drug-loaded nanoparticles transforms them into heaters that can produce heat up to ~44 °C. A very interesting property, given the fact that tumor cells are irreversibly damaged at this temperature, and locally heating a tumor mass for 30 min is enough to destroy it (Huber, 2005). In fact, the temperature of the magnetofluid rises from room temperature and reaches the minimum hyperthermia temperature (~41 °C) in 25 min. After ~35 min, the nanoparticle suspension reaches the temperature of 44 °C, which is maintained if the conditions are kept constant until the end of the experiment. This proves a good control of the temperature and heat flux, a basic requirement for hyperthermia if we keep in mind that when the temperature rises greater than 48 °C, it is hypothesized that healthy cells surrounding the tumor mass will begin to burn and be damaged (Gonzales and Krishnan, 2005; Lao and Ramanujan, 2004).

7. Concluding Remarks

The development of a multifunctional magnetic nanomedicine against cancer should be based on a complete physicochemical characterization of the parameters determining the magnetic responsiveness, antitumor drug loading and release, hyperthermia, and blood compatibility. The synthesis methodology for the preparation of the iron oxide core of the nanocomposites must be defined perfectly, given the fact that it will determine the magnetic responsiveness and hyperthermia effect of the nanomedicine. The influence of the synthesis conditions and the contributions of both the surface and the polymer matrix to the overall drug vehiculization can be clarified by both qualitative and quantitative methods. Special emphasis should be given to the most significant factors affecting drug vehiculization, for example, the monomer and surfactant concentrations, the pH, and the drug concentration. Such studies are crucial to reach conclusions regarding the potential introduction of the multifunctional antitumor nanomedicine into the clinic.

ACKNOWLEDGMENT

The research leading to this contribution has received funding from project PE2008-FQM-3993 (Junta de Andalucía, Spain).

REFERENCES

Adamson, A. W., and Gast, A. P. (1997). Physical Chemistry of Surfaces. 6th edn. John Wiley & Sons, Inc., New York.

Arias, J. L. (2011). Drug delivery strategies in targeting cancer: Current concepts and future developments. *Curr. Drug Targets* **12,** 1094–1095.

Arias, J. L., Gallardo, V., Gómez-Lopera, S. A., Plaza, R. C., and Delgado, A. V. (2001). Synthesis and characterization of poly(ethyl-2-cyanoacrylate) nanoparticles with a magnetic core. *J. Control. Release* **77,** 309–321.

Arias, J. L., Gallardo, V., Linares-Molinero, F., and Delgado, A. V. (2006). Preparation and characterization of carbonyl iron/poly(butylcyanoacrylate) core/shell nanoparticles. *J. Colloid Interface Sci.* **299,** 599–607.

Arias, J. L., Ruiz, M. A., Gallardo, V., and Delgado, A. V. (2008). Tegafur loading and release properties of magnetite/poly(alkylcyanoacrylate) (core/shell) nanoparticles. *J. Control. Release* **125,** 50–58.

Arias, J. L., Gómez-Gallo, A., Delgado, A. V., and Gallardo, V. (2009). Study of the stability of Kollidon® SR suspensions for pharmaceutical applications. *Colloids Surf. A Physicochem. Eng. Asp.* **338,** 107–113.

Arias, J. L., Clares, B., Morales, M. E., Gallardo, V., and Ruiz, M. A. (2011). Lipid-based drug delivery systems for cancer treatment. *Curr. Drug Targets* **12,** 1151–1165.

Armstrong, T. I., Davies, M. C., and Illum, L. (1997). Human serum albumin as a probe for protein adsorption to nanoparticles. *J. Drug Target.* **4,** 389–398.

Bee, A., Massart, R., and Neveu, S. (1995). Synthesis of very fine maghemite particles. *J. Magn. Magn. Mater.* **149,** 6–9.

Borchard, G., and Kreuter, J. (1996). The role of serum complement on the organ distribution of intravenously administered poly(methyl methacrylate) nanoparticles: Effects of pre-coating with plasma and with serum complement. *Pharm. Res.* **13,** 1055–1058.

Corot, C., Robert, P., Idee, J. M., and Port, M. (2006). Recent advances in iron oxide nanocrystal technology for medical imaging. *Adv. Drug Deliv. Rev.* **58,** 1471–1504.

Dash, B. C., Réthoré, G., Monaghan, M., Fitzgerald, K., Gallagher, W., and Pandit, A. (2010). The influence of size and charge of chitosan/polyglutamic acid hollow spheres on cellular internalization, viability and blood compatibility. *Biomaterials* **31,** 8188–8197.

Decuzzi, P., Pasqualini, R., Arap, W., and Ferrari, M. (2009). Intravascular delivery of particulate systems: Does geometry really matter? *Pharm. Res.* **26,** 235–243.

Depeyrot, J., Sousa, E. C., Aquino, R., Tourinho, F. A., Dubois, E., Bacri, J. C., and Perzynski, R. (2002). Rare earth doped maghemite EDL-MF: A perspective for nanoradiotherapy? *J. Magn. Magn. Mater.* **252,** 375–377.

Durán, J. D. G., Arias, J. L., Gallardo, V., and Delgado, A. V. (2008). Magnetic colloids as drug vehicles. *J. Pharm. Sci.* **97,** 2948–2983.

Elias, A., and Tsourkas, A. (2009). Imaging circulating cells and lymphoid tissues with iron oxide nanoparticles. *Hematology Am. Soc. Hematol. Educ. Program* 720–726.

Gonzales, M., and Krishnan, K. M. (2005). Synthesis of magnetoliposomes with monodisperse iron oxide nanocrystal cores for hyperthermia. *J. Magn. Magn. Mater.* **293,** 265–270.

Holgado, M. A., Álvarez-Fuentes, J., Fernández-Arévalo, M., and Arias, J. L. (2011). Possibilities of poly(D,L-lactide-co-glycolide) in the formulation of nanomedicines against cancer. *Curr. Drug Targets* **12,** 1096–1111.

Huber, D. L. (2005). Synthesis, properties, and applications of iron nanoparticles. *Small* **1,** 482–501.

Lao, L. L., and Ramanujan, R. V. (2004). Magnetic and hydrogel composite materials for hyperthermia applications. *J. Mater. Sci. Mater. Med.* **15,** 1061–1064.

Laurent, S., Forge, D., Port, M., Roch, A., Robic, C., Elst, L. V., and Muller, R. N. (2008). Magnetic iron oxide nanoparticles: Synthesis, stabilization, vectorization, physicochemical characterizations, and biological applications. *Chem. Rev.* **108,** 2064–2110.

Lyon, R. J. P. (1967). Infrared absorption spectroscopy. *In* "Physical Methods in Determinative Mineralogy," (J. Zussman, ed.), pp. 371–399. Academic Press, London, New York.

Maaßen, S., Fattal, E., Müller, R. H., and Couvreur, P. (1993). Cell culture for the assessment of toxicity and uptake of polymeric particulate drug carriers. *S.T.P. Pharm. Sci.* **3,** 11–22.

Maeng, J. H., Lee, D. H., Jung, K. H., Bae, Y. H., Park, I. S., Jeong, S., Jeon, Y. S., Shim, C. K., Kim, W., Kim, J., Lee, J., Lee, Y. M., *et al.* (2010). Multifunctional doxorubicin loaded superparamagnetic iron oxide nanoparticles for chemotherapy and magnetic resonance imaging in liver cancer. *Biomaterials* **31,** 4995–5006.

Massart, R. (1981). Preparation of aqueous magnetic liquids in alkaline and acidic media. *IEEE Trans. Magn.* **17,** 1247–1248.

Maver, U., Bele, M., Makovec, D., Čampelj, S., Jamnik, J., and Gaberšček, M. (2009). Incorporation and release of drug into/from superparamagnetic iron oxide nanoparticles. *J. Magn. Magn. Mater.* **321,** 3187–3192.

Merle, P., Si-Ahmed, S., Habersetzer, F., Abergel, A., Taieb, J., Bonyhay, L., Constantini, D., Dufour-Lamartinie, J., and Trépo, C. (2006). Phase 1 study of intra-arterial hepatic (IAH) delivery of doxorubicin-transdrug® (DT) for patients with advanced hepatocellular carcinoma (HCC). *J. Clin. Virol.* **36,** S179.

O'Brien, R. W., and White, L. R. (1978). Electrophoretic mobility of a spherical colloidal particle. *J. Chem. Soc. Faraday Trans.* **2,** 1607–1626.

Reddy, L. H., and Couvreur, P. (2008). Novel approaches to deliver gemcitabine to cancers. *Curr. Pharm. Des.* **14,** 1124–1137.

Sagnella, S., and Mai-Ngam, K. (2005). Chitosan based surfactant polymers designed to improve blood compatibility on biomaterials. *Colloids Surf. B Biointerfaces* **42,** 147–155.

Santos, J. G., Silveira, L. B., Oliveira, A. C., Garg, V. K., Lacava, B. M., Tedesco, A. C., and Morais, P. C. (2007). Mössbauer investigation of maghemite-based glycolic acid nanocomposite. *Hyperfine Interact.* **175,** 71–75.

Schulze, E., Ferrucci, J. T., Jr., Poss, K., Lapointe, L., Bogdanova, A., and Weissleder, R. (1995). Cellular uptake and trafficking of a prototypical magnetic iron oxide label in vitro. *Invest. Radiol.* **30,** 604–610.

Shubayev, V. I., Pisanic, T. R., II, and Jin, S. (2009). Magnetic nanoparticles for theragnostics. *Adv. Drug Deliv. Rev.* **61,** 467–477.

Silverstein, R. M., and Webster, F. X. (1998). Spectrometric Identification of Organic Compounds. 6th edn. John Wiley & Sons, Inc., New York.

Terreno, E., Castelli, D. D., Viale, A., and Aime, S. (2010). Challenges for molecular magnetic resonance imaging. *Chem. Rev.* **110,** 3019–3042.

van Oss, C. J. (2006). Interfacial Forces in Aqueous Media. 2nd edn. CRC Press, Boca Raton.

Vauthier, C., Dubernet, C., Fattal, E., Pinto-Alphandary, H., and Couvreur, P. (2003). Poly (alkylcyanoacrylates) as biodegradable materials for biomedical applications. *Adv. Drug Deliv. Rev.* **55,** 519–548.

Weissleder, R., Bogdanov, A., Neuwelt, E. A., and Papisov, M. (1995). Long-circulating iron oxides for MR imaging. *Adv. Drug Deliv. Rev.* **16,** 321–334.

Zhang, C., Jugold, M., Woenne, E. C., Lammers, T., Morgenstern, B., Mueller, M. M., Zentgraf, H., Bock, M., Eisenhut, M., Semmler, W., and Kiessling, F. (2007). Specific targeting of tumor angiogenesis by RGD-conjugated ultrasmall superparamagnetic iron oxide particles using a clinical 1.5-T magnetic resonance scanner. *Cancer Res.* **67,** 1555–1562.

Zhang, N., Yin, Y., Xu, S. J., and Chen, W. S. (2008). 5-fluorouracil: Mechanisms of resistance and reversal strategies. *Molecules* **13,** 1551–1569.

CHAPTER FIVE

Development and Use of Ceramide Nanoliposomes in Cancer

Rebecca J. Watters,* Mark Kester,*,† Melissa A. Tran,† Thomas P. Loughran Jr.,* *and* Xin Liu*

Contents

* Penn State Hershey Cancer Institute, Pennsylvania State College of Medicine, Hershey, Pennsylvania, USA
† Department of Pharmacology, Pennsylvania State College of Medicine, Hershey, Pennsylvania, USA

Methods in Enzymology, Volume 508
ISSN 0076-6879, DOI: 10.1016/B978-0-12-391860-4.00005-7

Abstract

Integration of C_6-ceramide into stealth pegylated nanoliposomes has led to the development of a promising preclinical therapeutic alone and in combination with other agents for treatment of cancer. Ceramide itself has been implicated as a bioactive lipid second messenger mediating cell senescence, cell cycle arrest, and apoptosis. Recent lipidomic analyses have demonstrated that specific ceramide species are differentially metabolized in individual cancers. Therapeutics that increase ceramide levels in cancer tissues have shown increased cell death and tumor inhibition. However, the use of ceramide itself as therapeutic has been problematic due to its inherent hydrophobicity and insolubility, therefore limiting the application for intravenous administration. Pegylated nanoliposomes eliminate this issue and are able to enhance the intracellular delivery of ceramide to cancer cells.

1. Introduction

1.1. Role of ceramide

The sphingolipid network is a diverse arrangement of prosurvival and proapoptotic signaling lipids (Ryland *et al.*, 2011). Ceramide is a fundamental and integral component of this pathway, responsible for regulating cellular differentiation, proliferation, and apoptosis (Kolesnick and Kronke, 1998). Ceramide can be formed and regulated through several different metabolic pathways (Fig. 5.1). The most well known is the *de novo* pathway that mediates the condensation of serine and palmitoyl-CoA forming ketosphinganine. This is then reduced to dihydrosphingosine (Merrill and Jones, 1990), which is then deacetylated by ceramide synthase into dihydroceramide. Next, dihydroceramide reductase catalyzes the oxidation of dihydroceramide, resulting in a *trans*-4,5 double bond, forming ceramide (Kolesnick and Kronke, 1998). Another pathway involves the hydrolysis of sphingomyelin by sphingomyelinase, which may be triggered by an extracellular signal, such as ionizing radiation, thus resulting in programmed cell death (Haimovitz-Friedman *et al.*, 1994). Last, ceramide can be produced by degradation of complex glycosphingolipids through acid hydrolases (Kolesnick and Kronke, 1998).

Some data indicate that dysfunctional ceramide metabolism or decreased levels of total ceramide are involved in cancer pathogenesis (Ryland *et al.*, 2011; Saddoughi *et al.*, 2008). However, recent lipidomic studies suggest that these findings are more complex, as it appears that ceramide species levels may increase and decrease and that the length of the fatty acid chain may play a role in tumorigenesis and therapeutic efficacy (Ryland *et al.*, 2011). In particular, several recent lipidomics studies have demonstrated that long-chain ceramides, such as C_{16}-, C_{24}-, and $C_{24:1}$-ceramides were

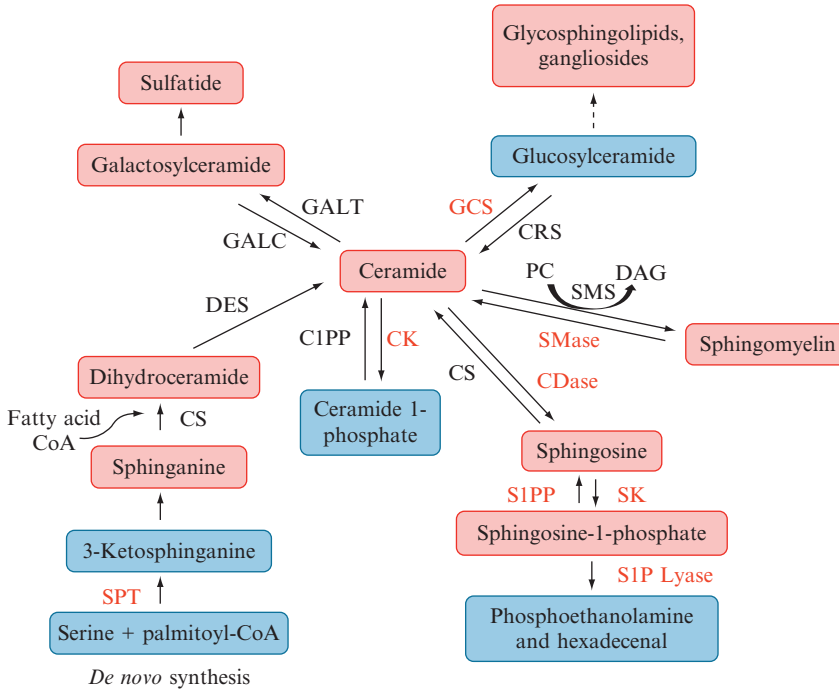

Figure 5.1 Sphingolipid metabolic pathway. Endogenous ceramide can be generated via *de novo* synthesis by condensation of serine and palmitoyl-CoA, sphingomyelin catabolism by sphingomylinases, catabolism of glycosphingolipids or dephosphorylation of metabolites like ceramide 1-phosphate, and sphingosine 1-phosphate. As described in detail in the chapter, several of these sphingolipid enzymes and metabolites are known to be deregulated in cancer (red). CK, ceramide kinase; C1PP, ceramide 1-phosphate phosphatase; CRS, cerebrosidase; CS, ceramide synthase; CDase, ceramidase; DAG, diacylglycerol; DES, dihydroceramide desaturase; GALC, galactosylceramidase; GALT, galactosyltransferase; GCS, glucosylceramide synthase; PC, phosphatidylcholine; SK, sphingosine kinase; S1PP, sphingosine 1-phosphate phosphatase; S1P Lyase, sphingosine 1-phosphate lyase; SMS, sphingomyelin synthase; SMase, sphingomyelinase; SPT, serine palmitoyltransferase. (Figure 5.1 and legend previously published from Ryland *et al.*, 2011.)

actually upregulated in head and neck (Karahatay *et al.*, 2007) and breast cancers (Schiffmann *et al.*, 2009) when compared to normal respective tissues (Ryland *et al.*, 2011). In addition, C_{16}-ceramides were discovered to be upregulated in pancreatic cancer patients (Ryland *et al.*, 2011). Experimental evidence indicates that the altered regulation of ceramide levels in cancer cells in combination with altered expression, and activity of enzymes in sphingolipid metabolism results in cellular proliferation and tumor growth (Saddoughi *et al.*, 2008). The use of exogenous short-chain ceramide that can further deregulate endogenous ceramide metabolism

and/or induce cell death may also be useful for therapeutic applications in cancer. Ceramide's role in inducing selective apoptosis in cancer cells compared to nontransformed cells makes it an attractive therapeutic (Barth *et al.*, 2011). However, there are several physicochemical properties of ceramide, such as poor bioavailability and lack of an appropriate solvent, that inhibit effective delivery (Stover and Kester, 2003; Tran *et al.*, 2008). In particular, the long-chain (C_{16-24}) hydrophobic region prevents solubilization in aqueous solutions. Short-chain ceramides, although having a smaller hydrophobic region, are also not particularly soluble or stable in commercial excipients (Khazanov *et al.*, 2008). In particular, the potential exists for precipitation into micelle suspensions when administered in aqueous solutions (Radin, 2001; Stover and Kester, 2003). Similar to the naturally occurring, endogenous form of ceramide, these short-chain forms are also at risk for possible metabolism by various enzymes in the sphingolipid pathway, such as glucosylceramide synthase (Messner and Cabot, 2010) and ceramidases (Ryland *et al.*, 2011). As a result, ceramide has been incorporated into nanoliposomal formulations by several groups to enhance its solubility through the incorporation into the lipid bilayer (Khazanov *et al.*, 2008; Shabbits and Mayer, 2003b; Stover and Kester, 2003; Tokudome *et al.*, 2009b) (Fig. 5.2). Nanoliposomes are 10^{-7} m in size, and therefore nanoscopic spheres comprising a phospholipid bilayer that encloses a hydrophilic aqueous core. In addition to nanoscale size for easier passive targeting, utilization of a pegylated formulation enables ceramide evasion of the reticuloendothelial system (Gabizon and Martin, 1997; Khazanov *et al.*, 2008; Stover and Kester, 2003). Nanoliposomal formulations that incorporated PEG-2000 (Khazanov *et al.*, 2008) conjugated to phosphatidylethanolamine (Stover *et al.*, 2005) or PEG-750 conjugated

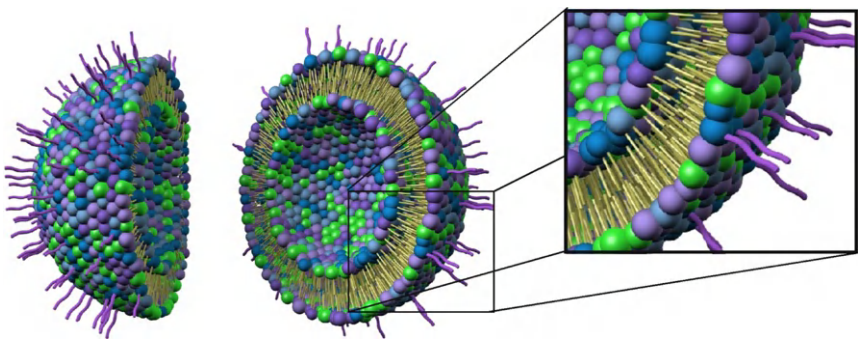

Figure 5.2 C_6-ceramide is incorporated into the hydrophobic lipid bilayer of the nanoliposome. Inset shows close-up of lipid bilayer with C_6-ceramide incorporated (shown in green). (Figure adapted from Barth *et al.*, 2011.)

to C_8-ceramide (Stover *et al.*, 2005) have proven to sterically stabilize ceramide nanoliposomes, yielding shelf life stability over a year (Khazanov *et al.*, 2008; Zolnik *et al.*, 2008). Moreover, nonpegylated ceramide nanoliposomes that utilize cholesterol or cholesterol derivative salt as a fusigen (Shabbits and Mayer, 2003a; Tokudome *et al.*, 2009a) have also been evaluated. In fact, nonpegylated nanoliposomes containing 15 mol% ceramide have proven efficacious in an ascites tumor model (Shabbits and Mayer, 2003a).

Our C_6-ceramide nanoliposome formulation is particularly successful *in vivo* (Barth *et al.*, 2011), because it is designed to carry a large molar fraction of C_6, by definition a bilayer-destabilizing lipid, maximizing the drug payload without sacrificing vesicular stability. The inclusion of PEG-C_8 stabilized the formulation, allowing for the incorporation of up to 30 mol% bioactive C_6 in a unilamelar 70 nm-sized homogenous formulation. Without the PEG-C_8, stable vesicles containing 30 mol% C_6 could not be prepared or extruded. Additionally, the inclusion of PEG-C_8 has been observed to facilitate time-release properties of liposomal bilayers, with the added benefit of enhanced bioavailability because of the polyethylene glycol chains. Moreover, pegylation allows for chemical modification of liposomal surfaces for targeting strategies.

Vehicles containing short-chain ceramide other than our C_6-ceramide nanoliposomes are currently being employed by several other groups (Barth *et al.*, 2011). Among these other particles are ceramide-containing calcium phosphate and phosphosilicate nanoparticles (CPSNPs; Barth *et al.*, 2011), ceramide-containing biodegradable nanoparticles (Morgan *et al.*, 2008), thermoresponsive linear-dendritic nanoparticles (Stover *et al.*, 2008), nanoemulsions, and polyethylene oxide-modified polyepsilon-caprolactone nanoparticles (Desai *et al.*, 2008; Devalapally *et al.*, 2007, 2008; van Vlerken *et al.*, 2007).

1.2. Efficacy of C_6-ceramide nanoliposome in cancer

Short-chain ceramide nanoliposomes induce apoptosis in *in vivo* breast cancer models (Shabbits and Mayer, 2003a; Stover *et al.*, 2005). For instance, C_6-ceramide nanoliposomes were found to inhibit phosphorylated Akt levels and to stimulate caspase-3/7 activity more than nonliposomal C_6-ceramide, concomitant with significantly inhibited cellular proliferation in breast cancer MDA-MB-231 cells (Stover and Kester, 2003). Further work has established ceramide nanoliposomes as an adjuvant therapeutic approach for conventional therapeutics. In MDA-MB-231 breast cancer cells as well as metastatic melanoma cell lines (UACC 903 and 1205 Lu), C_6-ceramide nanoliposomes incorporated into a therapeutic cocktail with Sorafenib, a known multikinase inhibitor (Tran *et al.*, 2008) synergistically reduce tumor cell burden. Overall, the combination cocktail resulted in

synergism of inhibition by targeting both MAPK and PI3K signaling pathways, resulting in a twofold increase in cellular apoptosis and a three- to fourfold decrease in proliferation. This combination treatment also demonstrated a 30% increase in tumor inhibition *in vivo* compared with single agent treatments alone (Tran *et al.*, 2008). C_6-ceramide nanoliposomes have also been tested in combination with gemcitabine and with encapsulation of D-threo-1-phenyl-2-decanoylamino-3-morpholino-1-propanol (PDMP), an inhibitor of glucosylceramide synthase. Specially, in a model of pancreatic cancer, these combinational therapies were shown to cooperatively inhibit PANC-1 tumor growth *in vivo* (Jiang *et al.*, 2011). In addition to breast cancer, pancreatic cancer, and melanoma, C_6-ceramide nanoliposomes have also proved effective in inhibiting *in vivo* growth of hepatocellular carcinoma (HCC; Tagaram *et al.*, 2011). In that study, human SK-HEP-1 cells were engrafted into athymic nude mice and treated with C_6-ceramide nanoliposomes. Such treatment induced apoptosis as well as reduced tumor vascularization and proliferation by targeting the phosphorylation of Akt. In the addition to the solid tumor models, C_6-ceramide nanoliposomes have proven effective in nonsolid leukemia models. We have found that C_6-ceramide induces complete remission in a cohort of a rat syngeneic model of aggressive natural killer cell-large granular lymphocyte (NK-LGL) leukemia (Liu *et al.*, 2010). This study also revealed that survivin, a member of the inhibitor of apoptosis (IAP) family, that plays an important role in regulation of NK cell survival through the ERK/MAPK pathway, was a target of C_6-ceramide nanoliposomes.

1.3. Selective mechanism of C_6-ceramide nanoliposome cancer tissue uptake

We have shown that the neutral nanoliposomal-C_6 partitions out of the liposomal bilayer into the plasma membrane bilayer without associated liposome/cell membrane fusion (Stover and Kester, 2003). During the formulation of the ceramide nanoliposomes, ceramide/phospholipid bilayer interactions are favored because of the chemical structure of ceramide, with the small hydroxyl head group and the saturated hydrophobic chains positioning themselves in the bilayer. This positioning can be envisioned as being similar to the way endogenous ceramide forms in the microdomain of the cellular bilayer membrane (Cremesti *et al.*, 2002; Finnegan *et al.*, 2004). The rapid bilayer exchange allows for immediate distribution of ceramide to all well-perfused tissues, including tumors, which may not result in adverse affects as ceramide appears to exhibit a neoplasm-selective targeting mechanism (Zolnik *et al.*, 2008). Indeed, extensive toxicology studies have shown no biologically significant changes in body weight, organ weight, clinical chemistries, hematology, gross pathology, or histology at the 50 mg/kg dose level in the Sprague–Dawley rat model, supporting a tumor-selective mechanism

(detailed information on the toxicology studies of the "Ceramide Nanoliposomes" can be found at http://ncl.cancer.gov/working_technical_reports.asp). In addition, the liposomal ceramide bilayer exchange mechanism also circumvents the lysosomal degradation pathway that might be encountered by following an endocytosis-mediated delivery route (Zolnik *et al.*, 2008). Furthermore, utilizing mouse mammary breast adenocarcinoma cells, we determined that liposomal-C_6 was delivered and accumulated in caveolae, caveolin-1-enriched lipid rafts, known to serve as signaling/docking platforms for a multitude of signaling cascades (Carver and Schnitzer, 2003; Schroeder *et al.*, 2001). In addition, liposomal C_6 also localizes within the mitochondria, possibly contributing to mitochondrial dysfunction and resultant cell death (Liu *et al.*, 2010; Stover *et al.*, 2005).

2. Preparation of Ceramide Nanoliposomes

Selection of appropriate lipids for liposome production may require producing several formulations to determine an optimal formulation. Lipids can be divided into several categories, including cationic, anionic, and neutral helper lipids. 1,2-Dioleoyl-*sn*-glycero-3-phosphoethanolamine (DOPE) and cholesterol are often referred to as "helper lipids" as they are added to increase stability and enhance cellular uptake by providing a neutral component to charged liposomes (Farhood *et al.*, 1995). The addition of pegylated lipids are essential, as they play a role in enhanced circulation time by masking the liposome from the mononuclear phagocytic system (Gabizon and Martin, 1997). Our C_6-ceramide nanoliposome formulation contains 12% PEG, thus allowing for this benefit. Cationic, neutral, and anionic lipids can be chosen to change the overall charge of the liposome and enhance interactions with molecules of interest.

Our C_6-ceramide nanoliposomes are prepared from the following lipids (Avanti Polar Lipids, Alabaster, AL) dissolved in chloroform ($CHCl_3$): 1,2-distearoyl-*sn*-glycero-3-phosphocholine (DSPC), DOPE, *N*-hexanoyl-D-erythro-sphingosine (C_6-ceramide), 1,2-distearoyl-*sn*-glycero-3-phosphoethanolamine-*N*-[methoxy polyethylene glycol-2000] (PEG-2000), and *N*-octanoyl-sphingosine-1-[succinyl(methoxy polyethylene glycol)-750] (PEG(750)-C_8), which are combined at a molar ratio of 3.75:1.75:3:0.75:0.75, respectively. This combination was chosen due to its stability after the testing of multiple formulations (Stover and Kester, 2003). In addition, we have also published a cationic C_6-ceramide formulation using egg phosphatidylcholine, DOPE, cholesterol, DOTAP, and C_6-ceramide in the following ratio 5:0.5:1.5:1:2, respectively (Stover and Kester, 2003). Lipids are mixed in a glass tube, dried under a stream of nitrogen, and then rehydrated with sterile saline to a final concentration of 25 mg/ml containing 30 mol% of C_6-ceramide.

Lipids are then incubated for 3 h above the lipid phase transition temperature at 60 °C, which is a critical step, with intermittent vortexing every 15–20 min to facilitate the rehydration. Lipids are considered rehydrated when no lipid is adhering to the glass tube. Next, the rehydrated lipids are sonicated at 60 °C for a period of 5–10 min, resulting in a clear suspension. This solution is then extruded using a 100-nm pore-diameter polycarbonate membrane using the Avanti Mini-Extruder (Avanti Polar Lipids; Liu *et al.*, 2010; Stover and Kester, 2003; Stover *et al.*, 2005; Tran *et al.*, 2008). The liposomes are passed 11 times through the extruder ending on the side opposite the starting point. In addition to the C_6-ceramide nanoliposomes, control "ghost" liposomes are manufactured by excluding C_6-ceramide in the preparation described above.

As previously mentioned, we also have incorporated the glucosylceramide synthase inhibitor, PDMP, in our C_6-ceramide nanoliposomes, to enhance the cytotoxicity of C_6. Our formulation was prepared with the following Avanti lipids as follows: DSPC, DOPE, PEG(2000)-DSPE, C_6-ceramide, PEG(750)-C_8), and PDMP in a 3.75:1.75:0.75:1.5:0.75: 1.5 ratio (Jiang *et al.*, 2011).

For short-term storage, nanoliposomes may be stored at 4 °C or at room temperature in saline (154 m*M*), at 25 mg/ml (Zolnik *et al.*, 2008). To ascertain stability over time, the liposome size is measured, since increased sample concentration can lead to aggregation as the electric fields in the charged particles interact with each other, thus altering diffusional properties. It is critical that the storage temperature never be less than 4 °C as this will affect the integrity of the liposome and cause the lipids to precipitate.

3. Characterization of the Ceramide Nanoliposomes

3.1. Incorporation of C_6-ceramide

The C_6-ceramide base nanoliposomes comprise ~30 mol% ceramide, and incorporation efficiency is determined by integrating trace amounts of [^{3}H] C_6-ceramide (American Radiolabeled Chemicals, St. Louis) in the formulation, extracting constituent lipids in $CHCl_3$/MeOH (2:1), and comparing radioactivity before and after extrusion using a scintillation counter. This may also be validated by extracting constituent lipids in $CHCl_3$/MeOH (2:1), followed by resolution on preheated silica gel 60 thin layer chromatography plates using a $CHCL_3$/MeOH/ddH_2O (60:25:4) solvent system, with lipids visualized in an iodine chamber (Stover and Kester, 2003). In addition, we have also made use of the dual labeled liposome, [^{3}H]DSPC/[^{14}C] C_6-ceramide (Zolnik *et al.*, 2008) to determine pharmacokinetic parameters.

3.2. Particle size measurement

The size of the nanoliposome is crucial, as vesicles <100 nm have reduced uptake into liver tissues, while vesicles >100 nm are subject to rapid clearance by the mononuclear phagocytic system (De Jong and Borm, 2008). Particle size is determined through the use of a Malvern Zetasizer Nano ZS (Malvern), which determines the diameter based on dynamic or static light scattering from 0.6 nm to 6 μm. This measurement includes the intensity-weighted average diameter for all size populations known as the Z-average (Z-avg), the broadness of particle size distribution via the polydispersity index (PdI), the volume-weighted average diameter over the major volume peak (Vol-Peak), and its percentage of the total population (Vol-Peak, vol%). Through the Stokes–Einstein equation, we can determine the hydrodynamic size (R_H) or relative size of the nanoliposomes:

$$R_H = \kappa T/6\pi\eta D$$

where R_H is the radius, T is the temperature, D is the diffusion coefficient, k is the Boltzmann constant, and η is for solvent viscosity.

Overall, the intensity fluctuation in scattered light is being measured with the principle that small particles diffuse quickly while larger ones diffuse slowly. Here, the particles are assumed to act as spheres with radii R_H. We assume the particles are fully suspended in solution and that the radius determined from the diffusional properties of the nanoliposomes is indicative of its size.

Our nanoliposomes are formed at 80 ± 15 nm in size and contain $\sim$30 molt; cell-permeable ceramide (Liu *et al.*, 2010; Stover and Kester, 2003; Stover *et al.*, 2005; Tran *et al.*, 2008; Fig. 5.3). Nanoliposomes are prepared in aqueous solutions at 25 mg/ml concentration for sizing and then diluted in a 1:10 ratio of nanoliposome suspension to dH_2O. The samples are measured a minimum of seven times at 25 °C. Typically, the formulation will be measured on the day of preparation, the next day, 1 week later, 1 month later, and 3 months later to monitor stability. Size may also be determined using transmission electron microscopy (TEM). In brief, liposomes are attached with 0.1% (w/v) aqueous solution of poly-L-lysine to formvar carbon-coated 400 mesh copper grids for 5 min. Next, negative staining is carried out by adding 1% phosphotungstic acid (pH 7.0) to the dried grids for 5 min. Samples are then visualized at 21,500 × magnification with 60 kV accelerating voltage with a transmission electron microscope (Stover and Kester, 2003). Effects on size stability are also determined by analyzing the effect of pH (0.1 *M* HCl–0.1 *M* NaOH), fetal bovine serum (FBS), time, temperature, and media changes on the nanoliposomes, with no appreciable change noted (NCL, 2007).

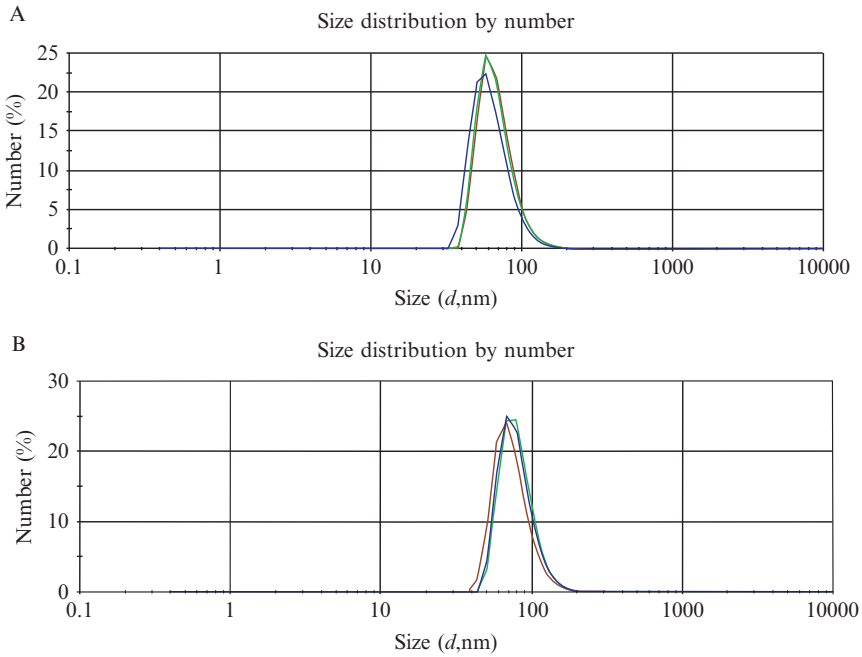

Figure 5.3 Comparison of particle size of C_6-ceramide and ghost nanoliposomes by dynamic light scattering. Nanoliposomes are prepared in aqueous solutions at 1 mg/ml concentration and then diluted in a 1:10 ratio of nanoliposome suspension to dH_2O. The samples are measured a minimum of seven times through the software at 25 °C. (A) Ghost liposomes average ~64 nm, (B) C_6-ceramide liposomes average ~79 nm.

3.3. Zeta-potential measurement

The zeta potential (ZP) can be used to evaluate the charge stability of a disperse system, such as liposomes; it is used to quantify the magnitude of the electrical charge of the lipid bilayer. A measurement is taken by applying an electric charge across the sample in a folded capillary flow cell. The particles that maintain a high ZP will be attracted to the electrode of opposite charge. The velocity will be proportional to the degree of ZP and is measured through Doppler anemometry, which analyzes speed and direction. A minimum of 10 measurements at two different concentrations are taken for each sample nanoliposome formulation, which are performed on a Zetasizer nano ZS (Malvern) at 100 V. Our average ZP value of ghost nanoliposomes is -10.7 ± 0.6 mV, whereas C_6-ceramide nanoliposomes have an average ZP of -13.9 ± 0.8 mV, as seen in Fig. 5.4 (NCL, 2007). Knowledge of ZP is critical for formulation, design, and quality control, as any differences in ZP could lead to drastically different characteristics for

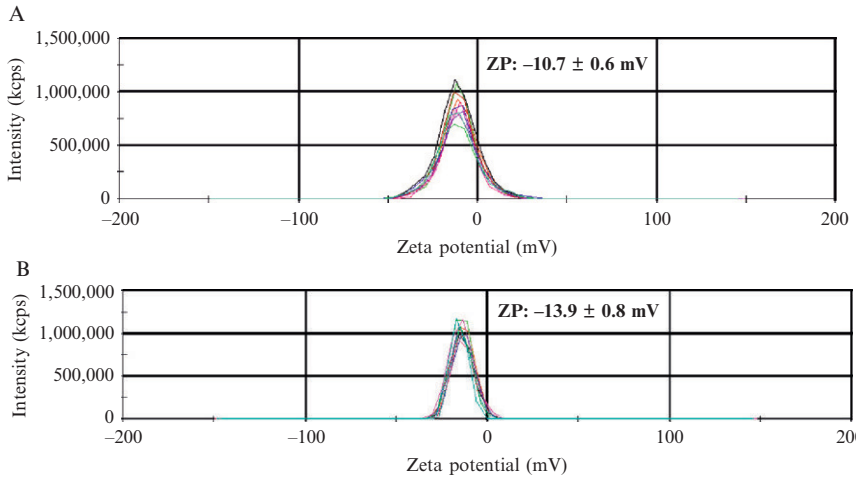

Figure 5.4 Determining the zeta potential of C_6-ceramide and ghost nanoliposomes. A folded capillary flow cell was used for zeta potential measurement at a voltage of 100 V. The zeta-potential of Ghost and C_6-ceramide nanoliposomes is measured at 25 °C. Samples are diluted in 10 m*M* NaCl to give a 1 mg/ml final concentration. A minimum of 10 measurements are taken for each sample. (A) Ghost nanoliposomes have an average ZP of -10.7 ± 0.6 mV, (B) C_6-ceramide has an average ZP of -13.9 ± 0.8 mV (NCL, 2007).

nanoliposomes. As a result, the greater the ZP, then the more likely that the particles will resist aggregation. In addition, different ZPs will change how the particles will be targeted *in vivo*.

4. Evaluation of C_6-Ceramide Nanoliposomes *In Vitro*

4.1. Delivery of C_6-ceramide nanoliposomes *in vitro*

C_6-ceramide nanoliposomes can be delivered effectively to both suspension and adherent cancer cells. First, we describe our suspension cell procedure with LGL leukemia cells. In particular, human NKL cells cultured in RPMI-1640 (Invitrogen) supplemented with 20% FBS from HyClone (Fisher Thermo Scientific) plus 100 IU/ml IL-2. Rat RNK16 cells are cultured in RPMI-1640 (Invitrogen) and supplemented with 10% FBS from HyClone (Fisher Thermo Scientific). All cells are maintained in a 37 °C humidified 5% CO_2 atmosphere incubator. The cells are plated at a density of 1×10^6 cells/ml in a six-well plate in a total of 4 ml, and C_6-ceramide nanoliposomes are added immediately after plating, in a

wide range, from 6.25 to 25 μ*M* ceramide (Liu *et al.*, 2010). The protocol differs slightly from adherent cells in that they are plated 24 h before treatment, enabling them to adhere (Stover and Kester, 2003; Stover *et al.*, 2005; Tagaram *et al.*, 2011; Tran *et al.*, 2008). To examine if ceramide is being delivered, downstream affects can be examined at the protein and RNA levels. Cells are collected 24–72 h after treatment for protein or RNA extraction and analyzed for expression of potential targets affected by ceramide treatment, in particular, survivin and pERK (Liu *et al.*, 2010) and PI3K/Akt (Jiang *et al.*, 2011; Tran *et al.*, 2008).

For protein extraction, cell lysates are harvested by addition of RIPA lysis buffer-containing phosphatase inhibitor and protease inhibitor cocktails (Sigma). Whole cell lysates are centrifuged ($\geq 10{,}000 \times g$) for 10 min at 4 °C to remove cell debris. Quantification of protein concentrations are performed utilizing the NanoDrop 2000 Spectrophotometer (Thermo Fisher Scientific), and 30 μg of protein are loaded per lane onto 10% precasted NuPAGE electrophoresis gels (Invitrogen). Following electrophoresis, samples are transferred to a polyvinylidene difluoride membrane (Pall Corporation). The blots are probed with antibodies of interest according to each supplier's recommendations.

For RNA extractions from cells, we utilize TRIzol Reagent (Invitrogen), following the manufacturer's instructions. qRT-PCR is performed using primer sets (IDTDNA) specific for targets of interest in an ABI PRISM 7900 sequence detector (Applied Biosystems). GAPDH or 18S are typically used as a control. In our laboratory, 4 μg of total RNA per sample is used to synthesize the first strand of cDNA using random hexamers and MMLV reverse transcription reagent (Invitrogen) in a total volume of 20 μl. A total of 1 μg of cDNA is applied in 10 μl PCR mix from the QuantiTect SYBR Green PCR kit (Qiagen). Amplification of triplicate cDNA template samples is performed for denaturation for 15 min at 95 °C, followed by 45 cycles of denaturation at 94 °C for 15 s, annealing at 55 °C for 30 s, and extension at 72 °C for 30 s. A standard curve of cycle thresholds using serial dilutions of cDNA samples is established and used to calculate the relative abundance of the target gene in the samples (Liu *et al.*, 2010). Values are then normalized to glyceraldehyde-3-phosphate dehydrogenase (GAPDH) (IDTDNA), which is obtained from a similar curve. The changes in fluorescence of SYBR green dye in every cycle are monitored and calculated by the ABI 7900 system software and the threshold cycle (Ct) for each reaction. The relative amount of PCR products generated from each primer set was determined based on the threshold cycle or Ct value. PCR analysis was performed on each cDNA in triplicate.

Additionally, nanoliposomal C_6-ceramide is able to deliver C_6-ceramide to the mitochondria, thus initiating antiproliferative and proapoptotic effects (Birbes *et al.*, 2002), resulting in mitochondrial dysfunction and ultimate cell death (Stover *et al.*, 2005). Confocal microscopy studies are

used to demonstrate this application. We have studied the accumulation of C_6 into 410.4 murine mammary adenocarcinoma cells by formulating a liposomal-C_6 vesicle with 10 mol% NBD-C_6 as a marker for C_6, with the remainder made with unlabeled C_6 to make a total of 30 mol% ceramide. Cells were plated at 2.0×10^4 per well in eight-well chamber slides and allowed to grow overnight. Liposomal-NBD-C_6 was added at 25 μmol/l for a 2-h treatment period. Cellular nuclei were counterstained with 4,6-diamidino-2-phenylindole (DAPI), and MitoTracker Deep Red 633 (Molecular Probes) was used as a marker for mitochondria, following the manufacturer's instructions. C_6 delivery and accumulation was evaluated by confocal microscopy at ×63 magnification (Leica Microsystems; Stover *et al.*, 2005). NBD-C_6 can be used in a similar manner to show the uptake of the liposomes into the cells using the above protocol, but omitting the MitoTracker Deep Red 633 (Molecular Probes).

4.2. Determination of *in vitro* cell viability by C_6-ceramide nanoliposomes

MTT (3-(4,5-dimethylthiazol-2-yl)-2,5-diphenyltetrazolium bromide), a colorimetric assay is performed to determine cell viability using the CellTiter96 AQueous One Solution assay kit (Promega). Leukemic suspension or adherent cancer cells are plated at 10,000 cells/well in a 96-well plate and incubated for a 24 h treatment. Afterward, the MTT reagent is added and incubated for 1–4 h. The relative viable cell number is determined by reading the plates at 490-nm wavelength in a Synergy HT Multi-Detection Microplate Reader (Bio-TEK). In addition, ATP production can be used as an indicator of cell viability. In particular, the ADP to ATP ratio levels are assessed by using a luciferin/luciferase-based ATP assay (Promega). Cells are plated at 10,000 cells/well in a 96-well white walled plate. After a 24 h treatment with C_6-ceramide nanoliposomes alone or with various combination agents, cells are incubated with the ATP assay mix reagent. After 10 min incubation, luminescence is measured using a luminometer. The ATP level is expressed as the percentage of luminescence intensity of treated cells as compared to cells treated with respective vehicle controls. As a positive control, 3-bromopyruvate (Sigma), which decreases ATP levels through mitochondrial depolarization (Ihrlund *et al.*, 2008) is used.

To determine the effect of C_6-ceramide nanoliposome on proliferation, a [^{3}H] thymidine proliferation assay can be utilized. Briefly, MDA-MB-231 cells are seeded at 3.5×10^4 cells/well in 24-well plates and grown overnight prior to 24 h of serum starvation. At hour 12 of serum starvation, cells are treated with liposomal or nonliposomal C_6 for the remainder of serum starvation. Following serum starvation, media are then supplemented with FBS (10% final concentration) for an additional 12 h, and cellular proliferation was assayed with the addition of 0.5 mCi/ml [^{3}H]thymidine for the

final 4 h of treatment. Cells are washed once with cold PBS and then twice with 10% trichloric acetic acid for 10 min. Cells are solubilized with 0.3 N NaOH, and [^{3}H]thymidine incorporation into acid-insoluble DNA is assessed with a scintillation counter. In addition, proliferation activity can also be determined using BrdU incorporation assays (Tran *et al.*, 2008).

4.3. Determination of *in vitro* cell apoptosis

Analysis of the effect of nanoliposomal C_6-ceramide on apoptosis can also be examined. Two-color flow cytometry with annexin-V (5 μl/sample; BD Pharmingen), and 7-amino-actinomycin D (7-AAD; 10 μl/sample; BD Pharmingen) are used to assess the degree of cellular apoptosis in cells treated with C_6-ceramide alone or in combination therapy. For each sample, 5×10^5 cells are plated in triplicate in 24-well plates in 0.5 ml volume and the percentage of specific apoptosis is calculated using the following formula: Apoptosis (%) = (% Annexin-V-allophycocyanin conjugate (APC) positive in assay well − % Annexin-V-APC positive in the control well) × 100/(100 − % Annexin-V-APC positive in the control well).

In addition to the annexinV/7-AAD assay, caspase assays can also be utilized to determine apoptosis. Caspase-3/7 enzymatic activity levels are measured using the Apo-ONE homogenous caspase-3/7 assay (Promega) and performed following the instructions of the manufacturer. The kit provides a caspase-3/7 substrate and rhodamine 110, bis-(*N*-CBZ-L-aspartyl-L-glutamyl-L-valyl-L-aspartic acid amide), which is cleaved by enzymatically active caspase-3/7 resulting in a fluorogenic cleavage product. MDA-MB-231 cells are seeded to a density of 6.0×10^3 cells/well in 96-well plates and grown for 48 h in culture media containing 10% FBS. Cells are then treated with liposomal or nonliposomal C_6 for 24 h in media containing 1% FBS.

4.4. Measurement of reactive oxygen species and mitochondrial membrane potential

It is documented that ceramide treatment results in increased production of reactive oxygen species (ROS) due to its ability to uncouple the electron transport chain and cause oxidative cell damage (Birbes *et al.*, 2002; Di Paola *et al.*, 2000; Garcia-Ruiz *et al.*, 1997). The amount of cytoplasmic ROS production is used to determine the level of cellular oxidative stress. Cells treated for 2–6 h with C_6-ceramide nanoliposomes are collected and resuspended in PBS containing freshly prepared 1–10 μ*M* (manufacturer suggests treatment range 1–10 μ*M*) H_2-DCF-DA (Molecular Probes) at 37 °C in the dark for 30 min. This reagent penetrates cells and emits green fluorescence on oxidation with H_2O_2. Next, the cells are incubated for 30 min with 2 μ*M* H_2-DCF-DA. The cells are then washed twice in PBS, and 10,000 events are analyzed immediately by cell flow cytometry at 488 nm excitation and

530 nm emissions (BD FACScalibur). H_2O_2 is used as a positive control at a 1 μM concentration.

In addition to ROS, measurement of mitochondrial membrane potential (MMP) can also be used to determine the effectiveness of C_6-ceramide nanoliposome treatment. We utilized JC-1, an MMP indicator to show changes in MMP for RNK16 and human NK-LGL cells. JC-1, a cationic and lipophilic dye (Invitrogen) specifically permeates mitochondrial membranes and fluoresces red when it aggregates in the matrix of healthy, high potential mitochondria, whereas it fluoresces green in cells with low MMP. Cells are collected after a 24 h treatment with C_6-ceramide nanoliposomes, and then incubated with 2 μg/ml JC-1 dye at a density of 5×10^5 cells/0.5 ml. After incubation for 20 min at 37 °C in the dark, samples are washed twice with PBS and then incubated for 15 min at 37 °C in the dark with Annexin-V-APC (BD Biosciences). Cells are immediately analyzed by flow cytometry on a BD FACScalibur at 488-nm excitation and collection of 10,000 events. Data are collected at 530-nm emission for green fluorescence and 590-nm for red fluorescence (BD FACScalibur).

5. Evaluation of C_6-Ceramide Nanoliposomes *In Vivo*

5.1. Determination of the maximum tolerated dose of C_6-ceramide nanoliposomes

C_6-ceramide nanoliposome concentrations for use in animal model systems are determined via a maximum tolerated dose (MTD) study. Typically, groups of three rats or mice receive intravenous (i.v.) injections of the C_6-ceramide nanoliposome at a starting concentration of 10 mg/kg. Animals are then monitored periodically for 24 h for signs of toxicity through liver enzyme analysis, complete blood count (CBC), and assessments of respiratory difficulties, gastrointestinal distress, spastic paralysis, and blindness. If these signs of toxicity are observed, then the same dose injection would be given every other day for 3–4 weeks for a total of 10–15 doses, with animals monitored daily for signs of delayed toxicity. Next, dose-escalation or reduction is followed with a modified Fibonacci sequence, until 2/3 of the animals demonstrate significant side effects. The next lower dose is then taken to be the MTD.

5.2. Pharmacokinetic and tissue distribution of C_6-ceramide nanoliposomes *in vivo*

Pharmacokinetics and biodistribution of C_6-ceramide nanoliposomes in tissues are performed following the i.v. administration of these nanoliposomes that have incorporated [^{3}H]C_6-ceramide (Stover and Kester, 2003),

or the dual labeled [^{3}H] DSPC and [^{14}C]C_6-ceramide (Zolnik *et al.*, 2008). Groups of three rats or mice are treated with the C_6-ceramide nanoliposomes at the MTD. The same dose of control, "ghost" nanoliposomes (containing no C_6-ceramide) with the amount of C_8-ceramide lipid adjusted accordingly to maintain a similar ratio to the C_6-ceramide nanoliposome, is injected into the animals as a control. At time points of 1 min, 10 min, 30 min, 1 h, 4 h, and 24 h, the animals are sacrificed, and the blood, spleen, liver, kidney, and heart tissues are extracted and rapidly washed and solubilized with Solvable (Perkin Elmer). The mass of total C_6 per milligram of tissue or blood is calculated from the radioactivity obtained from [^{14}C] C_6-ceramide and of [^{3}H]DSPC (both obtained from American Radiolabeled Chemicals) through scintillation counting, using dual label mode (Beckman Coulter LS6500) (Zolnik *et al.*, 2008).

5.3. Efficacy of C_6-ceramide nanoliposomes *in vivo*

We have successfully treated both leukemic rat and subcutaneous xenograft athymic nude mouse models with our C_6-ceramide nanoliposomes. In addition, we are also currently working on treating orthotopic hepatocellular and pancreatic cancer models. For LGL leukemia, we use male F344 rats of approximately 6 weeks in age that are inoculated intraperitoneally with 1×10^6 RNK16 cells. LGL leukemia then takes 4–5 weeks to develop and is monitored through CBC. Treatment commences once rats have elevated white blood cell and leukemic cell counts in blood. Rats are then injected three times a week via tail vein injections with 40 mg/kg C_6-ceramide nanoliposomes for 6 weeks. Such an approach resulted in complete remission in 5/14 rats (Liu *et al.*, 2010). For subcutaneous athymic nude mouse models, $1–10 \times 10^6$ cells (amount may vary depending on the aggressiveness of the cancer) are injected subcutaneously. In particular, for melanoma, 5×10^6 UACC 903 or 1205 Lu cells, for breast cancer, 10×10^6 MDA-MB-231 cells, and for HCC, 5×10^6 SK-HEP-1 cells are injected bilaterally into flanks of the mouse, resulting in two tumors per animal. Nanoliposomal ceramide is then delivered daily via i.v. injection at 36 mg/kg in combination with Sorafenib, a multikinase inhibitor shown to be effective in renal cell carcinoma, resulted in a 58% reduction in tumor size (Stover *et al.*, 2005; Tran *et al.*, 2008).

5.4. Determination of *in vivo* cell apoptosis

To assess the degree of C_6-ceramide-induced cellular apoptosis *in vivo*, the TUNEL *in situ* cell death fluorescence in detection kit (Roche) is utilized to determine DNA fragmentation in sections of spleen, liver, thymus, lymph node, stomach, kidney, and lung. Positive control slides are treated with 300 U/ml DNase for 1–10 min at 37 °C to induce DNA strand breaks, prior to TUNEL labeling.

6. Concluding Remarks

Liposomes have proven to be effective vehicles for delivery of many therapeutic agents to cancer, in particular the FDA-approved doxorubicin encapsulating nanoliposome (DOXIL; Ellerhorst *et al.*, 1999). However, there are many complexities associated with the design, such as avoidance of an immune response, increased circulation time, and effective targeting (Tran *et al.*, 2009). The main issue in the development of C_6-ceramide nanoliposomes focuses on the issue of selectivity. Currently, we rely on passive targeting, as most tumors have a "leaky vasculature," which is a result of irregular basement membranes containing ~200 nm gaps (Aagaard and Rossi, 2007). Due to this occurrence, cancer cells are more likely to accumulate the liposomes due to the principle of enhanced permeability and retention. As a result, our C_6-ceramide nanoliposomes have managed to selectively and effectively target cancerous cells, including melanoma, NK-LGL leukemic cells, and breast cancer cells while sparing melanocytes, PBMCs, and mammary epithelial cells, respectively (Barth *et al.*, 2011). However, a direct targeting approach would result in more efficacious delivery and treatment. Surfaces of cancer cells have many unique markers and proteins that could be exploited, thus allowing for more selectivity toward cancer cells versus normal surrounding cells. This could be performed through the conjugation of various antibodies or peptides to the liposome through maleimide or *N*-hydroxysuccinimide (NHS) chemistry.

In addition to targeting, another area being explored with the C_6-ceramide nanoliposomal formulation involves the encapsulation of siRNA/shRNA or drugs. Gene therapy is currently hindered by an effective delivery method, and our liposomes could provide an effective vehicle of delivering siRNA/shRNA to cancer cells while also providing a dose of C_6-ceramide in a nontoxic manner. We are presently working on second-generation C_6-ceramide nanoliposomes that encapsulate macromolecule-based therapeutics within minimally cationic, nontoxic formulations. We are also pursuing encapsulation of drugs within C_6 nanoliposomes as another second-generation option (Jiang *et al.*, 2011). Hydrophilic drugs may be loaded into the hydrophilic center of the liposomes utilizing a pH gradient, or may be included in the initial buffer solution used for hydrating the dried lipids (Salem *et al.*, 2005). For encapsulating hydrophobic drugs, the agent would need to be dried down at the beginning with the lipids before the rehydration step and eventual extrusion. Various methods including radiolabeling or HPLC/MS strategies can be used to determine encapsulation efficiency and release kinetics.

Our nanoliposomes have been fully characterized by the Nanotechnology Characterization Laboratory at NCI (Frederick, MD) and deemed to be efficacious with minimum toxicity (Zolnik *et al.*, 2008). Currently, we

propose to extend our findings by manufacturing and validating scaled-up, sterile-filtered, good manufacturing practice (GMP)-grade C_6-ceramide-nanoliposomes. The quantitative milestone will be the filing of an FDA-IND application to support first-in-man studies in HCC, where there is an unmet need for effective treatment resulting in 95% fatal cases within 7 months. This Phase I study will include Sorafenib-treated HCC patients to assess dose and toxicity. Our novel C_6-ceramide nanoliposome formulation has resulted in significant decreased cellular proliferation, increased cellular apoptosis, and inhibited tumor progression *in vivo* in a variety of cancer models, and as a result, we hope to accomplish these same goals in humans.

Conflict of Interest Statement. The Penn State Research Foundation has licensed ceramide-containing and ceramide-regulating nanoliposomes and calcium phosphosilicate nanoparticles to Keystone Nano, Inc. (State College, PA) for commercialization. M. K. serves as CMO of Keystone Nano, Inc.

REFERENCES

Aagaard, L., and Rossi, J. J. (2007). RNAi therapeutics: Principles, prospects and challenges. *Adv. Drug Deliv. Rev.* **59,** 75–86.

Barth, B. M., Cabot, M. C., and Kester, M. (2011). Ceramide-based therapeutics for the treatment of cancer. *Anticancer Agents Med. Chem.* **11**(9), 911–919.

Birbes, H., El Bawab, S., Obeid, L. M., and Hannun, Y. A. (2002). Mitochondria and ceramide: Intertwined roles in regulation of apoptosis. *Adv. Enzyme Regul.* **42,** 113–129.

Carver, L. A., and Schnitzer, J. E. (2003). Caveolae: Mining little caves for new cancer targets. *Nat. Rev. Cancer* **3,** 571–581.

Cremesti, A. E., Goni, F. M., and Kolesnick, R. (2002). Role of sphingomyelinase and ceramide in modulating rafts: Do biophysical properties determine biologic outcome? *FEBS Lett.* **531,** 47–53.

De Jong, W. H., and Borm, P. J. (2008). Drug delivery and nanoparticles:Applications and hazards. *Int. J. Nanomedicine* **3,** 133–149.

Desai, A., Vyas, T., and Amiji, M. (2008). Cytotoxicity and apoptosis enhancement in brain tumor cells upon coadministration of paclitaxel and ceramide in nanoemulsion formulations. *J. Pharm. Sci.* **97,** 2745–2756.

Devalapally, H., Duan, Z., Seiden, M. V., and Amiji, M. M. (2007). Paclitaxel and ceramide co-administration in biodegradable polymeric nanoparticulate delivery system to overcome drug resistance in ovarian cancer. *Int. J. Cancer* **121,** 1830–1838.

Devalapally, H., Duan, Z., Seiden, M. V., and Amiji, M. M. (2008). Modulation of drug resistance in ovarian adenocarcinoma by enhancing intracellular ceramide using tamoxifen-loaded biodegradable polymeric nanoparticles. *Clin. Cancer Res.* **14,** 3193–3203.

Di Paola, M., Cocco, T., and Lorusso, M. (2000). Ceramide interaction with the respiratory chain of heart mitochondria. *Biochemistry* **39,** 6660–6668.

Ellerhorst, J. A., Bedikian, A., Ring, S., Buzaid, A. C., Eton, O., and Legha, S. S. (1999). Phase II trial of doxil for patients with metastatic melanoma refractory to frontline therapy. *Oncol. Rep.* **6,** 1097–1099.

Farhood, H., Serbina, N., and Huang, L. (1995). The role of dioleoyl phosphatidylethanolamine in cationic liposome mediated gene transfer. *Biochim. Biophys. Acta* **1235,** 289–295.

Finnegan, C. M., Rawat, S. S., Puri, A., Wang, J. M., Ruscetti, F. W., and Blumenthal, R. (2004). Ceramide, a target for antiretroviral therapy. *Proc. Natl. Acad. Sci. USA* **101,** 15452–15457.

Gabizon, A., and Martin, F. (1997). Polyethylene glycol-coated (pegylated) liposomal doxorubicin. Rationale for use in solid tumours. *Drugs* **54**(Suppl. 4), 15–21.

Garcia-Ruiz, C., Colell, A., Mari, M., Morales, A., and Fernandez-Checa, J. C. (1997). Direct effect of ceramide on the mitochondrial electron transport chain leads to generation of reactive oxygen species. Role of mitochondrial glutathione. *J. Biol. Chem.* **272,** 11369–11377.

Haimovitz-Friedman, A., Kan, C. C., Ehleiter, D., Persaud, R. S., McLoughlin, M., Fuks, Z., and Kolesnick, R. N. (1994). Ionizing radiation acts on cellular membranes to generate ceramide and initiate apoptosis. *J. Exp. Med.* **180,** 525–535.

Ihrlund, L. S., Hernlund, E., Khan, O., and Shoshan, M. C. (2008). 3-Bromopyruvate as inhibitor of tumour cell energy metabolism and chemopotentiator of platinum drugs. *Mol. Oncol.* **2,** 94–101.

Jiang, Y., Divittore, N. A., Kaiser, J. M., Shanmugavelandy, S. S., Fritz, J. L., Heakal, Y., Tagaram, H. R., Cheng, H., Cabot, M. C., Staveley-O'Carroll, K. F., Tran, M. A., Fox, T. E., *et al.* (2011). Combinatorial therapies improve the therapeutic efficacy of nanoliposomal ceramide for pancreatic cancer. *Cancer Biol. Ther.* **12,** 574–585.

Karahatay, S., Thomas, K., Koybasi, S., Senkal, C. E., Elojeimy, S., Liu, X., Bielawski, J., Day, T. A., Gillespie, M. B., Sinha, D., Norris, J. S., Hannun, Y. A., and Ogretmen, B. (2007). Clinical relevance of ceramide metabolism in the pathogenesis of human head and neck squamous cell carcinoma (HNSCC): Attenuation of C(18)-ceramide in HNSCC tumors correlates with lymphovascular invasion and nodal metastasis. *Cancer Lett.* **256,** 101–111.

Khazanov, E., Priev, A., Shillemans, J. P., and Barenholz, Y. (2008). Physicochemical and biological characterization of ceramide-containing liposomes: Paving the way to ceramide therapeutic application. *Langmuir* **24,** 6965–6980.

Kolesnick, R. N., and Kronke, M. (1998). Regulation of ceramide production and apoptosis. *Annu. Rev. Physiol.* **60,** 643–665.

Liu, X., Ryland, L., Yang, J., Liao, A., Aliaga, C., Watts, R., Tan, S. F., Kaiser, J., Shanmugavelandy, S. S., Rogers, A., Loughran, K., Petersen, B., *et al.* (2010). Targeting of survivin by nanoliposomal ceramide induces complete remission in a rat model of NK-LGL leukemia. *Blood* **116,** 4192–4201.

Merrill, A. H., Jr., and Jones, D. D. (1990). An update of the enzymology and regulation of sphingomyelin metabolism. *Biochim. Biophys. Acta* **1044,** 1–12.

Messner, M. C., and Cabot, M. C. (2010). Glucosylceramide in humans. *Adv. Exp. Med. Biol.* **688,** 156–164.

Morgan, T. T., Muddana, H. S., Altinoglu, E. I., Rouse, S. M., Tabakovic, A., Tabouillot, T., Russin, T. J., Shanmugavelandy, S. S., Butler, P. J., Eklund, P. C., Yun, J. K., Kester, M., *et al.* (2008). Encapsulation of organic molecules in calcium phosphate nanocomposite particles for intracellular imaging and drug delivery. *Nano Lett.* **8,** 4108–4115.

NCL, T. R. (2007). NCL Technical Reports, NCL200702A.

Radin, N. S. (2001). Killing cancer cells by poly-drug elevation of ceramide levels: A hypothesis whose time has come? *Eur. J. Biochem.* **268,** 193–204.

Ryland, L. K., Fox, T. E., Liu, X., Loughran, T. P., and Kester, M. (2011). Dysregulation of sphingolipid metabolism in cancer. *Cancer Biol. Ther.* **11,** 138–149.

Saddoughi, S. A., Song, P., and Ogretmen, B. (2008). Roles of bioactive sphingolipids in cancer biology and therapeutics. *Dŭzgüneş Biochem.* **49,** 413–440.

Salem, I. I., Flasher, D. L., and Düzgüneş, N. (2005). Liposome-encapsulated antibiotics. *Methods Enzymol.* **391,** 261–291.

Schiffmann, S., Sandner, J., Birod, K., Wobst, I., Angioni, C., Ruckhaberle, E., Kaufmann, M., Ackermann, H., Lotsch, J., Schmidt, H., Geisslinger, G., and Grosch, S. (2009). Ceramide synthases and ceramide levels are increased in breast cancer tissue. *Carcinogenesis* **30,** 745–752.

Schroeder, F., Gallegos, A. M., Atshaves, B. P., Storey, S. M., McIntosh, A. L., Petrescu, A. D., Huang, H., Starodub, O., Chao, H., Yang, H., Frolov, A., and Kier, A. B. (2001). Recent advances in membrane microdomains: Rafts, caveolae, and intracellular cholesterol trafficking. *Exp. Biol. Med. (Maywood)* **226,** 873–890.

Shabbits, J. A., and Mayer, L. D. (2003a). High ceramide content liposomes with in vivo antitumor activity. *Anticancer Res.* **23,** 3663–3669.

Shabbits, J. A., and Mayer, L. D. (2003b). Intracellular delivery of ceramide lipids via liposomes enhances apoptosis in vitro. *Biochim. Biophys. Acta* **1612,** 98–106.

Stover, T., and Kester, M. (2003). Liposomal delivery enhances short-chain ceramide-induced apoptosis of breast cancer cells. *J. Pharmacol. Exp. Ther.* **307,** 468–475.

Stover, T. C., Sharma, A., Robertson, G. P., and Kester, M. (2005). Systemic delivery of liposomal short-chain ceramide limits solid tumor growth in murine models of breast adenocarcinoma. *Clin. Cancer Res.* **11,** 3465–3474.

Stover, T. C., Kim, Y. S., Lowe, T. L., and Kester, M. (2008). Thermoresponsive and biodegradable linear-dendritic nanoparticles for targeted and sustained release of a pro-apoptotic drug. *Biomaterials* **29,** 359–369.

Tagaram, H. R., Divittore, N. A., Barth, B. M., Kaiser, J. M., Avella, D., Kimchi, E. T., Jiang, Y., Isom, H. C., Kester, M., and Staveley-O'Carroll, K. F. (2011). Nanoliposomal ceramide prevents in vivo growth of hepatocellular carcinoma. *Gut* **60,** 695–701.

Tokudome, Y., Saito, Y., Sato, F., Kikuchi, M., Hinokitani, T., and Goto, K. (2009). Preparation and characterization of ceramide-based liposomes with high fusion activity and high membrane fluidity. *Colloids Surf. B Biointerfaces* **73,** 92–96.

Tran, M. A., Smith, C. D., Kester, M., and Robertson, G. P. (2008). Combining nanoliposomal ceramide with sorafenib synergistically inhibits melanoma and breast cancer cell survival to decrease tumor development. *Clin. Cancer Res.* **14,** 3571–3581.

Tran, M. A., Watts, R. J., and Robertson, G. P. (2009). Use of liposomes as drug delivery vehicles for treatment of melanoma. *Pigment Cell Melanoma Res.* **22,** 388–399.

van Vlerken, L. E., Vyas, T. K., and Amiji, M. M. (2007). Poly(ethylene glycol)-modified nanocarriers for tumor-targeted and intracellular delivery. *Pharm. Res.* **24,** 1405–1414.

Zolnik, B. S., Stern, S. T., Kaiser, J. M., Heakal, Y., Clogston, J. D., Kester, M., and McNeil, S. E. (2008). Rapid distribution of liposomal short-chain ceramide in vitro and in vivo. *Drug Metab. Dispos.* **36,** 1709–1715.

CHAPTER SIX

Multistage Nanoparticles for Improved Delivery into Tumor Tissue

Triantafyllos Stylianopoulos,[*] Cliff Wong,[†] Moungi G. Bawendi,[†] Rakesh K. Jain,[‡] *and* Dai Fukumura[‡]

Contents

Abstract

The enhanced permeability and retention (EPR) effect has been a key rationale for the development of nanoscale carriers to solid tumors. As a consequence of EPR, nanotherapeutics are expected to improve drug and detection probe delivery, have less adverse effects than conventional chemotherapy, and thus

[*] Department of Mechanical and Manufacturing Engineering, University of Cyprus, Nicosia, Cyprus
[†] Department of Chemistry, Massachusetts Institute of Technology, Cambridge, Massachusetts, USA
[‡] Edwin L. Steele Laboratory, Massachusetts General Hospital and Harvard Medical School, Boston, Massachusetts, USA

Methods in Enzymology, Volume 508
ISSN 0076-6879, DOI: 10.1016/B978-0-12-391860-4.00006-9

result in improved detection and treatment of tumors. Physiological barriers posed by the abnormal tumor microenvironment, however, can hinder the homogeneous delivery of nanomedicine in amounts sufficient to eradicate cancer. To effectively enhance the therapeutic outcome of cancer patients by nanotherapeutics, we have to find ways to overcome these barriers. One possibility is to exploit the abnormal tumor microenvironment for selective and improved delivery of therapeutic agents to tumors. Recently, we proposed a multistage nanoparticle delivery system as a potential means to enable uniform delivery throughout the tumor and improve the efficacy of anticancer therapy. Here, we describe the synthesis of a novel multistage nanoparticle formulation that shrinks in size once it enters the tumor interstitial space to optimize the delivery to tumors as well as within tumors. Finally, we provide detailed experimental methods for the characterization of such nanoparticles.

1. Introduction

Systemic administration of nanomedicines to solid tumors is a three-step process (Jain, 1987a,b, 2001; Jain and Baxter, 1988). Nanoparticles have to first travel through the blood vessels and reach the tumor tissue. Subsequently, the nanoparticles need to cross the tumor vessel walls and finally travel through the interstitial space to attack cancer cells. For optimal delivery and enhanced therapeutic efficacy, nanoscale drugs must have long circulation times in the bloodstream, and effective transport across the tumor vessel walls, as well as through the tumor interstitial space (Chauhan *et al.*, 2011; Jain and Stylianopoulos, 2010).

1.1. Considerations for vascular transport of nanoparticles

Provided the therapeutic agent is not toxic to normal organs, it is reasonable to prolong blood circulation time to allow longer interaction with the tumor tissue. Blood circulation time is determined by the clearance rate through renal excretion and interactions with the reticuloendothelial system in the liver and the spleen. Relatively, small nanoparticles with hydrodynamic diameter smaller than 6 nm have a blood half-life < 600 min and are rapidly cleared by the kidney, whereas the blood half-life of larger particles might exceed 1000 min (Choi *et al.*, 2010, 2007; Longmire *et al.*, 2008; Petros and DeSimone, 2010; Popovic *et al.*, 2010). Clearance from the reticuloendothelial system might vary significantly among the different types of nanoparticles and can be controlled by surface modifications (Franzen and Lommel, 2009; Longmire *et al.*, 2008). Today, coating the surface of a nanoparticle with a layer of polyethyleneglycol (PEG) is a common practice. Attachment of PEG to the surface sterically stabilizes nanoparticles and results in a near neutral surface charge. PEGylation protects nanoparticles from opsonization by

serum proteins and phagocytosis by Kupffer cells and hepatocytes (Klibanov *et al.*, 1990; Peracchia *et al.*, 1999; Storm *et al.*, 1995).

1.2. Considerations for transvascular transport of nanoparticles

Transport across the tumor vessel walls and through the tumor interstitial space is determined by the properties of the nanoparticle (size, shape, and charge) and the tumor architecture (Baish *et al.*, 2011; Jain, 1987a; Popovic *et al.*, 2010; Stylianopoulos *et al.*, 2010a,b). Tumor vessels are in general tortuous and nonuniformly distributed, typically exhibiting high vascular density in the periphery and lower in the center of the tumor (Chauhan *et al.*, 2011; Jain and Baxter, 1988; Vakoc *et al.*, 2009). In addition, many tumor vessels have an abnormal endothelial cell lining, detached pericytes, and an abnormally thick or thin basement membrane (Fig. 6.1; Jain, 1987a). As a result, the size of the pores of the vessel walls is heterogeneous. We have shown previously that the pore size ranges from 10 to 2000 nm in various tumors growing in animal models (Hashizume *et al.*, 2000; Hobbs *et al.*, 1998). Collectively, tumor vessels are nonuniformly leaky and have relatively larger pore size, on average, than normal vessels. This is the actual basis of the EPR effect.

Many normal vessels have a pore size in the range of 10 nm, much larger than the size of a chemotherapeutic molecule (<1 nm), but smaller than the size of most nanoparticle formulations. As a result, systemically administered chemotherapeutics are delivered effectively not only to tumors but also to normal tissues. Since chemotherapeutics are toxic to both cancer and normal cells, lack of preferential delivery results in significant adverse effects in normal tissues. On the contrary, a nanoparticle with size larger than the pore size of normal vessels could preferentially pass through the pores of tumor vessels and diminish the adverse effects.

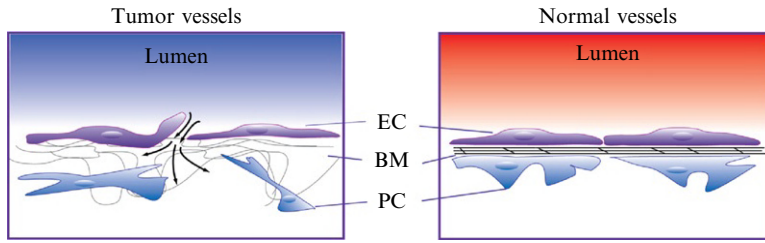

Figure 6.1 Contrary to normal vessels (right), tumor vessels (left) might have an abnormal endothelial cell (EC) lining, an abnormally thick or thin basement membrane (BM), and detached or absent pericytes (PC). As a result, nanoparticles can more easily pass through the tumor vessel wall.

1.3. Considerations for interstitial transport of nanoparticles

The hyperpermeability of tumor vessels combined with the absence of functional lymphatic vessels at the center of the tumor leads to a uniformly elevated interstitial fluid pressure (IFP) (Boucher and Jain, 1992; Boucher *et al.*, 1990, 1991; Gutmann *et al.*, 1992; Jain and Baxter, 1988; Less *et al.*, 1992; Roh *et al.*, 1991). IFP in many tumors might be as high as microvascular pressure (MVP), whereas in many cases, it can locally exceed MVP. This effect might diminish pressure gradients across the vessel walls and in the tumor interstitial space (Baxter and Jain, 1989, 1990; Jain and Baxter, 1988; Jain *et al.*, 2007). In such a case, the main mechanism of drug transport is diffusion, which can be a very slow process, particularly for large nanoparticles (Chary and Jain, 1989; Nugent and Jain, 1984; Pluen *et al.*, 2001; Ramanujan *et al.*, 2002).

In addition, in many tumors there is an accumulation of fibrillar collagen types I and III in the interstitial space, presumably due to increased activity of factors, such as transforming growth factor-β (TGF-β), that might stiffen the extracellular matrix and induce fibrosis (Branton and Kopp, 1999; Brown *et al.*, 2003; Butcher *et al.*, 2009; Diop-Frimpong *et al.*, 2011; Egeblad *et al.*, 2010; Huijbers *et al.*, 2010; Kauppila *et al.*, 1998; McKee *et al.*, 2006; Netti *et al.*, 2000). Increased fibrillar collagen may hinder the diffusion of nanoparticles in tumors. In particular, it has been shown that, in collagen-rich tumors, nanoparticles with hydrodynamic diameter larger than 60 nm might not be able to effectively penetrate the collagen network that comprises the tumor interstitium (Brown *et al.*, 2003; Diop-Frimpong *et al.*, 2011; McKee *et al.*, 2006; Netti *et al.*, 2000; Pluen *et al.*, 2001). These particles will cross the leaky tumor vessels, but because they cannot diffuse effectively, they are likely to accumulate in perivascular regions and cause only local effects (Yuan *et al.*, 1994). One approach to improve the delivery is to modify the collagen matrix (Brown *et al.*, 2003; Diop-Frimpong *et al.*, 2011; McKee *et al.*, 2006; Netti *et al.*, 2000). In the next section, we discuss an alternative approach—a multistage delivery system to overcome this challenge.

1.4. Multistage nanoparticle systems to optimize drug delivery

Currently, FDA-approved anticancer nanoparticles include Doxil® (ovarian cancers, metastatic breast cancers, and HIV-related Kaposi's sarcomas) and Abraxane® (metastatic breast cancers). The size of these nanoparticles is ~100 nm in diameter. Both Doxil® and Abraxane® are associated with significant reduction in the adverse effects as compared to conventional chemotherapy. However, the survival benefit is relatively modest presumably due to inadequate delivery to tumors (Gordon *et al.*, 2001; Gradishar *et al.*, 2005; Jain and Stylianopoulos, 2010). For optimal efficacy, a therapeutic agent

must reach tumors in amounts sufficient to destroy cancer cells, but at the same time should not cause significant adverse effects in normal tissues. In general, relatively small size nanoparticles have higher transvascular and interstitial transport (Popovic *et al.*, 2010). However, small particles might have a shorter blood half-life and be delivered to normal tissues, causing adverse effects. Therefore, the size of the particle needs initially to be relatively large to achieve high blood half-life and selective extravasation, but once it enters the tumor interstitium, it needs to have a small size for effective and uniform penetration. These contradicting/opposing demands for the size of nanomedicines have led to the development of multistage nanoparticles that are able to change their size in response to stimuli from the tumor microenvironment.

We describe the synthesis of a multistage nanoparticle delivery system which initially has a size of ~100 nm, but when it reaches the tumor, it shrinks its size to a ~10 nm particle that can more effectively diffuse throughout the tumor interstitial space (Fig. 6.2; Wong *et al.*, 2011). To achieve this size change in tumor tissues, the methodology makes use of matrix metalloproteinase (MMP) enzymes that are overexpressed in the microenvironment of many tumors to degrade the core of a ~100-nm gelatin nanoparticle so that smaller ~10 nm diagnostic or therapeutic agents can be released from its surface. Methods to assess the size change of the nanoparticle upon MMP activation, such as gel filtration chromatography

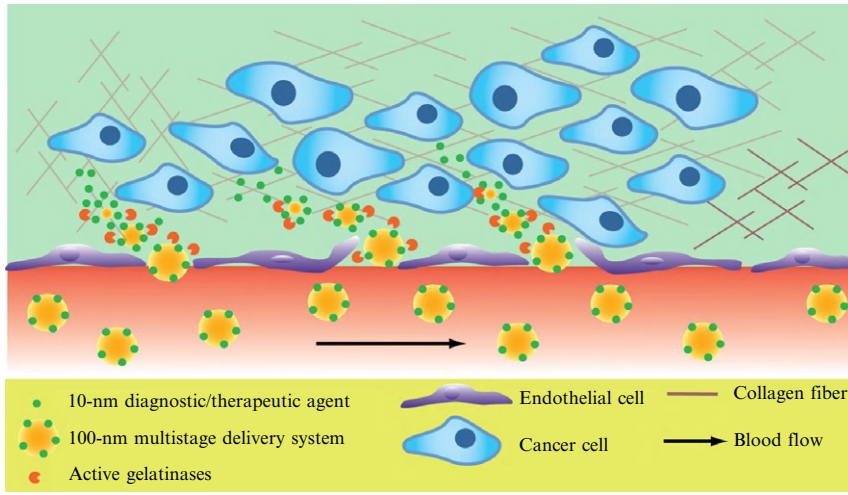

Figure 6.2 Schematic representation of the multistage nanoparticle delivery system. The initial 100-nm gelatin particle accumulates preferentially around leaky vessels in tumor tissue. Because of its large size, the 100-nm particle cannot penetrate the dense collagen matrix of the interstitial space. MMP-2 activity can degrade the gelatin core of the 100-nm particle and release smaller 10-nm particles from its surface. These particles can penetrate deep into the tumor due to their small size.

(GFC), fluorescence correlation spectroscopy (FCS), as well as diffusion measurements in collagen gels, are described in detail. *In vivo* techniques based on intravital microscopy (IVM) that are used to measure the delivery of multistage nanoparticles in animal models are also discussed. These techniques include systemic and local administration of the multistage nanoparticles in human tumor xenografts to estimate blood half-life, systemic delivery, and interstitial transport.

2. Synthesis of Gelatin-Quantum Dot Nanoparticles (QDGelNP)

2.1. Synthesis of gelatin nanoparticles

Reagents used for the synthesis of the gelatin particles include:

1. Gelatin type A ~175 bloom from porcine skin (Sigma).
2. Acetone (EMD Chemicals).
3. Deionized water (Thermo Scientific® Barnstead Nanopure).
4. HCl solution, 1 N (Sigma).
5. Glutaraldehyde solution (Grade I, 50%) (Sigma).
6. Glycine solution, 1 *M* (Sigma).
7. 10× PBS (EMD Chemicals).

To synthesize the gelatin nanoparticles, we perform the following steps (Wong *et al.*, 2011; Fig. 6.3): 0.625 g of gelatin is added to 12.5 ml of deionized water and heated to 40 °C in a 100-ml round-bottom flask until

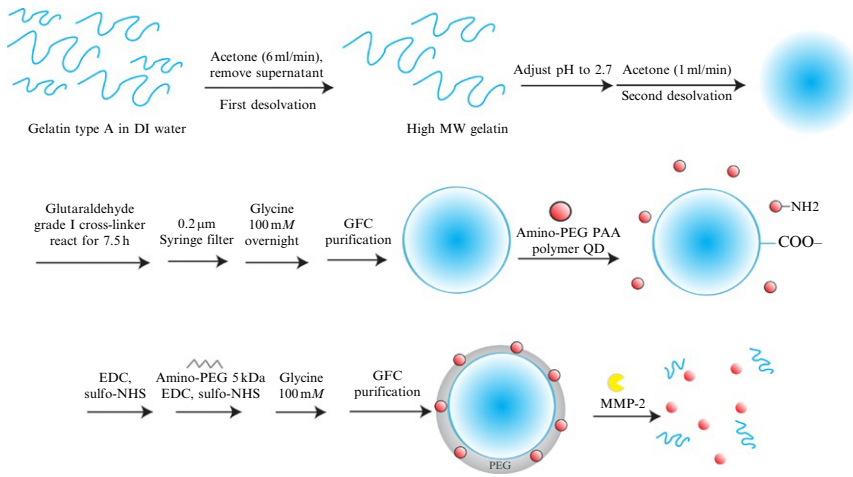

Figure 6.3 Stages of QDGelNP synthesis.

fully dissolved. The flask is then removed from heat and 12.5 ml of acetone are added to the solution at 6.0 ml/min using a PHD2000 syringe pump (Harvard Apparatus, Holliston, MA, USA) while stirring at 300 rpm. The high-molecular weight gelatin fraction will began precipitating onto the bottom of the round-bottom flask. The stirring is turned off when the acetone addition is complete. Exactly 1 min after the addition of acetone, the supernatant containing the low-molecular weight gelatin fraction is discarded. Deionized water (12.5 ml) is added to the remaining precipitate and heated again to 40 °C, until complete dissolution. Half the solution is removed and the pH of this half is adjusted to 2.7 with a 1 N HCl solution while recording the exact volume needed. The pH is monitored using a Thermo Orion PerpHecT Sure-Flow pH electrode (Thermo Fisher Scientific, Asheville, NC, USA). This electrode minimizes clogging but causes contamination with the pH electrode solution. Therefore, this half of the gelatin solution is discarded after recording the amount of HCl needed to change the pH to 2.7. This exact volume of 1 N HCl solution is added to the remaining half of gelatin solution to adjust the pH to 2.7 and used for the next step. Under constant stirring at 600 rpm and 40 °C, 20.75 ml of acetone are added at 1 ml/min using the syringe pump. Following addition of ~17 ml of acetone, the solution appears cloudy white. After the acetone addition is complete, 30 μl of 50% glutaraldehyde solution (Grade I) diluted in 1 ml acetone is added to the gelatin solution at 0.05 ml/min to crosslink the particles. Afterward, the solution is kept at 40 °C and stirred at 600 rpm for 7.5 h. The acetone is then evaporated slowly at 25 °C to a final volume of 5–6 ml using a rotary evaporator. The remaining solution is first filtered through a 0.45-μm syringe filter to prevent clogging and then through a 0.2-μm syringe filter for finer size selection. A 1 *M* glycine solution (0.2 ml) is added, and the solution is stored overnight at 4 °C. The glycine should quench any remaining reactive glutaraldehyde groups. GFC is used subsequently to purify the nanoparticles. We have also tried centrifugation and centrifugal filters to purify the nanoparticles, but they both result in an increase in the size of the particles. A 1 ml solution of the gelatin particles is injected into a Superose™ 6 GL 10/300 column (GE Healthcare, Piscataway, NJ, USA) with 1× PBS as the mobile phase. The peak eluting at the void volume is collected with 0.5 ml fractions. This procedure is repeated one more time, and the first concentrated fractions from both GFC runs are combined. This 1 ml solution is then taken to the next step for quantum dot (QD) conjugation and PEGylation.

2.2. Synthesis of gelatin-quantum dot nanoparticles

Reagents used for the synthesis of the QDGelNP include:

1. Gelatin nanoparticles (see Section 2.1).
2. Hydroxysulfosuccinimide sodium salt (sulfo-NHS) (Sigma).

3. *N*-(3-Dimethylaminopropyl)-*N′*-ethylcarbodiimide hydrochloride (EDC) (Sigma).
4. Methoxypolyethylene glycol amine 5000 (mPEG-amine 5 kDa) (Sigma).
5. HEPES buffer (EMD Chemicals).
6. Qdot® 565 ITK™ amino (PEG) quantum dot (Invitrogen).

The 1 ml gelatin nanoparticle (NP) solution is mixed with 20 μl of 8 μ*M* Qdot® 565 ITK™ amino (PEG) QDs in a 7-ml glass vial. The solution is gently stirred at 130 rpm for 30 min. High stir speeds result in particle aggregation. Afterwards, the pH is changed to 5 using 1 N HCl solution and then immediately adjusted to pH 6 using 1 N NaOH. The pH is checked by removing 1 μl of the solution using a 10 μl micropipette and applying it onto a pH strip. Stirring is continued for 30 min. EDC (0.4 mg, 2.1 μmol) and sulfo-NHS (0.4 mg, 1.9 μmol) are dissolved in 50 μl of deionized water and then added to the gelatin NP/QD mixture. The reaction proceeds for 3 h. Subsequently, mPEG-amine 5 kDa (20 mg, ~4 μmol) dissolved in 50 μl of deionized water is added to the gelatin NP/QD solution. Then, another solution of EDC (0.4 mg) and sulfo-NHS (0.4 mg) dissolved in 50 μl of deionized water is added. After 2 h of reaction, the pH is adjusted to 8 using 1 N NaOH, and the stirring continues for 1 h. A 1 *M* glycine solution (50 μl) is added to quench the reaction. After 30 min, the resulting solution is filtered through a 0.2 μm syringe filter to remove any aggregates. This solution is then purified using GFC with the Superose™ 6 column. The mobile phase for the GFC is 50 m*M* HEPES buffer at pH 7.5 for subsequent *in vitro* characterization of the QDGelNPs or PBS at pH 7.4 for subsequent *in vivo* experiments. The product eluting at the void volume is collected in 0.5 ml fractions, and the first concentrated fraction is used for further experiments.

3. Kinetics of QDGelNP Degradation

To measure the kinetics of MMP-2-induced QD release, QDGelNP are incubated with MMP-2 for various time intervals. QDGelNP (0.1 mg) in 50 m*M* HEPES and 2 m*M* $CaCl_2$ are incubated with 230 ng of MMP-2 for a maximum of 12 h at 37 °C. After incubation, an EDTA solution (200 m*M*) is added to obtain a final concentration of 20 m*M* EDTA to inhibit further MMP-2 cleavage. The samples before and after incubation are analyzed by GFC, with a Superose™ 6 GL 10/300 column on an Agilent 1100 series HPLC with an in-line degasser, autosampler, diode array detector, and fluorescence detector (Roseville, CA, USA). The injection volume is 45 μl and the mobile phase is 1 × PBS (pH 7.4) at a flow rate of 0.5 ml/min. The GFC chromatograms are detected by fluorescence, with 250 nm excitation wavelength and 565 nm emission wavelength, which

permits the measurement of only the QDs' elution profile. To normalize for changes in the QD fluorescence intensity over time and scattering effects, the integrated intensities of the chromatograms from 13 to 38 min are set to unity. The percentage of QDs that are released over time is then calculated. The peak corresponding to the free QDs is integrated (from 18 to 38 min) and then corrected for peak tailing from the peak eluting at void volume. The correction for peak tailing is done by supposing that for a certain integrated area of the peak at void volume, a fixed percentage of that integrated area will be added to the peak for individual QDs. We obtain the fixed percentage of 26.5% using QDGelNP before cleaving, which should elute completely at the void volume if not for peak tailing. A typical kinetic curve of gelatin degradation and QD release is shown in Fig. 6.4.

4. Multiphoton Fluorescence Correlation Spectroscopy

FCS is an accurate method to measure the diffusion coefficient of nanoparticles in a small focal volume allowing for two-component or anomalous diffusion measurements. It can be used with either confocal or multiphoton laser scanning microscopy, but it is restricted to low-concentration samples (Alexandrakis *et al.*, 2004; Schwille *et al.*, 1999). For multiphoton laser scanning microscopy, the laser is usually set to 800–900 nm, and it is aligned through the Pockel's cell. Photomultiplier

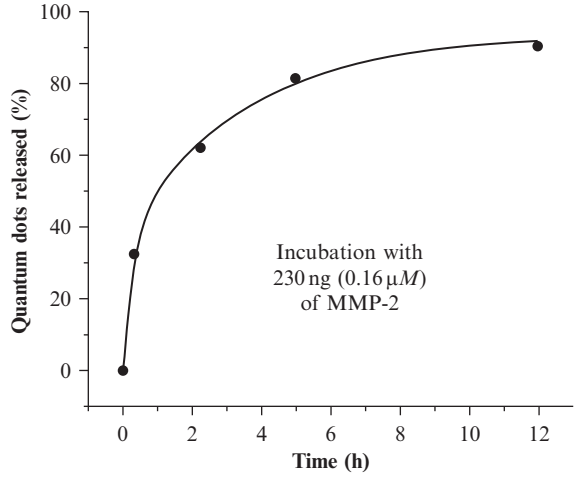

Figure 6.4 Kinetics of gelatin degradation and release of quantum dots (Wong *et al.*, 2011).

tubes (PMTs) are installed along with the appropriate band-pass filters to select the emission spectra of interest. One PMT is used for autocorrelation analysis, whereas two PMTs are required for cross-correlation. Fluctuations in fluorescence intensity are recorded as fluctuations in the photocurrent of the PMT. The PMTs are connected to a digital correlator card that performs the autocorrelation of the fluorescence intensity signal. The resulting autocorrelation curve is displayed on a computer that allows control of the data acquisition time and analysis of the autocorrelation curves. Usually, a $40\times$ or $60\times$ water emission objective is used with the microscope, and the whole system is controlled by suitable commercial software.

For *in vitro* studies, the samples of interest can be prepared by sealing a silicone perfusion chamber over a 22×50-mm glass coverslip. It is recommended to treat the coverslip surface with a 1% (w/v) casein in PBS solution to prevent nonspecific binding of nanoparticles to the surface of the glass. For *in vivo* diffusion measurements, the particles can be injected directly to the tumor microenvironment as described in Section 7.1. The concentration of the nanoparticles, the excitation power, and the acquisition time should be adjusted properly so that the diffusion measurements are not influenced by these parameters. The FCS technique is based on the analysis of fluctuations of fluorophores in the focal volume. Lower concentration of nanoparticles in the focal volume increases the intensity fluctuations and results in improvement in the quality of the FCS data (unless the signal intensity from the lower concentration sample becomes too dim). High excitation power can cause photobleaching of the particles, which might become more significant for longer acquisition times. We recommend that nanoparticle solutions of varying concentrations are tested, and the excitation power and acquisition time are tuned to get optimal conditions. We also recommend that the number of nanoparticles in the focal volume be larger than 80 but should not exceed 1000. Usually the excitation power is less than 25 mW, depending on the optical properties of the nanoparticles, and the acquisition time is from 60 to 90 s (Alexandrakis *et al.*, 2004; Stylianopoulos *et al.*, 2010b). Because FCS measurements are sensitive to random noise caused by aggregates or other sources, we suggest that 5–10 correlation curves are obtained from the same spot in the sample and their values are averaged. It is also crucial to place a cover over the sample, stage, and objective during the measurements to minimize ambient light noise.

To extract the apparent diffusion coefficient, D, the correlation curves are best-fitted to diffusion equations. For isotropic single-component diffusion, the mean-square displacement, $\langle r^2 \rangle$, of the particles is proportional to time, t: $\langle r^2 \rangle = 6Dt$. The equation for the correlation function, G, is:

$$G(t) = \frac{1}{N}\left(1 + \frac{t}{\tau_d}\right)^{-1}\left(1 + \frac{t}{K^2\tau_d}\right)^{-1/2} + G_{inf}, \qquad (6.1)$$

where N is the total number of particles in the focal volume; $K = z_o/r_o$ with z_o and r_o the axial and radial dimension of the focal volume, respectively; the characteristic time $\tau_d = r_o^2/8D$; and G_{inf} is an offset. The experimental data of $G(t)$ versus t is then fit to the above equation to determine the values of N, D, and G_{inf}.

When diffusion measurements are performed *in vivo* or in tissue phantoms (e.g., collagen gels), nanoparticles might exhibit a two-component diffusion resulting from the heterogeneous structure of the tissue. The slow component corresponds to the viscous phase of the tissue, characterized by high collagen density. The fast component corresponds to the aqueous phase, which is usual in the distant regions from the collagen fibers (Alexandrakis *et al.*, 2004; Chauhan *et al.*, 2009). For two-component diffusion, the correlation function takes the form:

$$G(t) = \frac{1}{N}\phi_1\left(1+\frac{t}{\tau_1}\right)^{-1}\left(1+\frac{t}{K^2\tau_1}\right)^{-1/2} + \frac{1}{N}\phi_2\left(1+\frac{t}{\tau_2}\right)^{-1}\left(1+\frac{t}{K^2\tau_2}\right)^{-1/2}, \tag{6.2}$$

where ϕ_1 and ϕ_2 ($\phi_2 = 1 - \phi_1$) are the population fractions of each component of the diffusion, $\tau_1 = r_o^2/8D_1$ and $\tau_2 = r_o^2/8D_2$ are the two characteristic times, and D_1 and D_2 are the two components of the diffusion coefficient. Regression of Eq. (6.2) to the experimentally obtained correlation curves determines the values of ϕ_1, D_1, and D_2.

For anomalous subdiffusion, the mean-square displacement of the particles is proportional to some power of time α ($0 < \alpha < 1$), that is, $\langle r^2\rangle = 6\Gamma t^\alpha$. In this case, the apparent diffusion coefficient depends on time and is given by the quantity $D(t) = \langle r^2\rangle/6t = \Gamma t^{\alpha-1}$. Anomalous diffusion is a generalization of normal diffusion (which occurs when $\alpha = 1$), and the autocorrelation functions are derived by replacing t/τ_d in Eq. (6.1) with $(t/\tau_d)^\alpha$ to yield

$$G(t) = \frac{1}{N}\left(1+\left(\frac{t}{\tau_d}\right)^\alpha\right)^{-1}\left(1+\frac{1}{K^2}\left(\frac{t}{\tau_d}\right)^\alpha\right)^{-1/2} + G_{inf}. \tag{6.3}$$

Finally, the dimensions of the focal volume, r_o and z_o, can be calculated by obtaining correlation curves of particles of known diffusion coefficient and fitting Eq. (6.1) to them. Such a calibration can be performed by obtaining correlation curves of fluorescent latex spheres of known diameter in water whose diffusion coefficient is given by the Stokes–Einstein relationship. Correlation curves of such particles can be measured and then Eq. (6.1) can be used to fit for K and r_o with known D. Subsequently, one can use these values of K and r_o to perform diffusion measurements of nanoparticles of interest.

5. *In Vitro* Measurements of Interstitial Penetration

In vitro measurements of the interstitial penetration of nanoparticles can be performed with collagen gels that mimic the interstitial space of tumors. The gels are usually prepared with rat tail collagen I (BD Biosciences, San Jose, CA, USA) with the addition of sodium hydroxide to convert the pH to alkaline and induce collagen gelation (Chauhan *et al.*, 2009; Ramanujan *et al.*, 2002; Stylianopoulos *et al.*, 2010b). With the addition of sodium hydroxide to the collagen, the solution is vortexed immediately to allow uniform distribution of sodium hydroxide, and it is placed into a microslide capillary tube (Vitrocom no. 2540, Mountain Lakes, NJ, USA). The capillary tube is filled partially, and the collagen is incubated overnight at 37 °C. A 20 μl mixture of QDGelNPs, either before or after incubation with MMP-2, is added to the capillary tube in contact with the free surface of the collagen gel. The particles penetrate the collagen structure, and depending on their size, they travel a different distance in the gel. The penetration distance can be measured with multiphoton laser scanning microscopy, and processing of the images with ImageJ or other image processing software. The diffusion of the particles in the tube can be considered one-dimensional and is governed by the following one-dimensional model:

$$C(x,t) \propto \operatorname{erfc}\left(\frac{x}{2\sqrt{D_{\text{eff}}t}}\right), \tag{6.4}$$

where erfc is the complementary error function. Fitting this equation to the concentration/intensity profile of the nanoparticles in the capillary tube for a given diffusion time, t, one can get the value of the effective diffusion coefficient D_{eff}. The time, t, in which particles are allowed to diffuse in the gel depends on how fast they move, and it usually ranges from 6 to 12 h.

6. *In Situ* Zymography

Before performing any *in vivo* studies, it is crucial to identify a tumor model that exhibits high MMP-2 activity, and thus, it can more easily cause degradation of the QDGelNPs. MMP-2 activity between different tumor models can be compared with *in situ* zymography. According to this technique (Mook *et al.*, 2003), a 1% (w/v) low gelatin temperature agarose in PBS is prepared and 4′,6-diamidino-2-phenylindole (DAPI) is added to reach a final concentration of 1.0 μg/ml. The agarose solution is then mixed with a 1.0 mg/ml solution of DQ gelatin at a 10:1 ratio. DQ gelatin contains

quenched FITC, which becomes unquenched under MMP degradation of the gelatin. The amount of degradation is related to the FITC intensity when imaged on a confocal microscope. Forty microliters of the agarose solution that contains DQ gelatin and DAPI are placed on top of cryostat sections (10 μm thick) of the tumors of interest and enclosed with a coverslip. Following solidification of the agarose at 4 °C, the gel and tumor section are incubated for 2 h at room temperature. Subsequently, confocal imaging is performed for DAPI and FITC. DAPI stains the cell nuclei, and since MMP-2 is secreted by cells, regions with high cellular density are expected to have high MMP activity, which is shown as increased FITC intensity. Fluorescence of FITC is detected by excitation at 460–500 nm and emission at 512–542 nm, and DAPI is detected by excitation at 340–380 nm and emission at 425 nm. Comparison of the FITC intensity for various tumor types can reveal the tumors that exhibit the highest MMP-2 activity.

7. Intravital Microscopy—*In Vivo* Measurements

In vivo validation of the multistage nanoparticle system is essential to prove its capability for long circulation times and deep penetration into tumor tissue. Experimental protocols involve the use of IVM to measure (i) diffusion of the particles in the interstitial space of tumors, (ii) intratumoral delivery following systemic administration, and (iii) blood half-life (Fukumura *et al.*, 2010; Jain *et al.*, 2002). IVM is a noninvasive technique that allows imaging at multiple time intervals and has increased imaging depth of up to 400 μm with minimal photodamage. Confocal laser scanning microscopy and multiphoton laser scanning microscopy are the two most common techniques of IVM. The latter offers significant advancements, such as improved signal-to-noise ratio and improved imaging depth (Brown *et al.*, 2001; Padera *et al.*, 2002). IVM requires four components: (i) a transparent window placed in the animal model to allow visualization, (ii) the optically active nanoparticles that serve as contrast agents and can be detected by the microscope, (iii) a laser microscope accompanied by a detection system, and (iii) mathematical models and computer programs that can be used to process the images and measure parameters of interest.

Animal models that are most often used in cancer studies are mice with compromised immune systems (e.g., nude or severe combined immunodeficient (SCID) mice). Transparent windows might be placed with a surgical operation on the dorsal skin, the mammary fat pad, or the brain of the mouse depending on the origin of the tumor of interest (Jain *et al.*, 2010). Placement of a window in other organs such as liver or pancreas is also

feasible (Jain *et al.*, 2002). The tumor source can be a suspension of cancer cells or a piece of tumor tissue that are implanted in the region where the tumor is expected to grow. Usually, the transparent window is placed first and then the cancer cells or the tumor fragment is implanted. However, if the tumor has a low chance of growing, it is common to reverse the order so that windows will be placed only to the mice whose tumor has grown. In principle, it is also possible to image spontaneously occurring tumors (Hagendoorn *et al.*, 2006; Kim *et al.*, 2010). Finally, to perform experiments, the tumor has to be vascularized, and thus, it is left to grow to a size of $\sim$5 mm. The time that takes the tumor to grow to that size might vary from a few days to weeks, depending on the tumor growth rate and the implantation procedure (e.g., number of cancer cells implanted).

7.1. Interstitial transport measurements of multistage nanoparticles

To investigate if the MMP-2 activity of a tumor tissue is sufficient to cause degradation of the gelatin nanoparticles, direct injection of the particles into the tumor and subsequent imaging of their distribution is performed. The 100 nm gelatin particles have to be equipped with a smaller (10 nm) optically active agent to be detectable by the microscope. QDs can be used as a model system because they have high resistance to photo and chemical degradation, narrow photoluminescence spectra, broad excitation spectral windows, and large two-photon absorption cross sections (Allen *et al.*, 2010; Popovic *et al.*, 2010; Stroh *et al.*, 2005). In addition, a control group of nondegradable QDs with the same size as the gelatin particles (100 nm) but with a different emission wavelength from the 10 nm QDs is required. A solution of both types of nanoparticles is made and a very small volume of it ($\sim$1 μl) is injected directly into the tumor of an anesthetized mouse, a technique known as intratumoral microinjection.

The injection has to be done very slowly to eliminate pressure gradients so that all injected particles stay at the injection site and do not move to the surrounding tumor tissue by convection. The injection rate is on the order of 0.05 μl/min. With a commercial needle, it is not feasible to inject such a low volume of nanoparticles at these slow rates. Instead, a needle made by a glass tube of 200 μm in diameter is used. The tube is initially heated in the middle and is pulled apart from its edges. Once the heated part melts, the tube breaks in two pieces and a "needle" with diameter on the order of a few micrometers is formed at the heated side of each piece. The tip of the needle is then carefully broken under a light microscope so that the lumen increases to $\sim$40 μm in diameter. The tube is then filled with the solution of the nanoparticles and connected with a plastic tube to a syringe filled with silicon oil. Silicon oil has a high viscosity, which makes the motion of the piston of the syringe more easily controllable. The glass tube penetrates the

surface of the tumor and the particles are released at a depth of 300–500 μm from the surface. A light microscope to better control the injection point and a system to control the penetration depth of the glass tube are required for improved accuracy. With the completion of the injection, the mouse is ready for intravital imaging.

Imaging of the nanoparticles is performed using a multiphoton laser scanning microscope (Fukumura *et al.*, 2010). The microscope is equipped with two PMTs carrying different emission filters so that both particle types (QDGelNPs and control) can be simultaneously detected. Comparison of images taken at different time intervals can reveal how fast the particles diffuse away from the injection point, which is directly related to their size, as smaller particles diffuse faster than larger one (Fig. 6.5).

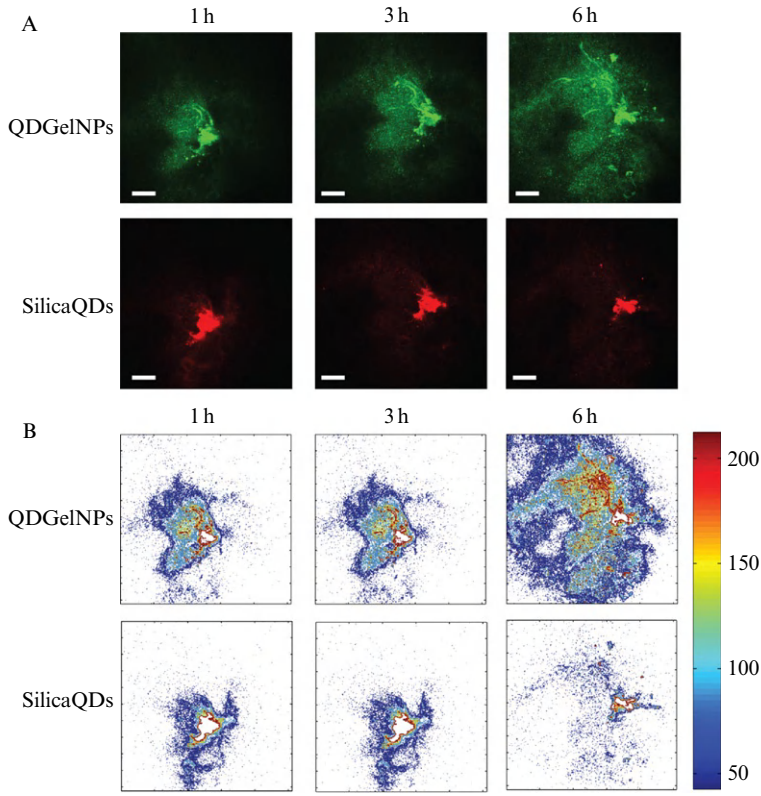

Figure 6.5 (A) Images of QDGelNPs and silica quantum dots (SilicaQDs) at 1, 3, and 6 h after intratumoral coinjection into HT1080 tumor xenograft. (B) Relative fluorescence intensity of the corresponding images from panel (A). QDGelNPs and SilicaQDs have the same initial size of 100 nm. Degradation of gelatin by MMP-2 results in 10 nm QD particles that travel faster in the tumor interstitial space. Scale bar: 100 μm (Wong *et al.*, 2011).

FCS is also a method that can be used with multiphoton microscopy to measure the diffusion coefficient of QD nanoparticles *in vivo* (Alexandrakis *et al.*, 2004).

The emission intensity of different types of nanoparticles might be quite different, and thus, simultaneous imaging requires suitable calibration of the multiphoton system. Before performing *in vivo* imaging, a solution containing both types of particles is placed in a capillary tube and imaged to determine the right emission filters to be used and the PMT sensitivity. The bandwidth of each emission filter should not allow the signal from the other particles to enter the PMT. PMT sensitivity should be calibrated so that the intensity of both types of nanoparticles in the solution is the same. The photoluminescence intensity also depends on the power of the laser. For animal studies, the laser power usually does not exceed 500–600 mW. Higher power of laser might damage the tissue and distort the quality of the images. The images are usually taken as multiple three-dimensional stacks. The average or maximum intensity z-projections of the stacks are extracted using an image processing software (e.g., ImageJ). Images of consecutive adjacent regions in the x and y directions are combined to form a mosaic of the entire injection site.

7.2. Delivery through the systemic circulation

Systemic administration of nanoparticles is most often performed with retro-orbital or tail-vein injection (Steel *et al.*, 2008). According to the retro-orbital injection, the mouse is anesthetized and 200 μl of the nanoparticle solution are injected into the retrobulbar sinus. The needle, whose length should not exceed 0.5 in., is inserted at a 45° angle to the eye, lateral to the medial canthus, and through the conjunctival membrane. It passes behind the globe of the eye to enter the retrobulbar sinus. This is a technique that requires proper training, because it can severely injured the animal, but it requires less than 5 min if it is performed proficiently. A mouse should, however, receive no more than one injection per day for each eye, and there should be 1–2 days between repeated injections. The tail vein is an alternative to the retro-orbital injection route. It does not require anesthesia, is safer, and allows administration of larger amounts of nanoparticles, but it is more time-consuming. The animal is first placed on a heat pad to increase blood flow to the tail vein. It is then transferred to a holding device, which restrains the motion of the mouse, while allowing access to the tail vein. Starting from the tip of the tail and moving toward the body, the needle is inserted to the tail vein as parallel to the tail as possible. One should be able to see the needle entering the vein, or the solution going into the vein.

Following systemic administration, multiphoton imaging is carried out to form a mosaic of the entire tumor, and the intensity of the nanoparticles is

measured. The normalized transvascular flux is calculated from the intensity of the particles using the equation (Brown *et al.*, 2001):

$$P_{\text{eff}} = \frac{J_{\text{t}}}{S_{\text{v}}(C_{\text{v}} - C)} = \lim_{t \to 0} \frac{\partial}{\partial t} \frac{\int_{r=R}^{\infty} C(r) r \mathrm{d}r}{(C_{\text{v}} - C)R}, \tag{6.5}$$

where J_{t} is the transvascular flux, S_{v} is the vessel surface area, C_{v} is the concentration of the probe in the vessel, C is the concentration of the probe immediately extravascular and is calculated based on the fluorescence intensity, P_{eff} is the effective permeability, t is the time after the initial image, r is the distance from the vessel central axis, and R is the vessel radius at that point along the vessel. The calculation is made as an average over the entire imaged volume for each tumor. Apart from transvascular flux, these images can show the interstitial penetration of the nanoparticles from the blood vessels and their distribution in the tumor interstitial space.

7.3. Blood circulation time

To measure the circulation time of nanoparticles, mice not bearing tumors may be used. Intravenous infusion of the particles is performed by retro-orbital or tail-vein injection. At different time intervals, starting 1 min before the injection of particles, a small quantity of blood ($\sim$13 μl) is collected by means of a tail-vein nick and mixed with 3 μl 50 m*M* EDTA. The samples are then imaged using multiphoton microscopy, and values of average intensities are extracted. Again, it is assumed that fluorescence intensity is proportional to the particle concentration. The clearance half-life is calculated by fitting a biexponential curve to the intensity data (Popovic *et al.*, 2010). The intensity data are characterized by a quick drop of the intensity at short times and a slow decrease at long times. The short time response is attributed to particle absorption by tissues, whereas the long time behavior is due to the clearance of the particles. Therefore, the clearance half-life corresponds to the long time exponent.

8. Conclusion and Perspective

In this chapter, we provide a detailed description of the methods for the formulation and characterization of a multistage nanoparticle delivery system that enables enhanced distribution to tumors. This multistage system is based on the enzymatic degradation of a $\sim$100-nm gelatin carrier and the release from its surface of smaller diagnostic or therapeutic agents. We have shown the proof of principle of this strategy by administering the multistage nanoparticles directly into the tumor. The gelatinase enzymatic activity in

HT1080 soft tissue sarcomas was sufficient to degrade the gelatin and release 10 nm QDs that were conjugated to the nanoparticle (Wong *et al.*, 2011). The next steps of the development of this multistage nanoparticle delivery system would be the optimization of the system via systemic administration and, ultimately, the creation of drug-loading multistage nanoparticles as well as the evaluation of their *in vivo* efficacy. These are necessary steps for the true evaluation of the hypothesis and for potentially moving toward clinical application.

It should be noted that there are other types of multistage nanoparticle delivery systems under development (Ferrari, 2005). For example, mesoporous silica particles function as carriers for the controlled release of therapeutic agents (Lu *et al.*, 2007; Tanaka *et al.*, 2010; Tasciotti *et al.*, 2008). These particles release their therapeutic load progressively while circulating in the bloodstream. Effort is also made for the optimal design of these particles to improve their margination and interaction with the abnormal tumor vasculature (Serda *et al.*, 2011). In addition, there are other promising strategies for cancer treatment, such as targeted nanoparticle delivery systems. These nanoparticles are equipped with peptides or targeting moieties that can selectively bind tumor endothelial cells or cancer cells (Davis *et al.*, 2010; Ruoslahti *et al.*, 2010), or enhance permeation to tumor tissue (Karmali *et al.*, 2009; Sugahara *et al.*, 2009). Ultimately, successful multistage nanoparticle systems are likely to combine different approaches and may even be customized for individual tumors and be adjustable during the course of treatment.

ACKNOWLEDGMENTS

This chapter is based on the paper by Wong *et al.* (2011). This research was supported by US National Cancer Institute Grants R01-CA126642 (to R. K. J. and M. G. B.), P01-CA080124 (to R. K. J. and D. F.), R01-CA096915 (to D. F.); Federal Shared Proton Beam Program Income (to R. K. J.); National Center for Research Resources S10-RR027070 (to D. F.); Department of Defense Breast Cancer Research Program BC095991 (R. K. J.); and a FP7 Marie-Curie International Reintegration Grant PIRG08-GA-2010-276894 (to T. S.).

REFERENCES

Alexandrakis, G., Brown, E. B., Tong, R. T., McKee, T. D., Campbell, R. B., Boucher, Y., and Jain, R. K. (2004). Two-photon fluorescence correlation microscopy reveals the two-phase nature of transport in tumors. *Nat. Med.* **10,** 203–207.

Allen, P. M., Liu, W., Chauhan, V. P., Lee, J., Ting, A. Y., Fukumura, D., Jain, R. K., and Bawendi, M. G. (2010). InAs(ZnCdS) quantum dots optimized for biological imaging in the near-infrared. *J. Am. Chem. Soc.* **132,** 470–471.

Baish, J. W., Stylianopoulos, T., Lanning, R. M., Kamoun, W. S., Fukumura, D., Munn, L. L., and Jain, R. K. (2011). Scaling rules for diffusive drug delivery in tumor and normal tissues. *Proc. Natl. Acad. Sci. USA* **108,** 1799–1803.

Baxter, L. T., and Jain, R. K. (1989). Transport of fluid and macromolecules in tumors. I. Role of interstitial pressure and convection. *Microvasc. Res.* **37,** 77–104.

Baxter, L. T., and Jain, R. K. (1990). Transport of fluid and macromolecules in tumors. II. Role of heterogeneous perfusion and lymphatics. *Microvasc. Res.* **40,** 246–263.

Boucher, Y., and Jain, R. K. (1992). Microvascular pressure is the principal driving force for interstitial hypertension in solid tumors: Implications for vascular collapse. *Cancer Res.* **52,** 5110–5114.

Boucher, Y., Baxter, L. T., and Jain, R. K. (1990). Interstitial pressure gradients in tissue-isolated and subcutaneous tumors: Implications for therapy. *Cancer Res.* **50,** 4478–4484.

Boucher, Y., Kirkwood, J. M., Opacic, D., Desantis, M., and Jain, R. K. (1991). Interstitial hypertension in superficial metastatic melanomas in humans. *Cancer Res.* **51,** 6691–6694.

Branton, M. H., and Kopp, J. B. (1999). TGF-beta and fibrosis. *Microbes Infect.* **1,** 1349–1365.

Brown, E. B., Campbell, R. B., Tsuzuki, Y., Xu, L., Carmeliet, P., Fukumura, D., and Jain, R. K. (2001). In vivo measurement of gene expression, angiogenesis and physiological function in tumors using multiphoton laser scanning microscopy. *Nat. Med.* **7,** 864–868.

Brown, E., McKee, T., diTomaso, E., Pluen, A., Seed, B., Boucher, Y., and Jain, R. K. (2003). Dynamic imaging of collagen and its modulation in tumors in vivo using second-harmonic generation. *Nat. Med.* **9,** 796–800.

Butcher, D. T., Alliston, T., and Weaver, V. M. (2009). A tense situation: Forcing tumour progression. *Nat. Rev. Cancer* **9,** 108–122.

Chary, S. R., and Jain, R. K. (1989). Direct measurement of interstitial convection and diffusion of albumin in normal and neoplastic tissues by fluorescence photobleaching. *Proc. Natl. Acad. Sci. USA* **86,** 5385–5389.

Chauhan, V. P., Lanning, R. M., Diop-Frimpong, B., Mok, W., Brown, E. B., Padera, T. P., Boucher, Y., and Jain, R. K. (2009). Multiscale measurements distinguish cellular and interstitial hindrances to diffusion in vivo. *Biophys. J.* **97,** 330–336.

Chauhan, V. P., Stylianopoulos, T., Boucher, Y., and Jain, R. K. (2011). Delivery of molecular and nanomedicine to tumors: Transport barriers and strategies. *Annu. Rev. Chem. Biomol. Eng.* **2,** 281–298.

Choi, H. S., Liu, W., Misra, P., Tanaka, E., Zimmer, J. P., Itty Ipe, B., Bawendi, M. G., and Frangioni, J. V. (2007). Renal clearance of quantum dots. *Nat. Biotechnol.* **25,** 1165–1170.

Choi, H. S., Liu, W., Liu, F., Nasr, K., Misra, P., Bawendi, M. G., and Frangioni, J. V. (2010). Design considerations for tumour-targeted nanoparticles. *Nat. Nanotechnol.* **5,** 42–47.

Davis, M. E., Zuckerman, J. E., Choi, C. H., Seligson, D., Tolcher, A., Alabi, C. A., Yen, Y., Heidel, J. D., and Ribas, A. (2010). Evidence of RNAi in humans from systemically administered siRNA via targeted nanoparticles. *Nature* **464,** 1067–1070.

Diop-Frimpong, B., Chauhan, V. P., Krane, S., Boucher, Y., and Jain, R. K. (2011). Losartan inhibits collagen I synthesis and improves the distribution and efficacy of nanotherapeutics in tumors. *Proc. Natl. Acad. Sci. USA* **108,** 2909–2914.

Egeblad, M., Rasch, M. G., and Weaver, V. M. (2010). Dynamic interplay between the collagen scaffold and tumor evolution. *Curr. Opin. Cell Biol.* **22,** 697–706.

Ferrari, M. (2005). Cancer nanotechnology: Opportunities and challenges. *Nat. Rev. Cancer* **5,** 161–171.

Franzen, S., and Lommel, S. A. (2009). Targeting cancer with 'smart bombs': Equipping plant virus nanoparticles for a 'seek and destroy' mission. *Nanomedicine (Lond.)* **4,** 575–588.

Fukumura, D., Duda, D. G., Munn, L. L., and Jain, R. K. (2010). Tumor microvasculature and microenvironment: Novel insights through intravital imaging in pre-clinical models. *Microcirculation* **17,** 206–225.

Gordon, A. N., Fleagle, J. T., Guthrie, D., Parkin, D. E., Gore, M. E., and Lacave, A. J. (2001). Recurrent epithelial ovarian carcinoma: A randomized phase III study of pegylated liposomal doxorubicin versus topotecan. *J. Clin. Oncol.* **19,** 3312–3322.

Gradishar, W. J., Tjulandin, S., Davidson, N., Shaw, H., Desai, N., Bhar, P., Hawkins, M., and O'Shaughnessy, J. (2005). Phase III trial of nanoparticle albumin-bound paclitaxel compared with polyethylated castor oil-based paclitaxel in women with breast cancer. *J. Clin. Oncol.* **23,** 7794–7803.

Gutmann, R., Leunig, M., Feyh, J., Goetz, A. E., Messmer, K., Kastenbauer, E., and Jain, R. K. (1992). Interstitial hypertension in head and neck tumors in patients: Correlation with tumor size. *Cancer Res.* **52,** 1993–1995.

Hagendoorn, J., Tong, R., Fukumura, D., Lin, Q., Lobo, J., Padera, T. P., Xu, L., Kucherlapati, R., and Jain, R. K. (2006). Onset of abnormal blood and lymphatic vessel function and interstitial hypertension in early stages of carcinogenesis. *Cancer Res.* **66,** 3360–3364.

Hashizume, H., Baluk, P., Morikawa, S., McLean, J. W., Thurston, G., Roberge, S., Jain, R. K., and McDonald, D. M. (2000). Openings between defective endothelial cells explain tumor vessel leakiness. *Am. J. Pathol.* **156,** 1363–1380.

Hobbs, S. K., Monsky, W. L., Yuan, F., Roberts, W. G., Griffith, L., Torchilin, V. P., and Jain, R. K. (1998). Regulation of transport pathways in tumor vessels: Role of tumor type and microenvironment. *Proc. Natl. Acad. Sci. USA* **95,** 4607–4612.

Huijbers, I. J., Iravani, M., Popov, S., Robertson, D., Al-Sarraj, S., Jones, C., and Isacke, C. M. (2010). A role for fibrillar collagen deposition and the collagen internalization receptor endo180 in glioma invasion. *PLoS One* **5,** e9808.

Jain, R. K. (1987a). Transport of molecules across tumor vasculature. *Cancer Metastasis Rev.* **6,** 559–593.

Jain, R. K. (1987b). Transport of molecules in the tumor interstitium: A review. *Cancer Res.* **47,** 3039–3051.

Jain, R. K. (2001). Normalizing tumor vasculature with anti-angiogenic therapy: A new paradigm for combination therapy. *Nat. Med.* **7,** 987–989.

Jain, R. K., and Baxter, L. T. (1988). Mechanisms of heterogeneous distribution of monoclonal antibodies and other macromolecules in tumors: Significance of elevated interstitial pressure. *Cancer Res.* **48,** 7022–7032.

Jain, R. K., and Stylianopoulos, T. (2010). Delivering nanomedicine to solid tumors. *Nat. Rev. Clin. Oncol.* **7,** 653–664.

Jain, R. K., Munn, L. L., and Fukumura, D. (2002). Dissecting tumour pathophysiology using intravital microscopy. *Nat. Rev. Cancer* **2,** 266–276.

Jain, R. K., Munn, L. L., and Fukumura, D. (2010). Intravital microscopy of normal and diseased tissues in mice. *In* "Live Cell Imaging: A Laboratory Manual," (R. D. Goldman and D. L. Spector, eds.), pp. 475–522. Cold Spring Harbor, NY, Cold Spring Harbor Laboratory Press.

Jain, R. K., Tong, R. T., and Munn, L. L. (2007). Effect of vascular normalization by antiangiogenic therapy on interstitial hypertension, peritumor edema, and lymphatic metastasis: Insights from a mathematical model. *Cancer Res.* **67,** 2729–2735.

Karmali, P. P., Kotamraju, V. R., Kastantin, M., Black, M., Missirlis, D., Tirrell, M., and Ruoslahti, E. (2009). Targeting of albumin-embedded paclitaxel nanoparticles to tumors. *Nanomedicine* **5,** 73–82.

Kauppila, S., Stenback, F., Risteli, J., Jukkola, A., and Risteli, L. (1998). Aberrant type I and type III collagen gene expression in human breast cancer in vivo. *J. Pathol.* **186,** 262–268.

Kim, P., Chung, E., Yamashita, H., Hung, K. E., Mizoguchi, A., Kucherlapati, R., Fukumura, D., Jain, R. K., and Yun, S. H. (2010). In vivo wide-area cellular imaging by side-view endomicroscopy. *Nat. Methods* **7,** 303–305.

Klibanov, A. L., Maruyama, K., Torchilin, V. P., and Huang, L. (1990). Amphipathic polyethyleneglycols effectively prolong the circulation time of liposomes. *FEBS Lett.* **268,** 235–237.

Less, J. R., Posner, M. C., Boucher, Y., Borochovitz, D., Wolmark, N., and Jain, R. K. (1992). Interstitial hypertension in human breast and colorectal tumors. *Cancer Res.* **52,** 6371–6374.

Longmire, M., Choyke, P. L., and Kobayashi, H. (2008). Clearance properties of nano-sized particles and molecules as imaging agents: Considerations and caveats. *Nanomedicine (Lond.)* **3,** 703–717.

Lu, J., Liong, M., Sherman, S., Xia, T., Kovochich, M., Nel, A. E., Zink, J. I., and Tamanoi, F. (2007). Mesoporous silica nanoparticles for cancer therapy: Energy-dependent cellular uptake and delivery of paclitaxel to cancer cells. *Nanobiotechnology* **3,** 89–95.

McKee, T. D., Grandi, P., Mok, W., Alexandrakis, G., Insin, N., Zimmer, J. P., Bawendi, M. G., Boucher, Y., Breakefield, X. O., and Jain, R. K. (2006). Degradation of fibrillar collagen in a human melanoma xenograft improves the efficacy of an oncolytic herpes simplex virus vector. *Cancer Res.* **66,** 2509–2513.

Mook, O. R., Van Overbeek, C., Ackema, E. G., Van Maldegem, F., and Frederiks, W. M. (2003). In situ localization of gelatinolytic activity in the extracellular matrix of metastases of colon cancer in rat liver using quenched fluorogenic DQ-gelatin. *J. Histochem. Cytochem.* **51,** 821–829.

Netti, P. A., Berk, D. A., Swartz, M. A., Grodzinsky, A. J., and Jain, R. K. (2000). Role of extracellular matrix assembly in interstitial transport in solid tumors. *Cancer Res.* **60,** 2497–2503.

Nugent, L. J., and Jain, R. K. (1984). Extravascular diffusion in normal and neoplastic tissues. *Cancer Res.* **44,** 238–244.

Padera, T. P., Stoll, B. R., So, P. T., and Jain, R. K. (2002). Conventional and high-speed intravital multiphoton laser scanning microscopy of microvasculature, lymphatics, and leukocyte-endothelial interactions. *Mol. Imaging* **1,** 9–15.

Peracchia, M. T., Fattal, E., Desmaele, D., Besnard, M., Noel, J. P., Gomis, J. M., Appel, M., d'Angelo, J., and Couvreur, P. (1999). Stealth PEGylated polycyanoacrylate nanoparticles for intravenous administration and splenic targeting. *J. Control. Release* **60,** 121–128.

Petros, R. A., and DeSimone, J. M. (2010). Strategies in the design of nanoparticles for therapeutic applications. *Nat. Rev. Drug Discov.* **9,** 615–627.

Pluen, A., Boucher, Y., Ramanujan, S., McKee, T. D., Gohongi, T., di Tomaso, E., Brown, E. B., Izumi, Y., Campbell, R. B., Berk, D. A., and Jain, R. K. (2001). Role of tumor-host interactions in interstitial diffusion of macromolecules: Cranial vs. subcutaneous tumors. *Proc. Natl. Acad. Sci. USA* **98,** 4628–4633.

Popovic, Z., Liu, W., Chauhan, V. P., Lee, J., Wong, C., Greytak, A. B., Insin, N., Nocera, D. G., Fukumura, D., Jain, R. K., and Bawendi, M. G. (2010). A nanoparticle size series for in vivo fluorescence imaging. *Angew. Chem. Int. Ed Engl.* **49,** 8649–8652.

Ramanujan, S., Pluen, A., McKee, T. D., Brown, E. B., Boucher, Y., and Jain, R. K. (2002). Diffusion and convection in collagen gels: Implications for transport in the tumor interstitium. *Biophys. J.* **83,** 1650–1660.

Roh, H. D., Boucher, Y., Kalnicki, S., Buchsbaum, R., Bloomer, W. D., and Jain, R. K. (1991). Interstitial hypertension in carcinoma of uterine cervix in patients: Possible correlation with tumor oxygenation and radiation response. *Cancer Res.* **51,** 6695–6698.

Ruoslahti, E., Bhatia, S. N., and Sailor, M. J. (2010). Targeting of drugs and nanoparticles to tumors. *J. Cell Biol.* **188,** 759–768.

Schwille, P., Haupts, U., Maiti, S., and Webb, W. W. (1999). Molecular dynamics in living cells observed by fluorescence correlation spectroscopy with one- and two-photon excitation. *Biophys. J.* **77,** 2251–2265.

Serda, R. E., Godin, B., Blanco, E., Chiappini, C., and Ferrari, M. (2011). Multi-stage delivery nano-particle systems for therapeutic applications. *Biochim. Biophys. Acta* **1810,** 317–329.

Steel, C. D., Stephens, A. L., Hahto, S. M., Singletary, S. J., and Ciavarra, R. P. (2008). Comparison of the lateral tail vein and the retro-orbital venous sinus as routes of intravenous drug delivery in a transgenic mouse model. *Lab. Anim. (N.Y.)* **37,** 26–32.

Storm, G., Belliot, S. O., Daemen, T., and Lasic, D. D. (1995). Surface modification of nanoparticles to oppose uptake by the mononuclear phagocyte system. *Adv. Drug Deliv. Rev.* **17,** 31–48.

Stroh, M., Zimmer, J. P., Duda, D. G., Levchenko, T. S., Cohen, K. S., Brown, E. B., Scadden, D. T., Torchilin, V. P., Bawendi, M. G., Fukumura, D., and Jain, R. K. (2005). Quantum dots spectrally distinguish multiple species within the tumor milieu in vivo. *Nat. Med.* **11,** 678–682.

Stylianopoulos, T., Diop-Frimpong, B., Munn, L. L., and Jain, R. K. (2010a). Diffusion anisotropy in collagen gels and tumors: The effect of fiber network orientation. *Biophys. J.* **99,** 3119–3128.

Stylianopoulos, T., Poh, M. Z., Insin, N., Bawendi, M. G., Fukumura, D., Munn, L. L., and Jain, R. K. (2010b). Diffusion of particles in the extracellular matrix: The effect of repulsive electrostatic interactions. *Biophys. J.* **99,** 1342–1349.

Sugahara, K. N., Teesalu, T., Karmali, P. P., Kotamraju, V. R., Agemy, L., Girard, O. M., Hanahan, D., Mattrey, R. F., and Ruoslahti, E. (2009). Tissue-penetrating delivery of compounds and nanoparticles into tumors. *Cancer Cell* **16,** 510–520.

Tanaka, T., Mangala, L. S., Vivas-Mejia, P. E., Nieves-Alicea, R., Mann, A. P., Mora, E., Han, H. D., Shahzad, M. M., Liu, X., Bhavane, R., Gu, J., Fakhoury, J. R., *et al.* (2010). Sustained small interfering RNA delivery by mesoporous silicon particles. *Cancer Res.* **70,** 3687–3696.

Tasciotti, E., Liu, X., Bhavane, R., Plant, K., Leonard, A. D., Price, B. K., Cheng, M. M., Decuzzi, P., Tour, J. M., Robertson, F., and Ferrari, M. (2008). Mesoporous silicon particles as a multistage delivery system for imaging and therapeutic applications. *Nat. Nanotechnol.* **3,** 151–157.

Vakoc, B. J., Lanning, R. M., Tyrrell, J. A., Padera, T. P., Bartlett, L. A., Stylianopoulos, T., Munn, L. L., Tearney, G. J., Fukumura, D., Jain, R. K., and Bouma, B. E. (2009). Three-dimensional microscopy of the tumor microenvironment in vivo using optical frequency domain imaging. *Nat. Med.* **15,** 1219–1223.

Wong, C., Stylianopoulos, T., Cui, J., Martin, J., Chauhan, V. P., Jiang, W., Popovic, Z., Jain, R. K., Bawendi, M. G., and Fukumura, D. (2011). Multistage nanoparticle delivery system for deep penetration into tumor tissue. *Proc. Natl. Acad. Sci. USA* **108,** 2426–2431.

Yuan, F., Leunig, M., Huang, S. K., Berk, D. A., Papahadjopoulos, D., and Jain, R. K. (1994). Microvascular permeability and interstitial penetration of sterically stabilized (stealth) liposomes in a human tumor xenograft. *Cancer Res.* **54,** 3352–3356.

CHAPTER SEVEN

Mitochondria-Specific Nanocarriers for Improving the Proapoptotic Activity of Small Molecules

Volkmar Weissig

Contents

Abstract

The efficiency and efficacy of drug action depends largely on how well an unaided drug molecule is able to reach its intracellular target or even its target

Midwestern University College of Pharmacy Glendale, Glendale, Arizona, USA

Methods in Enzymology, Volume 508
ISSN 0076-6879, DOI: 10.1016/B978-0-12-391860-4.00007-0

inside organelles such as mitochondria. Subsequently, the specific delivery of a drug to its site of action inside cells will dramatically improve its action. Mitochondria play a key role in apoptosis, and several clinically used, as well as experimental, drugs are known to trigger apoptosis by interacting directly with the target site at or inside mitochondria. During the past decade, a variety of mitochondria-specific pharmaceutical nanocarriers have been developed for the purpose of delivering therapeutic DNA or low-molecular weight compounds to mitochondria inside living mammalian cells. Here, the preparation of drug-containing, mitochondria-targeted nanocarriers is described and protocols for their *in vitro* and *in vivo* assessment are given.

1. Introduction

Considered as novel intracellular targets for anticancer drugs for the first time around 1998 (Decaudin *et al.*, 1998; Guchelaar *et al.*, 1997), mitochondria are being regarded today as prime targets for anticancer chemotherapy (Biasutto *et al.*, 2010; Chen *et al.*, 2010, Ralph *et al.*, 2010). During the late 1990s, the importance of subcellular, that is, organelle-specific drug delivery was widely underappreciated. With the exception of wide-ranging investigations of intracellular barriers, DNA constructs have to surmount on their way to and into the nucleus (Lechardeur and Lukacs, 2002), not much attention has been paid over a decade ago to factors controlling the intracellular distribution of internalized low-molecular weight compounds (Duvvuri *et al.*, 2004a). Subsequently, the faulty notion that once a drug is in the cytosol it will reach mitochondria anyway, because there are so many of them, was not unheard of, and early attempts to design mitochondria-targeted colloidal drug delivery systems were not particularly encouraged.

A large portion of the intracellular space is occupied by cell organelles. All these organelles possess distinctive lipid compositions, membrane-linked proteins, electrical charges/potentials, as well as intraluminal pH values (Duvvuri *et al.*, 2004a,b). Clearly, these organelle-specific properties have to play a role for the intracellular distribution of any small molecule which has entered the cell. Ten years ago, a quantitative structure–activity relationship (QSAR) model was developed that allows predicting the cellular uptake, the intracellular distribution, and potential intracellular sites of accumulation for low-molecular weight fluorescent dyes (Horobin, 2001). It was made evident that the overall size, the size of the aromatic system, the amphipathic character, the presence of planar aromatic rings, the electric charge, and the acid/base properties all control the intracellular fate of small molecules (Horobin, 2001). This QSAR approach was applied 5 years ago in combination with a Fick–Nernst–Planck physicochemical model to a set of more than 100 molecules known to accumulate at or in mitochondria

(Horobin *et al.*, 2007). It was concluded that a random, statistical interaction of low-molecular weight molecules with mitochondria can hardly be expected. Any potential drug will affect mitochondria only if the drug molecule's physicochemical properties "allow" it to interact with the mitochondrial network, or when the drug has been transported to mitochondrial sites by a mitochondria-targeted drug carrier system.

A serendipitous discovery made during the late 1990s opened the way for the design of organelle-specific drug carrier systems, in particular, for targeting to mitochondria. Dequalinium chloride, a bola-amphiphilic compound notorious for its selective accumulation inside respiring mammalian mitochondria (Gamboa-Vujicic *et al.*, 1993; Weiss *et al.*, 1987), was found to be able to self-assemble into colloidal vesicles termed "DQAsomes" (the term "nano" was not yet in vogue at this time) (Weissig *et al.*, 1998a,b).

Over the past 10 years, DQAsomes have been explored successfully as the first mitochondria-specific transfection vector. DQAsomes have been shown to meet all criteria for a mitochondria-targeted DNA delivery system. DQAsomes are able to bind pDNA and to protect it from nuclease digestion (Lasch *et al.*, 1999). Employing different experimental systems involving liposomes mimicking the composition of cytosolic and mitochondrial membranes (Weissig *et al.*, 2000), and energized isolated mitochondria (Weissig *et al.*, 2001), it was shown that DQAsome/DNA complexes (DQAplexes) selectively release the DNA upon contact with mitochondrial but not cytosolic membranes. Employing a novel protocol for selectively staining free pDNA in the cytosol of living cells, it was further demonstrated that DQAplexes appear to be able to escape from endosomes without losing their pDNA load. The complex then translocates to the site of mitochondria where a portion of the pDNA is released from its DQAsomal carrier (D'Souza *et al.*, 2003).

Most recently, the first study demonstrating the capability of DQAplexes to specifically transfect mitochondria has been published (Lyrawati *et al.*, 2011). Using immunofluorescence and a combination of immunohistochemical and molecular-based techniques, it has been shown that DQAsomes are capable of delivering an artificial mini-mitochondrial genome into mitochondria of a variety of mammalian cells. Despite low transfection efficiencies, the mini-genome's transcription into mRNA and subsequent translation into GFP protein inside the mitochondrial compartments could be established. Undoubtedly, further optimization of DQAsome-based mitochondrial transfection is needed to provide an effective means to manipulate the mitochondrial genome in living mammalian cells and to open the way toward the cure of mitochondrial DNA diseases via mitochondrial gene therapy.

Concomitantly with the exploration of DQAsomes as a transfection vector, they have also been proposed as a mitochondria-targeted colloidal

drug carrier system. To assess the utility of DQAsomes as a mitochondria-targeted colloidal drug carrier for proapoptotic low-molecular weight compounds, paclitaxel was chosen as a model drug based on studies published in 2000 (Andre *et al.*, 2000; Goncalves *et al.*, 2000), which showed for the first time that in addition to being an antimicrotubule agent paclitaxel also acts directly on mitochondria, causing the release of cytochrome *C*, subsequently triggering apoptosis. Protocols pertaining to the application of paclitaxel formulated into DQAsomes for anticancer chemotherapy are given in detail below.

Liposomes (artificial phospholipid vesicles) can be considered as the archetype of all pharmaceutical nanocarriers currently under development. These nanovesicles are able to sequester hydrophilic drug molecules in their aqueous inner space and lipophilic drugs in their phospholipid bilayer membranes. Liposomes were discovered at the beginning of the 1960s (Bangham *et al.*, 1965a,b) and proposed in the early 1970s as a drug carrier system (Gregoriadis, 1975, 1976a,b). About 20 years later, the US FDA approved Doxil® (Johnson & Johnson Corporation, NJ) and Daunoxome® (Gilead Sciences, Inc., CA) as the first liposome-based drug formulations. Doxil is a formulation of doxorubicin hydrochloride, whereas Daunoxome is a formulation of daunorubicin. In both formulations, polyethylene glycol linked to the liposome surface increases the vesicle's longevity in systemic circulation, which is prerequisite for an increased accumulation of the liposomal drug at sites of vascular damage, such as in solid tumors and at inflamed areas. On entering the interstitium of a solid tumor mediated by the enhanced permeability and retention effect, liposomes eventually disintegrate via an ill-defined mechanism and release the drug from its nanocarrier.

Once the drug has entered the tumor cell, it still has to find its way to its subcellular target, which is for many proapoptotic drugs the mitochondrial network. To render liposomes mitochondria-specific, the well-established mitochondriotropic triphenylphosphonium cation (Horobin *et al.*, 2007; Murphy and Smith, 2000; Smith *et al.*, 1999) has been rendered more hydrophobic, that is, linked to a lipid anchor, by reacting triphenylphosphine with stearyl bromide, yielding stearyl-triphenylphosphonium bromide (STPP) (Boddapati *et al.*, 2005). The detailed protocol for the synthesis of STPP is given below. Anchoring hydrophilic molecules to/into phospholipid membranes via modifying them with fatty acid or phospholipid residues is a well-known principle used by nature (Magee and Schlesinger, 1982; Schlesinger and Magee, 1982; Schmidt, 1983) and has been fully explored in liposome technology for the surface modification of liposomes (Torchilin *et al.*, 2003; Weissig *et al.*, 1986, 1989; Weissig and Gregoriadis, 1992). A typical protocol for preparing STPP liposomes is given below.

Utilizing hydrophobic fluorophores as model drugs, it has been demonstrated that STPP liposomes are able to transport selectively the hydrophobic molecule to the site of mitochondria. Confocal fluorescence microscopic images show an almost perfect colocalization of the fluorophore with previously labeled mitochondria (Boddapati *et al.*, 2008). It should be noted, however, that it seems highly unlikely that whole and intact liposomes are able to enter the cytosol and deliver selectively to mitochondria any drug, independent of its solubility. Attempts to show the colocalization of mitochondria with liposomes containing both a lipid and an aqueous fluorescence marker, for example, have failed (V. Weissig, unpublished). However, in all experiments aimed at demonstrating the ability of STPP liposomes to deliver a drug selectively to mitochondria, the fluorescence label was covalently linked to a phospholipid, the targeting ligand (TPP) was attached to stearic acid, and the drug itself was highly hydrophobic. Subsequently, all three components are "detained" within the liposomal bilayer membrane. Neither STPP nor the drug or the fluorophore is able to exist in solution as a monomer at measurable concentrations. It shall therefore be speculated that liposomal membrane fragments (and not whole liposomes) survive cell internalization and endosomal escape, reassemble into vesicular structures, possibly by including endosomal membrane lipids while still accommodating, that is, "holding together" the fluorescence marker, the targeting moiety, and the hydrophobic drug. If this hypothesis holds true, then mitochondriotropic STPP liposomes should be able to enhance significantly the proapoptotic activity of hydrophobic molecules, which are known to trigger apoptosis by directly acting on mitochondria. This hypothesis was undoubtedly confirmed in two publications. In the first paper (Boddapati *et al.*, 2008), ceramide, a sphingolipid signaling molecule, has been used mainly based on the observation that this lipid is able to form large stable pores in membranes, which, in turn, have been implied in playing a role for the mitochondrial membrane channel formation during apoptosis (Siskind and Colombini, 2000). In the second study, STPP liposomes have been employed to deliver sclareol to tumor cell mitochondria *in vitro* (Patel *et al.*, 2009). Sclareol (labd-14-ene-8,13 diol) is a labdane diterpene isolated from the plant *Salvia sclarea*, which has been shown to induce apoptosis possibly via both the mitochondrial and the death receptor pathways (Dimas *et al.*, 1999, 2001, 2007).

In addition, preliminary data obtained from ongoing studies show a significantly increased cytotoxicity of CD437 when incorporated into STPP liposomes (Weissig *et al.*, 2009). CD437 is a novel retinoid acid receptor (RAR)γ activator, which has been found to inhibit the growth and to induce the apoptosis of a wide variety of solid tumors via directly acting on mitochondria (Gonda *et al.*, 2008; Watanabe *et al.*, 2008).

Typical protocols for the formulation of hydrophobic proapoptotic small molecules into STPP liposomes and their subsequent *in vitro* and *in vivo* assessment are given below.

2. The Use of DQAsomes for Mitochondria-Targeted Delivery of Paclitaxel

2.1. DQAsomal formulation of paclitaxel

Dequalinium chloride (Sigma, St. Louis, MO; 26 mg; 10 m*M* final concentration) and 42 mg (10 m*M* final) paclitaxel (Natural Pharmaceuticals, Inc., Beverly, MA) are dissolved in methanol in a round-bottom flask, followed by removal of the organic solvent with a rotary evaporator. After adding 5 m*M* HEPES, pH 7.4, the suspension is sonicated with a probe sonicator until an opaque solution is obtained, which usually takes about 1 h. To prevent overheating of the sonicated material, the round-bottom flask is cooled with ice water. To remove any undissolved material, the colloidal solution containing DQAsomes with encapsulated paclitaxel is centrifuged for 10 min at 3000 × *g*.

The solubility of paclitaxel in water at 25 °C and pH 7.4 is 0.172 mg/l (0.2 μ*M*), which is extremely low, making any separation procedure of non-encapsulated paclitaxel from DQAsomes unnecessary; that is, in an aqueous environment, only paclitaxel encapsulated in DQAsomes will stay in colloidal solution. Nevertheless, for controls, a paclitaxel suspension can be probe sonicated under identical conditions used for the DQAsomal formulation of paclitaxel, but in the complete absence of dequalinium chloride. Upon centrifugation, no paclitaxel will be detectable in the supernatant using UV spectroscopy at 230 nm.

The amount of dequalinium in the DQAsomal paclitaxel formulation is measured using fluorescence spectroscopy (excitation 335 nm, emission 360 nm). At these wavelengths, paclitaxel does not display any fluorescence and therefore does not interfere with the determination of dequalinium. For measurements, 3 μl of the DQAsomal paclitaxel formulation are dissolved in 3 ml methanol, yielding a concentration of dequalinium that lies within the linear range of a standard curve obtained by measuring free dequalinium chloride in methanol.

The UV spectra of paclitaxel and dequalinium in methanol, however, strongly overlap between 200 and 240 nm. Therefore, before measuring the amount of paclitaxel encapsulated into DQAsomes, dequalinium has to be quantitatively removed from the preparation. To this end, a solid phase extraction (SPE) column (J.T. Baker, distributed by Taylor Scientific, St. Louis, MS) (Bakerbond Octadecyl 40 μm Prep LC Packing) is equilibrated with methanol and loaded with 1 ml water followed by the

application of 0.02 ml DQAsomes previously dissolved in methanol/water = 10/1 (v/v). Dequalinium is eluted quantitatively from the column by washing with a discontinuous methanol/water gradient (1 ml methanol/water (1:4, v/v), followed by 1 ml methanol/water (3:2, v/v)). Paclitaxel is eluted from the SPE column by washing with 1 ml 100% methanol and measured via UV spectroscopy at 230 nm. The lack of any absorption at 315 nm demonstrates the complete absence of dequalinium in the sample used for the determination of paclitaxel.

The preparation of DQAsomes in the presence of paclitaxel yields a stable colloidal solution of the drug with an average size distribution between 400 and 600 nm (Fig. 7.1; Cheng *et al.*, 2005). The quantitative compositions of such colloidal formulations are shown in Table 7.1 demonstrating that paclitaxel can be formulated into DQAsomes at an approximate maximal molar ratio of paclitaxel to dequalinium of 1:2.

The compositions of paclitaxel-containing DQAsomes upon storage for at least 2 weeks are shown in Fig. 7.2. Over a period of 10 days, the ratio of paclitaxel to dequalinium remains almost constant, indicating that paclitaxel remains stably incorporated in DQAsomes. However, from the gradual decrease of the total concentration of paclitaxel and of dequalinium over

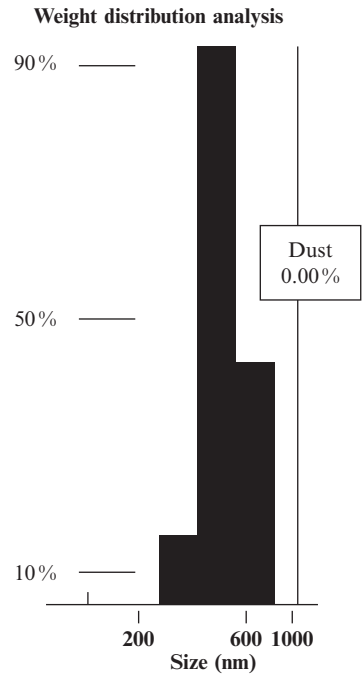

Figure 7.1 Size distribution of DQAsomal incorporated paclitaxel (0.67 mol paclitaxel/mol dequalinium). Data from Cheng *et al.* (2005).

Table 7.1 Quantitative composition of three independently prepared samples of DQAsomal encapsulated paclitaxel

Dequalinium (m*M*)	Paclitaxel (m*M*)	Molar ratio paclitaxel/dequalinium
8.96	6.0	0.67
7.54	4.91	0.65
9.94	4.31	0.43

Data from Cheng *et al.* (2005).

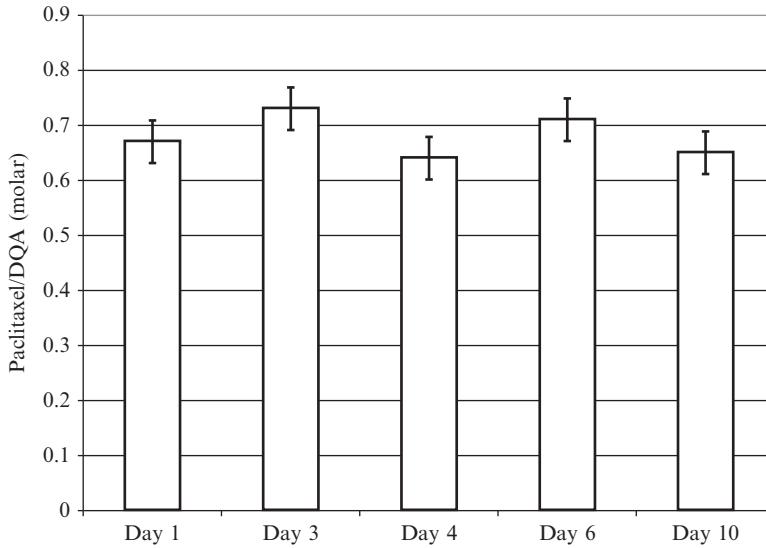

Figure 7.2 Composition of a preparation of DQAsomal encapsulated paclitaxel upon storage over 10 days at 4 °C. At the days indicated, the paclitaxel-containing DQAsome preparation was again centrifuged (10 min, 3000 rpm) to remove freshly formed precipitate followed by the determination of the dequalinium/paclitaxel ratio. Data from Cheng *et al.* (2005).

several days (data not shown), it can be concluded that paclitaxel-loaded DQAsomes tend to form larger aggregates, which are removable by centrifugation. Autoclaving of DQAsome-incorporated paclitaxel leads to the quantitative precipitation of paclitaxel, whereas "empty" DQAsomes remain in the supernatant.

Although empty DQAsomes are spherical vesicles of similar size, the vesicle character of colloidal paclitaxel incorporated into DQAsomes has not been demonstrated. Cryo-electron (not shown) and transmission electron microscopic images (Fig. 7.3) showed, with considerable

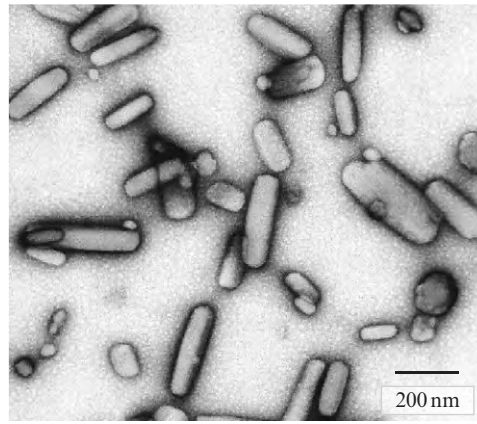

Figure 7.3 Negatively stained transmission electron microscopic image of paclitaxel-loaded DQAsomes (0.61 mol paclitaxel/mol dequalinium). Data from Cheng *et al.* (2005).

reproducibility, rod-shaped structures approximately 400 nm in length (Cheng *et al.*, 2005). Considering the reproducible stoichiometric composition of 2 mol dequalinium per 1 mol paclitaxel, it seems likely that the obtained colloidal solution of DQAsomal paclitaxel contains crystal-like solid nanoparticles instead of vesicles with encapsulated paclitaxel. Interestingly, electron microscopic images of colloidal solutions obtained when preparing DQAsomes in the presence of another drug, etoposide (VP-16), show the same rod-like structures (V. Weissig, 2005, unpublished). Attempts to determine exactly the nature of these DQAsomal drug preparations have not been made so far. Nevertheless, the formulation of paclitaxel in DQAsomes increases the solubility of the drug in comparison to free paclitaxel by a factor of roughly 3000, thereby presenting a possible alternative to Cremophor-based formulations of the highly insoluble paclitaxel.

A series of studies demonstrates that DQAsomal preparations of paclitaxel increase the drug's efficiency in triggering apoptosis by directly acting on mitochondria. First, fluorescence microscopic images of cells incubated with free fluorescently labeled paclitaxel and DQAsomal formulations thereof display a strikingly different intracellular drug disposition. While the free drug randomly diffuses throughout the cytosol, fluorescently labeled paclitaxel formulated with DQAsomes does colocalize with mitochondria (D'Souza *et al.*, 2008). Second, two apoptosis-specific assays based on changes of the nuclear morphology (chromatin condensation assay) and subsequent DNA laddering (DNA fragmentation assay) showed that DQAsomal

paclitaxel, in contrast to all controls, triggers cell death via apoptosis in cancer cells (D'Souza *et al.*, 2008). Third, in a tumor growth inhibition study with DQAsomal paclitaxel in nude mice bearing human colon carcinoma cells, DQAsomal paclitaxel inhibited tumor growth by about 50% in comparison to the free drug, which, at the concentration used, did not have any impact on tumor growth (Cheng *et al.*, 2005).

2.2. Chromatin condensation assay

In difference to healthy cells, the nuclei of apoptotic cells display highly condensed chromatin that can take the form of crescents around the periphery of the nucleus, or the entire nucleus can appear as a group of featureless, bright spherical beads (Fig. 7.4, insert). Such morphological changes in the nuclei of apoptotic cells can easily be visualized by fluorescence microscopy (Aizenman *et al.*, 2000; Druse *et al.*, 2005).

To assay chromatin condensation, that is, to count the number of apoptotic nuclei, Colo205 cells are plated in six-well plates such that they reach 50–70% confluency at the day of the experiment. Cells are washed three times with phosphate-buffered saline (PBS), and then 2 ml of serum-free

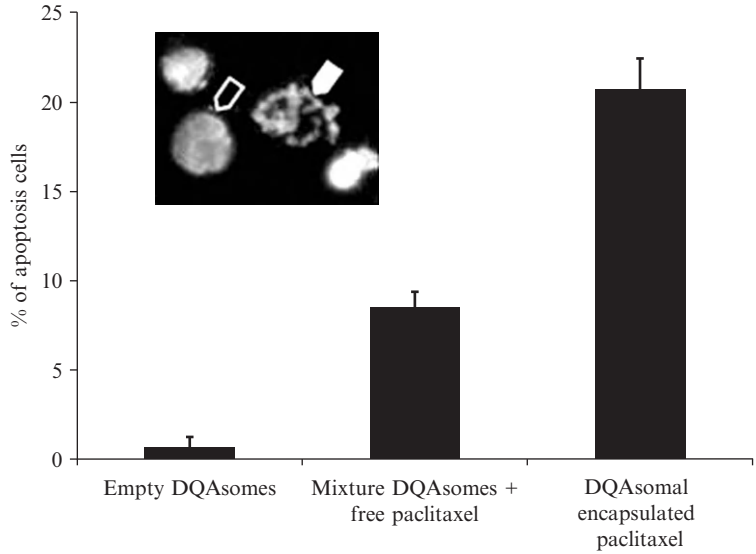

Figure 7.4 Nuclear morphology assay for determining apoptosis: quantitative estimation of apoptotic nuclei based on 400 cells counted for each group. Inset: representative image showing normal (open arrow) and apoptotic nuclei (solid arrow). Data from D'Souza *et al.* (2008).

RPMI-1640 medium are added. Cells are treated with drugs (negative control, 20 n*M* empty DQAsomes, 10 n*M* free paclitaxel mixed with 20 n*M* empty DQAsomes, and 10 n*M* paclitaxel formulated, i.e., incorporated into 10 n*M* DQAsomes), incubated for 2 h, followed by the addition of 10% FBS (final concentration). After further incubation for 20 h, the cells are stained with 10 mg/ml Hoechst 33342 for 10 min at 37 °C. Following trypsinization and washing with PBS, the stained cells are covered with fluoromount medium (Trevigen, Inc., Gaithersburg, MD). The nuclear morphology of cells can then be visualized using a Nikon Eclipse E400 epifluorescence microscope with a UV-2B filter.

Figure 7.4 shows a typical result of such an assay. Fluorescent nuclei were screened for normal morphology (unaltered chromatin) and apoptotic nuclei (identified as those with fragmented/scattered or condensed chromatin) were counted. Results were expressed as the percentage of apoptotic nuclei/400 nuclei. It can be seen that the percentage of apoptotic cells in samples treated with DQAsomal encapsulated paclitaxel is significantly higher in comparison to all controls.

2.3. DNA fragmentation assay

Colo205 cells are grown to 60% confluence in 25 cm^2 flasks, washed three times with PBS, followed by adding serum-free RPMI-1640 medium. Cells are treated for 20 or 30 h with 20 n*M* empty DQAsomes, 10 n*M* free paclitaxel, 20 nm empty DQAsomes mixed with 10 n*M* free paclitaxel, and 10 n*M* paclitaxel formulated into 20 n*M* DQAsomes followed by adding serum to a final concentration of 10%.

Genomic DNA of treated cells is extracted using the DNeasy Tissue Kit (Qiagen, Valencia, CA). Approximately, 3 mg of DNA sample is separated electrophoretically on a 1.4% agarose gel containing ethidium bromide (EtBr; 0.5 mg/ml). EtBr-stained DNA in the gel is then visualized under UV light and photographed. Alternatively, SYBR (Invitrogen, Carlsbad, CA) can be used as a less toxic stain.

2.4. Effect of paclitaxel formulated into DQAsomes on tumor growth in nude mice bearing human colon carcinoma cells

Female nude mice (Charles River Laboratory, Wilmington, MA; strain nu/nu, age 6–8 weeks, weight 20–22 g) are inoculated with 10–12 million Colo205 colon cancer cells s.c. into the left flank after having been appropriately anesthetized. Mice should form a palpable tumor about 1–2 mm in diameter within 7 days after inoculation.

Treatment is started 8 days after tumor inoculation, each injection is given i.p. in a volume of 150 µl. All groups involve eight mice and are treated as follows: untreated group: 5 m*M* HEPES, pH 7.4, is administered twice a week for 3 weeks. Free paclitaxel treated group: paclitaxel is suspended in 100% DMSO at a concentration of 20 m*M* and stored at 4 °C. Immediately before use, an appropriate amount is diluted into warmed medium. Paclitaxel (5.04 mg/kg/week) is administered twice a week for 1.5 weeks followed by administering 15.12 mg/kg/week for another 1.5 weeks. Empty DQAsome treated group: 3 mg/kg/week is administered twice a week for 1.5 weeks followed by administering 9.0 mg/kg/week for another 1.5 weeks. Group treated with paclitaxel encapsulated in DQAsomes: (3 mg dequalinium + 5.04 mg paclitaxel)/kg/week is administered twice a week for 1.5 weeks, followed by administering (9 mg dequalinium + 15.12 mg paclitaxel)/kg/week for another 1.5 weeks.

Tumor growth is determined by measurement of the diameter of the tumor nodule in two dimensions with a caliper twice a week. The apparent tumor volume is calculated during treatment using the following formula: tumor volume = (length × width^2)/2, with the length being greater than the width. The length and width of the tumor are measured in millimeter. Mice are sacrificed after 4 weeks by cervical dislocation following anesthesia, the tumor mass is isolated and weighed. Differences in apparent tumor volumes during treatment and postmortem tumor weights are compared using the non-parametric two-tailed Wilcoxon rank sum test (GraphPad Software, La Jolla, CA) for two independent samples. For easy representation of the difference in tumor volumes during the treatment between the control and the groups, the average tumor volume (mm^3) of the group versus days can be plotted. Tumor weights are plotted as box plots, which represent the median, quartiles, and extremes in a group.

The effects of DQAsomal paclitaxel versus the free drug and empty DQAsomes on tumor growth are shown in Figs. 7.5 and 7.6. It can be seen that at concentrations where free paclitaxel and empty DQAsomes do not show any impact on tumor growth, paclitaxel-loaded DQAsomes (with paclitaxel and dequalinium concentrations identical to controls) inhibit the tumor growth by about 50%. Correspondingly, the average tumor weight in the treatment group after sacrificing the animals after 26 days is approximately half of that in all controls. These results demonstrate that DQAsomes are able to increase the therapeutic potential of paclitaxel.

An independent study has confirmed the rod-like structure of paclitaxel formulated into DQAsomes, their colocalization with mitochondria as well as the resulting increased apoptotic activity of paclitaxel (Vaidya *et al.*, 2009). These authors also succeeded in further increasing the activity of DQAsomal paclitaxel by conjugating folic acid to the surface of DQAsomes making them specific for tumor cells overexpressing the folate receptor.

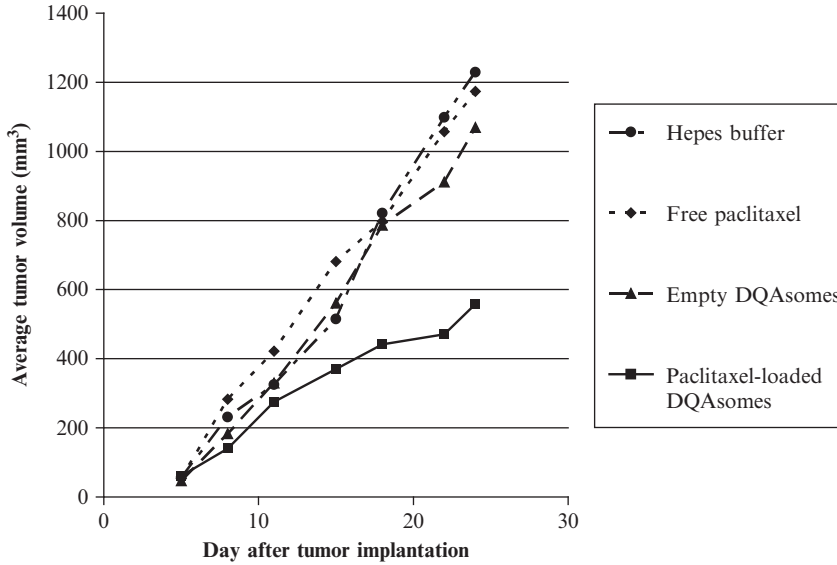

Figure 7.5 Tumor growth inhibition study in nude mice implanted with human colon cancer cells. The mean tumor volume from each group was blotted against the number of days. Each group involved eight animals. For clarity, error bars were omitted. Note that after 1.5 weeks the dose, normalized for paclitaxel, was tripled in all treatment groups. Data from Cheng *et al.* (2005).

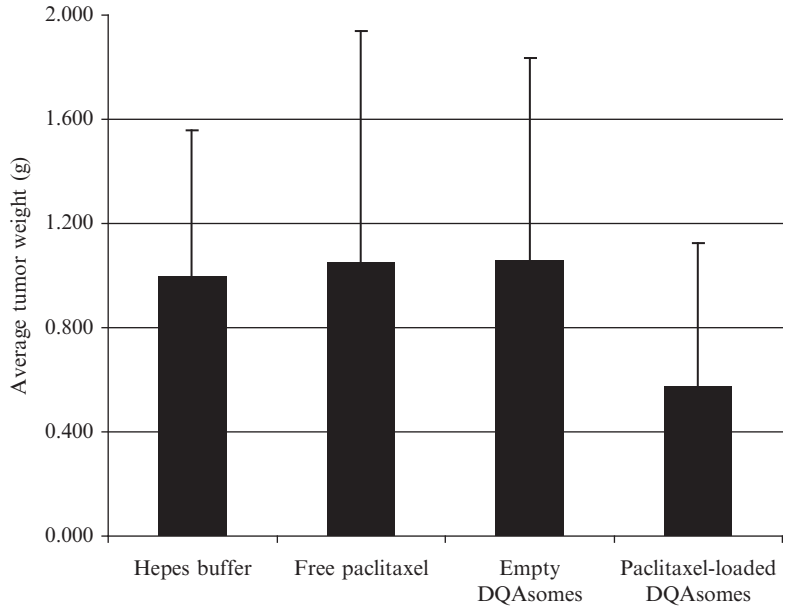

Figure 7.6 Average tumor weight ($n = 8$) at time of sacrifice of nude mice implanted with human colon cancer cells. For treatment group (paclitaxel-loaded DQAsomes) versus all three control groups combined $P = 0.054$ (Parametric Student T-test). Data from Cheng *et al.* (2005).

3. Mitochondriotropic Liposomes for the Delivery of Small Proapoptotic Molecules

3.1. Synthesis of stearyl-triphenylphosphonium bromide

Stearyl bromide (1.93 g, 5.5 mmol) and triphenylphosphine (1.52 g, 5.8 mmol) are heated under reflux for 20 h in freshly distilled anhydrous xylene (30 ml). The progress of the reaction can be monitored by thin layer chromatography (TLC) on silica gel plates (Silica Gel 60, F-254) using iodine as detection reagent. The solvent is removed on a rotary evaporator to obtain a crude yellowish oil. The crude is purified by silica gel column chromatography (75 g) using methanol:chloroform (5:95) as an eluent. Purified STPP, obtained as a colorless oil, crystallizes on standing and is recrystallized from ether to yield pure STPP at 35–45% yield. The product is characterized by ^{1}H NMR ($CDCl_3$) and ^{31}P NMR (with external 85% H_3PO_4 as reference) on a VARIAN Mercury 300 NMR spectrometer: ^{1}H NMR: 7.68–7.88 (m, 15H), 3.7–3.8 (m, 2H), 1.55–1.65 (t, 4H), 1.2–1.35 (m, 28H), 0.7–0.8 (t, 3H); ^{31}P NMR d: 25.34.

3.2. Surface modification of liposomes with stearyl-triphenylphosphonium bromide (preparation of STPP liposomes)

STPP liposomes are prepared by probe sonication according to Papahadjopoulos and Watkins (1967). However, any other common liposome preparation method can be chosen, depending upon the desired liposome properties and on the physicochemical nature of the low-molecular compounds to be entrapped (Düzgüneş, 2003; Mui *et al.*, 2003).

A mixture of lecithin, cholesterol, and STPP (PC/Ch/STPP = 65/15/20, molar ratio; final total lipid 25 mg/ml) is dissolved in chloroform, followed by removal of the organic solvent, using a rotary evaporator. After adding 5 m*M* HEPES (pH 7.4) to the dry lipid film, the sample is probe sonicated with a Sonic Dismembrator (Model 100, Fischer Scientific) at a power output of approximately 10 W for 30 min. To remove any titanium particles, which will be shed from the tip of the probe during sonication, the sample is centrifuged for 10 min at 3000 × *g*. The formed liposomes are separated from free, that is, non-incorporated, STPP by gel filtration chromatography on a Sephadex G-15 column.

Liposome size can be determined by dynamic light scattering analysis on a Beckman N4 Coulter Counter. The size of STPP liposomes with 20 mol% STPP and prepared following the above protocol was found to be 132 ± 59 nm (Boddapati *et al.*, 2005), which is slightly larger than one would have expected for liposomes prepared by probe sonication. Apparently, the

presence of 20 mol% STPP on the liposome surface seems to add to the vesicle's diameter. The liposome size does not change significantly upon storage at 4 °C over several weeks.

The zeta potential of STPP liposomes can be determined at 2.5 V, 657 nm, 2.00 Hz, and 25 °C using the Zeta Potential Analyzer Version 3.26 from Brookhaven Instruments Corporation. For each measurement, 10 µl liposome solution (total lipid 25 mg/ml; STPP content varying between 0 and 25 mol%) are added into 2 ml Hepes-buffered saline (HBS), pH 7.4 and incubated until temperature equilibration is attained. The zeta potential of STPP liposomes increases linearly with increasing amounts of incorporated STPP until it reaches a plateau between 15 and 20 mol% STPP (Fig. 7.7).

In addition to the zeta potential measurement, the liposomal incorporation of STPP can also be confirmed by ^{31}P NMR spectroscopy. The ^{31}P NMR spectrum (not shown) of STPP liposomes displays two chemical shifts correlating to the phosphorus in the lipid's phosphate groups and to the positively charged phosphorus of STPP (Boddapati *et al.*, 2005). No differences in both chemical shifts between the free compounds (i.e., free STPP and free phospholipid) and the liposome-incorporated molecules were found, indicating that the triphenylphosphonium group of STPP does not seem to interact with the bilayer membrane. This, in turn, suggests that STPP appears to be anchored in the lipid membrane as shown schematically in Fig. 7.8.

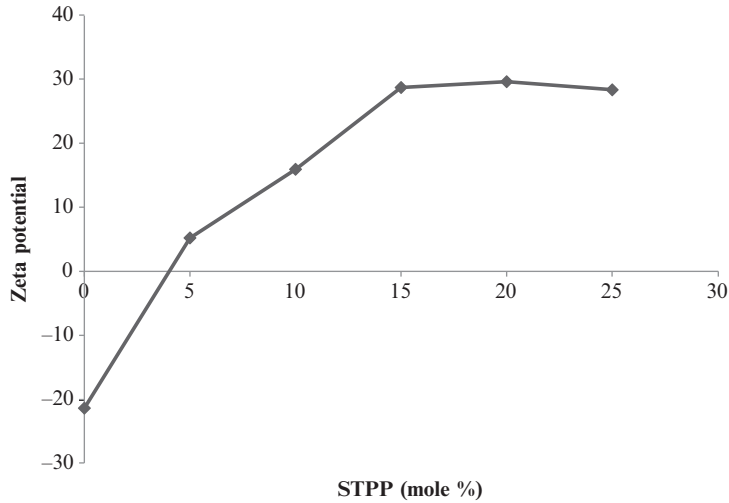

Figure 7.7 Zeta potential of liposomes with varying amounts of incorporated STPP. Data from Boddapati *et al.* (2005).

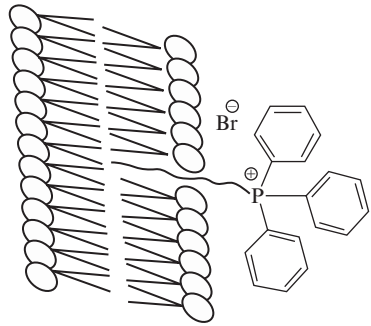

Figure 7.8 Schematic depiction of a mitochondriotropic triphenylphosphonium cation anchored in a liposomal phospholipid bilayer membrane via an alkyl residue (not drawn to molecular scale). From Boddapati *et al.* (2005).

3.3. Effect of ceramide incorporated into PEGylated STPP liposomes on the growth of murine 4T1 mammary carcinoma in Balb/c mice

STPP liposomes with incorporated ceramide are prepared following the above given protocol. In brief, the appropriate amount of ceramide-C6 (6-hexanoyl-D-erythro-sphingosine) required to make up 10 mol% of ceramide in the final liposome preparation is added to the appropriate mixture of lecithin, cholesterol, PEG5000-distearoylphosphatidylethanolamine ((DSPE) final concentration 3 mol%), and varying amounts of STPP in chloroform. The solvent is removed by rotary evaporation and the resulting dry thin lipid film is hydrated with 5 m*M* HEPES buffer, probe sonicated for 30 min and centrifuged for 10 min at 3000 $\times$ *g*. Liposomes are isolated by gel filtration on a Sephadex G-15 column and characterized for their size and zeta potential as described above.

To determine the maximal tolerated dose of STPP liposomes in mice, animals are divided into groups of six (female Balb/C mice), and liposomes containing STPP equivalent to 0.045, 01.15, 0.4.5, and 1.5 mg/kg are injected via tail vein (100 μl/mouse) on alternate days for a total of 10 doses over a 21-day period. The animals are monitored for changes in body weight, hydration, ataxia, and abnormal behavior. Doses of STPP can be considered safe if none of the mice in the group demonstrates any adverse effects during the 21-day test period.

To assess the biodistribution of PEG-STPP liposomes in tumor-bearing mice, STPP liposomes labeled with ^{111}In are prepared by the inclusion of 3 mol% PEG5000-PE and 0.5 mol% *N*-diethylenetriaminepentaacetic acid (DTPA)-PE. Following the preparation of the DTPA-PE containing liposomes, they are supplemented with 1 *M* citrate buffer and incubated for 1 h with ^{111}In–citrate complex at room temperature, and then dialyzed

overnight against HBS at 4 °C to remove free (unencapsulated) label. As a control, PEGylated liposomes without incorporated STPP are used. Female C57BL mice bearing LLC (Lewis Lung Carcinoma) tumors are injected via the tail vein with 5 μCi of the radiolabeled liposome dispersion, followed by sacrificing the animals after 24 h. Organs are then removed, weighed, and the radioactivity quantified as CPM using a Beckman 5500B gamma-counter. Following this procedure, it was found (Boddapati *et al.*, 2008) that 1.5 mol% STPP does not significantly change the expected biodistribution of PEG500-STPP liposomes in comparison to liposomes lacking the cationic ligand. Most importantly, the extent of liposomal tumor accumulation remains unchanged (not shown).

To assess the effect of liposomal ceramide on tumor growth, female Balb/c mice are inoculated by subcutaneous injection in the right hind flank region with mouse mammary carcinoma 4T1 cells (10^6 cells in 0.1 ml). Upon formation of measurable tumors, the mice are divided into three groups of five animals each for injection. The injections of a dose of liposomal ceramide equal to 6 mg/kg are repeated at a frequency of one injection per 2 days. Tumor growth is measured over the period of the injections and the tumor volumes of the groups compared.

Figure 7.9A shows the tumor volumes recorded over the course of the tumor growth inhibition study. In the case of buffer-treated as well as empty STPP-modified nanocarrier treated groups, 50% of the animals developed necrotic morbidity at day 12 and had to be euthanized as required by institutional humane treatment policy. However, all mice treated with ceramide in STPP-modified nanocarrier did not show any morbidity even after 18 days. Statistical analysis of tumor growth rate at the 12-day time point ($n = 6$) showed that the treatment with ceramide in the STPP-modified nanocarrier significantly inhibited the tumor growth rate compared to sham treatment (Fig. 7.9B). Further, there was no significant reduction in the tumor growth rate upon treatment with empty STPP-modified nanocarriers when compared to sham treatment, indicating that STPP-modified nanocarriers alone have no antitumor effect.

3.4. Formulation of CD437 into STPP liposomes and assessment of the drug's increased cytotoxicity *in vitro*

STPP liposomes are prepared by probe sonication, but any other liposome preparation method is applicable. A mixture of egg phosphatidylcholine (PC), cholesterol, STPP (synthesized as described above), and CD437 (available from Sigma) is dissolved in chloroform at a molar ratio PC/Ch/STPP/CD437 = 55/10/1/0.1 (total lipid 25 mg/ml). The amounts of CD437 can be varied but should not exceed 10 mol% of the total lipid. Following removal of the organic solvent using a rotary evaporator, 5 m*M* HEPES (pH 7.4) is added to the dry lipid film and the sample is then probe

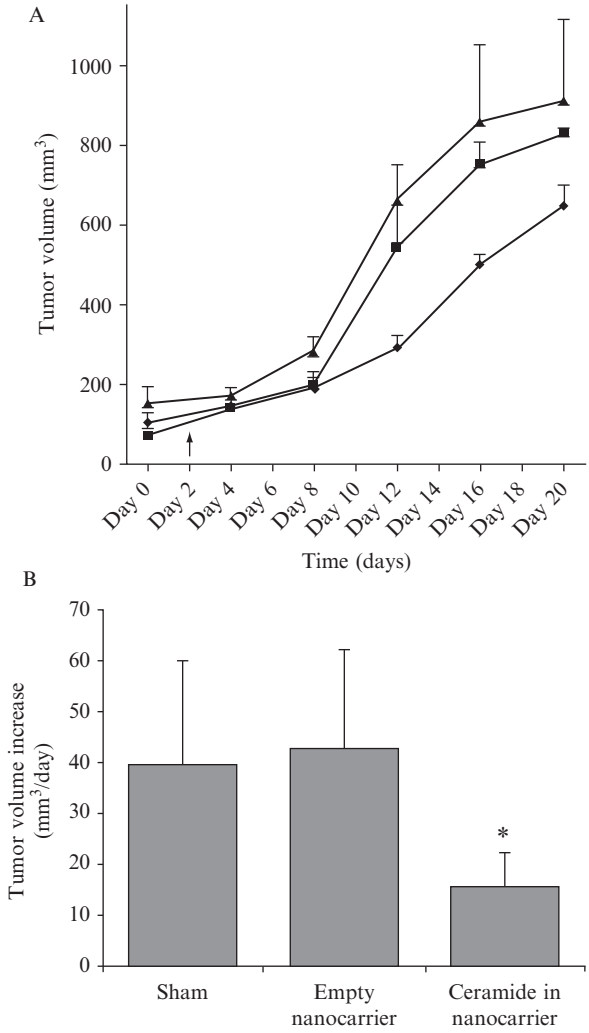

Figure 7.9 Tumor growth inhibition. (A) Tumor volume ($mm^3 \pm$ standard deviation) measured over time period of treatment in Balb/c mice bearing murine 4T1 mammary carcinoma tumors ($n = 6$): after treatment with buffer (▪), empty STPP liposomes (▲), and ceramide in STPP liposomes (◆). The arrow indicates the start of treatment. (B) Tumor growth in mm^3/day ± standard deviation at day 12 ($n = 6$) (*indicates a P value of < 0.05).

sonicated with a Sonic Dismembrator (Model 100, Fischer Scientific) at a power output of approximately 10 W for 30 min. To remove any titanium particles, which will have leaked from the probe during sonication, the sample is centrifuged for 10 min at about 3000 × *g*. The formed liposomes

with incorporated CD437 are separated from free non-incorporated CD437 by gel filtration chromatography on a Sephadex G-15 column.

The amount of liposome-encapsulated CD437 is determined by high-performance liquid chromatography (HPLC). Liposomes are lysed by adding Triton X-100 at a final concentration of 1% followed by adding 5 μl of internal standard (100 μg/ml all-*trans*-retinol acetate). Samples are then injected into an HPLC apparatus (Waters Alliance 2690, Separation Module with a Waters 717 autosampler). The separations of CD437 and internal standard are achieved on a chemically bonded reversed-phased C_{18} analytical column (Waters Symmetry, 150 × 4.6 mm, 3.5 μm particle size) with a Symmetry C_{18} guard column (5 μm, 3.9 × 20 mm). Isocratic elution with acetonitrile:water:glacial acetic acid (88:10:2, v/v) should be delivered at a flow rate of 1.0 ml/min. The volume of injection is set for 100 μl and the autosampler temperature is set at 4 °C. Eluents are detected by a Waters 2487 UV–visible absorbance detector at 325 nm. The standard curves are prepared daily by spiking and measuring known amounts of CD437 in the presence of the internal standard. Liposomal phospholipid can be quantified using any standard phosphate assay (Düzgüneş, 2003). The amount of encapsulated CD437 can be expressed in mg/ml as well as in mol CD437 per mol phospholipid.

To assess the cytotoxicity of liposomal CD437, COLO205 cells are grown in 96 well plates to 50–60% confluence, followed by incubation for 48 h with the appropriate amounts of drug-loaded liposomes, empty liposomes, the free drug, and mixtures of the free drug with empty liposomes. Following incubation, the cells are washed and 20 μl/well MTS reagent (CellTiter 96® AQueous One Solution Cell Proliferation Assay from Promega, Madison, WI) is added. After incubation for 4 h, the resultant absorbance is measured at 490 nm. As can be seen from Fig. 7.10, CD437 formulated in STPP liposomes possesses superior cytotoxicity over all controls.

3.5. Incorporation of sclareol into STPP liposomes and assessment of the drug's increased proapoptotic activity

Liposomes are prepared by the thin-film hydration method as described by Gabizon and Papahadjopoulos (1988). The lipid film is prepared by adding PC, dipalmitoylphosphatidylglycerol (DPPG) (Avanti Polar Lipids, Alabaster, AL), sclareol (Sigma–Aldrich, St. Louis, MO) and then either STPP (synthesized as described above) or 1,2-dioleoyl-3-trimethylammonium-propane (chloride salt) (DOTAP) in the molar ratios shown in Table 7.2. Liposomes containing DOTAP instead of STPP serve as a control: both molecules possess a positive charge, but in contrast to DOTAP, the charge in STPP is delocalized, which is a major prerequisite for this molecule's mitochondriotropism (Horobin *et al.*, 2007).

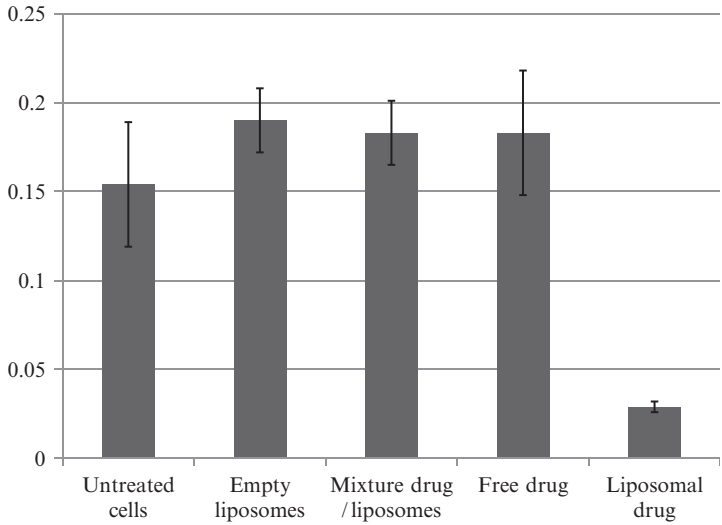

Figure 7.10 Cytotoxicity of CD437 formulated into STPP liposomes. Colon cancer cells were incubated with 200 n*M* CD437, either in free form as a mixture with empty STPP liposomes or incorporated into STPP liposomes.

Table 7.2 Summary of lipid compositions used to prepare sclareol-containing STPP and DOTAP liposomes

Formulation	Lipid composition	Molar ratio
Empty STPP liposomes	EPC:DPPG:STPP	8.87:0.1:0.136
Sclareol-containing STPP liposomes	EPC:DPPG:STPP: sclareol	8.87:0.1:0.136:5
Empty DOTAP liposomes	EPC:DPPG:DOTAP	8.87:0.1:0.136
Sclareol-containing DOTAP liposomes	EPC:DPPG:DOTAP: sclareol	8.87:0.1:0.136:5

Data from Patel *et al.* (2009).

After the removal of chloroform at 40 °C under vacuum in a rotary evaporator, the lipid film is hydrated with 0.292 *M* of sucrose (sucrose-to-lipid ratio, 2.24, w/w) for 1 h with occasional stirring to produce a crude suspension. This suspension is subjected to sonication for two 5-min periods interrupted by a 5-min resting period in an ice-water bath, using a probe sonicator (6 W, 60 Sonic Dismembrator; Fisher Scientific, Pittsburgh, PA). The resulting liposomal preparation is allowed to rest for 30 min and then centrifuged at 3000 rpm for 6 min at 25 °C in order to remove any titanium particles shed from the probe. Following lyophilization, the liposomal preparation is reconstituted to initial volume by adding HPLC-grade

water. After the addition of water, preparations are allowed to rest for 15 min with occasional stirring before use.

To assess the proapoptotic activity of sclareol-containing liposomes, an Annexin V Binding Assay can be used (Vybrant® Apoptosis Assay kit #3 from Invitrogen). The loss of cell membrane asymmetry is an early event in apoptosis, resulting in the surface exposure of phosphatidylserine, which, in turn, binds Annexin V, a specific phospholipid-binding protein (Overbeeke *et al.*, 1998; van den Eijnde *et al.*, 1998; van Engeland *et al.*, 1998). Human colon carcinoma (COLO205) cells are grown in a T25 culture flask until they are about 75% confluent. Cells are then treated for 8 h with sclareol incorporated in the above-described liposome formulations to achieve a 100 μ*M* final concentration of sclareol per flask. After incubation, cells are collected and centrifuged to obtain cell pellets. Cell pellets are resuspended in PBS. The cells are then counted by using a Neubauer Slide (Fisher Scientific, Pittsburgh, PA). Aliquots containing 0.2 million cells are used to measure apoptotic cells by flow cytometry, according to the manufacturer's protocol. Results can be expressed as the percent increase in cells undergoing apoptosis in treated cells over untreated control. Following this procedure, it was found (not shown) that there was an almost threefold increase in Annexin V binding in the case of cells treated with sclareol incorporated into mitochondria-targeted (i.e., STPP-containing) liposomes, compared to sclareol incorporated into non-mitochondria targeted, that is, DOTAP liposomes (Patel *et al.*, 2009).

To further elucidate which one of the apoptotic pathways (i.e., the extrinsic vs. the intrinsic pathway) is being activated by the liposomal drug formulations, caspase-8 and -9 activities can be measured by using the Caspase-8/FLICE and Caspase-9 Fluorometric assay kits (Biovision, Mountain View, CA), respectively. COLO205 cells are grown in a T75 culture flask until about 75% confluency, and then treated for 24 h with sclareol incorporated in either STPP or DOTAP liposomes, at a final sclareol concentration of 100 μ*M*. Following incubation, cells are collected and centrifuged to obtain cell pellets, which are resuspended in PBS. The cells are counted by using a Neubauer Slide. Aliquots containing 1 million cells are used to measure caspase-8 and -9 activities, according to the instructions supplied with the respective kits. Caspase activities are determined for treated as well as untreated cells. Results are expressed as the percent increase in caspase activity in treated samples over the untreated control. It was found (not shown) that both caspase-8 and -9 activities in cells treated with sclareol incorporated into STPP liposomes were significantly greater than in cells treated with sclareol incorporated into DOTAP liposomes. In addition, an apparent greater induction of caspase-9 activity suggests an increased induction of the mitochondria-mediated intrinsic pathway as a result of delivering the drug specifically to mitochondria (Patel *et al.*, 2009).

4. Conclusions

DQAsomes and STPP liposomes constitute the first available mitochondria-targeted pharmaceutical nanocarrier systems. This chapter describes in detail methods pertaining to the use of these novel drug carriers for the selective delivery of proapoptotic molecules to cancer cell mitochondria. Studies presented demonstrate clearly that the mitochondria-targeted delivery of drugs that are known to act significantly on mitochondria increases the efficiency and efficacy of such drugs *in vitro* as well as *in vivo*. In conclusion, nanocarrier-mediated drug delivery to mitochondria represents a new approach toward anticancer chemotherapy.

ACKNOWLEDGMENTS

All work in the author's laboratories has been financially supported over the years by the Mitochondrial Disease Association (Tucson, AZ), the United Mitochondrial Disease Foundation (Pittsburgh, PA), the Massachusetts Technology Transfer Center (Boston, MA), Northeastern University (Boston, MA), and Midwestern University Glendale (Glendale, AZ). The author would like to thank all his undergraduate and graduate of students who have contributed to these studies. In particular, the author is appreciative of the significant contributions from his former Ph.D. students Dr. Gerard D'Souza, Dr. Sarathi Boddapati, Dr. Shing-Ming Cheng, and Dr. Eyad Katrangi.

REFERENCES

Aizenman, E., Stout, A. K., Hartnett, K. A., Dineley, K. E., McLaughlin, B., and Reynolds, I. J. (2000). Induction of neuronal apoptosis by thiol oxidation: Putative role of intracellular zinc release. *J. Neurochem.* **75,** 1878–1888.

Andre, N., Braguer, D., Brasseur, G., Goncalves, A., Lemesle-Meunier, D., Guise, S., Jordan, M. A., and Briand, C. (2000). Paclitaxel induces release of cytochrome c from mitochondria isolated from human neuroblastoma cells. *Cancer Res.* **60,** 5349–5353.

Bangham, A. D., Standish, M. M., and Miller, N. (1965a). Cation permeability of phospholipid model membranes: Effect of narcotics. *Nature* **208,** 1295–1297.

Bangham, A. D., Standish, M. M., and Watkins, J. C. (1965b). Diffusion of univalent ions across the lamellae of swollen phospholipids. *J. Mol. Biol.* **13,** 238–252.

Biasutto, L., Dong, L. F., Zoratti, M., and Neuzil, J. (2010). Mitochondrially targeted anticancer agents. *Mitochondrion* **10,** 670–681.

Boddapati, S. V., Tongcharoensirikul, P., Hanson, R. N., D'Souza, G. G., Torchilin, V. P., and Weissig, V. (2005). Mitochondriotropic liposomes. *J. Liposome Res.* **15,** 49–58.

Boddapati, S. V., D'Souza, G. G., Erdogan, S., Torchilin, V. P., and Weissig, V. (2008). Organelle-targeted nanocarriers: Specific delivery of liposomal ceramide to mitochondria enhances its cytotoxicity in vitro and in vivo. *Nano Lett.* **8,** 2559–2563.

Chen, G., Wang, F., Trachootham, D., and Huang, P. (2010). Preferential killing of cancer cells with mitochondrial dysfunction by natural compounds. *Mitochondrion* **10,** 614–625.

Cheng, S. M., Pabba, S., Torchilin, V. P., Fowle, W., Kimpfler, A., Schubert, R., and Weissig, V. (2005). Towards mitochondria-specific delivery of apoptosis-inducing agents: DQAsomal incorporated paclitaxel. *J. Drug Deliv. Sci. Technol.* **15,** 81–86.

D'Souza, G. G., Rammohan, R., Cheng, S. M., Torchilin, V. P., and Weissig, V. (2003). DQAsome-mediated delivery of plasmid DNA toward mitochondria in living cells. *J. Control. Release* **92,** 189–197.

D'Souza, G. G., Cheng, S. M., Boddapati, S. V., Horobin, R. W., and Weissig, V. (2008). Nanocarrier-assisted sub-cellular targeting to the site of mitochondria improves the pro-apoptotic activity of paclitaxel. *J. Drug Target.* **16,** 578–585.

Decaudin, D., Marzo, I., Brenner, C., and Kroemer, G. (1998). Mitochondria in chemotherapy-induced apoptosis: A prospective novel target of cancer therapy (review). *Int. J. Oncol.* **12,** 141–152.

Dimas, K., Kokkinopoulos, D., Demetzos, C., Vaos, B., Marselos, M., Malamas, M., and Tzavaras, T. (1999). The effect of sclareol on growth and cell cycle progression of human leukemic cell lines. *Leuk. Res.* **23,** 217–234.

Dimas, K., Demetzos, C., Vaos, V., Ioannidis, P., and Trangas, T. (2001). Labdane type diterpenes down-regulate the expression of c-Myc protein, but not of Bcl-2, in human leukemia T-cells undergoing apoptosis. *Leuk. Res.* **25,** 449–454.

Dimas, K., Hatziantoniou, S., Tseleni, S., Khan, H., Georgopoulos, A., Alevizopoulos, K., Wyche, J. H., Pantazis, P., and Demetzos, C. (2007). Sclareol induces apoptosis in human HCT116 colon cancer cells in vitro and suppression of HCT116 tumor growth in immunodeficient mice. *Apoptosis* **12,** 685–694.

Druse, M., Tajuddin, N. F., Gillespie, R. A., and Le, P. (2005). Signaling pathways involved with serotonin1A agonist-mediated neuroprotection against ethanol-induced apoptosis of fetal rhombencephalic neurons. *Brain Res. Dev. Brain Res.* **159,** 18–28.

Duvvuri, M., Feng, W., Mathis, A., and Krise, J. P. (2004a). A cell fractionation approach for the quantitative analysis of subcellular drug disposition. *Pharm. Res.* **21,** 26–32.

Duvvuri, M., Gong, Y., Chatterji, D., and Krise, J. P. (2004b). Weak base permeability characteristics influence the intracellular sequestration site in the multidrug-resistant human leukemic cell line HL-60. *J. Biol. Chem.* **279,** 32367–32372.

Düzgüneş, N. (2003). Preparation and quantitation of small unilamellar liposomes and large unilamellar reverse-phase evaporation liposomes. *Methods Enzymol.* **367,** 23–27.

Gabizon, A., and Papahadjopoulos, D. (1988). Liposome formulations with prolonged circulation time in blood and enhanced uptake by tumors. *Proc. Natl. Acad. Sci. USA* **85,** 6949–6953.

Gamboa-Vujicic, G., Emma, D. A., Liao, S. Y., Fuchtner, C., and Manetta, A. (1993). Toxicity of the mitochondrial poison dequalinium chloride in a murine model system. *J. Pharm. Sci.* **82,** 231–235.

Goncalves, A., Braguer, D., Carles, G., Andre, N., Prevot, C., and Briand, C. (2000). Caspase-8 activation independent of CD95/CD95-L interaction during paclitaxel-induced apoptosis in human colon cancer cells (HT29-D4). *Biochem. Pharmacol.* **60,** 1579–1584.

Gonda, K., Tsuchiya, H., Sakabe, T., Akechi, Y., Ikeda, R., Nishio, R., Terabayashi, K., Ishii, K., Matsumi, Y., Ashla, A. A., Okamoto, H., Takubo, K., *et al.* (2008). Synthetic retinoid CD437 induces mitochondria-mediated apoptosis in hepatocellular carcinoma cells. *Biochem. Biophys. Res. Commun.* **370,** 629–633.

Gregoriadis, G. (1975). Letter: Enzyme-carrier potential of liposomes in enzyme replacement therapy. *N. Engl. J. Med.* **292,** 215.

Gregoriadis, G. (1976a). The carrier potential of liposomes in biology and medicine (first of two parts). *N. Engl. J. Med.* **295,** 704–710.

Gregoriadis, G. (1976b). The carrier potential of liposomes in biology and medicine (second of two parts). *N. Engl. J. Med.* **295,** 765–770.

Guchelaar, H. J., Vermes, A., Vermes, I., and Haanen, C. (1997). Apoptosis: Molecular mechanisms and implications for cancer chemotherapy. *Pharm. World Sci.* **19,** 119–125.

Horobin, R. W. (2001). Uptake, distribution and accumulation of dyes and fluorescent probes within living cells: A structure-activity modelling approach. *Adv. Colour Sci. Technol.* **4,** 101–107.

Horobin, R. W., Trapp, S., and Weissig, V. (2007). Mitochondriotropics: A review of their mode of action, and their applications for drug and DNA delivery to mammalian mitochondria. *J. Control. Release* **121,** 125–136.

Lasch, J., Meye, A., Taubert, H., Koelsch, R., Mansa-ard, J., and Weissig, V. (1999). Dequalinium vesicles form stable complexes with plasmid DNA which are protected from DNase attack. *Biol. Chem.* **380,** 647–652.

Lechardeur, D., and Lukacs, G. L. (2002). Intracellular barriers to non-viral gene transfer. *Curr. Gene Ther.* **2,** 183–194.

Lyrawati, D., Trounson, A., and Cram, D. (2011). Expression of GFP in the mitochondrial compartment using DQAsome-mediated delivery of an artificial mini-mitochondrial genome. *Pharm. Res.* **28,** 2848–2862.

Magee, A. I., and Schlesinger, M. J. (1982). Fatty acid acylation of eukaryotic cell membrane proteins. *Biochim. Biophys. Acta* **694,** 279–289.

Mui, B., Chow, L., and Hope, M. J. (2003). Extrusion technique to generate liposomes of defined size. *Methods Enzymol.* **367,** 3–14.

Murphy, M. P., and Smith, R. A. (2000). Drug delivery to mitochondria: The key to mitochondrial medicine. *Adv. Drug Deliv. Rev.* **41,** 235–250.

Overbeeke, R., Steffens-Nakken, H., Vermes, I., Reutelingsperger, C., and Haanen, C. (1998). Early features of apoptosis detected by four different flow cytometry assays. *Apoptosis* **3,** 115–121.

Papahadjopoulos, D., and Watkins, J. C. (1967). Phospholipid model membranes. II. Permeability properties of hydrated liquid crystals. *Biochim. Biophys. Acta* **135,** 639–652.

Patel, N. R., Hatziantoniou, S., Georgopoulos, A., Demetzos, C., Torchilin, V. P., Weissig, V., and D'Souza, G. G. (2009). Mitochondria-targeted liposomes improve the apoptotic and cytotoxic action of sclareol. *J. Liposome Res.* **20,** 244–249.

Ralph, S. J., Rodriguez-Enriquez, S., Neuzil, J., and Moreno-Sanchez, R. (2010). Bioenergetic pathways in tumor mitochondria as targets for cancer therapy and the importance of the ROS-induced apoptotic trigger. *Mol. Aspects Med.* **31,** 29–59.

Schlesinger, M. J., and Magee, A. I. (1982). Fatty acid acylation of membrane proteins. *Biophys. J.* **37,** 126–127.

Schmidt, M. F. (1983). Fatty acid binding: A new kind of posttranslational modification of membrane proteins. *Curr. Top. Microbiol. Immunol.* **102,** 101–129.

Siskind, L. J., and Colombini, M. (2000). The lipids C2- and C16-ceramide form large stable channels. Implications for apoptosis. *J. Biol. Chem.* **275,** 38640–38644.

Smith, R. A., Porteous, C. M., Coulter, C. V., and Murphy, M. P. (1999). Selective targeting of an antioxidant to mitochondria. *Eur. J. Biochem.* **263,** 709–716.

Torchilin, V. P., Weissig, V., Martin, F. J., Heath, T. D., and New, R. R. C. (2003). Surface modification of liposomes. *In* "Liposomes—A Practical Approach," (V. P. Torchilin and V. Weissig, eds.), pp. 193–229. Oxford University Press, Oxford.

Vaidya, B., Paliwal, R., Rai, S., Khatri, K., Goyal, A. K., Mishra, N., and Vyas, S. (2009). Cell-selective mitochondrial targeting: A new approach for cancer therapy. *Cancer Ther.* **7,** 141–148.

van den Eijnde, S. M., Boshart, L., Baehrecke, E. H., De Zeeuw, C. I., Reutelingsperger, C. P., and Vermeij-Keers, C. (1998). Cell surface exposure of phosphatidylserine during apoptosis is phylogenetically conserved. *Apoptosis* **3,** 9–16.

van Engeland, M., Nieland, L. J., Ramaekers, F. C., Schutte, B., and Reutelingsperger, C. P. (1998). Annexin V-affinity assay: A review on an apoptosis detection system based on phosphatidylserine exposure. *Cytometry* **31,** 1–9.

Watanabe, Y., Tsuchiya, H., Sakabe, T., Matsuoka, S., Akechi, Y., Fujimoto, Y., Yamane, K., Ikeda, R., Nishio, R., Terabayashi, K., Ishii, K., Gonda, K., *et al.* (2008). CD437 induces apoptosis in ovarian adenocarcinoma cells via ER stress signaling. *Biochem. Biophys. Res. Commun.* **366,** 840–847.

Weiss, M. J., Wong, J. R., Ha, C. S., Bleday, R., Salem, R. R., Steele, G. D., Jr., and Chen, L. B. (1987). Dequalinium, a topical antimicrobial agent, displays anticarcinoma activity based on selective mitochondrial accumulation. *Proc. Natl. Acad. Sci. USA* **84,** 5444–5448.

Weissig, V., and Gregoriadis, G. (1992). Coupling of amino group bearing ligands to liposomes. *In* "Liposome Technology," (G. Gregoriadis, ed.)Vol. III, pp. 231–248. CRC Press Inc., Boca Raton.

Weissig, V., Lasch, J., Klibanov, A. L., and Torchilin, V. P. (1986). A new hydrophobic anchor for the attachment of proteins to liposomal membranes. *FEBS Lett.* **202,** 86–90.

Weissig, V., Lasch, J., and Gregoriadis, G. (1989). Covalent coupling of sugars to liposomes. *Biochim. Biophys. Acta* **1003,** 54–57.

Weissig, V., Lasch, J., Erdos, G., Meyer, H. W., Rowe, T. C., and Hughes, J. (1998a). DQAsomes: A novel potential drug and gene delivery system made from Dequalinium. *Pharm. Res.* **15,** 334–337.

Weissig, V., Moegel, H.-J., Wahab, M., and Lasch, J. (1998b). Computer simulation of DQAsomes. *Proc. Int. Symp. Control Release Bioact. Mater.* **25,** 196–197.

Weissig, V., Lizano, C., and Torchilin, V. P. (2000). Selective DNA release from DQAsome/DNA complexes at mitochondria-like membranes. *Drug Deliv.* **7,** 1–5.

Weissig, V., D'Souza, G. G., and Torchilin, V. P. (2001). DQAsome/DNA complexes release DNA upon contact with isolated mouse liver mitochondria. *J. Control. Release* **75,** 401–408.

Weissig, V., David, J., Liu, X., Psaros, S., Voong, K., Kao, J., and Walker, A. (2009). Liposome-based delivery of CD437 to mitochondria enhances its cytotoxicity in vitro. Annual Meeting of the American Association of Pharmaceutical Sciences, Los Angeles, CA.

CHAPTER EIGHT

Targeting of Tumor Endothelium by RGD-Grafted PLGA-Nanoparticles

Fabienne Danhier,* Vincent Pourcelle,† Jacqueline Marchand-Brynaert,† Christine Jérôme,‡ Olivier Feron,§ *and* Véronique Préat*

Contents

* Louvain Drug Research Institute, Pharmaceutics and Drug Delivery, Université Catholique de Louvain, Brussels, Belgium
† Institute of Condensed Matter and Nanosciences, Organic and Medicinal Chemistry, Université Catholique de Louvain, Louvain-la-Neuve, Belgium
‡ Centre d'Etude et de Recherche sur les Macromolécules, Université de Liège, Liège, Belgium
§ Institute of Experimental and Clinical Research, Pole of Pharmacology, Université Catholique de Louvain, Brussels, Belgium

Methods in Enzymology, Volume 508
ISSN 0076-6879, DOI: 10.1016/B978-0-12-391860-4.00008-2

Abstract

The destruction of the neovessels in solid tumors can cause the death of tumor cells resulting from the lack of oxygen and nutrients. Peculiarities of the tumor vasculature, however, also position angiogenic endothelial cells as obvious targets to address cytotoxic drugs into the tumor. In particular, the identification of a three-amino acids sequence, arginine-glycine-aspartate (RGD), as a fundamental recognition site for proliferating endothelial attachment to the extracellular matrix leads to the development of tumor-targeting ligands for nanoparticles. The RGD peptide can target the $\alpha_v\beta_3$ integrin overexpressed by the tumor endothelium, and thereby increases the accumulation of drug-loaded RGD-grafted nanoparticles. RGD-nanoparticles may thus extravasate more efficiently and enter the tumor via the enhanced permeability and retention (EPR) effect. This combination of active and passive processes leads to the penetration of nanoparticles into the tumor tissue, followed by cellular uptake and intracellular delivery of the cytotoxic payload. Since cancer cells may also express $\alpha_v\beta_3$ integrin, the entrapping of RGD-nanoparticles into the tumor interstitial fluid may yet be facilitated through direct binding to cancer cells. Here, we describe methods used for the preparation of RGD-nanoparticles and for the validation of their potential of tumor endothelium targeting both *in vitro* and *in vivo*. We also illustrate how RGD-nanoparticles may be more suited than nontargeted modalities for the tumor delivery of poorly soluble and/or highly cytotoxic drugs, using different mouse tumor xenograft models.

1. Introduction

Although cancer cells are inherently more vulnerable to chemotherapy than the majority of normal cells, most anticancer drugs are nonselective and can cause injury to normal tissues. Efforts are now focused on attempts to kill cancer cells by more targeting ways while sparing normal cells (Haley and Frenkel, 2008; Lammers *et al.*, 2008). Because of the particular characteristics of the tumor microenvironment and tumor angiogenesis, it is possible to design drug delivery systems that specifically target anticancer drugs to tumors, exploiting vascular abnormalities of tumors. Nanoparticles can target them by a passive or active process. *Passive targeting* implies that nanoparticles, smaller than the fenestrations between endothelial cells, can enter the interstitium and be entrapped in the tumor tissues. The combination of leaky vasculature and poor lymphatic drainage results in the well-known enhanced permeability and retention (EPR) effect (Maeda *et al.*, 2000). *Active targeting* involves drug delivery to a specific site based on the molecular recognition. One approach is to couple a ligand to nanoparticles that can interact with a receptor at the target cell site (Danhier *et al.*, 2010a).

The angiogenic phenotype of the tumor vasculature and, in particular, some proteins or receptors expressed at the surface of the endothelial cells

lining the tumor blood vessels (Carmeliet and Jain, 2000; Ruoslahti, 2002) are considered as very attractive targets for addressing nanoparticles to tumors. The best example is the integrin adhesion molecule $\alpha_v\beta_3$, which is known to play key roles in angiogenesis by "integrating" extracellular stimuli into intracellular signaling (Hynes, 2002). More generally, the α_v integrin subunit is highly expressed on endothelial cells lining tumor and tumor cells but poorly expressed in resting endothelial cells and most normal organs (Brooks *et al.*, 1994). Targeting the $\alpha_v\beta_3$ integrin with drugs may thus provide an opportunity to destroy tumor vessels but sparing microvessels from normal tissues (Arap *et al.*, 1998; Murphy *et al.*, 2008). The RGD sequence (Arg-Gly-Asp) was first discovered in the early 1970s by E. Ruoslahti as a cell attachment site in fibronectin. Later, this sequence has been recognized as the minimal integrin sequence present in many natural ligands binding the $\alpha_v\beta_3$ receptor, including fibrinogen, fibronectin, vitronectin, plasminogen, thrombospondin, prothrombin, MMP-2, laminin, osteopontin, etc. (Sheldrake and Patterson, 2009). The RGD sequence is currently the basic module for a variety of molecules designed for the preferential binding to either $\alpha_v\beta_3$ integrin or other integrins (Temming *et al.*, 2005). RGD-targeted nanocarriers have indeed the potential to deliver various pharmacological agents to the $\alpha_v\beta_3$-expressing tumor vasculature. Interestingly, $\alpha_v\beta_3$ integrin is upregulated not only in angiogenic endothelial cells but also in several tumor cells. Hence, RGD-targeted nanocarriers can potentially consist in a double targeting.

Interestingly, two recent papers (Sugahara *et al.*, 2009, 2010) have shown that the iRGD cyclic peptide has the potential to selectively deliver a large variety of therapeutic or diagnostic agents to a tumor site. In a first step, the RGD motif of the iRGD cyclic peptide interacts with the α_v integrin present at the endothelial cell surface; in a second step, a protease cleaves iRGD and exposes the cryptic CendR motif RGDK that can interact with the neuropilin-1 receptor, and thereby increase tumor vascular permeability. Remarkably, this penetrating peptide works not only when it is conjugated to the payload but also when it is coadministered with small molecules, nanoparticles, or monoclonal antibodies (Feron, 2010).

Different RGD-targeted nanocarriers have been studied. The first results to show the inhibition of metastases with this kind of strategy were obtained with targeted nanoparticles loaded with doxorubicin (DOX) (Murphy *et al.*, 2008). The preferential activity of these nanoparticles on metastases suggests that growing metastatic tumors may have a greater dependence on angiogenic vessels. Other nanocarriers have been grafted with the RGD peptide such as polymeric micelle, *N*-(2-hydroxypropyl) methacrylamide (HPMA) conjugate or liposomes (Borgman *et al.*, 2009; Meng *et al.*, 2010; Zhan *et al.*, 2010). Poly (lactide-co-glycolide) (PLGA)-based nanoparticles decorated with the RGD peptide were designed for DOX *in vitro* (Wang *et al.*, 2009) and for paclitaxel (PTX) delivery both *in vitro* and *in vivo* (Danhier *et al.*, 2009a,b).

In this chapter, we describe the preparation of the nanoparticles and some experimental procedures to demonstrate both *in vitro* and *in vivo* the tumor targeting of PLGA-based RGD-nanoparticles loaded with anticancer drugs. Poly(lactide-co-glycolide) (PLGA) was chosen for its biodegradability properties, its biocompatibility, and its approval by FDA. Poly(ε-caprolactone-co-ethylene glycol) (PCL-PEG), an amphiphilic copolymer, was added to take advantage of PEG repulsive properties (Owens and Peppas, 2006), to provide a higher stability for nanoparticles in biological fluids, and to allow the grafting of targeting ligands at the nanoparticle surface (Garinot *et al.*, 2007). In these different studies, the paradigmatic examples of anticancer drugs taking advantage of the nanoparticles encapsulation are PTX, DOX, and the recently developed cyclin-dependent kinase (CDK) inhibitor JNJ-7706621. PTX is a drug isolated from the bark of *Taxus brevifolia* with documented cytotoxic activity against various types of solid tumors. Because of a low solubility, PTX is currently formulated (Taxol®) at 6 mg/ml in a vehicle composed of a 1:1 blend of Cremophor® EL and ethanol. However, Cremophor® EL causes side effects, for example, hypersensitivity and nephrotoxicity (Singla *et al.*, 2002). DOX is an anthracycline antibiotic and a highly potent antineoplastic agent approved for use against a wide spectrum of tumors, including acute leukemias, lymphomas, and a variety of solid tumors. Unfortunately, its long-term clinical use is compromised by its dose-dependent cardiotoxicity, which may lead to irreversible cardiomyopathy and subsequent congestive heart failure (Shan *et al.*, 1996). Finally, JNJ-7706621 is a 1,2,4-triazole-3,5-diamine derivative that inhibits CDK activity and is being developed as an antitumor agent. JNJ-7706621 is a potent inhibitor of CDK1, CDK2, and to a lesser extent, CDK4 activity (Lin *et al.*, 2005). JNJ-7706621 blocks progression of human cancer cells through the cell cycle, causing an accumulation of cells in the G_2/M phase, preventing cells from entering mitosis, and activating apoptosis. CDK inhibitors, including JNJ-7706621, are poorly soluble in aqueous medium (17 μg/ml) (Emanuel *et al.*, 2005).

2. Nanoparticle Formulation

2.1. Polymer synthesis and characterization

PLGA (22,000), PLGA-b-PEG (16,500–4600), and PCL-b-PEG (15,200–4600) (Table 8.1) polymers are synthesized. The RGD peptide (GRGDS) (97.0%) is purchased from NeoMPS, Strasbourg, France.

PLGA is prepared as previously described (Kricheldorf *et al.*, 1985) by copolymerization of lactide and glycolide, promoted by dibutyltin dimethoxide (Sigma-Aldrich, St. Louis, MO, USA) as the catalyst. To obtain the fluorescent-PLGA, fluorescein with a carboxylic acid function is prepared according to the method described previously (Cao *et al.*, 2005) and then is

Table 8.1 Chemical description of the polymers included in the formulations

Polymer	Mn (SEC) g/mol[a]	Mn (NMR) g/mol polyester-PEG	Mol% glycolide[b]
PLGA	22,000	–	25
Fluorescent-PLGA	23,600	–	29
PLGA-b-PEG	29,300	16,500–4600	26
PCL-b-PEG	22,400	15,200–4600	–

[a] Polystyrene calibration.
[b] Determined by NMR by the following formula: $(I_{4.7}/2)/(I_{5.2} + I_{4.7}/2) \times 100$, where $I_{4.7}$ is the signal intensity of the glycolide unit at 4.7 ppm ($CH_2OC = O$) and $I_{5.2}$ is the signal intensity of the lactide unit at 5.2 ppm ($CH(CH_3)OC = O$).

coupled to the MeO-PLGA-OH using *N*,*N*′-dicyclohexylcarbodiimide as the coupling agent and 4-(dimethylamino)pyridine as the catalyst (Freichels *et al.*, 2011a). *PLGA-b-PEG* is synthesized by a conventional ring-opening polymerization of D,L-lactide and glycolide using PEG as the macroinitiator and stannous octanoate as the catalyst (Zweers *et al.*, 2004). The *PCL-b-PEG* copolymer is also synthesized by ring-opening polymerization using triethylaluminum as the catalyst (Pourcelle *et al.*, 2009).

2.2. Photografting of PCL-b-PEG and fixation of the RGD peptide

The covalent fixation of the RGD peptide on PCL-b-PEG is illustrated in Fig. 8.1. This novel technique is inspired by "photoaffinity labeling" and is based on the photoactivation of a so-called molecular clip, *O*-succinimidyl 4-(*p*-azidophenyl) butanoate, directly coated or mixed in an inert polymeric matrix (Freichels *et al.*, 2011b; Pourcelle *et al.*, 2007). In this way, we can derivatize the unreactive polymer into activated ones bearing *N*-hydroxysuccinimide esters that can react with biomolecules. PCL-b-PEG is solubilized in a solution containing the molecular clip in order to have 2 mmol of the clip per gram of polymer. The polymer solution is cast on clean glass plates, and after solvent evaporation, it is dried under vacuum to a constant weight and removed from the plates as shavings. The polymer sample is irradiated at 254 nm under an argon atmosphere for 20 min, in a homemade reactor (rotating quartz flask of 15 ml; 3 UV lamps of 8 W placed at a distance of 4.5 cm). After washing with isopropanol:ethyl acetate (19:1, v/v) to remove unreacted clips and nonfixed compounds, the "NHS-activated" polymer is immersed in a 1 m*M* solution of the ligand (GRGDS) (NeoMPS) in phosphate buffer (0.1 *M*): acetonitrile (1:1, v/v) at pH 8 and shaken for 24 h at 20 °C. The peptide solution is removed by suction and the sample is then washed three times with 5 m*M* HCl, five times with deionized water, shaken overnight in deionized water, rinsed with MeOH, and dried under vacuum at 40 °C to a

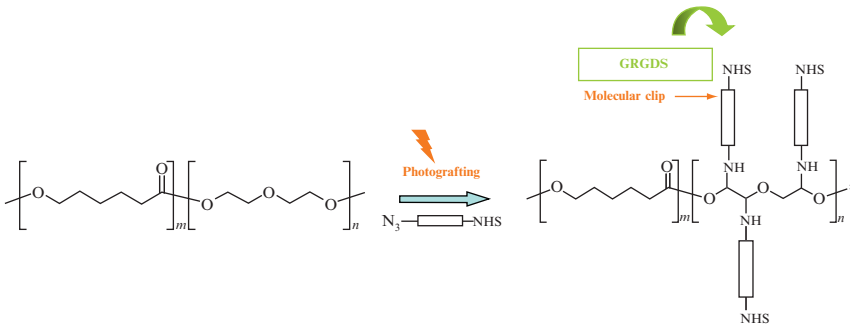

Figure 8.1 Covalent fixation of the ligands. GRGDS was covalently anchored on PCL-b-PEG in two steps. The first step is the photografting of activated NHS esters mainly on the PEG block of the PCL-b-PEG. The second step is the fixation of the GRGDS by displacement of the NHS (Pourcelle *et al.*, 2007).

constant weight (Pourcelle *et al.*, 2007, 2009). Following the same methodology, RGD-peptidomimetics (RGDp) may also be grafted at the nanoparticle surface. RGDp is prepared from L-tyrosine as scaffold, according to standard chemistry (Heckmann *et al.*, 2008) for the selective NH_2 and OH functionalizations. The triethylene glycol spacer-arm (for grafting on materials) is introduced via a sequence of reactions (nitration/reduction/acylation) (Biltresse *et al.*, 2004; Rerat *et al.*, 2009). The ligand grafting assessed by X-ray photoelectron spectroscopy (XPS) is approximately 0.4–0.5 molecules by PCL-b-PEG chain (Pourcelle *et al.*, 2007).

2.3. Preparation of drug-loaded nanoparticles

Nanoparticles are prepared by nanoprecipitation (Fessi *et al.*, 1989). PTX (Calbiochem, Darmastadt, Germany) (1 mg) is solubilized in 1 ml of acetone. This solution is added to the polymers: PLGA or fluorescent-PLGA (70 mg), PLGA-b-PEG (15 mg), PCL-b-PEG or PCL-b-PEG-g-GRGDS (15 mg) and mixed under magnetic stirring until the solubilization of the polymers (Table 8.2). This solution containing PTX and the polymers is completed until 10 ml with acetone. Finally, this solution is injected slowly with a glass syringe to 20 ml of water under magnetic stirring at room temperature overnight to allow the evaporation of acetone. To remove the nonencapsulated drug, the suspensions are filtered (1.2 µm) and then ultracentrifuged at 22,000 × *g* for 1 h at 4 °C. The pellets are suspended in adequate volume of ultra-purified water. FITC-covalently labeled PLGA is used to prepare fluorescent nanoparticles (Danhier *et al.*, 2009a).

These PLGA-based nanoparticles may also encapsulate other anticancer drugs such as DOX (5 mg) (Sigma-Aldrich) or a new CDK inhibitor, the

Table 8.2 Polymer composition of the different formulations used in this study

Formulation	Fluorescent-PLGA (70 mg)	PLGA-b-PEG (15 mg)	PCL-b-PEG (15 mg)	PCL-b-PEG-*g*-GRGDS (15 mg)
PTX-loaded nanoparticles *(PTX-NP)*	Y	Y	Y	NA
PTX-loaded nanoparticles grafted with the RGD peptide *(PTX-RGD-NP)*	Y	Y	NA	Y
Nonloaded nanoparticles *(NP)*	Y	Y	Y	NA
Nonloaded nanoparticles grafted with the RGD-peptidomimetic *(RGD-NP)*	Y	Y	NA	Y

NA: not applicable.
Y: Yes (included in formulations).

JNJ-7706621 compound (5 mg) (Johnson & Johnson, Janssen Pharmaceutica, Beerse, Belgium) (Danhier *et al.*, 2010b).

2.4. Physicochemical characterization of drug-loaded nanoparticles

The average size and size polydispersity of the nanoparticles are determined by photon correlation spectroscopy using a Malvern Nano ZS (Malvern Instruments, UK). The nanoparticles suspension (10 µl; polymer concentration 50 mg/ml) is diluted in 1 ml of ultra-purified water for the measurements. The Zeta (ζ) potential of the nanoparticles (10 µl; polymer concentration 50 mg/ml) is measured in KCl 1 m*M* (1 ml) with a Malvern Nano ZS at 25 °C. The instrument is calibrated with standard latex nanoparticles (Malvern Instruments). The size of PTX-loaded nanoparticles (PTX-NP) is 114 nm, while the size of PTX-loaded RGD-nanoparticles (PTX-RGD-NP) is slightly enhanced (138 nm). ζ potential of nanoparticles is close to neutrality, confirming the presence of PEG chains shielding the negative charges present at the nanoparticle surface. DOX-loaded nanoparticles (DOX-NP) or JNJ-7706621-loaded nanoparticles (JNJ-NP) present similar physicochemical characteristics than PTX-NP (Danhier *et al.*, 2009b).

The drug loading efficiency of PTX-NP is determined in triplicate by HPLC with UV detection at 227 nm (Agilent 1100 series, Agilent Technologies, Diegem, Belgium) (Danhier *et al.*, 2009a). The mobile phase (1.0 ml/min) consists of acetonitrile and water (70:30 v/v, respectively). The reverse phase column is a CC 125/4 Nucleodur 100-5 C18. The nanoparticles suspension (300 µl) is dissolved in acetonitrile (4.7 ml) and vigorously vortexed to get a

clear solution. The encapsulation efficiency is defined by the ratio of the measured amount of PTX encapsulated in nanoparticles to the initial amount of PTX encapsulated in nanoparticles Eq. (8.1). Experimental values are the average of at least three different formulations. The percentage of encapsulation of PTX-NP and PTX-RGD-NP is 72% and 61%, respectively.

$$\text{Encapsulation efficiency } (\%) = \frac{\text{Amount of drug in nanoparticles}}{\text{Initial amount of drug}} \times 100 \tag{8.1}$$

The amount of JNJ-7706621 entrapped in nanoparticles is determined in triplicate by HPLC (Agilent 1100 series, Agilent Technologies) (Danhier *et al.*, 2010b). The samples are eluted with a linear gradient of 0.2% ammonium acetate in water (A) and acetonitrile (B), from 100% (0 min) to 20% (12 min). A reverse phase column CC 125/4 Nucleodur 100-5 C18 (Macherey-Nagel, Germany) is maintained at 30 °C. The flow rate is set at 1.2 ml/min and the detection wavelength is 272 nm. Sample solution is injected at a volume of 10 µl. Nanoparticles are dissolved in acetonitrile and vigorously vortexed to get a clear solution. The percentage of encapsulation of JNJ-NP and JNJ-RGD-NP is 65% and 63%, respectively.

The DOX content in nanoparticles is determined after nanoparticles are dissolved in acetonitrile, using a spectrophotometer (HP8453 from Hewlett Packard) at 481 nm. The percentage of encapsulation is 88%.

3. *In Vitro* Antitumoral Activity

3.1. Cell viability by MTT assay

HeLa cells (ATCC, American Type Culture Collection, Manassas, VA, USA) are grown in DMEM (Gibco® BRL, Carlsbad, CA, USA) supplemented with 10% (v/v) fetal bovine serum and 100 IU/ml of penicillin G sodium and 100 µg/ml of streptomycin sulfate (Carlsbad, CA, USA). The cells are maintained in an incubator supplied with 5% CO_2/95% air humidified atmosphere at 37 °C.

HeLa cells are seeded in 96-well plates at the density of 2500 viable cells per well and incubated at 24 h to allow cell attachment. The cells are then incubated with Taxol® (Bristol-Myers Squibb, New York, USA), PTX-NP (PTX concentrations of 0.025, 0.25, 2.5, 12.5, and 25 µg/ml) and drug-free nanoparticles (polymers concentration 10 mg/ml) for 24, 48, and 72 h. At determined time, the formulations are replaced with DMEM containing MTT (5 mg/ml) (Sigma-Aldrich) and cells are then incubated for additional 4 h. MTT is aspirated off and DMSO is added to dissolve the formazan

crystals (Mosmann, 1983). Absorbance is measured at 570 nm using a BioRad microplate reader. Untreated cells are taken as control with 100% viability and cells without addition of MTT are used as blank to calibrate the spectrophotometer to zero absorbance. Triton X-100 1% is used as positive control of cytotoxicity. IC_{50} value for HeLa cells decreases from 15.5 μg/ml for Taxol® to 5.5 μg/ml for the PTX-NP after 24 h incubation. The grafting of the RGD peptide on the nanoparticles does not influence the IC_{50} value *in vitro* (i.e., same results are obtained with PTX-RGD-NP).

The same assay is performed with JNJ-NP at JNJ-7706621 concentrations from 0.011 to 22 μg/ml. After 24 and 48 h, an influence of the concentrations of JNJ-7706621 on cell viability can be observed. The presence of the RGD peptide at the nanoparticles surface does not influence the cell viability.

3.2. Apoptosis induced by drug-loaded nanoparticles

Apoptosis is identified morphologically by 4,6-diamidino-2-phenylindole (DAPI) staining. HeLa cells are seeded in 6-well plates containing a coverslip with 100,000 cells per well and cultured at 37 °C for 24 h. Cells are then incubated for 4 h with Taxol®, PTX-NP (PTX concentration of 25 μg/ml), and culture medium as control. Samples are then fixed with 4% paraformaldehyde in PBS at room temperature for 15 min, stained with 0.2 μg/ml DAPI in PBS at room temperature for 15 min, and washed twice with PBS and water. Coverslips are mounted onto glass slides. Slides are then examined using a fluorescent microscope with a 340/380 nm excitation filter and LP 430 nm barrier filter. Enumeration of apoptotic nuclei (about 200 cells are counted) is made on slides picked up at random by two independent experimenters. Clusters of apoptotic bodies are given as a single count (Kroning and Lichtenstein, 1998). The percentage of apoptotic cells induced by Taxol® and PTX-RGD-NP is not significantly different indicating that nanoparticles do not decrease apoptosis compared to Taxol®.

The induction of apoptosis of JNJ-7706621 is also studied by DAPI staining of the nuclei. It is demonstrated that the encapsulation of the drug in nanoparticles does not decrease apoptosis compared to a control suspension of JNJ-7706621(Danhier *et al.*, 2010b).

4. *In Vitro* Demonstration of Tumor Targeting

4.1. Fluorescence microscopy

To check if RGD-grafted nanoparticles can recognize $\alpha_v\beta_3$ integrins on endothelial cells, the association of PTX-NP and PTX-RGD-NP to human umbilical vein endothelial cells (HUVEC) that express the $\alpha_v\beta_3$ integrins is assessed by fluorescence microscopy (Danhier *et al.*, 2009b).

4.1.1. Association of nanoparticles to HUVEC

HUVEC (Clonetics, Lonza, Verviers, Belgium) are cultured in EGM-2 medium containing growth factors (Clonetics), 100 IU/ml of penicillin G sodium and 100 μg/ml of streptomycin sulfate and 10% (v/v) fetal bovine serum at 37 °C in a 5% CO_2/95% air humidified atmosphere. Culture flasks are precoated with gelatin 0.2% in ultra-purified water for 15 min and are dried for 6 h in sterile environment.

After the gelatin coating, 2 ml of the suspension of HUVEC 3×10^5 cells in EGM-2 medium (passage 3) is plated in Lab-Tek and incubated for 2 days to allow cell attachment. After 2 days, when the Lab-Tek is covered by cells, the medium is removed and replaced by fresh medium containing PTX-NP or PTX-RGD-NP for 2 h. After incubation, the medium is removed and cells are washed three times with HBSS, fixed with paraformaldehyde 4% in PBS, and mounted with Vectashield (Vector Lab Inc., Burlingame, CA) containing DAPI for nuclear staining. Cells are then examined using a fluorescent microscope (Axioskop 40, Zeiss) using the 350 nm (blue) and 470–490 nm (green) excitation filters and are photographed with an AxioCam MRc5 camera (Zeiss). The cells are also analyzed using a confocal laser scanning microscope (Axiovert 135 *M* microscope equipped with a BioRad MRC1024 confocal system). Sequential images are processed and overlaid using Adobe Photoshop version 5.5. Compared to nontargeted PTX-NP, a high level of association of fluorescent PTX-RGD-NP with HUVEC is demonstrated (Danhier *et al.*, 2009b).

4.1.2. Specificity of binding to $\alpha_v\beta_3$ integrin assessed by competition assay

To visualize the specificity of the RGD-NP for $\alpha_v\beta_3$ integrin, we have performed competition assay on HUVEC, using the same protocol that described above with some modifications. Two milliliters of HUVEC (passage 3) in EGM-2 medium is seeded in Lab-Tek 2-grid chamber for 2 days to allow cell attachment. Before the experiment, the medium is removed and cells are blocked with medium containing 5% bovine serum albumin (BSA) for 30 min to inhibit the specific binding. Then, the medium is removed and cells are preincubated with a 20-fold molar excess of GRGDS peptide or the anti-$\alpha_v\beta_3$ integrin monoclonal antibody (1/50 dilution) (GeneTex, Irvine, USA) for 15 min in serum-free medium (Murphy *et al.*, 2008). Finally, the medium is removed and replaced by fresh medium (1.86 ml) containing fluorescent RGD-NP (140 μl). HUVEC are then incubated for 1 h at 37 °C. An excess of GRGDS peptide or anti-$\alpha_v\beta_3$ integrin monoclonal antibody strongly inhibits the binding of the RGD-NP to HUVEC (Fig. 8.2) (Danhier *et al.*, 2009b).

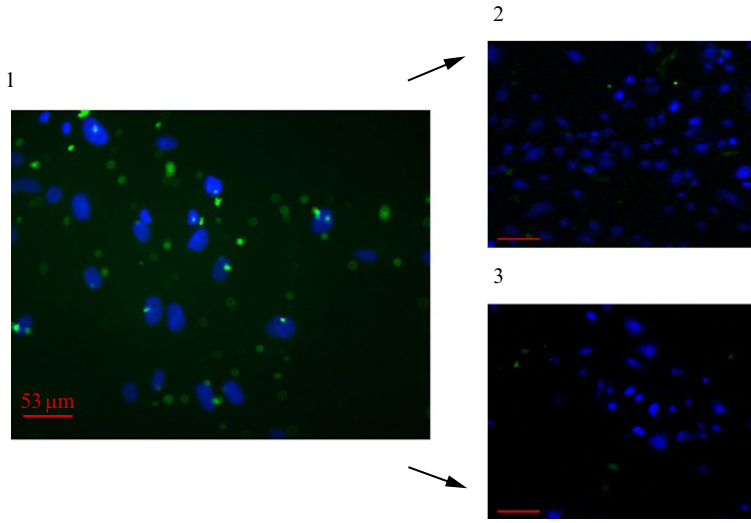

Figure 8.2 Detection of fluorescent PTX-loaded nanoparticles in HUVEC. DAPI staining was used to label nuclei. Fluorescent microscopy of HUVEC incubated for 1 h with fluorescent RGD-NP. (1) No pretreatment. (2) Pretreatment with a 20-fold molar excess of the GRGDS peptide. (3) Pretreatment with the anti-$\alpha_v\beta_3$ integrin monoclonal antibody (1/50 dilution) (adapted from Danhier *et al.*, 2009b).

4.1.3. Use of a fluorescent drug: DOX

To visualize the cellular distribution of both polymers and drugs, DOX (Sigma-Aldrich) is encapsulated in the same nanoparticles. The association of DOX-NP with HUVEC, 3×10^5 cells (passage 4) is assessed in Lab-Tek 2-grid chamber as described above ($n = 4$). DOX-NP or free nanoparticles are incubated 1 h at a concentration of 6 µg/ml DOX. Cells are then examined using a fluorescent microscope (Axioskop 40, Zeiss) using the 480 nm (red) excitation filters and are photographed with an AxioCam MRc5 camera (Zeiss) (Xiong *et al.*, 2005). Compared to nontargeted DOX-NP, a high level of association of DOX from DOX-RGD-NP with HUVEC is observed (Danhier *et al.*, 2009b).

4.2. Fluorimetry

To compare the association (binding and uptake) of NP and RGD-NP to HUVEC, a quantitative endothelial cell uptake assay is performed (Danhier *et al.*, 2009b). TNF-α is known to promote $\alpha_v\beta_3$ integrin expression at the surface of endothelial cells (Swerlick *et al.*, 1992).

4.2.1. Association of nanoparticles to HUVEC

Flat-bottom 48-well culture plates are coated with 0.2% gelatin for 2 h at room temperature and then blocked with 0.1% BSA for 30 min at 37 °C. HUVEC (passage 4) are resuspended in EGM-2 medium and plated at 2×10^4 cells/well for 24 h. HUVEC are then activated with TNF-α (4 ng/ml) for 4 h to enhance $\alpha_v\beta_3$ integrin expression (Griffioen *et al.*, 1996; Swerlick *et al.*, 1992). Cells are then incubated with 200 µl of fluorescent FITC-NP and RGD-FITC-NP at 4 °C for 30 min and at 37 °C for 30 min, 1, 2, or 4 h. At designated times, cells are lysed with Triton X-100 (0.05% v/v) after rinsing with PBS to remove unattached cells. The amount of uptaken nanoparticles is quantified directly through measurement of fluorescence emission using a Packard Fluorocount Microplate Fluorometer (Packard Instrument Company, Meriden, CT, USA). The fluorometer is calibrated with standard solution of 17.5–7000 µg/ml of fluorescent-PLGA (correlation coefficient of $R^2 = 0.9985$). The excitation/emission wavelengths for FITC are 485/530 nm. Cellular uptake (%) is calculated from the ratio of FITC concentrations to the initial FITC concentration. The measured FITC concentrations are calculated from the measured fluorescence intensity and the calibration curve (Lohbach *et al.*, 2006). While activation of HUVEC by TNF-α does not influence the cellular uptake of nontargeted NP, the cellular uptake of RGD-NP is significantly enhanced by TNF-α incubation, indicating that the cellular uptake of RGD-NP is mediated by the binding to $\alpha_v\beta_3$ integrins, which are expressed at higher levels at the cell surface following TNF-α incubation (Danhier *et al.*, 2009b).

4.2.2. Specificity of binding to $\alpha_v\beta_3$ integrin assessed by competition assay

A competition assay is performed by preincubating the activated cells with either a 20-fold molar excess of GRGDS peptide or the anti-$\alpha_v\beta_3$ integrin monoclonal antibody (1/50 dilution) for 15 min in serum-free medium. Fluorescent nanoparticles are incubated for 4 h (Murphy *et al.*, 2008). When the GRGDS peptide or the anti-$\alpha_v\beta_3$ integrin monoclonal antibody is preincubated with TNF-α-activated HUVEC, the cellular uptake of RGD-NP becomes equivalent to nontargeted NP, showing that the cellular uptake of RGD-NP is mediated by $\alpha_v\beta_3$ integrin binding (Danhier *et al.*, 2009b).

5. *In Vivo* Demonstration of Tumor Targeting

To demonstrate the tumor endothelium targeting of RGD-nanoparticles *in vivo*, immunohistochemistry is performed using fluorescent nanoparticles. Antitumor efficacy is also performed on tumor-bearing mice to confirm immunohistochemistry results (Danhier *et al.*, 2009b).

5.1. Tumor model

Syngeneic transplantable liver tumors (TLTs) (Danhier *et al.*, 2009a; Jordan *et al.*, 2003) are implanted in the gastrocnemius muscle in the rear leg of 8-week-old male NMRI mice (Janvier, Genest St. Isle, France). The treatments are applied when the tumor reaches 8.0 ± 0.5 mm (~7 days). Before injection, animals are anesthetized by inhalation of Isoflurane mixed with 21% oxygen in a continuous flow (1.5 l/min) delivered by a nose cone.

A431 cells (ATCC) are implanted on 4–5-week-old female nude athymic mice, bought from Janvier. A solid tumor is established upon S.C. injection of 0.1 ml of A431 human cancer cells suspension (1×10^7 cells/ml) to the right flank of the mice. Treatments are started when tumor reached a volume of 190 mm^3 (measurement with an electronic caliper).

5.2. Immunohistochemistry

The fluorescent nanoparticles suspension (NP and RGD-NP, 100 µl) are injected through the tail vein of TLT-bearing mice ($n = 4$). Two hours after injection, animals are sacrificed. Tumors are removed, covered with cryo-embedding compound OCT (Tissue-Tek, Sacura), snap frozen in liquid nitrogen, and stored at −80 °C until sectioning.

Sections (5 µm) are mounted onto charged superfrost-plus glass slides and stored at −80 °C until staining. The sections are fixed in ice-cold acetone, rehydrated in PBS, and immunostained with a rat anti-CD31 antibody (1:50) in 1% BSA in PBS for 1 h. Incubation with the secondary antibody Alexa 568 goat anti-rat (1:500) is conducted for 30 min at room temperature. The sections are then mounted with Vectashield containing DAPI. Sections are analyzed using a fluorescent microscope with 350 nm (blue), 470–490 nm (green), and 515–560 nm (red) excitation filters (Muether *et al.*, 2007). Sequential images are processed and overlaid using Adobe Photoshop version 5.5. Sequential sections of the tumor are analyzed for nuclear staining by DAPI (blue fluorescence), nanoparticles by modified fluorescein (green fluorescence), and blood vessels by CD31 immunohistochemistry (red fluorescence). As shown in Fig. 8.3, a higher green fluorescence is observed in the tumor upon RGD-NP injection when compared to nontargeted NP ($p < 0.001$). The green fluorescence of nanoparticles is colocalized with CD31 immunostaining (red fluorescence) indicating that the nanoparticles target the tumor endothelium (Danhier *et al.*, 2009b).

5.3. Effect of nanoparticles on tumor growth

When TLTs reached 8.0 ± 0.5 mm in diameter, the mice are randomly assigned to one of the following groups: group 1: PBS injection; group 2: nonloaded NP; group 3: PTX-NP; and group 4: PTX-RGD-NP. All the treatments are injected through the tail vein (PTX 1 mg/kg). After

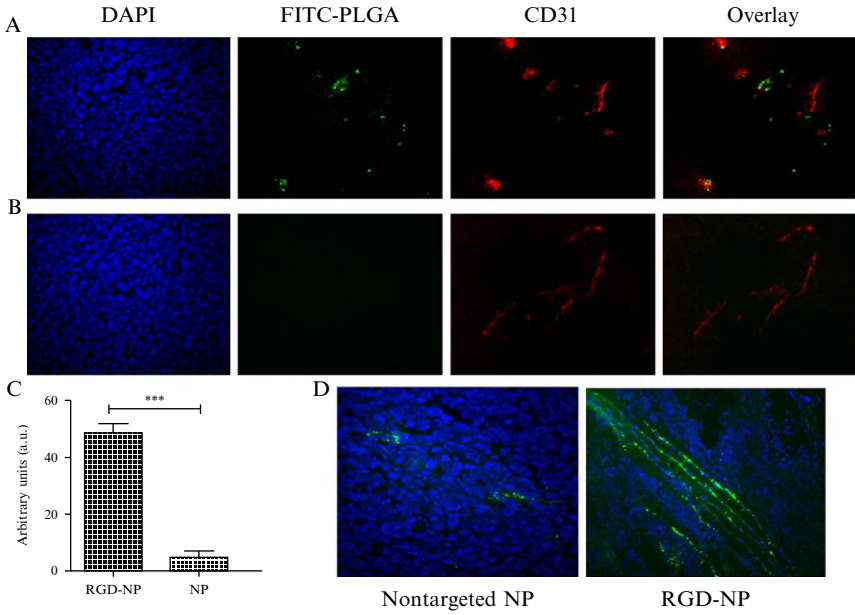

Figure 8.3 Fluorescent microscopy of TLTs growing in NMRI mice 2 h after injection of NP containing fluorescent-PLGA (green). Sections were stained with anti-CD31 to label endothelial cells (red) and counterstained with DAPI for nucleus detection (blue). (A) RGD-NP and (B) nontargeted NP. (C) Quantification of the fluorescent-PLGA signal from TLTs after NP and RGD-NP injection ($n = 4$). ***$p < 0.001$ (adapted from Danhier *et al.*, 2009b). (D) Fluorescent microscopy of TLTs growing in NMRI mice 4 h after injection of NP containing fluorescent-PLGA (green). Sections were stained with DAPI for nucleus detection (blue).

treatment, tumors are measured every day with an electronic caliper until they reached a diameter of 18 mm, at which time the mice are sacrificed. Changes in body weight are also monitored (Fig. 8.4A and B). PTX-RGD-NP inhibit tumor growth more efficiently than nontargeted nanoparticles. Indeed, the survival rate is significantly higher for mice treated with PTX-RGD-NP as compared to PTX-NP (Danhier *et al.*, 2009b).

Similar experiments are performed with two other anticancer drugs: a new CDK inhibitor, JNJ-7706621 (Fig. 8.4C and D), and DOX (Fig. 8.4E). Finally, PTX-(RGD)-NP are also tested on another tumor model (A-431), using similar treatment schedule and PTX dose than with TLT model (Fig. 8.4F). Regrowth delay of tumors is more important with RGD-NP than with nontargeted nanoparticles for all drugs tested (PTX, DOX, and JNJ-7706621). Moreover, the better efficiency of RGD-nanoparticles is demonstrated on two different tumor models: the hepatocarcinoma TLT and the human epidermoid carcinoma A431.

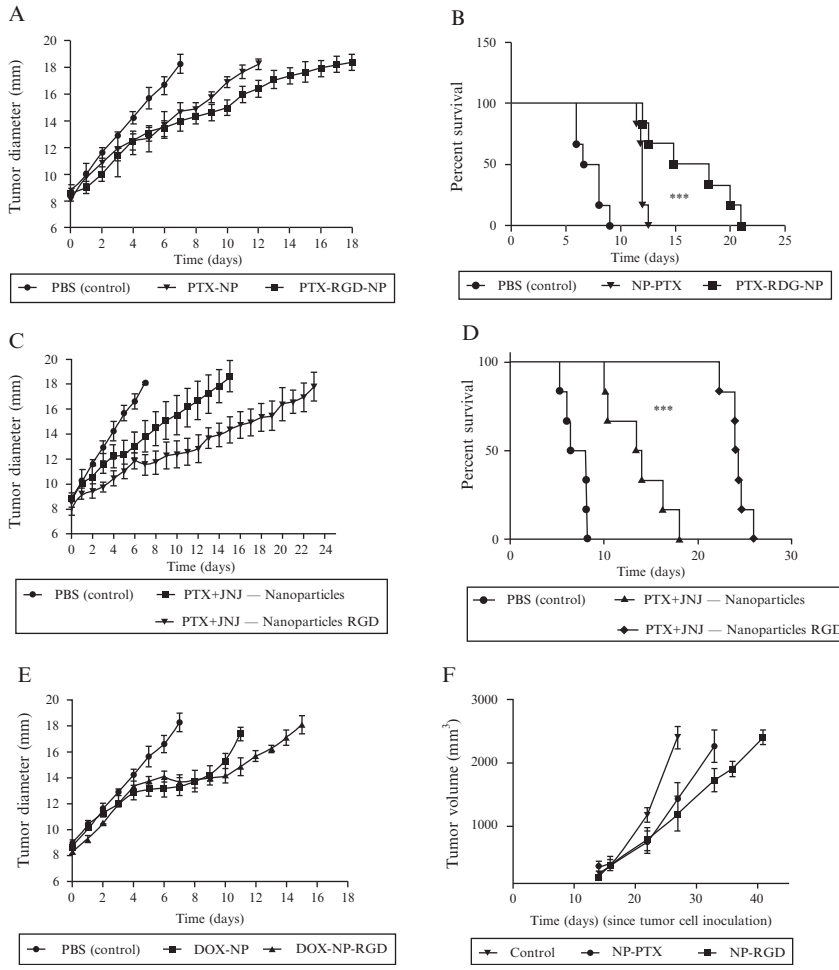

Figure 8.4 Antitumor effect of various treatments on tumor-bearing mice. (A and B) Antitumor effect of PTX-NP and PTX-RGD-NP (PTX concentration: 1 mg/kg) on TLT-bearing mice. (A) Tumor growth delays curves. Mean of tumor size ± SEM ($n = 6$). (B) Survival rates of tumor-bearing mice. ***$p < 0.001$. (C and D) Antitumor effect on TLT-bearing mice treated with the combination of PTX and JNJ-77006621 encapsulated in nanoparticles or in RGD-grafted nanoparticles. Mice received PTX at a dose of 1 mg/kg and 24 h post chemotherapy, mice received JNJ-7706621 each day for 5 consecutive days at a dose of 3.25 mg/kg/day. (C) Tumor growth delays curves. Mean of tumor size ± SEM ($n = 6$). (D) Survival rates of tumor-bearing mice. ***$p < 0.001$. (E) Antitumor effect of DOX-NP and DOX-RGD-NP (DOX concentration: 5 mg/kg) on TLT-bearing mice. (F) Antitumor effect of PTX-NP and PTX-RGD-NP (PTX concentration: 1 mg/kg) on A-431 tumor-bearing mice (adapted from Danhier *et al.*, 2009b, 2010a,b).

6. Concluding Remarks

The RGD peptide is an effective ligand for tumor targeting since it has been shown that integrin $\alpha_v\beta_3$ is overexpressed not only on tumoral endothelium but also on cancer cells, for a lot of cancer cell lines. The demonstration of the targeting of the tumor endothelium is performed both *in vitro* and *in vivo*. *In vitro*, the preferential association of RGD-grafted nanoparticles (compared to nontargeted nanoparticles) to HUVEC is demonstrated by both microscopy and fluorimetry. Competition assays clearly shows that this association is mediated by the binding of RGD moieties to $\alpha_v\beta_3$ integrin. *In vivo*, immunohistochemistry and antitumor efficacy study shows that RGD-nanoparticles target the tumor endothelium and delay tumor growth. To our knowledge, it is the first time that PLGA-based nanoparticles grafted with the RGD peptide have been studied *in vitro* and *in vivo*.

ACKNOWLEDGMENTS

The authors wish to thank Johnson & Johnson, Pharmaceutical Research and Development, Division of Janssen Pharmaceutica, Belgium for providing Paclitaxel and JNJ-7706621. This work was supported by the FRSM (Belgium). The authors also thank Bernard Ucakar (Université Catholique de Louvain) for his technical support.

REFERENCES

Arap, W., Pasqualini, R., and Ruoslahti, E. (1998). Cancer treatment by targeted drug delivery to tumor vasculature in a mouse model. *Science* **279,** 377–380.

Biltresse, S., Attolini, M., Dive, G., Cordi, A., Tucker, G. C., and Marchand-Brynaert, J. (2004). Novel RGD-like molecules based on the tyrosine template: Design, synthesis, and biological evaluation on isolated integrins alphaVbeta3/alphaIIbbeta3 and in cellular adhesion tests. *Bioorg. Med. Chem.* **12,** 5379–5393.

Borgman, M. P., Aras, O., Geyser-Stoops, S., Sausville, E. A., and Ghandehari, H. (2009). Biodistribution of HPMA copolymer-aminohexylgeldanamycin-RGDfK conjugates for prostate cancer drug delivery. *Mol. Pharm.* **6,** 1836–1847.

Brooks, P. C., Clark, R. A., and Cheresh, D. A. (1994). Requirement of vascular integrin alpha v beta 3 for angiogenesis. *Science* **264,** 569–571.

Cao, L. W., Wang, H., Li, J. S., and Zhang, H. S. (2005). 6-Oxy-(N-succinimidyl acetate)-9-(2′-methoxycarbonyl) fluorescein as a new fluorescent labeling reagent for aliphatic amines in environmental and food samples using high-performance liquid chromatography. *J. Chromatogr. A* **1063,** 143–151.

Carmeliet, P., and Jain, R. K. (2000). Angiogenesis in cancer and other diseases. *Nature* **407,** 249–257.

Danhier, F., Lecouturier, N., Vroman, B., Jérôme, C., Marchand-Brynaert, J., Feron, O., and Préat, V. (2009a). Paclitaxel-loaded PEGylated PLGA-based nanoparticles: In vitro and in vivo evaluation. *J. Control. Release* **133,** 11–17.

Danhier, F., Vroman, B., Lecouturier, N., Crokart, N., Pourcelle, V., Freichels, H., Jérôme, C., Marchand-Brynaert, J., Feron, O., and Préat, V. (2009b). Targeting of tumor endothelium by RGD-grafted PLGA-nanoparticles loaded with paclitaxel. *J. Control. Release* **140,** 166–173.

Danhier, F., Feron, O., and Préat, V. (2010a). To exploit the tumor microenvironment: Passive and active tumor targeting of nanocarriers for anti-cancer drug delivery. *J. Control. Release* **148,** 135–146.

Danhier, F., Ucakar, B., Magotteaux, N., Brewster, M., and Préat, V. (2010b). Active and passive tumor targeting of a novel poorly soluble cyclin dependent kinase inhibitor, JNJ-7706621. *Int. J. Pharm.* **392,** 20–28.

Emanuel, S., Rugg, C. A., Gruninger, R. H., Lin, R., Fuentes-Pesquera, A., Connolly, P. J., Wetter, S. K., Hollister, B., Kruger, W. W., Napier, C., Jolliffe, L., and Middleton, S. A. (2005). The in vitro and in vivo effects of JNJ-7706621: A dual inhibitor of cyclin-dependent kinases and aurora kinases. *Cancer Res.* **65,** 9038–9046.

Feron, O. (2010). Tumor-penetrating peptides: A shift from magic bullets to magic guns. *Sci. Transl. Med.* **2,** 1–5.

Fessi, H., Puisieux, F., Devissaguet, J. P., Ammoury, N., and Benita, S. (1989). Nanocapsule formation by interfacial polymer deposition following solvent displacement. *Int. J. Pharm.* **55,** R1–R4.

Freichels, H., Danhier, F., Préat, V., Lecomte, P., and Jérôme, C. (2011a). Fluorescent labeling of degradable poly(lactide-co-glycolide) for cellular nanoparticles tracking in living cells. *Int. J. Artif. Organs* **34,** 156–160.

Freichels, H., Pourcelle, V., Le Duff, C. S., Marchand-Brynaert, J., and Jérôme, C. (2011b). "Clip" and "Click" Chemistries combination: Toward easy PEGylation of degradable aliphatic polyesters. *Macromol. Rapid Commun.* **32,** 616–621.

Garinot, M., Fiévez, V., Pourcelle, V., Stoffelbach, F., des Rieux, A., Plapied, L., Theate, I., Friechels, H., Jérôme, Ch., Marchand-Brynaert, J., Schneider, Y. J., and Préat, V. (2007). PEGylated PLGA-based nanoparticles targeting M cells for oral vaccination. *J. Control. Release* **120,** 195–204.

Griffioen, A. W., Damen, C. A., Blijham, G. H., and Groenewegen, G. (1996). Tumor angiogenesis is accompanied by a decreased inflammatory response of tumor-associated endothelium. *Blood* **88,** 667–673.

Haley, B., and Frenkel, E. (2008). Nanoparticles for drug delivery in cancer treatment. *Urol. Oncol.* **26,** 57–64.

Heckmann, D., Meyer, A., Laufer, B., Zahn, G., Stragies, R., and Kessler, H. (2008). Rational design of highly active and selective ligands for the alpha5beta1 integrin receptor. *Chembiochem* **9,** 1397–1407.

Hynes, R. O. (2002). A reevaluation of integrins as regulators of angiogenesis. *Nat. Med.* **8,** 918–921.

Jordan, B. F., Sonveaux, P., Feron, O., Grégoire, V., Beghein, N., and Gallez, B. (2003). Nitric oxide-mediated increase in tumor blood flow and oxygenation of tumors implanted in muscles stimulated by electric pulses. *Int. J. Radiat. Oncol. Biol. Phys.* **55,** 1066–1073.

Kricheldorf, H. R., Jonte, J. M., and Berl, M. (1985). Polylactones. 3. Copolymerization of glycolide with l, l-lactide and other lactones. *Makromol. Chem.* **12,** 25–38.

Kroning, R., and Lichtenstein, A. (1998). Taxol can induce phosphorylation of BCL-2 in multiple myeloma cells and potentiate dexamethasone-induced apoptosis. *Leuk. Res.* **22,** 275–286.

Lammers, T., Hennink, W. E., and Storm, G. (2008). Tumour-targeted nanomedicines: Principles and practice. *Br. J. Cancer* **99,** 392–397.

Lin, R., Connolly, P. J., Huang, S., Wetter, S. K., Lu, Y., Murray, W. V., Emanuel, S. L., Gruninger, R. H., Fuentes-Pesquera, A. R., Rugg, C. A., Middleton, S. A., and Jolliffe, L. K. (2005). 1-Acyl-1H-[1,2,4]triazole-3,5-diamine analogues as novel and potent anticancer cyclin-dependent kinase inhibitors: Synthesis and evaluation of biological activities. *J. Med. Chem.* **48,** 4208–4211.

Lohbach, C., Neumann, D., Lehr, C. M., and Lamprecht, A. (2006). Human vascular endothelial cells in primary cell culture for the evaluation of nanoparticle bioadhesion. *J. Nanosci. Nanotechnol.* **6,** 3303–3309.

Maeda, H., Wu, J., Sawa, T., Matsumura, Y., and Hori, K. (2000). Tumor vascular permeability and the EPR effect in macromolecular therapeutics: A review. *J. Control. Release* **65,** 271–284.

Meng, S., Su, B., Li, W., Ding, Y., Tang, L., Zhou, W., Song, Y., and Caicun, Z. (2010). Integrin-targeted paclitaxel nanoliposomes for tumor therapy. *Med. Oncol.* **28,** 1180–1187.

Mosmann, T. (1983). Rapid colorimetric assay for cellular growth and survival: Application to proliferation and cytotoxicity assays. *J. Immunol. Methods* **65,** 55–63.

Muether, P. S., Dell, S., Kociok, N., Zahn, G., Stragies, R., Vossmeyer, D., and Joussen, A. M. (2007). The role of integrin alpha5beta1 in the regulation of corneal neovascularization. *Exp. Eye Res.* **85,** 356–365.

Murphy, E. A., Majeti, B. K., Barnes, L. A., Makale, M., Weis, S. M., Lutu-Fuga, K., Wrasidlo, W., and Cheresh, D. A. (2008). Nanoparticle-mediated drug delivery to tumor vasculature suppresses metastasis. *Proc. Natl. Acad. Sci. USA* **105,** 9343–9348.

Owens, D. E., III, and Peppas, N. A. (2006). Opsonization, biodistribution, and pharmacokinetics of polymeric nanoparticles. *Int. J. Pharm.* **307,** 93–102.

Pourcelle, V., Devouge, S., Garinot, M., Préat, V., and Marchand-Brynaert, J. (2007). PCL-PEG-based nanoparticles grafted with GRGDS peptide: Preparation and surface analysis by XPS. *Biomacromolecules* **8,** 3977–3983.

Pourcelle, V., Freichels, H., Stoffelbach, F., Auzely-Velty, R., Jérôme, C., and Marchand-Brynaert, J. (2009). Light induced functionalization of PCL-PEG block copolymers for the covalent immobilization of biomolecules. *Biomacromolecules* **10,** 966–974.

Rerat, V., Dive, G., Cordi, A. A., Tucker, G. C., Bareille, R., Amédée, J., Bordenave, L., and Marchand-Brynaert, J. (2009). αvβ3 integrin-targeting Arg-Gly-Asp (RGD) peptidomimetics containing oligoethylene glycol (OEG) spacers. *J. Med. Chem.* **52,** 7029–7043.

Ruoslahti, E. (2002). Specialization of tumour vasculature. *Nat. Rev. Cancer* **2,** 83–90.

Shan, K., Lincoff, A. M., and Young, J. B. (1996). Anthracycline-induced cardiotoxicity. *Ann. Intern. Med.* **125,** 47–58.

Sheldrake, H. M., and Patterson, L. H. (2009). Function and antagonism of beta3 integrins in the development of cancer therapy. *Curr. Cancer Drug Targets* **9,** 519–540.

Singla, A. K., Garg, A., and Aggarwal, D. (2002). Paclitaxel and its formulations. *Int. J. Pharm.* **235,** 179–192.

Sugahara, K., Teesalu, T., Karmali, P., Kotazmraju, V., Agemy, L., Girard, O., Hanahan, D., Mattrey, R., and Ruoshlati, E. (2009). Tissue-penetrating delivery of compounds and nanoparticles into tumors. *Cancer Cell* **16,** 510–520.

Sugahara, K., Teesalu, T., Karmali, P., Kotazmraju, V., Agemy, L., Greenwald, D., and Ruoslathi, E. (2010). Coadministration of a tumor-penetrating peptide enhances the efficacy of cancer drugs. *Sciences* **328,** 1031–1035.

Swerlick, R. A., Lee, K. H., Li, L. J., Sepp, N. T., Caughman, S. W., and Lawley, T. J. (1992). Regulation of vascular cell adhesion molecule 1 on human dermal microvascular endothelial cells. *J. Immunol.* **149,** 698–705.

Temming, K., Schiffelers, R. M., Molema, G., and Kok, R. J. (2005). RGD-based strategies for selective delivery of therapeutics and imaging agents to the tumour vasculature. *Drug Resist. Updat.* **8,** 381–402.

Wang, Z., Chui, W. K., and Ho, P. C. (2009). Design of a multifunctional PLGA nanoparticulate drug delivery system: Evaluation of its physicochemical properties and anticancer activity to malignant cancer cells. *Pharm. Res.* **26,** 1162–1171.

Xiong, X. B., Huang, Y., Lu, W. L., Zhang, X., Zhang, H., Nagai, T., and Zhang, Q. (2005). Enhanced intracellular delivery and improved antitumor efficacy of doxorubicin by sterically stabilized liposomes modified with a synthetic RGD mimetic. *J. Control. Release* **107,** 262–275.

Zhan, C., Gu, B., Xie, C., Li, J., Liu, Y., and Lu, W. (2010). Cyclic RGD conjugated poly (ethylene glycol)-co-poly(lactic acid) micelle enhances paclitaxel anti-glioblastoma effect. *J. Control. Release* **143,** 136–142.

Zweers, M. L., Engbers, G. H., Grijpma, D. W., and Feijen, J. (2004). In vitro degradation of nanoparticles prepared from polymers based on DL-lactide, glycolide and poly(ethylene oxide). *J. Control. Release* **100,** 347–356.

CHAPTER NINE

Peptide Nanofiber Scaffold for Brain Tissue Reconstruction

Gilberto Ka Kit Leung,[*] Yue Chun Wang,[*,†] *and* Wutian Wu[‡,§,¶,||]

Contents

Abstract

Traumatic brain injury (TBI) and neurosurgical procedures commonly result in tissue loss within the cerebral parenchyma. Regeneration is limited by the anatomical tissue gaps and the hostile microenvironment created by the trauma. A search for novel biomaterials that are neuroprotective and conducive to healing and regeneration is needed. One approach is with the use of RADA16-I, a type I self-assembling peptide nanofiber scaffold. We review the current evidence on the use of RADA16-I and describe our experience with its use in rodent models of surgical brain injury.

A cortical resection model is used to mimic the significant amount of tissue loss seen in TBI and clinical surgery. The use of RADA16-I as a carrier of

[*] Li Ka Shing Faculty of Medicine, Department of Surgery, The University of Hong Kong, Hong Kong SAR, China
[†] Department of Physiology, School of Medicine, Ji Nan University of China, Guangzhou, China
[‡] Department of Anatomy, The University of Hong Kong, Hong Kong SAR, China
[§] State Key Laboratory of Brain and Cognitive Sciences, The University of Hong Kong, Hong Kong SAR, China
[¶] Li Ka Shing Faculty of Medicine, Research Center of Reproduction, Development and Growth, The University of Hong Kong, Hong Kong SAR, China
[||] Joint Laboratory for Brain Function and Health (BFAH), Jinan University and The University of Hong Kong, Guangzhou, China

Methods in Enzymology, Volume 508
ISSN 0076-6879, DOI: 10.1016/B978-0-12-391860-4.00009-4

transplantable neuroprogenitor cells and a potential topical hemostatic agent is described. RADA16-I can bridge tissue gaps and reduce surrounding reactive changes. Embedment of transplantable cells within the tissue scaffold is feasible. RADA16-I achieves hemostasis almost instantaneously and is associated with less tissue damage when compared with other conventional methods. There are, however, certain limitations with the application of RADA16-I mainly due to its intrinsically low pH and need for prebuffering.

The use of peptide nanofiber scaffold is a promising approach for the reconstruction of the injured brain. New experimental models and research methods are required to fully explore its potential in minimizing secondary brain injuries and to promote neuronal regeneration.

Abbreviations

BSA	bovine serum albumin
DAPI	4,6-diamidino-2-phenylindole
ECM	extracellular matrix
GFAP	glial fibrillary acid protein
H&E	hematoxylin and eosin
MRI	magnetic resonance imaging
NPCs	neural progenitor cells
PBS	phosphate-buffered saline
SD	Sprague–Dawley
SAPNS	self-assembling peptide nanofiber scaffold
SBI	surgical brain injury
TBI	traumatic brain injury
TUNEL	terminal deoxynucleotidyl transferase biotin-dUTP nick end labeling

1. Introduction

Traumatic brain injury (TBI) and neurosurgical procedures commonly result in the formation of tissue gaps and raw surfaces within the cerebral parenchyma. Regeneration and functional recovery are limited by the hostile microenvironment caused by the mechanical trauma and the brain's intrinsic responses to injury. The latter is characterized by the disruption of the blood–brain barrier, extravasations of plasma proteins, cellular infiltration, ischemia, excitotoxicity, and free radical release (Bramlett and Dietrich, 2007). These events may lead to secondary cell death, demyelination, axonal degeneration,

and the formation of fluid-filled cavities that are initially lined by reactive gliosis and, subsequently, by glial scars. The presence of anatomical tissue gaps and glial scars acts as a physical and chemical barrier to axonal regrowth that may extend beyond the site of the initial injury (Silver and Miller, 2004). To promote healing and regeneration, it is necessary to bridge the tissue gap and to limit glial scar formation. The presence of a suitable 3-dimensional (3D) extracellular framework for cellular repopulation and reorganization is also important.

The use of biomaterial scaffolds is a novel approach in providing extracellular matrix (ECM)-like structures that are potentially conducive to cellular infiltration, proliferation, differentiation, and reorganization in experimental settings (Vasita and Katti, 2006; Willerth and Sakiyama-Elbert, 2007; Yarlagadda *et al.*, 2005). Tissue scaffolds may also reduce glial scar formation by modulating inflammatory reactions around the site of injury. The essential characteristics for these biomaterials include (i) biocompatibility; (ii) controlled biodegradation; (iii) lack of cytotoxicity and immunogenicity; (iv) amenability to design and modification; (v) ability to promote or inhibit cell-material interactions; (vi) easy production, purification, and processing; and (vii) chemical compatibility with physiological conditions (Holmes *et al.*, 2000). The ability to carry and deliver drugs or transplantable cells is another important consideration.

A variety of biomaterial scaffolds has been developed (Willerth and Sakiyama-Elbert, 2007). For tissue repair, scaffolds need to contain fibers that are significantly smaller than cells (i.e., nanofibers) so that the latter can migrate into and become embedded within the framework. To date, there are three fiber-fabrication techniques that can consistently produce nanofibers to this standard, namely, self-assembly, electrospinning, and phase separation (Barnes *et al.*, 2007). In this chapter, we focus on the self-assembling peptide nanofiber scaffold (SAPNS).

2. Self-Assembling Peptide Nanofiber Scaffold

2.1. Basic structures and properties

The SAPNS contains periodic repeats of alternating ionic hydrophilic and hydrophobic amino acids that give rise to a typical β-sheet structure with distinct polar and nonpolar surfaces. It is a promising scaffold material because of the design versatility afforded by the amino acid sequences and the variety of possible secondary, tertiary, and quaternary structures. Under the appropriate conditions, the β-sheets would spontaneously self-assemble to form nanofibers. The latter would further self-assemble to form a 3D nanofiber scaffold. The process is similar to that of polymerization (Gelain *et al.*, 2007; Zhang, 2008). A nanofiber scaffold so formed has pores of

around 5–200 nm in diameter, resembling the structures found in most ECM (Holmes *et al.*, 2000; Zhang *et al.*, 2002). As peptides are nontoxic, biocompatible, and biodegradable, SAPNS is potentially suitable for clinical use. These oligopeptides may contain synthetic amino acids, and by subjecting them to different process conditions (e.g., pH, salt content), a large variety of scaffolds may be designed and constructed. It also has the capacity to carry transplantable cells or drugs to provide the appropriate signaling for the promotion of neuroregeneration (Ashammakhi *et al.*, 2009).

One of the most widely studied SAPNSs is RADA16-I. It contains the amino acids alanine, lysine, and glutamate in repeated sequences of Arg-Ala-Asp-Ala (RADA). Individual nanofibers formed by RADA16-I have diameters of around 10 nm and form scaffolds with high hydration of greater than 99% water. RADA16-I has been studied extensively for use in tissue cultures for a variety of cell types and is commercially available in both powder and liquid forms (BD™ PuraMatrix™ Peptide Hydrogel, BD Science, Cambridge, MA; Zhang *et al.*, 1993, 1995). It has also been found to promote regeneration in experimental spinal cord and brain injuries. Ellis-Behnke *et al.* (2006b) performed a transection in the hamster brain and filled the wound with RADA16-I. The latter was found to "knit" the severed tissue almost seamlessly with axonal regrowth across the transection gap (Ellis-Behnke *et al.*, 2006b). Guo *et al.* (2007) examined the effect of RADA16-I in experimental spinal cord injury in rats by embedding Schwann cells and neuroprogenitor cells (NPCs) within RADA16-I. Again, the latter was found to integrate well within the injury site, and the transplanted cells were able to survive and differentiate within RADA16-I (Guo *et al.*, 2007). Using a cortical resection model, our group has demonstrated that treatment with RADA16-I was associated with less inflammatory response and better knitting of the injured cerebral cortex (Guo *et al.*, 2009). Another interesting property of RADA16-I is its ability to stop bleeding almost instantaneously. This adds an advantage when dealing with surgical trauma of the brain in both experimental and clinical settings (Ellis-Behnke *et al.*, 2006a).

2.2. Preparation for use

We use the liquid form of RADA16-I as a 1% solution (w/v) in our *in vivo* experiments. For other *in vitro* procedures, such as surface plating or encapsulating of cells, concentrations below 0.5% may be used instead. Since the gelation of this material is initiated by salt concentration at or greater than 1 m*M*, RADA16-I should not be combined with salt-containing buffers until gelation is desired. We produce 10% sucrose stocks in distilled water that are then kept refrigerated at −20 °C. The stock solution should remain clear and odorless during storage. Prior to use, the viscosity of the stock solution is decreased by vortexing it for 30 min. Bubbles may sometimes form which can be eliminated by centrifugation. The material is then

refiltered with a 0.20-μm membrane filter prior to application. RADA16-I can also be obtained in powder form from other researchers (Ellis-Behnke *et al.*, 2006b). The powder can be reconstituted readily as a solution by dissolving 10 mg of it in 1 ml of Milli-Q water (Millipore) in an Eppendorf tube, mixed, sonicated for 30 s, and then filtered. It can be left to sit at room temperature for 1 month prior to use.

The commercially available liquid form of RADA16-I has a pH of 2–2.5. When applied directly onto nervous tissue, this degree of acidity may cause significant injury and inflammatory reactions. Previous studies, however, have described the use of nonbuffered RADA16-I on the brain and did not report any significant adverse reactions (Ellis-Behnke *et al.*, 2006b; Guo *et al.*, 2009). We surmise that this may be due to the buffering effect provided by the copious amount of cerebrospinal fluid and blood surrounding the application sites. For experiments on the spinal cord, however, nonbuffered RADA16-I has been found to damage the host tissue (Guo *et al.*, 2007). This may be the result of the different microenvironment and/or the differences between the spinal cord and the brain in their responses to injury (Schnell *et al.*, 1999). In our experience with two different experimental models, we found that unbuffered RADA16-I would cause less inflammatory response in the brain when used in a cortical resection model than in a linear cortical incision model that involves less bleeding and a smaller injury (Guo *et al.*, 2009).

The self-assembly of RADA16-I is a spontaneous process under thermodynamic equilibrium by noncovalent interactions, such as ionic and hydrogen bonding. The formation of β-sheets is affected to different extents by the pH of the microenvironment. Between pH 1.0 and 4.0, RADA16-I forms typical β-sheets, which readily self-assemble into long nanofibers. Between pH 4.5 and 9.5, it forms smaller sized fibers as well as some aggregates. Above pH 9.5, the β-sheets may fail to form good nanofibers (Ye *et al.*, 2008). The data indicate that buffering RADA16-I to physiological pH does not significantly alter its self-assembly efficacy and has the benefit of avoiding additional injury to the host tissue. However, while buffering produces a more "brain-friendly" RADA16-I hydrogel, it has certain limitations. When unbuffered in its native form, RADA16-I can be applied readily as an injectable liquid. Not only is this more convenient for use, but it also allows better conformation of the hydrogel to the lesion cavity. Buffered RADA16-I gelates immediately and has to be transferred as a solid hydrogel into the lesion site. The hydrogel is fragile and must be handled very gently. The shapes and sizes of the hydrogel are variable and therefore may not conform readily within the lesion cavity. The need for pretreatment also lessens its potential use as a topical haemostatic and neuroprotective agent in clinical surgery.

The RADA16-I solution can be buffered with phosphate-buffered saline (PBS) in a ratio of 100 μl PBS for 50 μl RADA16-I. We perform

this on a small plastic dish right next to the surgical field to facilitate the transfer of the hydrogel. The amount of RADA16-I used would depend on the injury model. Once formed, we let the hydrogel stand for 1 min before transferring it onto the lesion site with a microscoop. Alternatively, the hydrogel can be pulled into a 1-ml syringe using a 20–22-gauge needle and then injected onto the lesion site using a 26-gauge needle. We find this method to be more difficult to use, as the transfer may introduce bubbles and the hydrogel may disintegrate.

3. Experimental Models

3.1. Surgical brain injury

Many experimental models of TBI have been developed to elucidate the primary and secondary sequelae underlying human TBI in an effort to identify potential neuroprotective or neuroregenerative therapies. The majority of these models involve the infliction of dynamic deformation or acceleration/deceleration injuries to the brain (Cernak, 2005; Morales *et al.*, 2005). Some of these (e.g., the diffuse axonal injury model) do not consistently give rise to tissue gaps, which somewhat precludes their use in studying biomaterial scaffolds. Others may cause edema, bleeding, and eventually cell death and tissue loss, but the resultant tissue gaps may vary in configurations and sizes. Moreover, the formation of these tissue gaps is a delayed and protracted process, and the application of biomaterial scaffolds would require a second operation. By contrast, experimental models primarily aimed at creating anatomical tissue gaps would produce standardized lesions and allow the immediate implantation of tissue scaffolds. These surgical brain injury (SBI) models mimic the situations encountered during neurosurgical procedures (e.g., brain tumor resection, hematoma evacuation) which often result in cell loss along with the disruption of supporting ECM in the surrounding brain (Jadhav and Zhang, 2008). In certain critical areas (e.g., brainstem, motor cortex), these injuries may cause significant neurological deficits (e.g., coma, hemiplegia). The intraoperative applications of scaffold materials exploit an opportune therapeutic window, whereby early neuroprotective and regenerative benefits can be provided (Wong *et al.*, 2008).

3.2. Cortical resection model

We use a cortical resection model to mimic the volume loss caused by SBI. The model has been described previously (Guo *et al.*, 2009). Briefly, adult female Sprague–Dawley (SD) rats (220–250 g) are put under general anesthesia by giving ketamine (80 mg/kg) and xylazine (10 mg/kg) intraperitoneally. The animal head is fixed on a stereotactic frame to place the skull in a

horizontal position. Following a dorsal midline skin incision on the head, a craniotomy is performed over one or both of the frontal lobes. We do not use electric drilling in making the craniotomy because drilling generates heat that may cause thermal injury to the underlying brain; instead, we use a metallic trephine (3 mm outer diameter) to raise a bone flap by manual drilling (Fig. 9.1). The dura is opened with micro scissors. A 1 × 2 mm rectangle of 2-mm thick cortical tissue is then resected at a site 2 mm lateral to the bregma. Bleeding from the cut surface is first stopped by filling the cavity with 20 μl 1% RADA16-I solution, which has known hemostatic properties. Thirty seconds later, the cavity is cleared to remove the coagulated blood. This is followed by the administration of fresh RADA16-I. The dura is closed with a 10/0 nylon suture (Ethicon Inc., Johnson & Johnson, Somerville, NJ) and covered with dura graft implant (DURAFORM^{TM}, Codman, Raynham, MA). The skull flap is replaced and secured with bone wax. The skin is closed with a 4/0 nylon suture (Ethicon Inc.).

The animals are allowed to survive postoperatively and are sacrificed at various time-points using an overdose of intraperitoneal pentobarbital. This is followed by transcardial perfusion with 4% paraformaldehyde in 0.1 *M* PBS (pH 7.4). The brains are extracted intact and postfixed overnight in perfusing solution, followed by cryoprotection in a 30% sucrose solution overnight at 4 °C. Figure 9.2 shows the macroscopic appearance of the harvested brain after treatment with RADA16-I and saline.

Tissue preparations for histological and immunohistochemical studies are performed in the standard manner. Briefly, the brain is embedded in optimal cutting temperature compound (OCT, Sacura, Torrance, CA). Coronal cryostat sections (30 μm) are made and mounted on gelatin-coated slides and stored at −20 °C. Cell morphology is studied with hematoxylin

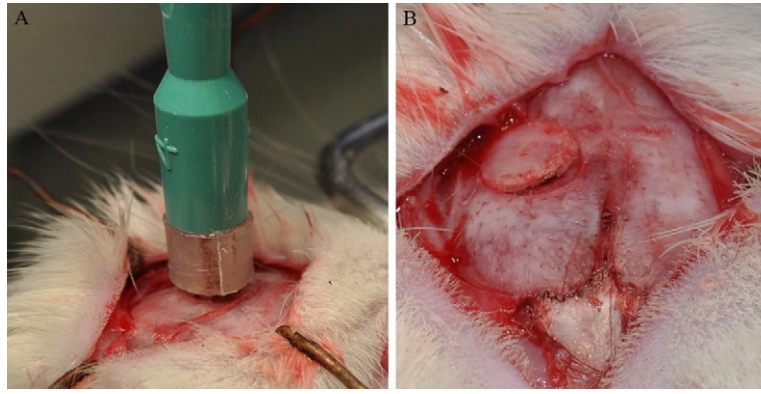

Figure 9.1 (A) A trephine for skull opening; (B) craniotomy bone flap is raised.

Figure 9.2 Macroscopic appearance after treatment with RADA16-I (*left hemisphere*) and saline (*right hemisphere*).

and eosin (H&E) (Sigma) dye. Frozen sections are air-dried at room temperature for 30 min and washed with PBS for 10 min. They are then blocked with 10% normal goat serum and 0.3% Triton X-100 (Triton® X-100, Sigma-Aldrich, St. Louis, MO) in PBS for 1 h at room temperature. Afterward, the sections are stained with various primary antibodies overnight at 4 °C, depending on the investigations required; washed in PBS three times; and incubated with the appropriate secondary antibodies for 2 h at room temperature. The slides are washed again in PBS three times and mounted with mounting medium (Dako, Carpinteria, CA) after counterstaining of the nuclei with 4,6-diamidino-2-phenylindole (DAPI, Sigma, St. Louis, MO).

3.3. Cell embedment within nanofiber scaffold

RADA16-I has the capacity to carry transplantable cells. For this purpose, the RADA16-I solution is first buffered with the culture medium carrying the transplanted cells. A variety of cells may be embedded for transplantation. We have previously described the use of NPCs in RADA16-I (Guo *et al.*, 2007). NPCs are obtained from the hippocampi of (E16) embryos of GFP-transgenic SD rats (Enomoto *et al.*, 2003). After collection and centrifugation, the cells are resuspended in DMEM/F12 supplemented with B27 supplement (2%, Gibco, Invitrogen, Grand Island, NY), N2 (1%, Gibco), epidermal growth factor (EGF, 20 ng/ml, Gibco), basic fibroblast growth factor (bFGF, 20 ng/ml, Sigma), penicillin (100 U/ml), and streptomycin

(100 μg/ml). They are then transferred to culture flasks at 1×10^5 cells/ml and cultured as neurospheres. The cells have to be mechanically dissociated and reseeded once a week. To embed the NPCs within RADA16-I, 1 μl of the cell suspension is mixed with 9 μl of 1% RADA16-I solution and then plated to a dish in DMEM/F12 with 10% fetal bovine serum (FBS; Gibco). Gelation would occur immediately. To further stabilize the hydrogel, the medium is changed twice at 1, 10, and 30 min after plating and once every 3 days thereafter. The hydrogel is ready for transplantation on day 7.

In vivo transplantation of the NPC-containing RADA16-I hydrogel can be achieved by transferring it directly into the lesion cavity with the assistance of a microscoop. Immunohistochemical studies of the transplant culture is performed using primary antibodies that may include mouse anti-nestin (1:2000; BD Biosciences, Cambridge, MA) for NPCs; rabbit anti-GFAP (1:1000; Chemicon) for astrocytes; mouse anti-Rip (1:50, gift from Dr Xu XM, Kentucky Spinal Cord Injury Research Center, Louisville, KY) for oligodendrocytes; mouse anti-β-tubulin III (1:500; Sigma) for neurons; mouse anti-NF200 (1:400; Sigma) for axons; rabbit anti-5HT (serotonin, 1:200; Sigma, St. Louis, MO) for raphespinal axons; rabbit anticalcitonin gene-related peptide (CGRP, 1:200; Sigma) for primary sensory axons; mouse anti-ED1 (1:1000; Serotec, Raleigh, NC) for macrophages; and mouse antimyelin basic protein (anti-MBP, New England Biolabs, Ipswich, MA, 1:1000) for myelin. The procedure for tissue preparation is as described above.

Ex vivo assessment of the embedded cells within RADA16-I cultures can be performed 4 weeks after the embedding by a two-photon confocal microscope (Zeiss LSM510 META, Jena, Germany). For immunohistochemical studies, the NPC neurospheres are plated on poly-L-lysine-coated coverslips and grown in culture medium. These are then fixed 1 h later with 4% paraformaldehyde, cryoprotected in 30% sucrose, cut into 10 μm cryostat sections, and mounted on to gelatin-coated slides. Subsequent immunostaining is performed as described above.

3.4. Other SBI models

We have also used another SBI model aimed at studying the use of RADA16-I as a topical hemostatic and neuroprotective agent and to investigate if RADA16-I promotes healing across the incision site. The animal is anesthetized and positioned as described above. Following dura opening, a right cortical incision (length, 2 mm anterior–posterior; depth, 1 mm; centered 2 mm lateral to the sagital suture and 1 mm anterior to the coronal suture) by a stereotactically guided microknife is made under an operating microscope. The incision is designed to transect a cortical vessel. Bleeding from the transected vessel is stopped by topically applying RADA16-I.

We compare RADA16-I with other hemostatic techniques commonly used in neurosurgical procedures, such as bipolar electrocautery. The latter is an integral adjunct in modern neurosurgical procedures (Vellimana *et al.*, 2009). It involves the passing of electric current through electrodes mounted on the two prongs of a forceps. The current and the heat so generated then result in hemostatic coagulation. We use a commercially available ICC Biploar machine (ERBE, Germany) and standardize the duration and voltage of coagulation to 2 s and 20 W, respectively. The voltage is controlled by a foot switch connected to the bipolar machine, and the application time can be set with a custom-made digital timer. The distance between the two prongs of the forceps is also fixed.

Immediately prior to sacrifice, we subject the animals to magnetic resonance imaging (MRI). The volume of T2-hyperintensity is used to assess the degree of brain edema and inflammatory responses. Our preliminary findings demonstrate that RADA16-I results in a smaller cortical lesion and lesser degree of reactive changes around the site of injury (Figs. 9.3–9.5).

There are various histological techniques for assessing the spatiotemporal distribution of degenerating cells, including H&E staining, suppressed silver methods, and terminal deoxynucleotidyl transferase biotin-dUTP nick end labeling (TUNEL). Eosin staining is technically simple and reproducible but does not result in the selective and unequivocal labeling of degenerating neurons. The suppressed silver method can be used to selectively stain degenerating neurons; however, the technique is time-consuming and laborious. TUNEL labeling detects fragmented DNA during the later stages of apoptosis but is not specific for neurons or glial cells. Moreover, we find that our SBI models produce mainly necrosis, but little apoptosis. To study the extent of cellular degeneration, we examine the surrounding tissue with Fluoro-Jade series. Fluoro-Jade B is a high-affinity fluorescent marker for

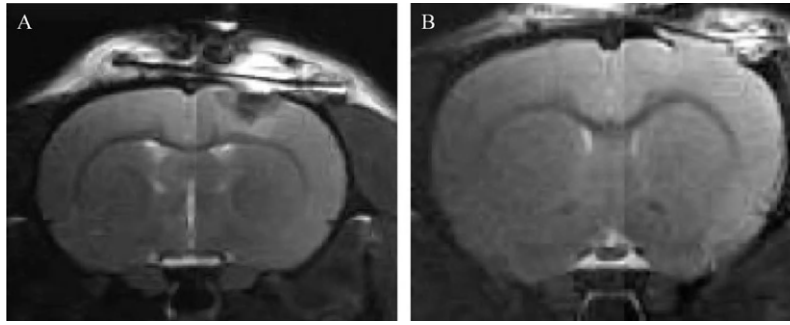

Figure 9.3 MRI study (Day 7) showing the area of T2-hyperintense area around the lesion site in the right frontal lobe after treatment with (A) electrocautery and (B) RADA16-I.

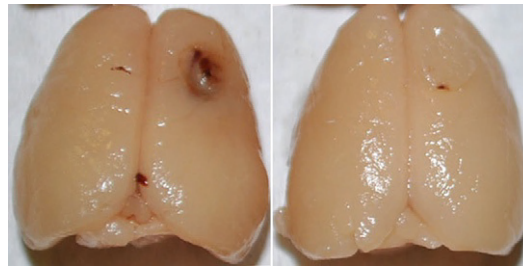

Figure 9.4 Macroscopic appearance after treatment with electrocautery (*left*) and RADA16-I (*right*).

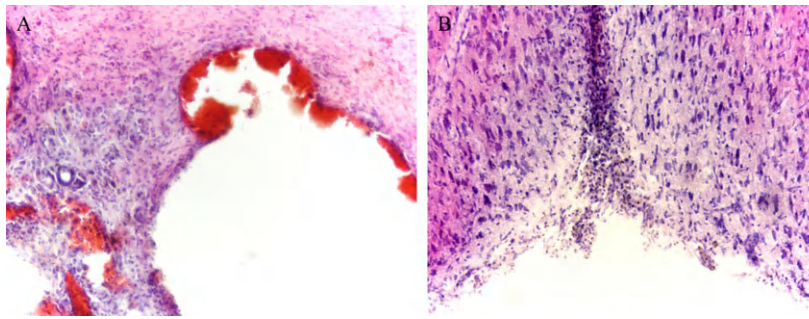

Figure 9.5 Hematoxylin and eosin staining examination showing the lesions after treatment with (A) electrocautery and (B) RADA16-I.

the localization of neuronal degeneration. It has high sensitivity and specificity for neuronal degeneration (Tanaka *et al.*, 2006). To study the extent of cellular degeneration, we examine the surrounding tissue with Fluoro-Jade B (Fluoro-Jade® B, Millipore, Billerica, MA) according to the manufacturer's instructions. Briefly, tissue sections are first incubated in a solution of 1% NaOH in 80% ethanol for 5 min followed by hydration in graded ethanol (75%, 50%, and 25%; 5 min each) and distilled water for 2 min and then incubated in a solution of 0.06% potassium permanganate for 10 min on a shaker, followed by washing with distilled water for 2 min. The sections are then incubated in a 0.0004% staining solution of Fluoro-Jade B and 0.0004% DAPI for 20 min, followed by three changes of distilled water for 2 min each. Excess water is removed by briefly draining the slides vertically on a paper towel, and the sections are air-dried, cleared in xylene at least a minute (2 × 5 min), and cover-slipped. Our initial findings indicate that Fluoro-Jade positivity is less extensive after treatment with RADA16-I (Fig. 9.6).

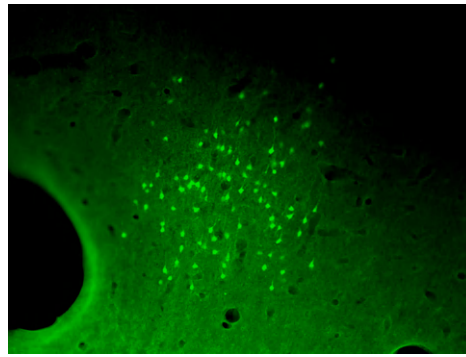

Figure 9.6 Immunohistochemical staining using fluoro-jade B showing the presence of degenerative neurons deep at the site of injury after electrocautery.

Ellis-Behnke *et al.* (2006b) have developed a model that involves a cut wound in the midbrain and have studied the regeneration of the associated visual pathway and function. Treatment with RADA16-I was found to promote axonal regrowth and functional recovery (Ellis-Behnke *et al.*, 2006b). Although this is a robust experimental model, the injury is relatively uncommon in a clinical setting. Conversely, the SBI models described in this chapter are more realistic. However, there are certain methodological limitations. First, unlike the spinal cord in which the majority of axons run longitudinally within nerve sheaths and may potentially regenerate as such, the topography of the cerebral neurons adopts a highly complex 3D geometry. Regeneration within and across a tissue gap in the brain requires a complex pattern of axonal regrowth. Assessments by means of axonal labeling and/or functional studies are more difficult to accomplish than in spinal cord injury studies. Second, the cortical resection and the associated resultant cavity are more difficult to standardize because of their 3D geometry, as well as the tendency for the surrounding brain to swell and alter the cavity's configuration.

4. Conclusion

The use of a peptide nanofiber scaffold is a novel and promising approach to facilitate the healing and regeneration of injury within the brain. RADA16-I has been found to bridge tissue gaps in various SBI models and provides a supportive microenvironment for astrocytes and microglial cells to migrate into and survive within the lesion sites. It may also act as a carrier of transplantable cells. RADA16-I is potentially suitable

for clinical use because of its biocompatible constituents. However, the need for buffering may limit its application. Future investigations may focus on the development of peptide nanofiber scaffolds with intrinsic pH that is closer to physiological values. The use of nanofiber scaffolds as potential carriers of growth factors and neuroprotective agents should be explored. It is critical to work with experimental models that produce consistent tissue gaps, permit the ready application of nanofiber scaffolds, and that are subject to quantitative assessment of neuronal regrowth and functional recovery within the cerebrum.

REFERENCES

Ashammakhi, N., Wimpenny, I., Nikkola, L., and Yang, Y. (2009). Electrospinning: Methods and development of biodegradable nanofibres for drug release. *J. Biomed. Nanotechnol.* **5,** 1–19.

Barnes, C. P., Sell, S. A., Boland, E. D., Simpson, D. G., and Bowlin, G. L. (2007). Nanofiber technology: Designing the next generation of tissue engineering scaffolds. *Adv. Drug Deliv. Rev.* **59,** 1413–1433.

Bramlett, H. M., and Dietrich, W. D. (2007). Progressive damage after brain and spinal cord injury: Pathomechanisms and treatment strategies. *Prog. Brain Res.* **161,** 125–141.

Cernak, I. (2005). Animal models of head trauma. *NeuroRx* **2,** 410–422.

Ellis-Behnke, R. G., Liang, Y. X., Tay, D. K., Kau, P. W., Schneider, G. E., Zhang, S., Wu, W., and So, K. F. (2006a). Nano hemostat solution: Immediate hemostasis at the nanoscale. *Nanomedicine* **2,** 207–215.

Ellis-Behnke, R. G., Liang, Y. X., You, S. W., Tay, D. K., Zhang, S., So, K. F., and Schneider, G. E. (2006b). Nano neuro knitting: Peptide nanofiber scaffold for brain repair and axon regeneration with functional return of vision. *Proc. Natl. Acad. Sci. USA* **103,** 5054–5059.

Enomoto, M., Shinomiya, K., and Okabe, S. (2003). Migration and differentiation of neural progenitor cells from two different regions of embryonic central nervous system after transplantation into the intact spinal cord. *Eur. J. Neurosci.* **17,** 1223–1232.

Gelain, F., Lomander, A., Vescovi, A. L., and Zhang, S. (2007). Systematic studies of a self-assembling peptide nanofiber scaffold with other scaffolds. *J. Nanosci. Nanotechnol.* **7,** 424–434.

Guo, J., Su, H., Zeng, Y., Liang, Y. X., Wong, W. M., Ellis-Behnke, R. G., So, K. F., and Wu, W. (2007). Reknitting the injured spinal cord by self-assembling peptide nanofiber scaffold. *Nanomedicine* **3,** 311–321.

Guo, J., Leung, K. K., Su, H., Yuan, Q., Wang, L., Chu, T. H., Zhang, W., Pu, J. K., Ng, G. K., Wong, W. M., Dai, X., and Wu, W. (2009). Self-assembling peptide nanofiber scaffold promotes the reconstruction of acutely injured brain. *Nanomedicine* **5,** 345–351.

Holmes, T. C., de Lacalle, S., Su, X., Liu, G., Rich, A., and Zhang, S. (2000). Extensive neurite outgrowth and active synapse formation on self-assembling peptide scaffolds. *Proc. Natl. Acad. Sci. USA* **97,** 6728–6733.

Jadhav, V., and Zhang, J. H. (2008). Surgical brain injury: Prevention is better than cure. *Front. Biosci.* **13,** 3793–3797.

Morales, D. M., Marklund, N., Lebold, D., Thompson, H. J., Pitkanen, A., Maxwell, W. L., Longhi, L., Laurer, H., Maegele, M., Neugebauer, E., Graham, D. I., Stocchetti, N., *et al.* (2005). Experimental models of traumatic brain injury: Do we really need to build a better mousetrap? *Neuroscience* **136,** 971–989.

Schnell, L., Fearn, S., Klassen, H., Schwab, M. E., and Perry, V. H. (1999). Acute inflammatory responses to mechanical lesions in the CNS: Differences between brain and spinal cord. *Eur. J. Neurosci.* **11,** 3648–3658.

Silver, J., and Miller, J. H. (2004). Regeneration beyond the glial scar. *Nat. Rev. Neurosci.* **5,** 146–156.

Tanaka, K. F., Ochi, N., Hayashi, T., Ikeda, E., and Ikenaka, K. (2006). Fluoro-Jade: New fluorescent marker of Rosenthal fibers. *Neurosci. Lett.* **407,** 127–130.

Vasita, R., and Katti, D. S. (2006). Nanofibers and their applications in tissue engineering. *Int. J. Nanomedicine* **1,** 15–30.

Vellimana, A. K., Sciubba, D. M., Noggle, J. C., and Jallo, G. I. (2009). Current technological advances of bipolar coagulation. *Neurosurgery* **64,** 11–18.

Willerth, S. M., and Sakiyama-Elbert, S. E. (2007). Approaches to neural tissue engineering using scaffolds for drug delivery. *Adv. Drug Deliv. Rev.* **59,** 325–338.

Wong, D. Y., Krebsbach, P. H., and Hollister, S. J. (2008). Brain cortex regeneration affected by scaffold architectures. *J. Neurosurg.* **109,** 715–722.

Yarlagadda, P. K., Chandrasekharan, M., and Shyan, J. Y. (2005). Recent advances and current developments in tissue scaffolding. *Biomed. Mater. Eng.* **15,** 159–177.

Ye, Z., Zhang, H., Luo, H., Wang, S., Zhou, Q., Du, X., Tang, C., Chen, L., Liu, J., Shi, Y. K., Zhang, E. Y., Ellis-Behnke, R., *et al.* (2008). Temperature and pH effects on biophysical and morphological properties of self-assembling peptide RADA16-I. *J. Pept. Sci.* **14,** 152–162.

Zhang, S. (2008). Designer self-assembling peptide nanofiber scaffolds for study of 3-d cell biology and beyond. *Adv. Cancer Res.* **99,** 335–362.

Zhang, S., Holmes, T., Lockshin, C., and Rich, A. (1993). Spontaneous assembly of a self-complementary oligopeptide to form a stable macroscopic membrane. *Proc. Natl. Acad. Sci. USA* **90,** 3334–3338.

Zhang, S., Holmes, T. C., DiPersio, C. M., Hynes, R. O., Su, X., and Rich, A. (1995). Self-complementary oligopeptide matrices support mammalian cell attachment. *Biomaterials* **16,** 1385–1393.

Zhang, S., Marini, D. M., Hwang, W., and Santoso, S. (2002). Design of nanostructured biological materials through self-assembly of peptides and proteins. *Curr. Opin. Chem. Biol.* **6,** 865–871.

CHAPTER TEN

Detection and Treatment of Intravascular Thrombi with Magnetofluorescent Nanoparticles

S. Sibel Erdem,* Irina Y. Sazonova,† Tetsuya Hara,‡ Farouc A. Jaffer,‡ *and* Jason R. McCarthy*

Contents

Abstract

Thrombosis, the formation of a clot within a blood vessel, underlies a number of life-threatening cardiovascular disorders such as heart attack, ischemic stroke, pulmonary embolism, and deep vein thrombosis. These conditions affect the lives of millions of people worldwide and result in significant morbidity and mortality. It is thus crucial to develop novel methodologies to enhance the detection and treatment of these disorders. Thrombolysis, or the dissolution

* Center for Systems Biology, Harvard Medical School and Massachusetts General Hospital, Charlestown, Massachusetts, USA
† Section of Cardiology, Department of Medicine, Medical College of Georgia, Georgia Health Sciences University, Augusta, Georgia, USA
‡ Cardiology Division, Cardiovascular Research Center, Harvard Medical School and Massachusetts General Hospital, Boston, Massachusetts, USA

Methods in Enzymology, Volume 508
ISSN 0076-6879, DOI: 10.1016/B978-0-12-391860-4.00010-0

of blood clots, relies upon the administration of exogenous plasminogen activators (PAs) that lyse fibrin. Yet, there are several drawbacks to the use of current PAs, including significant risks of uncontrolled bleeding and suboptimal efficacy and pharmacokinetics. Nanomaterials are well positioned to address these priority issues in thrombolysis, via the alteration of PA pharmacokinetics and biodistribution. Additionally, due to the multifunctional nature of nanoparticles, these thrombolytics may be targeted to the site of occlusion, effectively concentrating the drug where it is most needed. Herein, we describe the methodology associated with the synthesis of a novel thrombus-targeted fibrinolytic nanoagent. At each step of the synthesis, we analyze the nanomaterials, including their physical properties and their ability to bind to thrombosis targets of interest. The effect of the conjugation of tPA to the nanoparticle surface on the amidolytic and fibrinolytic activities of nanoagents is also investigated. Lastly, the *in vivo* binding of the targeted thrombolytic to intravascular thrombi is examined.

1. Introduction

Hemostasis is responsible for the prevention of blood loss in response to vessel injury. It is a delicate balancing act between the formation of clots (thrombosis) and their dissolution (thrombolysis or fibrinolysis). Under certain circumstances, this physiological process may become overwhelmed, promoting the formation of pathological thrombosis, and resulting in vessel occlusion. Depending upon its location and size, this thrombus causes vascular ischemia that may result in death or significant tissue injury, leading to many long-term health problems.

Thrombi are initially formed by the adherence of platelets to damaged endothelium, a result of the exposure of subendothelial proteins to the blood. This initial hemostatic plug is strengthened by the deposition of fibrin and its cross-linking, a process that is mediated by the coagulation cascade, a series of interconnected coagulation factors. Clinically, when thrombosis is suspected, patients undergo multiple tests, including conventional vessel imaging modalities, including ultrasound, X-ray computed tomography, echocardiography, and magnetic resonance (MR) imaging, with sensitivities and specificities reaching greater than 85–90%. While results from these tests can be used to determine the location of a thrombus and its severity, they provide little biological information about the clot, including its constitution and age, factors that are important in the determination of optimum therapeutic strategies.

Several molecular imaging strategies have thus been developed to study thrombus formation *in vivo*. Platelets have been labeled with radionuclides or fluorophores and injected into animals prior to the induction of thrombosis (Falati *et al.*, 2002; Flaumenhaft *et al.*, 2007; Sim *et al.*, 2004), whereas

antibody and peptide affinity ligands have been used to localize imaging agents to fibrin (Falati *et al.*, 2002; Lanza *et al.*, 1996; McCarthy *et al.*, 2009; Thakur *et al.*, 2000). We have used one coagulation factor, in particular, tissue transglutaminase-activated factor XIII (FXIIIa), to effectively localize nanoparticles to thrombi (McCarthy *et al.*, 2009). The peptide-targeted agent is based on the amino terminus of α_2-antiplasmin, $N_{13}QEQVSPLTLLK_{24}$, which is specifically cross-linked into thrombi by the FXIIIa via a covalent bond between the glutamine 14 residue and the ε-amino group of a lysine residing within fibrin. FXIIIa, a hallmark of acute thrombi, plays a role not only in the stabilization of thrombi by cross-linking fibrin strands, thereby conferring stability, but also in covalently embedding α_2-antiplasmin into the clot, effectively increasing fibrinolytic resistance (Jaffer *et al.*, 2004; Tung *et al.*, 2003).

Whereas the molecular imaging agents described above may not ultimately serve as diagnostic agents in clinical medicine, they may be further viable as scaffolds to improve the efficaciousness of thrombosis therapies. Currently, pathological thrombosis is treated with a combination of antiplatelet, anticoagulant, and thrombolytic therapies. The latter, thrombolysis, is affected by the administration of plasminogen activators (PAs, e.g., tissue PA (tPA) or streptokinase (SK)), enzymes that catalyze the activation of the zymogen plasminogen to the active plasmin, which, in turn, cleaves fibrin, lysing the clot. While this approach sounds relatively simple, it possesses suboptimal efficacy, including incomplete lysis, thereby decreasing vascular patency, as well as reocclusion after the cessation of therapy (Anderson and Willerson, 1993; Murray and Lopez, 1997). There are also significant, life-threatening, bleeding consequences that may arise due to the suppression of hemostasis, including intracerebral hemorrhage, which can result in death or significant neurological deficit (Anderson and Willerson, 1993). It is thus important to develop alternative thrombolytics with potentially increased safety profiles and greater therapeutic windows.

In this chapter, we discuss the synthesis of thrombolytic nanoagents based upon the targeting of recombinant tPA-modified iron oxide nanoparticles to thrombi via the FXIIIa-sensitive peptide affinity ligand described above. These nanoagents are expected to modulate the pharmacokinetics and biodistribution of the PA, potentially increasing the efficacy of therapy.

2. Synthesis of Cross-linked Dextran-Coated Iron Oxide Nanoparticles

Dextran-coated monocrystalline iron oxide nanoparticles (MION) have been used clinically for almost two decades and have found utility in the detection of metastases (Harisinghani *et al.*, 2001; Saini *et al.*, 2000), the

imaging of angiogenesis (Tang *et al.*, 2005), the examination of primary tumors (Enochs *et al.*, 1999), and the detection of atherosclerotic lesions (Kooi *et al.*, 2003). Their usefulness is a result of their innate localization to inflammatory sites and uptake by phagocytic cells, such as macrophages. Whereas the targeting of these particles to sites of interest via affinity ligands would seem facile, the dextran coating is only weakly bound to the iron oxide core, resulting in an equilibrium in which the dextran can dissociate from the particle. If modified with ligands, including those used in targeting, imaging, or therapy, the biodistribution of the dissociated dextran would deviate from that of the particle, giving confounding results. To circumvent this dissociation and provide sites for further modification, the dextran coating of MION can be cross-linked and aminated, providing for superb stability under harsh conditions as well as excellent performance in biological systems without a change in size, blood half-life, or loss of its dextran coat (Josephson *et al.*, 1999). The resulting particle, CLIO (cross-linked dextran-coated iron oxide nanoparticle), behaves similar to MION, in that it can be utilized to image inflammation but can also be targeted to sites of interest, including thrombosis, as described here.

CLIO synthesis begins with the cross-linking of dextran-coated MION. MION can be purchased from the Center for Systems Biology at the Massachusetts General Hospital (MGH) in Boston, MA. Alternatively, dextran-coated iron oxide nanoparticles are available from a number of vendors, although they have not been tested in this protocol. Five volumes of 5 *M* aqueous sodium hydroxide is added to three volumes of MION over 15 min while stirring at room temperature. Two volumes of epichlorohydrin are then added slowly to the mixture and stirred vigorously for 8 h, at which time three volumes of 30% of ammonium hydroxide is added (Josephson *et al.*, 1999). The mixture is stirred for an additional 10 h, followed by the removal of excess epichlorohyrdin and ammonia by diafiltration using citrate buffer (pH 8). The resulting CLIO is concentrated to approximately 10 mg Fe/ml via centrifugal filtration using Amicon Ultra-4 filters with 100 kDa nominal molecular weight cutoff, Amicon Ultra-4, Millipore, Billerica, MA. The resulting CLIO is stored in Nalgene bottles at 4 °C and has been shown to be stable for several years.

2.1. Determination of iron concentration

It is crucial to know the concentration of iron in solution for all subsequent experiments, particularly when determining injection doses for *in vivo* experimentation. Thus, methodologies have been established for its determination spectroscopically via the dissolution of the particles and comparison to standards. In this assay, 10 μl of CLIO is mixed with 1 ml of 6 *M* hydrochloric acid (HCl) and 10 μl of 3% hydrogen peroxide. The solution is kept at room temperature for 1 h, and the optical density

(OD) of the solution at 410 nm is measured. Concomitantly, standard solutions of Fe containing 0.1–4.0 mg of Fe/ml in 6 *M* HCl should also be prepared and measured. The concentration of CLIO is then calculated from the slope of the plot of the OD versus the concentration of iron in the standard solutions.

3. Modification of CLIO with Fluorescent Dyes

Whereas CLIO is innately useful for MR imaging, due to its relaxivity-altering capabilities, its modification with fluorophores allows for its use in optical imaging, particularly *in vivo* near-infrared fluorescence imaging. In this instance, we use VivoTag 680 (VT680), which can be purchased from Perkin Elmer (Woburn, MA) and is comparable to other dyes such as Cy 5.5 (GE Healthcare) and Alexa Fluor 680 (Invitrogen, Carlsbad, CA). The maximum absorption of the dye (λ_{max}) is 670 nm, while its emission maximum is 688 nm. In typical syntheses, 1 mg of dye is reacted with 20 mg of CLIO (20 mg Fe) yielding approximately three dye molecules per particle. This number has been optimized through experimentation, as the coupling of more dyes to the particle surface can result in intermolecular quenching and diminish the overall brightness of the particle. As the surface of CLIO is functionalized with amines, succinimidyl ester- or isothiocyanate-activated fluorophores provide for facile reactions, although carboxylic acid bearing dyes can be reacted with the particle in the presence of appropriate coupling agents.

To synthesize CLIO-VT680, 1 mg of the dye is initially dissolved in dimethyl sulfoxide (DMSO) (not more than 40% of the total volume of the reaction) and is added to 20 mg of the CLIO prepared above (Scheme 10.1). The reaction is allowed to proceed for 3 h, at which time the product is purified by size exclusion chromatography (Sephadex G-25), using phosphate-buffered saline as the eluent (Dulbecco's phosphate-buffered saline (PBS), pH 7.4). It is important to note that calcium- and magnesium-free PBS should be used, since the presence of divalent cations can cause precipitation of the material. The purified CLIO-VT680 is concentrated using centrifugal filtration (100 kDa nominal molecular weight cutoff, Amicon Ultra-4, Millipore, Billerica, MA) to approximately 4 mg Fe/ml and should be stored in the dark at 4 °C to prevent photobleaching of the dye.

3.1. Spectrophotometric determination of particle and dye concentrations

As a next step, the concentrations of the dye-labeled particles (in mg Fe/ml solution) and fluorophores (VT680) are examined spectrophotometrically. The concentration of iron is determined comparatively, using

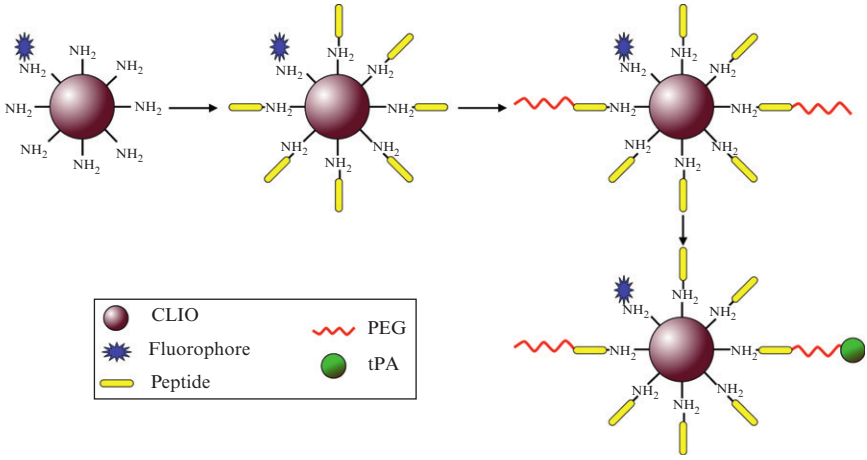

Scheme 10.1 Layer by layer synthesis of theranostic particles. Reproduced with permission from McCarthy *et al.* (2011).

CLIO as a standard, as its concentration had been determined relatively accurately using the dissolution process discussed above. The concentration of the dye is calculated from the OD at its λ_{max} using the Beer–Lambert Law. In this procedure, 10 μl of CLIO is diluted to 3 ml with PBS buffer and the OD is measured at 300 nm. Ten microliters of CLIO-VT680 is also diluted to 3 ml with PBS buffer and the absorption of that solution is determined at 300–680 nm. All measurements are performed in triplicate to ensure accuracy and minimize error. An arbitrary example is demonstrated further below.

If we assume that the initial concentration of the standard solution of CLIO is 8 mg Fe/ml and it is 300 times diluted with PBS, then the final concentration of the solution would be 2.6×10^{-2} mg Fe/ml. If this solution has an OD of 1.5 and diluted imaging agent solution has OD of 0.3 at 300 nm, Eq. (10.1) is used to calculate the concentration of CLIO-VT680 in mg Fe/ml.

$$\frac{[\mathrm{CLIO}]_{\mathrm{dil}}}{\mathrm{OD}_{\mathrm{CLIO}}} = \frac{[\mathrm{CLIO-VT680}]_{\mathrm{dil}}}{\mathrm{OD}_{\mathrm{CLIO-VT680}}} \tag{10.1}$$

where $[\mathrm{CLIO}]_{\mathrm{dil}}$ is the concentration of the diluted standard sample (CLIO), and $\mathrm{OD}_{\mathrm{CLIO}}$ is the absorption of the diluted standard sample at 300 nm. $[\mathrm{CLIO\text{-}VT680}]_{\mathrm{dil}}$ stands for concentration of the diluted imaging agent (CLIO-VT680) and $\mathrm{OD}_{\mathrm{CLIO\text{-}VT680}}$ refers to absorption of the dye-labeled agent at 300 nm. Thus:

$$\frac{(2.6 \times 10^{-2}\,\text{mg Fe/ml})}{1.5\,\text{AU}} = \frac{[\text{CLIO} - \text{VT680}]_{\text{dil}}}{0.3\,\text{AU}}$$

$$[\text{CLIO} - \text{VT680}]_{\text{dil}} = 5.1 \times 10^{-3}\,\text{mg Fe/ml}$$

$[\text{CLIO-VT680}]_{\text{dil}}$ is multiplied by the dilution factor (D) to determine the concentration of the original sample, as shown in Eq. (10.2) below

$$[\text{CLIO} - \text{VT680}] = [\text{CLIO} - \text{VT680}]_{\text{dil}} \times \text{D}$$
$$\frac{5.1 \times 10^{-3}\,\text{mg Fe/ml} \times 3\,\text{ml}}{1 \times 10^{-2}\text{ml}} = 1.54\,\text{mg Fe/ml} \tag{10.2}$$

The concentration of the VT680 is calculated from the absorption of the dye at its maximum, 680 nm, in the diluted solution and its extinction coefficient using the Beer–Lambert Law as follows (Eq. (10.3))

$$A = \frac{\varepsilon c l}{D} \tag{10.3}$$

where A is the absorption of the dye in diluted solution (arbitrary units), ε is the extinction coefficient of the dye ($\text{l mol}^{-1}\ \text{cm}^{-1}$), c is the concentration of the dye (M) and l is the path length of the cuvette (cm). As stated before, D refers to the dilution factor. For the diluted solution above, with an OD of 0.067 AU at 680 nm, the concentration of VT680 is:

$$0.067\text{AU} = \frac{\left(2 \times 10^{5} 1\ \text{mol}^{-1}\,\text{cm}^{-1}\right)(c)\ (1\,\text{cm})/3\ \text{ml}}{1 \times 10^{-2}\,\text{ml}}, \quad c = 1.00 \times 10^{-4} M$$

3.2. Conjugation of targeting ligands to CLIO-VT680

To enable thrombus targeting, the nanoagent is next modified with a peptide-based affinity ligand sensitive to FXIIIa. In order to facilitate the modification of CLIO-VT680 with the FXIII peptide, the peptide sequence is modified at its N-terminus with a glycine and at its C-terminus with a tryptophan spacer and a cysteine, allowing for its conjugation to the particle via a thioether linkage. To a suspension of CLIO-VT680 in PBS, succinimidyl iodoacetate (SIA) is added. This reagent is dissolved in DMSO before addition to the particles, as it is not soluble in aqueous buffer. Importantly, the amount of DMSO used should be 20–30% of the volume of the buffer, in order for the SIA to remain in solution. In this reaction, 1 mg of SIA is used per milligram of Fe to achieve maximum

loading. More specifically, 10 mg SIA is dissolved in DMSO (300 μl) and is added to 10 mg of CLIO-VT680 (10 mg, 9.4 mg Fe/ml) in PBS. The reaction is carried out at room temperature for 4 h, at which time the product can be purified by size exclusion chromatography (Sephadex G-25, PBS), as was done for the CLIO-VT680. The collected suspension can be used without any further treatment. Importantly, iodoacetate-modified CLIO-VT680 is susceptible to hydrolysis, thus it is important to immediately react it with a thiol containing ligand, such as the peptide described below.

The targeting peptide used in our example was purchased from the Peptide Synthesis/Protein Sequencing Core at the MGH in Boston, MA and was synthesized on Rink Amide resin, using an automated synthesizer and traditional Fmoc chemistries. The targeting peptide (FXIII), GNQEQVSPLTLLKC-NH_2, with the N-terminus *t*-butoxycarbonyl (Boc)-protected, was received on resin. In order to isolate the peptide, the resin is swelled in *N*,*N*-dimethylformamide for 15 min and filtered, followed by suspension in a cleavage cocktail consisting of trifluoroacetic acid (TFA), triisopropylsilane, and water (95:2.5:2.5, 5 m) for 3 h. At the conclusion of the reaction, the resin is filtered and the supernatant containing the peptide is precipitated by the addition of an excess amount of diethyl ether. The peptide is further purified by high-performance liquid chromatography (HPLC) on a Varian ProStar HPLC. Gradients are run with buffer A (H_2O/0.1% TFA) and buffer B (acetonitrile/10% buffer A/0.1% TFA) from 80% A to 20% A over the course of 30 min, with the peptide eluting at 12.8 min.

At the last step of the synthesis of the FXIII-targeted nanoagent, the purified peptide (10 mg), whose the N-terminus had been deprotected during the cleavage from the solid support, is added to a suspension of the SIA-modified CLIO-VT680 (10 mg, 9.4 mg Fe/ml) at 1:1 mass ratio (Scheme 10.1). This reaction is allowed to proceed at room temperature for 16 h. The FXIII-targeted nanoagent is purified by size exclusion column chromatography using PBS as the eluting solvent to yield CLIO-VT680-FXIII. A control nanoagent is also synthesized for this study. The control peptide, GNAEQVSPLTLLKC-NH_2 (CXIII), with a single amino acid mutation of the glutamine-14 residue to alanine, on Rink Amide resin, is also purchased from the Peptide Synthesis/Protein Sequencing Core at the MGH. This single amino acid mutation is the key factor that prevents the peptide's ability to bind the thrombus (Jaffer *et al.*, 2004; Tung *et al.*, 2003). An identical methodology to that described above is used to isolate and purify the CXIII peptide, and subsequently conjugate it to CLIO-VT680, giving the control agent, CLIO-VT680-CXIII. As was described in Section 3.1, the concentrations of the dye-labeled CLIO-VT680-FXIII and CLIO-VT680-CXIII particles are determined spectrophotometrically.

4. *In Vitro* Determination of Clot Binding Efficacy

The ability of the synthesized nanoagents to bind to their desired target can be readily ascertained *in vitro* using the optical properties of the nanoparticles and clots comprising fresh frozen plasma (FFP) (McCarthy *et al.*, 2009). FFP is obtained from deidentified, outdated blood products from the MGH Blood Bank, based upon a protocol approved by the Institutional Review Board at MGH. FFP clots are created in 96-well plates by mixing 180 μl of FFP, 10 μl of 0.4 *M* $CaCl_2$, and 10 μl of thrombin (0.1 U/ul; PBS), followed by incubation at 37 °C for 90 min. At this point, 6 μg of each of the nanoparticle preparations (2 mg Fe/ml) is added and incubated at 37 °C for 30 min more. To remove any unbound nanoagents, the clots are washed twice with PBS and centrifuged at 500 rpm for 10 min. The washing procedure is repeated an additional two times, and the clots are removed from the 96-well plate and laid out on a glass plate for fluorescence reflectance imaging (FRI) in the 680 nm channel. White light and fluorescence images are acquired on a Siemens BonSAI system, although any FRI system with the appropriate imaging channels can be used (e.g., Carestream Image Station, Carestream Health, Rochester, NY). The images are then analyzed using ImageJ software (NIH), where the clots are selected as regions of interest (ROI) in the white light image, which are subsequently applied to the fluorescence image. These ROIs are then utilized to determine the integrated signal intensity, the area within the ROI, and the signal per area. Target-to-background ratios (TBRs) are calculated as a ratio of the average signal per area for each of the nanoagents as compared to clots incubated with just PBS. As can be seen in Fig. 10.1A, the FXIII-targeted

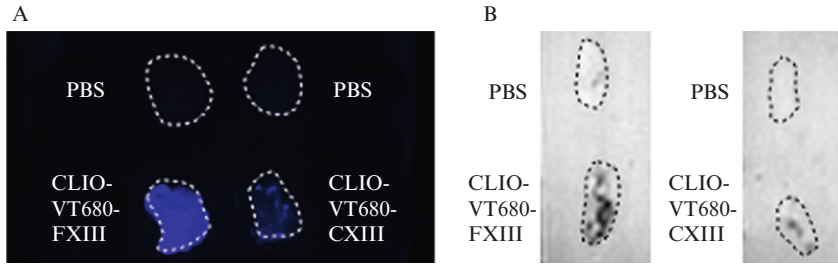

Figure 10.1 (A) FRI image of the gel in the VT680 channel demonstrates clearly the strong binding of the targeting agent to the FFP clot. (B) T2*-weighted MR image of FFP clots depicting strong T2 decreases in clots incubated with CLIO-FXIII and CLIO-CXIII. Reproduced with permission from McCarthy *et al.* (2009).

imaging agent (CLIO-VT680-FXIII) demonstrates a considerably greater fluorescence signal (2.5-fold higher TBR) than clots incubated with the control agent, CLIO-VT680-CXIII (McCarthy *et al.*, 2009).

As these particles are based upon an iron oxide core, they are also useful for MR imaging, making them truly multimodal. As opposed to gadolinium chelates, which serve as T_1 imaging agents, iron oxides are primarily T_2 imaging agents and result in negative enhancements in the images (depending upon the pulse sequence). To demonstrate nanoagent binding by MR imaging, representative clots from the above FRI experiment are embedded in 2% agar and imaged using a T_2*-weighted pulse sequence with the following imaging parameters: multislice 2D fast low angle shot (FLASH) sequence, repetition time (TR) 500 ms, echo time (TE) 8 ms, flip angle 30°, matrix 128 × 128, in-plane resolution 0.3 × 0.3 mm, slice thickness 0.8 mm, and eight averages (McCarthy *et al.*, 2009). As shown in Fig. 10.1B, the clots incubated with CLIO-VT680-FXIII demonstrated a decrease in signal because of the presence of the targeted nanoagents, whereas the clots treated with PBS or CLIO-VT680-CXIII show minimal darkening.

5. Synthesis of Thrombolytic Nanoagents

In order to affect targeted thrombolysis, a PA must be conjugated to the thrombus-targeted nanoscaffold. Some examples include urokinase and SK, each of which has been previously conjugated to a nanoparticle (Bi *et al.*, 2009; Marsh *et al.*, 2007, 2011). In this instance, we chose to use recombinant tPA. There are two main reasons for this: (1) tPA is used clinically in the treatment of a number of thrombus sequelae, including myocardial infarction and stroke and (2) tPA contains one free cysteine (Cys 83) in the growth factor domain, thereby providing a handle by which it can be conjugated to the nanoparticle in a controlled manner. Synthesis of the thrombolytic nanoagent starts with addition of a discrete polyethylene glycol (PEG) linker to the previously synthesized thrombus-targeted agent (CLIO-VT680-FXIII). This PEG must be heterobifunctional, containing an amine-reactive succinimidyl ester and a thiol-reactive maleimide, to facilitate reaction with the amino termini of the peptide-modified particle and tPA. It is also important to have a spacer between the fibrinolytic drug and the particle to minimize steric interactions. However, it is also crucial to assure that the avidity of the nanoparticle is not greatly influenced by the addition of the therapeutic moiety. Therefore, the PEG spacer is used in a substoichiometric ratio to the peptide on the particle (McCarthy *et al.*, 2011). Briefly, Mal-dPEG$_{24}$-NHS ester (0.9 mg in 240 µl DMSO, Quanta Biodesign, Powell, Ohio) is added to a suspension of CLIO-VT680-FXIII,

(9 mg, 7 mg Fe/ml) in PBS (pH 7.4). The reaction is allowed to proceed for 3 h, at which time the product is purified by size exclusion chromatography (Sephadex G-25, PBS) to give CLIO-FXIII-PEG.

A solution of tPA (6 mg, 1 mg/ml in sterile water) is added to a suspension of CLIO-FXIII-PEG, (9 mg, 15 mg Fe/ml) in PBS (pH 7.4) (Scheme 10.1). The resulting solution is exchanged into Tris buffer (pH 7.5) by centrifugal filtration using Amicon Ultra-4 filtration units (4 kDa) cutoff filters. The resulting solution is allowed to react for 24 h and is then purified by centrifugal filtration (Waters, 100 kDa cutoff) via extensive washing with PBS. The suspension should then be transferred to a 15-ml conical tube and centrifuged at 2000 rpm for 10 min to remove any white precipitate that may be present to give the thrombolytic nanoagent CLIO-FXIII-PEG-tPA, which should be stored at 4 °C. This precipitate is a tPA degradation product and cannot be removed during the filtration. It should be noted that the identical synthetic methodology is employed for the synthesis of the control agent CLIO-CXIII-PEG-tPA as well.

5.1. Characterization of the thrombolytic nanoagent

5.1.1. Determination of the number of tPA per particle

The number of tPA molecules conjugated to the particle surface can be calculated using the Bradford protein assay (Bio-Rad Protein Assay Kit II, Bio-Rad, Hercules, CA). Initially, a standard curve is generated using bovine serum albumin (BSA). The BSA standard is dissolved in 20 ml of ultra pure water, resulting in a solution with 1.44 mg BSA/ml. This solution is further diluted to 0.5, 0.4, 0.3, 0.2, 0.1, and 0.05 mg BSA/ml solution. Concomitantly, 1 ml of the Protein Assay Dye Reagent is diluted to 5 ml with distilled, deionized water. Ten microliters of each diluted protein solution is then added to 200 μl of diluted Protein Assay Dye Reagent in a 96-well plate. Following the 10-min incubation time, the OD of the mixture is read at 562 nm using a plate reader. A standard curve is then generated by plotting the OD versus the protein concentration. The protein concentration of the targeted and control agents, as well as free tPA are then measured. Similar to the standards, 10 μl of each of the solutions is added to 200 μl of the diluted Protein Assay Dye Reagent, which is incubated for 10 min, and its OD is read at 562 nm. Using the equation for the slope of the experimentally obtained standard curve, equation 10.4 is used for calculating the concentration of tPA in solution. Importantly, the concentration of the free tPA is known, as 2 ml of tPA is reconstituted in 1 ml sterile water. Thus, the concentration determined using the protein assay should match that of the dilution.

$$y = 0.9478x + 0.475 \tag{10.4}$$

For CLIO-FXIII-PEG-tPA (0.9 mg Fe/ml), the OD at 562 nm is 1, which will be used for the explanation of the calculations, below. The number of milligrams of tPA per milliliter of solution is calculated using Eq. (10.4) as shown below.

$$\begin{aligned} x &= \frac{1 - 0.475}{0.9478} \\ &= 0.562\,\text{mg/ml} \end{aligned}$$

The number of moles of tPA is calculated by dividing the number of milligrams by the molecular weight of tPA, as shown in Eq. (10.5), where n is the number of moles, m is the number of grams, and M is the molecular weight of the substance.

$$\begin{aligned} n &= \frac{m}{M} \\ &= \frac{(0.562\,\text{mg}/1000\,\text{g/mg})}{70,000\,\text{g/mol}} \\ &= 8 \times 10^{-9}\,\text{mol} \end{aligned} \tag{10.5}$$

Since the calculated number of moles is in 1 ml of solution, it is converted to liters to calculate the molarity of tPA using the Eq. (10.6), where C is the concentration, n is the number of moles, and V is the volume (L) of the solution.

$$\begin{aligned} C &= \frac{n}{V} \\ C_1 &= \frac{8 \times 10^{-9}\,\text{mol}}{1 \times 10^{-3}\text{l}} \\ &= 8 \times 10^{-6} M \end{aligned} \tag{10.6}$$

To calculate the number of tPA per particle, the concentration of CLIO must be calculated as well. Based on previous reports (Josephson *et al.*, 1999), we know that there are approximately 8000 Fe atoms per particle of CLIO. The molecular weight of CLIO is calculated using Eq. (10.7), where MW is the molecular weight of CLIO and 55.85 g/mol is the atomic weight of an Fe atom.

$$\begin{aligned} \text{MW} &= 8000\ \text{Fe atoms/particle} \times 55.85\,\text{g/mol} \\ &= 446,800\ \text{g/mol} \end{aligned} \tag{10.7}$$

The concentration of Fe is calculated by dividing the initial Fe concentration in the CLIO-FXIII-PEG-tPA (0.9 mg/ml or 0.9 g/l) by the number of grams of Fe as shown below (Eq. (10.8)).

$$C_2 = \frac{0.9\,\text{g/l}}{446,800\ \text{g/mol}} = 2 \times 10^{-6} M \tag{10.8}$$

As the final step of the calculations, the concentration of tPA (C_1) is divided by the concentration of CLIO (C_2) to give the number of tPA per particle, as shown in Eq. (10.9).

$$\text{Number of tPA per CLIO} = \frac{C_1}{C_2} = \frac{8 \times 10^{-6}\,M}{2 \times 10^{-6}\,M} = 4 \tag{10.9}$$

5.1.2. Analysis of *in vitro* enzymatic efficiency

The enzymatic efficiency of CLIO-FXIII-PEG-tPA is examined to determine whether the conjugation of tPA to the nanoparticle affects its proteolytic activity. The amidase kinetic parameters of CLIO-FXIII-PEG-tPA are determined by measuring the cleavage of the *p*-nitroanilide chromogenix substrate, S2288. S-2288 (Diapharma, West Chester, Ohio) is a short tPA-specific peptide, H-D-isoleucyl-L-prolyl-L-arginine-*p*-nitroanilide dihydrochloride, which upon amidolytic cleavage generates *p*-nitroanilide, a chromophore that can be monitored at 405 nm. In this assay, free tPA or CLIO-FXIII-PEG-tPA (100 n*M* tPA) is added to a well containing the assay buffer (0.1 *M* Tris–HCl, 0.1 *M* NaCl, pH 8.4) and S-2288 (0.15–1.5 m*M*) at 37 °C. The change in absorbance is measured at 405 nm for 10 min at 37 °C in a thermostatted plate reader (Synergy HT, Bio-Tech). The data are plotted as the change in absorption per minute (ΔOD_{405}/min) versus the concentration of the substrate and analyzed by Michaelis–Menten curve fitting to give the catalytic efficiency (k_{cat}/K_m, $mM^{-1}\,s^{-1}$) using GraphPad Prism software. As compared to free tPA, this assay revealed that the CLIO-based tPA conjugates demonstrate a 15% decrease in overall catalytic efficiency on a weight basis. This finding can be related with the steric constraint as a result of conjugation of tPA to the surface of CLIO and/or a decrease in the efficiency of the binding of tPA to the substrate.

6. *In Vitro* Clot Binding

As was done previously for CLIO-VT680-FXIII, the clot binding efficacy of the fully synthesized thrombolytic nanoagent must be ascertained to ensure that the addition of tPA is not detrimental to the thrombus targeting. Importantly, tPA must be inhibited prior to addition to the clots, as a failure to do so will result in clot dissolution. Inhibition of tPA is accomplished by the use of PPACK (Enzo Life Sciences, Farmingdale, NY), a low-molecular-weight inhibitor of serine proteases. To the tPA bearing agents (CLIO-FXIII-PEG-tPA and CLIO-CXIII-PEG-tPA), PPACK (1 mg/200 μl water) is added in one to one mass ratio. To be more specific, to 0.1 mg of CLIO (based upon the weight of iron), 0.1 mg of PPACK is added. The mixture is incubated at room temperature for 20 min, and the inhibition of tPA is confirmed via the S2288 chromogenic assay, as described in Section 5.1.2.

Clot binding experiments are performed as described in Section 3, with the clots being imaged in the VT680 channel of the FRI system. As can be seen in Fig. 10.2, FRI reveals that FXIII-targeted agents possess significantly higher TBRs at each stage of the synthesis (TBR of 9.8 for CLIO-FXIII-PEG-tPA vs. 4.5 for CLIO-PEG-tPA and 3.7 for CLIO-CXIII-PEG-tPA, ANOVA $p < 0.05$). The background fluorescence of the nontargeted agents can be likely attributed to nonspecific adherence of the CLIO-based agents to the plasma clots.

7. *In Vivo* Determination of Nanoagent Binding to Arterial and Venous Thrombi

Whereas demonstrating the *in vitro* binding and activity of the synthesized agents is indeed important, the *in vivo* capabilities are paramount. To investigate the *in vivo* targeting ability, a murine model of venous and arterial thrombosis is used, in conjunction with intravital fluorescence microscopy (IVFM). For thrombosis induction, the femoral vessels are damaged via the application of a solution of ferric chloride ($FeCl_3$) to the outer surface, as approved by the Subcommittee on Research Animal Care at MGH. This results in the formation of a thrombus within the vessel, the severity of which is controlled by the concentration of the $FeCl_3$ solution and the length of time that the solution is allowed to remain in contact with the vessel. To induce thrombosis, mice are initially anesthetized using an intraperitoneal (IP) ketamine (50 mg/ml, 330 μl), xylazine (100 mg/ml, 50 μl), and sterile saline (380 μl) mixture. Each mouse receives a 50 μl IP induction dose of the resulting mixture, followed by 20–30 μl IP hourly for continued

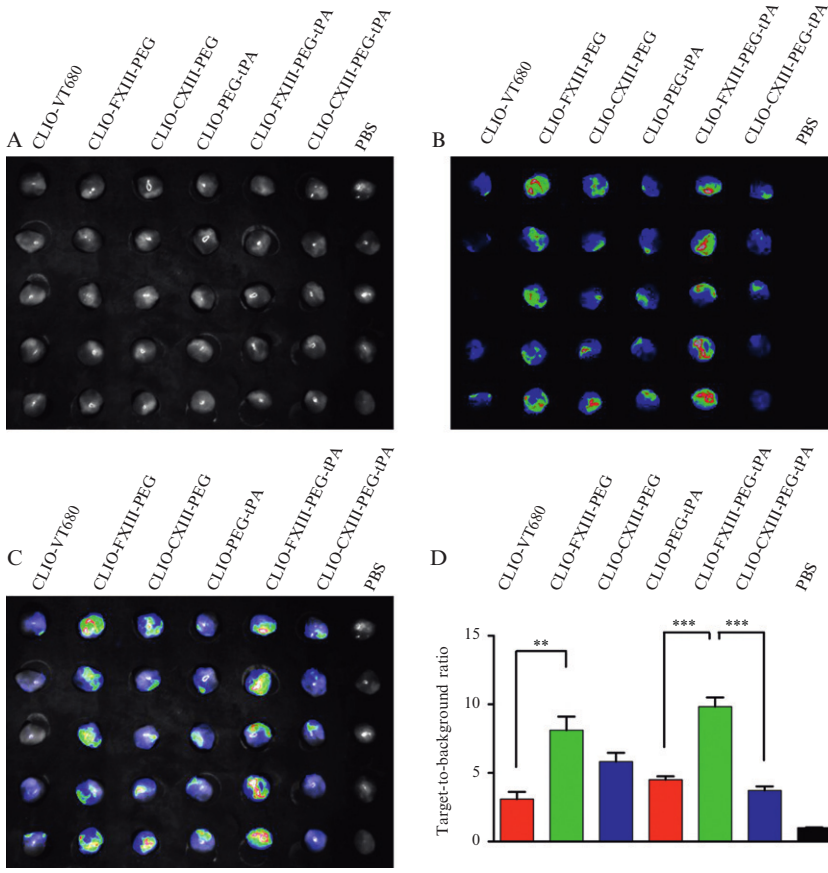

Figure 10.2 *In vitro* binding of synthesized nanoagent to FFP clots. (A) White light image of FFP clots; (B) fluorescence reflectance image of nanoagent binding in the VT680 channel; (C) merged white light and fluorescence images depicting clot binding; (D) quantification of clot target-to-background ratio. All results are relative to PBS-treated clots ($^{**}P = 0.0017$, $^{***}P < 0.0001$). Reproduced with permission from McCarthy *et al.* (2011).

anesthesia. After surgical resection of the overlying tissue, $FeCl_3$ is locally applied to the femoral vein using a 1-mm strip of Whatman No.1 filter paper soaked in 7.5% $FeCl_3$ in distilled water (McCarthy *et al.*, 2009). The filter paper is applied to the anterior surface of the vein for 5 min. Thereafter, the filter paper is removed and the vessel is washed with PBS. At 60 min after induction, the respective thrombus-targeted agent (CLIO-FXIII-PEG-tPA) or control agent (CLIO-CXIII-PEG-tPA) is administered via retro-orbital injection, although intravenous injection via the tail vein may also be used

successfully.. All agents are injected at 7.5 mg Fe/kg mouse (100 μl total volume). At 90 min after thrombus induction, 100 μl of fluorescein-labeled dextran (FITC-dextran, 5 mg/ml, λ_{ex} 490, λ_{em} 525 nm) is coinjected to provide a fluorescence angiogram of the vessels. At 120 min after thrombus induction (60 min after injection of the agent), multichannel IVFM is performed.

IVFM studies employ a multichannel laser scanning fluorescence microscope optimized for intravital imaging (Veilleux *et al.*, 2008). For fluorophore excitation, two different light sources are used. An excitation beam at 491 nm, suitable for fluorescein, is generated by a single diode-pumped solid state laser, (Dual Calypso, Cobolt AB, Solna, Sweden). For VT680, the 635-nm excitation light is generated by a diode laser (Radius, Coherent Inc., Santa Clara, CA). These laser beams are deflected into a custom-designed video-rate (30 frames/s) x–y scanner (polygon, galvanometer) and then focused onto the femoral vein with a 17 times, N.A. = 0.9, water-immersion microscope objective lens, EAF-30-1 (LOMO, Northbrook, IL). Each fluorescence signal is epicollected by a corresponding photomultiplier tube, R3896 (Hamamatsu Photonics, Bridgewater, NJ). The FITC-dextran fluorescence is collected through a 509–547 nm bandpass filter, and VT680 fluorescence is collected through a 667–722 nm bandpass filter. The two-dimensional images in the x–y plane (500 × 500 pixels) are acquired by a frame grabber (Snapper-8/24 PCI, Active Silicon, North Chelmsford, MA) installed on a Macintosh computer (Power Mac G4). The imaging speed was 30 frames/s and each static image is an average of 30 frames. Z-stacks (2.0 μm steps with 700 μm × 700 μm field of view) are collected throughout the entire thrombus region.

The acquired image stacks are initially converted into a two-dimensional summation image using ImageJ, and the thrombus is identified as a filling defect, or an area devoid of signal, in the fluorescein channel angiogram images. This region is then manually traced in ImageJ, and the area and integrated density in the VT680 channel are used to calculate the signal per area. A normal, nonthrombosed ROI segment is also chosen as background. TBRs are then calculated as a ratio of the signal in the thrombosed region to the nonthrombosed region.

Figure 10.3A and B shows single composite image slices, consisting of the VT680 and FITC channels taken from the z-stack acquired during the IVFM experiment. The dark void in the image is the location of the thrombus, while the green is the fluorescence signal of the FITC-dextran used to delineate the lumen of the vessels. In mice injected with CLIO-FXIII-PEG-tPA (Fig. 10.3A), the binding of the probe to the thrombus is readily observable as a red fluorescence signal along the periphery of the clot, a signal that is not seen in the animals treated with the control agent (CLIO-CXIII-PEG-tPA). When the entire cohort of mice is analyzed as

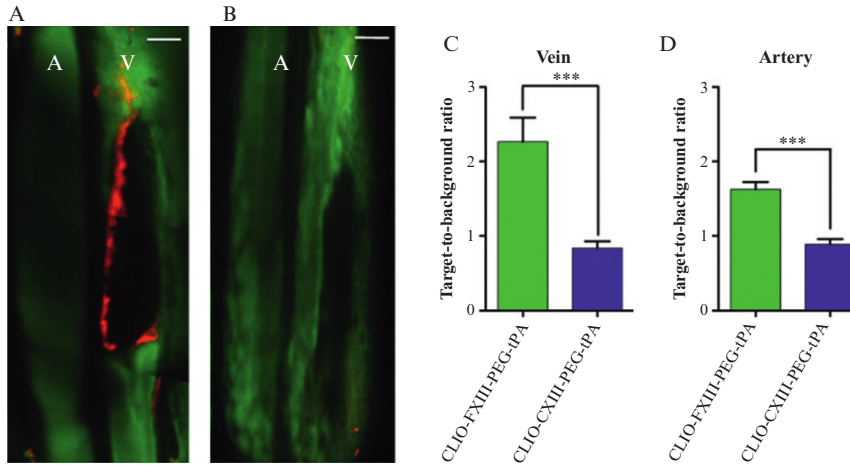

Figure 10.3 *In vivo* examination of nanoagent binding to arterial and venous thrombi. Representative IVFM images of the localization to intravascular thrombi of CLIO-FXIII-PEG-tPA (A) and CLIO-CXIII-PEG-tPA (B), demonstrating significant binding of the FXIIIa-targeted agent to the periphery of the thrombus. Target-to-background ratios were calculated for the veins (C) and arteries (D) in all *in vivo* experiments. Scale bars, 100 μm. ($^{***}P < 0.0001$) A, artery; V, vein. Reproduced with permission from McCarthy *et al.* (2011).

described above, the targeted nanoagent demonstrates significantly higher TBRs than the control agent (Fig. 10.3C and D).

8. Concluding Remarks

The morbidity and mortality associated with thrombosis and its sequelae, including myocardial infarction, stroke, pulmonary embolism, and deep vein thrombosis, make thrombotic vascular disease a topic of great interest. While the angiographic or passive detection of thrombi is routine, clinical molecular imaging agents may eventually yield information about the constitution of the clot, as well as its age, thereby informing decisions as to the optimal therapeutic strategy. These same imaging agents may also enable the generation of more efficacious therapeutics. As the administration of exogenous PAs, such as tPA, results in unacceptable levels of deleterious side effects, including intracerebral hemorrhage (Armstrong and Collen, 2001; NINDS Study Group, 1995), the modification of their pharmacokinetics and biodistribution via appending to targeted nanoagents might mitigate these issues, enhancing the therapeutic windows of these thrombolytics.

REFERENCES

Anderson, H. V., and Willerson, J. T. (1993). Thrombolysis in acute myocardial infarction. *N. Engl. J. Med.* **329,** 703–709.

Armstrong, P. W., and Collen, D. (2001). Fibrinolysis for acute myocardial infarction: Current status and new horizons for pharmacological reperfusion, part 1. *Circulation* **103,** 2862–2866.

Bi, F., Zhang, J., Su, Y., Tang, Y. C., and Liu, J. N. (2009). Chemical conjugation of urokinase to magnetic nanoparticles for targeted thrombolysis. *Biomaterials* **30,** 5125–5130.

Enochs, W. S., Harsh, G., Hochberg, F., and Weissleder, R. (1999). Improved delineation of human brain tumors on MR images using a long-circulating, superparamagnetic iron oxide agent. *J. Magn. Reson. Imaging* **9,** 228–232.

Falati, S., Gross, P., Merrill-Skoloff, G., Furie, B. C., and Furie, B. (2002). Real-time in vivo imaging of platelets, tissue factor and fibrin during arterial thrombus formation in the mouse. *Nat. Med.* **8,** 1175–1181.

Flaumenhaft, R., Tanaka, E., Graham, G. J., De Grand, A. M., Laurence, R. G., Hoshino, K., Hajjar, R. J., and Frangioni, J. V. (2007). Localization and quantification of platelet-rich thrombi in large blood vessels with near-infrared fluorescence imaging. *Circulation* **115,** 84–93.

Harisinghani, M. G., Jhaveri, K. S., Weissleder, R., Schima, W., Saini, S., Hahn, P. F., and Mueller, P. R. (2001). MRI contrast agents for evaluating focal hepatic lesions. *Clin. Radiol.* **56,** 714–725.

Jaffer, F. A., Tung, C. H., Wykrzykowska, J. J., Ho, N. H., Houng, A. K., Reed, G. L., and Weissleder, R. (2004). Molecular imaging of factor XIIIa activity in thrombosis using a novel, near-infrared fluorescent contrast agent that covalently links to thrombi. *Circulation* **110,** 170–176.

Josephson, L., Tung, C. H., Moore, A., and Weissleder, R. (1999). High-efficiency intracellular magnetic labeling with novel superparamagnetic-Tat peptide conjugates. *Bioconjug. Chem.* **10,** 186–191.

Kooi, M. E., Cappendijk, V. C., Cleutjens, K. B., Kessels, A. G., Kitslaar, P. J., Borgers, M., Frederik, P. M., Daemen, M. J., and van Engelshoven, J. M. (2003). Accumulation of ultrasmall superparamagnetic particles of iron oxide in human atherosclerotic plaques can be detected by in vivo magnetic resonance imaging. *Circulation* **107,** 2453–2458.

Lanza, G. M., Wallace, K. D., Scott, M. J., Cacheris, W. P., Abendschein, D. R., Christy, D. H., Sharkey, A. M., Miller, J. G., Gaffney, P. J., and Wickline, S. A. (1996). A novel site-targeted ultrasonic contrast agent with broad biomedical application. *Circulation* **94,** 3334–3340.

Marsh, J. N., Senpan, A., Hu, G., Scott, M. J., Gaffney, P. J., Wickline, S. A., and Lanza, G. M. (2007). Fibrin-targeted perfluorocarbon nanoparticles for targeted thrombolysis. *Nanomedicine (Lond.)* **2,** 533–543.

Marsh, J. N., Hu, G., Scott, M. J., Zhang, H., Goette, M. J., Gaffney, P. J., Caruthers, S. D., Wickline, S. A., Abendschein, D., and Lanza, G. M. (2011). A fibrin-specific thrombolytic nanomedicine approach to acute ischemic stroke. *Nanomedicine (Lond.)* **6,** 605–615.

McCarthy, J. R., Patel, P., Botnaru, I., Haghayeghi, P., Weissleder, R., and Jaffer, F. A. (2009). Multimodal nanoagents for the detection of intravascular thrombi. *Bioconjug. Chem.* **20,** 1251–1255.

McCarthy, J. R., Sazonova, I. Y., Erdem, S. E., Hara, T., Thompson, B. D., Patel, P., Botnaru, I., Reed, G. L., Weissleder, R., and Jaffer, F. A. (2011). Multifunctional nanoagent for thrombus-targeted fibrinolytic therapy. *Nanomedicine (Lond.)* DOI 10.2217/NNM.11.179.

Murray, C. J., and Lopez, A. D. (1997). Alternative projections of mortality and disability by cause 1990-2020: Global Burden of Disease Study. *Lancet* **349,** 1498–1504.

NINDS Study Group, (1995). Tissue plasminogen activator for acute ischemic stroke. The National Institute of Neurological Disorders and Stroke rt-PA Stroke Study Group. *N. Engl. J. Med.* **333,** 1581–1587.

Saini, S., Sharma, R., Baron, R. L., Turner, D. A., Ros, P. R., Hahn, P. F., Small, W. C., Delange, E. E., Stillman, A. E., Edelman, R. R., Runge, V. M., and Outwater, E. K. (2000). Multicentre dose-ranging study on the efficacy of USPIO ferumoxtran-10 for liver MR imaging. *Clin. Radiol.* **55,** 690–695.

Sim, D. S., Merrill-Skoloff, G., Furie, B. C., Furie, B., and Flaumenhaft, R. (2004). Initial accumulation of platelets during arterial thrombus formation in vivo is inhibited by elevation of basal cAMP levels. *Blood* **103,** 2127–2134.

Tang, Y., Kim, M., Carrasco, D., Kung, A. L., Chin, L., and Weissleder, R. (2005). In vivo assessment of RAS-dependent maintenance of tumor angiogenesis by real-time magnetic resonance imaging. *Cancer Res.* **65,** 8324–8330.

Thakur, M. L., Pallela, V. R., Consigny, P. M., Rao, P. S., Vessileva-Belnikolovska, D., and Shi, R. (2000). Imaging vascular thrombosis with 99mTc-labeled fibrin alpha-chain peptide. *J. Nucl. Med.* **41,** 161–168.

Tung, C. H., Ho, N. H., Zeng, Q., Tang, Y., Jaffer, F. A., Reed, G. L., and Weissleder, R. (2003). Novel factor XIII probes for blood coagulation imaging. *Chembiochem* **4,** 897–899.

Veilleux, I., Spencer, J. A., Biss, D. P., Cote, D., and Lin, C. P. (2008). Cell tracking with video rate multimodality laser scanning microscopy. *IEEE J. Select. Topic. Quant. Electron.* **14,** 10–18.

CHAPTER ELEVEN

Imaging the Efficacy of Anti-Inflammatory Liposomes in a Rabbit Model of Atherosclerosis by Non-Invasive Imaging

Mark E. Lobatto,[*,†] Claudia Calcagno,[*] Josbert M. Metselaar,[‡] Gert Storm,[‡] Erik S. G. Stroes,[†] Zahi A. Fayad,[*] *and* Willem J. M. Mulder[*,†]

Contents

Abstract

Nanomedicine can provide a potent alternative to current therapeutic strategies for atherosclerosis. For example, the encapsulation of anti-inflammatory drugs into liposomes improves their pharmacokinetics and biodistribution, thereby

* Translational and Molecular Imaging Institute, Mount Sinai School of Medicine, New York, USA
† Department of Vascular Medicine, Academic Medical Center, Amsterdam, The Netherlands
‡ Utrecht Institute for Pharmaceutical Sciences, Utrecht University, Utrecht, The Netherlands

Methods in Enzymology, Volume 508
ISSN 0076-6879, DOI: 10.1016/B978-0-12-391860-4.00011-2

enhancing bioavailability to atherosclerotic plaques and improving therapeutic efficacy. The evaluation of this type of experimental therapeutics can greatly benefit from *in vivo* evaluation to assess biological changes, which can be performed by non-invasive imaging techniques, such as ^{18}F-fluorodeoxyglucose positron emission tomography/computed tomography (FDG-PET/CT) and dynamic contrast enhanced magnetic resonance imaging (DCE-MRI). Here, we will illustrate the methods for inducing atherosclerosis in a rabbit model, the production of anti-inflammatory liposomes and monitoring of therapeutic efficacy of experimental therapeutics with the above-mentioned imaging techniques.

1. Introduction

The primary cause of cardiovascular disease, atherosclerosis, is a chronic systemic disease characterized by subendothelial lipid deposits with an inflammatory reaction (Libby, 2002). To date, most interventions for the treatment of atherosclerosis have focused on altering systemic lipid levels. A promising alternative approach to reduce the risk of vascular events caused by atherosclerosis is to directly target local inflammation at the level of the vessel wall (Libby *et al.*, 2011). A potential drawback of an anti-inflammatory strategy is the thin line between inhibiting local inflammation in the vessel wall versus inducing systemic immunosuppression. One way to limit the systemic effects of an anti-inflammatory regimen is to attain local delivery of drugs by encapsulating anti-inflammatory drugs in nanoparticles, for example, in liposomes. This method has been investigated in a variety of diseases implicated with inflammation, including cancer, multiple sclerosis, and rheumatoid arthritis (Metselaar and Storm, 2005). Drugs encapsulated in long-circulating liposomes accumulate at inflammatory regions to a higher extent than the free drug due to enhanced vascular permeability (Maurer *et al.*, 2001). At these sites, long-circulating nanoparticles will extravasate from the circulation and stay retained locally. This targeting phenomenon is commonly referred to as the enhanced permeability and retention (EPR) effect (Fang *et al.*, 2011).

Previously, it has been established that polyethylene glycol (PEG)-coated liposomes, encapsulating the anti-inflammatory drug prednisolone phosphate, effectively target atherosclerotic lesions in a rabbit model of atherosclerosis, and aggressively attenuate atherosclerotic plaque inflammation (Lobatto *et al.*, 2010). To a large degree this is attributed to nonspecific targeting of plaques, which results in an improved bioavailability of the liposomal formulation over free circulating corticosteroids.

Since atherosclerosis is a systemic disease of the vasculature, the evaluation of therapeutic interventions was traditionally based on the incidence of cardiovascular events or on secondary endpoints, such as measuring

systemic lipid levels or circulating biomarkers. The past two decades have witnessed tremendous progress in the direct visualization of atherosclerotic plaque morphology and activity by non-invasive imaging (Sanz and Fayad, 2008). These imaging techniques include various forms of magnetic resonance imaging (MRI) as well as positron emission tomography (PET). One of the most exciting developments in non-invasive imaging of atherosclerosis is the possibility to evaluate therapeutic efficacy at earlier stages of drug development, without the need, for example, to monitor major cardiac events in longitudinal studies (Lindsay and Choudhury, 2008). This strategy can vastly speed up the process of drug development or rejection and facilitates the translation of therapeutics into clinical medicine. A variety of imaging techniques for the evaluation of therapeutic efficacy are now in clinical use, such as intravascular ultrasound of coronary arteries, or the measurement of carotid intima-media thickness by ultrasound (de Groot *et al.*, 2008; Nissen *et al.*, 2003). Other modalities, which provide information on biological plaque processes instead of plaque morphology, such as ^{18}F-fluorodeoxyglucose positron emission tomography/computed tomography (FDG-PET/CT), have also been included in clinical trials recently (Fayad *et al.*, 2011).

FDG-PET/CT is used to visualize, quantify, and characterize atherosclerotic plaque inflammation non-invasively by detecting early metabolic changes in response to treatment, before changes in plaque size and morphology are appreciable (Rudd *et al.*, 2010). Additional information on plaque volume, composition, endothelial permeability and plaque neovascularization can be provided by high-resolution MRI and dynamic contrast enhanced magnetic resonance imaging (DCE-MRI) (Calcagno *et al.*, 2010a; Sanz and Fayad, 2008).

In larger animal models of atherosclerosis, such as the rabbit, the aforementioned clinical imaging methods can be applied to evaluate therapeutic efficacy. In this chapter, we will describe the preparation and development of an experimental rabbit model of atherosclerosis, as well as methods for producing clinically translatable liposomal anti-inflammatory formulations, and we will conclude with providing a guideline on the setup and evaluation of therapeutic efficacy of such liposomal nanoparticles with the non-invasive imaging modalities, FDG-PET/CT and DCE-MRI.

2. Experimental Animal Model of Atherosclerosis

A variety of animal models of atherosclerosis are available, ranging from genetically engineered mouse models to Watanabe hyperlipedimic rabbits and Yukutan swine models. For the purpose of the studies described

here, we recommend New Zealand white rabbits. These rabbits have several advantages over the other animal models, as they are large enough to be imaged on clinical scanners with sufficient spatial resolution, are easy to handle, and the aorta is less prone to be affected by motion artifacts, all preferable for the imaging procedures described later on.

2.1. Procedure: Balloon angioplasty of the aorta in a rabbit model

Although there is some degree of variability in the procedures used to induce atherosclerosis in this animal model, most methods include a combination of a high cholesterol diet for varying periods of time and a balloon injury of the aorta. The balloon injury will denude the aorta of endothelial cells and will enhance the uptake of cholesterol and macrophages in the vessel wall, thereby creating atherosclerotic lesions (Weidinger *et al.*, 1991).

Rabbits can be purchased from several vendors and are usually 4 months old at the initiation of the atherogenic diet (Fitzgerald *et al.*, 2011). We use a combination of a high cholesterol diet (4.7% palm oil and 0.3% cholesterol-enriched diet, and 4.85% palm oil and 0.15% cholesterol-enriched diet; Research Diet Inc., New Jersey, USA) and a repeated balloon injury of the aorta by a femoral angioplasty under fluoroscopic guidance 2 and 6 weeks after diet initiation. Procedures are performed under sterile conditions and under general anesthesia while monitoring vital functions. Anesthesia is induced by an intramuscular injection of Ketamine (20 mg/kg; Vedco, Missouri, USA) and Xylazine (10 mg/kg; Vedco, Missouri, USA). After general anesthesia, the inguinal area of the extremity that will undergo angioplasty is shaved and prepped with povidone-iodine solution. The rabbit is then placed in the supine position with the hindlimb stretched out, and the foot is taped down to the operating table to ensure a stable position of the extremity, and subsequently covered in sterile drapes in appropriate fashion. An approximately 5–7 cm longitudinal skin incision is made in the medial thigh, starting at the center of the inguinal ligament with care to avoid damaging the underlying structures. After dissection, the femoral neurovascular bundle can be identified in the proximal inguinal region. When dissecting the femoral artery from the surrounding tissue, special care should be taken to avoid damage to the femoral nerve. Care must also be taken to circumferentially dissect the vessel; once a stretch of 2–3 cm has been freed from the surrounding tissue, the blood flow is constricted by applying a suture to the distal end of the exposed femoral artery, using a silk 2-0 suture (Ethicon) to ease catheter insertion later on. In addition, 1.0% Lidocaine can be added for the purpose of attaining vasodilatation. To avoid blood loss and to maintain overview, a vascular loop can be placed around the proximal part of the artery. An incision is made in the artery length-wise with a #11 scalpel blade, and a catheter introducer (BD, New Jersey, USA) is inserted to ease the

introduction of a 4-F Fogarty embolectomy catheter (Edwards Lifesciences, California, USA) (Fig. 11.1A). Once the catheter is inserted, the vascular loop is removed to advance the catheter up to the thoracic descending aorta. The catheter and attached manometer can be filled with Iopamidol (Bracco Diagnostics, New Jersey, USA) to adequately track the balloon under fluoroscopic guidance.

The balloon is inflated gently to a pressure of 2.0 atm with a manometer. To denude the aorta of endothelial cells the catheter is pulled back over the entire length of the aorta down to the iliac bifurcation (Fig. 11.1B).

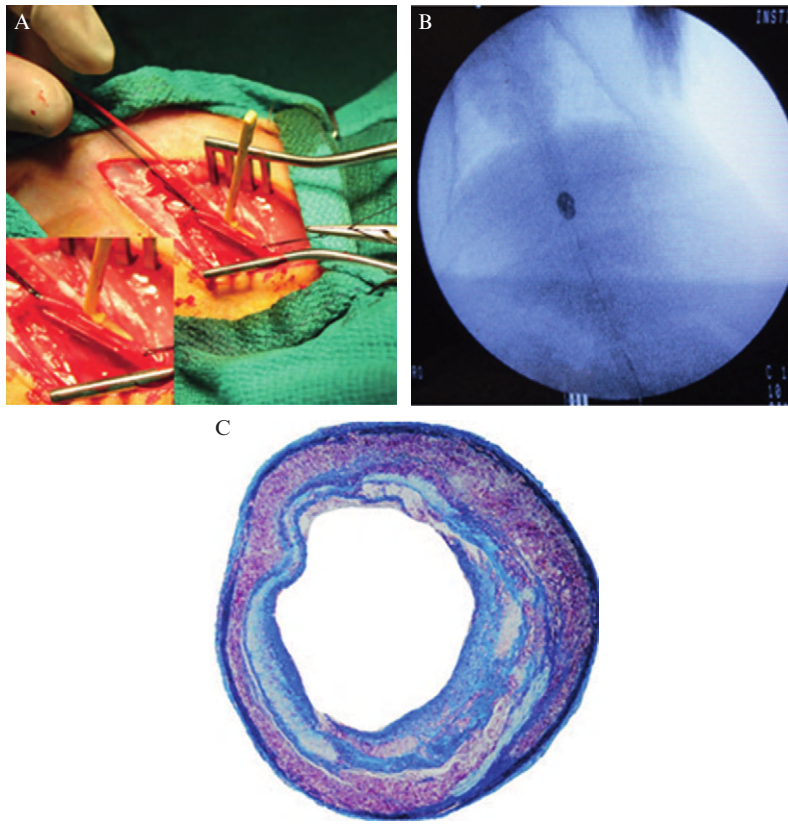

Figure 11.1 The induction of atherosclerosis in a New Zealand White rabbit. (A) After 2 and 6 weeks of a high cholesterol-enriched diet, a femoral angioplasty is performed by exposing the femoral artery under surgical conditions and introducing a 4-F embolectomy catheter. (B) The balloon is subsequently inflated, while pulling back the inflated balloon over the length of the aorta to denude the aorta of endothelial cells. (C) After 6 months rabbits will have advanced atherosclerotic lesions, evidenced by histology with a Masson's trichrome stain.

While retracting the catheter, the balloon should be deflated slowly when encountering resistance to avoid creating aortic aneurysms. The pullback procedure is repeated two additional times. The catheter is removed subsequently, and the femoral artery is ligated. The procedure is completed when hemostasis is ensured, the subcutaneous tissue is approximated with two interrupted Vicryl 3-0 sutures, and the skin is closed with a Prolene continuous monofilament suture 2.0 (Ethicon). The same procedure is repeated 4 weeks later from the contralateral extremity. After 6 months of initiating the diet, the rabbits will have grown advanced atherosclerotic lesions, as shown in Fig. 11.1C.

3. Liposome Preparation

3.1. Liposome preparation in the laboratory

Long-circulating PEG liposomes can be prepared of a mixture of dipalmitoyl phosphatidyl choline (DPPC), cholesterol, and PEG 2000 distearoyl phosphatidylethanolamine (PEG-DSPE) in a molar ratio of 62%, 33%, and 5%, respectively. Anti-inflammatory properties are acquired by encapsulating a corticosteroid in the aqueous interior of the liposome. To ensure an optimal inclusion efficiency, the water-soluble disodium phosphate ester derivative of the corticosteroid is used. Upon release at the target site, mainly induced by local phagocytes and extracellular enzymes, the inactive phosphate derivative is converted into the active drug. To obtain the desired long-circulating behavior, the liposomes need to comply with a particle diameter specification roughly between 75 and 150 nm. However, to avoid problems with sterile filtration on the one hand and with low steroid content on the other hand, the liposomes are kept below 120 nm and above 80 nm, respectively. The incorporation efficiency of the drug in liposomes is typically between 1.5% and 3% at a molar lipid starting concentration of 100 m*M* and is dependent on particle size. This translates to a final content between 1.5 and 3.0 mg/ml of corticosteroid within the formulation.

The most straightforward manufacturing method of lab scale liposomal corticosteroid batches involves extrusion. Briefly, a lipid solution is prepared in ethanol, containing DPPC, cholesterol, and PEG-DSPE in a round bottom flask, which is then evaporated under rotation to create a lipid film. This lipid film is hydrated with an aqueous solution of corticosteroid phosphate. The resulting coarse lipid dispersion is subsequently downsized by repeated extrusion at elevated temperatures (above 60 °C) through a series of polycarbonate filter membranes. Unencapsulated prednisolone is removed by dialysis against 0.9% phosphate buffered saline, using dialysis cassettes with a molecular weight cut-off value of 30,000 kD. Extrusion is a suitable method for lab batches of corticosteroid liposomes up to 100 ml.

3.2. Good manufacturing practice (GMP) production of anti-inflammatory liposomes

Manufacturing of larger quantities by extrusion is more complex because it requires large and expensive equipment in which temperature is difficult to control. Stepping up from small to large-scale extrusion equipment does not necessarily lead to a product with comparable specifications. Furthermore, the formulation shows the tendency to clog the extrusion membrane and changing the extrusion membranes in large-scale equipment during the manufacturing process is not straightforward. Therefore, to manufacture larger batches of liposomal corticosteroid product under GMP conditions, we opted for an alternative method named high-shear homogenization. In this method, the coarse lipid dispersion is led through an interaction chamber under high pressure, which creates high flow speeds and shear forces that effectively downsize the liposomes. Homogenization allows a more continuous process that leads to identical results, whether small or large volumes of formulations are processed, as long as the manufacturing circumstances (temperature and pressure) are kept the same.

To manufacture 1 l of corticosteroid liposomes under GMP conditions, 62.5 g corticosteroid phosphate derivative is dissolved in 450 ml of sterile water for injection. The lipid components (45.0 g DPPC, 13.4 g PEG-DSPE, and 12.6 g cholesterol) are dissolved in 50 ml ethanol by heating to 70 °C under continuous stirring. The alcoholic lipid solution is then injected into the aqueous prednisolone sodium phosphate solution under vigorous stirring, creating a coarse lipid dispersion.

Downsizing the liposomes to the desired particle diameter occurs by high-shear homogenization. The homogenizer is first sterilized by continuous circulation of 500 ml 1 *M* sodium hydroxide and subsequently rinsed with phosphate buffered water for injections until the pH reaches 7.4. The coarse lipid dispersion is homogenized by three consecutive runs, while keeping the temperature of the dispersion between runs at 70 °C, by placing the lipid dispersion on a hot magnetic stirrer. After the third run the fine liposome dispersion is gradually cooled down to room temperature.

To clear the formulation from unencapsulated corticosteroid and ethanol, the fine liposome dispersion is transferred to a sterile crossflow filtration unit, and filtered using polysulfonate membrane capsules with a cut-off of 100 kD. A sterile phosphate buffered (pH 7.6) sucrose solution (10%) is prepared and added to the retentate in the filtration unit to compensate for the loss of permeate from the unit (which is unencapsulated aqueous corticosteroid solution). When a total of 15 l sucrose solution has been added, the dispersion can be considered devoid of unencapsulated prednisolone sodium phosphate and ethanol.

Finally, the liposome dispersion is sterile-filtered by dead-end filtration using a 0.45–0.2 μm Sartobran-P filter unit connected to a membrane

pump. The filtered dispersion is collected into 10 ml injection vials using 1.6 mm × 1.6 mm platinum-catalyzed silicone tubing. The injection vials are subsequently stoppered, sealed with aluminum caps and labeled. The final liposomal product is stored between 2 and 8 °C. The most important quality control tests and specifications with regard to the final liposomal corticosteroid product are listed in Table 11.1.

Shelf life stability studies with the liposomal corticosteroid product have indicated that it remains stable for at least 2 years when stored between 2 and 8 °C. During this time no significant changes in particle size was observed, nor do measurable amounts of the incorporated corticosteroid leak from the liposomal interior. The chemical stability of both the active ingredient and the lipid excipients remains excellent under these storage conditions. Storage at ambient or higher temperatures indicates that cholesterol will eventually pose the most critical stability problem, as it slowly degrades at these temperatures.

Table 11.1 Quality control tests and specifications of anti-inflammatory liposomes

Item/test method	Specification
1. Appearance	A clear to mildly turbid fluid
2. Dynamic light scattering	
Particle diameter	80–120 nm
Polydispersity index	≤ 0.25
3. HPLC assay encapsulated drug identification	Retention time of the corticosteroid reference standard equals the retention time of the liposomal corticosteroid
Content	1.5–3.0 mg/ml
Content uniformity	All vials within 85.0–115.0%, relative standard deviation less or equal to 6.0%
4. HPLC assay free drug in permeate	≤ 0.05 mg/ml
5. HPLC assay lipid excipients identification	Retention time of the lipid reference standard equals the retention time of the lipid in the product
Content	80–120% of the starting lipid concentration in the formulation
6. pH of the dispersion	Within the range of 6.50–8.50
7. Bacterial endotoxins	<20 EU/vial
8. Sterility	Sterile (as determined by a Steritest Compact test (Millipore, Massachusetts, USA))
9. Residual ethanol	<100 ppm

4. Imaging as a Readout for Therapeutic Efficacy of Drugs in Atherosclerosis

^{18}F-FDG in combination with PET/CT is used as a molecular imaging technique to assess metabolically active processes and is the gold standard for detection of metastases in cancer. Recently, several studies have demonstrated that ^{18}F-FDG uptake correlates with atherosclerotic plaque inflammation. Human carotid arteries that are implicated in stroke have shown an increased uptake of ^{18}F-FDG (Rudd *et al.*, 2002). In addition, increased uptake has also been observed in patients with acute coronary syndromes (Rogers *et al.*, 2010). FDG-PET/CT is therefore increasingly used as a marker to assess metabolically active atherosclerotic plaques, as well as to assess the therapeutic efficacy of anti-atherosclerosis drugs (Rudd *et al.*, 2010). This technique can be executed with high reproducibility, which is of major importance for drug efficacy studies (Rudd *et al.*, 2007). For the purpose of this chapter we will describe a technique to measure drug efficacy of experimental therapeutics in a rabbit model.

4.1. FDG-PET/CT image acquisition

FDG-PET/CT imaging of rabbits can be performed using clinically available PET/CT scanners. Rabbits have to be fasted for 4 h prior to radiotracer injection to avoid interference with ^{18}F-FDG uptake, while water can be provided *ad libitum*. With a catheter placed in the marginal ear vein, rabbits are injected with 1 mCi/Kg ^{18}F-FDG, followed by a 5 ml saline flush. It is useful to note the exact amount of ^{18}F-FDG that has been injected, as well as the weight of the animal, as this is essential for subsequent image analysis. For the interpretation of the data it is also recommended to have ^{18}F-FDG circulate for 180 min prior to imaging, as it has been reported that this will maximize the contrast between the plaque and background activity, and will therefore give a more accurate representation of actual ^{18}F-FDG plaque uptake (Rudd *et al.*, 2002). For the evaluation of therapeutic efficacy it is required to obtain a scan prior to injection of the drug to be evaluated. Time points after therapeutic drug administration can be chosen according to drug half-life and expected duration of drug activity. Rabbits are imaged supine under general anesthesia, dosed as earlier, while secured with a blanket. It is vital to empty the bladder with a catheter before imaging as the renal clearance of FDG and ensuing accumulation in the bladder will heavily impair the analysis of FDG uptake in the distal aorta.

Rabbits are scanned in a single-bed position in three-dimensional mode for 10 min, covering the region of the thoracic descending aorta down to the iliac bifurcation ($\sim$15.5 cm). Reconstruction is then performed which typically can give a reconstructed slice thickness of 4.25 mm.

4.2. FDG-PET/CT image analysis

For image analysis, the PET/CT images are then calibrated to the injected dose of ^{18}F-FDG and animal weight. The images can be analyzed on the locally available workstation by measuring arterial ^{18}F-FDG uptake in the aorta, after drawing a region of interest (ROI) around the aorta on slices of coregistered transaxial PET/CT images. A suggestion is to start at the superior mesenteric artery and end at the iliac bifurcation to ensure that the same anatomic region is covered in each individual rabbit. On each image slice, the mean standard uptake value (SUV) of ^{18}F-FDG in the artery is calculated as the mean pixel activity within the ROI. The SUV is the decay-corrected tissue concentration of ^{18}F-FDG (in kBq/g), corrected for the injected ^{18}F-FDG dose and body weight (in kBq/g); this is a well-recognized method for the analysis of PET data. To ensure proper data for SUV comparison with serially scanned animals it is advised to use the exact same injection and imaging acquisition times. After analysis of the aorta, the SUV average can be compared to preinjection data. Although the value of FDG-PET data is becoming increasingly validated, it is suggested to confirm and correlate values with immunohistochemistry. Macrophage density count has been used as the histological standard to validate SUV, which can be obtained through immunohistochemical staining with RAM-11 (Dako, California, USA) (Zhang *et al.*, 2006). Because nuclear imaging is involved with this technique, it is essential to involve the radiation safety officer within the local institute to account for relevant safety precautions.

4.3. DCE-MRI background

DCE-MRI is a non-invasive imaging technique used to study the extent and characteristics of the microvasculature in many physiological and pathological instances (Choyke *et al.*, 2003; Notohamiprodjo *et al.*, 2010; Padhani, 2002). It consists of the rapid serial acquisition of MRI images during the injection of a contrast agent (CA; most often a gadolinium chelate). The CA acts by shortening the proton relaxation times of target tissues, which results in a change in the MR signal during data acquisition. After appropriate conversion to concentration, CA uptake curves are analyzed using either compartmental modeling or non-model based approaches to infer the extent and properties of tissue microvasculature (Roberts *et al.*, 2006; Sourbron, 2010; Tofts *et al.*, 1999).

In recent years, DCE-MRI has been adopted to study the formation of new vessels, neovascularization, in atherosclerotic plaques in both rabbit models as well as human subjects with carotid disease (Calcagno *et al.*, 2008; Dong *et al.*, 2011; Kerwin *et al.*, 2003). The extent of neovascularization in atherosclerotic disease has been shown to correlate with inflammation, and

plaques that are prone to rupture (Moreno *et al.*, 2004). Current approaches for DCE-MRI of atherosclerosis can be classified into "bright blood" and "black-blood" techniques. Bright blood techniques are *T*1-weighted, spoiled gradient echo (SPGR)-based acquisitions, and allow the determination of the CA concentration in the blood plasma (the so-called arterial input function, AIF), which is required to extract kinetic parameters. Using bright blood acquisitions, a positive significant correlation between DCE-MRI measures and neovascularization in human carotid plaques has been demonstrated (Kerwin *et al.*, 2006). A positive significant correlation between DCE-MRI measures and several atherosclerosis risk factors has been confirmed as well (Kerwin *et al.*, 2006). Because of their intrinsically poor vessel lumen/wall delineation, bright blood techniques are usually not suited for imaging early atherosclerotic lesions and/or animal models, where the vessel wall thickness can be less than 2 mm. In these cases, black-blood techniques are advantageous.

Black-blood techniques typically consist of *T*1-weighted turbo spin echo (TSE) acquisitions, and allow better vessel lumen/wall delineation than bright blood techniques. Since they do not allow for direct acquisition of the AIF from the dynamic scan, either a population AIF, relative modeling or non-model based approaches are used for their analysis. Using non-model based approaches, a positive significant relationship between neovascularization in aortic plaque of atherosclerotic rabbits and the DCE-MRI parameter area under the curve (AUC) is observed (Calcagno *et al.*, 2008). Additionally, good reproducibility of the technique and its potential as a readout for anti-inflammatory therapy was shown recently (Calcagno *et al.*, 2010b).

4.4. DCE-MRI acquisition

The acquisition of DCE-MRI scans is performed under anesthesia (dosed as earlier). If necessary, another half a dose of anesthesia can be administered 45–60 min after induction during long scanning procedures, or anesthesia can be sustained by the use of Isofluorane. Slightly different protocols can be used for DCE-MRI acquisition. Here we will describe a comprehensive image acquisition and analysis protocol.

Doses of CA are 0.1 or 0.2 mmol/kg for the full-dose DCE scan (depending on the desired signal-to-noise ratio, SNR) and 0.01 mmol/kg for the test bolus. The CA can be administered by either manual injection or using a power injector. If the manual injection is chosen, one syringe is prepared with the full-dose of CA, one syringe with the test bolus dose diluted to the volume of the full dose, and two syringes with 10-ml saline. When performing manual injections one researcher needs to be inside the MRI room during the dynamic scan. For both test and full-dose administration, after acquisition of a few precontrast frames, the CA is first injected

through intravenous injection, followed by the saline flush. If the CA is delivered through a power injector, syringes are prepared with a test dose, a full dose and saline. If the power injector cannot deliver fractions of ml, both CA doses will be diluted to the same lowest possible volume. After placing the syringes on the power injector, the line is filled with saline and checked for the presence of air. After positioning the rabbit in the MRI (see below), the line is connected to the catheter. The injection can be delivered at a rate of 0.5 ml/s, after a chosen number (minimum of three) of precontrast images. The set of syringes will have to be exchanged between the test and full-dose injection.

The rabbits are scanned with a conventional volume knee coil on the clinically available MRI scanner, with sufficient padding to support the head and legs of the animal during imaging. The animal is positioned in the coil, head first-supine, making sure that the abdomen is approximately at the center of the coil. If a power injector is used, the line is connected to the catheter in the marginal ear vein.

After performing localizer scans, a time-of-flight acquisition should be performed from the left renal artery to the iliac bifurcation. This acquisition is useful for slice planning of subsequent scans and for serial studies to identify anatomical fiducial markers to be used for image coregistration. Subsequently, conventional black-blood TSE acquisitions for morphological plaque characterization are performed. Black-blood imaging can be achieved using spatial saturation or double inversion pulses. Depending on the scope of the study, $T1$ and/or $T2$ and/or proton density (PD) weighted imaging is performed. Typical imaging parameters for $T1$/$T2$/PD-weighted images are as follows: acquisition type, two dimensional (2D); slice thickness, 3 mm; inter-slice gap, 0.3 mm; number of slices, 25–30; echo time (TE), 5.6/39/5.6 ms; repetition time (TR), 800/2000/2000 ms; FOV, 12×12 cm^2; in-plane spatial resolution, 0.5×0.5 mm^2; echo train length, 7; and signal averages, 16. Spectral fat suppression is applied to null the signal from the peri-adventitial fat. Following anatomical images, a test bolus (Kershaw and Cheng, 2011) is acquired to sample the AIF, using a single slice, single-shot saturation prepared gradient echo acquisition. Typical imaging parameters are: acquisition type, 2D; slice thickness, 3-mm; TE, 2.1 ms; TR, 4.3 ms; flip angle (FA), 12°; FOV, 12×12 cm^2; in-plane spatial resolution, 1×1 mm^2; and signal averages, 1; time resolution $\sim$0.5 s; acquisition duration, $\sim$3 min.

For the purpose of signal intensity normalization, a SPGR PD-weighted image without saturation preparation is acquired before the test bolus, using the same imaging parameters detailed below, except for FA (4°) and TR (300 ms). Following test bolus acquisition, a group of slices is selected for DCE-MRI based on the precontrast TSE scans. Before DCE acquisition, $T1$ mapping is acquired with a method of choice (Haacke *et al.*, 1999) to facilitate signal conversion to concentration during

the analysis process. For the purpose of signal normalization, a TSE PD-weighted scan can be performed on the slices selected for DCE imaging, using the same imaging parameters detailed above (if not acquired before). *T*1-weighted black-blood DCE-MRI is performed on selected axial slices. Typical imaging parameters are as follows: acquisition type, 2D; slice thickness, 3 mm; inter-slice gap, 0.3 mm; number of slices, 4–6; TE, 5–10 ms; TR, 400–700 ms; FOV, 12 × 12 cm^2; in-plane spatial resolution, 0.5 × 0.5 mm^2; echo train length, 7–9; and signal averages, 1; time resolution: 20–40 s; acquisition duration 10–15 min. Following DCE, a *T*1-weighted postcontrast image of the same slices can be acquired with the same parameters used for DCE acquisition (except increased number of averages) for vessel wall delineation.

4.5. DCE-MRI analysis

After denoising and intra-series coregistration for image analysis (Kerwin *et al.*, 2002), ROIs are placed in the vessel lumen and wall (for test-bolus and full-dose scan, respectively) and propagated through the dynamic series. After appropriate scaling of MR signal values, AIF, and vessel wall ROI curves can be converted to concentration by choosing one of the following equations (Haacke *et al.*, 1999):

$$C(t) \propto \frac{(\mathrm{SI}(t) - \mathrm{SI}(0))}{\mathrm{SI}(0)}, \tag{11.1}$$

where $C(t)$ is the CA concentration at time t, $\mathrm{SI}(t)$ is the MR signal at time t, and $\mathrm{SI}(0)$ is the precontrast MR signal.

$$\mathrm{SI}(t) = M_0 \frac{\sin\alpha(1 - E1(t))}{1 - E1(t)\cos\alpha}, \quad \text{where } E1(t) = \mathrm{e}^{-TR/T1(t)}, \tag{11.2}$$

where M_0 is the bulk magnetization, α is the FA and $T1(t)$ is the longitudinal relaxation time at time t. After normalizing for either a PD-weighted image or the precontrast MR signal to account for M_0, this equation can be solved for $T1(t)$. The CA concentration can then be calculated as:

$$\frac{1}{T1(t)} = \frac{1}{T1(0)} + \mathrm{r1} \cdot C(t), \tag{11.3}$$

where $T1(0)$ is the precontrast $T1$ (which can be either calculated from a $T1$-mapping sequence or assumed), and r1 is the CA relaxivity (which can be found in the literature).

Once converted to concentration, the test bolus has to be linearly scaled to the full-dose injected and corrected for hematocrit, before being used for kinetic modeling. It is also worth mentioning that since the values derived from Eq. (11.1) are only deemed linearly proportional to the real concentration and the linearity constant may vary depending on the acquisition used, this method should not be used if test bolus data are used for analysis. After conversion to concentration, parameters can be extracted from the DCE data using the following approaches:

1. if test bolus data are available, either a regular or modified Tofts model can be used (Tofts *et al.*, 1999)
2. if only black-blood data are available, kinetic modeling can still be performed if a population AIF is available from the literature (Parker *et al.*, 2006) or previous experiments. In alternative, non-model based approaches (Roberts *et al.*, 2006) or relative modeling approaches (Yankeelov *et al.*, 2005) can be used

Parameters extracted from kinetic modeling can provide information about the extent of plaque neovascularization (v_p, fractional blood volume), blood flow/permeability (K^{trans}, and K_{ep}, the transfer constants from the tissue to the plasma compartments) and the distribution volume of the CA (v_e, the fractional extravascular extracellular space volume) (Tofts *et al.*, 1999). These parameters can give an indication about the extent and characteristics of plaque neovasculature and inflammation, and track their changes upon intervention with anti-inflammatory therapies.

Kinetic modeling is typically performed using in-house software, using either nonlinear or linear least squares methods when possible. Among non-model based parameters, despite its unclear relationship with physiological variables, the AUC of the normalized signal intensity versus time, has been correlated positively with plaque neovascularization, and was proven to be useful in tracking the response to anti-inflammatory therapy seen in Fig. 11.2 (Calcagno *et al.*, 2010a,b; Lobatto *et al.*, 2010).

5. Concluding Remarks

Although considerable progress has been made in the treatment of atherosclerosis, there is a continuous search and necessity for new methods to manage this disease. The use of nanoparticles encapsulating anti-inflammatory drugs targeting the atherosclerotic vessel wall can be a very efficient strategy in the right setting, for example, after a cardiovascular event, to accomplish systemic vascular silencing of inflammation to minimize future events. The methods for creating experimental atherosclerotic lesions and formulating anti-inflammatory liposomes are well-established

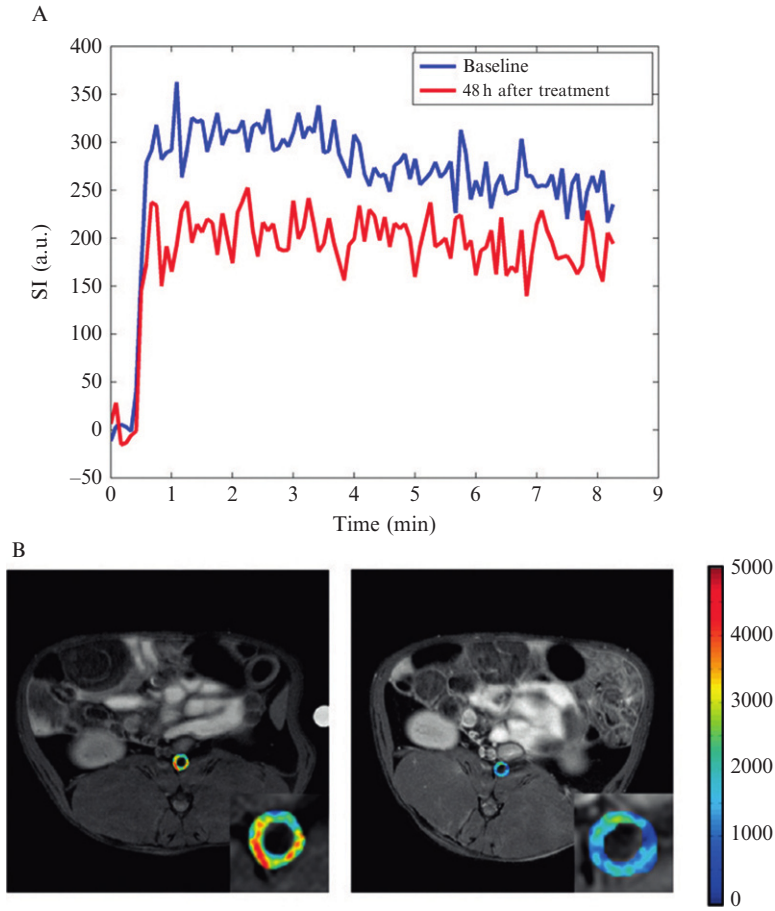

Figure 11.2 Evaluating therapeutic efficacy of experimental therapeutics by dynamic contrast enhanced MRI. (A) An example of a graph showing a decrease in area under the curve (AUC) in response to treatment of liposome-encapsulated prednisolone phosphate in a rabbit. (B) Overlays on anatomical MR images of AUC maps on the aorta display changes before (left) and 2days after treatment (right). (B) reprinted with permission from Lobatto *et al*. (2010) © 2010 American Chemical Society.

nowadays, although the particular combination for this application is novel. Importantly, the ability of non-invasive imaging modalities, such as FDG-PET/CT and DCE-MRI, to provide early insights into drug efficacy of experimental therapeutics can greatly speed up the process of drug development, and will facilitate translating nanotherapeutics into clinical medicine.

ACKNOWLEDGMENTS

M.E.L. is supported by the International Atherosclerosis Society and by the Foundation "De Drie Lichten" in The Netherlands. This work was supported by the National Heart, Lung, and Blood Institute, National Institutes of Health, as a Program of Excellence in Nanotechnology (PEN) Award, Contract #HHSN268201000045C, as well as by R01 EB009638 (Z.A.F.) and R01 CA155432 (W.J.M.M.).

REFERENCES

Calcagno, C., Cornily, J. C., Hyafil, F., Rudd, J. H., Briley-Saebo, K. C., Mani, V., Goldschlager, G., Machac, J., Fuster, V., and Fayad, Z. A. (2008). Detection of neovessels in atherosclerotic plaques of rabbits using dynamic contrast enhanced MRI and 18F-FDG PET. *Arterioscler. Thromb. Vasc. Biol.* **28,** 1311–1317.

Calcagno, C., Mani, V., Ramachandran, S., and Fayad, Z. A. (2010a). Dynamic contrast enhanced (DCE) magnetic resonance imaging (MRI) of atherosclerotic plaque angiogenesis. *Angiogenesis* **13,** 87–99.

Calcagno, C., Vucic, E., Mani, V., Goldschlager, G., and Fayad, Z. A. (2010b). Reproducibility of black blood dynamic contrast-enhanced magnetic resonance imaging in aortic plaques of atherosclerotic rabbits. *J. Magn. Reson. Imaging* **32,** 191–198.

Choyke, P. L., Dwyer, A. J., and Knopp, M. V. (2003). Functional tumor imaging with dynamic contrast-enhanced magnetic resonance imaging. *J. Magn. Reson. Imaging* **17,** 509–520.

de Groot, E., van Leuven, S. I., Duivenvoorden, R., Meuwese, M. C., Akdim, F., Bots, M. L., and Kastelein, J. J. (2008). Measurement of carotid intima-media thickness to assess progression and regression of atherosclerosis. *Nat. Clin. Pract. Cardiovasc. Med.* **5,** 280–288.

Dong, L., Kerwin, W. S., Chen, H., Chu, B., Underhill, H. R., Neradilek, M. B., Hatsukami, T. S., Yuan, C., and Zhao, X. Q. (2011). Carotid artery atherosclerosis: Effect of intensive lipid therapy on the vasa vasorum—Evaluation by using dynamic contrast-enhanced MR imaging. *Radiology* **260,** 224–231.

Fang, J., Nakamura, H., and Maeda, H. (2011). The EPR effect: Unique features of tumor blood vessels for drug delivery, factors involved, and limitations and augmentation of the effect. *Adv. Drug Deliv. Rev.* **63,** 136–151.

Fayad, Z. A., Mani, V., Woodward, M., Kallend, D., Abt, M., Burgess, T., Fuster, V., Ballantyne, C. M., Stein, E. A., Tardif, J. C., Rudd, J. H., Farkouh, M. E., *et al.* (2011). Safety and efficacy of dalcetrapib on atherosclerotic disease using novel non-invasive multimodality imaging (dal-PLAQUE): A randomised clinical trial. *Lancet* **378,** 1547–1559.

Fitzgerald, K. T., Holladay, C. A., McCarthy, C., Power, K. A., Pandit, A., and Gallagher, W. M. (2011). Standardization of models and methods used to assess nanoparticles in cardiovascular applications. *Small* **7,** 705–717.

Haacke, E. M., Brown, R. W., Thompson, M. R., and Venkatesan, R. (1999). Magnetic Resonance Imaging, Physical Principles and Sequence Design. Wiley, New York.

Kershaw, L. E., and Cheng, H. L. (2011). A general dual-bolus approach for quantitative DCE-MRI. *Magn. Reson. Imaging* **29,** 160–166.

Kerwin, W. S., Cai, J., and Yuan, C. (2002). Noise and motion correction in dynamic contrast-enhanced MRI for analysis of atherosclerotic lesions. *Magn. Reson. Med.* **47,** 1211–1217.

Kerwin, W., Hooker, A., Spilker, M., Vicini, P., Ferguson, M., Hatsukami, T., and Yuan, C. (2003). Quantitative magnetic resonance imaging analysis of neovasculature volume in carotid atherosclerotic plaque. *Circulation* **107,** 851–856.

Kerwin, W. S., O'Brien, K. D., Ferguson, M. S., Polissar, N., Hatsukami, T. S., and Yuan, C. (2006). Inflammation in carotid atherosclerotic plaque: A dynamic contrast-enhanced MR imaging study. *Radiology* **241,** 459–468.

Libby, P. (2002). Inflammation in atherosclerosis. *Nature* **420,** 868–874.

Libby, P., Ridker, P. M., and Hansson, G. K. (2011). Progress and challenges in translating the biology of atherosclerosis. *Nature* **473,** 317–325.

Lindsay, A. C., and Choudhury, R. P. (2008). Form to function: Current and future roles for atherosclerosis imaging in drug development. *Nat. Rev. Drug Discov.* **7,** 517–529.

Lobatto, M. E., Fayad, Z. A., Silvera, S., Vucic, E., Calcagno, C., Mani, V., Dickson, S. D., Nicolay, K., Banciu, M., Schiffelers, R. M., Metselaar, J. M., van Bloois, L., *et al.* (2010). Multimodal clinical imaging to longitudinally assess a nanomedical anti-inflammatory treatment in experimental atherosclerosis. *Mol. Pharm.* **7,** 2020–2029.

Maurer, N., Fenske, D. B., and Cullis, P. R. (2001). Developments in liposomal drug delivery systems. *Expert Opin. Biol. Ther.* **1,** 923–947.

Metselaar, J. M., and Storm, G. (2005). Liposomes in the treatment of inflammatory disorders. *Expert Opin. Drug Deliv.* **2,** 465–476.

Moreno, P. R., Purushothaman, K. R., Fuster, V., Echeverri, D., Truszczynska, H., Sharma, S. K., Badimon, J. J., and O'Connor, W. N. (2004). Plaque neovascularization is increased in ruptured atherosclerotic lesions of human aorta: Implications for plaque vulnerability. *Circulation* **110,** 2032–2038.

Nissen, S. E., Tsunoda, T., Tuzcu, E. M., Schoenhagen, P., Cooper, C. J., Yasin, M., Eaton, G. M., Lauer, M. A., Sheldon, W. S., Grines, C. L., Halpern, S., Crowe, T., *et al.* (2003). Effect of recombinant ApoA-I Milano on coronary atherosclerosis in patients with acute coronary syndromes: A randomized controlled trial. *JAMA* **290,** 2292–2300.

Notohamiprodjo, M., Reiser, M. F., and Sourbron, S. P. (2010). Diffusion and perfusion of the kidney. *Eur. J. Radiol.* **76,** 337–347.

Padhani, A. R. (2002). Dynamic contrast-enhanced MRI in clinical oncology: Current status and future directions. *J. Magn. Reson. Imaging* **16,** 407–422.

Parker, G. J., Roberts, C., Macdonald, A., Buonaccorsi, G. A., Cheung, S., Buckley, D. L., Jackson, A., Watson, Y., Davies, K., and Jayson, G. C. (2006). Experimentally-derived functional form for a population-averaged high-temporal-resolution arterial input function for dynamic contrast-enhanced MRI. *Magn. Reson. Med.* **56,** 993–1000.

Roberts, C., Issa, B., Stone, A., Jackson, A., Waterton, J. C., and Parker, G. J. (2006). Comparative study into the robustness of compartmental modeling and model-free analysis in DCE-MRI studies. *J. Magn. Reson. Imaging* **23,** 554–563.

Rogers, I. S., Nasir, K., Figueroa, A. L., Cury, R. C., Hoffmann, U., Vermylen, D. A., Brady, T. J., and Tawakol, A. (2010). Feasibility of FDG imaging of the coronary arteries: Comparison between acute coronary syndrome and stable angina. *JACC Cardiovasc. Imaging* **3,** 388–397.

Rudd, J. H., Warburton, E. A., Fryer, T. D., Jones, H. A., Clark, J. C., Antoun, N., Johnstrom, P., Davenport, A. P., Kirkpatrick, P. J., Arch, B. N., Pickard, J. D., and Weissberg, P. L. (2002). Imaging atherosclerotic plaque inflammation with [18F]-fluorodeoxyglucose positron emission tomography. *Circulation* **105,** 2708–2711.

Rudd, J. H., Myers, K. S., Bansilal, S., Machac, J., Rafique, A., Farkouh, M., Fuster, V., and Fayad, Z. A. (2007). (18)Fluorodeoxyglucose positron emission tomography imaging of atherosclerotic plaque inflammation is highly reproducible: Implications for atherosclerosis therapy trials. *J. Am. Coll. Cardiol.* **50,** 892–896.

Rudd, J. H., Narula, J., Strauss, H. W., Virmani, R., Machac, J., Klimas, M., Tahara, N., Fuster, V., Warburton, E. A., Fayad, Z. A., and Tawakol, A. A. (2010). Imaging atherosclerotic plaque inflammation by fluorodeoxyglucose with positron emission tomography: Ready for prime time? *J. Am. Coll. Cardiol.* **55,** 2527–2535.

Sanz, J., and Fayad, Z. A. (2008). Imaging of atherosclerotic cardiovascular disease. *Nature* **451,** 953–957.

Sourbron, S. (2010). Technical aspects of MR perfusion. *Eur. J. Radiol.* **76,** 304–313.

Tofts, P. S., Brix, G., Buckley, D. L., Evelhoch, J. L., Henderson, E., Knopp, M. V., Larsson, H. B., Lee, T. Y., Mayr, N. A., Parker, G. J., Port, R. E., Taylor, J., *et al.* (1999). Estimating kinetic parameters from dynamic contrast-enhanced T(1)-weighted MRI of a diffusable tracer: Standardized quantities and symbols. *J. Magn. Reson. Imaging* **10,** 223–232.

Weidinger, F. F., McLenachan, J. M., Cybulsky, M. I., Fallon, J. T., Hollenberg, N. K., Cooke, J. P., and Ganz, P. (1991). Hypercholesterolemia enhances macrophage recruitment and dysfunction of regenerated endothelium after balloon injury of the rabbit iliac artery. *Circulation* **84,** 755–767.

Yankeelov, T. E., Luci, J. J., Lepage, M., Li, R., Debusk, L., Lin, P. C., Price, R. R., and Gore, J. C. (2005). Quantitative pharmacokinetic analysis of DCE-MRI data without an arterial input function: A reference region model. *Magn. Reson. Imaging* **23,** 519–529.

Zhang, Z., Machac, J., Helft, G., Worthley, S. G., Tang, C., Zaman, A. G., Rodriguez, O. J., Buchsbaum, M. S., Fuster, V., and Badimon, J. J. (2006). Non-invasive imaging of atherosclerotic plaque macrophage in a rabbit model with F-18 FDG PET: A histopathological correlation. *BMC Nucl. Med.* **6,** 3.

CHAPTER TWELVE

Lipid Nanoparticles for Drug Targeting to the Brain

Maria Luisa Bondì,* Roberto Di Gesù,† *and* Emanuela Fabiola Craparo†

Contents

Abstract

In this chapter, the main production methods of lipid nanostructures such as solid lipid nanoparticles and nanostructured lipid carriers, and their application are described. In particular, we describe the strategies commonly used to obtain lipid nanoparticles to overcome the blood–brain barrier (BBB) for the treatment of several brain diseases.

The use of these carriers as targeted drug delivery systems is associated with many advantages that include excellent storage stability, easy production without the use of any organic solvent, the possibility of steam sterilization and lyophilization, and large scale production. They exhibit good stability during long-term storage, consist of physiologically well-tolerated ingredients often already approved for pharmaceutical applications in humans, and are generally recognized as safe. Under optimized conditions, they can be produced to incorporate several drugs and therapeutic proteins. Formulation in solid lipid

* Istituto per lo Studio dei Materiali Nanostrutturati (ISMN), Consiglio Nazionale delle Ricerche, Palermo, Italy
† Dipartimento di Scienze e Tecnologie Molecolari e Biomolecolari (STEMBIO), Università di Palermo, Palermo, Italy

Methods in Enzymology, Volume 508
ISSN 0076-6879, DOI: 10.1016/B978-0-12-391860-4.00012-4

nanostructures confers improved drug loading and protein stability, targeting, and sustained release of the incorporated molecules. Moreover, their lipophilic features lead them to the central nervous system by an endocytotic mechanism, overcoming the BBB.

Many drugs have been incorporated into solid lipid nanosystems and several therapeutic applications may be foreseen, such as targeting with molecules useful for treatment of brain diseases.

1. Introduction

In the past decade, an emerging interest has been growing toward brain drug targeting and the issues surrounding this field have been discussed widely (Abbott, 2004; Ghersi *et al.*, 2004; Lawrence, 2002; Pardridge, 2002; Ricci *et al.*, 2006; Su and Sinko, 2006). These issues, along with poor knowledge regarding the physiology of the central nervous system (CNS) have been the main limiting factors in the development of effective drugs and appropriate drug delivery systems (DDSs) for brain targeting (Lawrence, 2002; Pardridge, 2002; Ricci *et al.*, 2006).

A worrying updated picture of the worldwide CNS pathology incidence displayed that, in Europe alone, about 35% of the total burden of all diseases is caused by brain diseases (Pardridge, 2002) and about 1.5 billion people worldwide suffer from CNS disorders. Moreover, because of an average lifespan increase to almost 70 years, at which age about 50% of the population starts revealing evidence of Alzheimer's disease (AD) (Ghersi *et al.*, 2004), an increase of the global burden of CNS disorders from the current 11% to 14%, is expected by 2020 (Blasi *et al.*, 2007). For genetic, age and related reasons, most of the degenerative CNS pathologies, such as Creutzfeldt-Jakob's disease, Parkinson's disease (PD), AD, and Huntington's disease, multiple sclerosis, and amyotrophic lateral sclerosis, are developing as a consequence of wrong lifestyle and increased risk factors, such as alcohol, drugs, or dietary abuse, as well as stress (Croquelois *et al.*, 2007; Meyerhoff, 2001). In addition, CNS involvement may occur because of primary effects of human immunodeficiency virus (HIV) infection or secondary effects of immune suppression. About 75% of patients with acquired immune deficiency syndrome eventually develop some features of subacute encephalitis and other secondary effects, such as primary CNS lymphoma and progressive multifocal leukoencephalopathy (Bell *et al.*, 2006; Croquelois *et al.*, 2007; Kaul and Lipton, 2006; Levy and Bredesen, 1988; Oliveira *et al.*, 2006). This emergency is becoming particularly serious in developing countries as a result of a wide and uncontrolled spread of HIV infection.

In this context, the synthetic-chemical strategy appears to be very hard. In fact, innovative molecules must have several features such conformational

affinity for receptors or hydrophilic/lipophilic balance to improve a suitable pharmacokinetic profile. In effect, the most important factor limiting the development of new drugs for the CNS is the blood–brain barrier (BBB), because it limits the brain penetration of several molecules. Essentially, 100% of large-molecule pharmaceutics, including peptides, recombinant proteins, monoclonal antibodies, RNA interference (RNAi)-based drugs and gene therapeutics, do not cross the BBB (Pardridge, 2001). A common misconception is that small molecules readily cross the BBB, but >98% of all small molecules do not cross the BBB either. For this reason, the pharmaceutical technology contribution to this area is of paramount importance (Ghersi *et al.*, 2004; Guerin *et al.*, 2004; Jain, 2005; Johanson *et al.*, 2005). In the context of an effective drug deposition to the CNS, several targeted drug delivery systems (TDDSs) have been developed (Badruddoja and Black, 2006; Butowski and Chang, 2005; Craparo *et al.*, 2011; Gaillard *et al.*, 2005; Lungwitz *et al.*, 2005; Tiwari and Amiji, 2006; Vyas *et al.*, 2006), whereas other carriers developed for different aims, have been transformed into a possible brain targeting application (Garcia-Garcia *et al.*, 2005; Roney *et al.*, 2005). Among others, nanoparticles (NPs) have been considered as carriers of choice to overcome the BBB (Aktas *et al.*, 2005; Göppert and Müller, 2005; Koziara *et al.*, 2003; Müller and Keck, 2004; Tiwari and Amiji, 2006). In particular, solid lipid nanostructures have recently been reappraised as potential TDDS for brain targeting (Begley, 2004; Göppert and Müller, 2005; Müller and Keck, 2004; Tiwari and Amiji, 2006; Wissing *et al.*, 2004). They are nano-sized particles ranging from 1 to 500 nm that are able to entrap lipophilic or hydrophilic drugs. Their chemical–physical characteristics such as size, surface charge, morphology, and matrix composition play a fundamental role in their biodistribution. To achieve brain targeting, these carriers can be surface-modified by site-specific molecules, and consequently, they are able to specifically carry drugs across the BBB by active transport mechanisms.

2. Blood–Brain Barrier

The BBB is the specialized system of capillary endothelial cells that protects the brain from harmful substances in the bloodstream, while supplying the brain with the required nutrients for proper function. Unlike peripheral capillaries that allow relatively free exchange of substances across/between cells, the BBB strictly limits transport into the brain through both physical (tight junctions) and metabolic (enzymes) barriers (Fundaro *et al.*, 2000). Thus, the BBB is often the rate-limiting factor in determining permeation of therapeutic drugs into the brain.

The BBB is a unique and selective barrier of endothelial cells that line cerebral capillaries, together with perivascular elements, such as closely

associated astrocytic end-feet processes, perivascular neurons and pericytes (Abbott *et al.*, 2006; Newton, 2006). The endothelial cells of the BBB are distinguished from those in the periphery by increased mitochondrial content, a lack of fenestrations, minimal pinocytotic activity (Hawkins *et al.*, 2006), and the presence of complex tight junctions due to the interaction of several transmembrane proteins, such as occludin, claudins, and junctional adhesion molecules-JAMs that divide the membranes of the endothelial cells into two distinct sides, luminal (blood side) and abluminal (brain side; Abbott *et al.*, 2006; Begley, 2003; Newton, 2006; Pardridge, 2005). The BBB performs many functions: first, maintaining the internal environment of the brain, maintaining brain interstitial fluid (ISF) and the cerebrospinal fluid (CSF) composition within extremely fine limits, far more so than the somatic extracellular fluid, so that the neurons can perform their complex integrative functions (Begley, 2003, 1996). Second, a major function of the BBB is neuroprotection. Over a lifetime CNS will be exposed to a wide range of neurotoxic metabolites and acquired xenobiotics, which may cause cell damage and death. BBB protects the brain from fluctuations in ionic composition that can occur after a meal or exercise, which could disturb synaptic and axonal signaling. The barrier helps to keep the centrally and peripherally acting neurotransmitters separate. Finally, the continual turnover and drainage of CSF and ISF by bulk flow helps to clear larger molecules and brain metabolites, thus maintaining brain microenvironment (Hawkins and Davis, 2005). The ability of a particular substance to cross the BBB and enter the brain is dependent upon several factors, but in general, there is a relationship between lipophilicity and brain penetration for these solutes, and the more lipid-soluble a molecule, the more readily it will enter the CNS. Some of these lipophilic substances do not, however, enter the brain as readily as one might expect or predict from their lipid solubility. These solutes, and in many cases their metabolites, are actively removed from the CNS by efflux transporters.

3. Solid Lipid Nanoparticles (SLN)

The use of TDDS is the major way of achieving noninvasive brain drug delivery. Various colloidal delivery systems have been tried by many researchers to obtain a controlled release of many drugs; these systems include liposomes, microspheres, lipid microspheres, niosomes, polymeric NPs, and solid lipid nanoparticles (SLNs; Craparo *et al.*, 2011; Denora *et al.*, 2009; Gabathuler, 2010). For a delivery system to be effective, a high drug loading, physical and chemical stability, and a low incidence of toxicity of the carrier are important factors. Further, the *in vivo* fate of the carrier, the

process and production choices and the overall costs are other parameters that must be evaluated (Gualbert *et al.*, 2003; Shusta, 2005). In this context, lipid nanostructures have been proposed as alternative carriers to polymeric NPs to overcome some of their common problems. Lipid NPs are generally made up of biocompatible lipids and natural surfactants. More recently, modification of SLN, the so-called nanostructured lipid carriers (NLC) and lipid drug conjugated nanoparticles (LDC-NPs) show a higher drug loading capacity (LC) and a longer term stability during storage than SLN. Important advantages include the possibility to include lipophilic or hydrophilic drugs (Cecchell *et al.*, 2007; Chen *et al.*, 2001; Reddy and Venkateshwarlu, 2004).

In general, size not exceeding a maximum diameter of 200 nm, neutral surface charge, sphericity, and an adequate deformability are crucial characteristics to ensure prolonged blood circulation and a relatively low rate of mononuclear phagocyte system (MPS) uptake. Moreover, chemical modification of the nanocarrier surface with certain hydrophilic polymers, such as poly(ethylene glycols) (PEGs) and/or the use of a surfactant (such as polysorbate and Epikuron), represents the most frequent way to sterically stabilize them by a polymer-mediated protection and to impart the *in vivo* longevity to drug carriers (Juillerat-Jeanneret, 2008; Park *et al.*, 2008). PEG chains can be physically adsorbed on the particle surface or covalently bonded to fully formed lipid nanocarriers by using PEGylated lipids as starting material (Denora *et al.*, 2009; Hu *et al.*, 2007). To increase the accumulation specifically in the required pathological site, nanocarriers may be actively targeted by incorporating surface-grafted recognition moieties that impart an affinity for cellular receptors or components that are present on and/or upregulated by specific cells (Byrne *et al.*, 2008).

SLN and NLC can be formulated by using several methods: oil-in-water (o/w) microemulsion, nanoprecipitation, and hot and cold high-pressure homogenization (HPH) techniques.

The o/w microemulsion technique (Fig. 12.1) is preferable when substances are unstable to the high-mechanical stress produced by HPH. However, using this method, huge amounts of surfactants and cosurfactants have to be used. In the nanoprecipitation method (Fig. 12.2), an organic solvent miscible with water must be used to dissolve lipids.

Either the hot or the cold homogenization techniques (Figs. 12.3 and 12.4, respectively) have in common an initial step consisting of the lipid melting at approximately 5–10 °C above the mixture melting point, although larger particle sizes and a broader size distribution are observed in cold-homogenized samples, compared to the hot homogenization.

All the methods mentioned above will be described in detail in the following examples.

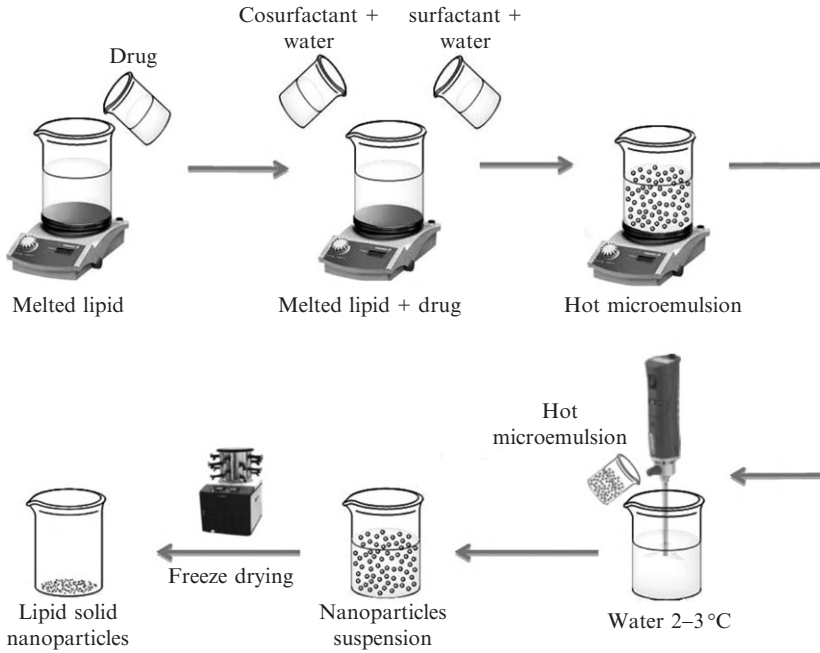

Figure 12.1 **Schematic diagram for the preparation of lipid nanostructures via the o/w microemulsion technique: heating the lipid above its melting point and addition of the drug; addition of the surfactant and cosurfactant aqueous solutions to the melted lipid; dispersion of the warm microemulsion in cold water (2–3 °C); and freeze-drying procedure.**

4. SLN Containing Riluzole

We described previously the preparation of SLN loaded with riluzole (Bondì *et al.*, 2010a). This drug is a potent neuroprotective agent that is useful in the treatment of various models of neurodegeneration (Bondì *et al.*, 2008; Miller *et al.*, 2007). Riluzole prevents acute cell damage induced by glutamate in degenerative diseases of motor neurons and protects dopamine neurons in PD (Storch *et al.*, 2000). Riluzole-loaded SLNs were successfully prepared using the o/w microemulsion technique (Fig. 12.1). Briefly to prepare the lipid phase, Compritol 888 ATO (0.25 mmol) is heated to 5–10 °C above its melting point and the drug (0.43 mmol) is added. Successively, an aqueous suspension of Epikuron 200 (0.05 mmol) and an aqueous solution of taurocholate sodium salt (0.24 mmol) are added, obtaining a warm clear microemulsion at 75 °C (±1 °C). Riluzole-loaded SLNs are obtained by dispersing the warm o/w microemulsion in cold water (100 ml, 2–3 °C) under mechanical stirring. The obtained colloidal

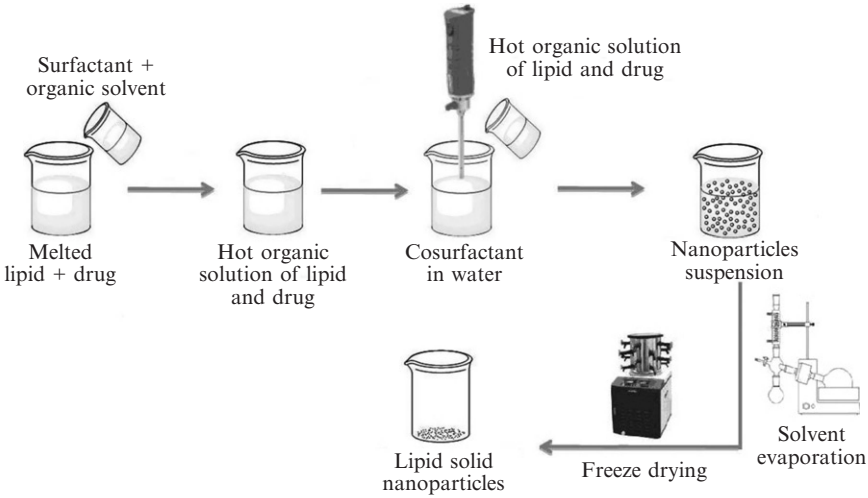

Figure 12.2 Schematic diagram for the preparation of lipid nanostructures via the nanoprecipitation method: dissolution of the lipid in the organic solvent miscible in water and addition of the drug; addition of the organic solution in an aqueous phase containing the surfactant(s); evaporation by rotavapor to remove organic solvent; and freeze-drying procedure.

milk dispersion is centrifuged at 110,000 × *g* for 1 h at 2 °C. NPs are then suspended in water, freeze-dried for obtaining a dried powder that is utilized for further characterization. The average diameter and width of distribution (polydispersity index, PDI) of drug-loaded SLNs are determined by photon correlation spectroscopy (PCS) by using a Zetasizer Nano ZS (Malvern Instruments Ltd, Malvern, UK) that utilizes the noninvasive back-scattering technique. The dried sample is appropriately diluted with filtered (0.2 μm filter), double-distilled water, and the reading is carried out at a fixed angle of 173° with respect to the incident beam. The average diameter and PDI of riluzole-loaded SLNs were about 88 nm and 0.27, respectively. The ζ-potential values are measured using principles of the laser Doppler velocitometry by using a Zetasizer Nano ZS. The sample is dispersed in the proper suspending medium, specifically an aqueous solution of NaCl (0.9%, w/v), filtered (0.2 μm), double-distilled water or 0.01 *M* phosphate buffered saline (PBS) at pH 7.4. In our experiments, the ζ-potential values were between −45 and −9 mV.

Moreover, an adequate HPLC method to determine the amount of riluzole entrapped in SLNs, or the amount of drug released from SLNs is developed. The HPLC analysis is performed at room temperature using an LC Star 9012 Solvent Delivery System (Varian, Turin, Italy) equipped with a reversed-phase C18 column (Bondapak®, 5 μm, 250 × 46 mm i.d., Waters, MA, USA). A mixture of an aqueous solution of sodium bibasic phosphate

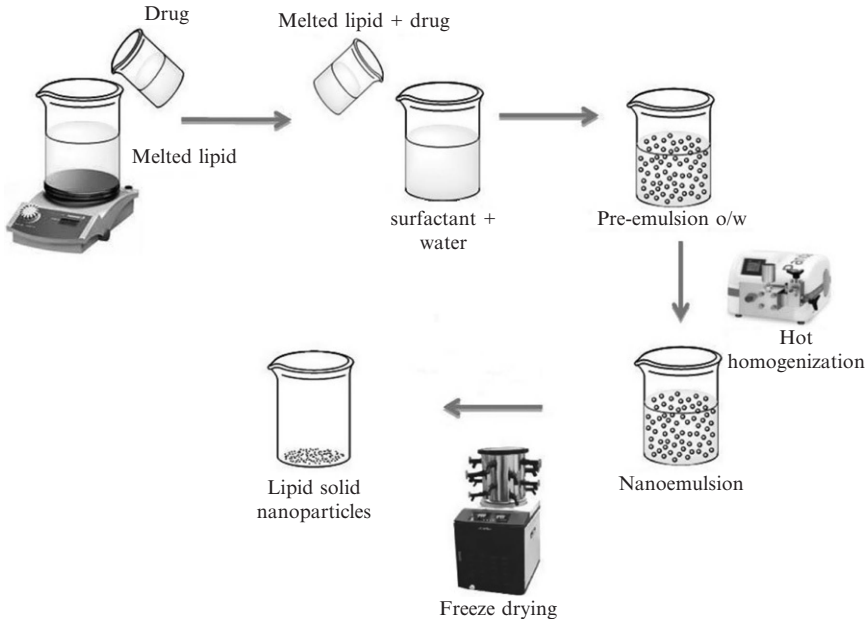

Figure 12.3 **Schematic diagram for the preparation of lipid nanostructures via the hot HPH technique: heating the lipid above its melting point and addition of the drug; addition of the melted lipid in a hot aqueous phase containing the surfactant(s) and formation of the primary emulsion by vigorous stirring with a high speed stirrer; homogenization in a heated homogenizer for several homogenization cycles; and freeze-drying procedure.**

(pH 9)/CH_3OH (20:80 v/v) with a flow rate of 1 ml/min is used as the mobile phase. The drug peak is measured at a wavelength of 289 nm and quantitatively determined by comparison with a standard curve obtained using riluzole ethanolic solutions at known concentrations. To determine the amount of riluzole entrapped into SLNs, 5 mg of freeze-dried, drug-loaded SLNs are dissolved in a mixture (10 ml) of ethanol and dichloromethane (4:1 v/v). The organic solution obtained is filtered through a 0.45-μm PTFE membrane filter and analyzed by HPLC. The LC%, expressed as the weight percent ratio between the loaded riluzole and the dried system (lipid matrix and riluzole), was 14.5% (w/w).

Finally, to verify the capability of SLNs to carry the entrapped riluzole into the brain, *in vivo* studies on rats are performed, and the differences in biodistribution between the drugs, free or blended into SLNs, are evaluated. The experiments are carried out in adult male Sprague–Dawley rats that are immunized using a model of multiple sclerosis (experimental allergic encephalomyelitis, EAE). For these experiments, free riluzole or riluzole-loaded SLNs are dispersed in the vehicle (20% w/w, Tween 80), diluted in a

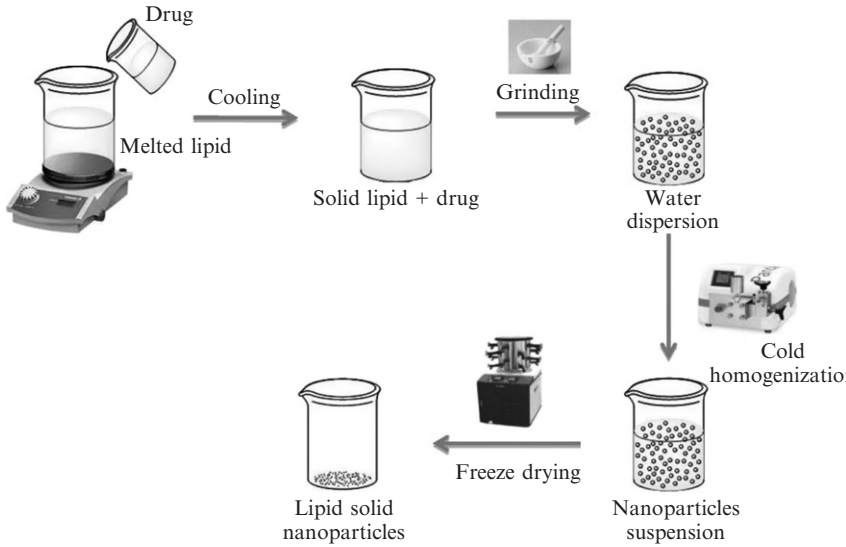

Figure 12.4 Schematic diagram for the preparation of lipid nanostructures via the cold HPH technique: heating the lipid above its melting point and addition of the drug; cooling and grinding the lipid; addition of the lipid in a cold aqueous phase containing the surfactant(s) and homogenization in a homogenizer for several homogenization cycles; and freeze-drying procedure.

saline solution to obtain the proper drug concentration (8 mg drug/ml) and stored at 4 °C. These two formulations are administered to rats by the intraperitoneal route, at the dose of 8 mg/kg of body weight and at room temperature. As riluzole has a neuroprotective action, it is administered, free or blended into SLNs, as a pretreatment before the appearance of clinical signs of EAE, which are usually observed from day 14 following the onset of the disease. The animals are divided into two groups, each of which received intraperitoneally one of the two formulations described above. The treatment begins on day 7 after the immunization. At this preventive stage, the BBB is believed to still be intact because the inflammatory process is absent (Oliveira *et al.*, 2006). Two separate sets of animals with EAE are used to evaluate the effects of riluzole, free or blended into SLNs. Rats treated with riluzole-loaded SLNs developed clinical signs of EAE later than those treated with free riluzole, demonstrating that this system has a greater efficacy than free riluzole. A total of 14 days after immunization, a significant difference between the positive control (EAE plus vehicle) and treated (EAE plus riluzole-loaded SLN) group was observed. Six of the ten control rats developed severe EAE and the other four died. By contrast, none of the (EAE plus riluzole-loaded SLN) treated rats died. When the riluzole-loaded SLNs are administered, the amounts of drug found in the brain after 8 and

16 h postinjection were equal to 1.31 and 0.07 μg riluzole/g tissue weight, respectively. However, when free riluzole was administered, the amounts of drug found in the brain were equal to 1.01 and 0.02 μg riluzole/g tissue weight, respectively. In blood serum, riluzole was found only 8 h postinjection and its blood concentration was higher when the free drug was administered compared with the drug-loaded SLNs. In particular, when the drug-loaded SLNs were administered, the amount of drug found in blood serum 8 h postinjection was equal to 0.42 μg riluzole/g tissue weight, whereas when the free riluzole is administered, the amount of drug found in blood serum was equal to 0.64 μg riluzole/g tissue weight. This result means that the riluzole that had blended into SLNs crossed the BBB more easily than the free drug, and this process led to a reduction of drug concentration in the bloodstream. This phenomenon could be due to endocytosis or transcytosis of these nanoparticulate carriers through the endothelial cells lining the blood capillaries of the brain (Joshi and Müller, 2009; Kaur *et al.*, 2008). Other processes, such as tight-junction modulation or P-glycoprotein inhibition, could also occur and contribute to the potential brain release and targeting of drug-loaded systems. Moreover, the drug biodistribution was also exploited in organs such as the liver, spleen, heart, kidneys, and lungs to determine the potential reduction of drug toxicity when riluzole is administered into the lipid carrier. The drug entrapped into SLNs accumulated in the non target organs to a much lower extent than the free drug. All these results demonstrate that the use of the carrier not only increases the targeted release of riluzole to the brain, but also reduces indiscriminate biodistribution in non target organs, with a reduction in side and toxic effects.

5. SLN Containing Ferulic Acid (FA)

We have described the preparation of SLN loaded with FA (Bondì *et al.*, 2009; Picone *et al.*, 2009), a molecule with high antioxidant (Scott *et al.*, 1993) and anti-inflammatory activities (Fernandez *et al.*, 1998). It has been also suggested that FA can act as a free radical scavenger (Kanski *et al.*, 2002; Kikuzaki *et al.*, 2002; Ogiwara *et al.*, 2002). Further, administration of FA induces resistance to Aβ42 toxicity in mice, and it has been suggested that it may be a useful chemopreventive agent against AD (Yan *et al.*, 2000). Moreover, inhibition of the formation as well as destabilization of preformed amyloid fibrils has been suggested (Ono and Yamada, 2005).

FA-loaded SLNs are prepared via the o/w microemulsion method (Fig. 12.1) by using Compritol 888 ATO as the lipid matrix, Epikuron 200 as a surfactant, and taurocholate sodium salt as a cosurfactant. The lipid phase is prepared by heating Compritol 888 ATO to 5–10 °C above

its melting point, and FA is dissolved in the melted lipid matrix. An aqueous suspension of Epikuron 200 (0.075 *M*) and an aqueous solution of taurocholate sodium salt (0.715 *M*) are added successively, thus obtaining a warm clear microemulsion. FA-loaded SLN are obtained by dispersing the warm o/w microemulsion in cold water under mechanical stirring. SLNs are purified by centrifugation at 140,000 × *g* for 1 h, and freeze-dried by a Modulyo freeze-dryer (FreeZone® Freeze Dry System, Labconco Corporation, Kansas City, Missouri, USA) for subsequent characterization.

To determine the amount of FA entrapped into SLNs, 5 mg of freeze-dried SLNs are dissolved in 25 ml of tetrahydrofuran (THF). The organic solution is filtered through 0.45 μm (PTFE membrane) filters and analyzed by HPLC. To ensure that the drug is not absorbed on the PTFE membrane, several THF solutions of drug at known concentrations are filtered and the concentration values before and after filtration are evaluated by HPLC analysis. No significant differences in drug concentration were observed. Results are expressed as LC% (w/w), that is, the relative percentage of loaded drug with respect to the lipid phase (matrix lipid + drug). The HPLC analysis is performed at room temperature using a Shimadzu Instrument equipped with a reversed-phase C18 column (Bondapak®, 3 μm, 150 × 4.6 mm i.d., Supelco-Milan, Italy). A mixture of THF, H_2O, and CH_3COOH (60:35:5 v/v) with a flow rate of 0.2 ml/min is used as the mobile phase. The HPLC column system is connected to a UV-Vis detector (Shimadzu, Germany). The drug peak is measured at 318 nm and measured by comparison with a standard curve obtained using FA solutions in THF at known concentrations.

Finally, to test the activity of free FA against Aβ toxicity and to investigate if the entrapment of FA into SLNs may improve the effectiveness of free FA, *in vitro* experiments on LAN5 neuroblastoma cells treated with rAβ42 oligomers are carried out. As a first approach, the morphological effect with respect to the corresponding controls is observed. Cells treated with rAβ42 oligomers and FA free or loaded into SLNs, instead, appear to recover the regular morphology of neurons. Moreover, results of a dose-response study showed that cells treated with rAβ42 alone or with empty SLNs showed a mortality of ∼40% when compared with the control. When free FA at concentrations of 14 m*M* and 28 m*M* was utilized, a recovery of cell viability of ∼15% and 20%, respectively, was observed. Further, when FA at the highest concentration (28 m*M*) entrapped into SLNs was employed, the best result, in terms of cell viability, was obtained. Under these conditions, a total recovery of rAβ42-induced toxicity was detected, indicating that these SLNs are good carriers for improving the protective effect of FA.

Furthermore, Aβ is able to generate free radicals and cause oxidative damage (Ghersi *et al.*, 2004). Then, the ability of FA, free or loaded into SLNs, in reducing ROS produced by Aβ treatment can also be investigated.

Intracellular ROS are measured by flow cytofluorimetry. The cells were incubated with 1 μ*M* dichlorofluorescein diacetate (DCFH-DA) (Sigma-Aldrich, Milan) in PBS for 10 min at room temperature in the dark. After washing, cells were dissolved in PBS and then analyzed by flow cytometry for fluorescence-positive cells analysis. rAβ42 oligomers induced a significantly higher ROS percentage generation with respect to the other three conditions. In particular, in the presence of FA entrapped into SLNs, rAβ42-induced intracellular ROS formation was completely inhibited. Proteolytic enzymes of the caspase family play a central role in initiating and sustaining the event leading to apoptotic cell death.

To investigate the possibility that FA, free or incorporated into the SNLs, can interfere with the apoptotic process activated by rAβ42, a caspase 9 luminometric assay is utilized. In our laboratory, we use LAN5 cells treated with rAβ42 oligomers alone or in the presence of FA or FA-loaded SLNs. Cells treated with oligomers in the presence of FA-loaded SLN showed a strong reduction of activation of caspase 9 in comparison to cells treated with oligomers alone, indicating that the DDS induced a positive protective effect. In conclusion, β-amyloid is a key factor in free radical generation and oxidative damage activating a cascade of events leading to apoptotic cell death. The suppression or the reduction of the oxidative stress seems to be a promising therapeutic intervention for neurodegenerative diseases. The use of DDS loaded with antioxidant molecules such as FA appears to be potentially useful for an effective therapy of AD.

6. SLN Containing Curcumin

Curcumin is a natural low-molecular-weight polyphenol extracted from the rhizome of *Curcuma longa*, and has a wide range of pharmacological activities such as anticancer, antioxidant, anti-amyloid, and anti-inflammatory properties, although its clinical application has been limited because of its poor aqueous solubility (Sahu *et al.*, 2008; Sou *et al.*, 2008; Wang *et al.*, 2006). To increase its aqueous solubility and bioavailability, attempts have been made through encapsulation in lipid NPs (Sou *et al.*, 2008).

We have described the preparation of SLN containing curcumin using the nanoprecipitation technique (Fig. 12.2; Bondì *et al.*, 2010b). Briefly, to prepare the lipid phase, the selected lipid or mixture is heated to 5–10 °C above its melting point. An ethanolic solution of Epikuron 200 (0.14 mmol) is added, under stirring, to the melted lipid (0.70 mmol). For obtaining drug-loaded NPs, curcumin (0.27 mmol) was added, under mechanical stirring, to the melted lipid before the addition of the Epikuron solution. To obtain NLC, the hot solution is dispersed in cold, double-distilled water

(100 ml at 2–3 °C) containing taurocholate (sodium salt) (0.69 mmol), by using an Ultra Turrax T25 (IKA, D-Staufen-Germany) equipped with dispersing tool S25N 10G (IKA, D-Staufen-Germany) at 6500 rpm for 10 min. Then, NLC are submitted to exhaustive dialysis using Visking dialysis tubing (18/32″; molecular weight cut-off 12,000–14,000 Da), freeze-dried (FreeZone® Freeze Dry System, Labconco Corporation, Kansas City, Missouri, USA), and stored at room temperature. Ethanol is completely removed from the NPs during purification.

In particular, Imwitor, Compritol 888 ATO, Precirol ATO as lipid components are used. Indeed, Epikuron 200 and taurocholate sodium salt are chosen as surfactant and cosurfactant, respectively. Since some physical–chemical and technological properties, such as size, surface charge, PDI, and LC% are quite critical for the biopharmaceutical behavior of NLC, all the obtained samples, after preparation and purification, are characterized in terms of particle size, PDI, and zeta potential.

Typical data indicate that the average diameter of the samples were all in the nanometric scale, ranging between 105 and 135 nm. Moreover, all these systems possessed low PDI values, which indicated a good dimensional homogeneity of particles that, together with small size, render them suitable to be injected intravenously, to minimize their uptake by macrophages. The zeta potential values of the obtained samples were high and negative, assuring a considerable potential stability of all the aqueous NLC dispersions. The LC% values, expressed as weight percent ratio between entrapped curcumin and the total dried sample weight and evaluated by HPLC analysis, were high, ranging between 21.1% and 27.4% (w/w). Drug release studies conducted in PBS at pH 7.4 and in human plasma, in order to investigate the drug release profiles in media mimicking biological fluids, showed a release profile considerably slow. It was found that, after 24 h of incubation, the total amount of unreleased curcumin was found in the NPs. The presence of a high amount of unreleased curcumin is of great importance, considering that curcumin-loaded NLC could reach the target site (such as a tumor), and there release the drug.

In vitro experiments on LAN5 cells showed that curcumin loaded into NLC is internalized inside the cells, and possess a higher efficacy to inhibit cell viability and to induce Hsp70 protein production, a marker of curcumin activity inside the cells, than the free drug. The best results in terms of the reduction of cell viability and induction of Hsp70 protein were obtained when the NLC sample, obtained by using Compritol as the lipid matrix, was tested. Its composition probably favors the internalization process of the NPs into LAN5 cells as visualized by the *in vitro* fluorescence assay. These results suggested that these systems are potential carriers for parenteral administration of curcumin, and open up avenues for systemic therapy of human cancers.

7. SLN Containing Camptothecin

Camptothecin (CA), an alkaloid with a peculiar anticancer mechanism, acts with a unique mechanism of action, targeting the nuclear enzyme topoisomerase I (Yang *et al.*, 1999). CA inhibits the growth of a wide range of tumors (Giovanella *et al.*, 1991, 1989; Potmesil, 1994). The interaction between CA and topoisomerase I was thought to occur through the attack of a nucleophilic site on the enzyme at the acyl position in the lactone of the CA structure, which plays an important role in its biological activity (Potmesil, 1994). The opening of the lactone under alkaline conditions to form the acid salt or carboxylate species results in loss of *in vitro* activity and apparently decreases the *in vivo* anticancer activity. The poor water solubility of the lactone form, instability in biological pH values and low biological activity, and the severe toxicity of the carboxylate form precluded the use of CA in clinical applications.

To overcome these problems, the drug is incorporated into stearic acid (SA)-based SLN by using the hot HPH method (Fig. 12.3). For this purpose, CA (100 mg) and soybean lecithin (1.5 g) are dissolved in 10 ml absolute ethanol, the pH is adjusted to 8.0 with ammonium hydroxide, and then SA is added. The mixture is heated until 85 °C and sonicated for 30 min. Then the ethanol is evaporated to produce a nearly clear, melted lipid phase. In addition, an aqueous phase is prepared by dissolving poloxamer 188 (0.5 g) and glycerol (2.25 g) in 100 ml of distilled water. The melted lipid is first dispersed in the aqueous phase, which is previously heated to the same temperature (85 °C), by magnetic stirring and sonication. This premix is passed through a preheated (80–90 °C) high-pressure homogenizer 15M-8BA (APV, Crawley, Sussex, UK) for five cycles at 6000-psi. The hot dispersion is filtered through 0.45 μm filters and allowed to cool quickly to 4 °C, forming a CA-loaded SLN (CA-SLN) suspension, which is stored at 4 °C or lyophilized for long term storage. The manufacturing process and storage of CA-SLN are conducted under nitrogen atmosphere. The zeta potential of the CA-SLN is measured by the electrophoretic mobility of the NPs in a U-type tube at 20 °C. The CA-SLN suspension (100 ml) is ultrafiltered using a XHH Hollow Fiber Ultrafiltration membrane (MW 10,000). The concentrations of CA in the CA-SLN suspension (100 μl) and in the ultrafiltrate (500 μl) are assayed by HPLC after dilution with methanol. HPLC analysis was performed at room temperature using a Waters 720 liquid chromatography (Waters Assoc., Milford, MA, USA) epuipped with a reversed-phase column (Ultrasil ODS, 250 mm × 4.6 mm internal diameter, 10 μm particle size) (Altex, Berkeley, CA, USA). A mixture of methanol-water/75:25 v/v with a flow rate of 0.7 ml/min was used as the mobile phase. The drug peak was measured at wavelength of 254 nm (Lon and Ahmed, 1990).

Finally, C57BL/6J mice, body weight between 17 and 21 g, are used for biodistribution studies. The CA-SLN suspension and CA-Sol are injected intravenously into the tail vein. At the predetermined time, blood samples are collected and placed into test tubes containing 10 μl of heparin solution, whereas the plasma is separated immediately by centrifugation. The animals are dissected and each tested organ is removed. Every organ sample is weighed accurately, homogenized, and acidified to pH 3.0. Blood, plasma, and tissue concentration data of CA obtained from mice are pooled to provide the mean concentration data. The area under the concentration–time curve (AUC) and the mean residence time (MRT) are determined. The value of absolute bioavailability (F) is defined as follows:

$$F = (\mathrm{AUC}_{\mathrm{CA-SLN}} \times \mathrm{dose}_{\mathrm{CA-Sol}})/(\mathrm{AUC}_{\mathrm{CA-Sol}} \times \mathrm{dose}_{\mathrm{CA-SLN}}).$$

Compared with CA-Sol, the value of F for CA-SLN was 4.9, and the MRT of CA-SLN increased about 18 times in plasma compared with the same dose of CA-Sol. This may be caused by the coating of poloxamer 188 on the surface of CA-SLN (Ricci *et al.*, 2006) and the sustained release of CA from CA-SLN. A prolonged residence in various organs was achieved with CA-SLN. The MRT of CA-SLN increased more than four times compared with the same dose of CA-Sol in every measured organ, probably because of the increased internalization of the CA-SLN inside various tissues that could then release their content at a slow rate. Moreover, CA-SLN greatly enhanced the brain CA concentrations and maintained the high drug level for a longer time. Compared with the same dose of CA-Sol, the $C_{\max}$ (the maximum concentration) of CA-SLN increased by more than 180%. The AUC/dose of CA-SLN was 10.4-fold greater and MRT increased four times. These results indicate that CA-SLN could successfully target CA to the brain and could greatly improve the efficacy of CA to treat brain cancers.

8. LDC-NPs Containing Diminazene

Diminazene is an antitrypanosomal drug used widely in veterinary medicine. *Trypanosoma brucei gambiense* and *T. brucei rhodiense*, transmitted by the tse–tse fly, after a hemolymphatic stage, enter into the CNS where they cannot be reached by hydrophilic drugs, and cause the so called human African trypanosomiasis ("sleeping sickness"). Clinical treatment of trypanosomiasis today consists of a drug therapy with rather old and toxic drugs (i.e., having very severe side effects). No drug can be given orally; all drugs have to be administered i.v. under hospital care. All clinical drugs in use show problems of availability, affordability, toxicity, and resistance. Because of its high polarity, diminazene cannot cross the BBB.

To deliver diminazene to the brain of infected mice, the drug is conjugated with SA or oleic acid (OA) to obtain lipid-drug conjugates (as described below), which are used as starting materials to prepare LDC-NP (Olbrich *et al.*, 2004). The choice of the LDC formulation is made to overcome the low drug LC of SLNs (especially for hydrophilic drugs) as one of the disadvantages of this delivery system. In this way, LDC-NP possess a diminazene LC of up to 33% (w/w) and are produced using the cold HPH technique (Fig. 12.4). Diminazene base is prepared by the addition of excess 1 *M* potassium hydroxide solution to an aqueous solution of diminazene diaceturate. Diminazene free base (*D*), a red precipitate, is filtered with S&S filter paper (Schleicher & Schull, Dassel, Germany) and washed three times with water for injection. It is dried at 40 °C and successively stored at 4 °C. The binary fatty acid salts of diminazene are prepared by dissolving the drug and fatty acid in 96% ethanol (Caelo), and consequent evaporation of the solvent at 40 °C under reduced pressure. SA diminazene and oleic acid diminazene (OAD) formulations are dried at 40 °C for 24 h. Fatty acid diminazene NPs are prepared by dispersing the bulk material with 1% polysorbate 80 and 2.25% glycerol solution in a mortar to form a predispersion. This predispersion is homogenized with an APV LAB 40 homogenizer (APV-Gaulin, Lubeck, Germany) using 1500 bar and cycle numbers between 20 and 27. After five cycles, the samples replaced in ice to avoid high temperatures of the dispersion. Particle size analysis by PCS and zeta potential measurements are performed using a Zetasizer 4 (Malvern Instruments, UK). Results are expressed using the volume distribution in terms of diameter 90% (LD 90%) values. That means that 90% of the particle population possesses a diameter below this size.

Finally, cytotoxicity is evaluated on granulocytes, obtained from blood of healthy volunteers by density centrifugation using Polymorphprep®, and is expressed as LD_{50} values. For this purpose, granulocytes are used because these cells are involved in the development of "sleeping sickness." By using LDC-NP, the cytotoxicity of the formulations was reduced significantly compared to pure polysorbate 80 solutions. In case of OAD-based LDC-NP, the addition of diminazene was not able to reduce the cytotoxicity of the formulation. The two-dimensional electrophoresis (2-DE) analysis of the protein adsorption patterns on the different LDC-NPs showed strong enrichment of the apolipoproteins A-I and AIV. Apo E has been reported to be the key factor for BBB passage (Kreuter and Alyautdin, 2000), and was found to be adsorbed on LDC-NPs after incubation in human serum, in addition to the proteins Apo A-I and A-IV (Olbrich *et al.*, 2002). The higher amount of adsorbed key plasma proteins could also result in higher levels of drug-containing particles reaching the brain and being transcytosed as described for LDL particles, where Apo A-I and Apo E could be identified as key factors for the uptake via LDL receptors (Dehouck *et al.*, 1997; Pitas *et al.*, 1987).

In conclusion, plasma protein adsorption patterns indicated the avoidance of hepatic uptake with the possibility of increased uptake via the LDL receptors at the BBB. Due to the high drug load, much higher intracerebral drug levels can be reached, allowing the administration of a lower dose to the patients, thereby reducing side effects.

9. SLN Containing Atazanavir

Atazanavir sulfate (Reyataz®, Bristol Meyer Squibb, MW: 802.9 g/mol) is an azapeptide inhibitor of HIV-1 protease frequently used in the treatment of HIV infection. Atazanavir is highly selective for HIV-1 protease and exerts protease inhibition-associated cytotoxicity at concentrations 6500- to 23,000-fold higher than those required for therapeutic antiviral activity (Gong *et al.*, 1999; Rabasseda *et al.*, 1999). Thus, because of its superior clinical profile, lower toxicity, and frequent use, Atazanavir is an attractive candidate for encapsulation in a nanoparticulate DDS for brain targeting.

Atazanavir-loaded SLNs are formulated by thin film hydration, using a microemulsion technique as already described (Fig. 12.1; Chattopadhyay *et al.*, 2008). SA (25 mg) is dissolved in 1 ml of 3% (w/w) Pluronic®F68 aqueous solution. Atazanavir, dissolved in methanol (1.25 mg for a total drug loading of 5% w/w), s added to the lipid-surfactant solution. The resulting mixture of Atazanavir, SA, and Pluronic®F68 is then stirred for approximately 30 min. The organic solvents are then evaporated under nitrogen to form a thin lipid film, and the dried film is subsequently treated with 0.5 ml of deionized water maintained at approximately 80–82 °C. The resultant emulsion is then subjected to alternate cycles of heat and vortexing for 5 min to facilitate the rapid formation of a microemulsion (Koziara *et al.*, 2005). Once a clear phase is obtained, the microemulsion is ultrasonicated with intermittent periods of vortexing for 3 min to further reduce the particle size. SLN containing Atazanavir are formed by dispersing the microemulsion in 4.5 ml of deionized water maintained at a temperature of 2–4 °C. Maximum Atazanavir loading into SLNs is determined by adding increasing amounts of Atazanavir (1%, 2%, 5%, 7.5%, 10%, and 20%). The encapsulation efficiency of Atazanavir in SLNs is determined by centrifugal filtration using an ultrafiltration membrane. Briefly, 1.5 ml of the freshly prepared Atazanavir-loaded SLNs are placed in the filter unit of a 5000-MW cut off centrifugal filter device (Amicon® Ultra-4, Millipora) prerinsed with deionized water. The device is centrifuged at 2000 × *g* to obtain an ultrafiltrate. The amount of unencapsulated Atazanavir present in the ultrafiltrate is measured by UV spectrophotometry Agilent 8453 UV spectrophotometer (Agilent Technologies, Waldbronn, Germany) at 249 nm. The concentration is obtained from a standard curve of Atazanavir prepared in deionized distilled water.

To account for any loss of Atazanavir due to adsorption onto the ultrafiltration membrane, the adsorption of Atazanavir on the membrane was evaluated by separate filtration studies of aqueous solutions of Atazanavir at equivalent drug loading concentrations.

The average diameter of SLNs is measured by PCS at a fixed angle of 90° using a He–Ne laser at 633 nm a Nicomp Zetasizer 380 Instrument (Malvern Instruments Ltd, Worcestershire, UK). Each SLN sample is diluted 1:50 with deionized, 0.22 μm filtered water (Millipore) until a count rate of 200–300 kHz is achieved. Volume-weighted Gaussian analysis is used for reporting the particle size distribution. Particle size is determined using two 5-min cycles for each sample. Zeta potential is a key factor in evaluating the stability of a colloidal dispersion (Komatsu *et al.*, 1995), and the surface charge on the particle is determined using the same instrument utilizing microelectrophoresis principles. A typical sample is prepared by diluting the SLNs with 0.1% Pluronic®F68 aqueous solution. The sample is placed in 4.5 ml, 10 mm pathlength polystyrene cuvettes (Fisher Scientific, USA).

Finally, the viability of hCMEC/D3 cells in the presence or absence of free Atazanavir, blank as well as Atazanavir-loaded SLNs over a period of 24 h is evaluated by the 3-[4,5-dimethylthiazol-2-yl]-2,5-diphenyltetrazoliumbromide (MTT) assay. The hCMEC/D3 cell line is an extensively characterized human brain endothelial cell line, which mimics most of the key characteristics of the BBB, even in the absence of cocultured glial cells. It is a useful model for screening CNS drug candidates, as well as for DDS to the brain.

The free aqueous Atazanavir and surfactant (Pluronic® F68) solution showed little or no reduction in cell viability over a wide concentration range. The cell viability was approximately 100% for blank and Atazanavir-loaded SLNs at a concentration corresponding to 200 n*M* of free Atazanavir. Increasing the concentration of blank SLNs and Atazanavir-loaded SLNs to 500 n*M* dropped the cell viability to approximately 60%. Exposure to varying concentrations of surfactant (Pluronic® F68) solution showed little or no reduction in cell viability. Drug uptake of [^{3}H]-Atazanavir-loaded SLNs, or blank SLNs in the presence of [^{3}H]-Atazanavir aqueous solution, or [^{3}H]-Atazanavir aqueous solution prepared in Hank's buffered salt solution is evaluated in confluent hCMEC/D3 monolayer cells. The amount of cellular drug uptake is measured using a liquid scintillation counter (Beckman LS5000 TD, Beckman Coulter, Inc.). Accumulation of [^{3}H]-Atazanavir is standardized to the cellular protein concentration (mg/ml) determined by the Bradford colorimetric method (Guerin *et al.*, 2004), using bovine serum albumin (Sigma-Aldrich, Milan, Italy) as the standard. hCMEC monolayer cells are treated with [^{3}H]-Atazanavir-loaded SLNs or [^{3}3H]-Atazanavir aqueous solution (all treatments are equivalent to 200 n*M* of free Atazanavir). The results showed that there is a significant difference in the uptake of Atazanavir when delivered by the formulations at

the early time points up to 60 min. Furthermore, there is a significant difference ($p < 0.05$) in Atazanavir accumulated by the cells treated with SLN-encapsulated drug and the other two treatments at 120 min.

In conclusion, results from cell viability studies coupled with higher drug cellular uptake suggest that SLNs can effectively deliver Atazanavir to human brain endothelial cells, *in vitro*.

10. Concluding Remarks

The methods and the studies described in this chapter demonstrate that many biologically actives molecules can be entrapped into SLN and that these systems are more efficacious than the free drug in several brain disease models. Targeting of these systems to CNS may further enhance the therapeutic effect of many macromolecular drugs. The success of drug loaded into solid lipid nanostructures suggests that they may be used effectively for treatment of several brain diseases. Further studies are necessary to find effective combination of SLN-encapsulated drugs and to identify others drugs that show increased therapeutic efficacy when carried by SLN.

REFERENCES

Abbott, N. J. (2004). Evidence for bulk flow of brain interstitial fluid: Significance for physiology and pathology. *Neurochem. Int.* **45,** 545–552.

Abbott, N. J., Rönnbäck, L., and Hansson, E. (2006). Astrocyte-endothelial interactions at the blood–brain barrier. *Nat. Rev. Neurosci.* **7,** 41–53.

Aktas, Y., Yemisci, M., Andrieux, K., Gursoy, R. N., Alonso, M. J., Fernandez-Megia, E., Novoa-Carballal, R., Quiñoa, E., iguera, R., Sargon, M. F., Celik, H. H., Demir, A. S., *et al.* (2005). Development and brain delivery of chitosan–PEG nanoparticles functionalized with the monoclonal antibody OX26. *Bioconjug. Chem.* **16,** 1503–1511.

Badruddoja, M. A., and Black, K. L. (2006). Improving the delivery of therapeutic agents to CNS neoplasms: A clinical review. *Front. Biosci.* **11,** 1466–1478.

Begley, D. J. (1996). The blood–brain barrier: Principles for targeting peptides and drugs to the central nervous system. *Proc. Natl. Acad. Sci. USA* **48,** 136–146.

Begley, D. (2003). Efflux mechanisms in the central nervous system: A powerful influence on drug distribution within the brain. *In* "Spinal Cord and Brain Barriers in Health and Disease," (W. J. Sharma, ed.), pp. 83–97.

Begley, D. J. (2004). Delivery of therapeutic agents to the central nervous system: The problems and the possibilities. *Pharmacol. Ther.* **104,** 29–45.

Bell, J. E., Anthony, I. C., and Simmonds, P. (2006). Impact of HIV on regional and cellular organisation of the brain. *Curr. HIV Res.* **4,** 249–257.

Blasi, P., Giovangioli, S., Schoubben, A., Ricci, M., and Rossi, C. (2007). Solid lipid nanoparticles for targeted brain drug delivery. *Adv. Drug Deliv. Rev.* **59,** 454–477.

Bondì, M. L., Craparo, E. F., Giammona, G., and Drago, F. (2008). Vol. WO2008/000448 A2.

Bondì, M. L., Montana, G., Craparo, E. F., Picone, P., Capuano, G., Di Carlo, G., and Giammona, G. (2009). Ferulic acid-loaded lipid nanostructures as drug delivery systems

for Alzheimer's disease: Preparation, characterization and cytotoxicity studies. *Curr. Nanosci.* **5,** 26–32.

Bondì, M. L., Craparo, E. F., Giammona, G., and Drago, F. (2010a). Brain-targeted solid lipid nanoparticles containing riluzole: Preparation, characterisation and biodistribution. *Nanomedicine* **5,** 25–32.

Bondì, M. L., Craparo, E. F., Picone, P., Di Carlo, M., Di Gesù, R., Capuano, G., and Giammona, G. (2010b). Curcumin entrapped into lipid nanosystems inhibits neuroblastoma cancer cell growth and activate Hsp70 protein. *Curr. Nanosci.* **6,** 439–445.

Butowski, N., and Chang, S. M. (2005). Small molecule and monoclonal antibody therapies in neurooncology. *Cancer Control* **12,** 116–124.

Byrne, J. D., Betancourt, T., and Brannon-Peppas, L. (2008). Active targeting schemes for nanoparticle systems in cancer therapeutics. *Adv. Drug Deliv. Rev.* **60,** 1615–1626.

Cecchell, R., Berezowski, V., Lundquis, S., Culot, M., Renftel, M., Dehouck, M. P., and Fenart, L. (2007). Modelling of the blood–brain barrier in drug discovery and development. *Nat. Rev. Drug Discov.* **6,** 650–661.

Chattopadhyay, N., Zastre, J., Wong, H. L., Wu, X. Y., and Bendayan, R. (2008). Solid lipid nanoparticles enhance the delivery of the HIV protease inhibitor, atazanavir, by a human brain endothelial cell line. *Pharm. Res.* **25,** 2262–2271.

Chen, D., Yang, T., Liang, W., and Zhang, Q. (2001). In vitro and in vivo study of two types of long circulating solid lipid nanoparticles containing Paclitaxel. *Chem. Pharm. Bull.* **49,** 1444–1447.

Craparo, E. F., Bondì, M. L., Pitarresi, G., and Cavallaro, G. (2011). Nanoparticulate systems for drug delivery and targeting to the central nervous system. *CNS Neurosci. Ther.* **17,** 670–677.

Croquelois, A., Assal, G., Annoni, J. M., Staub, F., Gronchi, A., Bruggimann, L., Dieguez, S., and Bogousslavsky, J. (2007). Diseases of the nervous system: Patients' aetiological beliefs. *J. Neurol. Neurosurg. Psychiatry* **76,** 582–584.

Dehouck, B., Fenart, C., Dehouck, M.-P., Pierce, A., Torpier, G., and Cechelli, R. A. (1997). A new function for then LDL receptor: Transcytosis of LDL across the blood brain barrier. *J. Cell Biol.* **138,** 887–889.

Denora, N., Trapani, A., Laquintana, V., Lopedota, A., and Trapani, G. (2009). Recent advances in medicinal chemistry and pharmaceutical technology-strategies for drug delivery to the brain. *Curr. Top. Med. Chem.* **9,** 182–196.

Fernandez, M. A., Saenz, M. T., and Garcia, M. D. (1998). Anti-inflammatory activity in rats and mice of phenolic acids isolated from Scrophularia frutescens. *J. Pharm. Pharmacol.* **50,** 1183–1186.

Fundaro, A., Cavalli, R., Bagoni, A., Vighetto, D., Zara, G. P., and Gasco, M. R. (2000). Non-stealth and stealth solid lipid nanoparticles(sln) carrying doxorubicin: Pharmacokinetic and tissue distribution after i.v. administration to rats. *Pharm. Res.* **42,** 337–343.

Gabathuler, R. (2010). Approaches to transport therapeutic drugs across the blood–brain barrier to treat brain diseases. *Neurobiol. Dis.* **37,** 48–57.

Gaillard, P. J., Visser, C. C., and de Boer, A. G. (2005). Targeted delivery across the blood-brain barrier. *Expert Opin. Drug Deliv.* **12,** 299–309.

Garcia-Garcia, E., Andrieux, K., Gil, S., and Couvreur, P. (2005). Colloidal carriers and blood-brain barrier (BBB) translocation: A way to deliver drugs to the brain? *Int. J. Pharm.* **298,** 274–292.

Ghersi, G., Egea, M., and Sugiyama, Y. (2004). transfer in the choroid plexus. Multiplicity and substrate specificities of transporters. *Adv. Drug Deliv. Rev.* **56,** 1693–1694.

Giovanella, B. C., Stchlin, S., Wall, M. E., Wani, M. C., Nicholas, A. W., Liu, L. F., Silber, R., and Potmesil, M. (1989). DNA topoisomerase I targeted chemotherapy of human colon cancer in xenografts. *Science* **246,** 1046–1048.

Giovanella, B. C., Hinz, R., Kozielski, A., Slehlin, L. S., Jr., Silber, R., and Pormesil, M. (1991). Complete growth inhibition of human cancer xenografts in nude mice by treatment with 20-(S)- camptothecin. *Cancer Res.* **51,** 3052–3055.

Gong, Y., Robinson, B., Rose, R., Deminie, C., Spicer, T., and Markowitz, M. (1999). Antiviral activity and resistance profile of an HIV-1 protease inhibitor BMS-232632. 38th Interscience Conference on Antimicrobial Agents and Chemotherapy.

Göppert, T. M., and Müller, R. H. (2005). Polysorbate-stabilized solid lipid nanoparticles as colloidal carriers for intravenous targeting of drugs to the brain: Comparison of plasma protein adsorption patterns. *J. Drug Target.* **13,** 179–187.

Gualbert, J., Shahgaldian, P., and Coleman, A. W. (2003). Interactions of amphiphilic calyx [4]arene-based solid lipid nanoparticles with bovine serum albumin. *Int. J. Pharm.* **257,** 69–73.

Guerin, C., Olivi, A., Weingart, J. D., Lawson, H. C., and Brem, H. (2004). Recent advances in brain tumor therapy: Local intracerebral drug delivery by polymers. *Invest. New Drugs* **22,** 27–37.

Hawkins, B. T., and Davis, T. P. (2005). The blood–brain barrier/neurovascular unit in health and disease. *Pharmacol. Rev.* **57,** 173–185.

Hawkins, R. A., O'Kane, R. L., Simpson, I. A., and Viñaz, J. R. (2006). Branched-chain amino acids: Metabolism, physiological function, and application. *J. Nutr.* **136,** 218–226.

Hu, Y., Xie, J., Wah, T. Y., and Wang, C. H. (2007). Effect of PEG conformation and particle size on the cellular uptake efficiency of nanoparticles with the HepG2 cells. *J. Control. Release* **118,** 7–17.

Jain, K. K. (2005). Nanotechnology-based drug delivery for cancer. *Technol. Cancer Res. Treat.* **4,** 407–416.

Johanson, C. E., Duncan, J. A., Stopa, E. G., and Baird, A. (2005). Enhanced prospects for drug delivery and brain targeting by the choroid plexus-CSF route. *Pharm. Res.* **22,** 1011–1037.

Joshi, M. D., and Müller, R. H. (2009). Lipid nanoparticles for parenteral delivery of actives. *Eur. J. Pharm. Biopharm.* **71,** 161–172.

Juillerat-Jeanneret, L. (2008). The targeted delivery of cancer drugs across the blood-brain barrier: Chemical modifications of drugs or drug-nanoparticles? *Drug Discov. Today* **13,** 1099–1106.

Kanski, J., Aksenova, M., Stoyanova, A., and Butterfield, D. A. (2002). Ferulic acid antioxidant protection against hydroxyl and peroxyl radical oxidation in synaptosomal and neuronal cell culture systems in vitro: Structure-activity studies. *J. Nutr. Biochem.* **13,** 273–281.

Kaul, M., and Lipton, S. A. (2006). Mechanisms of neuronal injury and death in HIV-1 associated dementia. *Curr. HIV Res.* **4,** 307–318.

Kaur, I. P., Bhandari, R., and Bhandari, S. (2008). Potential of solid lipid nanoparticles in brain targeting. *J. Control. Release* **127,** 97–109.

Kikuzaki, H., Hisamoto, M., Hirose, K., Akiyama, K., and Taniguchi, H. (2002). Antioxidant properties of ferulic acid and its related compounds. *J. Agric. Food Chem.* **50,** 2161–2168.

Komatsu, H., Kitajima, A., and Okada, S. (1995). Pharmaceutical characterization of commercially available intravenous fat emulsions: Estimation of average particle size, size distribution and surface potential using photon correlation spectroscopy. *Chem. Pharm. Bull.* **43,** 1412–1415.

Koziara, J. M., Lockman, P. R., Allen, D. D., and Mumper, R. J. (2003). In situ blood-brain barrier transport of nanoparticles. *Pharm. Res.* **20,** 1772–1778.

Koziara, J. M., Mumper, R. J., Oh, J. J., Akers, W. S., and Ferraris, S. P. (2005). Blood compatibility of cetyl alcohol/polysorbate-based nanoparticles. *Pharm. Res.* **22,** 1821–1828.

Kreuter, J., and Alyautdin, R. N. (2000). Using nanoparticles to target drugs to the central nervous system. *In* "The Blood Brain Barrier and Drug Delivery to the CNS," (M. W. Bradbury, D. J. Begley, and J. Kreuter, eds.), pp. 205–223. Marcel Dekker, New York.

Lawrence, R. N. (2002). Sir Richard Sykes contemplates the future of the pharma industry. *Drug Discov. Today* **7,** 645–648.

Levy, R. M., and Bredesen, D. E. (1988). Central nervous system dysfunction in acquired immunodeficiency syndrome. *In* "AIDS and The Nervous System," (M. L. Rosenblum and R. M. Levy, eds.), Vol. 1, pp. 27–64.

Lon, J. P., and Ahmed, A. E. (1990). Determination of camptothecin in biological fluids using reversed phase high-performance liquid chromatography with fluorescence detection. *J. Chromatogr. Biomed. Appl.* **530,** 367–376.

Lungwitz, U., Breunig, M., Blunk, T., and Gopferich, A. (2005). Polyethyleniminebased non-viral gene delivery systems. *Eur. J. Pharm. Biopharm.* **60,** 247–266.

Meyerhoff, J. D. (2001). Effects of alcohol and HIV infection on the central nervous system. *Alcohol Res. Health* **25,** 288–298.

Miller, R. G., Mitchell, J. D., and Lyon, M. (2007). Riluzole for amyotrophic lateral sclerosis (ALS)/motor neuron disease (MND), Vol. CD001447.

Müller, R. H., and Keck, C. M. (2004). Drug delivery to the brain-realization by novel drug carriers. *J. Nanosci. Nanotechnol.* **4,** 471–483.

Newton, H. B. (2006). Advances in strategies to improve drug delivery to brain tumors. *Expert Rev. Neurother.* **6,** 1495–1509.

Ogiwara, T., Satoh, K., Kadoma, Y., Muratami, Y., Unten, S., Atsumi, T., Sakagami, H., and Fujisawa, S. (2002). Radical scavenging activity and cytotoxicity of ferulic acid. *Anticancer Res.* **22,** 2711–2717.

Olbrich, C., Müller, R. H., and Kayser, O. (2002). Lipid drug conjugate nanoparticles as novel carrier system for the hydrophilic antitrypanosomal drug Diminazene aceturate. *J. Drug Target.* **10,** 387–396.

Olbrich, C., Gessner, A., Schroder, W., Kayser, O., and Muller, R. H. (2004). Lipid–drug conjugate nanoparticles of the hydrophilic drug diminazene—Cytotoxicity testing and mouse serum adsorption. *J. Control. Release* **96,** 425–435.

Oliveira, J. F., Greco, D. B., Oliveira, G. C., Christo, P. P., Guimaraes, M. D., and Oliveira, R. C. (2006). Neurological disease in HIV-infected patients in the era of highly active antiretroviral treatment: A Brazilian experience. *Rev. Soc. Bras. Med. Trop.* **39,** 146–151.

Ono, K., and Yamada, M. (2005). Ferulic acid destabilizes preformed beta-amyloid fibrils in vitro. *Biochem. Biophys. Res. Commun.* **336,** 444–449.

Pardridge, W. M. (2001). Brain drug targeting: The future of brain drug development. Cambridge University Press.

Pardridge, W. M. (2002). Why is the global CNS pharmaceutical market so underpenetrated? *Drug Discov. Today* **7,** 5–7.

Pardridge, W. M. (2005). Molecular biology of the blood–brain barrier. *Mol. Biotechnol.* **30,** 57–69.

Park, J. H., Lee, S., Kim, J. H., Park, K., Kim, K., and Kwon, I. C. (2008). Polymeric nanomedicine for cancer therapy. *Prog. Polym. Sci.* **33,** 113–137.

Picone, P., Bondì, M. L., Montana, G., Bruno, A., Pitarresi, G., Giammona, G., and Di Carlo, M. (2009). Ferulic acid inhibits oxidative stress and cell death induced by Ab oligomers: Improved delivery by solid lipid nanoparticles. *Free Radic. Res.* **43,** 1133–1145.

Pitas, R. E., Boyles, J. K., Lee, S. H., Hui, D., and Weisgraber, K. H. (1987). Lipoproteins and their receptors in the central nervous system. Characterization of the lipoproteins in cerebrospinal fluid and identification of apolipoprotein B, E, (LDL receptors) in the brain. *J. Biol. Chem.* **262,** 14352–14560.

Potmesil, M. (1994). Camptothecins: From bench research to hospital wards. *Cancer Res.* **54,** 1431–1439.

Rabasseda, X., Silvestre, J., and Castañer, J. (1999). BMS-232632. Anti-HIV, HIV-1 protease inhibitor. *Drugs Future* **24,** 375–380.

Reddy, J. S., and Venkateshwarlu, V. (2004). Novel delivery systems for drug targeting to the brain. *Drugs of Future* **29,** 63–83.

Ricci, M., Blasi, P., Giovagnoli, S., and Rossi, C. (2006). Delivering drugs to the central nervous system: A medicinal chemistry or a pharmaceutical technology issue? *Curr. Med. Chem.* **13,** 1757–1775.

Roney, C., Kulkarni, P., Arora, V., Antich, P., Bonte, F., Wu, A., Mallikarjuana, N. N., Manohar, S., Liang, H. F., Kulkarni, A. R., Sung, H. W., Sairam, M., *et al.* (2005). Targeted nanoparticles for drug delivery through the blood-brain barrier for Alzheimer's disease. *J. Control. Release* **108,** 193–214.

Sahu, A., Bora, U., Kasoju, N., and Goswami, P. (2008). Synthesis of novel biodegradable and self-assembling methoxy poly(ethylene glycol)–palmitate nanocarrier for curcumin delivery to cancer cells. *Acta Biomater.* **4,** 1752–1761.

Scott, B. C., Butler, J., Halliwell, B., and Aruoma, O. I. (1993). Evaluation of the antioxidant actions of ferulic acid and catechins. *Free Radic. Res. Commun.* **19,** 241–253.

Shusta, E. V. (2005). Blood–brain barrier genomics, proteomics, and new transporter discovery. *NeuroRx* **2,** 151–161.

Sou, K., Inenaga, S., Takeoka, S., and Tsuchida, E. (2008). Loading of curcumin into macrophages using lipid-based nanoparticles. *Int. J. Pharm.* **352,** 287–293.

Storch, A., Burkhardt, K., and Ludolph, A. C. (2000). Protective effects of riluzole on dopamine neurons: Involvement of oxidative stress and cellular energy metabolism. *J. Neurochem.* **75,** 2259–2269.

Su, Y., and Sinko, P. J. (2006). Drug delivery across the blood-brain barrier: Why is it difficult. How to measure and improve it? *Expert Opin. Drug Deliv.* **3,** 419–435.

Tiwari, S. B., and Amiji, M. M. (2006). A review of nanocarrier-based CNS delivery systems. *Curr. Drug Deliv.* **3,** 219–232.

Vyas, T. K., Shahiwala, A., Marathe, S., and Misra, A. (2006). Intranasal drug delivery for brain targeting. *Curr. Drug Deliv.* **2,** 299–309.

Wang, Z., Zhang, Y., Banerjee, S., Li, Y., and Sarkar, F. H. (2006). Notch-1 down-regulation by curcumin is associated with the inhibition of cell growth and the induction of apoptosis in pancreatic cancer cells. *Cancer* **106,** 2503–2513.

Wissing, S. A., Kayser, O., and Müller, R. H. (2004). Solid lipid nanoparticles for parenteral drug delivery. *Adv. Drug Deliv. Rev.* **56,** 1257–1272.

Yan, J. J., Cho, J. Y., Kim, H. S., Kim, K. L., Jung, J. S., Huh, S. O., Suh, H. W., Kim, Y. H., and Song, D. K. (2000). Protection against beta-amyloid peptide toxicity in vivo with long-term administration of ferulic acid. *Br. J. Pharmacol.* **133,** 89–96.

Yang, S., Zhu, J., Lu, Y., Liang, B., and Yang, C. (1999). Body distribution of camptothecin solid lipid nanoparticles after oral administration. *Pharm. Res.* **16,** 751–757.

CHAPTER THIRTEEN

Transport of a Caspase Inhibitor Across the Blood–Brain Barrier by Chitosan Nanoparticles

Müge Yemişci,[*] Yasemin Gürsoy-Özdemir,[*] Seçil Caban,[†] Ebru Bodur,[‡] Yılmaz Çapan,[†] *and* Turgay Dalkara[*]

Contents

* Institute of Neurological Sciences and Psychiatry and, Department of Neurology, Faculty of Medicine, Hacettepe University, Ankara, Turkey
† Department of Pharmaceutical Technology, Faculty of Pharmacy, Hacettepe University, Ankara, Turkey
‡ Department of Medical Biochemistry, Faculty of Medicine, Hacettepe University, Ankara, Turkey

Methods in Enzymology, Volume 508
ISSN 0076-6879, DOI: 10.1016/B978-0-12-391860-4.00013-6

Abstract

The current treatment of neurological and psychiatric diseases is far beyond being satisfactory. In addition to highly complex disease mechanisms, the blood–brain barrier (BBB) also remains as a challenge by limiting the delivery of the majority of currently available therapeutics to the central nervous system. Several approaches taking advantage of molecular and physicochemical characteristics of the BBB have been developed recently to improve drug delivery to the brain.

Here, we introduce a nanomedicine that can efficiently transport BBB-impermeable peptides to the brain. This nanomedicine is made of chitosan nanoparticles into which considerable amounts of a peptide can be incorporated. The nanoparticle surface is modified with polyethylene glycol to enhance the plasma residence time by preventing their capture by the reticuloendothelial system. Monoclonal antibodies against the transferrin receptor (TfR), which is highly expressed on the brain capillary endothelium, are conjugated to nanoparticles via biotin–streptavidin bonds. The activation of TfR by the nanoparticle–antibody complex induces transcytosis and thus delivers the loaded drug to the brain. Penetration of nanoparticles to the brain can be illustrated *in vivo* by intravital microscopy as well as *ex vivo* by fluorescence or electron microscopy. *N*-Benzyloxycarbonyl-Asp(OMe)-Glu(OMe)-Val-Asp(OMe)-fluoromethyl ketone (Z-DEVD-FMK)-loaded nanoparticles rapidly release their contents within brain parenchyma, inhibit ischemia-induced caspase-3 activity, and thereby provide neuroprotection.

1. Introduction

The blood–brain barrier (BBB) is formed by endothelial cells lining cerebral microvessels. They have no fenestrations, and the junctions between them are sealed by tight junction proteins to limit paracellular diffusion (Abbott *et al.*, 2006). Although this structure is fundamental for the normal function of the central nervous system (CNS), it also introduces a significant challenge in the treatment of brain diseases, as it severely restricts the transport of therapeutic drugs from blood to the brain. Only small molecules (<400 Da) that are lipid soluble pass the BBB in pharmacologically significant amounts (Pardridge, 2007). Essential nutrients like hexoses, amino acids, or peptides are transported by specific carriers or transporters located on the BBB (Begley, 1996; Pardridge, 2007). Similarly, only a small number of hydrophilic therapeutic agents can pass through the BBB by diffusion or facilitated transport, whereas some of these agents are pumped back into the circulation by efflux systems (Begley, 1996; Kreuter, 2001). Therefore, novel strategies are needed urgently to deliver therapeutics across BBB.

One of the recently developed strategies is the use of endogenous transporters localized on the brain capillary endothelium as drug carriers (Aktaş *et al.*, 2005; Kreuter, 2001). The transferrin receptor (TfR), especially the subtype-1, is highly expressed on the luminal side of brain capillary endothelium and could prompt receptor-mediated transcytosis across the BBB when activated (Jefferies *et al.*, 1984; Pardridge *et al.*, 1991). Although directly linking a therapeutic agent to the ligand of this receptor is a plausible strategy to deliver the agent to the brain, this approach can only deliver a limited amount of the drug, when the ratio of drug molecule to carrier protein is around one. On the other hand, it is possible to increase significantly this ratio by loading large amounts of therapeutic molecules into nanoparticles targeted to the carrier systems on the BBB. Indeed, conjugation of nanoparticles with monoclonal antibodies against the TfR1 (TfRMAb) has been shown to direct nanoparticles, together with their contents, into the CNS after systemic administration (Aktaş *et al.*, 2005).

Chitosan polymers are biocompatible and do not cause allergic reactions or immune rejection. Surface modifications, like adding hydrophilic coatings such as polyethylene glycol (PEG), increase the stability and half-life of chitosan nanoparticles in the systemic circulation by preventing their elimination via the reticuloendothelial system (Brigger *et al.*, 2002). Therefore, a larger dose of therapeutic agents can effectively be delivered across the BBB into the CNS with these nanoparticles targeted to the brain by bypassing systemic degradation. The enhanced brain delivery also reduces potential systemic side effects (Zensi *et al.*, 2009).

Caspase-3, among other caspases, is a potent mediator of apoptosis and plays an important role in neuronal death following global or focal cerebral ischemia (Chen *et al.*, 1998; Namura *et al.*, 1998). Caspase-3 is found as an inactive precursor and is cleaved into active subunits following an apoptotic signal (Chen *et al.*, 1998; Namura *et al.*, 1998). Importantly, administration of caspase-3 inhibitors or knocking out the caspase-3 gene leads to increased cell survival following cerebral ischemia, highlighting the critical role of caspases in ischemic injury (Hara *et al.*, 1997; Namura *et al.*, 1998; Schielke *et al.*, 1998). One of these inhibitors, *N*-benzyloxycarbonyl-Asp(OMe)-Glu(OMe)-Val-Asp(OMe)-fluoromethyl ketone (Z-DEVD-FMK), is a specific and irreversible inhibitor of caspase-3 and was shown to decrease infarct volume in experimental models of ischemia when given intracerebroventricularly (Hara *et al.*, 1997). Unfortunately, similar to several other caspase inhibitors, this peptide is unable to pass the BBB and cannot achieve therapeutic levels within the brain parenchyma after systemic administration.

Here, we introduce preparation of a nanomedicine that can transport Z-DEVD-FMK across the BBB and describe the methods evaluating its penetration to the brain and its effect on ischemia-induced caspase activity and stroke.

2. Preparation of Nanoparticles

Chitosan nanoparticles are prepared and loaded with Z-DEVD-FMK (Bachem, USA) and then targeted to the brain by conjugating them with an antibody against the TfR1 on the brain capillary endothelium, according to a previously developed method (Aktaş *et al.*, 2005; Karatas *et al.*, 2009). Chitosan polymers are first modified with PEG chains (PEGylation) to increase the plasma residence time of nanoparticles by inhibiting their capture and elimination via the reticuloendothelial system (Fig. 13.1). The PEGylated polymer (MeO-PEG-OCH_2CO_2H) is synthesized from commercially available MeO-PEG-OH (Sigma-Aldrich, St. Louis, MO) according to previously described procedures (Fernandez-Megia *et al.*, 2007; Royer and Anantharmaiah, 1979).

Briefly, the PEGylated and biotinylated chitosan (CS-PEG-BIO) is dissolved (1 mg/ml) in ultrapure water having an electrical resistance of 18 *M*Ω cm at 25 °C. Nanoparticles are formed from the polymer with ionic gelation by adding a tripolyphosphate (TPP; Sigma, St. Louis, MO) solution (0.84 mg/ml) as a cross-linker onto the chitosan solution in aqueous medium. Concentrations of the polymer and cross-linker solutions and the

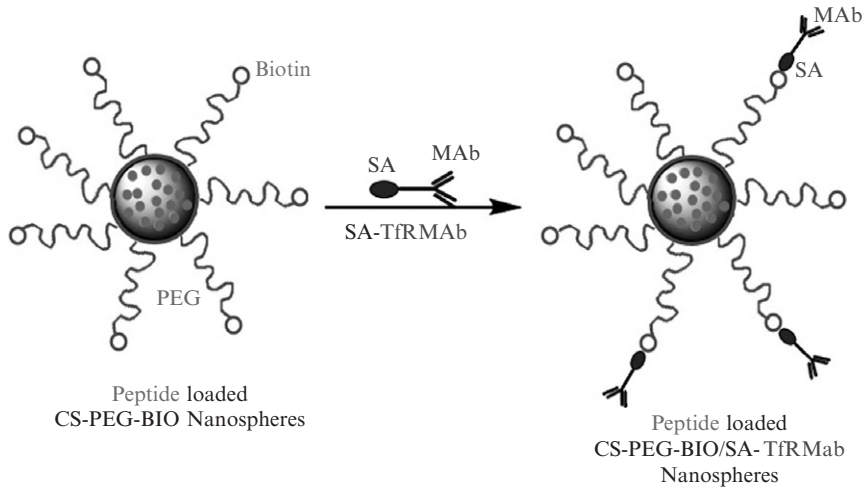

Figure 13.1 Schematic view of nanoparticles. Peptides such as caspase-3 inhibitor Z-DEVD-FMK or Nile red are loaded into chitosan nanoparticles. Their surface is then modified by adding poly(ethylene glycol) (PEG) chains and biotin (CS-PEG-BIO nanoparticles). Anti-mouse transferrin antibodies are conjugated with nanoparticles by means of biotin–streptavidin bonds (modified from Karatas *et al.*, 2009, with permission) (For interpretation of the references to color in this figure legend, the reader is referred to the Web version of this chapter.)

timing are kept constant in all batches to avoid undesirable aggregation or precipitation of nanoparticles as well as a highly variable particle size. The TPP solution is added drop wise onto the polymer solution while stirring. A fixed TPP dropping rate is used to obtain uniform batches. Z-DEVD-FMK (0.133 mg/ml) is incorporated into the polymer before the addition of TPP. The amount of Z-DEVD-FMK solution added is determined depending on the targeted loading concentration (e.g., 10.5 or 42 μl to obtain 50 or 188 ng/ml, respectively; see Section 4.2). The nanoparticle suspension is then centrifuged at 10,000 rpm (9277 × *g*) at 4 °C for 1 h and the supernatant is discarded.

2.1. Conjugation of streptavidin-monoclonal antibody complex with CS-PEG-BIO nanoparticles

Traut's Reagent (4 mg/ml) (2-immunothiolane, Pierce, Thermo Fisher Scientific Inc., Rockford, IL) solution is added into borate buffer and mixed with a Streptavidin (Sigma) solution (7 mg/250 μl water) in equal volumes for 90 min to obtain thiolate streptavidin. One hundred microliters of anti-TfR monoclonal antibody (TfRMAb; functional grade, purified, anti-mouse CD71, clone R17217, eBioscience, San Diego, CA) solution (1 mg/ml) is stirred with 5 μl of *m*-maleimidobenzoyl-*N*-hydroxysuccinimide (Sigma) solution (5 mg/ml in dimethylformamide) for 30 min at ambient conditions to transform some of the amino groups into maleimide groups. Equal volumes of the streptavidin solution and the antibody solution are then added into the CS-PEG-BIO nanoparticle suspension (500 μl). Finally, the mixture is vortexed for 1 min and kept at room temperature for 30 min.

2.2. Characterization of nanoparticles

Particle size and zeta potential measurements of the nanoparticles are performed in triplicate with standard protocols, as described before (Aktaş *et al.*, 2005; Karatas *et al.*, 2009). The drug amount adsorbed into the nanoparticles is calculated by the difference between the total amount of the peptide used and the amount of the nonencapsulated drug, which remains dissolved in the suspension.

For *in vitro* drug release studies, phosphate buffered saline (PBS, pH 7.4) is used as the medium in Eppendorf tubes in a water bath at 37 °C on a horizontal shaker. The supernatants are filtered through cellulose acetate filters before measuring the concentrations. Quantitation of Z-DEVD-FMK is achieved with HPLC (Agilent Technologies 1200 Series apparatus with HP CHEMSTATION software) and a cyano column (150 × 4.6 mm; particle size 5 μm; Clipeus, Higgins Analytical, Inc.). Mobile phase is a mixture of water:acetonitrile (80:20) containing 0.1% TFA. Twenty microliters of the

mobile phase is injected at a flow rate of 1 ml/min. Z-DEVD-FMK is detected at 215 nm wavelength (Aktaş *et al.*, 2005).

3. *In Vivo* Experiments with Nanoparticles Loaded with a Caspase Inhibitor

The penetration of nanoparticles into the brain *in vivo* can be monitored by using intravital fluorescence microscopy and can be verified by histopathologic evaluation of brain sections obtained from mice treated with nanoparticles (Karatas *et al.*, 2009). The *in vivo* neuroprotective effect of nanoparticles loaded with a caspase inhibitor is evaluated by using an experimental model of focal cerebral ischemia (Karatas *et al.*, 2009).

3.1. *In vivo* monitoring of nanoparticle penetration into the brain parenchyma by intravital fluorescent microscopy

Swiss albino mice are anesthetized with isoflurane during surgery and with urethane (750 mg/kg, intraperitoneal, followed by 500 mg/kg 30 min later) during the experiment. Physiologic parameters are closely monitored during the experiments: Body temperature is continuously measured by a rectal probe and kept at 37.0 ± 0.2 °C with a homeothermic blanket (Harvard Apparatus, Holliston, MA). Systolic blood pressure is monitored noninvasively by using a cuff and tail probe (NIBP controller; AD Instruments). Pulse rate and oxygen saturation are followed online by an oxymeter using a mini Y clip attached on the left lower extremity (V3304 Tabletop Pulse Oximeter; SurgiVet, Dublin, OH).

A cranial window of 5 × 5 mm is opened over the parietotemporal cortex, leaving the dura mater and cortex intact, blood pressure and oxygenation are maintained within normal limits in order to avoid cerebrovascular dysfunction. When drilling the cranial window, caution is taken for not heating the brain, hence, the cranium is frequently washed with saline. The cranium is firmly fixed to make sure that there is no head movement with the respiration of the animal. The window is sealed with dental acrylic and then filled with artificial cerebrospinal fluid (124 m*M* NaCl, 5 m*M* KCl, 1.25 m*M* NaH_2PO_4, 1.3 m*M* $MgSO_4$, 2.4 m*M* $CaCl_2$, 25 m*M* $NaHCO_3$, 10 m*M* glucose, pH 7.4) heated to 37 °C. The lightening conditions are kept constant for the recording of sequential fluorescence images throughout the experiment.

TfRMAb-conjugated or -unconjugated nanoparticles loaded with Nile red are administered intravenously via the tail vein of mice in order to assess the penetration of nanopheres into the brain parenchyma *in vivo*. Nile red is chosen as it emits intense fluorescence, is not biodegradable, can be reliably

detected by spectrophotometry, and can be efficiently loaded to nanoparticles (Gessner *et al.*, 2001). Fluorescent images are recorded under a Nikon Eclipse E600 microscope at 100 × magnification in dark by using a camera and imaging software (Nikon DXM1200 and NIS Elements Advanced Research v.2.32, Nikon) at baseline and after the injection of nanoparticles (1, 5, 10, 20, and 30 min after injection and then every 15 min for 3 h) using the same exposure time and gain settings. Images are saved in TIFF format to calculate the mean fluorescence intensity within the imaged area using the same imaging software.

The fluorescence emitted from TfRMAb-free nanoparticles, since they cannot pass the BBB, is as a reflection of Nile red fluorescence coming from nanoparticles in the brain circulation. On the other hand, the fluorescent signal emitted from TfRMAb-conjugated nanoparticles reflects the total pool of nanoparticles within the brain as well as circulation. Therefore, the difference between the fluorescent signals obtained in experiments performed with conjugated and unconjugated nanoparticles corresponds to the net signal coming from the nanoparticles penetrating the brain. Our experiments showed that the fluorescence from unconjugated nanoparticles peaked within 10 min of administration and gradually diminished over a period of 2 h, reflecting the elimination kinetics of circulating nanoparticles (Fig. 13.2). The fluorescence from TfRMAb-conjugated nanoparticles, however, continued to increase after the 10th minute of injection, and a significant signal was sustained during a 3-h follow up. The net difference between these curves suggests that nanoparticles functionalized with TfRMAb successfully penetrate into the brain tissue and this penetration starts as early as 10 min after systemic administration and reaches a peak within 75 min (Karatas *et al.*, 2009).

3.2. Determination of tissue Nile red concentration to evaluate nanoparticle distribution

UV spectrophotometry can be used to determine the tissue Nile red concentration in the brain, liver, and spleen. Tissues are homogenized (20%, w/v) in 25 m*M* HEPES (pH 7.4), 2 m*M* EDTA, 2 m*M* EGTA, 2 m*M* DTT, 5 m*M* $MgCl_2$, %0.1 Triton X-100 containing 10 μg/ml protease inhibitor cocktail and 3 ml of 1% phosphoric acid is added to 500 μl of homogenate to precipitate proteins followed by 3 ml of butanol to extract the lipid phase. The mixture is vortexed for 1 min at 2000 rpm and centrifuged at 2500 × *g* for 15 min. After this process, the extracted lipids as well as Nile red can be found in the upper butanol phase. Nile red in this media was found to have an absorbance peak at 549 nm through spectrophotometric analysis (Karatas *et al.*, 2009). No significant Nile red accumulation was detected in liver or spleen homogenates (Fig. 13.2). However, in brain homogenates of mice injected with TfRMAb-conjugated nanoparticles, there was a strong

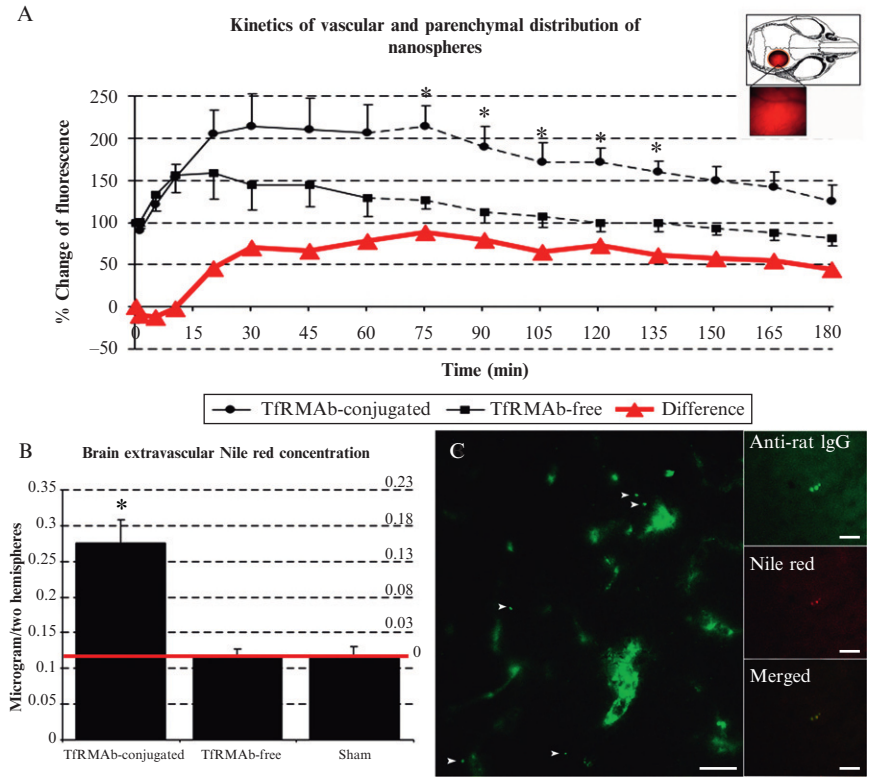

Figure 13.2 (A) Nanoparticles are rapidly transported to brain parenchyma after systemic administration. The graph illustrates the change in fluorescence recorded from the brain over the course of 3 h after injection of Nile red-loaded to TfRMAb-conjugated or -unconjugated nanoparticles. The difference between the two lines (red line) reflects the fluorescence coming from the nanoparticles within the parenchyma and illustrates the time course of nanoparticle penetrance to the brain. (B) Nile red concentration in brain postvascular tissue increased only when TfRMAb-conjugated nanoparticles were administered. The graph illustrates spectrophotometric measurements at 549 nm from brain homogenates obtained 1 h after injection of TfRMAb-conjugated or -unconjugated nanoparticles or from sham-operated mice. Only values above the horizontal red line, below which values correspond to the tissue background readings, were taken into consideration. (C) Penetration of the nanoparticles to the parenchyma was confirmed by fluorescent microscopy on brain sections obtained 1 h after injection. FITC-conjugated anti-rat IgG antibody (green) labeled the nanoparticles bearing TfRMAb, clearly demonstrating that the nanoparticles were dispersed within the extracellular space outside the vessel lumens. Vessels were visualized by nonspecific labeling obtained with a high concentration of the antibody. Some FITC-conjugated nanoparticles exhibited green as well as red fluorescence because they had not released within an hour all the Nile red that was loaded (right). A lower concentration of the antibody was used to stain these sections; hence, vessels were not labeled. Scale bars: (C) left panel, 15 μm; (C) right panels, 5 μm (reprinted from Karatas *et al.*, 2009, with permission).

spectrophotometric signal at 549 nm (Karatas *et al.*, 2009). These findings are consistent with the idea that TfRMAb conjugated to nanoparticles, being selective to the TfR type 1 on cerebral vasculature (Lee *et al.*, 2000), lead to preferential accumulation of nanoparticles in the brain.

3.3. Histological demonstration of nanoparticles within the brain parenchyma

The penetration of nanoparticles into the brain can also be demonstrated by using FITC-labeled nanoparticles and immunofluorescence microscopy. However, it is recommended that the examiner should familiarize himself with the appearance of nanoparticles first *in vitro* and then in sections prepared from mouse brains to which nanoparticles were directly injected. Nanoparticles appear as discrete fluorescent dots or as small aggregates in suspensions containing FITC-labeled nanoparticles (1 mg in 200 µl saline; Fig. 13.3). FITC-labeled nanoparticles (1 mg in 200 µl saline) are injected with a microsyringe into the right frontal cortex. Mice are immediately decapitated and the brains are kept at −80 °C until use. Frozen coronal sections of 20 µm thickness, passing through the injection site are then obtained and examined under fluorescence microscopy (Nikon Eclipse E600, λ_{ex} 450–490 nm). Nanoparticles are observed as fluorescent spherical particles, sometimes forming aggregates on brain sections, similar to their appearance in suspension (Fig. 13.3).

FITC-labeled (1 mg in 200 µl saline) TfRMAb-conjugated or -unconjugated nanoparticles are injected intravenously to mice via the tail vein. Mice are transcardially perfused with saline to flush the intravascular content, including the nanoparticles, and are then decapitated 1 and 2 h after injection. The sections are coverslipped with mounting medium containing Hoechst-33258 to counterstain the nuclei. The systemically administered TfRMAb-conjugated nanoparticles were distributed in both hemispheres (Fig. 13.3). The nanoparticles were localized in the brain parenchyma, outside the vascular lumen identified by the surrounding endothelial nuclei. However, no evidence for nanoparticle penetration into brain was observed in mice injected with nanoparticles not conjugated with TfRMAb (Aktaş *et al.*, 2005).

TfRMAb-conjugated nanoparticles loaded with Nile red can also be used to determine the passage of the nanoparticles through the BBB with help of their red fluorescence. At the end of the above described experiments performed with intravital fluorescence microscopy (Karatas *et al.*, 2009), mice are transcardially perfused with saline to flush all the intravascular content, including the nanoparticles loaded with Nile red. The brain, liver, and spleen are removed, immediately frozen, and kept at −80 °C until use. Fresh-frozen, 20 µm-thick coronal brain sections are cut, fixed with 96% ethanol for 10 min and washed with PBS. An antibody against the rat

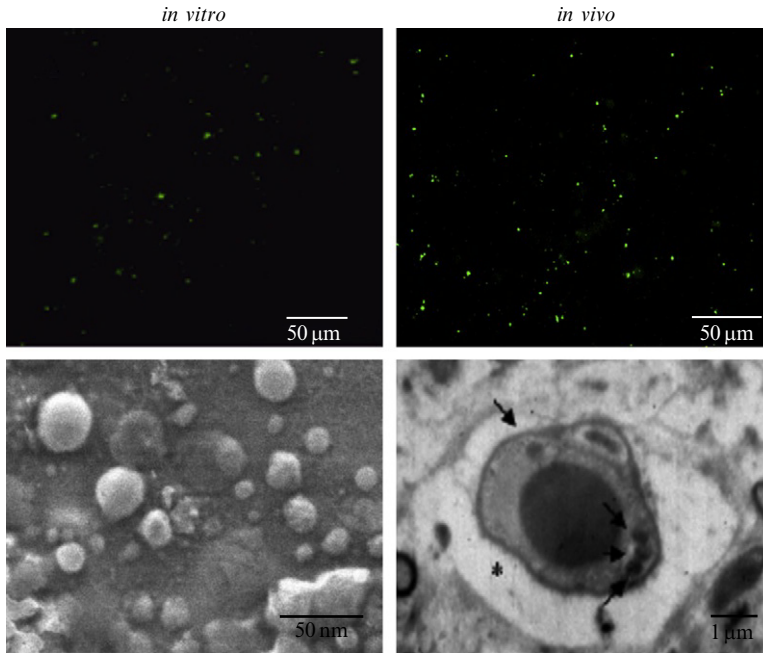

Figure 13.3 Nanoparticles can be visualized by fluorescence microscopy as well as electron microscopy. The column on the left illustrates nanoparticles in aqueous milieu *in vitro*. FITC-labeled nanoparticles are identified as small dots under the fluorescence microscope, and electron dense particles with the electron microscope. After i.v. administration (right column), FITC-labeled nanoparticles are visible in brain tissue sections similar to those observed with *in vitro* imaging. The electron micrograph clearly shows that nanoparticles are transferred into the brain capillary endothelium from circulation (modified from Aktaş *et al.*, 2005, with permission). (For the color version of this figure, the reader is referred to the Web version of this chapter.)

IgG2a is employed to visualize the nanoparticles conjugated with TfRMAb because the TfRMAb is a rat IgG2a. Therefore, the sections are immunostained by using FITC-conjugated goat anti-rat IgG antibody (Sigma, at 1:100 and 1:200 dilutions, in PBS) at room temperature for 60 min to detect TfRMAb-conjugated nanoparticles via the green fluorescence of FITC. Colocalization of the green fluorescence of FITC with the red fluorescence of Nile red ensures that the observed fluorescent dots are nanoparticles (Fig. 13.2). Sections are also coverslipped with mounting medium containing Hoechst 33258 to identify endothelial nuclei. Fluorescence microscopy of these brain sections showed that nanoparticles functionalized with TfRMAb were dispersed within the brain parenchyma, outside the vessel lumens, confirming the successful transfer of nanoparticles across the BBB (Fig. 13.2). Negative controls are carried out by omitting the anti-rat IgG antibody (Karatas *et al.*, 2009).

3.4. Electron microscopy

Nanoparticles can be identified unequivocally by electron microscopy. For this purpose, 1 mm^3 specimens from the frontal cortex, striatum, and the occipital cortices of the hemispheres are examined with transmission electron microscopy. The specimens are fixed in 2.5% gluteraldehyde for 24 h, and after washing in phosphate buffer (pH 7.4), they are fixed in 1% osmium tetroxide (in phosphate buffer) and dehydrated in graded alcohol. After washing the tissues with propylene oxide and embedding them in epoxy-resin embedding media, semithin (2 μm) and ultrathin (60 nm) sections are cut with an LKB-Nova (Bromma, Sweden) ultramicrotome having a glass knife. The sections are stained with methylene blue and examined under a Nikon Optiphot (Japan) light microscope. After trimming, the semi and ultrathin sections are collected on copper grids, stained with uranyl acetate and lead citrate, and examined with a JEOL JEM 1200 EX (Japan) transmission electron microscope. The TfRMAb-conjugated, peptide-unloaded nanoparticles were detected as dense spherical particles with an approximate diameter of 200 nm within the endothelium of the brain blood vessels as well as brain parenchyma (Fig. 13.3; Aktaş *et al.*, 2005).

4. The Neuroprotective Effect of Nanoparticles Loaded with a Caspase Inhibitor

4.1. Focal cerebral ischemia model

Male Swiss albino mice (25–30 g) are housed under diurnal lighting conditions and fasted overnight but allowed *ad libitum* access to water before the experiment. The intraluminal filament middle cerebral artery occlusion (MCAo) model is used to induce focal cerebral ischemia (Gursoy-Ozdemir *et al.*, 2000). In this model, after ligation of the right common and external carotid arteries with a 5-0 silk suture, a nylon filament (8-0) is inserted into the right common carotid artery through a small incision proximal to the bifurcation in anesthetized mice and is advanced up to origin of middle cerebral artery (MCA) via the internal carotid artery (10 mm from the bifurcation) to cause cessation of blood flow in the MCA territory. The tip of filament is coated with silicone resin/hardener mixture (Xantropen M Haereus Kulzer, and Optosil-Xantropen Activator, Bayer) to provide smooth move in the lumen. The filament is withdrawn after 2 h of MCAo to establish reperfusion. Throughout the experiments, the regional cerebral blood flow (rCBF) is monitored by laser Doppler (PF-318 of PeriFlux PF 2B; Perimed) using a fiber optic flexible probe placed over the temporal bone 2 mm posterior, 6 mm lateral to the bregma, and away from large pial vessels. This is instrumental to confirm occlusion and

reperfusion. Physiologic parameters (blood pressure, body temperature, rCBF, pulse rate, and tissue oxygen saturation) are also monitored closely during cerebral ischemia, as described above. There must be no significant differences between the physiologic parameters of the experimental groups, so that the changes determined in infarct volumes could be attributed to the effect of the therapeutics.

4.2. Neuroprotection study groups

To evaluate the neuroprotective effect of nanoparticles loaded with Z-DEVD-FMK, various groups of mice are subjected to 2 h of MCAo and 24 h of reperfusion. Control groups receive either drug unloaded TfRMAb-conjugated nanoparticles or TfRMAb-unconjugated nanoparticles loaded with the peptide. The treatment groups receive injections of TfRMAb-conjugated nanoparticles loaded with 50 ng/mg of Z-DEVD-FMK (low-dose group) or 188 ng/mg of Z-DEVD-FMK (high-dose group). Nanoparticles (1 mg of nanoparticle in 10 μl of saline) are administered just before induction of ischemia via the tail vein in all experimental groups, except in one group of mice that are treated with nanoparticles loaded with a high dose of the caspase inhibitor just before establishing reperfusion (postischemia treatment group; Karatas *et al.*, 2009).

The neuroprotective effect of nanoparticles loaded with the caspase inhibitor can be assessed by neurological evaluation of mice, the infarct volume and caspase activity. Twenty hours after reperfusion, prior to scarification, the neurologic deficit is scored in each animal, with a previously validated scale ranging from 0 to 3; 0 designating no significant neurologic deficit and 3 designating severe neurologic deficit (Huang *et al.*, 1994). Treatment with TfRMAb-conjugated nanoparticles containing Z-DEVD-FMK leads to significant improvement in neurological deficits. The mean ± SEM neurological deficit scores 24 h after reperfusion were 2.8 ± 0.2 in the peptide-free (blank) nanoparticle group, 2.6 ± 0.2 in the TfRMAb-unconjugated nanoparticle group, 2.0 ± 0.2 in the low-dose Z-DEVD-FMK group, 1.5 ± 0.3 in the high-dose Z-DEVD-FMK group, and 2.3 ± 0.2 in the high-dose Z-DEVD-FMK/postischemia group ($p < 0.05$ when compared with the peptide-free (blank) and the TfRMAb-unconjugated group; Karatas *et al.* 2009).

For evaluation of the infarct volume, mice are anesthetized with a lethal dose of chloral hydrate 24 h after reperfusion. Mice are transcardially perfused with 100 ml of heparinized ultra pure water (10 IU/ml) followed by 4% paraformaldehyde and then decapitated. Brains are stored in 4% paraformaldehyde for 48 h, after which 2-mm thick coronal sections are serially cut, starting from the frontal pole. Slices are then embedded in paraffin and 5 μm-thick sections are obtained from the posterior surface of each slab and stained with hematoxylin and eosin. The boundary of the infarct area,

characterized by reduced eosin staining under light microscopy, is outlined using an image analysis software (ImageJ 1.59, NIH, Bethesda, MD) to calculate the infarct volume. We found that the infarct volumes in mice receiving Z-DEVD-FMK-free (blank) and TfRMAb-unconjugated nanoparticles were 43 ± 4 and 50 ± 4 mm^3, respectively (Fig. 13.4). Treatment with nanoparticles loaded with Z-DEVD-FMK significantly and dose-dependently decreased the infarct volume ($p < 0.05$). The volumes were 33 ± 3 mm^3 with low-dose Z-DEVD-FMK, 26 ± 4 mm^3 with high-dose Z-DEVD-FMK and 32 ± 2 mm^3 with high-dose Z-DEVD-FMK, when administered postischemia (Karatas *et al.*, 2009). The neuroprotection obtained in the posttreatment group in which Z-DEVD-FMK was given 2 h after ischemia is of clinical importance, because the therapeutic time window in stroke patients is limited to the first 3 h after stroke onset and the delayed treatment is usually ineffective.

4.3. Determination of caspase-3 activity

Caspase-3 activity in the ischemic brain tissue can also be utilized to assess the effect of systematically administered Z-DEVD-FMK-loaded nanoparticles. Caspases are enzymes of the cysteine–aspartic acid protease family. They are present in cells as zymogens and are activated upon proteolytic cleavage. Assays of caspase-3 activity must take into account several factors, one of which is the efficiency of the active-site histidine and cysteine pair. The histidine imidazole has a pK_a of 6 and cysteine has a pK_a of 8. The optimal caspase-3 activity occurs at pH 7.4 (the intracellular value). It should also be kept in mind that the cysteine side chain must be protonated. For this reason, in all assays, the concentration of active site cysteine is maintained by addition of the reducing agent, dithiothreitol (DTT) at a final concentration of 2 m*M*. Membrane penetration is achieved by the strong hydrophobic reagent 0.1% TX-100, whereas 2 m*M* EGTA, 2 m*M* EDTA, 5 m*M* $MgCl_2$ are added to the buffer composition to keep the intracellular cofactor concentrations constant.

As previous studies showed a peak in caspase-3 activity 1 h after reperfusion (Ma *et al.*, 1998, 2001), mice are sacrificed 2 h after MCAo and 1 h of reperfusion. Brains kept on ice are weighed and homogenized (20%, w/v) using an Omni 5000 homogenizer (Kennisaw, GA) at 3000 rpm in 25 m*M* HEPES, pH 7.4, 2 m*M* EDTA, 2 m*M* EGTA, 2 m*M* DTT, 5 m*M* $MgCl_2$, 0.1% Triton X-100, and 10 μg/ml protease inhibitor mixture. The homogenates are centrifuged at 4 °C, 12,000 × *g* for 20 min. The clear supernatants are used for caspase-3 activity and protein determination. All assays are done at least in duplicate. Caspase-3 activity is determined using the fluorogenic caspase-3 substrate (*N*-acetyl)-Asp-Glu-Val-Asp-7-amino-4-trifluoromethyl-coumarin (Ac-DEVD-AFC) ApoScreen Kit from ICN Biomedicals (Solon, OH). Briefly, 25 μl of tissue homogenate is added to each well in a 96-well

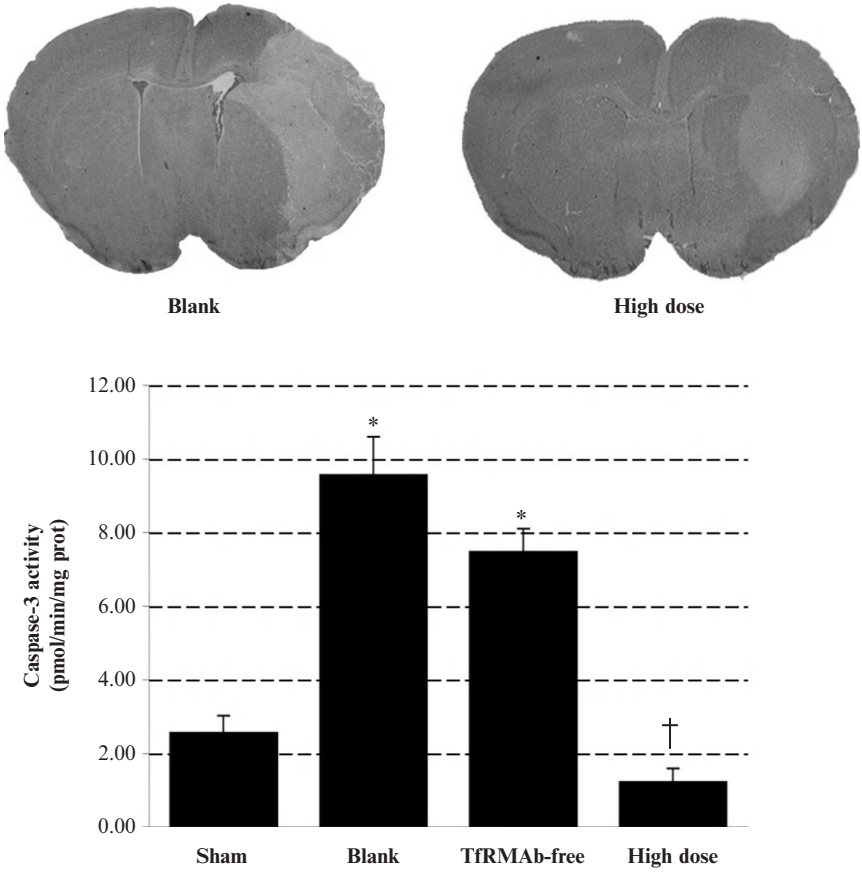

Figure 13.4 Caspase inhibitor-loaded nanoparticles suppress the ischemia-induced increase in caspase-3 activity and provide neuroprotection after systemic administration. Coronal brain sections stained with hematoxylin and eosin illustrate the representative infarct areas (pale) from mice subjected to 2 h of ischemia and 24 h of reperfusion, and treated with blank (control), or high-dose Z-DEVD-FMK-loaded nanoparticles. Caspase-3 activity was detected in hemispheres obtained from mice subjected to either sham surgery or 2 h MCA occlusion and 1 h reperfusion. Nanoparticles loaded with a high dose of Z-DEVD-FMK and conjugated with TfRMAb antibody (high-dose) significantly inhibited caspase-3 activity, whereas nanoparticles not loaded with the peptide (blank) or unconjugated with TfRMAb (TfRMAb-free) were ineffective. *Significant difference when compared with the sham-operated group. †No significant difference when compared with the sham-operated group. Prot, protein (modified from Karatas *et al.*, 2009, with permission). (For the color version of this figure, the reader is referred to the Web version of this chapter.)

plate already containing 222.5 µl of 100 m*M* HEPES, pH 7.4, and 2 m*M* DTT. The reaction is initiated by the addition of fluorogenic 2.5 µl of Ac-DEVD-AFC at a final concentration of 200 µ*M*. Parallel samples are incubated for

25 min with the competitive inhibitor Z-DEVD-FMK (final concentration 40 μM) before adding the substrate. Activity measurements utilizing an end point assay are performed at baseline and 35 min later (excitation 400, emission 505 nm) with a spectrofluorometric plate reader (SpectraMax M2, Molecular Devices, Sunnyvale, CA) and software (SOFTmax Pro 3.1.1, Molecular Devices). Caspase-3 activity (fluorescence units per milligram protein per minute of reaction time) is calculated from the slope of the difference between substrate utilization velocity in the samples with and without caspase-3 inhibitor. This measurement is then converted to picomoles of substrate cleaved per milligram of protein per minute, based on a standard curve for amino-4-trifluoromethylcoumarin. The protein concentration in the supernatant is determined by the Bradford assay. These assays also confirmed the efficient transfer of nanoparticles across the BBB by showing that caspase-3 activity was suppressed significantly in mice receiving conjugated nanoparticles loaded with high-dose Z-DEVD-FMK when compared to mice receiving peptide-free (blank) or TfRMAb-unconjugated nanoparticles ($p < 0.05$; Fig. 13.4; Karatas *et al.*, 2009).

5. Concluding Remarks

Brain-targeted nanoparticles loaded with BBB-impermeable drugs create new and exciting opportunities for treatment of CNS disorders. These nanomedicines not only have the potential of achieving therapeutic drug levels in the brain but may also decrease their systemic side effects by selectively targeting therapeutics to the brain. Although currently used pharmacological end points are useful as screening tools, we need advanced technologies that will allow us to study the *in vivo* kinetics of nanoparticle penetration to the CNS to further develop these novel drug carriers (e.g., by modifying the particle size, shape, and surface characteristics). Moreover, identification of the most efficient carrier (e.g., the insulin receptor) on human brain capillary endothelial cells is necessary to translate these nanotechnologies to the clinic, despite the fact that the mouse TfR system currently provides a satisfactory experimental model.

ACKNOWLEDGMENTS

We wish to thank all of our colleagues including our collaborators in France (Patrick Couvreur, Karine Andrieux from Universite´ Paris Sud) and Spain (Eduardo Fernandez-Megia, Ramon Novoa-Carballal, Ricardo Riguera from Universidad de Santiago de Compostela) for their important contributions to the development of the nanoparticles used in studies cited in the chapter. Dr. Turgay Dalkara's work is supported by the Turkish Academy of Sciences.

REFERENCES

Abbott, N. J., Rönnbäck, L., and Hansson, E. (2006). Astrocyte-endothelial interactions at the blood-brain barrier. *Nat. Rev. Neurosci.* **7,** 41–53.

Aktaş, Y., Yemisci, M., Andrieux, K., Gürsoy, R. N., Alonso, M. J., Fernandez-Megia, E., Novoa-Carballal, R., Quiñoá, E., Riguera, R., Sargon, M. F., Celik, H. H., Demir, A. S., *et al.* (2005). Development and brain delivery of chitosan-PEG nanoparticles functionalized with the monoclonal antibody OX26. *Bioconjug. Chem.* **16,** 1503–1511.

Begly, D. M. (1996). The blood-brain-barrier: Principles for targeting peptides and drugs to the central nervous system. *J. Pharm. Pharmacol.* **48,** 136–146.

Brigger, I., Morizet, J., Aubert, G., Chacun, H., Terrier-Lacombe, M. J., Couvreur, P., and Vassal, G. (2002). Poly(ethylene glycol)-coated hexadecylcyanoacrylate nanoparticles display a combined effect for brain tumor targeting. *J. Pharmacol. Exp. Ther.* **303,** 928–936.

Chen, J., Nagayama, T., Jin, K., Stetler, R. A., Zhu, R. L., Graham, S. H., and Simon, R. P. (1998). Induction of caspase-3-like protease may mediate delayed neuronal death in the hippocampus after transient cerebral ischemia. *J. Neurosci.* **18,** 4914–4928.

Fernandez-Megia, E., Novoa-Carballal, R., Quinoa, E., and Riguera, R. (2007). Conjugation of bioactive ligands to PEG-grafted chitosan at the distal end of PEG. *Biomacromolecules* **8,** 833–842.

Gessner, A., Olbrich, C., Schröder, W., Kayser, O., and Müller, R. H. (2001). The role of plasma proteins in brain targeting: Species dependent protein adsorption patterns on brain-specific lipid drug conjugate (LDC) nanoparticles. *Int. J. Pharm.* **214,** 87–91.

Gursoy-Ozdemir, Y., Bolay, H., Saribas, O., and Dalkara, T. (2000). Role of endothelial nitric oxide generation and peroxynitrite formation in reperfusion injury after focal cerebral ischemia. *Stroke* **31,** 1974–1981.

Hara, H., Friedlander, R. M., Gagliardini, V., Ayata, C., Fink, K., Huang, Z., Shimizu-Sasamata, M., Yuan, J., and Moskowitz, M. A. (1997). Inhibition of interleukin 1beta converting enzyme family proteases reduces ischemic and excitotoxic neuronal damage. *Proc. Natl. Acad. Sci. USA* **94,** 2007–2012.

Huang, Z., Huang, P. L., Panahian, N., Dalkara, T., Fishman, M. C., and Moskowitz, M. A. (1994). Effects of cerebral ischemia in mice deficient in neuronal nitric oxide synthase. *Science* **265,** 1883–1885.

Jefferies, W. A., Brandon, M. R., Hunt, S. V., Williams, A. F., Gatter, K. C., and Mason, D. Y. (1984). Transferrin receptor on endothelium of brain capillaries. *Nature* **312,** 162–163.

Karatas, H., Aktaş, Y., Gursoy-Ozdemir, Y., Bodur, E., Yemisci, M., Caban, S., Vural, A., Pinarbasli, O., Capan, Y., Fernandez-Megia, E., Novoa-Carballal, R., Riguera, R., *et al.* (2009). A nanomedicine transports a peptide caspase-3 inhibitor across the blood-brain barrier and provides neuroprotection. *J. Neurosci.* **29,** 13761–13769.

Kreuter, J. (2001). Nanoparticulate systems for brain delivery of drugs. *Adv. Drug Deliv. Rev.* **47,** 65–81.

Lee, H. J., Engelhardt, B., Lesley, J., Bickel, U., and Pardridge, W. M. (2000). Targeting rat anti-mouse transferrin receptor monoclonal antibodies through bloodbrain barrier in mouse. *J. Pharmacol. Exp. Ther.* **292,** 1048–1052.

Ma, J., Endres, M., and Moskowitz, M. A. (1998). Synergistic effects of caspase inhibitors and MK-801 in brain injury after transient focal cerebral ischaemia in mice. *Br. J. Pharmacol.* **124,** 756–762.

Ma, J., Qiu, J., Hirt, L., Dalkara, T., and Moskowitz, M. A. (2001). Synergistic protective effect of caspase inhibitors and bFGF against brain injury induced by transient focal ischaemia. *Br. J. Pharmacol.* **133,** 345–350.

Namura, S., Zhu, J., Fink, K., Endres, M., Srinivasan, A., Tomaselli, K. J., Yuan, J., and Moskowitz, M. A. (1998). Activation and cleavage of caspase-3 in apoptosis induced by experimental cerebral ischemia. *J. Neurosci.* **18,** 3659–3668.

Pardridge, W. M. (2007). Drug targeting to the brain. *Pharm. Res.* **24,** 1733–1744.

Pardridge, W. M., Buciak, J. L., and Friden, P. M. (1991). Selective transport of an anti transferrin receptor antibody through the blood-brain barrier *in vivo*. *J. Pharmacol. Exp. Ther.* **259,** 66–70.

Royer, G. P., and Anantharmaiah, G. (1979). Peptide synthesis in water and the use of immobilized carboxypeptidase Y for deprotection. *J. Am. Chem. Soc.* **101,** 3394–3396.

Schielke, G. P., Yang, G. Y., Shivers, B. D., and Betz, A. L. (1998). Reduced ischemic brain injury in interleukin-1 beta converting enzyme-deficient mice. *J. Cereb. Blood Flow Metab.* **18,** 180–185.

Zensi, A., Begley, D., Pontikis, C., Legros, C., Mihoreanu, L., Wagner, S., Büchel, C., von Briesen, H., and Kreuter, J. (2009). Albumin nanoparticles targeted with Apo E enter the CNS by transcytosis and are delivered to neurones. *J. Control. Release* **137,** 78–86.

CHAPTER FOURTEEN

Nanotechnology as a Promising Strategy for Alternative Routes of Insulin Delivery

Catarina Pinto Reis* *and* Christiane Damgé†

Contents

Abstract

Since its discovery, insulin has been used as highly specific and effective therapeutic protein to treat type 1 diabetes and later was associated to oral antidiabetic agents in the treatment of type 2 diabetes. Generally, insulin is administered parenterally. Although this route is successful, it still has several limitations, such as discomfort, pain, lipodystrophy at the injection sites and peripheral hyperinsulinemia, which may be the cause of side effects and some complications. Thus, alternative routes of administration have been developed, namely, those based on nanotechnologies. Nanoparticles, made of synthetic or natural materials, have been shown to successfully overcome the inherent

* CBIOS-LNBN (Laboratory of Nanoscience and Biomedical Nanotechnology) and Faculty of Sciences and Health Technologies, Lusophone University of Humanities and Technologies, Lisbon, Portugal
† EA 3452, University Henri Poincaré, Faculty of Pharmacy, Nancy, France

Methods in Enzymology, Volume 508
ISSN 0076-6879, DOI: 10.1016/B978-0-12-391860-4.00014-8

barriers for insulin stability, degradation, and uptake across the gastrointestinal tract and other mucosal membranes. This review describes some of the many attempts made to develop alternative and more convenient routes for insulin delivery.

1. Introduction

Diabetes mellitus is a chronic metabolic disease characterized by an abnormal elevation of blood glucose levels which can lead to chronic micro- and macrovascular complications including neuropathy, nephropathy, retinopathy, and cardiovascular diseases. The incidence of diabetes largely increases around the world. The number of diabetic patients has grown from 30 million in 1985 to the current 171 million in 2000 and is expected to grow to 366 million people in 2025 (Damgé *et al.*, 2008).

Diabetes can be briefly classified in two main types: (i) type 1 diabetes which is caused by an autoimmune destruction of insulin beta cells in the pancreas and is controlled by parenteral administration of insulin; (ii) type 2 diabetes which is characterized by variable degrees of insulin resistance, impaired secretion of insulin and increased glucose production, and is generally controlled by oral antidiabetic agents when life style changes are no more efficient; and finally, when these therapeutics failed to reduce glycemia, these patients are also treated with insulin.

Conventionally, the treatment of diabetes is based on the subcutaneous (s.c.) administration of exogenous insulin in order to supply its physiological secretion. Although this parenteral route of administration is satisfactory in terms of efficacy, it can result in peripheral hyperinsulinemia which has been associated with hypertension, development of atherosclerosis, and increased insulin resistance in peripheral and muscle tissues (Del Prato *et al.*, 1994). Additionally, the burden of daily injections can also result in a psychological discomfort, pain, high probability of infections, and local deposition of insulin leading to local lipodystrophy at the injections sites. Thus, this can lead to poor patient compliance.

Despite progresses in devices for the injection of insulin, several approaches for alternative routes of administration of insulin have been developed such as oral, buccal, nasal, rectal, pulmonary, ocular, and transdermal routes (Brange and Langkjoer, 1997; Owens *et al.*, 2003; Peppas and Kavimandan, 2006). However, the oral route is considered to be the most convenient and physiological. Indeed, insulin absorbed by the intestinal epithelium reaches the liver through the portal vein and can directly inhibit hepatic glucose output (Peppas and Kavimandan, 2006). The effect of insulin on the liver is essential in the maintenance of glucose homeostasis. Parenteral administration of insulin never mimics the natural secretion of

insulin by the pancreatic islets of Langerhans since it is first delivered to peripheral tissues (Peppas and Kavimandan, 2006) and only 20% of injected insulin can target the liver.

However, insulin, a 51 amino acid peptide, cannot be orally administered because it is unstable in the gastrointestinal tract (GIT); it is degraded by proteolytic enzymes; and finally, it is less absorbed by the intestinal epithelium (<0.5% under physiological conditions) mainly due to the large size and hydrophilicity of the molecule (Damgé *et al.*, 2008; Reis *et al.*, 2008a).

Other routes of administration of insulin have also been explored such as the inhaled insulin, nasal, buccal, and transdermal insulin because these absorption surfaces of insulin are very large but bioavailabilities are generally low.

Thus, novel strategies based on nanotechnologies may be promising to improve the bioavailability of insulin using these alternative routes of administration, which are always better accepted by patients than the classical s.c. administration with insulin pens. The concept is based on the encapsulation of insulin in particular drug carriers able to protect the hormone against enzymes and to improve its uptake through the intestinal wall or other mucosae.

Nanoparticles are solid colloidal drug carriers ranging from 10 to 1000 nm in size. They are composed of natural, semisynthetic, or synthetic polymers that may or may not be biodegradable (Soppimath *et al.*, 2001). Nanoparticles are a collective name for nanospheres and nanocapsules. Nanocapsules comprise a vesicular structure with an inner core surrounded by a polymeric wall. Nanospheres are full polymeric structures. Insulin may be adsorbed at the surface of the polymer or entrapped in the polymer. However, in the case of nanocapsules, insulin is usually inside the inner core of the nanoparticulate system (Damgé *et al.*, 2008; Pinto Reis *et al.*, 2006b).

The next section will explore several current methods of alternative delivered insulin using nanotechnologies, including their progress to date, their limitations, and hopeful future.

2. Oral Administration of Insulin

2.1. The barriers for oral administration of insulin

The GIT is a major organ that possesses a very highly absorptive surface—the small intestine—representing a surface of 250 m^2 in an adult human. Indeed, the initial function of the GIT is to digest and absorb nutrients, water, and vitamins from the food. However, it is considered as a barrier for the entry of pathogens, toxins, and undigested macromolecules. Thus, before reaching the bloodstream, insulin orally administered encounters several organs: the mouth, the pharynx, the esophagus, the stomach, the

small intestine (subdivided in three parts: duodenum, jejunum, and ileum), and the colon. The epithelium that lines the small intestine is mainly composed of columnar epithelial cells (enterocytes) involved in the absorption of nutrients, and goblet cells that secrete mucus. At the luminal side of enterocytes, the plasma membrane forms a brush border which increases the absorptive area of the intestine by approximately two orders of magnitude. It is lined by a glycocalix—a sulfated mucopolysaccharide sheet. Together with mucus, a viscous fluid composed of highly glycosylated proteins (mucins) secreted by goblet cells, enzymes, electrolytes, and water hinder the absorption of proteins and peptides. Tight junctions between the adjacent cells also prevent the absorption of large molecules and particles. The small intestine has another particularity: lymphoid nodules, individually or aggregated into Peyer's patches. They are dispersed through the intestinal epithelium and more abundant in the ileum than in the jejunum. This follicle-associated epithelium is composed of enterocytes, a few goblet cells and M cells. These latter structures attracted the attention of scientists for a long time because they are specialized in the uptake of particles and organisms and are involved in the immunological responses of the mucosa.

During the transit through the GIT, insulin is mainly degraded in the stomach and in the duodenum. Pepsinogen secreted from the gastric glands is converted to pepsin by hydrogen chloride also produced by the gastric glands together with mucus. Then, pepsin is able to degrade proteins by cleavage of peptide bonds between aromatic amino acids such as phenylalanine, tryptophan, and tyrosine. In the duodenum, insulin is in presence of trypsin, chymotrypsin, and carboxypeptidases secreted in the intestinal lumen from the pancreas. Trypsin is the most efficient enzyme for the degradation of insulin. However, other enzymes located in the brush border membrane, such as peptidases, also contribute to insulin degradation. In addition, there is also a specific cytosolic enzyme called insulin-degrading enzyme, which completely denaturates insulin inside enterocytes.

Finally, insulin reaches the intestine where it is less absorbed, due to its large molecular weight and hydrophilicity. Therefore, in order to escape all these barriers, insulin was associated to appropriate carrier formulations that will protect it against enzymes and improve its absorption, leading to a higher bioavailability.

2.2. Polymeric nanoparticles

The polymers used for the manufacturing of nanoparticles are synthetic or more natural materials. The most largely used synthetic polymers are polyalkylcyanoacrylates, the copolymers of lactic and glycolic acid (PLGA) and poly-ε-caprolactone (PCL).

Damgé *et al.* (1988) reported that the intragastric administration in diabetic rats of insulin encapsulated in polyisobutylcyanocrylate (PIBCA)

nanocapsules induced a sustained reduction of blood glucose levels that lasted for 1–3 weeks, depending on the dose of insulin. However, controls such as free insulin and insulin adsorbed at the surface of these nanocapsules (both cases mean insulin non-encapsulated) did not show any effect on glycemia. Thus, this pilot work demonstrated for the first time that insulin encapsulated to a polymeric colloidal biodegradable drug carrier, remained biologically active after oral administration in diabetic rats. These authors showed that the nanocapsules produced by the interfacial polymerization method protected insulin from the degradation of proteolytic enzymes and facilitated the absorption of insulin-loaded nanocapsules through a paracellular pathway and through a transcellular pathway via the M cells of the Peyer's patches (Aprahamian *et al.*, 1987; Damgé *et al.*, 1990, 2000). The nanocapsules responsible for such therapeutic effects comprised polymeric colloidal particles less than 300 nm in diameter made of an oily core surrounded by a polymeric wall. Poloxamer 188 was used as a surfactant during formulation. Further, our laboratory elucidated the role played by the oily phase and surfactant agents in the protection and absorption of insulin-loaded nanocapsules. Thus, we developed full polymeric PIBCA nanoparticles by the emulsion polymerization method (Damgé *et al.*, 1997) and investigated their biological effects after oral administration in diabetic rats. We observed a sustained reduction of blood glucose levels, which lasted up to 10–13 days when nanoparticles were dispersed in an oily medium containing surfactant agents (poloxamer 188 and deoxycholic acid), whereas they were without any effect after suspension in water. This indicates that oil and surfactant agents play a considerable role in the protection of insulin against proteolytic enzymes and in the absorption of insulin by the GIT. Finally, the biological efficacy of PIBCA nanocapsules was confirmed in alloxan-induced diabetic dogs (Damgé *et al.*, 1995) and in non=obese diabetic mice, a genetically autoimmune type 1 diabetic model (Sai *et al.*, 1996). These findings are in agreement with those of other laboratories. Radwan and Aboul-Enein (2002) reported that orally administered, insulin-loaded poly(ethylcyanoacrylate) nanospheres retained their biological activity up to 12 days in 50% of diabetic rats in the presence of glycyrrhizic acid and capric acid as absorption enhancers. However, Radwan (2001) only found a blood glucose reduction that lasted from 2 h up to more than 8 h after oral administration of PIBCA nanospheres in the presence of surfactants to diabetic rats. After oral administration of PIBCA nanospheres to diabetic rats, blood glucose levels decreased from the second hour onward, over a 40 h period (Mesiha *et al.*, 2005). In addition, Cournarie *et al.* (2002) only detected a significant but rapid increase in plasma insulin levels (30 min to 1 h postadministration) after oral administration of insulin-loaded PIBCA nanocapsules to diabetic rats without decrease of glycemia. According to these authors, insulin-resistance that was developed by their diabetic rats should explain these results. Later, studies

showed that insulin did not react with the alkylcyanoacrylate monomer during nanocapsule formation and was located within the oily core rather than adsorbed on the surface (Aboubakar *et al.*, 1999) and that the prolonged action of insulin-loaded nanoparticles could be due to the retention of a proportion of the colloidal system in the GIT (Pinto Reis *et al.*, 2006a).

Diabetes is a chronic disease that requires a long-term treatment for several decades. Thus, the fate of the polymers used must be well controlled. A more accepted polymer by the pharmaceutical companies is composed of PLGA. However, the relative bioavailability is low. As known, relative bioavailability measures the bioavailability of different drug formulations compared with the same drug taken as a standard; but it can also result from the comparison of several routes of administration (e.g., oral route vs. subcutaneous route). Thus, it was proposed to improve the formulation by coating PLGA nanoparticles with chitosan or by rendering the insulin molecule more lipophilic (Cui *et al.*, 2006). It was also proposed to prevent the release of insulin in the stomach using a pH sensitive cellulose copolymer (HPMCP-55), leading to the formation of PLGA-Hp55 nanoparticles (Cui *et al.*, 2007). These modifications improved the relative bioavailabilities of insulin to about 7–8%. Finally, Carino *et al.* (2000) prepared PLGA nanoparticles with fumaric anhydride oligomer and iron oxide additives (FAO/PLGA) and found a 11.4% increase over intraperitoneal insulin.

Another formulation was based on the combination of two polymers: PCL, a biodegradable polymer generally used in the manufacture of surgical threads, and Eudragit RS, a nondegradable mucoadhesive polymer used in the manufacture of capsules (Damgé *et al.*, 2007). When these nanoparticles were orally administered in diabetic rats, they reduced glycemia for a prolonged period (from 4 h up to 24 h) with a relative bioavailability of 13% versus s.c. administration of insulin. Finally, to improve the efficacy of these nanoparticles, regular insulin was replaced by the fast acting analog, aspart-insulin (Damgé *et al.*, 2010). In this molecule, the amino acid B28, which is normally proline, is substituted with an aspartic acid residue. This analog has increased charge repulsion, which prevents the formation of hexamers and thus becomes faster acting insulin. After oral administration in diabetic rats, insulin nanoparticles prolonged the postprandial peak suppression by more than 24 h in comparison with regular insulin working only 6–8 h. This effect may be explained by the monomeric configuration of aspart-insulin, which is probably taken up more efficiently by the intestinal mucosa than regular insulin.

Advances in nanotechnology applied to insulin are focused around a search for formulations with lower toxicity, and more simple and scaleable methodologies using biodegradable and naturally occurring polymers, such as alginate, chitosan, gelatin, or pectin. The preparation of these nanoparticles generally uses mild conditions for the insulin molecule, for example,

alginate gels in the presence of divalent cations such as calcium. These gels are pH-sensitive. They undergo shrinkage in an acidic pH, protecting the peptide against degradation in the stomach; then they swell in the neutral medium of the intestine, releasing the peptide in the intestinal medium. Insulin was first encapsulated into alginate beads prepared by extrusion/gelation. Then, they were coated with chitosan (Sarmento *et al.*, 2007a), and the bioavailability increased by a factor four after oral administration in diabetic rats. Insulin-loaded alginate-dextran nanospheres were also prepared by nanoemulsion dispersion followed by triggered *in situ* gelation (Pinto Reis *et al.*, 2007). This method was based on emulsification/internal gelation, which was developed initially for production of microparticles. Insulin encapsulation efficiency was 82.5%. Alginate-dextran particles suppressed insulin release in acidic media and promoted a sustained release at near-neutral conditions. Nanoencapsulated insulin was bioactive, as demonstrated through both *in vivo* and *in vitro* bioassays (Pinto Reis *et al.*, 2007). In order to improve the biological efficacy of this formulation, Reis *et al.* (2008b) coated these alginate-dextran nanoparticles with chitosan, albumin, and PEG and observed after oral delivery of these nanoparticles in diabetic rats, a sustained reduction of glycemia, increased plasma levels of insulin and a pharmacological bioavailability of 40% by comparison with s.c. administration.

Ongoing investigations are looking to improve the oral bioavailability of insulin using chitosan particulate systems (Pan *et al.*, 2002). Chitosan has been used as a unique polymer or a copolymer or a coating material.

Chitosan nanoparticles were prepared by ionotropic gelation. The insulin association efficiency spanned a broad range from 2% to 85%, depending on process and formulation parameters, and was highly sensitive to formulation pH. Interaction of insulin with the chitosan nanoparticles rendered the protein more susceptible to acid and enzymatic hydrolyses, the effects being more evident in nanoparticles prepared at pH 5.3 than at pH 6.1. These insulin-loaded nanoparticles were effective at lowering serum glucose levels of diabetic rats when orally administered at doses of 50 and/or 100 IU/kg (Ma *et al.*, 2005). The 100 IU/kg-dose (nanoparticles formed at pH 5.3) sustained serum glucose at prediabetic levels for at least 11 h. In comparison, nanoparticles formulated at pH 6.1 had a faster onset of action (2 h vs. 10 h), but lower efficiency.

Novel functionalized graft copolymer nanoparticles consisting of chitosan and monomers of methylmethacrylate, *N*-dimethylaminoethyl methacrylate hydrochloride, and *N*-trimethylaminoethyl methacrylate chloride, which show a higher solubility than chitosan in a broader pH range, have been prepared by free radical polymerization (Qian *et al.*, 2006). Insulin-loaded nanoparticles showed maximal encapsulation efficiency of 100%. *In vitro*, nanoparticles provided an initial burst release followed by a slowly sustained release for more than 24 h. Plasma glucose reduction of 10–20%, 20–30%, and 30–40% resulted from nanoparticles formed with

methylmethacrylate, *N*-dimethylaminoethyl methacrylate hydrochloride, and *N*-trimethylaminoethyl methacrylate chloride, respectively.

Polymethacrylic acid-chitosan-polyethylene glycol nanoparticles were prepared under mild aqueous conditions, via polyelectrolyte complexation but *in vivo* trials were not performed (Sajeesh and Sharma, 2005). The same group changed the formulation by incorporation of cyclodextrin and conducted mucoadhesive studies using freshly excised rat intestinal mucosa (Sajeesh and Sharma, 2006). The particles were found to be weakly adhesive.

Chitosan was also associated with sulfate dextran (Sarmento *et al.*, 2006). An association efficiency of 85% was obtained. Insulin was almost fully retained at pH below 5.2 for up to 24 h, and at pH 6.8 the release of insulin proceeded at a controlled rate.

Nanoparticles composed of chitosan and poly(γ-glutamic acid) were prepared by a simple ionic-gelation method (Lin *et al.*, 2007). Nanoparticles with a positive surface charge (or shelled with chitosan) could transiently open the tight junctions between Caco-2 cells and thus increased the paracellular permeability. Insulin-loaded nanoparticles reduced blood glucose level in a diabetic rat model to around 55% of basal values, lasting up to 10 h.

Besides alginate and chitosan, other natural materials such as gelatin and pectin can be used as matrix encapsulation polymers. Cheng and Lim (2004) encapsulated insulin into pectin nanoparticles with an encapsulation efficiency of 93.3%. Release profiles showed a burst effect within the first hour, with little insulin being released thereafter in simulated gastric and intestinal fluids. The burst effect was pH dependent. Increasing the pH from 2 to 3 enhanced the association efficiency by threefold.

2.3. Mucoadhesive nanoparticles

Bio- or mucoadhesive nanoparticles have been developed to increase the concentration of the peptide at the apical pole of absorptive cells and thus to create an insulin concentration gradient favoring its uptake through the intestinal epithelium. The adsorption of nanoparticles at the surface of the intestinal epithelium results from the interaction of the positively charged nanoparticles and the negatively charged, hydrophilic glycoproteins from the mucus. Thus, the interaction between nanoparticles and the intestinal surface depends on the charges and the hydrophobic properties of the drug carrier. For example, chitosan and its derivatives, or polyethylene glycol formulated in insulin nanoparticles interact strongly with the mucus, improving the absorption of insulin and its biological efficacy after oral administration.

The therapeutic efficacy of mucoadhesive nanoparticles has been improved by the addition of protease inhibitors that protect insulin against degradation by enzymes.

2.4. Lipidic nanoparticles

The formulations based on lipids have the great advantage of being less toxic or nontoxic. The use of liposome-based systems for oral insulin delivery has been investigated extensively in animal studies. Varying reductions in blood glucose have been reported depending on factors including lipid composition, presence or absence of surfactant, size, surface charge, and the physical state of the phospholipid bilayer employed (Choudhari *et al.*, 1994). Liposomes are susceptible to enzymatic degradation and bile salt dissolution, although they can be stabilized by polymerization, coating with chitosan and polyvinyl alcohol or by incorporation of sodium taurocholate, dipalmitoyl phosphatidylethanol, or sorbitan monoesters.

Other investigations suggested multiple emulsions as potential oral carriers for insulin, but emulsions cannot be considered as nanoparticular drug carriers.

Insulin-loaded solid lipid nanoparticles (SLNs) have also been developed. Sarmento *et al.* (2007b) noted a sustained but slight hypoglycemic effect that lasted 24 h after oral administration in diabetic rats. Further, insulin-loaded SLNs were modified with wheat germ agglutinin-*N*-glutaryl-phosphatidylethanolamine (WGA-SLNs) to stabilize those (Zhang *et al.*, 2006). WGA was chosen for its relatively good resistance to acidic pH and enzymatic degradation. After oral administration to healthy rats, insulin-loaded SLNs rapidly reduced blood glucose levels, the maximal effect being noted after 1 h. However, this effect was less intense, but sustained up to 6 h; the relative bioavailability remained low, around 5% in comparison with an s.c. injection. More recently, Yang *et al.* (2010) improved the entrapment efficiency of insulin by preparing gel-core-SLNs with the hydrogel core and lipid shell, but the pharmacological availability remained low (6%).

2.5. Miscellaneous formulations

Other polymers and techniques to prepare insulin polymeric carriers have been developed to encapsulate insulin, such as terpolymers of *N*-isopropylacrylamide, butyl methacrylate, or acrylic acid.

Calcium phosphate-PEG-insulin-casein (CAPIC) particles composed of a hydrophobic core (calcium phosphate-PEG-insulin), surrounded by a hydrophilic layer (mostly casein) that may protect insulin from the harsh acidic environment of the stomach, appeared also to be effective (Morçol *et al.*, 2004). After oral administration in nonobese diabetic mice, this formulation worked fast (as early as 1 h postadministration) and for a sustained period (at least 12 h in fasted mice).

In another formulation, vitamin B_{12} was coupled to dextran nanospheres; when this formulation was administered orally in diabetic rats, the pharmacological bioavailability of insulin was improved (Chalasani *et al.*, 2007).

Finally, biocompatible self-assembled "nanocubicles" and insulin-loaded gold nanoparticles were also prepared and investigated in diabetic animals after oral delivery.

2.6. Intestinal absorption of insulin-loaded nanoparticles

Basically, four different pathways are possible for nanoparticle-associated insulin or free insulin to reach the bloodstream from the intestinal lumen: (i) insulin may be released from the nanoparticles in close contact with the apical membrane of enterocytes and may be absorbed by a receptor-mediated transport of free insulin; (ii) nanoparticles may be absorbed by transcytosis through enterocytes; (iii) nanoparticles less than 200 nm in diameter may be taken up by the intestinal mucosa through a paracellular pathway via intercellular spaces between adjacent cells; and finally, (iv) nanoparticles may be taken up by a transcellular pathway by M cells of Peyer's patches.

Insulin-loaded nanoparticles should be degraded in the intestinal lumen in order to release their insulin. However, this degradation depends on the polymer used. A protective role of the mucus against poly(alkylcyanoacrylate) degradation has been reported *in vitro*, resulting in the presence of insulin-loaded nanocapsules in the vicinity of brush border membranes from enterocytes at the apical part of the villi (Aprahamian *et al.*, 1987). By contrast, nanocapsules appeared to be degraded in the lumen of the crypts, where mucus was reduced and isolated gold-labeled insulin colloidal particles could be released. It is quite possible that other polymers behave differently when in contact with the mucus layer. Mucoadhesion of nanoparticulate polymers is an important factor that prolonges the retention time in the GIT, leading to the promotion of insulin absorption. Mucoadhesiveness can be explained by the interaction of the electropositive nanoparticles and the electronegative mucus layer, which covers the intestinal epithelium. An example is given by the electropositively charged insulin nanoparticles composed of PCL/Eudragit RS or alginate shelled with chitosan/albumin/PEG, which strongly adhered to the luminal part of the intestinal epithelium after administration in an *in situ* isolated intestinal loop in the rat (Damgé *et al.*, 2007; Reis *et al.*, 2008b).

Free insulin released by the nanoparticles at the vicinity of the brush border membrane should be transported within the cytoplasm of enterocytes by transcytosis (Bendayan *et al.*, 1990). Indeed, in the presence of antiproteases (aprotinin) and a surfactant agent (sodium cholate), gold-labeled insulin particles detected in the lumen of the intestinal tract were absorbed through the endosomal compartment of epithelial cells rather than passing between cells. Then, they were internalized through invaginations of the luminal plasma membrane and transferred to the basolateral membrane where they were released into the interstitial space to reach the

circulation. Insulin receptors present along the intestinal epithelium should play a role in insulin uptake via receptor-mediated transport and allow the transport of 60–500 nm particles (Delie and Blanco-Prieto, 2005; Swaan, 1998). Receptor-mediated transport could explain the presence of insulin-labeled gold particles in enterocytes after oral administration of insulin-loaded poly(isobutylcyanoacrylate) nanocapsules in the rat (Pinto-Alphandary *et al.*, 2003). However, insulin should also be degraded inside the cytoplasm of absorptive cells by the specific insulin-degrading enzyme (Aboubakar *et al.*, 1999). As a consequence, the exact amount of insulin arriving in the blood compartment through transcytosis remains unknown. Nevertheless, Bendayan *et al.* (1990) found a significant reduction of blood glucose after the introduction of insulin (associated to antiproteases and surfactants) in the intestinal lumen of normal and diabetic rats.

A paracellular transport is possible only after opening the tight junctions that maintain the integrity of the intestinal epithelium. This transport more often occurs at the tip of the villi, where absorptive cell desquamation occurs continuously. Indeed, poly(isobutylcyanoacrylate) nanocapsules less than 150 nm in diameter have been observed in the intercellular spaces between absorptive cells (Aprahamian *et al.*, 1987; Damgé *et al.*, 1990). They were also recovered in the lumen of capillaries, being in close contact with endothelial cells and red cells, demonstrating the absorption of nanoparticles through a paracellular pathway.

The paracellular uptake of insulin nanoparticles can be improved by cationic polymers such as chitosan or poly(acrylate), which reversibly open the tight junctions between enterocytes, allowing the transport of macromolecules (Radwan and Aboul-Enein, 2002). Chitosan acts via the electrostatic interaction between positively charged chitosan in solution and the negatively charged components of cell membranes. It has been shown that chitosan decreases the transepithelial electrical resistance of monolayers of Caco-2 cells (derived from a colonic adenocarcinoma)—a well accepted *in vitro* model that mimics the epithelial barrier (Radwan and Aboul-Enein, 2002). Chitosan is thought to act through tight junction disruption, leading to the enhancement of the absorption of insulin and a reduction in blood glucose levels after oral administration of insulin-loaded chitosan nanoparticles in the rat (Qian *et al.*, 2006). Ma *et al.* (2005) conjugated FITC to chitosan and confirmed the presence of the labeling agent at different stages of intestinal villi 3 h after oral administration to diabetic rats. We have also reported marked labeling on the epithelium of intestinal villi in an *in situ* isolated intestinal loop of the rat, following the delivery of FITC-labeled insulin-loaded alginate–dextran nanoparticles shelled with albumin–chitosan–PEG (Pinto Reis *et al.*, 2008b). It is interesting to note that the surface charge of nanoparticles is an important factor for the disruption of tight junctions. Indeed, positively charged nanoparticles of chitosan have been found to transiently

open tight junctions but negatively charged nanoparticles of poly (g-glutamic acid) had no effect (Norris *et al.*, 1998).

A more classical insulin nanoparticle uptake pathway concerns translocation through M cells of the follicle-associated epithelium. These cells are able to take up small and large particles, up to 15 μm in diameter. However, small particles were taken up to a greater extent than larger particles. This uptake can be nonspecific or specific, using the properties of the polymers to bind to specific transporters such as lectins or transferrins. In addition, nanoparticles were observed in the cytoplasm of M cells, then in the intercellular spaces containing phagocytic cells, including lymphocytes and macrophages (Damgé *et al.*, 2000). However, according to Pinto-Alphandary *et al.* (2003), poly(isobutylcyanoacrylate) nanocapsules should also be degraded, because free insulin-labeled gold particles were found under the M cells, in the intercellular pockets, and also in the underlining capillaries. Thus, there is a possibility that free insulin and insulin-loaded particulates can escape the lymphatics and eventually reach the bloodstream.

Using insulin labeled with FITC, Sarmento *et al.* (2007a), using alginate chitosan nanoparticles, and Damgé *et al.* (2007), using PCL/Eudragit RS nanoparticles, found marked labeling in the dome of Peyer's patches after the oral administration of insulin nanoparticles. However, this labeling was the most intense when insulin-loaded alginate nanospheres were coated with chitosan, albumin, and PEG (Reis *et al.*, 2008b).

Finally, insulin-loaded nanoparticles or free insulin have been shown to penetrate into blood capillaries through the fenestrations of their basement membrane, which generally have diameters from 500 nm to 5 μm. Indeed, nanocapsules, gold-labeled nanoparticles, as well as colloidal gold particles representing free insulin were observed inside intravillus blood capillaries (Aprahamian *et al.*, 1987; Pinto-Alphandary *et al.*, 2003).

Thus, different mechanisms coexist to allow insulin-loaded nanoparticles to be taken up by the intestinal epithelium. These depend on the nature of the polymer forming the nanoparticle and the coating material.

It is generally accepted that hydrophobic nanoparticles should be taken up more extensively by the intestinal epithelium than hydrophilic nanoparticles (Pinto Reis *et al.*, 2006a). Indeed, aminated nanoparticles are transported more efficiently through follicle-associated epithelium-like cells than carboxylated nanoparticles, suggesting an influence of nanoparticle hydrophobicity and surface functional groups on cellular uptake (Pinto Reis *et al.*, 2006a). In fact, hydrophobic nanoparticles seem to have a higher affinity for M cells than for absorptive cells (Delie and Blanco-Prieto, 2005). Indeed, they penetrate poorly into the mucus, which is dense over epithelial cells. Thus, not only the surface charge, but also the hydrophobic/hydrophilic balance, is important factors in the intestinal uptake of nanoparticles.

3. Buccal Administration of Insulin

The buccal mucosa has excellent accessibility, low enzymatic activity, a large absorptive area with a spread of vascularization, and a relatively immobile mucosa which may be an important factor for increasing the residence time of the drugs. In addition, the ease of access to the systemic circulation through the internal jugular vein allows drugs to bypass the hepatic first-pass metabolism, which may also increase bioavailability of drugs. Other advantages of buccal administration include the convenient route and painless administration, facility to modulate the selection of excipients, versatility in the design of multidirectional or unidirectional release systems for local or systemic action, and a predictable drug concentration in the blood. The major disadvantage of this route is that insulin may enter directly into peripheral circulation resulting in peripheral hyperinsulinemia similar to that seen with injectable insulin.

The exact mechanism of insulin absorption via this route is still not known, but one study showed that peptide transport across the buccal mucosa may occur via passive diffusion (Veuillez *et al.*, 2001). The role of absorption enhancers in the buccal transport of proteins is crucial. Reductions in blood glucose of up to 30% relative to intramuscular insulin have been reported, but those studies have lacked reproducibility (Aungst and Rogers, 1988). Besides the reproducibility, many absorption enhancers have some side effects, often causing irritation of the buccal mucosa. An additional problem of the buccal delivery of insulin is the unpleasant taste of buccal formulations.

In terms of multiparticulate system strategies, Ishida *et al.* (1981) were among the first to pioneer the mucoadhesive drug delivery system by administering insulin across the buccal mucosa in beagle dogs. Later, transferosomes have also been developed to enhance insulin bioavailability. Compared with s.c. administration of insulin solution, the relative pharmacological bioavailability and the relative bioavailability in the experimental group treated with vesicles were 15.59% and 19.78%, respectively. It is also anticipated that the effects of salivary scavenging and accidental swallowing of the delivery system, in addition to the barrier properties of the buccal mucosa, will remain major limitations in the development of buccal drug delivery systems.

Pelleted mucoadhesive polymeric nanoparticles for the buccal delivery of insulin were an attempt to develop an alternative buccal delivery system for insulin (Venugopalan *et al.*, 2001). A significant hypoglycemic response was observed after 7 h. In another related work, insulin was formulated into mucoadhesive buccal tablets using Carbopol 934, hydroxypropyl cellulose, or hydroxypropylmethyl cellulose and different absorption promoters. Additionally, Insulin Buccal Spray, a formulation with soybean lecithin

and propanediol combined as an absorption enhancer, improved the hypoglycemic effect of insulin in diabetic rabbits and rats (Xu *et al.*, 2002). The hypoglycemic effect lasted over 5 and 4 h in diabetic rabbits and rats, respectively. Biodel, Inc. is developing a rapid-acting sublingual insulin called Viatab™. This formulation has been tested in laboratory models and was not toxic.

One strategy to deliver insulin through the buccal mucosa in humans is already being tested by Generex Biotechnology Corp.: Oral-Lyn. *Oralyn*® involves a miceller insulin liquid formulation made from a combination of absorption enhancers and is administered through a *RapidMist*™ as a fine spray into the mouth (Modi *et al.*, 2002). Studies with healthy and type 1 diabetic individuals showed that it was fast acting (around 25 min) and had a rapid glycemic response (maximum effect at 45–50 min). This oral insulin formulation controlled postprandial glucose levels in both type 1 and 2 diabetics (Cernea *et al.*, 2005). The spray was thought effective for meal-related insulin requirements, since it was adsorbed and acted rapidly. Local tolerability appeared acceptable, but bioavailability remained low, necessitating repeated administrations.

The multitude of techniques already tested illustrates the inherent difficulties associated with the buccal route of insulin administration. So far, efficacy studies have only been presented as abstracts in conference proceedings, and safety reports of buccal insulin are not usually presented.

4. Nasal Administration of Insulin

The nasal cavity has a large epithelial surface area ($\sim$150 m^2), with highly vascularized and accessible mucosa. Two of the barriers to the nasal absorption of insulin are active mucociliary clearance and proteolytic enzymes (Owens *et al.*, 2003). There are many factors that influence the bioavailability of intranasal insulin, such as the physicochemical properties of the particles, timing, dosing, and frequency of administration and type, volume and concentration of insulin, or absorption enhancers. For this reason, most nasal formulations have low bioavailability values ranging from 8% to 15% (Cefalu, 2004).

A significant number of articles were published in pharmaceutical journals about novel approaches for nasal insulin in the past years but only focused on studies in animals. One of the first studies used rabbits (Fernández-Urrusuno *et al.*, 1999). Insulin-loaded chitosan nanoparticles were prepared by an ionic gelation method using tripolyphosphate as the counterion. Those nanoparticles were nasally administered to rabbits (5 IU/kg) and reduced the plasma glucose levels to 60% of the original value, whereas the chitosan insulin solution only achieved a reduction to 85%. Later, a similar chitosan-insulin formulation was prepared and

administered nasally to rats (2 IU/kg) and sheep (Dyer *et al.*, 2002). Although hypoglycemic effects were noted, the bioavailability of insulin was 1.3% for chitosan nanoparticles, 3.6% for the chitosan insulin solution, and 17% for the chitosan insulin powder.

Later, Simon *et al.* (2005) used nanocomplexes that comprise insulin and amine-modified polyesters. The biovailabilities of insulin after nasal administration of these nanocomplexes in healthy and diabetic rats ranged from 2.8% to 8.3%.

Other research groups focused on chitosan derivatives such as PEGylated-trimethyl-chitosan insulin complexes or thiolated chitosan derivatives (Mao *et al.*, 2005), or even chitosan associated to another polymer, such as alginate (Goycoolea *et al.*, 2009). In the last example, chitosan-alginate nanoparticles exhibited a capacity to enhance the systemic absorption of insulin after nasal administration to conscious rabbits. Chitosan was also associated to metallic nanoparticles (Bhumkar *et al.*, 2007). Gold chitosan nanoparticles decreased blood glucose 2 h after administration to diabetic rats. Reductions ranged from 30% to 20% for oral (50 IU/kg) and nasal (10 IU/kg) delivery, respectively. Serum gold level studies also demonstrated a significant improvement in the uptake of chitosan-reduced gold nanoparticles. In this study, the use of chitosan has a dual purpose, by acting as a reducing agent in the synthesis of gold nanoparticles and also promoting the penetration and uptake of insulin across the oral and nasal mucosa in diabetic rats.

Like chitosan, other polymers were also used in nasal insulin delivery; for example, starch (Jain *et al.*, 2008). Insulin-loaded starch nanoparticles led to a pronounced blood glucose reduction around 70%, and this effect lasted for 6 h.

Only two articles were published in the past year reporting a clinical study in humans when insulin was applied to the nose. Insulin was administered through a nasal spray named Nasulin (Stote *et al.*, 2010). However, it seems that CPEX Pharmaceuticals has abandoned their Nasulin project after Phase 2a trials.

It also appears that the number of other companies that are active in this area of research has decreased in the past few years. Those formulations tested result in unacceptable levels, dose variability, combined with nasal irritation in 25% of the patients. Insulin absorption was observed to be fast, but bioavailability was less than 20% (Owens *et al.*, 2003). As is the case with buccal mucosa administration, nasal administration directs the insulin into the peripheral circulation.

5. Pulmonary Administration of Insulin

Pulmonary delivery of insulin appears to be the first reported alternative to injections (Cefalu, 2004). In fact, transpulmonary delivery of proteins and peptides may be expected to have higher systemic absorption

than other noninvasive routes, since it provides a large surface area, a thin alveolar epithelium and the enzyme activity is relatively low.

Pulmonary drug delivery systems include a variety of pressurized metered dose inhalers, dry powder inhalers, nebulizers, and aqueous mist inhalers. An example of a pulmonary drug delivery system is the inhaled dry powder formulation of insulin named as Exubera, which was available on the market in the United States. However, in 2007, Pfizer has announced that they will no longer manufacture or market Exubera. At the time of Exubera's discontinuation, several other companies were pursuing inhaled insulin. Nevertheless, by March 2008, all of these products, except MannKind's *Afrezza*, had been discontinued as a result of nonacceptance by patients and physicians, uncertainties in the regulatory environment, and an evaluation of its commercial and clinical potentials. Lately, in January of 2011, MannKind Corporation announced that the FDA rejected *Afrezza* and asked for two more clinical trials.

In terms of the development of nanotechnology, it seems that particles smaller than about 260 nm can escape from the uptake by alveolar macrophages and can be transported by various mechanisms across cellular membranes from the lung to blood.

One of the first studies involved polybutylcyanoacrylate nanoparticles prepared by the emulsion polymerization method (Zhang *et al.*, 2001). These nanoparticles were administered via the pulmonary route to rats, and reduced glycemia as a function of the administered dose of insulin. The relative pharmacological bioavailability of insulin released from these nanoparticles was 57% compared to s.c. administration. Likewise, insulin-loaded chitosan nanoparticles were also prepared, then encapsulated into microspheres, and tested in rats (Grenha *et al.*, 2005). With this formulation, the blood glucose levels decreased to 90% of initial values after 60 min of intratracheal administration to nondiabetic rats, whereas reduction to 60% was obtained with an insulin solution.

At the same time, SLN were developed by the reverse micelle-double emulsion method (Liu *et al.*, 2008). In this case, the fasting plasma glucose level was reduced to 39% and the insulin level was increased to approximately 170 μIU/ml 4 h after pulmonary administration of insulin nanoparticles. In this study, a pharmacological bioavailability of 24% and a relative bioavailability of 22% were obtained, using s.c. insulin as a reference. When labeled, nanoparticles were found to be effectively and homogeneously distributed in the lung alveoli.

A novel system made of insulin-loaded SLN was investigated for prolonged drug release (Bi *et al.*, 2009). After intratracheal instillation in diabetic rats, this formulation showed a prolonged hypoglycemic effect, and a relative pharmacological bioavailability of 44%.

Recently, a complex made of phospholipids and proteins with insulin was prepared and tested in animal models (Zhang *et al.*, 2009). Compared

with s.c. injection, the relative pharmacological bioavailability of the insulin dry powder was 32.6%.

In general, all of the pulmonary insulin formulations have demonstrated adequate pharmacokinetic and pharmacodynamic features compared to s.c. insulin administration. In those formulations, insulin absorbed through lung alveoli enters directly into the peripheral circulation, providing no advantage over injectable insulin other than elimination of the discomfort of injection. Moreover, cytosolic biodegradation is thought to be the main determinant of insulin bioavailability; however, the lung is highly immunotolerant, and this is an important advantage (Owens *et al.*, 2003), but as the administration of insulin into the lungs could be lifelong, critical questions concerning long-term safety are still under investigation.

6. Transdermal Administration of Insulin

The skin is the largest organ of the human body, and thus, transdermal drug delivery is an appealing alternative to s.c. insulin delivery, since it offers good patient compliance and the possibility of controlled release over time, while avoiding possible drug degradation in the GIT or first-pass liver effects. Despite these advantages, the human skin is an extremely effective barrier that protects against and is impermeable to foreign molecules. The impermeability of skin is due predominately to the intercellular lipid layer of the *stratum corneum*. Attempts to optimize transdermal drug delivery have involved breaking down or removing the lipid barrier by a variety of chemical, electrical, or physical methods.

A large number of chemical absorption enhancers belonging to several different classes, such as surfactants, fatty acids, and fatty esters, have allowed limited enhancement of skin absorption, but they have some limitation, such as skin irritation and inability to deliver large molecules.

Another possibility to facilitate the transdermal absorption of large hydrophilic proteins is to coadminister a short synthetic cyclic peptide that increases the insulin stability (Chen *et al.*, 2006). The coadministration of this peptide and insulin to the abdominal skin of diabetic rats resulted in elevated systemic levels of insulin and suppressed serum glucose levels for at least 11 h. The effect was dose dependent. Time-lapse studies have suggested that the peptide creates a transient opening of the skin barrier that allows macromolecular drugs to reach the systemic circulation.

Lecithin vesicles containing insulin were also developed (Guo *et al.*, 2000). The entrapment efficiencies of conventional and flexible vesicles were 35% and 81%, respectively. When flexible vesicles were nonocclusively applied to the abdominal skin of mice, the blood glucose level decreased by 21% at 1 h, and 61% at 5 h, and was still at a decreased level ($>$ 50% decrease) at 18 h.

An advanced study involving $CaCO_3$ nanoparticles that were transdermally applied to the back skin of normal and diabetic mice increased slightly the serum insulin level, but bioavailability was low (0.9%) (Higaki *et al.*, 2006).

More recently, one of the most advanced technologies to overcome low skin permeability to insulin has employed iontophoresis, combined with absorption enhancers, electroporation, and sonophoresis. Several devices have been developed (Kanikkannan *et al.*, 1999). The major challenges in this area are the development of portable, cost-effective devices, and suitable semisolid formulations that are compatible with both the device and the skin, because the combination of absorption enhancers and iontophoresis causes greater skin irritation than when either is used alone.

In general, it seems that a transdermal delivery system for insulin is an attractive option. Although progress in the transdermal delivery of insulin and other peptides seems encouraging, it is still doubtful whether this delivery route provides a general approach to the noninvasive delivery of insulin, mainly because of the poor permeation capacity of insulin and the high susceptibility of the skin to adverse immunological reactions.

7. Pharmaceutical Industrial Advances

A number of alternative routes for the delivery of insulin have been developed during the last several decades, including the oral, nasal, pulmonary, and transdermal routes. Nanotechnologies have allowed the improvement of the protection of insulin against enzyme degradation, and facilitated the absorption of insulin-loaded nanoparticles or free insulin liberated from the particles through different epithelia. However, the oral route is the most physiological, whereby insulin reaches directly the liver, in contrast to s.c. delivery, which induces hyperinsulinism often associated with hypertension, development of atherosclerosis, and increased insulin resistance in peripheral and muscle tissues. In addition, the oral route also potentially avoids adverse effects, such as weight gain and hypoglycemia. Despite the great number of formulations based on nanotechnologies that were developed and investigated generally in small animals, only a few formulations have undergone clinical development.

The buccal and oral formulations proposed for clinical applications were based either on the addition of absorption enhancers or on the chemical modification of the insulin molecule. Buccal insulin with Oral-lyn was developed by Generex (Toronto, Canada), the SNAC-insulin capsule formulation was from Emisphere, and finally, hexyl-PEG-modified peroral insulin was developed by Nobex, a company that sold its assets and intellectual property to Biocon, an Indian company based in Bangalore. These two latter formulations are based on the chemical modification of the

insulin molecule or the use of absorption enhancers. Oral-lyn from Generex uses the formation of microfine mixed micelles made from the combination of absorption enhancers that encapsulate and protect insulin. Oral-lyn has been applied successfully to type 1 and type 2 diabetic patients, resulting in an appropriate control of glycemia. Emisphere has developed insulin tablets combining insulin with sodium *N*-(8-[2-hydroxybenzoyl] amino) caprylate (SNAC). SNAC-insulin acts as fast-acting insulin in healthy human subjects. Despite phase I and IIa clinical trials, Emisphere has stopped its activity in this area. Nobex's technology concerns the chemical modification of the insulin molecule by the covalent attachment of one or more low molecular weight amphiphilic oligomers. This covalent modification of insulin increases its solubility and improves its stability against proteolytic enzymes. The so obtained hexyl-insulin monoconjugate-2 is equivalent to short-acting insulin and reduces postprandial glycemia in type 2 diabetics.

Nowadays, only a few companies continue to transfer their technology into clinical development. Diabetology, a small UK-based company, uses an enteric coated capsule filled with a dry powder mixture containing insulin, stabilizer, and solubilizer. This formulation protects insulin from gastric degradation. The coating shell dissolves with neutral pH in the jejunum, and the capsule content is subsequently released. The so-called Capsulin induced a significant hypoglycemic action over a period of 6 h associated with only a small increase in circulating plasma insulin concentrations after an oral administration in diabetic patients. The large Indian company Biocon is in phase 3 studies with IN-105, a human insulin molecule conjugated at position B29 with polyethylene glycol via an acyl chain. IN-105 is well tolerated and reduces 2 h postprandial glucose excursion in a dose-dependent manner. The small Israel-based company Oramed is in phase 2b of clinical development with their insulin capsule, ORMD-0801. Finally, the small U.S.-based company Diasome works on the concept of hepatic-directed vesicles loaded with insulin (HDV-I) attached to a specific proprietary hepatocyte-targeting molecule. This system specifically targets encapsulated insulin to the hepatocytes and mimics physiological insulin. In contrast to all other oral insulin formulations, HDV-I is presumed to have a high potency; it is formulated as an oral gel capsule with only 5 IU of insulin.

8. Concluding Remarks

All formulations based on nanotechnologies that were investigated and largely published in small animal studies were long acting insulins. By contrast, formulations investigated in human studies were always short-acting and intermediary-acting insulins, but their bioavailability after oral administration remains consistently low (Damgé *et al.*, 2008; Heinemann,

2011; Iyer *et al*., 2010). This implies the use of large amounts of insulin, and the consequent high cost. This also implies that most of the insulin ingested is not absorbed and remains in the GIT. Although most of the insulin will certainly be degraded in the GIT by proteases, the sustained contact of a large concentration of insulin with the intestinal mucosa could act as a trophic factor, leading to an increased risk of several cancers including colon cancer. Finally, even if insulin *per se* may not be toxic, the chemical compounds employed in the various delivery systems as excipients or absorption promoters need to be safe and effective in long-term toxicological and clinical studies.

In conclusion, alternative routes of delivery of insulin will be very useful. The development of new formulations using nanotechnologies could enable the improvement of the low bioavailabilities generally observed with oral administration. Nevertheless, by replicating the physiological route of insulin secretion and absorption, oral insulin may have a significant advantage by avoiding peripheral hyperinsulinism. Such insulin formulations should also lead to an earlier treatment with insulin in type 2 diabetes, and a better adherence and compliance, resulting in improved glycemic control in the population.

REFERENCES

Aboubakar, M., Puisieux, F., Couvreur, P., Deyme, M., and Vauthier, C. (1999). Study of the mechanism of insulin encapsulation in poly(isobutylcyanoacrylate) nanocapsules obtained by interfacial polymerization. *J. Biomed. Mater. Res*. **47,** 568–576.

Aprahamian, M., Michel, C., Humbert, W., Devissaguet, J. P., and Damgé, C. (1987). Transmucosal passage of polyalkylcyanoacrylate nanocapsules as a new drug carrier in the small intestine. *Biol. Cell* **61,** 69–76.

Aungst, B. J., and Rogers, N. J. (1988). Site dependence of absorption-promoting actions of laureth-9, Na salicylate, Na2EDTA, and aprotinin on rectal, nasal, and buccal insulin delivery. *Pharm. Res*. **5,** 305–308.

Bendayan, M., Ziv, E., Ben-Sasson, R., Bar-On, H., and Kidron, M. (1990). Morphocytochemical and biochemical evidence for insulin absorption by the rat ileal epithelium. *Diabetologia* **33,** 197–204.

Bhumkar, D. R., Joshi, H. M., Sastry, M., and Pokharkar, V. B. (2007). Chitosan reduced gold nanoparticles as novel carriers for transmucosal delivery of insulin. *Pharm. Res*. **24,** 1415–1426.

Bi, R., Shao, W., Wang, Q., and Zhang, N. (2009). Solid lipid nanoparticles as insulin inhalation carriers for enhanced pulmonary delivery. *J. Biomed. Nanotechnol*. **5,** 84–92.

Brange, J., and Langkjoer, L. (1997). Insulin formulation and delivery. *In* "Protein Delivery: Physical Systems," (L. Sanders and W. Hendren, eds.), pp. 343–411. Plenum Press, New York.

Carino, G. P., Jacob, J. S., and Mathiowitz, E. (2000). Nanosphere based oral insulin delivery. *J. Control. Rel*. **65,** 261–269.

Cefalu, W. T. (2004). Concept, strategies, and feasibility of noninvasive insulin delivery. *Diabetes Care* **27,** 239–246.

Cernea, S., Kidron, M., Wohlgelernter, J., and Raz, I. (2005). Dose-response relationship of an oral insulin spray in six patients with type 1 diabetes: A single-center, randomized, single-blind, 5-way crossover study. *Clin. Ther.* **27,** 1562–1570.

Chalasani, K. B., Russell-Jones, G. J., Yandrapu, S. K., Diwan, P. V., and Jain, S. K. (2007). A novel vitamin B12-nanosphere conjugate carrier system for peroral delivery of insulin. *J. Control. Rel.* **117,** 421–429.

Chen, Y., Shen, Y., Guo, X., Zhang, C., Yang, W., Ma, M., Liu, S., Zhang, M., and Wen, L. P. (2006). Transdermal protein delivery by a coadministered peptide identified via phage display. *Nat. Biotechnol.* **24,** 455–460.

Cheng, K., and Lim, L.-Y. (2004). Insulin-loaded calcium pectinate nanoparticles: Effects of pectin molecular weight and formulation pH. *Drug Dev. Ind. Pharm.* **30,** 359–367.

Choudhari, K. B., Labhasetwar, V., and Dorle, A. K. (1994). Liposomes as a carrier for oral administration of insulin: Effect of formulation factors. *J. Microencapsul.* **11,** 319–325.

Cournarie, F., Auchere, D., Chevenne, D., Lacour, B., Seiller, M., and Vauthier, C. (2002). Absorption and efficiency of insulin after oral administration of insulin-loaded nanocapsules in diabetic rats. *Int. J. Pharm.* **242,** 325–328.

Cui, F., Shi, K., Zhang, L., Tao, A., and Kawashima, Y. (2006). Biodegradable nanoparticles loaded with insulin-phospholipid complex for oral delivery: Preparation, *in vitro* characterization and *in vivo* evaluation. *J. Control. Rel.* **114,** 242–250.

Cui, F. D., Tao, A. J., Cun, D. M., Zhang, L. Q., and Shi, K. (2007). Preparation of insulin loaded PLGA-Hp55 nanoparticles for oral delivery. *J. Pharm. Sci.* **96,** 421–427.

Damgé, C., Michel, C., Aprahamian, M., and Couvreur, P. (1988). New approach for oral administration of insulin with polyalkylcyanoacrylate nanocapsules as drug carrier. *Diabetes* **37,** 246–251.

Damgé, C., Michel, C., Aprahamian, M., Couvreur, P., and Devissaguet, J. (1990). Nanocapsules as carriers for oral peptide delivery. *J. Control. Rel.* **13,** 233–239.

Damgé, C., Hillaire-Buys, D., Puech, R., Hoeltzel, A., Michel, C., and Ribes, G. (1995). Effects of orally administered insulin nanocapsules in normal and diabetic dogs. *Diab. Nutr. Metab.* **8,** 3–9.

Damgé, C., Vranckx, H., Balschmidt, P., and Couvreur, P. (1997). Poly(alkylcyanoacrylate) nanospheres for oral administration of insulin. *J. Pharm. Sci.* **86,** 1403–1409.

Damgé, C., Aprahamian, M., Humbert, W., and Pinget, M. (2000). Ileal uptake of polyalkylcyanoacrylate nanocapsules in the rat. *J. Pharm. Pharmacol.* **52,** 1049–1056.

Damgé, C., Maincent, P., and Ubrich, N. (2007). Oral delivery of insulin associated to polymeric nanoparticles in diabetic rats. *J. Control. Rel.* **117,** 163–170.

Damgé, C., Pinto Reis, C., and Maincent, P. (2008). Nanoparticle strategies for the oral delivery of insulin. *Expert Opin. Drug Deliv.* **5,** 1–24.

Damgé, C., Socha, M., Ubrich, N., and Maincent, P. (2010). Poly(epsilon-caprolactone)/Eudragit nanoparticles for oral delivery of Aspart-insulin in the treatment of diabetes. *J. Pharm. Sci.* **99,** 879–889.

Del Prato, S., Leonetti, F., Simonson, D. C., Sheehan, P., Matsuda, M., and De Fronzo, R. A. (1994). Effect of sustained physiologic hyperinsulinaemia and hyperglycaemia on insulin secretion and insulin sensitivity in man. *Diabetologia* **37,** 1025–1035.

Delie, F., and Blanco-Prieto, M. J. (2005). Polymeric nanoparticulates to improve oral bioavailability of peptide drugs. *Molecules* **10,** 65–80.

Dyer, A. M., Hinchcliffe, M., Watts, P., Castile, J., Jabbal-Gill, I., Nankervis, R., Smith, A., and Illum, L. (2002). Nasal delivery of insulin using novel chitosan based formulations: A comparative study in two animal models between simple chitosan formulations and chitosan nanoparticles. *Pharm. Res.* **19,** 998–1008.

Fernández-Urrusuno, R., Calvo, P., Remuñán-López, C., Vila-Jato, J. L., and Alonso, M. J. (1999). Enhancement of nasal absorption of insulin using chitosan nanoparticles. *Pharm. Res.* **16,** 1576–1581.

Goycoolea, F. M., Lollo, G., Remuñán-López, C., Quaglia, F., and Alonso, M. J. (2009). Chitosan-alginate blended nanoparticles as carriers for the transmucosal delivery of macromolecules. *Biomacromolecules* **10,** 1736–1743.

Grenha, A., Seijo, B., and Remuñán-López, C. (2005). Microencapsulated chitosan nanoparticles for lung protein delivery. *Eur. J. Pharm. Sci.* **25,** 427–437.

Guo, J., Ping, Q., and Zhang, L. (2000). Transdermal delivery of insulin in mice by using lecithin vesicles as a carrier. *Drug Deliv.* **7,** 113–116.

Heinemann, L. (2011). New ways of insulin delivery. *Int. J. Clin. Pract.* **65**(Suppl. 170), 31–46.

Higaki, M., Kameyama, M., Udagawa, M., Ueno, Y., Yamaguchi, Y., Igarashi, R., Ishihara, T., and Mizushima, Y. (2006). Transdermal delivery of $CaCO_3$-nanoparticles containing insulin. *Diabetes Technol. Ther.* **8,** 369–374.

Ishida, M., Machida, Y., Nambu, N., and Nagai, T. (1981). New mucosal dosage form of insulin. *Chem. Pharm. Bull.* **29,** 810–816.

Iyer, H., Khedkar, A., and Verma, M. (2010). Oral insulin—A review of current status. *Diabetes Obes. Metab.* **12,** 179–185.

Jain, A. K., Khar, R. K., Ahmed, F. J., and Diwan, P. V. (2008). Effective insulin delivery using starch nanoparticles as a potential trans-nasal mucoadhesive carrier. *Eur. J. Pharm. Biopharm.* **69,** 426–435.

Kanikkannan, N., Singh, J., and Ramarao, P. (1999). Transdermal iontophoretic delivery of bovine insulin and monomeric human insulin analogue. *J. Control. Rel.* **59,** 99–105.

Lin, Y. H., Mi, F. L., Chen, C. T., Chang, W. C., Peng, S. F., Liang, H. F., and Sung, H. W. (2007). Preparation and characterization of nanoparticles shelled with chitosan for oral insulin delivery. *Biomacromolecules* **8,** 146–152.

Liu, J., Gong, T., Fu, H., Wang, C., Wang, X., Chen, Q., Zhang, Q., He, Q., and Zhang, Z. (2008). Solid lipid nanoparticles for pulmonary delivery of insulin. *Int. J. Pharm.* **356,** 333–344.

Ma, Z., Lim, T. M., and Lim, L.-Y. (2005). Pharmacological activity of peroral chitosan-insulin nanoparticles in diabetic rats. *Int. J. Pharm.* **293,** 271–280.

Mao, S., Germershaus, O., Fischer, D., Linn, T., Schnepf, R., and Kissel, T. (2005). Uptake and transport of PEG-graft-trimethyl-chitosan copolymer-insulin nanocomplexes by epithelial cells. *Pharm. Res.* **22,** 2058–2068.

Mesiha, M. S., Sidhom, M. B., and Fasipe, B. (2005). Oral and subcutaneous absorption of insulin poly(isobutylcyanoacrylate) nanoparticles. *Int. J. Pharm.* **288,** 289–293.

Modi, P., Mihic, M., and Lewin, A. (2002). The evolving role of oral insulin in the treatment of diabetes using a Rapid Mist^{TM} system. *Diabetes Metab. Res. Rev.* **18,** S38–S42.

Morçol, T., Nagappan, P., Nerenbaum, L., Mitchell, A., and Bell, S. J. (2004). Calcium phosphate-PEG-insulin-casein (CAPIC) particles as oral delivery systems for insulin. *Int. J. Pharm.* **277,** 91–97.

Norris, D. A., Puri, N., and Sinko, P. J. (1998). The effect of physical barriers and properties on the oral absorption of particulates. *Adv. Drug Deliv. Rev.* **34,** 135–154.

Owens, D. R., Zinman, B., and Bolli, G. (2003). Alternative routes of insulin delivery. *Diabet. Med.* **20,** 886–898.

Pan, Y., Li, Y. J., Zhao, H. Y., Zheng, J. M., Xu, H., Wei, G., Hao, J. S., and Cui, F. D. (2002). Bioadhesive polysaccharide in protein delivery system: Chitosan nanoparticles improve the intestinal absorption of insulin *in vivo*. *Int. J. Pharm.* **249,** 139–147.

Peppas, N. A., and Kavimandan, N. J. (2006). Nanoscale analysis of protein and peptide absorption: Insulin absorption using complexation and pH-sensitive hydrogels as delivery vehicles. *Eur. J. Pharm. Sci.* **29,** 183–197.

Pinto Reis, C., Neufeld, R. J., Ribeiro, A. J., and Veiga, F. (2006a). Nanoencapsulation II. Biomedical applications and current status of peptide and protein nanoparticulate delivery systems. *Nanomedicine* **2,** 53–65.

Pinto Reis, C., Neufeld, R. J., Ribeiro, A. J., and Veiga, F. (2006b). Nanoencapsulation I. Methods for preparation of drug-loaded polymeric nanoparticles. *Nanomedicine* **2,** 8–21.

Pinto Reis, C., Ribeiro, A. J., Houng, S., Veiga, F., and Neufeld, R. J. (2007). Nanoparticulate delivery system for insulin: Design, characterization and *in vitro/in vivo* bioactivity. *Eur. J. Pharm. Sci.* **30,** 392–397.

Pinto-Alphandary, H., Aboubakar, M., Jaillard, D., Couvreur, P., and Vauthier, C. (2003). Visualization of insulin-loaded nanocapsules: *In vitro* and *in vivo* studies after oral administration to rats. *Pharm. Res.* **20,** 1071–1084.

Qian, F., Cui, F., Ding, J., Tang, C., and Yin, C. (2006). Chitosan graft copolymer nanoparticles for oral protein drug delivery: Preparation and characterization. *Biomacromolecules* **7,** 2722–2727.

Radwan, M. A. (2001). Enhancement of absorption of insulin-loaded polyisobutylcyanoacrylate nanospheres by sodium cholate after oral and subcutaneous administration in diabetic rats. *Drug Dev. Ind. Pharm.* **27,** 981–989.

Radwan, M. A., and Aboul-Enein, H. Y. (2002). The effect of oral absorption enhancers on the *in vivo* performance of insulin-loaded poly(ethylcyanoacrylate) nanospheres in diabetic rats. *J. Microencapsul.* **19,** 225–235.

Reis, C. P., Ribeiro, A. J., Veiga, F., Neufeld, R. J., and Damgé, C. (2008a). Polyelectrolyte biomaterial interactions provide nanoparticulate carrier for oral insulin delivery. *Drug Deliv.* **15,** 127–139.

Reis, C. P., Veiga, F., Ribeiro, A. J., Neufeld, R. J., and Damgé, C. (2008b). Nanoparticulate biopolymers deliver insulin orally. *J. Pharm. Sci.* **97,** 5290–5305.

Sai, P., Damgé, C., Rivereau, A. S., Hoeltzel, A., and Gouin, E. (1996). Prophilactic oral administration of metabolically active insulin entrapped in isobutylcyanoacrylate nanocapsules reduces incidence of diabetes in non obese diabetic mice. *J. Autoimmun.* **9,** 713–722.

Sajeesh, S., and Sharma, C. P. (2005). Novel pH responsive polymethacrylic acid-Chitosan-polyethylene glycol nanoparticles for oral peptide delivery. *J. Biomed. Mater. Res. B Appl. Biomater.* **76,** 299–305.

Sajeesh, S., and Sharma, C. P. (2006). Cyclodextrin-insulin complex encapsulated polymethacrylic acid based nanoparticles for oral insulin delivery. *Int. J. Pharm.* **325,** 147–154.

Sarmento, B., Ribeiro, A., Veiga, F., and Ferreira, D. (2006). Development and characterization of new insulin containing polysaccharide nanoparticles. *Colloids Surf. B Biointerfaces* **53,** 193–202.

Sarmento, B., Ribeiro, A., Veiga, F., Sampaio, P., Neufeld, R., and Ferreira, D. (2007a). Alginate/chitosan nanoparticles are effective for oral insulin delivery. *Pharm. Res.* **24,** 2198–2206.

Sarmento, B., Martins, S., Ferreira, D., and Souto, E. B. (2007b). Oral insulin delivery by means of solid lipid nanoparticles. *Int. J. Nanomed.* **2,** 743–749.

Simon, M., Wittmar, M., Kissel, T., and Linn, T. (2005). Insulin containing nanocomplexes formed by self-assembly from biodegradable amine-modified poly(vinyl alcohol)-graft-poly(l-lactide): Bioavailability and nasal yolerability in rats. *Pharm. Res.* **22,** 1879–1886.

Soppimath, K. S., Aminabhavi, T. M., Kulkarni, A. R., and Rudzinski, W. E. (2001). Biodegradable polymeric nanoparticles as drug delivery devices. *J. Control. Rel.* **70,** 1–20.

Stote, R., Marbury, T., Shi, L., Miller, M., and Strange, P. (2010). Comparison pharmacokinetics of two concentrations (0.7% and 1.0%) of Nasulin, an ultra-rapid-acting intranasal insulin formulation. *J. Diabetes Sci. Technol.* **4,** 603–609.

Swaan, P. W. (1998). Recent advances in intestinal macromolecular drug delivery via receptor-mediated transport pathways. *Pharm. Res.* **15,** 826–834.

Venugopalan, P., Sapre, A., Venkatesan, N., and Vyas, S. P. (2001). Pelleted bioadhesive polymeric nanoparticles for buccal delivery of insulin: Preparation and characterization. *Pharmazie* **56,** 217–219.

Veuillez, F., Kalia, Y. N., Jacques, Y., Deshusses, J., and Buri, P. (2001). Factors and strategies for improving buccal absorption of peptides. *Eur. J. Pharm. Biopharm.* **51,** 93–109.

Xu, H. B., Huang, K. X., Zhu, Y. S., Gao, Q. H., Wu, Q. Z., Tian, W. Q., Sheng, X. Q., Chen, Z. X., and Gao, Z. H. (2002). Hypoglycaemic effect of a novel insulin buccal formulation on rabbits. *Pharmacol. Res.* **46,** 459–467.

Yang, R., Gao, R. C., Cai, C. F., Xu, H., Li, F., He, H. B., and Tang, X. (2010). Preparation of gel-core-solid lipid nanoparticle: A novel way to improve the encapsulation of protein and peptide. *Chem. Pharm. Bull.* **58,** 1195–1202.

Zhang, Q., Shen, Z., and Nagai, T. (2001). Prolonged hypoglycemic effect of insulin-loaded polybutylcyanoacrylate nanoparticles after pulmonary administration to normal rats. *Int. J. Pharm.* **218,** 75–80.

Zhang, N., Ping, Q., Huang, G., Han, X., Cheng, Y., and Xu, W. (2006). Transport characteristics of wheat germ agglutinin-modified insulin-liposomes and solid lipid nanoparticles in a perfused rat intestinal model. *J. Nanosci. Nanotechnol.* **6,** 2959–2966.

Zhang, Y., Zhu, J., Tang, Y., Chen, X., and Yang, Y. (2009). The preparation and application of pulmonary surfactant nanoparticles as absorption enhancers in insulin dry powder delivery. *Drug Dev. Ind. Pharm.* **35,** 1059–1065.

CHAPTER FIFTEEN

Chitosan-Coated Solid Lipid Nanoparticles for Insulin Delivery

Pedro Fonte,[*] Fernanda Andrade,[†] Francisca Araújo,[*] Cláudia Andrade,[*] José das Neves,[†] *and* Bruno Sarmento[*,†]

Contents

Abstract

The delivery of therapeutic proteins like insulin, exploiting routes of administration different from the traditional injectable forms, has been investigated extensively, taking advantage of the nanotechnology tools available nowadays in the massive drug delivery system pipeline. In this chapter, we describe in detail the preparation of solid lipid nanoparticles (SLN), further coated with the

[*] Health Sciences Research Center, Instituto Superior de Ciências da Saúde, Norte, Rua Central de Gandra, Gandra, Portugal
[†] Department of Pharmaceutical Technology, Faculty of Pharmacy, University of Porto, Rua Aníbal Cunha, Porto, Portugal

Methods in Enzymology, Volume 508
ISSN 0076-6879, DOI: 10.1016/B978-0-12-391860-4.00015-X

mucoadhesive polymer chitosan, intended for intestinal absorption of insulin after oral administration. We give special focus on the characterization of the SLN and of the biomacromolecule by itself after encapsulation, because of the intrinsic labile properties of insulin during the manufacturing process. We also describe methods to determine the *in vitro* intestinal permeability of insulin that solid lipid and chitosan-coated SLN can afford, as well as *in vivo* models to evaluate the hypoglycemic effect in diabetic animals.

1. Introduction

Insulin has been usually administered subcutaneously for the treatment of diabetes mellitus. Several attempts have been made to find alternative routes of insulin administration that improve patient compliance and avoid injections (Cefalu, 2004; Ghilzai, 2003; Owens, 2002). Among all routes, oral delivery is the most desirable one since it is noninvasive thus avoiding the contamination/infection risks associated with injectables, and is physiologically advantageous, because it better mimics the normal insulin pathway after endogenous secretion (Hoffman and Ziv, 1997; Owens, 2002). However, insulin, as other polypeptides, presents formulation challenges such as poor chemical and physical stability and short plasma half-time. This often leads to low bioavailability, mainly resulting from degradation in the stomach, digestion and inactivation in the intestinal cavity by proteolytic enzymes, and poor permeability through the intestinal epithelium because of its lack of lipophilicity and high molecular weight (Carino and Mathiowitz, 1999).

Solid lipid nanoparticles (SLN) are submicron colloidal carriers (usually 50–1000 nm), composed of lipids that are solid at body and room temperature, and dispersed either in an aqueous surfactant solution or water (Rawat *et al.*, 2006). The lipids that compose SLN can be complex acylglycerol mixtures, highly purified triacylglycerols or waxes. SLN gained increased interest among nanoparticulate systems in the past years mainly due to their biocompatibility, good tolerability, biodegradation (Almeida and Souto, 2007; Sarmento *et al.*, 2007b), and even by the possibility of large industrial scale production (Muller *et al.*, 2000). It has been reported that lipid nanoparticles encapsulating therapeutic proteins can improve their bioavailability, prolong their blood residence time, and/or modify their biodistribution (Garcia-Fuentes *et al.*, 2005). In fact, SLN are able to protect proteins from enzymatic degradation in the intestinal environment and enhance their selective uptake, resulting in prolonged therapeutic effect (Sarmento *et al.*, 2007b). Therefore, SLN have been proposed for the oral delivery of insulin for the treatment of diabetes mellitus (Liu *et al.*, 2007; Sarmento *et al.*, 2007b; Trotta *et al.*, 2005; Zhang *et al.*, 2006). Actually, SLN

and other lipid-based drug delivery systems are known to enhance the oral absorption of many drugs (Charman, 2000; Charman *et al.*, 1997). When SLN are administered orally, they can be absorbed either through the membranous epithelial cells (M-cells) of the Peyer's patches in the gut-associated lymphoid tissue (GALT) or transcellularly (Damge *et al.*, 2008).

Surface modification of nanoparticles with chitosan, a natural cationic polysaccharide derived from chitin, is a promising strategy to enhance the penetration of encapsulated macromolecules, such as insulin, through mucosal surfaces. This biopolymer has been used for developing drug delivery systems because of its good biocompatibility, biodegradability, low toxicity, antimicrobial, mucoadhesive, and absorption enhancing properties (Braz *et al.*, 2011). Insulin-loaded chitosan nanoparticles have been shown to yield a significant hypoglycemic effect when administered orally to diabetic animal models (Cui *et al.*, 2009; Reis *et al.*, 2008; Sarmento *et al.*, 2007c,d). In fact, the mucoadhesive properties of chitosan may enhance drug uptake, because the contact with the intestinal epithelium is maintained for longer periods and the penetration of the active drug is improved because of the prolonged concentration gradient between the intestinal membrane and nanoparticles. Further, chitosan is an effective permeability enhancer as it reversibly changes tight junctions (Cano-Cebrian *et al.*, 2005; Smith *et al.*, 2005).

Recently, our group demonstrated the ability of chitosan-coated SLN to enhance the intestinal uptake of insulin by showing its physiologic effect after oral administration to rats (Fonte *et al.*, 2011). Comparatively to uncoated SLN, we were able to reach a significant improvement of the hypoglycemic effect. This is probably due to chitosan mucoadhesive properties which promote the intestinal insulin uptake while overcoming the degradation of insulin in the gastrointestinal tract. Nevertheless, there is a major limitation in the oral delivery of insulin-loaded nanoparticles, besides the rate of permeation of nanoparticles through the intestinal epithelium, which is the elimination of nanoparticles by the mononuclear phagocyte system (MPS) (Champion *et al.*, 2008; Yin *et al.*, 2007). Macrophages present in tissues such as the lymph nodes, liver, spleen, and bone marrow are also an additional factor in the elimination of nanoparticles. The role of PEG (Owens and Peppas, 2006) and some hydrophilic polysaccharide (Lemarchand *et al.*, 2004) coating in avoiding phagocytosis of nanoparticles by macrophages is reported in the literature. Recently, we have demonstrated that chitosan-coated SLN were not internalized by the murine macrophage cell line, RAW 264.7, while uncoated SLN were taken up by these cells (Sarmento *et al.*, 2011). Chitosan was able to provide stealth properties to SLN, resulting in the absence of phagocytosis. All these findings open perspectives for the optimization of long-time blood circulating chitosan nanoparticles.

2. Preparation of Chitosan-Coated SLN

The described method for the preparation of chitosan-coated SLN is based on those developed previously by our group for the delivery of insulin (Fonte *et al.*, 2011; Sarmento *et al.*, 2011). It is based on the initial preparation of negatively charged SLN by a water-in-oil-in-water (w/o/w) emulsion method, followed by their coating with low molecular weight chitosan. The coating mechanism of SLN is simple adsorption resulting from the electrostatic interaction of chitosan (positively charged) with the negatively charged surface of SLN. Besides being simple and robust, the method is considered adequate because of its mild nature (no heat or chemical functionalization is involved), thus assuring the integrity of insulin's structure and its functionality. The oral administration of chitosan-coated insulin SLN to diabetic rats had resulted in a significant hypoglycemic effect up to 24 h, which was more pronounced than the one obtained after the administration of noncoated insulin-loaded SLN (Fonte *et al.* 2011). These results confirmed that this association under *in vivo* conditions remains stable.

2.1. Materials

Different lipids, either alone or in mixture, have been used by our group to produce SLN for the delivery of insulin. Examples include cetyl palmitate, Witepsol 85E (triglycerides of C10–C18 saturated fatty acids), Compritol 888 ATO (glycerol dibehenate EP), and Precirol ATO 5 (glyceryl mono-/di-/tri-palmitate/stearate) (Fonte *et al.*, 2011; Sarmento *et al.*, 2007b, 2011). All lipids can be obtained from Gattefossé (Nanterre, France) or Sasol (Brunsbüttel, Germany). Human zinc-insulin (lyophilized human biosynthetic insulin) is provided by Lilly Portugal (Queijas, Portugal), and chitosan (50 kDa, degree of deacetylation of 85%) is from Sigma-Aldrich Química, S.A. (Sintra, Portugal). All other materials are of analytical grade or equivalent.

2.2. Preparation protocol

The following protocol describes the detailed steps for obtaining insulin-loaded chitosan-coated SLN. Different SLN formulations can be coated with chitosan and are presented in Table 15.1. Variations in composition and operation parameters can result in changes in the final properties of nanoparticles (e.g., size, zeta potential, polydispersity index, insulin association).

Table 15.1 Insulin-loaded SLN formulations developed in our group

	Sarmento *et al.* (2007b)	Sarmento *et al.* (2011)	Fonte *et al.* (2011)
Internal water phase	Insulin (7 mg) in hydrochloride acid solution (0.1*M*; 0.5 ml)	Insulin (1 mg) in hydrochloride acid solution (0.1*M*; 0.2 ml)	Insulin (7 mg) in hydrochloride acid solution (0.1*M*; 0.2 ml)
Oil (lipid) phase	Cetyl palmitate (200 mg) dissolved in dichloromethane (4 ml)	Witepsol 85E, Compritol 888 ATO, or Precirol ATO 5 (200 mg) dissolved in dichloromethane (2 ml)	Witepsol 85E (200 mg) dissolved in chloroform (4 ml)
External water phase	Poloxamer 407 (2%, w/v; 25 ml)	Tween 80 or poloxamer 407 (2%, w/v; 20 ml)	Tween 80 (2%, w/v; 25 ml)

1. The lipid(s) are dissolved in the organic solvent in a 20 ml glass test tube by vortexing—this is the oil (lipid) phase. To minimize solvent evaporation, handling open tubes should be avoided. These operations should be carried out in a fume hood, and the appropriate measures should be followed to minimize exposure to organic solvents during this and the following steps.
2. The insulin is dissolved in hydrochloride acid solution (0.1 *M*) by gentle shaking—this is the internal water phase. We have replaced insulin by FITC-labeled insulin for fluorescence tracking purposes without affecting significantly the process or final properties of SLN.
3. The internal water phase is added to the lipid(s) organic solution and mixed for 30 s, using an Ultra-Turrax T25 mechanical homogenizer (IKA®-Werke GmbH & Co. KG, Staufen, Germany) at 20,000 rpm, or a sonicator (VibraCell model VCX130W equipped with a 6 mm sonication probe, Sonics & Materials, Inc., Newtown, CT, USA) at 70% amplitude—this step produces the w/o emulsion. To avoid solvent evaporation due to the temperature increase during mixing, particularly when using the sonicator, the test tube should be placed in an ice bath.
4. This emulsion is poured into a 50 ml glass beaker containing the external water phase and mixed for 30 s, using the mechanical homogenizer (20,000 rpm) or the sonicator (70% amplitude)—this is the w/o/w emulsion.

5. The previous emulsion is stirred magnetically at 300 rpm for 3 h to allow for organic solvent evaporation—this step produces the SLN dispersion.
6. The SLN dispersion is transferred into a beaker containing a 20 ml solution of 0.5% (w/v) chitosan and 2% (w/v) surfactant (the same used in step 4) in 1% (w/v) acetic acid, and keep under magnetic stirring overnight—the product is termed the chitosan-coated SLN dispersion. The final colloidal dispersion presents typically a final pH value around 4. We have replaced chitosan by FITC-labeled chitosan for fluorescence tracking purposes without significantly affecting the final properties of the SLN.

The obtained chitosan-coated SLN usually present diameters in the nano-range (200–800 nm) but microparticles can also be obtained for some lipid(s)/surfactant pairs (e.g., 1100–2200 nm for Precirol ATO 5/Tween 80) (Sarmento *et al.*, 2011). Sonication usually leads to lower diameters of SLN as compared to mechanical homogenization. Also, the use of poloxamer 407 generally leads to smaller SLN as compared to Tween 80 (Sarmento *et al.*, 2011). Different organic solvents from the ones indicated have also been used successfully in the preparation of SLN, namely acetone, diethyl ether, and ethyl acetate (Fonte *et al.*, 2011). In the case of acetone and ethyl acetate, partial miscibility of these solvents with water leads to emulsion destabilization and thus higher nanoparticle diameter. In general, noncoated SLN present zeta potentials of -15 to -25 mV, whereas values of $+11$ to $+38$ mV are observed for chitosan-coated SLN (Fonte *et al.*, 2011; Sarmento *et al.*, 2011). Further, there is an increase in diameter upon chitosan coating or aggregation (as reflected by increased polydispersity index values) because of the interaction of one chitosan molecule with multiple nanoparticles (Sarmento *et al.*, 2011). Insulin association efficiency is variable, but values are typically in the range of 39–66%.

3. Physicochemical Characterization of SLN

3.1. Determination of particle size and polydispersity index

The measurement of particle size is generally performed using photon correlation spectroscopy (PCS) also called quasi-elastic light scattering (QELS) or dynamic light scattering (DLS), which is based on the scattering of a laser light by submicron particles in suspension in a time-dependent manner (Xu, 2002b). The diffusion of particles over time (Brownian motion) causes fluctuations in the intensity of the light scattered at a certain detection angle (varying from 10° to 90°). The technique is based on the principle that smaller particles move with higher velocity than larger particles. Random Brownian motion of particles causes the intensity of light scattered from the particles to form a moving speckle pattern. This

movement can be detected as a change in intensity with time with suitable optics and a photomultiplier. Larger particles move more slowly than small particles, so that the rate of fluctuation of the light scattered from them also slower. PCS uses the rate of change of these light fluctuations to determine the size distribution of the particles scattering light. This correlation between the time and the light intensity variation results in a diffusion coefficient that is converted to particle size, resulting in an average of effective hydrodynamic diameter and polydispersity index, which is a measure for the width of the distribution (Xu, 2002b).

The measurements are generally carried out at 20–25 °C, with the detection angle fixed at 90°, and can be performed using different instruments, such as the Malvern ZetaSizer 5000, the ZetaSizer Nano ZS (Malvern Instruments, UK), or the 90Plus Particle Size Analyzer (Brookhaven Instruments Corporation, Holtsville, NY).

Samples are diluted with purified and deionized water (usually 18.2 MΩ·cm or lower) or a buffer solution to achieve suitable concentration for determination, placed in a cell appropriate for the instrument, and measured. A dilution is usually required for very concentrated samples to eliminate the multiple scattering resulting from particle aggregates (particle–particle interactions), or for standardization purposes (Xu, 2002b). It is necessary to ensure that the cell walls are clean (appropriate lab wipes should be used) and unscratched and that there are no bubbles in the liquid. This may interfere with the laser beam and give wrong results.

3.2. Determination of the zeta potential

Zeta potential (ζ) is the surface charge of the particle and can be determined by measuring the velocity of the particle moving in a cell under the influence of an applied electric field (electrophoretic mobility). The electrophoretic mobility of the particles is related to the electric field strength and to the particle's electric potential at the boundary between the moving particle and liquid and is defined as the electrophoretic velocity (u) per unit of the applied electric field (E)—see Eq. (15.1) (Clogston and Patri, 2011; Xu, 2002a).

$$\mu = u/E \tag{15.1}$$

For colloidal particles, the usual units are μm cm/V s, although the SI units are m^2/V s.

The relationship between zeta potential and electrophoretic mobility is given by the Henry equation (Eq. (15.2)).

$$\mu = \frac{2\zeta\varepsilon}{3\eta} f(Ka) \tag{15.2}$$

where ε is the dielectric constant, η is the viscosity of the dispersing liquid, and $f(Ka)$ is Henry's function (generally 1 or 1.5).

The Smoluchowski approximation—Eq. (15.3)—of the Henry equation is commonly used, because most of the determinations of the zeta potential are made in aqueous solutions with moderate electrolyte concentration, for which $f(Ka)$ takes the value of 1.5.

$$\mu = \frac{\zeta \varepsilon}{\eta} \tag{15.3}$$

For small particles (generally < 200 nm) in liquids with low dielectric constant and determinations in nonaqueous solutions, $f(Ka)$ assumes the value of 1, corresponding to the Hückel approximation Eq. (15.4) (Xu, 2002a).

$$\mu = \frac{2\zeta \varepsilon}{3\eta} \tag{15.4}$$

There are different techniques available for electrophoretic mobility determination, namely, electrophoretic light scattering (ELS), laser doppler anemometry (LDA), and phase analysis light scattering (PALS).

Basically, the sample is diluted in purified and deionized water having a conductivity adjusted to 50 μS/cm by addition of a 0.9% NaCl solution and placed in the appropriate measuring cell in order to cover the electrodes (Sarmento *et al.*, 2007b). When the electric field is applied, the particles move toward the electrode of opposite charge. A laser beam passes through the sample and the fluctuation in the intensity of the light scattered by the particles is proportional to their velocity. Then the software calculates the electrophoretic mobility and transforms the values into the zeta potential. The instruments used for zeta potential measurements are, in many cases, the same used for particle size determination. It is necessary to ensure that the electrodes are covered with liquid and that there are no bubbles. Like in the case of size determination, the cell walls need to be clean and unscratched.

The magnitude of the zeta potential provides an indication of the possible stability of colloidal systems. It is generally assumed that colloidal systems possessing a zeta potential higher than |30 mV| are strongly charged, and consequently, stable because of particle–particle repulsion (i.e., aggregation is avoided), whereas particles between -10 and $+10$ mV are considered approximately neutral (Clogston and Patri, 2011).

3.3. Morphological analysis of SLN

The morphological analysis of nanoparticles is performed using microscopic techniques such as scanning electron microscopy (SEM) or transmission electron microscopy (TEM). For SEM images, freeze-dried SLN are

mounted on metal stubs using adhesive tape, gold coated under vacuum and examined on a JSM-840 SEM from JEOL Ltd. (Tokyo, Japan) (Fonte *et al.*, 2011). In the case of TEM images, the samples are deposited on a grid, treated with uranyl acetate, and observed in an EM 902A TEM from Zeiss (Göttingen, Germany) (Sarmento *et al.*, 2007b). The images are captured with a camera attached to the microscope.

SLN typically exhibit a spherical shape, and a dense lipid matrix without aggregation (Fig. 15.1) (Sarmento *et al.*, 2007b), whereas chitosan-coated SLN aggregate to some extent (Fig. 15.2), which could be explained by the stickiness of the polymer. However, this low aggregation is reverted because the particles can be resuspended easily (Fonte *et al.*, 2011). Additionally, microscopy images are used to reinforce size and dispersion values, as previously described.

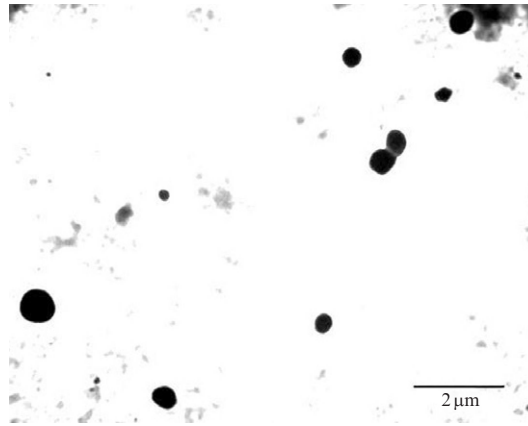

Figure 15.1 TEM micrographs of insulin-loaded SLN. Reprinted with permission from Sarmento *et al.* (2007b).

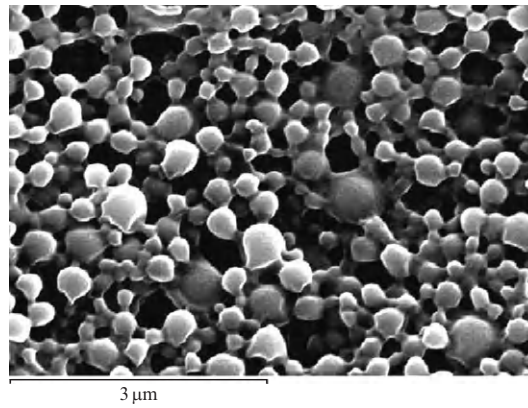

Figure 15.2 SEM microphotographs of insulin-loaded, chitosan-coated SLN. Reprinted with permission from Fonte *et al.* (2011).

3.4. Stability of SLN

The stability of nanoparticles is determined by monitoring their mean particle size and zeta potential over time. After production, samples are stored at 4 °C in aqueous solution, and then the size and zeta potential are measured on regular intervals up to 60 days of shelf-life (Sarmento *et al.*, 2006a). Stability tests may be performed for a period exceeding 60 days, if necessary. Morphological analysis can also be performed.

3.5. Insulin association efficiency and loading capacity

The association efficiency (AE), defined as the amount of insulin associated with the particles, is determined indirectly by the difference between the total amount used to prepare the systems, and the amount of insulin remaining in the aqueous phase after SLN isolation, according to Eq. (15.5). The aqueous phase is recovered after centrifugation of the SLN suspension (UL 80 ultracentrifuge, rotor type 55-S, Beckman Instruments, Germany) for 45 min at 50,000 rpm (corresponding to approx. 200,000 × *g*) (Sarmento *et al.*, 2011). The insulin concentration in the supernatant is determined by high performance liquid chromatography (HPLC) with UV detection (see Section 3.7).

$$\text{AE}\% = \frac{\text{total amount of insulin} - \text{free insulin in supernatant}}{\text{total amount of insulin}} \times 100 \tag{15.5}$$

The loading capacity (LC), defined as the mass percentage of insulin of the total mass of the particles, is calculated using Eq. (15.6). The total weight of the nanoparticles (dry mass) is obtained by freeze-drying an aliquot of a particle suspension before centrifugation (Fonte *et al.*, 2011).

$$\text{LC}\% = \frac{\text{total amount of insulin} - \text{free insulin in supernatant}}{\text{total weight of nanoparticles}} \times 100 \tag{15.6}$$

3.6. Insulin release from SLN

To estimate the insulin release profile from nanoparticles after oral administration, gastrointestinal conditions are simulated during the study. Insulin-loaded SLN (200 mg) are placed into 20 ml of HCl buffer at pH 1.2 and incubated at 37 °C for 2 h under magnetic stirring (100 rpm). At predetermined time points, 0.4 ml samples are collected for insulin determination and replaced by fresh medium. After 2 h, the same nanoparticles are isolated

by centrifugation as described previously, transferred to 20 ml of phosphate buffer at pH 6.8 and incubated at 37 °C for an additional 4 h period under magnetic stirring (100 rpm). At determined times, 0.4 ml samples are collected for insulin determination and replaced by fresh medium (Sarmento *et al.*, 2007c). The replacement of the removed samples with fresh medium is important to maintain the sink conditions. It is important not forget to take into account this dilution factor in the calculations of the amount of insulin released.

3.7. Insulin determination by HPLC-UV

Insulin concentration in the supernatant for AE and LC determination and in samples collected in release studies is determined using a reversed-phase HPLC-UV method developed and validated by our group (Sarmento *et al.*, 2006b).

The mobile phase of the chromatographic method consists of acetonitrile:0.1% (v/v) trifluoroacetic acid (TFA) aqueous solution initially set to a ratio of 30:70 (v/v), which is linearly changed to 40:60 (v/v) over 5 min. From 5 to 10 min the ratio is kept constant at 40:60 (v/v). The mobile phase is pumped at a constant flow rate of 1 ml/min, the injection volume is 20 µl and the detection wavelength used is 214 nm. The HPLC system is equipped with an XTerra RP 18 column, 5 µm particle size, 4.6 mm internal diameter × 250 mm length (Waters, USA) and a LiChrospher® 100 RP-18, 5 µm particle size guard column (Merck, Germany). All experiments are performed at room temperature, and the total area of the peak is used to quantify insulin. The calibration curves are prepared using human insulin standard solutions at concentrations of 3, 6, 12.5, 25, and 100 µg/ml in acetate buffer pH 4.7 (Sarmento *et al.*, 2011).

3.8. Analysis of insulin integrity

During the production of SLN, insulin is exposed to variations in conditions such as temperature, pH, or agitation/sonication that could lead to denaturation due to its labile nature with consequent loss of activity. It is important to know that the encapsulated insulin maintains its conformational structure. The maintenance of insulin integrity after encapsulation can be performed using different methods namely circular dichroism (CD) or Fourier transform infrared (FTIR) spectroscopy. The existence of differences between the spectra of insulin before and after encapsulation obtained by these techniques is associated with changes in its structure and/or conformation (Sarmento *et al.*, 2007a).

CD spectroscopy consists of the use of circularly polarized light to study the conformation of asymmetrical molecules. Proteins absorb right- and left-circularly polarized light differently according to their optical activity.

It is possible to obtain CD spectra using near (240–340 nm) or far (190–240 nm) UV radiation to analyze tertiary and secondary protein structure, respectively (Bloemendal and Jiskoot, 2005).

To probe insulin's secondary structure, CD spectra are obtained at room temperature on an Olis DSM 10 Spectrophotometer (Georgia, USA), using an insulin concentration of 0.2 mg/ml. In the far-UV region, CD spectra are recorded in a 0.01 cm cell from 250 to 190 nm, using a step size of 0.5 nm, a bandwidth of 1.5 nm, and an averaging time of 5 s, with the lamp housing purged with nitrogen to remove oxygen. For all spectra, an average of five scans is usually obtained. CD spectra of the appropriate reference are recorded and subtracted from the protein spectra. The molar ellipticity for insulin is calculated according to Eq. (15.7). Insulin concentration is determined by UV absorption at 276 nm using an extinction coefficient of 1.08 for 1.0 mg/ml (Sarmento *et al.*, 2007a).

$$\text{Molar ellipticity} = \frac{\text{CD sinal} \times \text{MRW}}{\text{insulin concentration} \times \text{cell path length}} \qquad (15.7)$$

where MRW is the mean residual weight of each insulin residue (115 Da). For these measurements, it is essential that the cell walls are clean and unscratched.

Atoms within molecules oscillate around an equilibrium point and the wavelength of that oscillation is in the infrared (IR) region (1–100 μm). In IR spectroscopy, the IR radiation passes through a sample where some of the radiation is absorbed and other transmitted. The absorption of radiation excites the vibrational motions of atoms whose energy corresponds to specific bonds or functional groups such as O—H, S—H, or C═O. The resulting spectrum represents a fingerprint of the sample with absorption peaks, which correspond to the frequencies of vibrations between the bonds of the atoms that constitute the molecules. The spectrum is plotted using a wavenumber scale that ranges from 10 to 10,000 cm^{-1} (van de Weert *et al.*, 2005). The amide groups of protein generate a number of characteristic IR bands that can be used to determine protein conformation and secondary structure. In particular, the amide I band, which is in the region of 1600–1700 cm^{-1}, is primarily due to the amide C═O stretching vibrations (Jiang *et al.*, 2011).

IR spectra are measured using a Bomem IR spectrometer (Bomem, Canada). The hydrated samples are placed in a cell with CaF_2 crystal windows and a 6 μm spacer. For solid samples, aliquots corresponding to 2 mg of insulin are gently mixed with 300 mg of micronized KBr powder and compressed into disks at a force of 10 kN for 2 min using a manual tablet press (Perkin-Elmer, Norwalk, USA). For each spectrum, a 256-scan interferogram is collected with a 4 cm^{-1} resolution in the mid-IR region at room temperature. Insulin spectra are obtained according to a double subtraction procedure and insulin-free systems and water vapor spectra are collected

under identical conditions for blank subtraction. The second-derivative spectra are obtained with a seven-point Savitsky–Golay derivative function and the baselines are corrected using a 3–4-point adjustment. In addition, spectra are area-normalized in the amide I region from 1710 to 1590 cm^{-1} using the Bgrams software (Galactic Industries, Salem, NH, USA) and area-overlap compared to an insulin aqueous standard solution of 10 mg/ml, in an appropriated buffer (Origin software, OriginLab Co., Northampton, MA, USA) (Sarmento *et al.*, 2007a).

During the formation of KBr disks, it is important to ensure that insulin/SLN are homogeneously dispersed into KBr and that the obtained disks have equal thickness throughout its diameter with no cracks. The disk should be handled carefully to avoid breakage.

4. Biological Characterization of Insulin-Loaded SLN

4.1. Insulin bioactivity

The maintenance of the biological activity of insulin after encapsulation can be assessed by a commercially available enzyme-linked immunosorbent assay (ELISA) (Mercodia, Uppsala, Sweden). This ELISA kit comprises a solid phase two-site enzyme immunoassay. It is based on the direct sandwich technique in which two monoclonal antibodies are directed against separate antigenic determinants of the insulin molecule. During incubation, the insulin in the sample reacts with peroxidase-conjugated anti-insulin antibodies and anti-insulin antibodies bound to the microtitration well. A simple washing step removes unbound enzyme-labeled antibody. The bound conjugate is detected by reaction with 3,3′,5,5′-tetramethylbenzidine. The reaction is stopped by adding an acid solution to give a colorimetric endpoint that is read at 450 nm.

Aliquots of samples taken during release assays are accurately diluted with purified and deionized water according to the ideal concentration range of the method (1–200 mU/l) and the manufacturer's protocol (Sarmento *et al.*, 2006a).

4.2. *In vitro* permeability studies

The permeability of chitosan-coated SLN can be assessed by *in vitro* studies using relevant cell monolayers. To evaluate the effect of chitosan on insulin absorption, the *in vitro* experiments can be performed in the well-established intestinal cell models like Caco-2 cell monolayer model and in an improved Caco-2/HT29 coculture cell monolayer model, which can better simulate the mucosal intestinal tissue.

Enterocyte Caco-2 cells (passages 70–75) and mucus-producing intestinal HT29 cells (passages 18–25) are maintained separately in Dulbecco's modified Eagle medium (DMEM) supplemented with 2 m*M* L-glutamine, 1% penicillin-streptomycin, 1% nonessential amino acids, and 10% heat-inactivated fetal bovine serum (further referred simply as complete DMEM). Both cell lines are cultured at 37 °C in an atmosphere of 5% CO_2/95% air and 90% relative humidity. The cells are routinely subcultured once a week after treatment with trypsin–EDTA (0.25%, 0.53 m*M*) and seeded at a density of 4×10^5 cells per 75 cm^2 flask. The medium is changed every other day. For experimental studies, Caco-2, HT29, and the mixture of Caco-2/HT29 (90:10 ratio) cells are seeded at a density of 1×10^5 cells/cm^2 onto Transwell® plates (4.1 cm^2 area, Corning Life Sciences, Acton, MA, USA) and maintained in complete DMEM. The medium is changed every other day.

All the cell monolayers are used after 21 days in culture. Monolayer development during this time is monitored by measuring the transepithelial electric resistance (TEER) using the EVOM equipment (World Precision Instruments, Aston, UK).

Insulin permeability experiments are performed at 37 °C from the apical to the basolateral chamber for both insulin encapsulated into nanoparticles (either chitosan-coated or not) and insulin in aqueous solution. The initial apical concentration is set to 100 μg/ml in a final volume of 1.5 ml. The transport experiments are run in HBSS at 37 °C. The basolateral samples are collected at different time points, and the insulin is determined by the previously described HPLC-UV (Sarmento *et al.*, 2006b). The TEER values are measured during the experiment in order to evaluate the integrity of the cell monolayer.

Figure 15.3 shows that the insulin transport through Caco-2 cell monolayer is increased upon encapsulation into SLN, and this effect is even higher when insulin is encapsulated into chitosan-coated SLN (Fonte *et al.*, 2011). The difference between uncoated SLN and chitosan-coated SLN on increasing insulin permeation is more prominent after 1 h, probably because of a delayed insulin release from nanoparticles. Thus, chitosan-coated SLN demonstrate better permeation-enhancing properties as compared to uncoated SLN. This is mainly due to chitosan mucoadhesive and permeability enhancing properties (Cano-Cebrian *et al.*, 2005; Yin *et al.*, 2009). Further, insulin can be released from the nanoparticles attached to the cell monolayer or transported inside the nanoparticles by the transcellular pathway.

During the experiments, the TEER values can decrease slightly because of the effect of chitosan on the tight junctions between intestinal cells. This decrease should not be below 80% of the initial values, thus assuring that the integrity of cell monolayers is maintained

The role of chitosan on insulin intestinal absorption is better understood using a Caco-2/HT29 coculture monolayer model, taking advantage of the

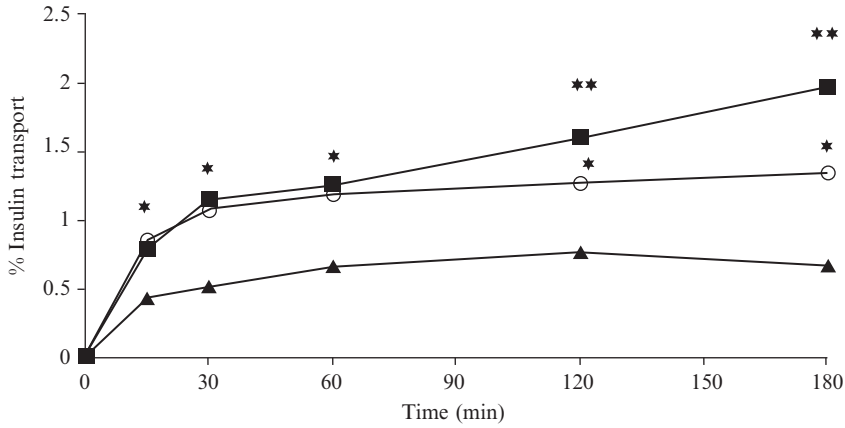

Figure 15.3 Cumulative transport of insulin across Caco-2 cell monolayers when encapsulated into SLN (empty circles) and into chitosan-coated SLN (filled squares), and compared with insulin in aqueous solution (filled triangles). $n = 3$; mean ± SD; (*) $p < 0.05$, SLN and chitosan-coated SLN showed statistically significant differences from insulin solution control; (**) $p < 0.05$, chitosan-coated SLN showed statistically significant differences from SLN. Reprinted with permission from Fonte *et al.* (2011).

mucous-secreting properties of HT29 cells. Figure 15.3 shows that the permeability of insulin is higher on the coculture model as compared to the Caco-2 model. The presence of HT29 mucus-producing goblet cells seems to have an important role on insulin permeation. In fact, the permeation rates of insulin, either in solution or encapsulated into SLN or chitosan-coated SLN, are twofold to threefold higher as compared to the Caco-2 cell monolayer model.

As indicated before, the TEER values can slightly decrease during the experiment, but this decrease must not be below 80% of the initial value, in order to assure the integrity of the monolayer.

These results show that the mucus present on the surface of the apical side of the cell monolayer facilitates the paracellular transport of the encapsulated insulin, which may also be related with the decreased value of TEER for coculture systems. Moreover, the absorption of insulin from SLN is higher in presence of the HT29 cells, highlighting the possible role of mucus on the retention of nanoparticles and the protein itself on the intestinal epithelium, prolonging its therapeutic window. Further, the percentage of insulin transport for chitosan-coated SLN through the Caco-2/HT29 coculture monolayer is higher than through the Caco-2 monolayer, highlighting that the enhancement of the nanoparticle mucoadhesion properties can be performed to promote the contact of proteins with the intestinal epithelium, increasing the concentration at the site of absorption (Garcia-Fuentes *et al.*, 2005), and increase its permeation either para- or transcellularly (Fig. 15.4) (Fonte *et al.*, 2011).

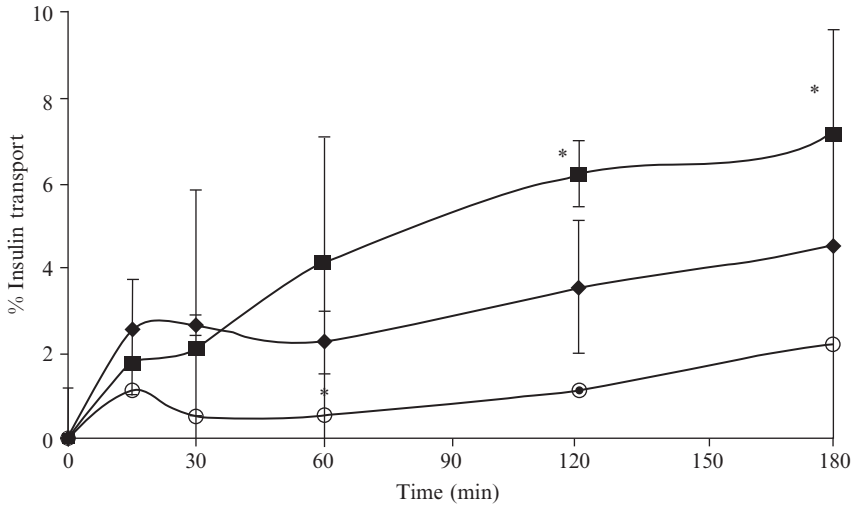

Figure 15.4 Cumulative transport of insulin across Caco-2/HT29 coculture monolayer when encapsulated into SLN (filled diamonds) and into chitosan-coated SLN (filled squares), and compared with insulin in aqueous solution (circles). $n = 3$; mean $\pm$ SD; (*) $p < 0.05$, chitosan-coated SLN showed statistically significant differences from insulin solution control. Reprinted with permission from Fonte *et al.* (2011).

In summary, the enhancement of insulin permeation as enhanced by its encapsulation in chitosan-coated SLN is verified *in vitro* using the Caco-2 intestinal cell monolayer. This effect is even more pronounced when the mucus-producing HT29 cells are included in the Caco-2 cell monolayer model.

4.3. Pharmacological activity of insulin-loaded SLN

In vivo studies are performed in diabetic animal (e.g., rat) to assess the pharmacological activity of insulin encapsulated into SLN. All experiments need to be carried out in accordance with Good Animal Laboratory Practice guidelines and approval of the local ethical committees. The work described here was performed according to the Federation of European Laboratory Animal Science Association Guide for the Care and Use of Laboratory Animals

Exposure of the animals to stress is of extreme importance in causing a disturbance to glycemia, and appropriate measures should be put into practice to minimize it.

Male Wistar rats weighing 200–250 g are housed in controlled environmental conditions of temperature (22 $\pm$ 2 °C) and relative humidity (45–65%) with lighting on a standard 12 h on/12 h off cycle. The rats are fed with

standard diet feed (Mucedola Top Certificate, Italy) and provided with tap water *ad libitum*. Diabetes is induced by a single intraperitoneal injection of streptozocin (50 mg/ml in citrate buffer, pH 4.5) at a dose of 50 mg/kg of body weight. After 2 weeks, rats presenting fasted blood glucose levels above 250 mg/dl are used for experiments. Diabetic rats are fasted for 12 h before the beginning of the experiment and remain fasted afterward for 24 h with free access to water (Fonte *et al.*, 2011; Sarmento *et al.*, 2007c).

SLN and chitosan-coated SLN dispersions (1.0 ml PBS) are administered intragastrically to rats by means of a gavage needle at an insulin dose of 25 IU/kg, based on the total insulin content of SLN. Control rats are similarly administered with equivalent volumes of insulin oral solution (25 IU/kg, in PBS). Also, a control group treated with subcutaneous insulin (2.5 UI/kg) is included in the experiment (Fonte *et al.*, 2011).

Blood samples are collected from the tip of the tail vein after needle puncture. A 0.1 ml aliquot is collected before and after administration at regular time points. Plasma glucose levels are determined using the Medisense Precision Xceed Kit (Abbott, Portugal; range 10–600 mg/dl) and expressed as the percentage of the baseline plasma glucose levels. The serum insulin concentration is measured by ELISA as described above. Results are shown as the mean (±SEM) of at least six animals.

Plots of plasma glucose levels versus time are used to evaluate the cumulative hypoglycemic effect after insulin administration. This effect is quantified by determining the area above the curve (AAC) by using the trapezoidal method. Pharmacological availability (PA) of peroral insulin-loaded into SLN and in solution is determined as the relative measure of the cumulative reduction in glucose blood levels as compared to the control insulin administered subcutaneously at a dose of 2.5 IU/kg (corresponding to 100% availability), using the following equation (Fonte *et al.*, 2011; Sarmento *et al.*, 2007c):

$$\mathrm{PA} = \frac{\mathrm{AAC\ oral/dose\ oral}}{\mathrm{AAC\ s.c./dose\ s.c.}} \times 100 \tag{15.8}$$

The encapsulation of insulin into SLN improves its pharmacological activity after oral administration as compared to the insulin solution (Fig. 15.5). The hypoglycemic effect is sustained for a longer time in the case of chitosan-coated SLN, highlighting the role of chitosan in conferring mucoadhesiveness to SLN and as an absorption enhancer of insulin (Fonte *et al.*, 2011). Although the PA values of 5.1–8.3% SLN and 17.7% for chitosan-coated SLN are low, the hypoglycemic effect is more prolonged when compared to subcutaneous insulin (Fonte *et al.*, 2011; Sarmento *et al.*, 2007b).

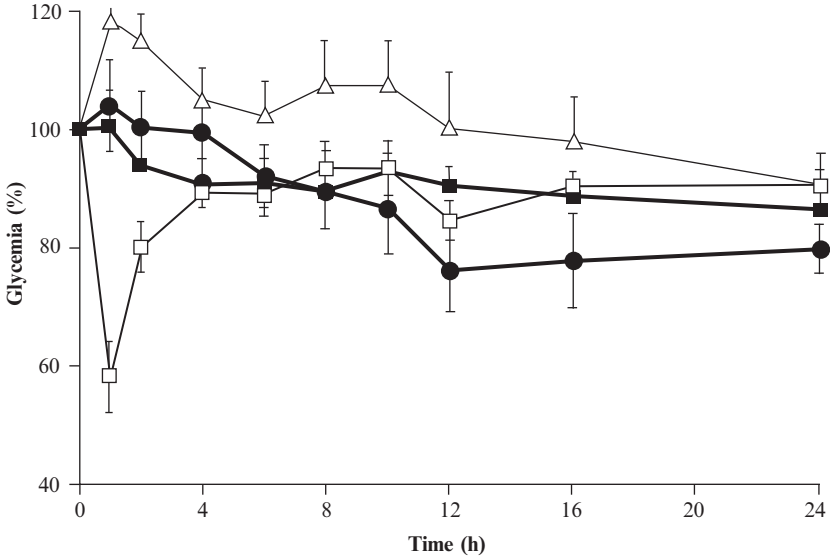

Figure 15.5 Percentage reduction of plasma glucose concentration in diabetic rats after administration of subcutaneous insulin, 2.5 UI/kg (empty squares); oral insulin solution, 25 IU/kg (empty triangles); insulin-loaded SLN, 25 IU/kg (filled squares); and insulin-loaded chitosan-coated SLN, 25 IU/Kg (filled circles). $n = 6$; mean $\pm$ SEM. Reprinted with permission from Fonte *et al.* (2011).

These results show that insulin-loaded SLN are suitable systems for the oral administration of insulin. SLN are able to protect insulin against chemical degradation in the gastrointestinal tract and enhance its absorption through intestinal epithelium. Moreover, chitosan coating seems to further enhance the intestinal absorption properties of insulin-loaded SLN, which may contribute to the development of an optimized oral insulin formulation.

ACKNOWLEDGMENTS

This work was supported by Fundação para a Ciência e a Tecnologia, Portugal (PTDC/SAU-FCF/104492/2008, SFRH/BPD/35996/2007, and PTDC/SAU-FCF/70651/2006).

REFERENCES

Almeida, A. J., and Souto, E. (2007). Solid lipid nanoparticles as a drug delivery system for peptides and proteins. *Adv. Drug Deliv. Rev.* **59,** 478–490.

Bloemendal, M., and Jiskoot, W. (2005). Circular dichroism spectroscopy. *In* "Methods for Structural Analysis of Protein Biopharmaceuticals," (D. Crommelin and W. Jiskoot, eds.), pp. 83–130. AAPS Press, Arlington, VA.

Braz, L., Rodrigues, S., Fonte, P., Grenha, A., and Sarmento, B. (2011). Mechanisms of Chemical and Enzymatic Chitosan Biodegradability and its Application on Drug Delivery, Biodegradable Polymers: Processing, Degradation and Applications. Nova Publishers, New York, USA. pp. 325–364.

Cano-Cebrian, M. J., Zornoza, T., Granero, L., and Polache, A. (2005). Intestinal absorption enhancement via the paracellular route by fatty acids, chitosans and others: A target for drug delivery. *Curr. Drug Deliv.* **2,** 9–22.

Carino, G. P., and Mathiowitz, E. (1999). Oral insulin delivery. *Adv. Drug Deliv. Rev.* **35,** 249–257.

Cefalu, W. T. (2004). Concept, strategies, and feasibility of noninvasive insulin delivery. *Diabetes Care* **27,** 239–246.

Champion, J. A., Walker, A., and Mitragotri, S. (2008). Role of particle size in phagocytosis of polymeric microspheres. *Pharm. Res.* **25,** 1815–1821.

Charman, W. N. (2000). Lipids, lipophilic drugs, and oral drug delivery-some emerging concepts. *J. Pharm. Sci.* **89,** 967–978.

Charman, W. N., Porter, C. J., Mithani, S., and Dressman, J. B. (1997). Physiochemical and physiological mechanisms for the effects of food on drug absorption: The role of lipids and pH. *J. Pharm. Sci.* **86,** 269–282.

Clogston, J. D., and Patri, A. K. (2011). Zeta potential measurement. *Methods Mol. Biol.* **697,** 63–70.

Cui, F., Qian, F., Zhao, Z., Yin, L., Tang, C., and Yin, C. (2009). Preparation, characterization, and oral delivery of insulin loaded carboxylated chitosan grafted poly(methyl methacrylate) nanoparticles. *Biomacromolecules* **10,** 1253–1258.

Damge, C., Reis, C. P., and Maincent, P. (2008). Nanoparticle strategies for the oral delivery of insulin. *Expert Opin. Drug Deliv.* **5,** 45–68.

Fonte, P., Nogueira, T., Gehm, C., Ferreira, D., and Sarmento, B. (2011). Chitosan-coated solid lipid nanoparticles enhance the oral absorption of insulin. *Drug Deliv. Transl. Res.* **1,** 299–308.

Garcia-Fuentes, M., Torres, D., and Alonso, M. J. (2005). New surface-modified lipid nanoparticles as delivery vehicles for salmon calcitonin. *Int. J. Pharm.* **296,** 122–132.

Ghilzai, N. M. K. (2003). New developments in insulin delivery. *Drug Dev. Ind. Pharm.* **29,** 253–265.

Hoffman, A., and Ziv, E. (1997). Pharmacokinetic considerations of new insulin formulations and routes of administration. *Clin. Pharmacokinet.* **33,** 285–301.

Jiang, Y., Li, C., Nguyen, X., Muzammil, S., Towers, E., Gabrielson, J., and Narhi, L. (2011). Qualification of FTIR spectroscopic method for protein secondary structural analysis. *J. Pharm. Sci.* **100,** 4631–4641.

Lemarchand, C., Gref, R., and Couvreur, P. (2004). Polysaccharide-decorated nanoparticles. *Eur. J. Pharm. Biopharm.* **58,** 327–341.

Liu, J., Gong, T., Wang, C., Zhong, Z., and Zhang, Z. (2007). Solid lipid nanoparticles loaded with insulin by sodium cholate-phosphatidylcholine-based mixed micelles: Preparation and characterization. *Int. J. Pharm.* **340,** 153–162.

Muller, R. H., Mader, K., and Gohla, S. (2000). Solid lipid nanoparticles (SLN) for controlled drug delivery—A review of the state of the art. *Eur. J. Pharm. Biopharm.* **50,** 161–177.

Owens, D. R. (2002). New horizons-alternative routes for insulin therapy. *Nat. Rev. Drug Discov.* **1,** 529–540.

Owens, D. E., 3rd, and Peppas, N. A. (2006). Opsonization, biodistribution, and pharmacokinetics of polymeric nanoparticles. *Int. J. Pharm.* **307,** 93–102.

Rawat, M., Singh, D., and Saraf, S. (2006). Nanocarriers: Promising vehicle for bioactive drugs. *Biol. Pharm. Bull.* **29,** 1790–1798.

Reis, C. P., Veiga, F. J., Ribeiro, A. J., Neufeld, R. J., and Damge, C. (2008). Nanoparticulate biopolymers deliver insulin orally eliciting pharmacological response. *J. Pharm. Sci.* **97,** 5290–5305.

Sarmento, B., Ribeiro, A., Veiga, F., and Ferreira, D. (2006a). Development and characterization of new insulin containing polysaccharide nanoparticles. *Colloids Surf. B Biointerfaces* **53,** 193–202.

Sarmento, B., Ribeiro, A., Veiga, F., and Ferreira, D. (2006b). Development and validation of a rapid reversed-phase HPLC method for the determination of insulin from nanoparticulate systems. *Biomed. Chromatogr.* **20,** 898–903.

Sarmento, B., Ferreira, D., Jorgensen, L., and van de Weert, M. (2007a). Probing insulin's secondary structure after entrapment into alginate/chitosan nanoparticles. *Eur. J. Pharm. Biopharm.* **65,** 10–17.

Sarmento, B., Martins, S., Ferreira, D., and Souto, E. B. (2007b). Oral insulin delivery by means of solid lipid nanoparticles. *Int. J. Nanomedicine* **2,** 743–749.

Sarmento, B., Ribeiro, A., Veiga, F., Ferreira, D., and Neufeld, R. (2007c). Oral bioavailability of insulin contained in polysaccharide nanoparticles. *Biomacromolecules* **8,** 3054–3060.

Sarmento, B., Ribeiro, A., Veiga, F., Sampaio, P., Neufeld, R., and Ferreira, D. (2007d). Alginate/chitosan nanoparticles are effective for oral insulin delivery. *Pharm. Res.* **24,** 2198–2206.

Sarmento, B., Mazzaglia, D., Bonferoni, M. C., Neto, A. P., Monteiro, M. C., and Seabra, V. (2011). Effect of chitosan coating in overcoming the phagocytosis of insulin loaded solid lipid nanoparticles by mononuclear phagocyte system. *Carbohydr. Polym.* **84,** 919–925.

Smith, J. M., Dornish, M., and Wood, E. J. (2005). Involvement of protein kinase C in chitosan glutamate-mediated tight junction disruption. *Biomaterials* **26,** 3269–3276.

Trotta, M., Cavalli, R., Carlotti, M. E., Battaglia, L., and Debernardi, F. (2005). Solid lipid micro-particles carrying insulin formed by solvent-in-water emulsion-diffusion technique. *Int. J. Pharm.* **288,** 281–288.

van de Weert, M., Hering, J., and Haris, P. (2005). Fourier transform infrared spectroscopy. *In* "Methods for Structural Analysis of Protein Biopharmaceuticals," (D. Crommelin and W. Jiskoot, eds.), pp. 131–166. AAPS Press, Arlington, VA.

Xu, R. (2002a). Electrophoretic Light Scattering—Zeta Potential Measurement, Particle Characterization: Light Scattering Methods. Kluwer Academic Publishers, Dordecht, Netherlands. pp. 289–343.

Xu, R. (2002b). Photon Correlation Spectroscopy—Submicron Particle Characterization, Particle Characterization: Light Scattering Methods. Kluwer Academic Publishers, Dordecht, Netherlands. pp. 223–288.

Yin, Y., Chen, D., Qiao, M., Wei, X., and Hu, H. (2007). Lectin-conjugated PLGA nanoparticles loaded with thymopentin: Ex vivo bioadhesion and in vivo biodistribution. *J. Control. Release* **123,** 27–38.

Yin, L., Ding, J., He, C., Cui, L., Tang, C., and Yin, C. (2009). Drug permeability and mucoadhesion properties of thiolated trimethyl chitosan nanoparticles in oral insulin delivery. *Biomaterials* **30,** 5691–5700.

Zhang, N., Ping, Q., Huang, G., Xu, W., Cheng, Y., and Han, X. (2006). Lectin-modified solid lipid nanoparticles as carriers for oral administration of insulin. *Int. J. Pharm.* **327,** 153–159.

CHAPTER SIXTEEN

Peptide Nanomedicines for Treatment of Acute Lung Injury

Ruxana T. Sadikot

Contents

Abstract

Acute lung injury (ALI) and acute respiratory distress syndrome (ARDS) represent a heterogenous group of lung disease in critically ill patients. Despite the increased understanding of the molecular pathogenesis of ARDS, the mortality remains unacceptably high, ranging from 34% to 64%. Hence, ARDS represents an unmet medical need with an urgency to develop effective pharmacotherapies. Several promising targets that have been identified as potential therapies for ARDS have been limited because of difficulty with delivery. In particular, delivery of peptides and proteins to the lung is an ongoing challenge. Nanobiotechnology and nanoscience are the basis of innovative techniques to deliver drugs targeted to the site of inflamed organs, such as the lungs. Nanoscale drug delivery systems have the ability to improve the pharmacokinetics and pharmakodynamics of agents allowing an increase in the biodistribution of therapeutic agents to target organs, resulting in improved efficacy with reduction in drug toxicity. These systems are exploited for therapeutic purpose to carry the drug in the body in a controlled manner from the site of administration to the therapeutic target. Hence, it is an attractive strategy to test potential targets

Jesse Brown VA Medical Center, Section of Pulmonary, Critical Care Medicine, University of Illinois at Chicago, Chicago, Illinois, USA

Methods in Enzymology, Volume 508
ISSN 0076-6879, DOI: 10.1016/B978-0-12-391860-4.00016-1

for ALI/ARDS using nanotechnology. To this end, we have identified several potential targets and proposed the delivery of these agents using nanomicelles to improve the drug delivery.

1. Introduction

In recent years, nanomedicine has become an attractive concept for the targeted delivery of therapeutic and diagnostic compounds to the lung (Dames *et al.*, 2007; Foldvari and Elsabahy, 2011). Nanoscale drug delivery systems have the ability to improve the pharmacokinetics and increase the biodistribution of therapeutic agents to target organs, thereby resulting in improved efficacy and reduced drug toxicity (Kim *et al.*, 2010; Koo *et al.*, 2005; Singh, 2010). Nanocarriers are particularly designed to target inflammation and cancer that have a permeable vasculature. Among the various drug delivery systems considered for pulmonary application, the use of biodegradable polymeric nanoparticles represent several advantages for the treatment of respiratory diseases (Bailey and Berkland, 2009; Buxton, 2009). A number of different strategies have been proposed for modification of nanoparticle characteristics to control their behavior within biological environments, like cell-specific targeted drug delivery or modified biological distribution of drugs, both at the cellular and organ level. This method of delivery is particularly attractive for inflammatory conditions such as acute lung injury (ALI) and acute respiratory distress syndrome (ARDS).

Despite recent advances in diagnostic and therapeutic modalities, ALI and ARDS still represent an unmet medical need because it is associated with appreciable morbidity and mortality (30–40%) and substantial medical expenditure (Girard and Bernard, 2007; Matthay, 2008; Matthay and Ware, 2000; Rubenfeld and Herridge, 2007). Hence, there is an urgent need to develop and test new drugs to treat this devastating disorder. Unfortunately, contemporary drug development approaches to address this challenge that center on mono–metabolic pathway inhibitors are hindered by diverse mechanisms underlying ALI and ARDS pathogenesis and by nonselective drug effects that could predispose to serious adverse events.

To overcome both barriers, we emulated the clinical success of combination therapy in cancer and HIV (Shey *et al.*, 2009) by devising an innovative nanopharmacotherapeutic strategy consisting of a combination of three long-acting and safe nanomedicines that selectively target and inhibit three distinct key intracellular proinflammatory signaling cascades activated in ALI. Accordingly, we have harnessed unique attributes of three novel, long-acting, biocompatible, and biodegradable antiinflammatory nanomedicines. They consist of two amphipathic peptide drugs, human glucagon-like peptide-1(7–36) amide (GLP-1), triggering receptor expressed on myeloid cells (TREM-1)

peptide and 17-allylamino-17-demethoxygeldanamycin (17-AAG), a water-insoluble cytotoxic drug. This innovative approach consists of self-assembly of each drug with U.S. FDA-generally regarded as safe (GRAS) distearoylphosphatidylethanolamine covalently linked to polyethylene glycol of molecular weight 2000 (DSPE-PEG_{2000}), a component of U.S.FDA-approved Doxil®, that forms long-acting, biocompatible, and biodegradable, sterically stabilized phospholipid nanomicelles (SSM) in aqueous milieu (size, ~15 nm; Rubinstein and Önyüksel, 2007a,b; Sadikot *et al.*, 2008a,b, 2009).

2. Sterically Stabilized Phospholipid Nanomicelles

SSM are a novel, long-acting, biocompatible, and biodegradable phospholipid-based drug delivery vehicles that acts as versatile carrier platform for peptide and water-insoluble drugs. This approach entails self-assembly of distearoylphosphatidylethanolamine covalently linked to polyethylene glycol of molecular weight 2000 (DSPE-PEG_{2000}) with drugs to form SSM in aqueous milieu (size, ~15 nm in diameter) (Koo *et al.*, 2005; Sadikot *et al.*, 2009).

These nanomicelles are composed of a hydrophilic corona that houses amphipathic peptide drugs, such as TREM-1 peptide and GLP-1, and a hydrophobic core that accommodates water-insoluble drugs, such as 17-AAG. They are simple to prepare and, unlike liposomes, can be stored in lyophilized form without lyo- or cryo–protectants for extended periods of time. Nanomicelles stabilize TREM-1 peptide and GLP-1 in active biological form (α-helix) which is preferred for ligand–receptor interactions and prevents rapid peptide degradation *in vivo*, thereby prolonging bioactivity (Al-Sabah and Donnelly, 2004; Alana *et al.*, 2006). In addition, SSM solubilize high concentrations of 17-AAG. Unlike surfactant micelles, the low critical micellar concentration (~1 μ*M*) of these nanoparticles prevents their disintegration upon dilution in biological fluids. Importantly, the PEG_{2000} moiety of SSM confers steric hindrance in the circulation, while their nanosize mitigates renal clearance and extravasation from intact microvessels. This, in turn, prolongs the circulation time of drug-loaded nanomicelles and promotes preferential extravasation from hyperpermeable lung microcirculation, the hallmark of ALI, into the injured lung.

This innovative, passively targeted therapeutic strategy amplifies drug delivery to the lung, thereby maximizing efficacy and enhancing the resolution of inflammation while reducing collateral damage to innocent bystander organs. These nanomicelles are FDA-approved for human studies (Lim *et al.*, 2011; Sadikot *et al.*, 2009).

3. Nanotechnology for Drug Delivery to the Lung

3.1. Nanoparticle drug delivery

Systemic delivery of nanoparticles is based on the principle of passive targeting. Passive targeting occurs as a result of extravasation of the nanoparticles at the diseased site where the microvasculature is leaky (Pison *et al.*, 2006). Examples of diseases where passive targeting of nanocarriers can be achieved are tumor and inflamed tissues. Microvascular leakiness in ALI and ARDS is the result of increased permeability, and the presence of cytokines and other vasoactive factors that enhance permeability (Matthay and Ware, 2000). Thus, drugs used for treatment of ALI and ARDS can be administered systemically and will localize to the lungs by passive targeting. This innovative, passively targeted therapeutic strategy amplifies drug delivery to the lung thereby maximizing efficacy and enhancing resolution of inflammation while reducing collateral damage to innocent bystander organs as occurs in patients with ALI and ARDS.

Among various drug delivery systems considered for pulmonary application, nanoparticles demonstrate several advantages for the treatment of respiratory diseases, including prolonged drug release, cell-specific targeted drug delivery, or modified biological distribution of drugs, both at the cellular and organ level (Azarmi *et al.*, 2008; Roy and Vij, 2010; Rudolph *et al.*, 2010; Yang *et al.*, 2008). Nanoparticles composed of biodegradable lipid-based nanomicelles and polymers fulfill many requirements placed on these delivery systems, such as the ability to be transferred into an aerosol, stability against forces generated during aerosolization, biocompatibility, targeting of specific sites, or cell populations in the lung, release of the drug in a predetermined manner, and degradation within an acceptable period of time (Roy and Vij, 2010; Yacobi *et al.*, 2008). Clearly, further studies are warranted to establish the role of aerosolized nanopreparations for inhalational therapy.

3.2. Nanoparticle delivery to the lung

We have used nanomicellar preparations for the delivery of targeted drugs to the lungs using a systemic approach. Micelles are self-assemblies of amphiphiles that form supramolecular core-shell structures in the aqueous environment (Koo *et al.*, 2005). Hydrophobic interactions are the predominant driving force in the assembly of the amphiphiles in the aqueous medium when their concentrations exceed the CMC. SSM were developed and patented in our laboratory as versatile carriers for peptide and

water-insoluble drugs (Rubinstein and Önyüksel, 2007a,b; Sadikot *et al.*, 2008a,b, 2009).

Systemic delivery of these agents is based on the principle of passive targeting (Kim *et al.*, 2010; Koo *et al.*, 2005). Passive targeting occurs due to extravasation of the nanoparticles at the diseased site where the microvasculature is leaky (Liu *et al.*, 2009). Examples of diseases where passive targeting of nanocarriers can be achieved are tumor and inflamed tissues. Leakiness in ALI/ARDS is the result of increased permeability and the presence of cytokines and other vasoactive factors that enhance permeability. Thus, agents used for treatment of ALI/ARDS can be administered systemically and will localize to the lungs by passive targeting.

We hypothesize that this innovative, passively targeted therapeutic strategy amplifies drug delivery to lung thereby maximizing efficacy and enhancing resolution of inflammation while reducing collateral damage to innocent bystander organs that occurs in patients with sepsis and ARDS.

Controlled drug delivery systems have also become increasingly attractive options for inhalation therapies (Klingler *et al.*, 2009; Mansour *et al.*, 2009; Roy and Vij, 2010). The large surface area of the lungs and the minimal barriers impeding access to the lung periphery make this organ a suitable portal for a variety of therapeutic interventions (Beck-Broichsitter *et al.*, 2010; Bur *et al.*, 2009; Buxton, 2009). The blood–barrier between the alveolar space and the pulmonary capillaries is very thin to allow for rapid gas exchange. Alveoli are small and there are approximately 300 million of them in each lung. Although alveoli are tiny structures, they have a very large surface area in total ($\sim$100 m^2) for performing efficient gas exchange, making it an attractive organ for direct drug delivery (Rudolph *et al.*, 2010; Smola *et al.*, 2008). Among the various drug delivery systems considered for pulmonary application, nanoparticles demonstrate several advantages for the treatment of respiratory diseases, such as prolonged drug release, cell-specific targeted drug delivery, or modified biological distribution of drugs, both at the cellular and organ level (Azarmi *et al.*, 2008; Bailey and Berkland, 2009; Pison *et al.*, 2006; Sung *et al.*, 2007; Yang *et al.*, 2008). Nanoparticles composed of biodegradable polymers fulfill many requirements placed on these delivery systems, such as ability to be transferred into an aerosol, stability against forces generated during aerosolization, biocompatibility, targeting of specific sites or cell populations in the lung, release of the drug in a predetermined manner, and degradation within an acceptable period of time (Rytting *et al.*, 2008; Schleh *et al.*, 2011; Yacobi *et al.*, 2008). Further studies are needed to establish the role of aerosolized nanopreparations for inhalational therapy.

4. ALI and Nanomedicine

4.1. Acute lung injury/acute respiratory distress syndrome

ALI and ARDS arise from direct and indirect injury to the lungs and result in a life-threatening form of respiratory failure with diffuse, bilateral lung injury, and severe hypoxemia caused by noncardiogenic pulmonary edema which affects approximately 1 million people worldwide annually (Girard and Bernard, 2007; Rubenfeld and Herridge, 2007). As with inflammatory processes elsewhere in the body, lung inflammation is accompanied by many cellular and biochemical processes; some of them specific to the syndrome and includes injury to both the pulmonary capillary endothelium and the alveolar epithelium. The importance of ALI has been highlighted by the emergence of SARS (severe acute respiratory syndrome). ALI and ARDS are a leading cause of morbidity and mortality in the United States (Matthay and Ware, 2000). The major reason underlying the lag in improvement in outcome is the lack of novel and specific therapies for ALI and ARDS (Matthay, 2008). Thus, ARDS represents an unmet medical need and there is an urgent need to develop novel therapies for this condition.

The molecular pathobiology of ARDS is being extensively defined and the role of several molecules including pattern recognition receptors present on the immune cells, such as Toll-like receptors and downstream signaling molecules, such as NF-κB and effector molecules, such as TNF-α and IL-1β are being investigated in the pathogenesis and treatment of ALI and ARDS. Targeting central molecules such as NF-κB attenuates lung inflammation but has major limitations, because inhibition of NF-κB is immunosuppressive and compromises host defense (Sadikot *et al.*, 2006). However, because of the complex nature of the disease targeting single cytokine or chemokine has also failed to attenuate lung inflammation as these are not sufficient singly to attenuate lung inflammation in ARDS.

Thus, we propose innovative approaches that involve: (1) targeting multiple upstream molecules TREM-1 (Bouchon *et al.*, 2000, 2001), reactive oxygen species (ROS), and Hsp90 that lead to activation of NF-κB, ultimately leading to ALI and ARDS, with poor outcomes in many cases; (2) developing a novel approach to deliver inhibitors of these molecules *in vivo*. We have previously shown that these individual nanoformulations are effective at attenuating lung inflammation; and (3) using combination therapeutic approach that involves three distinct intracellular metabolic pathways likely to be successful as it is in patients with cancer (Sadikot and Rubinstein, 2009; Sadikot *et al.*, 2004).

4.2. Nanomedicine therapy for acute lung injury

Nanoparticles have potential application in medical field including diagnostics and therapeutics. Nanoscale drug delivery systems have the ability to improve the pharmacokinetics and increase the biodistribution of therapeutic agents to target organs which results in improved efficacy and reduces drug toxicity (Koo *et al.*, 2005; Rudolph *et al.*, 2010). Nanocarriers are particularly designed to target inflammation and cancer that have permeable vasculature. Additionally many nanocarriers have the desirable advantage of improving solubility of hydrophobic compounds in the aqueous media to render them suitable for parenteral administration. In particular, delivery systems have shown to increase the stability of a wide variety of therapeutic agents, such as hydrophobic molecules, peptides, and oliginucleotides (Koo *et al.*, 2005).

These systems are exploited for diagnostic and therapeutic purposes to carry the drug in the body in a controlled manner from the site of administration to the therapeutic target (Mazzone, 2009). This implies the passage of the drug molecules and drug delivery system across numerous physiological barriers, which represents the most challenging goal in drug targeting. Nanoparticles can be constructed by various methodology so that effect can be targeted at desired site (Koo *et al.*, 2005).

To begin to address the potential of nanotechnology for treatment of ARDS, we developed novel, long-acting, biocompatible, and biodegradable phospholipid micelles (size, ~15 nm) to modulate key signaling molecules that are critical to the inflammatory response in ALI and ARDS (Matthay and Ware, 2000). We selected molecules that initiate and propagate inflammatory response by distinct mechanisms so that multiple pathways can be targeted either singly or by a combinatorial approach as in diseases like HIV (Shey *et al.*, 2009). Among these TREM-1(Bouchon *et al.*, 2000, 2001), ROS, and Hsp90 were initially selected to modulate the inflammatory response in the lung (Sadikot *et al.*, 2004, 2008a,b).

Realizing the short half-life of peptide drugs (min) hampers their clinical use, we invented micellar TREM-1 peptide and GLP-1 where each peptide drug is stabilized in its active form (α-helix) and its bioactivity is prolonged for hours *in vivo*. Likewise, water-insolubility of 17-AAG, a selective Hps90 inhibitor, constrains its use in humans. Accordingly, self-association of 17-AAG with these micelles overcomes this limitation while at the same time increasing its stability and bioavailability. These long-acting micellar drugs provide significant advancement in the treatment of experimental of ALI which could then be extended to critically ill patients. Nanoparticles can be introduced by systemic administration (oral, dermal, intravenous, etc.) or directly introduced into the lung through inhalation, intranasal, or oropharyngeal aspiration.

In a recent study, we tested the efficacy of GLP-1 nanomicelles in a mouse model of lipopolysaccharide (LPS) induced lung injury (Lim *et al.*, 2011; Sadikot *et al.*, 2008a,b). *In vivo* administration of GLP1-SSM to LPS-induced ALI mice resulted in significant downregulation of lung inflammation, with dose-dependent antiinflammatory activity observed. Similar therapeutic activity was not detected for GLP-1 in saline, indicating that the SSM nanocarriers played a critical role in protecting the enzyme-labile GLP-1 and delivering it to inflamed tissues *in vivo*. This study demonstrated for the first time that the lipid-based nanoformulation of GLP-1 is effective at attenuating inflammation in ALI/ARDS (Lim *et al.*, 2011). We have also tested the efficacy of TREM-1 nanomiceller peptide in a model of LPS-induced sepsis and lung injury and shown that TREM-1 nanomicelles are more efficacious than the naked peptide at abrogating inflammation (Sadikot *et al.*, 2008a,b). Studies with other nanomiceller preparations such as 17-AAG for treatment of ALI/ARDS are currently ongoing in our laboratory. Together, our studies demonstrate the feasibility of translating the use of these nanomiceller preparations for translational human studies to the clinics to treat this devastating disease. We hypothesize that combinatorial administration of nanomicelles that modulate distinct signaling pathways will prove to be more potent, however, will need further studies to optimize the administration of the nanopreparations.

5. Summary

Nanotechnology is an emerging science involving manipulation of materials at the nanometer scale. Nanomedicine, the medical application of nanotechnology, promises an endless range of applications from biomedical imaging to drug delivery and therapeutics. These novel approaches using nanotechnology are revolutionizing the future of medicine. Advances in nanotechnology are proving to be beneficial in therapeutic field such as drug discovery, drug delivery, and gene/protein delivery. Nanoparticulate drug delivery systems, designed as multifunctional engineered nanoparticles, appear to be particularly attractive and promising for drug delivery to organs such as the lung since they combine several opportunities like uniform distribution of drug dose among all ventilated alveoli allowing for uniform cellular drug internalization. Besides sustained release of drugs in plasma and organs, other potential advantages of the system include the possibility of reduction in drug dosage, adverse effects, and drug interactions. Although the field of nanomedicine offers multiple opportunities, it still is in its infancy and the research has to proceed in order to obtain a specific targeting of the drug combined with minimum side effects. Ongoing studies offer several exciting prospects for the application of engineered nanomaterials for drug delivery in years to come.

ACKNOWLEDGMENT

Supported by the Department of Veterans Affairs (VA Merit Grant).

REFERENCES

Alana, I., Parker, J. C., Gault, V. A., Flatt, P. R., O'Harte, F. P., Malthouse, J. P., and Hewage, C. M. (2006). NMR and alanine scan studies of glucose-dependent insulinotropic polypeptide in water. *J. Biol. Chem.* **281,** 16370–16376.

Al-Sabah, S., and Donnelly, D. (2004). The primary ligand-binding interaction at the GLP-1 receptor is via the putative helix of the peptide agonists. *Prot. Peptide Lett.* **11,** 9–14.

Azarmi, S., Roa, W. H., and Loebenberg, R. (2008). Targeted delivery of nanoparticles for the treatment of lung diseases. *Adv. Drug Deliv. Rev.* **60,** 863–875.

Bailey, M. M., and Berkland, C. J. (2009). Nanoparticle formulations in pulmonary drug delivery. *Med. Res. Rev.* **29,** 196–212.

Beck-Broichsitter, M., Gauss, J., Gessler, T., Seeger, W., Kissel, T., and Schmehl, T. (2010). Pulmonary targeting with biodegradable salbutamol-loaded nanoparticles. *J. Aerosol Med. Pulm. Drug Deliv.* **23**(1), 47–57.

Bouchon, A., Dietrich, J., and Colonna, M. (2000). Cutting edge: Inflammatory responses can be triggered by TREM-1, a novel receptor expressed on neutrophils and monocytes. *J. Immunol.* **164,** 4991.

Bouchon, A., Facchetti, F., Weigand, M. A., and Colonna, M. (2001). TREM-1 amplifies inflammation and is a crucial mediator of septic shock. *Nature* **410,** 1103.

Bur, M., Henning, A., Hein, S., Schneider, M., and Lehr, C. M. (2009). Inhalative nanomedicine—Opportunities and challenges. *Inhal. Toxicol.* **21**(Suppl. 1), 137–143.

Buxton, D. B. (2009). Nanomedicine for the management of lung and blood diseases. *Nanomedicine (London)* **4**(3), 331–339.

Dames, P., Gleich, B., Flemmer, A., Hajek, K., Seidl, N., Wiekhorst, F., Eberbeck, D., Bittmann, I., Bergemann, C., Weyh, T., Trahms, L., Rosenecker, J., *et al.* (2007). Targeted delivery of magnetic aerosol droplets to the lung. *Nat. Nanotechnol.* **2**(8), 495–499.

Foldvari, M., and Elsabahy, M. (2011). Nanotechnology enables superior medical therapies. *Curr. Drug Deliv.* **8**(3), 225–226.

Girard, T. D., and Bernard, G. R. (2007). Mechanical ventilation in ARDS: a state-of-the-art review. *Chest.* **131**(3), 921–929.

Kim, B. Y., Rutka, J. T., and Chan, W. C. (2010). Nanomedicine. *N. Engl. J. Med.* **363**(25), 2434–2443.

Klingler, C., Müller, B. W., and Steckel, H. (2009). Insulin-micro- and nanoparticles for pulmonary delivery. *Int. J. Pharm.* **377**(1–2), 173–179.

Koo, O. M., Rubinstein, I., and Önyüksel, H. (2005). Role of nanotechnology in targeted drug delivery and imaging: A concise review. *Nanomedicine* **1,** 193.

Lim, S. B., Rubinstein, I., Sadikot, R. T., Artwohl, J. E., and Onyüksel, H. A. (2011). Novel peptide nanomedicine against acute lung injury: GLP-1 in phospholipid micelles. *Pharm. Res.* **28**(3), 662–672.

Liu, M., Zhang, H., and Slutsky, A. S. (2009). Acute lung injury: a yellow card for engineered nanoparticles? *J. Mol. Cell. Biol.* **1**(1), 6–7.

Mansour, H. M., Rhee, Y. S., and Wu, X. (2009). Nanomedicine in pulmonary delivery. *Int. J. Nanomedicine* **4,** 299–319.

Matthay, M. A. (2008). Treatment of acute lung injury: Clinical and experimental studies. *Proc. Am. Thorac. Soc.* **5,** 297.

Matthay, M. A., and Ware, L. B. (2000). The acute respiratory distress syndrome. *N. Engl. J. Med.* **342,** 1334.

Mazzone, P. (2009). Nanomedicine: Sniffing out lung cancer. *Nat. Nanotechnol.* **4**(10), 621–622.

Pison, U., Welte, T., Giersig, M., and Groneberg, D. A. (2006). Nanomedicine for respiratory diseases. *Eur. J. Pharmacol.* **533,** 341–350.

Roy, I., and Vij, N. (2010). Nanodelivery in airway diseases: Challenges and therapeutic applications. *Nanomedicine* **6**(2), 237–244.

Rubenfeld, G. D., and Herridge, M. S. (2007). Epidemiology and outcomes of acute lung injury. *Chest* **131,** 554.

Rubinstein, I., and Önyüksel, H. (2007). Biocompatible, biodegradable and sterically stabilized phospholipid nanomicelles improve cryopreservation of oral keratinocytes: A preliminary investigation. *Int. J. Pharm.* **338,** 333.

Rudolph, C., Gleich, B., and Flemmer, A. W. (2010). Magnetic aerosol targeting of nanoparticles to cancer: Nanomagnetosols. *Methods Mol. Biol.* **624,** 267–280.

Rytting, E., Nguyen, J., Wang, X., and Kissel, T. (2008). Biodegradable polymeric nanocarriers for pulmonary drug delivery. *Exp. Opin. Drug Deliv.* **5,** 629–639.

Sadikot, R. T., and Rubinstein, I. (2009). Long-acting, multi-targeted nanomedicine: Addressing unmet medical need in acute lung injury. *J. Biomed. Nanotechnol.* **5**(6), 614–619.

Sadikot, R. T., Christman, J. W., and Blackwell, T. S. (2004). Molecular targets for modulating lung inflammation and injury. *Curr. Drug Targets* **5,** 581.

Sadikot, R. T., Zeng, H., Joo, M., Everhart, M. B., Sherrill, T. P., Li, B., Cheng, D. S., Yull, F. E., Christman, J. W., and Blackwell, T. S. (2006). Targeted immunomodulation of the NF-kappaB pathway in airway epithelium impacts host defense against *Pseudomonas aeruginosa*. *J. Immunol.* **176,** 4923.

Sadikot, R. T., Mohanty, P. S., Onyuksel, H., and Rubinstein, I. (2008a). Sterically stabilized phospholipid nanomicellar 17-allylaminodemethoxygeldanamycin inhibits lipopolysaccharide-induced activation of nuclear factor-κB in bone marrow-derived macrophages. *Am. J. Respir. Crit. Care Med.* **177**(Suppl.), A75.

Sadikot, R. T., Lim, S. B., Onyuksel, H., and Rubinstein, I. (2008b). TREM-1 self-associated with sterically stabilized phospholipid nanomicelles attenuates acute lung inflammation in mice. *Am. J. Respir. Crit. Care Med.* **177**(Suppl.), A982.

Sadikot, R. T., Lim, S., Wang, X., Christman, J. W., Onyuksel, H., and Rubinstein, I. (2009). Salutary effects of nanomicellar GLP-1 administered after onset of LPS-induced acute lung inflammation in mice. *Am. J. Respir. Crit. Care Med.* **179**(Suppl.), A5646.

Schleh, C., Rothen-Rutishauser, B., and Kreyling, W. G. (2011). The influence of pulmonary surfactant on nanoparticulate drug delivery systems. *Eur. J. Pharm. Biopharm.* **77**(3), 350–352.

Shey, M., Kongnyuy, E. J., Shang, J., and Wiysonge, C. S. (2009). A combination drug of abacavir-lamivudine-zidovudine (Trizivir$^{(R)}$) for treating HIV infection and AIDS. *Cochrane Database Syst. Rev.* **8,** CD005481.

Singh, S. (2010). Nanomedicine-nanoscale drugs and delivery systems. *J. Nanosci. Nanotechnol.* **10**(12), 7906–7918.

Smola, M., Vandamme, T., and Sokolowski, A. (2008). Nanocarriers as pulmonary drug delivery systems to treat and to diagnose respiratory and non respiratory diseases. *Int. J. Nanomedicine* **3**(1), 1–19.

Sung, J. C., Pulliam, B. L., and Edwards, D. A. (2007). Nanoparticles for drug delivery to the lungs. *Trends Biotechnol.* **25,** 563–570.

Yacobi, N. R., Demaio, L., Xie, J., Hamm-Alvarez, S. F., Borok, Z., Kim, K. J., and Crandall, E. D. (2008). Polystyrene nanoparticle trafficking across alveolar epithelium. *Nanomedicine* **4**(2), 139–145.

Yang, W., Peters, J. I., and Williams, R. O., III (2008). Inhaled nanoparticles—A current review. *Int. J. Pharm.* **356,** 239–247.

CHAPTER SEVENTEEN

Nanoparticle-Mediated Treatment of Pulmonary Arterial Hypertension

W. Mosgoeller,* R. Prassl,† *and* A. Zimmer‡,1

Contents

* Institut für Krebsforschung, Borschkegasse 8a, Klinik für Innere Medizin I, Medical University Vienna, Vienna, Austria
† Institute of Biophysics and Nanosystems Research, Austrian Academy of Sciences and Ludwig Boltzmann Institute for Lung Vascular Research, Graz, Austria
‡ Institute of Pharmaceutical Sciences, Department of Pharmaceutical Technology, Karl-Franzens-University of Graz, Graz, Austria
1 Corresponding author.

Methods in Enzymology, Volume 508
ISSN 0076-6879, DOI: 10.1016/B978-0-12-391860-4.00017-3

Abstract

Nanomedicine is an emerging field with great opportunities to improve the treatment of diseases which are currently not curable. Pulmonary arterial hypertension (PAH) is one of these diseases treatable by inhalation of medicines that provide novel depots for drugs with short pharmacological half-lives to improve the quality of life for patients. In this context, nanostructured drug delivery systems such as liposomes and polymeric nanoparticles are depot forms that can also act as penetration enhancers and solubilizers of drugs. The pulmonary use of these drug carriers will improve the therapeutic effect of potent drugs that are currently not fully applicable. This review focuses on the design and characterization of drug delivery systems with the potential to improve the treatment options for hypertonic conditions (like PAH). Liposomes as well as polymeric nanoparticles based on lactic acid, proticles and nanocrystalline drugs have good potential to be developed toward clinical use. Preparation methods and characterization techniques of nanoparticles such as light scattering or microscopy are provided.

1. Introduction

1.1. Pulmonary arterial hypertension

Pulmonary arterial hypertension (PAH) is a progressive and fatal disease. It is characterized by vasoconstriction and obliteration of the precapillary arterioles, which reduces the cross-sectional area for blood flow. The resulting chronic elevation of the pulmonary arterial pressure (Palevsky *et al.*, 1989; Wagenvoort and Wagenvoort, 1970; Wood, 1958) typically causes right heart failure, and the patients die within 3 years after diagnosis (D'Alonzo *et al.*, 1991).

1.1.1. Prevalence and relevance of PAH

PAH can occur without underlying conditions (idiopathic) or may be associated with other lung diseases (for review, see Shlobin and Nathan, 2011). Asthma and chronic obstructive pulmonary disease (COPD) are complex inflammatory airway diseases leading to PAH (Stevenson and Birrell, 2011). COPD will be among the most important diseases in the Western world. Owing to its frequency, it is by far the most common cause of pulmonary hypertension (Zakynthinos *et al.*, 2011).

PAH is diagnosed not only in adults. In children, it is frequently associated with congenital heart diseases, where treatment options cannot be extrapolated from adults. For these patients, it is possible to survive for 30 years or more before continuous disease management and pharmacologic treatment become part of their life (Tulloh, 2009). However, in about 50% of PAH cases in young patients, the histopathology is comparable to adults,

resulting in guidelines recommending similar diagnostic and therapeutic algorithms as for adults (Barst *et al.*, 2011).

Less frequently observed are respiratory problems in patients with chronic liver diseases. A liver disease associated with specific pulmonary and vascular abnormalities is the hepatopulmonary syndrome (Yeshua *et al.*, 2009). The pathomechanism remains enigmatic; however, there is good potential for inhalable drugs to become part of the disease management.

1.1.2. Treatment

Despite some progress in therapeutic research, the *ultima ratio* treatment for PAH is lung transplantation (George *et al.*, 2011). Currently, the most effective drugs have a very short half-life, rendering systemic administration difficult. Treprostinil is a prostacyclin analog that has been demonstrated to be effective when administered by continuous subcutaneous or intravenous infusion and more recently by nebulization (Nadler and Edelman, 2010). Because of the risks and inconveniences associated with the administration of prostacyclins, they are normally prescribed to patients with progressed disease only. Prostacyclin drugs approved for the therapy of PAH include intravenous infusions of epoprostenol and trepostinil, as well as subcutaneous infusion of treprostinil and inhalation of iloprost (Ewert *et al.*, 2011; Gomberg-Maitland and Olschewski, 2008). The noninvasive route of drug administration via inhalation seems to be the most promising strategy to achieve effective pulmonary vasodilatation. As a future perspective, this goal could be accomplished using nanotechnology. Likewise, the use of modern nebulizers guarantees deep pulmonary deposition of the required doses. Inhalation therapy may be a safer and easier route for drug administration and allow for an earlier treatment onset. For a more comprehensive review on inhalation therapy, the reader is referred to a recent paper by Gupta and Ahsan (2010).

PAH, asthma, and COPD share pathological features, such as inflammation, smooth muscle contraction, and vascular wall remodeling. In both asthma and COPD, the pathomechanisms involve complex inflammatory airway diseases characterized by airflow obstruction (Stevenson and Birrell, 2011). No existing drug has the potential to deal with these various pathomechanisms. A relatively young treatment concept is the inhalation of vasoactive peptides (Petkov *et al.*, 2003). Like other substances for the treatment of PAH, peptides are characterized by a very short half-life. Although applicable for systemic approaches, inhalation therapy is limited by rapid enzymatic degradation of the peptide in the bronchial fluid (Bolin *et al.*, 1995). Therefore, the development of long-acting VIP analogs, in combination with appropriate drug delivery systems, may provide clinically useful agents for the treatment of pulmonary hypertension in asthma and COPD (Burian *et al.*, 2010; Wu *et al.*, 2011).

Formulations to protect sensitive drugs or peptides from degradation and extend their half-lives are desirable. Inhalable and biodegradable nanoparticles have the potential to build up a substance depot that can be dispersed in the bronchial tree upon inhalation. In this way, drugs/peptides encapsulated in nanoparticles are protected from inactivation until they are released, which certainly reinforces their clinical potential.

2. Nanoparticles for Drug Delivery

Several nanocarrier-based drug delivery systems are already approved for clinical applications (for reviews see Allen and Cullis, 2004; Couvreur and Vauthier, 2006; Wagner *et al.*, 2006). Nanomedicine addresses a central problem in pharmacotherapy: the selective delivery of biologically active compounds from the site of administration directly to the therapeutic target. Thereby, the nanocarriers can serve as depot to deposit the drug at a defined region in the body, delivering it in a controlled and sustained release mode to selected tissues (Torchilin, 2005, 2009). More generally, pharmaceutical nanocarriers aim to reduce drug degradation and inactivation upon administration and aim to reduce adverse side effects. Nanocarriers are also intended to enhance drug absorption by facilitating diffusion through the epithelium, ultimately improving the pharmacokinetics and tissue distribution of the drug.

To date, growing interest is devoted to pulmonary delivery of therapeutics via inhalation using nanotechnology (for reviews, see Buxton, 2009; Konduri *et al.*, 2005; Mansour *et al.*, 2009; Smola *et al.*, 2008). The pulmonary drug delivery route offers several advantages for the treatment of respiratory diseases, as being noninvasive and more efficient than intravenous administration, avoiding first-pass metabolism. Nanoparticles can be inhaled and dispersed into the lung to directly bring the effective drug to the target organ. By this way, high drug concentrations can be delivered to the lung, which provides a huge surface area for drug absorption. Further, nanoparticles can overcome the main shortcoming of peptides/drugs, that is, the short half-life resulting from degradation and inactivation upon inhalation. However, to enable nanoparticle-mediated inhalation therapy, the development of stable controlled release formulations and the design of advanced inhalation devices are indispensable. Following these lines, preliminary successful approaches are reported in literature, in which liposomes and polymers appear to be the most promising candidates for pulmonary delivery.

2.1. Liposomes

Liposomes are excellent carriers for therapeutic drugs and have been investigated extensively as transport vehicles for small molecules, lipophilic compounds, peptides, and protein drugs. The chemical and structural versatility of

lipid species and the use of defined lipid mixtures and coadditives make them attractive candidates for different medical applications. In general, liposomal formulations could act as efficient storage, transport, and release systems and offer many advantages, such as high drug loading capacity, long half-life, good stability, also providing options for targeting. Liposomes have a high biocompatibility *in vivo* and have been proven to be nontoxic in human and animal studies (Waldrep *et al.*, 1997). The properties of liposomal carriers can be modified easily by coating the surface with various ligands. Such surface modifications modulate particle characteristics, such as stability, permeability, metabolic lifetime, mucoadhesion, or cellular uptake. In particular, polymer-coated liposomes have shown the highest potential for drug delivery. The most prominent of which are sterically stabilized liposomes (Stealth® liposomes) being coated with polyethylene glycol. They exhibit a significantly longer lifetime in circulation, and a reduced uptake by the reticuloendothelial system compared to unmodified plain liposomes. Similar effects are obtained for coating with other polymers, which form a dense layer around the liposome surface with the prospect to exert steric hindrance against opsonization and destabilization.

In summary, liposomes are promising entities for pharmacological applications, and several liposomal products have already reached the market (Torchilin, 2005, 2006; Wagner *et al.*, 2006). Until now, most liposomal formulations have been designed for intravenous application; however, encouraging results have been reported for inhalable liposomes, for example, amphotericin B, amikacin, beclomethasone, or cyclosporine A being on the market or at least in the clinic. In case of PAH, the proof of principle that vasodilatory drugs can be formulated as liposomal aerosol was demonstrated for VIP (Stark *et al.*, 2007) and iloprost (Kleemann *et al.*, 2007). The latter study revealed that iloprost-loaded liposomes can be nebulized without substantial loss of particle integrity. However, the encapsulation efficiency for iloprost is low and only slightly improved at acidic pH. In this study, about 4.4% iloprost encapsulation was achieved at pH 4.7 using DPPC/cholesterol (70/30 mol%) liposomes, corresponding to 11 μg iloprost/ml. For Stealth® liposomes, the incorporation rate was even worse. However, the daily dose of inhaled iloprost needed by PAH patients is about 30 μg (Olschewski *et al.*, 2002). This means that patients have to inhale just about 3 ml of iloprost-loaded liposomes, provided that the liposomes are retained in the lung for 24 h, and slowly release their payload (Kleemann *et al.*, 2007). If applicable, inhaled iloprost-liposomes would improve significantly patient compliance. Unfortunately, relevant data concerning drug release profiles and biological activity *in vitro* and *in vivo* are not available yet, and await further clarification. Apart from that, further approaches are aimed at improving the stability and encapsulation efficiency for iloprost.

The liposomal system established for aerosolic VIP delivery will be presented below in more detail.

Considering aerosolic applications, a proper liposome carrier has to meet certain criteria. First of all, the liposomal formulation has to be stable, and the liposomes should be below 200 nm in size to reach the lower bronchioles (Abu-Dahab *et al.*, 2001; Labiris and Dolovich, 2003). On the other hand, the liposomes have to be big enough to accommodate sufficient amounts of peptide/drugs. Once the drug is encapsulated, the liposomes should shield their payload from degradation in the pulmonary microenvironment, and enable a controlled, retarded release of the drugs.

Finally, the formulation has to survive the mechanical stress exerted by the inhalation device without loss of integrity because of particle aggregation, rupture, and spontaneous drug release.

Concerning toxicity, it has to be mentioned that many lipid components commonly used for liposome preparation are abundantly present in the lung surfactant fluid (Mansour *et al.*, 2009). Hence, liposomes are well tolerated by the lungs.

2.2. Micelles

Micelles are self-assembled supramolecular structures consisting of amphiphilic macromolecules. Once in contact with water, the lipid- or polymer-amphiphiles assemble to form nanoscopic core-shell structures that can be exploited as reservoirs for hydrophobic drugs. Only recently, Harada-Shiba *et al.* (2009) reported on the use of PEG-based cationic micelles (polyplex nanomicelles) for intratracheal gene transfer to the lung of rats with monocrotaline-induced PAH. Applying these nanocarriers, a remarkable therapeutic efficacy was achieved without compromising biocompatibility or inducing inflammation.

Other promising micellar drug delivery systems are sterically stabilized micelles consisting of self-assembled PEGylated-lipid molecules. In a recent paper by Gill *et al.*, 2011 a lipid-based micellar system for paclitaxel was presented as a controlled release formulation for pulmonary application in cancer therapy (Gill *et al.*, 2011). It is conceivable that a similar system could be adopted to transport drugs for PAH treatment.

2.3. Polymeric nanoparticles

The use of polymeric nanoparticles is derived from earlier investigations with microspheres and so-called submicron particles. As published previously, the deposition for particles in the pulmonary tract will be best if the aerosol droplets are in the range of 1–3 μm (Sakagami, 2006). Generating aqueous droplets in this range would have the chance to carry numerous nanoparticles in one droplet. Also the aim of nanocrystals seems to be attractive, since smaller particles below 100 nm are reported to accumulate

in the alveolar region due to increased mobility through diffusion (Patton and Byron, 2007).

The first study was designed to test the feasibility of polymeric microspheres as an inhalable carrier for prostaglandin E1 (PGE1) for the treatment of PAH. Poly(lactic-*co*-glycolic acid) (PLGA) microspheres are prepared by a double emulsion–solvent evaporation method (Gupta *et al.*, 2010). Since the solubility of prostaglandins and other drugs used for pulmonary delivery is limited, the advantage of the encapsulation of an inclusion complex of PGE1 and 2-hydroxypropyl-β-cyclodextrin (HPβCD) is also under investigation by the same group (Gupta *et al.*, 2011). In addition, a new strategy to deliver macromolecules to the lung is to form complexes with cationic polymers such as polyethyleneimine (PEI). Although the toxicity of such cationic polymers is a critical issue, successful drug delivery can be demonstrated (Thomas *et al.*, 2005). In combination with PGE1, PEI, and PLGA, polymer complexes are formed that are further coated with polyvinyl alcohol (PVA). The main idea behind this new technique is the controlled release by an osmotic pressure gradient (Gupta and Ahsan, 2011).

Another strategy to treat PAH that is not fully developed for nanoscaled carriers is the application of nitric oxide (NO) releasing agents to the lung tissue. Since NO is the strongest vasodilator but also has the shortest half-life, a depot formulation will be an attractive approach. In combination with polyethylene oxide-*co*-lactic acid (PELA), the encapsulation of a small hydrophilic prodrug (PROLI/NO) has been shown (Jeh *et al.*, 2004). So far, not all of these innovations are demonstrated to work properly, not even when formulated as nanoparticles, and need further investigations in the future.

New developments to treat PAH include nuclear factor κB (NF-κB) as a therapeutic target. Bioabsorbable polymeric nanoparticles formulated from a poly (ethylene glycol)-*block*-lactide/glycolide copolymer (PEG-PLGA) enabled the delivery of a NF-κB decoy oligodeoxynucleotide which is directed against the NF-κB binding site in the promoter region (Morishita *et al.*, 1998). These nanoparticles are shown to prevent monocrotaline-induced NF-κB activation in a rat model of monocrotaline-induced PAH (Kimura *et al.*, 2009).

Considering the delivery of oligonucleotides with nanoparticles, protamine-oligonucleotide nanoparticles—so-called proticles—are a new technique to deliver peptides to the lung. Our group has demonstrated the development of proticles as drug carriers for VIP. In a recent study, we have modified the composition of this self-assembled proticle system to achieve both appropriate binding efficiency of VIP to the proticle matrix and nanoparticle stability. Oligonucleotides which are used as biodegradable macromolecules to form the proticle matrix together with VIP and protamine by self assembly are designed as noncoding scrambled oligonucleotides (Ortner *et al.*, 2010; Wernig *et al.*, 2008). These oligonucleotides can be applied as pharmaceutical excipient only. We have found satisfactory encapsulation efficiency

(up to 80%), VIP release (77–87%), and an appropriate nanoparticle size (177–251 nm). Investigations on rat pulmonary arteries have shown a modified VIP response of proticle-associated VIP. We have noted differences in the profile of artery relaxation where VIP proticles lead to a 20–30% lower relaxation maximum than aqueous VIP solutions, followed by a prolonged vasodilation (Wernig *et al.*, 2008).

2.4. Nanocrystals and nanoprecipitates

Efficient administration of drugs represents a leading challenge in pulmonary medicine. Dry powder aerosols are of great interest compared to traditional aerosolized liquid formulations in that they may offer improved stability, and simple device design. Dry nanoparticle powders may be exhaled when smaller than 100 nm as a result of their small size, however, they tend to agglomerate and need further a basic excipient as a carrier with appropriate aerodynamic flow capabilities. In addition, nanoparticles are desired to enhance the dissolution rate of poorly soluble drugs.

Nanoparticles of the hypertension drug nifedipine are coprecipitated with stearic acid to form a colloid exhibiting a negative surface charge. Nifedipine nanoparticle colloids are destabilized by using sodium chloride to disrupt the electrostatic repulsion between the particles to achieve agglomerated nanoparticles of a controlled size. Such nanoprecipitates have been found to be well suited for pulmonary delivery after the aerodynamic performance is determined by cascade impaction (Plumley *et al.*, 2009).

Because particle size and agglomeration are a crucial issue for the delivery of nanoscaled material to the lung, nanocrystals can also be formulated as solid dispersion (Onoue *et al.*, 2011). Tranilast, an antiallergic agent that has a potential for the cotreatment of pulmonary inflammation during PAH, can be processed as wet-milled crystalline particles with a mean diameter of 122 nm. Such formulations have demonstrated high inhalation performance with an emitted dose and a fine particle fraction of ca. 98% and 60%, respectively (Kawabata *et al.*, 2011).

3. Preparation of Nanoparticles

3.1. Liposomes

Liposomes can be prepared by different well-established procedures (see Düzgüneş, 2003; Mozafari, 2005, and references therein). The most commonly used preparation method for liposomes is the dry lipid film rehydration technique. Here, selected phospholipids are dissolved in proper organic solvents and aliquots thereof are mixed at defined molar ratios in glass vials or round bottom flasks. The organic solvents are evaporated under a

stream of nitrogen and residual traces of solvent are removed in high vacuum overnight. The dry lipid film is resuspended in buffer and hydrated well above the gel-to-liquid crystalline phase transition temperature of the major lipid components. Heating is performed in a water bath or a heating oven. To obtain a homogeneous suspension, the mixture is vortexed vigorously. To further improve the homogeneity, the preparation can be subjected to repeated freeze and thaw cycles. While doing so, the tubes containing the liquid samples are plunged into liquid nitrogen or ice-cold acetone, kept there for 30 s before thawing and vortexing. The cycle is repeated three to six times. When appropriate, the liposome suspensions are extruded by passing them through size-controlled polycarbonate membranes with filter pore sizes of either 200 or 100 nm, using a size extruder. For pharmaceutical applications, the most commonly used lipids are neutral lipids such as phosphatidylcholine. Other excipients are cholesterol and small amounts (about 5 mol%) of PEGylated lipids, which are included to obtain steric stabilization. Drugs are often loaded into liposomes directly during the lipid film rehydration step. In particular cases, the lipid composition is adapted to the nature of the drug or to the chemical characteristics of the coating material. For example, for VIP, which is a cationic peptide, a phospholipid composition containing negatively charged lipids is shown to be more effective than a pure neutral zwitterionic formulation. To create negatively charged liposomes, phosphatidylglycerols can be used as adjunct. Alternatively, phosphatidic acid or dicetylphosphate are applicable. To proceed with the example of VIP as model drug, it is found that VIP molecules, which are associated to acidic liposomes, become immobilized and are transformed from random coil to the alpha-helical secondary structure (Gololobov *et al.*, 1998; Rubinstein *et al.*, 1999), which is the preferred conformation for receptor recognition. It is conceivable that such an interaction is mediated primarily by electrostatic attractions, which could occur between the polar amino acid residues and the negatively charged phospholipid headgroups or/and the negative charge of the phosphate group of PEGylated lipids. Apart from that, VIP penetrates the lipid bilayer and becomes stabilized in part by the hydrophobic effect (Stark *et al.*, 2007).

For VIP, various liposomal formulations have been tested using either plain liposomes (Gao *et al.*, 1994; Sethi *et al.*, 2005; Suzuki *et al.*, 1995) or sterically stabilized liposomes (Dagar *et al.*, 2001; Onyuksel *et al.*, 2006; Sejourne *et al.*, 1997; Stark *et al.*, 2007). The latter have also been explored for treatment of hypertension (Rubinstein, 2005; Rubinstein *et al.*, 2006), also with respect to inhalative pulmonary application (Hajos *et al.*, 2008; Stark *et al.*, 2008).

As a representative example for liposomes, which are designed for pulmonary delivery of vasodilatory drugs, we will explain how VIP-loaded sterically stabilized liposomes are manufactured in our laboratory (Fig. 17.1).

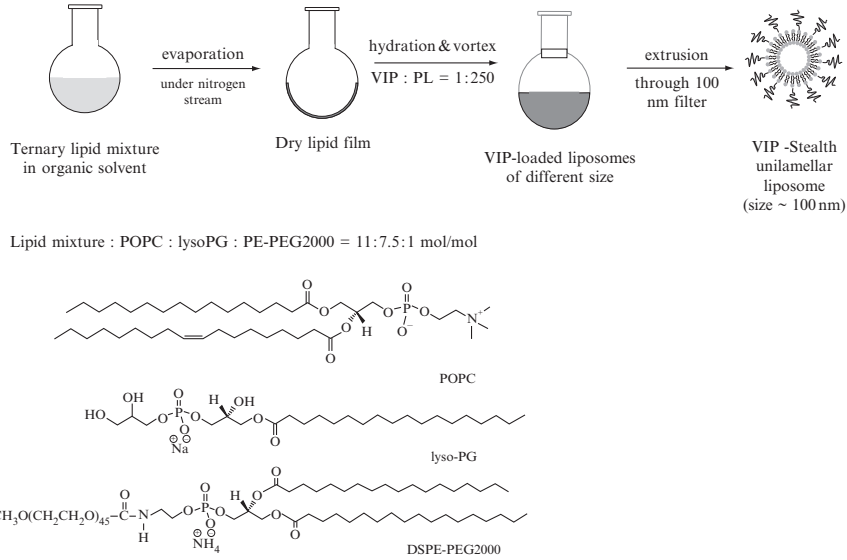

Figure 17.1 Preparation of VIP-loaded liposomes according to Stark *et al.* (2007).

3.2. Preparation of liposomes for pulmonary application of VIP

Stable spherical unilamellar liposomes are formed from a ternary lipid mixture consisting of palmitoyl-oleoyl-phosphatidylcholine (POPC), lyso-stearyl-phosphatidylglycerol (lyso-PG), and distearoylphosphatidyl-ethanolamine covalently linked to polyethylene glycol with a molecular weight of 2000 (DSPE-PEG2000). Phosphatidylglycerol is used to confer an overall negative charge to the liposomes with the purpose of stabilizing the positively charged peptide. Besides, glycerophospholipids are well tolerated by the lung being abundantly present in pulmonary surfactants. The lysolipid, which has only one hydrocarbon chain and a cone shaped geometry, is expected to promote positive curvature and enhance membrane permeabilty. It is verified that the lysolipid in the applied concentration range is nontoxic to cells. All lipids are purchased from Avanti Polar Lipids (Alabaster, AL). VIP (amino acid sequence HSDAVFTDNYTRLRKQ-MAVKKYLNSILN-NH_2) is synthesized by piCHEM (Graz, Austria) using FMOC solid-phase peptide synthesis methodology (FMOC-SPPS). The peptide is purified by RP-HPLC.

For the preparation of our formulation, we use the dry lipid film rehydration technique. First, stock solutions of DSPE-PEG2000, lyso-PG, and POPC (100 m*M*) are prepared in chloroform, chloroform:methanol 9:1 (v/v), and chloroform:methanol 2:1 (v/v), respectively. Second, aliquot amounts of lipid stock solutions are mixed to yield a molar ratio of

DSPE-PEG2000:lyso-PG:POPC of 5:38:57 mol%, with a total lipid concentration of 30 mg/ml. To create a lipid film, the organic solvents are evaporated under a stream of nitrogen, and residual traces of solvent are removed in high vacuum overnight. The dry lipid film is suspended in 1 ml buffer consisting of 10 m*M* Tris–HCl, pH 7.4 (Tris-buffer), and hydrated at 40 °C using a sand bath for 60 min with repeated vortexing (every 10 min for about 30 s). Typically, rehydration is performed above the phase transition temperature of the main lipid component, when the lipids are in the fluid phase. In case of POPC, the phase transition temperature is below 0 °C; nonetheless to warm up the sample to moderate temperatures leads to the formation of a more homogeneous suspension. For peptide loading, hydration is performed with 1 ml Tris-buffer containing 0.5 mg VIP. The suspensions are treated in the same way as described above for empty liposomes.

Finally, the lipid suspensions are extruded by pressing them through polycarbonate filters (Millipore, Vienna, Austria) with 100 nm pore size, using a LiposoFast pneumatic extruder (Avestin, Inc. Ottawa, ON). The extrusion step is repeated at least 21 times. During the passage through the filter, the liposomes become peeled like onions, whereas the removed shells reassemble to closed bilayers. After several repetitions of decomposition and assembly, the liposomes end up with a size approximately the same as the pore size of the filter. Similar to rehydration, the extrusion is performed with the lipids in the fluid phase. Using the lipid composition described above, size extrusion has turned out not to be absolutely necessary, as the main population of liposomes is already in a size range of 100–120 nm before extrusion, and only a subpopulation of particles with sizes up to 600 nm is detected in the unextruded preparation. The freshly prepared liposomes are stored in the cold room at 4 °C. Care has to be taken to avoid oxidation of unsaturated phospholipids. This can be done by storing the formulation under an argon or nitrogen atmosphere. Liposome formulations treated in this manner are stable for at least 4 weeks.

To determine peptide loading efficiency, a fluorescently labeled peptide (VIP(Cy3)) is used. Different concentrations of peptide are applied for the hydration step. After preparation and extrusion, gel filtration chromatography using a Sephadex G-75 column (Amersham Biosciences, Uppsala, Sweden) is performed. VIP associated with the lipid fraction elutes first, together with the liposomes, and can be quantified by fluorescence spectroscopy. Free VIP (Cy3), which is also used as a control, does not elute as a single band, but smears along the column. At a molar phospholipid:VIP ratio of 250:1, we attain a saturation concentration for VIP loading. Higher amounts of VIP cannot be incorporated. Varying the phospholipid concentration (10, 20, 30, or 40 mg phospholipid/ml) results in similar loading capacities of liposomes corresponding to about 0.004 mole VIP/mole phospholipid. The

phospholipid concentration is routinely determined by a modified Bartlett inorganic phosphate assay (Bartlett, 1959).

The encapsulated peptide concentration is in a range suited for PAH treatment, in which a daily administration of 200 μg free VIP via inhalation is required (Petkov *et al.*, 2003). This dose would correspond to a total volume of about 400 μl of our formulation to be inhaled per day. However, one has to keep in mind that the therapeutic dose of VIP might be much lower because of the protective effects of the liposomes.

3.3. Preparation of PEG-PLGA nanoparticles

PEG-PLGA nanoparticles with encapsulated decoy oligonucleotides directed against nuclear factor κB (NF-κB) are prepared using an emulsion–solvent diffusion method. Briefly, nanoparticles are prepared by a modified-SESD (spontaneous emulsification solvent diffusion) method using various solvent systems consisting of two water-miscible organic solvents, in which one solvent (e.g., acetone) has more affinity to PLGA than to PVA and the other has more affinity to PVA (e.g., alcohol) than to PLGA (Murakami *et al.*, 1999).

The typical operating procedure is as follows: 500 mg of PLGA are dissolved in 12.5 ml of the solvent mixture consisting of acetone plus ethanol or methanol (ratio 6:4, w/w). The polymer solution obtained is then added into 50 ml of an aqueous PVA solution (4%, w/w) in a 100-ml glass flask, using a peristaltic pump at a flow rate of 2 ml/min while continuously stirring at 400 rpm with a propeller mixer. For purification, the formed dispersion is transferred into a 1000-ml glass flask, and purified water is added up to 500 ml. The dispersion is condensed to 25 ml by means of ultrafiltration (Minitan® System, Millipore, Location, Japan), and purified water can be added up to 500 ml. This dilution–condensation process has to be repeated three times to remove the residual PVA and organic solvents. Finally the yield, particle size, size distribution, and PVA content of the PLGA nanoparticles are evaluated, and the phase separation behaviors of the polymers can be investigated. The average diameter of PEG-PLGA nanoparticles will be around 44 nm (Kimura *et al.*, 2009).

3.4. Preparation of nanoparticle precipitates

Nanoparticles are prepared by the rapid mixing of ethanol with dissolved nifedipine and stearic acid into a larger aqueous volume, known as a solvent/antisolvent precipitation technique. In a common experiment, 10 mg of nifedipine and 1 mg of stearic acid are completely dissolved in 1 ml of ethanol and allowed to stir overnight. This solution is added to 29 ml of cold deionized water via pipette injection under probe sonication (Fisher Sonic Dismembrator, model 500) at 60% amplitude for 20 s. The resulting colloid

can be frozen at −20 °C and lyophilized, or stored in a 4 °C refrigerator until further processing into nanoparticle agglomerates. At this time, samples can be taken from the solution for sizing and imaging. All solution vials and reaction vessels have to be kept covered from any light sources, as nifedipine exhibits considerable photosensitivity (~10% in 24 h) to UV and visible light spectra.

In the next step, nanoparticle colloids are destabilized via ionic force interactions to control agglomeration. Briefly, 30 ml of the nanoparticle suspension are taken from refrigeration and solid sodium chloride is added to 0.1 *M*. Directly after addition, the suspensions are subject to vigorous mixing via homogenization at 20,000 rpm. Samples are left to sit at room temperature for ~4 h and then are transferred to a −20 °C freezer before being lyophilized in a freeze dryer (Labconco, FreeZone 1). Some samples can be allowed to settle for 24 h and excess water can be decanted prior to freeze drying. This procedure will facilitate the elimination of most of the salt used as an agglomerating agent. Drying is continued for 36–48 h to remove residual water. Finally, the lyophilized powder can be stored in glass vials at room temperature until further characterization (Plumley *et al.*, 2009).

3.5. Preparation of VIP-loaded proticles

VIP-loaded proticles are prepared in aqueous solution by mixing the indicated mass ratios of oligonucleotides (ON), VIP, and protamine to achieve final concentrations of 100 μg/ml ON, 100 or 200 μg/ml VIP, and 60 or 80 μg/ml protamine in MilliQ water. Batch sizes are in the range of 1 ml nanoparticle suspension. Proticle composition is given as a mass ratio in the following sequence ON:VIP:protamine, for example, 1:1:0.6. Proticles are formed by the compounds' self-assembly within the first few seconds of incubation (Ortner *et al.*, 2010; Wernig *et al.*, 2008). Nanoparticle formation is a result of strong ionic interactions between the charged biomolecules. Reproducibility of proticle formation can be guaranteed by mixing of equal volumes, accurate mixing of proticle suspensions with a pipette, followed by vortexing for 5 s, as described earlier by our group (Lochmann *et al.*, 2005; Weyermann *et al.*, 2005b).

3.6. Nano-crystalline solid dispersions

A wet-milled tranilast formulation can be prepared with a NanoMill-01 system (Elan Drug Technologies, Dublin, Ireland). Briefly, 882 mg of crystalline tranilast (Kissei Pharmaceutical Company, Ltd., Nagano, Japan) is weighed and added to a 100-ml stainless chamber. Polystyrene beads (46.7 g) with a diameter of 0.5 mm are placed into the chamber, and 44.1 ml of 5 mg/ml hydroxypropyl cellulose SL (HPC-SL) solution, dissolved in deionized water, with 0.2 mg/ml SDS added. The tranilast colloidal suspension has

to be micronized at 3600 rpm for 90 min with the NanoMill system upon cooling of the chamber to 5 °C. After wet-milling the tranilast suspension is collected in a 300-ml flask and is frozen with a LyoStar II R freeze-dryer (SP Industries Inc., Warminster, Pennsylvania) at −70 °C for 3 h under ambient pressure. Primary drying is carried out for 12 h at −30 °C under a chamber vacuum pressure of 150 mTorr. Secondary drying is carried out for 4 h at 40 °C again under a chamber vacuum pressure of 150 mTorr. The amount of tranilast in the obtained dry powder can be measured by an internal standard method using a Waters Acquity UPLC system (Waters, Milford, MA). Final formulations suitable for inhalation are prepared by adsorption of the micronized tranilast to a lactose carrier (Respitose SV-003). With this procedure, a particle size distribution can be achieved with a 90% of drug crystals below 5 μm (Onoue *et al.*, 2011).

4. Physicochemical Characterization of Nanoparticles

4.1. Particle size measurements

4.1.1. Dynamic light scattering

The particle size (hydrodynamic diameter) and the broadness of the size distribution of particles dispersed in liquids (polydispersity index) can be measured by dynamic light scattering (DLS). The method is based on photon correlation spectroscopy (PCS), which is provided in many particle size instruments from different companies worldwide. Our group has published methods based on instruments of Malvern Instruments, UK. In earlier studies, a Zetasizer 3000 HSA was used, and newer publications have applied the NanoSizer ZS. The study which describes the preparation and characterization on VIP-loaded proticles determined the particle size distribution of different formulations (mass ratio ON:VIP: protamine 1:1:0.6; 1:1:0.8; 1:2:0.6) and also a primary complex between ON and VIP (mass ratio 1:2) has been measured. The instrument system is equipped with a 10 mW He–Ne-laser (633 nm), and the scattered light can be detected at an angle of 90°, or alternatively by a back scatter photo diode. Results are expressed as Z-average representing the averaged particle diameter. Further, the polydispersity index is given representing the broadness of the size distribution and a particle size distribution based on Malvern's optimized CONTIN algorithm can be computed. Typically, measurements are carried out in a plastic UV/VIS spectroscopy cuvette at 25 °C with samples prepared as dilution in the dispersions supernatant. With VIP-loaded proticles, one would be able to conduct a successful measurement by diluting 50 μl of the nanosuspension with 1 ml MilliQ Water just prior to the measurement (Ortner *et al.*, 2010; Wernig *et al.*, 2008). A similar procedure is reported

by Onoue *et al.* (2011) who have used an N5 submicron particle size analyzer (Beckman Coulter Inc., Brea, CA). Approximately 25 µl of the nanocrystal dispersion is diluted with ca. 4 ml of distilled water and dispersed homogeneously. The measurements are also performed at 25 °C at a measurement angle of 90°. The size distribution, which is calculated by histogram analysis of the scattering intensity, is given as cumulative values of the diameter 10% (D 10), 50% (D 50), and 90% (D 90), which means that 10%, 50%, or 90% of the measured particles are below this size (Onoue *et al.*, 2011).

4.1.2. Laser diffraction

In addition to DLS static light scattering, laser diffraction (LD) has improved its unique size range recently headed by the Malvern Instruments Mastersizer 3000 that includes an optimized Mie scatter theory. This LD instrument covers the broadest size range from 10 to 3.5 mm, with an exceptional resolution in the submicron range. Main advantage of the technology is not only the wide size range but also the possibility to measure dry powders and aerosols, which is not possible by DLS. A typical measurement in solution is conducted by the addition of the particle dispersion into the measurement chamber until a laser obscuration between 5% and 7% is reached. The "diameter 50%" (LD 50), 90% (LD 90), and 95% (LD 95) (volume distribution) of the measured particles are below this size, can be evaluated (Onoue *et al.*, 2011). In comparison to DLS, the LD also has the advantage of being able to measure the volume distribution directly, whereas the DLS measures an intensity-based mean particle diameter.

4.1.3. Electrical sensing zone method

In addition to LD, the particle size distribution of agglomerated nanoparticles in solution can be analyzed using the electrical sensing zone method (ESZ). This technique is provided by Beckman Coulter with its latest Multisizer 3 instrument. Using the Coulter principle, the Multisizer 3 Coulter Counter® provides number, volume, mass, and surface area size distributions in one measurement, with an overall sizing range of 0.4–1200 µm. The main advantage over DLS and LD is its response that is unaffected by particle color, shape, composition, or refractive index (Plumley *et al.*, 2009).

4.1.4. Aerodynamic assessment

To address the question whether nanoparticles alter the size of aerosol particles generated by nebulization, LD techniques can be used. With this technique, the median droplet size (DV50) and droplet size distributions of nebulized spray mists can be determined. Our group has investigated the impact of liposomes on droplet size distribution during nebulization using a Malvern Spraytec instrument (Malvern Instruments, Herrenberg, Germany). Briefly, liposomes are nebulized at room temperature with an atomization rate of 0.30 ml/min. The spray mist is collected for further

examination of liposome size with DLS as reported above. For example, we have used a commercially available open-circuit mouthpiece ventilator (MPV Truma, Putzbrunn, Germany). At each time-point during the spray event, we have recorded the entire size distribution of the aerosol. We observed no changes in particle size with time and determined a DV50 value of about 6 μm. The spray pattern in terms of volume frequency (%) showed the droplet size distribution ranging from 1 to 20 μm, with 90% of the droplets being below 14 μm in size. By this technique, we could show that nebulized liposomes did not change the droplet size of the spray mist, and neither was the size of the liposomes affected upon nebulization (Hajos *et al.*, 2008).

Dry powders of the nanoparticles are analyzed by time-of-flight measurement using an AerosizerLD (Amherst Instruments) equipped with a 700 μm aperture operating at 4 psi. For this procedure, 5 mg of the powder is added to the aerosizer, and data are collected until a minimum of 10,000 particles are measured. A cascade impactor is then used to collect data on powder performance. Briefly, eight filters are weighed and set onto collection plates that are housed within eight airtight stages arranged serially and stacked on a level setting. Air is then pumped through the stages at a rate of 30 l/min via a vacuum pump and about 10 mg of the samples are introduced at the top of the impactor device. The powders are allowed to deposit among the stages for 20 s, after which time the air flow is stopped. Filters are then removed from the stages and weighed as reported (Plumley *et al.*, 2009).

4.2. Tap density and angle of repose of dry nanoparticles

Dry nanoparticles powders are characterized via a tap density test and a test for angle of repose which will give a measure about the flowability of dry powders and will be important for powder inhaler formulations. The tapped and untapped (bulk) densities are determined by demarcating a small cuvette with known volumes, then inserting a small mass of powder into the cuvette (bulk density) and tapping it vertically against a padded bench top 50 times (tapped density). The mass is divided by the initial and final volumes. From these values, the Hausner ratio (tapped density/bulk density) and Carr's index (Ci) ((tapped density–bulk density)/tapped density × 100%) are also determined for each of the samples.

The angle of repose for each nano powder is measured via the fixed cone height method. Briefly, a glass funnel with an internal stem diameter of 5 mm is placed 1 cm over a glass slide. Particles are allowed to flow gently through the funnel until a cone is formed which has reached the funnel orifice. The angle of the cone to the horizontal is then recorded. This test should be performed in triplicate for each sample (Plumley *et al.*, 2009).

4.3. Surface charge

The surface charge of particles is an important measure to characterize particles in terms of aggregation propensity and colloidal stability. Unfortunately, the surface charge of a particle defined to be the Nernst potential cannot be determined directly. Therefore colloids are often characterized by the Zeta-potential, which is defined to be the potential in the shear plane of the particle. This Zeta-potential can be determined by the measurement of the electrophoretic mobility. Electrophoretic mobility measurements can be easily performed by different instruments, such as a Zetasizer Nano ZS (Malvern Instruments, UK), or a Brookhaven, ZetaPALS (Brookhaven Instruments Corporation, USA) (Plumley *et al.*, 2009). Since the Zeta-potential is highly dependent on the ionic strength and the pH of the solvent, a typical measurement has to be performed with a defined buffer solution with constant pH and ion concentration. In our group, often MilliQ water is used as solvent that has to be adjusted with a 0.9% (w/v) sodium chloride solution to reach a conductivity of 50 μS/cm and a pH in the range of 5.5–6.5 (Ortner *et al.*, 2010).

According to the VIP proticle formulations mentioned above, the zeta potential of different formulations of VIP-loaded proticles (mass ratio ON: VIP:protamine 1:1:0.6; 1:1:0.8; 1:2:0.6) and a primary complex between ON and VIP (mass ratio 1:2) is determined by measuring the electrophoretic mobility (Zetasizer HSA 3000, Malvern, Herrenberg, Germany). Typically, the samples are diluted with a buffer solution (1:7, v/v) immediately before the measurement starts. In general, the measured electrophoretic mobility is converted to the zeta potential, applying the Helmholtz–Smoluchowski equation. Due to an overload of protamine, which is an arginine-rich peptide, positively charged proticles can be achieved without VIP. However, in combination with VIP, the primary complex between oligonucleotides and VIP has the lowest Zeta-potential with approximately –45 mV and the highest Zeta-potential with approximately –15 mV as the ternary complex (Wernig *et al.*, 2008).

4.4. Structure of nanoparticles

Scanning electron microscopy (SEM) and transmission electron microscopy (TEM) can be used to obtain information on particle morphology. Different techniques can be applied to visualize liposomes, polymers, and nanoparticles as described earlier (Liu, 2005; Mühlfeld *et al.*, 2007). For the investigation of nanoparticles, five different EM techniques are briefly described below. They all yield complementary information on, for example, particle sizes, shapes, lamellarity, surface coating, or crystallinity of drugs.

4.4.1. Scanning electron microscopy

SEM can be applied to visualize the surface of nanoparticles. The procedure presented here was applied for VIP-loaded proticles (Wernig *et al.*, 2008). Briefly, the nanoparticle suspensions are freeze-dried in the presence of 5% mannitol. The freeze-dried samples can be sputtered with chromium (coating thickness $\approx$9 nm) in a gas discharge apparatus (GEA005—specimen penetration energy $\approx$10 eV) under argon atmosphere ($\approx 8 \times 10^{-2}$ Pa). Ultrahigh-resolution imaging is performed at low acceleration voltage using a Zeiss ULTRA 55 field emission SEM (FESEM) with GEMINI® technology (Graz University of Technology, Austria) to obtain high-contrast surface imaging.

4.4.2. Negative staining TEM

Ammonium molybdate (5%), phosphotungstic acid (1%), and uranyl acetate (2%) can be used as staining agents for liposomes. For VIP-loaded liposomes, uranyl acetate has been found to give the best contrast and the most homogeneous distribution of the dye. Briefly, 10 µl of liposomes (3 mg/ml) are placed on a carbon-over-Pioloform-coated copper grid and incubated for 1 min. The excess of the sample is blotted with filter paper and immediately replaced by 10 µl of staining agent, which is allowed to settle for 2 min, and then blotted again. Visualization of the samples is performed using a Zeiss EM 902 transmission electron microscope (Oberkochen, Germany) at an acceleration voltage of 80 kV. Digital images are made using a Proscan Slow Scan CCD camera at 1 K $\times$ 1 K resolution.

4.4.3. Ultrathin sectioning for standard TEM

For this method, liposomes are fixed with 1% aqueous OsO_4 over night at 4 °C. A fine, cloudy precipitate is formed and the clear supernatant is carefully removed. Absolute (100%) ethanol is added and after 1–2 h the precipitate condenses to form a loose pellet. The ethanol is replaced by propylene oxide as intermedium, and the pellet passes through increasing concentrations of epon in propylene oxide. The pellet is finally polymerized by incubation with epon at 60 °C for 24 h. Ultrathin sections of about 90 nm thickness are cut from the epon-embedded nanoparticle block, and doublestained with uranyl acetate (2%) and lead citrate. The sections are viewed with the same instrument as described above.

4.4.4. Freeze fracturing TEM

Liposomes are mixed with 30% glycerol (v/v), frozen in liquid propane, and stored in liquid nitrogen. Samples are fractured in a Balzers BAF400D freeze-etching apparatus (Balzers, Liechtenstein) under vacuum with a pressure between 1.3×10^{-4} and 1.3×10^{-5} Pa. Replicas are produced

by vacuum-deposition of the surface with platinum and carbon, controlled with a quartz crystal thin-film monitor. To clean the replicas, they are put into sodium hypochlorite solution (10% active chlorine) for about 3 h and stored overnight in 50% NaOH. Before mounting them on an uncoated copper grid, replicas are washed with distilled water at least three times. Visualization of the grids is accomplished with the same system as described above for negative staining at an acceleration voltage of 50 kV.

Using this method, drying or staining steps during which the liposomes may suffer from different pH or salt conditions, are not necessary, but images prepared by freeze fracturing do not reflect the real size of the liposomes since the fracture plane does not necessarily go through the center of the particles (Egelhaaf *et al.*, 1996).

4.4.5. Cryo-transmission electron microscopy

This technique relies on a very rapid temperature decrease with the goal to obtain frozen hydrated particles in vitreous ice. Briefly, a drop of the sample solution is placed on a copper grid coated with a perforated polymer film. Excess solution is subsequently removed by blotting with a filter paper. It is highly important that the sample film is prepared and handled in an experimental chamber with controlled temperature and humidity. Vitrification of the thin film is achieved by rapidly plunging the EM grid into liquid ethane or propane. The vitrified specimen is thereafter mounted onto a cold-stage kept at liquid nitrogen temperature and examined at this temperature with the electron microscope.

Some representative electron microscopic images of nanoparticles designed for pulmonary application are shown in Fig. 17.2.

4.4.6. Small angle X-ray scattering

Small angle X-ray scattering (SAXS) is a biophysical technique to obtain information about the inner organization of nanoparticles in terms of internal order, lamellarity, crystallinity, or porosity. The scattering curve directly shows the presence of single uncorrelated bilayers typical for unilamellar vesicles, Bragg peaks characteristic for multilamellar liposomes, or reflections characteristic of the formation of a nonlamellar phase. Parameters like axial bilayer thickness, the phospholipid headgroup–headgroup distance, the area occupied by the phospholipid headgroup and the thickness of the water layer can be determined. Further, the integrity of the bilayer or changes in bilayer organization upon drug incorporation can be monitored readily.

To perform SAXS measurements, only about 50 μl of liposomes are needed. Nonetheless, the samples should be concentrated before measurement to a total lipid concentration of at least 20 mg/ml. In case of VIP-loaded liposomes, which serve here as representative example, SAXS measurements are performed with an integrated SWAXS camera system (HECUS X-ray Systems, Graz, Austria) equipped with a semitransparent

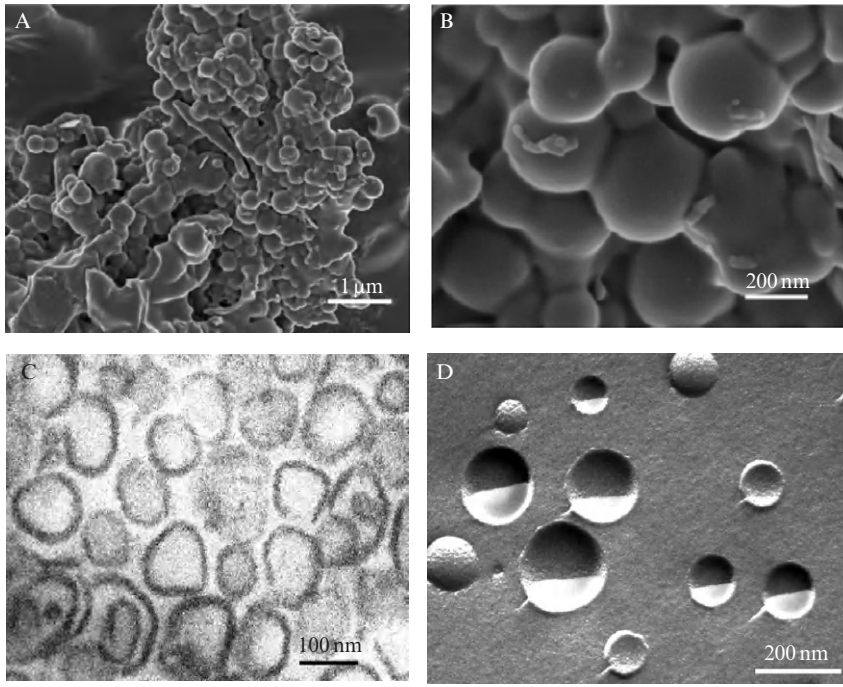

Figure 17.2 Electron micrographs of nanoparticles intended for pulmonary application. (A) SEM images of freeze-dried VIP-loaded proticles embedded in manitol. (B) The enlarged image confirms nanoparticle size and spherical morphology. The smaller irregular structures are noted to be primary complexes between oligonucleotides and VIP (reprinted from Wernig *et al.*, 2008). (C) TEM image of extruded liposomes. The liposomes are osmium-fixed, epon-embedded, and ultrathin sections, about 90 nm thick were cut and uranyl/lead stained (reprinted from Stark *et al.*, 2007). (D) Freeze-fracture image of plain liposomes prepared by extrusion through polycarbonate filters with a pore size of 100 nm (K. Gradauer, unpublished results).

Ni-filtered beam-stop, a position-sensitive detector and a data collection unit. The camera is attached to a conventional Cu-anode generator (Seifert-GE ID 3003, Ahrensburg, Germany) operated at 2 kW. The X-ray beam size is set to 0.5 mm. SAXS patterns are recorded in a q-range between 0.088 and 3.0 nm^{-1}, where $q = (4\pi \sin \theta)/\lambda$ is the scattering vector, 2θ the scattering angle, and $\lambda = 0.154$ nm the wavelength of the X-ray beam. Samples are transferred into 1 mm thin-walled quartz glass capillaries and equilibrated at 20 °C for 10 min using a programmable Peltier unit. An exposure time of 1 h is chosen to obtain good counting statistics at higher q values. The data are buffer background corrected, normalized to intensity, and corrected for slit collimation geometry. Detector channel numbers are converted to wave vectors using a silver stearate standard.

The data can be analyzed using different commercially available software program packages. Indirect Fourier transform can be performed with the program GIFT (Bergmann *et al.*, 2000) or with the program GNOM (Svergun, 1992). SAXS analysis of liposomal formulations can be easily performed using the program GAP (global analysis program) (Pabst, 2006; Pabst *et al.*, 2003). This program is particularly suitable to determine the organization of the lipid bilayers.

5. Biological Efficacy Assessment

During the development of nanocarriers, biological tests have two main functions: (i) to estimate the release kinetics and (ii) to test for the dose-response (release efficacy) after release from the nanocarrier.

5.1. *In vitro* cell culture related tests

A cell biology laboratory is required to test the biological activity of nanoencapsulated drugs. Depending on the cellular mechanisms and the type of interaction with the pharmaceutical nanoformulations, different approaches are necessary. As already mentioned above, the main focus during *in vitro* testing is (i) on the release kinetics, which describes a potential retard effect, and (ii) the drug efficacy (area under the curve). Typical *in vitro* test protocols will measure any specific cellular response under controlled conditions. First, the suitability of the cell lines used has to be proven. As an example, Fig. 17.3 shows an immunohistochemical staining of the VIP

Figure 17.3 Endothelial cells are cultured, fixed, and immmunostained with immunoglobulines to visualize the expression of so-called VPAC-2 receptors (brown) by this cell type.

receptor, VPAC-2, to ensure that the used cell line is suitable for subsequent release and efficacy tests with VIP encapsulated into nanocarriers.

The intracellular generation of cyclic-AMP (cAMP) in human pulmonary artery smooth muscle cells (hPASMACS) is often used to determine the concentration–time response of vasodilatory drugs. This assay can be applied for both prostacyclin- and VIP-loaded nanoparticles.

Briefly, cells are grown in 12-well plates (1×10^5 cells/well, 2 ml VascuLife® SMC Smooth Muscle Cell Culture Medium, at 37 °C, 5% CO_2) to 80% confluence (passages 8–10 are used). After washing with phosphate buffered saline (PBS), the cells are incubated with 1 ml medium containing different amounts of drug-loaded nanoparticles. The cells are kept for certain time points (0–3 h) at 37 °C. Subsequently, the cells are washed with cold PBS and resuspended in cell lysis buffer. After two cycles of freeze (− 20 °C) and thaw, the cell lysate is transferred to Eppendorf tubes and spun at $600 \times g$ for 10 min at 4 °C. The supernatant is stored at − 20 °C for cAMP determination. An aliquot is taken for total protein estimation and used to normalize cAMP concentrations. Any commercially available cAMP assay with competitive ELISA can be used for cAMP quantification according to the instructions provided by the producer.

5.2. *Ex vivo–in vitro* testing with a myograph

The primary targets of drugs developed for PAH-treatment are the blood vessel walls. Therefore, the testing of the relaxing efficacy under controlled conditions starts at an early phase *in vitro*. For these studies, a myograph system can be used. In general, preconstricted vessels will be exposed to nanoparticle formulations to assess the vasodilative effects and the pharmacokinetics.

5.2.1. Rat lung artery preparations

While mice are too small, rats or hamsters provide pulmonary arteries of suitable size to be tested. The procedure is not an animal-experiment *per se*, but an experiment on surviving organs, therefore, no particular regulations on animal experimentation have to be observed. We have also used human arteries obtained with the patient's permission after they underwent lobectomy (e.g., as treatment for lung cancer) to confirm the animal tissue results in human tissue.

The heart and lungs are excised en bloc from anesthesized animals, and pinned on a wax surface in a petri dish containing cold Krebs-Henseleit (KH) solution (in m*M* 118.40—NaCl; 5.01—KCl; 1.20—KH_2PO_4; 2.5—$CaCl_2$; 1.2—$MgCl_2$; 10.1—glucose; 25—$NaHCO_3$) in an orientation that facilitated identification of the pulmonary arteries (Fig. 17.4).

The pulmonary arterial tree is rapidly dissected from the lung parenchyma with small scissors and forceps. The common pulmonary artery and the left and right extrapulmonary artery segments are opened longitudinally

Figure 17.4 Heart and lungs prepared en bloc to obtain and dissect the pulmonary artery originating from the right ventricle (picture by Anaid Shabazian).

and divided into two pulmonary artery preparations (consisting of common and left or right pulmonary artery). The preparations are cut as zigzag segments (to obtain a segment of 1.3–1.5 cm in length) and mounted in thermostatically controlled (37 °C) organ baths. The organ baths contained 9 ml oxygenated KH solution gassed with 95% O_2 and 5% CO_2 (pH 7.4).

Then the activity of the arterial stripes under investigation can be recorded isotonically under a resting load of 1 g. The mechanical signals (artery extension and contraction) are processed by bridge amplifiers (Hugo Sachs Elektronik, Germany) and are recorded on ink writers. Under these conditions, the arterial segments are viable for 5 h or even longer.

5.2.2. Post-experiment vitality test of the mounted arteries

At the end of each experiment, papaverine hydrochloride (10 μ*M*), an endothelium-independent vasodilator, is added to the arterial strips to confirm that the arteries have retained their functionality during the whole experiment.

5.2.3. Lung artery physiology: Data analysis

The span of the recordings depends on the length of the artery-segments and varies from preparation to preparation and experiments. Therefore, the recorded precontraction by phenylephrine is taken as 100% reference for maximal contraction. As illustrated in Fig. 17.5, the vasorelaxation induced by each concentration of acetylcholine (ACh) or drug can be expressed as a percentage of the 100% precontraction, recorded immediately before the

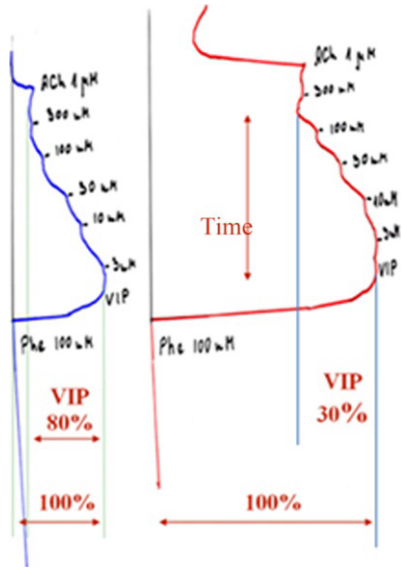

Figure 17.5 Two examples of artery contraction (and relaxation) obtained with the myograph. The maximal contraction after phenylephrine addition to the water bath is taken as 100% and the relaxation is expressed as percentage of the maximal contraction reaction. Note that in the same recording, both the response and the time to reach the maximum response is monitored; this procedure allows to test for release kinetics and retardation time.

first addition of the vasodilatory drug. With these relaxation, data statistical analysis can be performed with Student's *t*-test.

5.2.4. Endothelial function

After mounting, the arterial strips are equilibrated in their baths for 2–3 h during which the KH solution is renewed three times. Depending on the substance and the specific research question, the endothelium should stay intact or it can be mechanically removed by rubbing the intimal surface with a small wooden stick (Cardell *et al.*, 1997). This treatment destroys the endothelium, which can be used in control experiments. As ACh is known as an endothelium-specific vasorelaxing agent, the degree of endothelial destruction can be examined, by contracting the isolated pulmonary artery with a submaximal concentration (EC_{80}) of the α_1-adrenoceptor agonist L-phenylephrine (Phe) hydrochloride (Phe; 0.1 μ*M*) and testing the ability of ACh (1 μ*M*) to relax the arterial strips. As anticipated from the work of Furchgott and Zawadzki (1980) if any Ach-inducible relaxation is absent, then the endothelium had been rubbed off completely.

5.2.5. ecNOs-blockade by L-NAME

For mechanistic studies, in case NO plays a role is in the intracellular pathway (e.g., sildenafil, VIP), inhibition of NO production by preincubation with the nitric oxide synthase inhibitor N^{ω}-nitro-L-arginine methyl ester (L-NAME, 0.5 m*M*) (Rees *et al.*, 1989) can be performed. The precontraction with a submaximal concentration (EC_{80}) of Phe (0.1 μ*M*) is as usual (Haghighi *et al.*, 2002).

5.2.6. Practical applications of biological test systems

Because myograph recordings allow for the analysis of dose-effects and time-effects (retarded release), myograph measurements are particularly well suited in the development of nano-formulated vasoactive substances and their release from nanoparticles. The myograph technique has been employed successfully to develop liposomes as peptide carriers (Stark *et al.*, 2007), test them for the retardation effect (Hajos *et al.*, 2008), and measure the potential to protect against rapid enzymatic degradation (Stark *et al.*, 2008).

Another technique to observe and measure substance release from particles is the so-called time-lapse microscopy employed by Ortner and coworkers. The authors show that VIP-loaded proticles are stable in size and substance content in physiologic solutions by fluorescence correlation spectroscopy. With confocal laser scanning microscopy, proticles are observed to specifically target tumor cells before they unload their "cargo" (Ortner *et al.*, 2010).

5.3. Toxicology

To have a rough estimate of the toxicologic side effects, we recorded the vitality of the arteries (performance deterioration over time) during the tests with the myograph. Typically, the specific toxicologic testing of nanoformulated drugs should identify and test three possibilities for toxicologic reactions: (i) the substance, (ii) the carrier-material, and (iii) effects attributable to the particle size (nonspecific cellular uptake of nanoparticles). Other cytotoxicity tests that can be done in most cell biology labs are: (i) MTT assay for cytotoxicity, (ii) lactate dehydrogenase measurement (LDH), and (iii) NRU (neutral red uptake) (for review, see Weyermann *et al.*, 2005a).

6. Concluding Remarks

The growing interest in innovative nanotechnology-based pharmaceutics is well justified to improve inhalable drug delivery systems for the treatment of respiratory diseases. Nanoparticles are developed to bring effective amounts of drugs directly to the diseased organ, for example, the lung. This innovative strategy requires stable nanoparticle formulations in

combination with advanced inhalation devices providing defined nebulization properties. Most important, however, is that the nanoparticles have to shield their payload from rapid degradation and inactivation until they reach their target in the lung. Finally, the nanoparticles have to release the active drug in a controlled, retarded manner. To date, many different nanoparticle formulations or nanoparticle complexes have been explored for pulmonary drug delivery.

Since nanoparticle drug formulations offer many advantages over traditional liquid dose formulations, problems associated with cytotoxicity, proper upscaling techniques, and high production costs need to be overcome. In particular, pulmonary controlled release of vasodilatory drugs from nanoparticles for local treatment of PAH has the potential to substantially improve the disease management by the patient and doctors. Further improvements in inhalation therapy mediated by nanoparticle drug delivery systems are the focus of current research.

REFERENCES

Abu-Dahab, R., Schäfer, U. F., and Lehr, C. M. (2001). Lectin-functionalized liposomes for pulmonary drug delivery: Effect of nebulization on stability and bioadhesion. *Eur. J. Pharm. Sci.* **14,** 37–46.

Allen, T. M., and Cullis, P. R. (2004). Drug delivery systems: Entering the mainstream. *Science* **303,** 1818–1822.

Barst, R. J., Ertel, S. I., Beghetti, M., and Ivy, D. D. (2011). Pulmonary arterial hypertension: A comparison between children and adults. *Eur. Respir. J.* **37,** 665–677.

Bartlett, G. R. (1959). Phosphorus assay in column chromatography. *J. Biol. Chem.* **234,** 466–468.

Bergmann, A., Fritz, G., and Glatter, O. (2000). Solving the generalized indirect Fourier transformation (GIFT) by Boltzmann simplex simulated annealing (BSSA). *J. Appl. Cryst.* **33,** 1212–1216.

Bolin, D. R., Michalewsky, J., Wasserman, M. A., and O'Donnell, M. (1995). Design and development of a vasoactive intestinal peptide analog as a novel therapeutic for bronchial asthma. *Biopolymers* **37,** 57–66.

Burian, B., Storka, A., Marzluf, B. A., Yen, Y. C., Lambers, C., Robibaro, B., Vonbank, K., Mosgoeller, W., and Petkov, V. (2010). Vasoactive intestinal peptide (VIP) receptor expression in monocyte-derived macrophages from COPD patients. *Peptides* **31,** 603–608.

Buxton, D. B. (2009). Nanomedicine for the management of lung and blood diseases. *Nanomedicine* **4,** 331–339.

Cardell, L. O., Hjert, O., and Uddman, R. (1997). The induction of nitric oxide-mediated relaxation of human isolated pulmonary arteries by PACAP. *Br. J. Pharmacol.* **120,** 1096–1100.

Couvreur, P., and Vauthier, C. (2006). Nanotechnology: Intelligent design to treat complex disease. *Pharm. Res.* **23,** 1417–1450.

Dagar, S., Sekosan, M., Lee, B. S., Rubinstein, I., and Onyuksel, H. (2001). VIP receptors as molecular targets of breast cancer: Implications for targeted imaging and drug delivery. *J. Control. Release* **74,** 129–134.

D'Alonzo, G. E., *et al.* (1991). Survival in patients with primary pulmonary hypertension. Results from a national prospective registry. *Ann. Intern. Med.* **115,** 343–349.

Düzgüneş, N. (2003). Preparation and quantitation of small unilamellar liposomes and large unilamellar reverse-phase evaporation liposomes. *Methods Enzymol.* **367,** 23–27.

Egelhaaf, S. U., Wehrli, E., Müller, M., Adrian, M., and Schurtenberger, P. (1996). Determination of the size distribution of lecithin liposomes: A comparative study using freeze fracture, cryoelectron microscopy and dynamic light scattering. *J. Microsc.* **184,** 214–228.

Ewert, R., Glaser, S., Bollmann, T., and Schaper, C. (2011). Inhaled iloprost for therapy in pulmonary arterial hypertension. *Expert Rev. Respir. Med.* **5,** 145–152.

Furchgott, R. F., and Zawadzki, J. V. (1980). The obligatory role of endothelial cells in the relaxation of arterial smooth muscle by acetylcholine. *Nature* **288,** 373–376.

Gao, X. P., Noda, Y., Rubinstein, I., and Paul, S. (1994). Vasoactive intestinal peptide encapsulated in liposomes: Effects on systemic arterial blood pressure. *Life Sci.* **54,** 247–252.

George, M. P., Champion, H. C., and Pilewski, J. M. (2011). Lung transplantation for pulmonary hypertension. *Pulm. Circ.* **1,** 182–191.

Gill, K. K., Nazzal, S., and Kaddoumi, A. (2011). Paclitaxel loaded PEG(5000)-DSPE micelles as pulmonary delivery platform: Formulation characterization, tissue distribution, plasma pharmacokinetics, and toxicological evaluation. *Eur. J. Pharm. Biopharm.* **79,** 276–284.

Gololobov, G., Noda, Y., Sherman, S., Rubinstein, I., Baranowska-Kortylewicz, J., and Paul, S. (1998). Stabilization of vasoactive intestinal peptide by lipids. *J. Pharmacol. Exp. Ther.* **285,** 753–758.

Gomberg-Maitland, M., and Olschewski, H. (2008). Prostacyclin therapies for the treatment of pulmonary arterial hypertension. *Eur. Respir. J.* **31,** 891–901.

Gupta, V., and Ahsan, F. (2010). Inhalational therapy for pulmonary arterial hypertension: Current status and future prospects. *Crit. Rev. Ther. Drug Carrier Syst.* **27,** 313–370.

Gupta, V., and Ahsan, F. (2011). Influence of PEI as a core modifying agent on PLGA microspheres of PGE 1, a pulmonary selective vasodilator. *Int. J. Pharm.* **413,** 51–62.

Gupta, V., Rawat, A., and Ahsan, F. (2010). Feasibility study of aerosolized prostaglandin E1 microspheres as a noninvasive therapy for pulmonary arterial hypertension. *J. Pharm. Sci.* **99,** 1774–1789.

Gupta, V., Davis, M., Hope-Weeks, L. J., and Ahsan, F. (2011). PLGA microparticles encapsulating prostaglandin E1-hydroxypropyl-β-cyclodextrin (PGE1-HPβCD) complex for the treatment of pulmonary arterial hypertension (PAH). *Pharm. Res.* **28,** 1733–1749.

Haghighi, M. K., Pollock, D., and Hosseinei, H. F. (2002). Vasorelaxant effects of atropine: Role of nitric oxide/ endothelium derived relaxing factor. *Indian J. Pharmacol.* **34,** 244–250.

Hajos, F., Stark, B., Hensler, S., Prassl, R., and Mosgoeller, W. (2008). Inhalable liposomal formulation for vasoactive intestinal peptide. *Int. J. Pharm.* **357,** 286–294.

Harada-Shiba, M., *et al.* (2009). Intratracheal gene transfer of adrenomedullin using polyplex nanomicelles attenuates monocrotaline-induced pulmonary hypertension in rats. *Mol. Ther.* **17,** 1180–1186.

Jeh, H. S., Lu, S., and George, S. C. (2004). Encapsulation of PROLI/NO in biodegradable microparticles. *J. Microencapsul.* **21,** 3–13.

Kawabata, Y., Aoki, Y., Matsui, T., Yamamoto, K., Sato, H., Onoue, S., and Yamada, S. (2011). Stable dry powder inhaler formulation of tranilast attenuated antigen-evoked airway inflammation in rats. *Eur. J. Pharm. Biopharm.* **77,** 178–181.

Kimura, S., Egashira, K., Chen, L., Nakano, K., Iwata, E., Miyagawa, M., Tsujimoto, H., Hara, K., Morishita, R., Sueishi, K., Tominaga, R., and Sunagawa, K. (2009). Nanoparticle-mediated delivery of nuclear factor KB decoy into lungs ameliorates monocrotaline-induced pulmonary arterial hypertension. *Hypertension* **53,** 877–883.

Kleemann, E., Schmehl, T., Gessler, T., Bakowsky, U., Kissel, T., and Seeger, W. (2007). Iloprost-containing liposomes for aerosol application in pulmonary arterial hypertension: Formulation aspects and stability. *Pharm. Res.* **24,** 277–287.

Konduri, K. S., Nandedkar, S., Rickaby, D. A., Düzgüneş, N., and Gangadharam, P. R. J. (2005). The use of sterically stabilized liposomes to treat asthma. *Methods Enzymol.* **391,** 413–427.

Labiris, N. R., and Dolovich, M. B. (2003). Pulmonary drug delivery. Part II: The role of inhalant delivery devices and drug formulations in therapeutic effectiveness of aerosolized medications. *Br. J. Clin. Pharmacol.* **56,** 600–612.

Liu, J. (2005). Scanning transmission electron microscopy and its application to the study of nanoparticles and nanoparticle systems. *J. Electron Microsc.* **54,** 251–278.

Lochmann, D., Weyermann, J., Georgens, C., Prassl, R., and Zimmer, A. (2005). Albumin-protamine-oligonucleotide nanoparticles as a new antisense delivery system. Part 1: Physicochemical characterization. *Eur. J. Pharm. Biopharm.* **59,** 419–429.

Mansour, H. M., Rhee, Y. S., and Wu, X. (2009). Nanomedicine in pulmonary delivery. *Int. J. Nanomedicine* **4,** 299–319.

Morishita, R., Higaki, J., Tomita, N., and Ogihara, T. (1998). Application of transcription factor 'decoy' strategy as means of gene therapy and study of gene expression in cardiovascular disease. *Circ. Res.* **82,** 1023–1028.

Mozafari, M. R. (2005). Liposomes: An overview of manufacturing techniques. *Cell. Mol. Biol. Lett.* **10,** 711–719.

Mühlfeld, C., Rothen-Rutishauser, B., Vanhecke, D., Blank, F., Gehr, P., and Ochs, M. (2007). Visualization and quantitative analysis of nanoparticles in the respiratory tract by transmission electron microscopy. *Part. Fibre Toxicol.* **4**.

Murakami, H., Kobayashi, M., Takeuchi, H., and Kawashima, Y. (1999). Preparation of poly(DL-lactide-co-glycolide) nanoparticles by modified spontaneous emulsification solvent diffusion method. *Int. J. Pharm.* **187,** 143–152.

Nadler, S. T., and Edelman, J. D. (2010). Inhaled treprostinil and pulmonary arterial hypertension. *Vasc. Health Risk Manag.* **6,** 1115–1124.

Olschewski, H., *et al.* (2002). Inhaled iloprost for severe pulmonary hypertension. *N. Engl. J. Med.* **347,** 322–329.

Onoue, S., Aoki, Y., Kawabata, Y., Matsui, T., Yamamoto, K., Sato, H., Yamauchi, Y., and Yamada, S. (2011). Development of inhalable nanocrystalline solid dispersion of Tranilast for airway inflammatory diseases. *J. Pharm. Sci.* **100,** 622–633.

Onyuksel, H., Sejourne, F., Suzuki, H., and Rubinstein, I. (2006). Human VIP-alpha: A long-acting, biocompatible and biodegradable peptide nanomedicine for essential hypertension. *Peptides* **27,** 2271–2275.

Ortner, A., Wernig, K., Kaisler, R., Edetsberger, M., Hajos, F., Köhler, G., Mosgoeller, W., and Zimmer, A. (2010). VPAC receptor mediated tumor cell targeting by protamine based nanoparticles. *J. Drug Target.* **18,** 457–467.

Pabst, G. (2006). Global properties of biomimetic membranes: Perspectives on molecular features. *Biophys. Rev. Lett.* **1,** 57–84.

Pabst, G., Koschuch, R., Pozo-Navas, B., Rappolt, M., Lohner, K., and Laggner, P. (2003). Structural analysis of weakly ordered membrane stacks. *J. Appl. Cryst.* **63,** 1378–1388.

Palevsky, H. I., Schloo, B. L., Pietra, G. G., Weber, K. T., Janicki, J. S., Rubin, E., and Fishman, A. P. (1989). Primary pulmonary hypertension. Vascular structure, morphometry, and responsiveness to vasodilator agents. *Circulation* **80,** 1207–1221.

Patton, J. S., and Byron, P. R. (2007). Inhaling medicines: Delivering drugs to the body through the lungs. *Nat. Rev. Drug Discov.* **6,** 67–74.

Petkov, V., *et al.* (2003). Vasoactive intestinal peptide as a new drug for treatment of primary pulmonary hypertension. *J. Clin. Invest.* **111,** 1339–1346.

Plumley, C., Gorman, E. M., El-Gendy, N., Bybee, C. R., Munson, E. J., and Berkland, C. (2009). Nifedipine nanoparticle agglomeration as a dry powder aerosol formulation strategy. *Int. J. Pharm.* **369,** 136–143.

Rees, D. D., Palmer, R. M., Hodson, H. F., and Moncada, S. (1989). A specific inhibitor of nitric oxide formation from L-arginine attenuates endothelium-dependent relaxation. *Br. J. Pharmacol.* **96,** 418–424.

Rubinstein, I. (2005). Human VIP-alpha: An emerging biologic response modifier to treat primary pulmonary hypertension. *Expert Rev. Cardiovasc. Ther.* **3,** 565–569.

Rubinstein, I., Patel, M., Ikezaki, H., Dagar, S., and Onyuksel, H. (1999). Conformation and vasoreactivity of VIP in phospholipids: Effects of calmodulin. *Peptides* **20,** 1497–1501.

Rubinstein, I., Ikezaki, H., and Onyuksel, H. (2006). Intratracheal and subcutaneous liposomal VIP normalizes arterial pressure in spontaneously hypertensive hamsters. *Int. J. Pharm.* **316,** 144–147.

Sakagami, M. (2006). In vivo, in vitro and ex vivo models to assess pulmonary absorption and disposition of inhaled therapeutics for systemic delivery. *Adv. Drug Deliv. Rev.* **58,** 1030–1060.

Sejourne, F., Rubinstein, I., Suzuki, H., and Alkan-Onyuksel, H. (1997). Development of a novel bioactive formulation of vasoactive intestinal peptide in sterically stabilized liposomes. *Pharm. Res.* **14,** 362–365.

Sethi, V., Onyuksel, H., and Rubinstein, I. (2005). Liposomal vasoactive intestinal peptide. *Methods Enzymol.* **391,** 377–395.

Shlobin, O. A., and Nathan, S. D. (2011). Pulmonary hypertension secondary to interstitial lung disease. *Expert Rev. Respir. Med.* **5,** 179–189.

Smola, M., Vandamme, T., and Sokolowski, A. (2008). Nanocarriers as pulmonary drug delivery systems to treat and to diagnose respiratory and non respiratory diseases. *Int. J. Nanomedicine* **3,** 1–19.

Stark, B., Debbage, P., Andreae, F., Mosgoeller, W., and Prassl, R. (2007). Association of vasoactive intestinal peptide with polymer-grafted liposomes: Structural aspects for pulmonary delivery. *Biochim. Biophys. Acta* **1768,** 705–714.

Stark, B., Andreae, F., Mosgoeller, W., Edetsberger, M., Gaubitzer, E., Koehler, G., and Prassl, R. (2008). Liposomal vasoactive intestinal peptide for lung application: Protection from proteolytic degradation. *Eur. J. Pharm. Biopharm.* **70,** 153–164.

Stevenson, C. S., and Birrell, M. A. (2011). Moving towards a new generation of animal models for asthma and COPD with improved clinical relevance. *Pharmacol. Ther.* **130,** 93–105.

Suzuki, H., Noda, Y., Paul, S., Gao, X. P., and Rubinstein, I. (1995). Encapsulation of vasoactive intestinal peptide into liposomes: Effects on vasodilation in vivo. *Life Sci.* **57,** 1451–1457.

Svergun, D. I. (1992). Determination of the regularization parameter in indirect-transform methods using perceptual criteria. *J. Appl. Cryst.* **25,** 495–503.

Thomas, M., Lu, J. J., Ge, Q., Zhang, C., Chen, J., and Klibanov, A. M. (2005). Full deacylation of polyethylenimine dramatically boosts its gene delivery efficiency and specificity to mouse lung. *Proc. Natl. Acad. Sci. USA* **102,** 5679–5684.

Torchilin, V. P. (2005). Recent advances with liposomes as pharmaceutical carriers. *Nat. Rev. Drug Discov.* **4,** 145–160.

Torchilin, V. P. (2006). Multifunctional nanocarriers. *Adv. Drug Deliv. Rev.* **58,** 1532–1555.

Torchilin, V. (2009). Multifunctional and stimuli-sensitive pharmaceutical nanocarriers. *Eur. J. Pharm. Biopharm.* **71,** 431–444.

Tulloh, R. (2009). Etiology, diagnosis, and pharmacologic treatment of pediatric pulmonary hypertension. *Paediatr. Drugs* **11,** 115–128.

Wagenvoort, C. A., and Wagenvoort, N. (1970). Primary pulmonary hypertension: A pathological study of the lung vessel in 156 clinically diagnosed cases. *Circulation* **42,** 1163–1184.

Wagner, V., Dullaart, A., Bock, A. K., and Zweck, A. (2006). The emerging nanomedicine landscape. *Nat. Biotechnol.* **24,** 1211–1217.

Waldrep, J. C., Gilbert, B. E., Knight, C. M., Black, M. B., Scherer, P. W., Knight, V., and Eschenbacher, W. (1997). Pulmonary delivery of beclomethasone liposome aerosol in volunteers—Tolerance and safety. *Chest* **111,** 316–323.

Wernig, K., Griesbacher, M., Andreae, F., Hajos, F., Wagner, J., Mosgoeller, W., and Zimmer, A. (2008). Depot formulation of vasoactive intestinal peptide by protamine-based biodegradable nanoparticles. *J. Control. Release* **130,** 192–198.

Weyermann, J., Lochmann, D., and Zimmer, A. (2005a). A practical note on the use of cytotoxicity assays. *Int. J. Pharm.* **288,** 369–376.

Weyermann, J., Lochmann, D., Georgens, C., and Zimmer, A. (2005b). Albumin-protamine-oligonucleotide-nanoparticles as a new antisense delivery system. Part 2: Cellular uptake and effect. *Eur. J. Pharm. Biopharm.* **59,** 431–438.

Wood, P. (1958). Pulmonary hypertension with special reference to the vasoconstrictive factor. *Br. Heart J.* **20,** 557–570.

Wu, D., Lee, D., and Sung, Y. K. (2011). Prospect of vasoactive intestinal peptide therapy for COPD/PAH and asthma: A review. *Respir. Res.* **12,** 45.

Yeshua, H., Blendis, L. M., and Oren, R. (2009). Pulmonary manifestations of liver diseases. *Semin. Cardiothorac. Vasc. Anesth.* **13,** 60–69.

Zakynthinos, E., Daniil, Z., Papanikolaou, J., and Makris, D. (2011). Pulmonary hypertension in COPD: Pathophysiology and therapeutic targets. *Curr. Drug Targets* **12,** 501–513.

CHAPTER EIGHTEEN

Nanomedicines for Inflammatory Diseases

Fatima A. Khaja,* Otilia M. Y. Koo,*,† *and* Hayat Önyüksel*

Contents

Abstract

Inflammation is the body's natural defense mechanism in response to many diseases including infection, cancer, and autoimmune disease. Since the birth of nanotechnology at the end of the twentieth century, scientists have been utilizing the pathophysiologic features of inflammation, mainly leaky

* Department of Biopharmaceutical Sciences, College of Pharmacy, University of Illinois at Chicago, Chicago, Illinois, USA
† Drug Product Science and Technology, Bristol-Myers Squibb Company, New Brunswick, New Jersey, USA

Methods in Enzymology, Volume 508
ISSN 0076-6879, DOI: 10.1016/B978-0-12-391860-4.00018-5

vasculature and the overexpression of biomarkers, to design nanomedicines that can deliver drugs with passive and active targeting mechanisms to inflamed tissue sites and achieve effective therapy. Recent advances in nanomedicine research have provided scientists with nanocarriers of many unique and tunable properties to match the specific requirements for the treatment of different inflammatory disease conditions. In this chapter, we describe some of the materials and methods used in the preparation and characterization of these nanomedicines, approaches used for the evaluation of their efficacy on a cellular and organ level, as well as available animal models. We also show how safety and biodistribution studies using anti-inflammatory nanomedicines are conducted in our laboratory for the treatment of rheumatoid arthritis animal models.

1. Introduction

Inflammation is a fundamental, yet complex, process designed to protect the human body by eliminating both the causes and consequences of injury, such as microbes, toxins, and necrotic cells. Most of these factors reside in the extravascular space where they elicit a series of cellular reactions that activates the inflammatory response. Therefore, plasma proteins, circulating cells, and tissue phagocytes (the body's defenders against foreign invaders) have to be recruited to the extravascular space, to rid the organism of these factors (Kumar *et al.*, 2010). Inflammation has many features, some of which have been described by the early Egyptians, such as redness, swelling, heat, and pain. Throughout early medicine, physicians had been concentrating on palliative treatment of these symptoms while the causative element subsided. It was not until 1964, that Cotran and Majno described the phenomenon of vascular leakage in inflammation (Cotran and Majno, 1964), a concept scientists now utilize in the emerging field of nanomedicine.

Inflammation can either be acute or chronic in its time course. Acute inflammation has a rapid onset, usually caused by stimuli such as infection and foreign bodies and, lasts for a few hours to a few days. Chronic inflammation, on the other hand, has a duration of weeks to several months, causing degeneration of connective tissue in one or more body parts (Kumar *et al.*, 2010). A comprehensive list of inflammatory diseases would exceed 100; hence, this chapter will focus on conditions where the availability of effective long-term therapy remains scarce. These include; rheumatoid arthritis (RA), ocular inflammation, and inflammatory bowel disease (IBD). Although anti-inflammatory drugs are available for the treatment of many inflammatory conditions, their low bioavailability and nontargeted biodistribution often limit their success in controlling disease symptoms. Therefore, there remains a significant need for an effective anti-inflammatory medication. Nanoencapsulation of anti-inflammatory agents is one

approach that scientists have been considering to achieve better bioavailability and targeting (Koo *et al.,* 2011; Plevy and Targan, 2011; Ulbrich and Lamprecht, 2010).

The two main morphologic features of chronic inflammation that scientists have been exploiting to engineer the perfect nanomedicine are: vascular permeability or leakage and the overexpression of biomarkers. Vascular leakage is believed to be caused by the contraction of endothelial cells lining the arterioles and capillaries supplying the inflamed tissue. This phenomenon is elicited by histamine, bradykinin, leukotrienes, and other mediators (Lampugnani and Dejana. 1997), and results in inter-endothelial spaces ranging up to 700 nm in size, depending on the inflammatory state and disease (Moghimi *et al.,* 2001). These fenestrations allow the escape of exudate containing plasma proteins and circulating cells to the extracellular tissues. Therefore, the same process can also be used for passive targeting of anti-inflammatory nanomedicines. Nanoparticles with appropriate size can extravasate into these interstitial spaces and be retained at the site of inflammation by the enhanced permeability and retention (EPR) effect (Maeda *et al.,* 2000). The overexpression of biological markers or receptors on cell surfaces is a common feature of both cancer and inflammatory diseases. This phenomenon has been studied widely in the last decade to specifically target nanomedicines to the desired site by the chemical conjugation of a targeting ligand on the surface of circulating nanocarriers (Moghimi *et al.,* 2001). We have shown recently the use of the overexpression of vasoactive intestinal peptide receptors (VIP-R) on activated T lymphocytes, macrophages, and overproliferating synoviocytes, to successfully target camptothecin nanomedicine through surface conjugation of vasoactive intestinal peptide (VIP) to the inflamed joints of RA animal models (Koo *et al.,* 2011). VIP-R are ideal targets in this case, as they are overexpressed in inflamed peripheral tissues, but not on the luminal surface of blood vessels (Fahrenkrug *et al.,* 2000). In addition, VIP has shown anti-inflammatory benefits at the clinical and pathological levels, as its therapeutic effects are associated with the downregulation of both inflammation and autoimmune responses (Delgado *et al.*, 2001). Unfortunately its instability, short systemic half-life, and hypotensive effects have limited its application and transition from the bench to bedside. Hence, we have developed sterically stabilized micelles conjugated with VIP (SSMs–VIP) that have successfully enhanced and prolonged the activity of the peptide and reduced its side-effects on the mean systemic arterial pressure (Sethi *et al.*, 2003).

Nanomedicines can be defined as carrier systems in the nanosize range (preferably 10–100 nm), containing encapsulated, dispersed, adsorbed, or conjugated drugs and imaging agents (Koo *et al.*, 2005b). These nanoscale systems have tunable physical and chemical properties, giving them numerous advantages over other traditional oral or parenteral formulations. First, their chemical composition and possible arrangement of individual monomers

allows for the encapsulation of a wide variety of hydrophobic drugs, peptides, and oligonucleotides, where the payload is dependent on the overall size of the nanocarrier (Cesur *et al.*, 2009; Gao *et al.*, 2011; Kuzmis *et al.*, 2011). Second, their size and surface chemistry can be used to achieve passive and active targeting to the site of inflammation. The targeting ability results in the accumulation of therapeutic agents at inflammed sites in higher concentrations than in healthy tissues. This helps reduce major adverse effects observed with conventional medicines and enhances the efficacy, pharmacokinetic (PK) properties, and biodistribution of a given formulation (Cho *et al.*, 2008).

This chapter discusses two different categories of nanoparticles: lipid-based and polymeric nanomedicines that are being studied in the treatment of chronic inflammatory diseases such as RA, ocular inflammation, and IBD. Experimental methods used in the preparation and characterization of selected nanocarriers, that is, sterically stabilized phospholipid micelles, liposomes, solid lipid nanoparticles, Polylactic glycolic acid (PLGA), and chitosan polymers, that fall under the previously mentioned categories and have been studied for these inflammatory diseases, will be discussed. In addition, techniques and animal models used for the evaluation of *in vitro* and *in vivo* efficacy and biodistribution of these nanomedicines are given.

2. Nanomedicine Preparations

2.1. Materials and methods of preparation of lipid-based nanomedicines

Sterically stabilized phospholipid micelles (SSM): These are composed of DSPE-PEG_{2000} monomers [distearoylphosphatidylethanolamine-(polyethylene glycol-2000)] and have been studied in our laboratory for the delivery of hydrophobic molecules (Cesur *et al.*, 2009; Koo *et al.*, 2006; Krishnadas *et al.*, 2003), and peptide drugs (Kuzmis *et al.*, 2011; Lim *et al.*, 2011). These nanocarriers are ideal for drug delivery for multiple reasons: (i) Their phospholipid composition makes them biocompatible and relatively non-toxic; (ii) their hydrophobic core is suitable for incorporation of water insoluble drugs, (iii) their low critical micelle concentration (CMC) ensures their stability upon dilution and systemic injection, (iv) the hydrophilic corona composed of the PEG layer renders them sterically stabilized and protects them against uptake by the mononuclear phagocyte system and enables their active targeting by the chemical conjugation of ligands to the far ends of PEG, and (v) their small uniform size of $\sim$15 nm (Ashok *et al.*, 2004) makes them suitable for passive targeting through the leaky vasculature of inflamed tissues and cancer (Koo *et al.*, 2011). SSMs have been studied in our laboratory for inflammation by the targeted delivery of camptothecin and VIP as anti-inflammatory agents for the treatment of

RA (Koo *et al.*, 2005a; Sethi *et al.*, 2003). For laboratory scale, incorporating water insoluble molecules into SSM can be achieved by the coprecipitation and reconstitution technique. This briefly involves dissolving both the hydrophobic drug and DSPE-PEG_{2000} lipid (purchased from LIPOID GmbH. Ludwigshafen, Germany) in methanol as an organic solvent. A thin film is then formed by rotary evaporation of organic solvent under a stream of argon gas followed by reconstitution of the film with isotonic buffer, for example, phosphate buffered saline (PBS, pH 7.4). The resulting nanomedicine is in the form of a colloidal clear dispersion with the hydrophobic drug molecule encapsulated in the core of the SSM nanocarriers. Peptide nanomedicines on the other hand, can be prepared by simply incubating the peptide solution in PBS with the preformed SSMs in aqueous media at a specific lipid to peptide molar ratio at room temp (25 °C) for 2 h (Lim *et al.*, 2011). SSMs have also shown to be successful in increasing the shelf-life of incorporated drugs and can be stored with great stability as a lyophilized powder (Koo *et al.*, 2005a).

Alternatively *liposomes,* which are lipid bilayers with hydrophilic cores, are also suitable for water soluble anti-inflammatory agents. Small PEGylated liposomes (<150 nm) have been studied extensively as carriers of anti-inflammatory drugs such as prednisone and other corticosteroids (Ulbrich and Lamprecht, 2010) and have recently shown to yield rapid and durable disease remission in arthritis rat models (van den Hoven *et al.*, 2011). In this study, PEGylated liposomes were prepared by the typical film rehydration and extrusion method as follows: Phospholipids such as dipalmitoylphosphatidylcholine (DPPC), cholesterol, and DSPE-PEG_{2000} are dissolved in ethanol at a molar ratio of 1.85:1.0:0.15, respectively. The dry lipid film is formed by rotary evaporation and then rehydrated with isotonic buffer containing the soluble anti-inflammatory drug. Liposomes are then extruded through polycarbonate membranes to obtain the desired particle size (90–100 nm), and the unencapsulated drug is removed from solution by dialysis against PBS, using a dialysis membrane with a 10,000 molecular weight cutoff.

Solid lipid nanoparticles (SLNs) have also been studied extensively for inflammatory diseases because of their mucoadhesive properties (Serpe *et al.*, 2010; Seyfoddin *et al.*, 2010). SLNs consisting of a lipid matrix dispersed in aqueous solution and stabilized by surfactants are shown to be effective controlled release formulations. For the preparation of SLNs, hot, cold, or high pressure homogenization techniques are usually followed, in which the lipid matrix, such as stearic acid, is melted and mixed with the hydrophobic drug, for example, dexamethasone, and surfactants such as lecithin. A warm aqueous solution of cosurfactants, for example, 0.5% (w/w) poloxamer 188 is then added with rapid stirring ~8000 g (Yadav *et al.*, 2009). The resulting microemulsion is then dispersed into cold water (2–3 °C) in a homogenizer for 4 h to allow for the hardening of the SLNs, and the particles can be recovered by centrifugation (Ye *et al.*, 2008).

2.2. Materials and methods of preparation of polymeric nanomedicines

PLGA and polylactic acid (*PLA*) polymeric nanoparticles have been used recently for the delivery of anti-inflammatory drugs, although efficient drug encapsulation in these nanoparticles remains a challenging task. These polymeric nanomedicines are prepared by the solvent diffusion method that involves dissolving PLGA or PLA or a mixture of both with the hydrophobic drug to be encapsulated, for example, tacrolimus, in methylene chloride or other organic solvents. The solution is then poured into 1% (w/w) polyvinyl alcohol aqueous solution, the resulting emulsion is then sonicated, the organic solvent is removed by evaporation, and nanoparticles are collected by centrifugation at 40,000 g (Meissner *et al.*, 2006). Water soluble drugs, for example, betamethasone phosphate, can also be incorporated by their addition to the aqueous phase before the formation of nanoparticles. Stealth polymeric nanoparticles can be obtained by the incorporation of PEG-modified polymers during preparation (Ishihara *et al.*, 2010).

Chitosan nanomedicines are composed of natural polymeric nanoparticles consisting of the cationic polysaccharide, chitosan, and anti-inflammatory compounds. These nanoparticles are considered appropriate delivery systems for ocular applications as they interact with the negatively charged cornea and conjunctiva, allowing for prolonged residence time (Ulbrich and Lamprecht, 2010). These nanomedicines are prepared by mixing chitosan and an anti-inflammatory drug, for example, indomethacin, dissolved in acetic acid and dichloromethane, respectively, with tripolyphosphate. The mixture is then stirred at 30 °C for 30 min with moderate speed to achieve spontaneous ionic gelation of the nanoparticles resulting from the evaporation of organic solvents (Badawi *et al.*, 2008). The size of the formed nanoparticles is controlled by adjusting the ratio of chitosan to tripolyphosphate solution. The nanoparticles can be collected by centrifugation at 9000 g for 30 min and washed with distilled water to remove remaining traces of acetic acid (Wen *et al.*, 2011).

2.3. Methods of conjugating targeting agents

Coupling techniques for the conjugation of targeting ligands to nanomedicines involve the reaction between two activated groups on both the targeting ligand and the distal end of monomer constituents of the nanoparticle. These conjugations mostly involve the reaction between a carboxylic acid and primary amine, a maleimide and a thiol group, or between a hydrazide and an aldehyde (Dagar *et al.*, 2001; Koning *et al.*, 2006; Koo *et al.*, 2005b). We have previously coupled VIP to the distal end of DSPE-PEG_{3400} for the targeted delivery of our SSM nanocarrier to VIP receptors overexpressed in inflamed tissues (Delgado *et al.*, 2001). This technique involves a reaction between amines and *N*-hyrdroxysuccinimide (NHS) groups as a linking agent. VIP (synthesized at the Protein Research Laboratory, Resource Center, University of Illinois at

Chicago, Chicago, IL) and DSPE-PEG_{3400}-NHS [DSPE-PEG_{3400}-N-succinimidyl propionate] (obtained from Nektar Therapeutics Inc., Huntsville, AL) in the molar ratio of 1:5 (VIP:DSPE-PEG_{3400}-NHS) are dissolved separately in isotonic buffer (pH 7.4), then DSPE-PEG_{3400}-NHS is added in small increments to the VIP solution over 1–2 min at 4 °C with gentle stirring, followed by the addition of glycine to terminate the reaction and consume the remaining NHS moiety. The conjugation is tested using SDS-PAGE and subsequent staining with Coomassie blue R-250 and silver stain. The resulting DSPE-PEG_{3400}-VIP is purified by HPLC and incubated with preformed SSM to be incorporated within the preformed nanocarriers (Dagar *et al.*, 2001a).

3. Physicochemical Characterization of Nanomedicines

3.1. Size- and zeta-potential measurements

Particle sizes and surface charge of anti-inflammatory nanomedicines can be controlled and are designed depending on their intended application. Neutral nanoparticles with sizes smaller than that of the vascular pore cutoff, are likely to escape surface opsonization and will have significantly low uptake by the reticuloendothelial system. These particles will circulate longer in blood and can be passively targeted to inflamed tissues. On the other hand, particles intended for uptake by macrophages should be of larger size and distinct surface charge to facilitate their interaction and internalization by macrophages (Moghimi *et al.*, 2001). Particle size and surface charge are determined by measuring the hydrodynamic diameter and zeta potential of the particle using dynamic light scattering and electrophoretic light scattering techniques, respectively. Instruments such as Malvern, NICOMP-380 (Agilent Technologies. Santa Carla, CA.), or Brookhaven Zeta-Sizer are available for these measurements (Badawi *et al.*, 2008; Vukovic *et al.*, 2011). When monitoring light scattering at multiple angles, for example, 30°, 90°, and 120°, the observed difference in measurements may be indicative of a nonspherical or an oblate particle shape. Size and shape confirmation of the nanomedicine can also be confirmed by imaging the particles via transmission electron microscopy (TEM) or scanning electron microscopy (SEM), as shown in Fig. 18.1 (Koo *et al.*, 2005a). It is worth noting that zeta potential and TEM measurements are preferred on low salt or salt-free samples.

Advanced techniques such as small-angle X-ray scattering (SAXS) and small-angle neutron scattering (SANS) are also used for studying the shape and internal structure of nanoparticles (Ashok *et al.*, 2004). We have found that the contrast of mixed egg yolk phosphatidylcholine (PC) (obtained from LIPOID GmbH. Ludwigshafen, Germany) and (DSPE-PEG) and DSPE-PEG micelles is different for X-rays and neutrons, and by combining SANS and SAXS, complementary information about the micelle structure can be obtained.

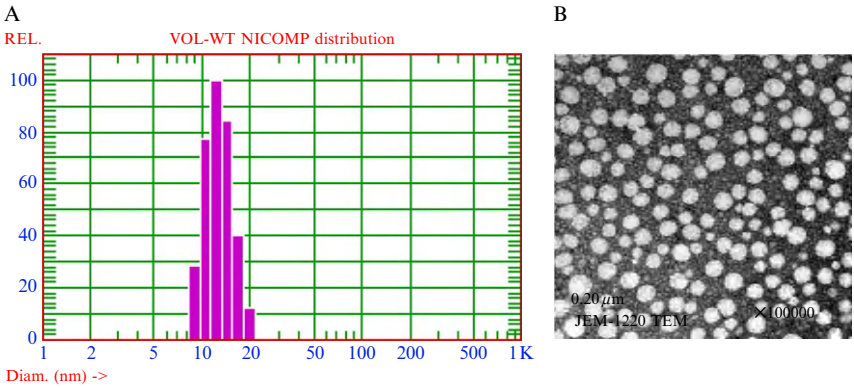

Figure 18.1 (A) Results of SSM particle size distribution as obtained by a NICOMP380 particle size analyzer. The measurement was performed at a 90° angle at room temperature (25 °C) and a pressure of $p = 1$ atm, solvent viscosity of $h = 0.933$ cP, and refractive index of $n = 1.333$. SSMs have a mean hydrodynamic diameter of 15 ± 3 nm. (B) TEM image of camptothecin-containing SSMs (CPT-SSM) and CPT particles obtained using a JEOL JEM-1220 instrument. The dispersion was observed at 100-kV for morphology, images were recorded by a multiscan camera using the Gatan Digital Micrograph 2.5 software (Koo *et al.*, 2005a,b).

The detailed structure of the micelles was determined by fitting a model for SANS and SAXS data simultaneously (Ashok *et al.*, 2004; Vukovic *et al.*, 2011).

3.2. Drug content and release measurements

Drug loading capacity is dependent on many factors such as size, charge, and hydrophobicity of the nanoparticle and encapsulated drug. The loading capacity of polymeric nanoparticles can be usually improved by changing the ratio of the composing polymers or their molecular weights (Ishihara *et al.*, 2010), while drug loading capacity of phospholipid micelles maybe increased by the addition of a second phospholipid, for example, PC during the preparation process (Krishnadas *et al.*, 2003). The drug content of self-assembled nanomedicines is usually determined by measuring the concentration of unencapsulated drug in the dispersion media using reverse-phase HPLC linked to UV–VIS or other detectors. In the case of solid particles, such as SLNs or liposomes in formulations that can be washed to remove unencapsulated drug, the drug content is measured after its extraction from the nanoparticles by dissolving in a suitable solvent, for example, methanol, centrifugation, then measuring the drug content in the supernatant (Ye *et al.*, 2008).

In vitro drug release on the other hand, is carried out by reverse dialysis bag technique in which the nanomedicine is incubated in a dialysis bag (donor chamber), with a molecular weight cutoff smaller than that of the nanomedicine, in a beaker large enough to give sink conditions and contains isotonic buffer, for example, PBS, pH 7.4 (recipient chamber), at physiological

temperature, 37 °C for 24–48 h with continuous light agitation (Attama *et al.*, 2008). The experiment is performed under sink conditions to avoid the interference of solubilized drug with its release from the nanoparticles. Samples are withdrawn from the recipient chamber at different time intervals, and the drug concentration is determined to evaluate the rate of release of drug from the nanomedicine (Vega *et al.*, 2006).

3.3. Nanomedicine storage stability and lyophilization

Satisfactory shelf stability is a requirement for successful introduction of any new dosage form to the market. Many lipid-containing nanomedicines are subject to chemical and physical instability during storage due to oxidation and hydrolysis or aggregation in aqueous environments; hence such formulations need to be lyophilized to ensure a longer shelf-life and stability. Lyophilization or freeze-drying is a relatively slow and expensive process that involves three main steps: First, freezing of the nanoparticle aqueous dispersion overnight by decreasing the temperature to −40 °C (at a rate of 0.25 °C/min). Second, a primary drying step is applied where the temperature of the shelf, on which the sample vials are placed, is maintained at −40 °C for 3.5 h to transfer heat from the shelf to the frozen solution. The ice in the sample sublimes and the water is transferred from the product to the condenser, with the temperature ranging from −77.5 °C to −83.6 °C. Third, a secondary drying step for an additional 7 h at 0 °C within a chamber pressure of -55×10^{-3} mm Hg, allows for additional removal of absorbed water from the product (Abdelwahed *et al.*, 2006; Koo *et al.*, 2005a). Small laboratory freeze-dryers such as Labconco FreeZone (Lim *et al.*, 2011) are also available for laboratory experimental batches and do not require the long cycles involved with industrial freeze-dryers. The final product should be in the form of an elegant cake with minimal shrinkage from the original frozen mass (Fig. 18.2). The addition of cryoprotective agents, such as, glycerol or mannitol, can be used in some nanomedicine formulations to immobilize the nanoparticles and maintain the integrity of the produced cake (Abdelwahed *et al.*, 2006). On the contrary, nanoparticles that are surface-conjugated with PEG can be successfully freeze-dried without the use of any cryo- or lyoprotectors (Lim *et al.*, 2008).

4. Assessment of the Therapeutic Effectiveness of Nanomedicines

4.1. Evaluation of cellular uptake

Internalization of nanomedicines into target cells takes place through a variety of pathways including phagocytosis, macropinocytosis, clathrin-mediated endocytosis or nonclathrin-mediated endocytosis (Koo *et al.*, 2005b).

Figure 18.2 Freeze-dried cakes of camptothecin nanomedicines (CPT–SSM) at an initial concentration of 15 m*M* DSPE-PEG_{2000} and CPT:DSPE-PEG_{2000} molar ratio = 0.004:1. $N = 4$, of 1 ml filled vials placed in different positions on the tray, and subjected to a controlled lyophilization cycle by the Virtis Genesis 25 EL freeze dryer, including slow freezing of the samples by decreasing the temperature at 0.25 °C/min to − 40 °C. In the first step of the freeze-drying process, the shelf temperature was maintained at 0 °C for 3.5 h, followed by an additional drying step of 7 h at 0 °C under a pressure of -55×10^{-3} mmHg. The condenser temperature ranged from − 77.5 °C to − 83.6 °C.

To evaluate cellular uptake of a nanomedicine, cell lines expressing receptors compatible with the targeting ligand of interest, are treated with a formulation of the nanoparticle tagged with a fluorophore. For this evaluation, cell lines are usually purchased from suppliers such as the American type culture collection (ATCC) (Cesur *et al.*, 2009), isolated from animals or humans as primary cell cultures (Serpe *et al.*, 2010), or bioengineered to mimic an organ of interest (Attama *et al.*, 2008). Cells are maintained at 37 °C in a 5% CO_2 incubator in Dulbecco's modified eagle medium (DMEM), or other suitable media, supplemented with 10–20% (v/v) serum, such as fetal bovine serum (FBS) or other sera, depending on type of cells used. We have performed cell uptake studies with MCF-7 cells that overexpress VIP-R, using quantum dots (QD) encapsulated in sterically stabilized mixed micelles surface-conjugated with VIP ("SSMM–VIP"), to evaluate cellular uptake of the nanomedicine (Rubinstein *et al.*, 2008). For these experiments cells are seeded in culture flasks 24 h before treatment. On the following day, culture media are removed and replaced with media containing QD–SSMM–VIP and incubated at 37 °C for various time intervals. The cells are then washed with PBS and imaged under a fluorescence microscope (Rubinstein *et al.*, 2008). Other techniques for evaluating cellular uptake include trypsinizing the treated cells and analyzing them for fluorescent content using fluorescence activated cell sorting (FACS) by flow cytometry instruments, as performed by Koning *et al.* (2006).

4.2. Available animal models

Disease animal models are essential to allow the investigation of disease states in ways that are inaccessible in humans. For the success and validity of the research, and to refine and improve the outcome of the conducted study, it is crucial to select the most appropriate animal model that is representative of human cases. Below we will illustrate some animal models that are suitable for the *in vivo* efficacy determination of nanomedicines in RA, ocular inflammation, and IBD as examples of inflammatory diseases.

RA nanomedicines are most commonly studied in adjuvant-induced arthritis (AIA) and collagen-induced arthritis (CIA) rat and mouse models. The AIA model is induced by intradermal injection of heat-inactivated *Mycobacterium tuberculosis* in incomplete Freund's adjuvant (IFA) in the base of Lewis rats' tails (Ishihara *et al.*, 2010; van den Hoven *et al.*, 2011). CIA is induced by immunization of genetically susceptible strains of mice through intradermal injections of type II collagen emulsified in IFA, followed by a second booster after 21 days (Delgado *et al.*, 2001; Koo *et al.*, 2011). The arthritic scores can then be obtained after 28 days of immunization. AIA models achieve more rapid onset of arthritis (within 10 days) with the development of a robust, easily measurable polyarticular inflammation, marked bone resorption and periosteal bone proliferation. CIA models on the other hand, are characterized by marked cartilage destruction, immune complex deposition on articular structure, bone resorption and periosteal proliferation, together with synovitis and periarticular inflammation (Hegen *et al.*, 2008).

The rabbit is the most commonly used animal species in ocular investigations to establish correlations between human and animal studies. The rabbit eye is known to be comparable to the human eye in terms of size; however, differences such as higher mucus and lower tear production may result in certain nanomedicine effects that cannot be translated to humans (Araujo *et al.*, 2009). Corneal inflammation can be induced in rabbit eyes by the addition of erosive chemicals such as 1 N NaOH or sodium arachidonate (SA). The efficacy of anti-inflammatory nanomedicines can then be evaluated either by treatment of the NaOH inflamed corneas 60–90 min later with anti-inflammatory nanomedicine, for example, indomethacin-containing chitosan-nanoparticles (Badawi *et al.*, 2008), or by evaluating the ability of the nanomedicine to prevent corneal lesions before the addition of the erosive chemical. Vega *et al.* (2006) studied the preventative effects of flurbiprofen-PLGA nanoparticles by applying the nanomedicine prior to SA solution in PBS. Inflammation was monitored 60, 90, 120, 150 min later using the Draize scoring system (Draize *et al.*, 1944; Vega *et al.*, 2006).

Many mouse models have been established for studying IBD, including Crohn's disease and ulcerative colitis. These include genetically engineered mice produced by knockout of T cell receptor-α (TCRα), interleukin (IL)-2, and IL-10, as well as congenic mouse strains. For example, SAMP1 (Mizoguchi and Mizoguchi. 2010), is a congenic mouse strain available from

national animal suppliers, such as The Jackson Laboratory, and can spontaneously develop IBD when housed under normal conditions. Alternatively, chemically induced colitis can be developed in wild-type (WT) mice by the addition of 5% dextran sulfate sodium (DSS) to their drinking water for 7–10 days (Meissner *et al.*, 2006), or the intrarectal administration of trinitrobenzene sulfonic acid (TNBS), resulting in acute intestinal injury (Lee *et al.*, 2010). T cell transfer IBD mice models, on the other hand, can be obtained 5–8 weeks after the transfer of naive T cells from healthy WT mice into syngeneic recipients that lack T and B cells. A protocol developed by Ostanin *et al.* (2009) is found useful in studying immunological mechanisms responsible for the induction, perpetuation, and regulation of the chronic disease. It is worth noting that, according to Plevy and Targan (2011), all IBD animal models are useful for addressing mechanistic questions about disease-related immune responses, and the screening of nanomedicines for therapeutic efficacy; but their utility in predicting therapeutic responses in people is still deficient.

4.3. Evaluation of *In Vivo* efficacy

To evaluate the *in vivo* efficacy of anti-inflammatory nanomedicines appropriate animal disease models are monitored for a period of time with continuous or intermittent administration of nanomedicine. Animals (rats or mice) are then sacrificed, tissues or organs to which nanomedicine delivery is intended are isolated and studied for their morphology, to determine whether the nanomedicine-treatment results in significant subsidence of inflammation. In our previous study, on developing CPT–SSM as an anti-arthritic nanomedicine, CIA mouse models, with arthritis score ≥ 2, were treated with CPT–SSM at respective doses. Animals were monitored for arthritic symptoms using two parameters; paw swelling (assessed by measuring paw thickness using a 0- to 10-mm digital caliper), and clinical arthritis scores (assessed by radiographic analysis using the following scoring system: 0, no swelling; 1, slight swelling and erythema; 2, pronounced edema; 3, joint rigidity) (Koo *et al.*, 2011).

The presence of T lymphocytes, B cells, and macrophages in the synovium of CIA mouse models was also used to evaluate the efficacy of CPT–SSM nanomedicine (Koo *et al.*, 2011). These inflammatory cells are found to increase with the progression of arthritis, while their lower levels are a good indication of the effectiveness of the nanomedicine. Furthermore, measurements are performed on CIA mice hind limbs, after their isolation from euthanized animals, by immunohistochemical staining. Briefly, the limbs are fixed in 10% buffered formalin, then decalcified in order to undergo microtomoy to obtain tissue sections. Decalcification is performed by a trained Veterinarian, briefly the tissues are placed in a weak acid e.g. 5% formic acid for 1–2 days that leaches the calcium from the bones but leaves the protein scaffolding. The samples are then embedded in paraffin, sectioned onto microscopic slides and stained with hematoxylin/eosin (H&E). The joint sections are further stained with antimouse CD3, CD79a antibodies, and lysozyme (purchased from

DakoCytomation, Carpinteria, CA) to identify T cells, B cells, and macrophages, respectively. For this, joint sections are deparaffinized in xylene, washed in alcohol, and then placed in 3% hydrogen peroxide in methanol for 15 min. For CD3 and CD79 antigen unmasking, slides are microwaved in citrate buffer, pH 6, whereas for lysozyme antigen unmasking, trypsin 0.1% is used for 40 min at 37 °C. Avidin and biotin blocking is applied and rinsed, primary antibody is then applied to positive slides, while buffer or negative control serum is applied to negative slides. Secondary antibodies (obtained from BioGenex Supersensitive Multilink, San Ramon, CA) are added, followed by labeling reagent and diaminobenzidine (DAB) to slides before counterstaining in hematoxylin, dehydration, mounting, and scoring (Fig. 18.3; Koo *et al.*, 2011).

For evaluating the efficacy of anti-inflammatory nanomedicines in ocular inflammation, the treated eyes are monitored for the period of study for signs of inflammation of the cornea, iris, and conjunctiva, according to the Draize scoring method (Draize *et al.*, 1944). Badawi *et al.* (2008) monitored the changes in the transparency of the cornea, or corneal perforation, and phthisis for 21 days after chitosan–indomethacin nanomedicine treatment of chemically injured corneas. The rabbits are examined using a hand-held slit lamp and a digital camera to photograph the corneas. The results are compared to those of drug-free nanoparticle-treated animals.

In the case of IBD nanomedicines, efficacy in animals is monitored through the physical appearance, consistency of feces, the presence of gross blood in stool, and body weight (Lee *et al.*, 2010). Other quantifiable methods can be used, such as measuring the activity of myeloperoxidase, as it is a reliable index of the severity of inflammation caused by infiltration of activated neutrophil into inflamed tissue, on distal colon specimens of treated animals (Meissner *et al.*, 2006). For this, nanomedicine-treated animals are euthanized, colon specimens are minced in hexadecyltrimethylammonium bromide 0.5% in 50 m*M* PBS, and homogenized on ice, sonicated for 10 s, freeze-thawed three times, and centrifuged at 100–500 g for 5 min. The supernatant is then added to o-dianisidine hydrochloride and 0.0005% hydrogen peroxide, and the absorbance is measured at 460 nm. The change in absorbance is used to determine the unit activity of myeloperoxidase, which is the amount that degrades 1 μmol of peroxidase per minute at 25 °C (Krawisz *et al.*, 1984). The efficacy of orally administered tacrolimus-containing nanoparticles was compared to subcutaneous formulation based on the myeloperoxidase activity observed in the two groups of treated animals (Fig. 18.4; Meissner *et al.*, 2006).

5. Assessment of Nanomedicine Safety and Bioavailability

After nanomedicine administration and during the *in vivo* studies, groups of treated animals are monitored on a daily basis by observing their well being, body weights, and behavioral parameters, in comparison to

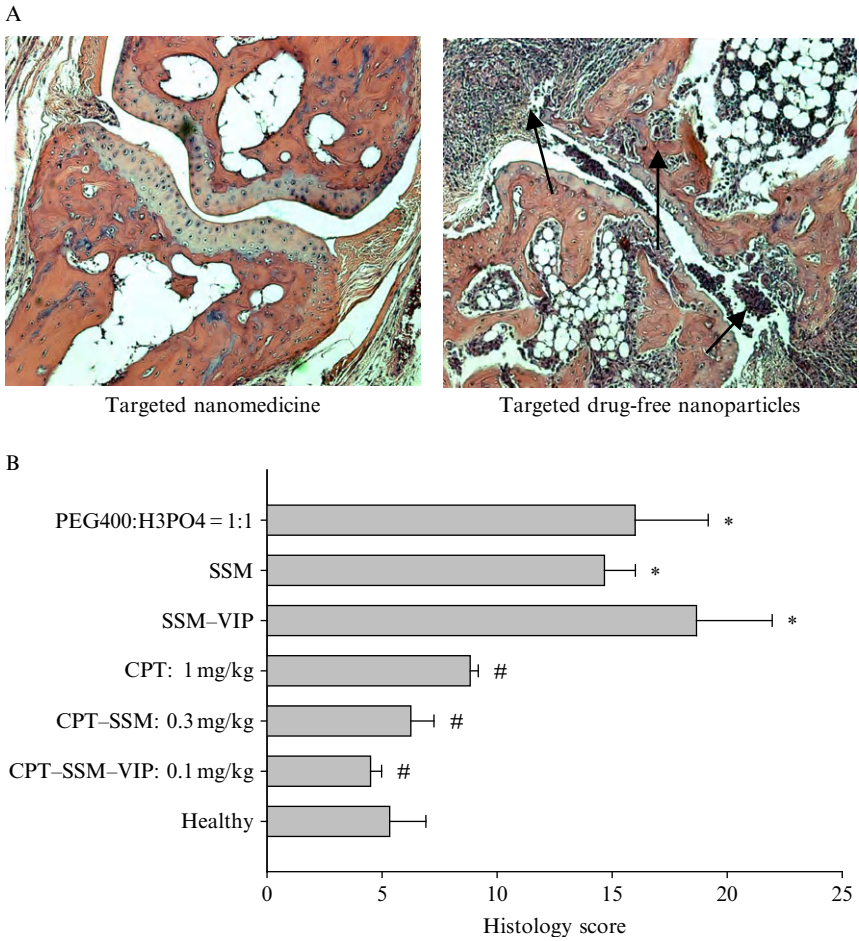

Figure 18.3 CPT–SSM–VIP abrogates CIA-characteristic inflammation of the synovial tissue, cartilage destruction and bone erosion. (A) Representative histopathology of a joint section of targeted nanomedicine treated (left), and targeted nanoparticle control (right) mice on day 60 (magnification $\times 100$). Arrows represent abnormal infiltration of inflammatory cells and bone/cartilage destruction. (B) Average pooled histological scores of paw sections taken from mice injected with various treatments at effective dose levels and controls. Results are expressed as mean $\pm$ S.E.M. (six mice/group). $^{*}p < 0.05$ versus normal mice; $\#p < 0.05$ versus empty controls (Koo *et al.*, 2011).

control groups, to physically evaluate the efficacy and toxicity of the studied nanomedicine. To confirm these observations, one has to monitor quantifiable parameters that validate or dismiss the suitability of the study and treatment. In this section, we will discuss a few of these parameters and techniques used to evaluate them.

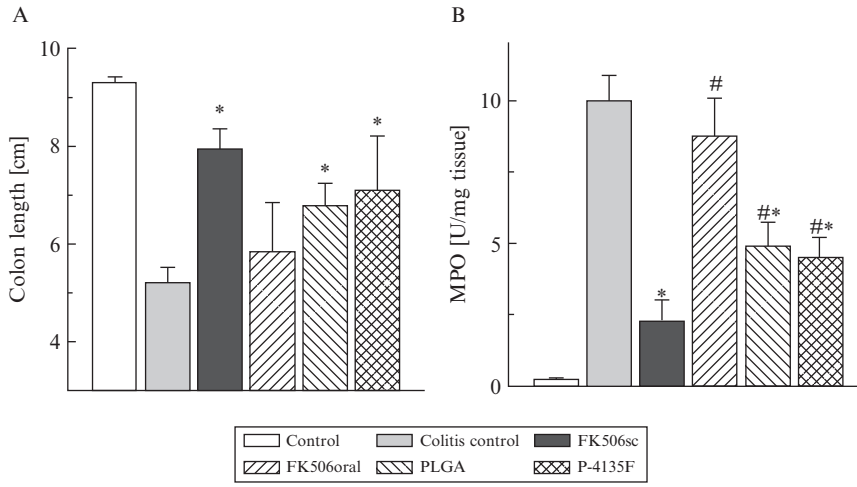

Figure 18.4 Results of *in vivo* efficacy of tacrolimus nanoparticles after a 7-day treatment of dextran sulfate sodium (DSS)-induced IBD in mice: Control (healthy animals), colitis control (DSS models receiving saline), FK506sc (DSS animals treated with subcutaneous injection of free tacrolimus), FK506oral (DSS animals treated with oral tacrolimus), PLGA (DSS animals treated with tacrolimus-PLGA nanoparticles), and P-4135F (DSS animals treated with tacrolimus-Eudragit nanoparticles). (A) Determination of colon length after final drug administration ($n = 6$ animals). $\star p < 0.05$ compared with colitis control mice given saline. $\#p < 0.05$ compared with the tacrolimus subcutaneous group. Data are shown as mean ± S.D. (B) Determination of myeloperoxidase (MPO) activity after final drug administration for $n = 6$ animals. $\star p < 0.05$ compared with colitis control mice given saline. $\#p < 0.05$ compared with the tacrolimus subcutaneous group. Data are shown as mean ± S.D. (Meissner *et al.*, 2006)

5.1. Serum biochemistry

Serum biochemistry profiling is one of the most important parameters for the evaluation of nanomedicines as they are often indicative of the progression of disease or the effectiveness and safety of therapy. Profiling serum biochemistry includes assessment of blood cell count with differentials and measurement of enzymes and biochemicals related to liver as well as renal functions. In our CPT–SSM nanomedicine study against RA, we analyzed blood counts and serum chemistry of the euthanized CIA mice and compared them to non-CIA and nontreated mice (Koo *et al.*, 2011).

Serpe *et al.* (2010) measured the efficacy of their dexamethasone and butyrate loaded SLNs in decreasing the secretion of the inflammatory mediators, IL-1β, TNF-α, IL-10, INF-γ by determining their concentration in the supernatant of peripheral blood mononuclear cells (PBMC) isolated from five IBD patients at 4 and 24 h of incubation by specific sandwich enzyme immunoassay. As for using serum biochemistry for safety

assessments, liver function tests including alanine aminotransferase (ALT) and aspartate aminotransferase (AST) enzymes, serum protein concentration, such as globulin and albumin, and renal function tests including creatinine, and blood urea nitrogen are usually performed by standard colorimetric kits such as Biometrieux solutions (Meissner *et al.*, 2006), and the results are then evaluated for indications of liver and renal toxicity.

5.2. Biodistribution and pharmacokinetics of nanomedicines

For biodistribution studies, animals are treated by IV administration with nanoparticles containing radiolabeled (^{3}H) drugs. At predetermined times (e.g., 12, 24, 48 h), a group of animals are sacrificed and major organs, including the liver, spleen, kidney, heart, lungs, intestines, and the treated area of interest are collected, weighed, and assessed for radioactivity of drug content using a gamma counter. Concentrations in the organs are calculated, and biodistribution is determined. Visualization of nanoparticle binding to other body parts such as the vasculature can also be performed. According to Koning *et al.* (2006), binding of liposomes to the vasculature is assessed by intravital microscopy after IV administration of rhodamine B sulfonyl-diacyl-phosphtidylethanolamine labeled liposomes into mice. The vasculature inflammation is then viewed under a fluorescence microscope, for example, a Leica DM-RXA (Koning *et al.*, 2006).

For PK studies, fluorophore- radionuclide- or drug-containing nanoparticles are administered using different routes. Blood samples are then collected at certain time points, for example, 1, 4, 8, and 24 h in tubes containing anticoagulants, such as EDTA or heparin sodium. Samples can be discolored, if necessary, by incubating at 50 °C with 0.1 *M* EDTA and 30% hydrogen peroxide in a volume ratio of 1:0.5:1. For nanoparticles containing radionuclides, for example, ^{67}Ga, blood samples are analyzed by scintillation counting or a gamma counter (Koning *et al.*, 2006), whereas for drug-containing nanoparticles, the drug content can be determined by HPLC or other sensitive analytical techniques. Plasma concentration–time curves are then plotted, and the area under the curve (AUC) is calculated using the trapezoidal rule. Other PK parameters for the studied nanomedicine can be assessed using designated PK programs (van den Hoven *et al.*, 2011). Meanwhile, for ocular PK, eyes are dissected after animal euthanasia and samples of ocular tissues, including the cornea, aqueous humor, lens, iris, and others are collected for HPLC analysis and PK evaluation (Zhang *et al.*, 2009).

PK of small molecules, including absorption, distribution, metabolism, and elimination (ADME) are usually studied through physiologically based pharmacokinetic models (PBPK). However, it is important to note that the PK of the free and nanomedicine-associated drug molecules can be significantly different. According to a recent review by Li *et al.* (2010), because of the differences between drug molecules loaded in nanoparticles and free

drug molecules, modifications of the PKPB modeling are needed for the proper understanding of the fate of the nanomedicine in the human body (Li *et al.*, 2010).

5.3. Cell viability and tissue histopathology

Direct applying of nanomedicines to cells and tissues may lead to toxicity resulting in their limited application *in vitro* and *in vivo*. Hence, evaluation of the biological activity and efficacy of the studied nanomedicine should be accompanied by a study of their biocompatibility and tolerance. *In vitro* cytotoxicity study can be performed to test for cell viability *in vitro*, especially when using cytotoxic drug-containing nanomedicines, for example, camptothecin. For this, several assays can be performed on the nanomedicine-treated cell cultures, depending on the culture type and agent studied. An example is the sulforhodamine B colorimetric assay that determines cell viability after treatment by measuring the cellular protein content (Vichai and Kirtikara, 2006). In this technique, cells are seeded in 96-well plates, at a density of 10^3–10^5 cells/well, and incubated at conditions suitable for cell culture, as mentioned above in the section on the evaluation of cellular uptake. On the next day, cells are treated with various concentrations of drug-free and drug-encapsulating nanoparticles, and incubated for another 24 h. Cells are then fixed as a monolayer to plates by incubating with 10–20% trichloroacetic acid for 1 h at 4 °C. Plates are washed, air dried and stained with 0.4% sulforhodamine B in 1% (v/v) acetic acid for 30 min, the optical density is measured at 560 nm, and cell viability is calculated and expressed as LD_{50} values (Koo *et al.*, 2005a).

For evaluating tissue histopathology, organs or tissues are placed in 10% formalin, then embedded in paraffin and stained with H&E for histopathological analysis under light microscopy. The presence of inflammatory markers and inflammatory cellular proliferation can also be assessed on these H&E specimens. In our work, using the CIA mouse model, the hind limbs of CIA treated animals were evaluated for cartilage destruction before and after treatment. Destruction is graded on a scale of 0–3, ranging from the appearance of dead chondrocytes to complete loss of articular cartilage. In addition, bone erosion is graded in the range from normal bone (0) to fully eroded cortical bone structure (3). These evaluations are usually performed by a qualified, "blinded" histopathologist, and the viability of tissues before and after treatment are measured accordingly (Koo *et al.*, 2011).

For ocular drug delivery, nanomedicines should have suitable biocompatible properties and ocular tolerability. To evaluate ocular tolerance, measurements such as histological modification to the corneal surface are usually performed. A special device was developed by Araujo *et al.* (2009) to study the modifications to the corneal structure before and after the application of nanomedicine. Otherwise, the corneal epithelium can be assessed

for this purpose by SEM. Diebold *et al.* (2007) evaluated the tolerance of their liposome–chitosan nanomedicine by macroscopic monitoring of the animals' eyes, followed by evaluation of eyeballs and lids, after fixation in paraffin. They used the following criteria: alteration in the ocular surface epithelia, edema in lid tissues, and the presence of inflammatory cells or other abnormalities (Diebold *et al.*, 2007). In the case of IBD, tissues from the distal and proximal colon are evaluated after histological staining for the presence of ulceration, inflammatory cells, signs of edema, surface epithelial hyperplasia and others (Yadav *et al.*, 2009).

6. Concluding Remarks

In recent years, considerable interest has been directed towards developing more effective anti-inflammatory nanomedicines that overcome the side-effects observed with conventional anti-inflammatory drugs. By controlling the release of these drugs and targeting them to the site of action we hope to accomplish such goals. Several approaches have been proposed to obtain a nanomedicine for specific inflammatory diseases; therefore it is crucial to choose the appropriate preparation, characterization, and evaluation techniques before moving with the nanomedicine to clinical applications. Here, we have described some techniques that can be helpful in achieving these goals, with hopes to move anti-inflammatory nanomedicine products to the market in the near future.

ACKNOWLEDGMENTS

Our Camptothecin-SSM study for the treatment of rheumatoid arthritis was supported, in part, by DOD grant BCRP, #DAMD 17-02-1-0415, VA Merit Review and NIH grants R01 AG024026, R01 HL72323, and C06RR15482. This investigation was conducted in a facility constructed with support from grant C06RR15482 from the NIH National Center for Research Resources. O.M.Y.K. was a recipient of the UIC University Fellowship.

REFERENCES

Abdelwahed, W., Degobert, G., Stainmesse, S., and Fessi, H. (2006). Freeze-drying of nanoparticles: Formulation, process and storage considerations. *Adv. Drug Deliv. Rev.* **58,** 1688–1713.

Araujo, J., Gonzalez, E., Egea, M. A., Garcia, M. L., and Souto, E. B. (2009). Nanomedicines for ocular NSAIDs: Safety on drug delivery. *Nanomedicine* **5,** 394–401.

Ashok, B., Arleth, L., Hjelm, R. P., Rubinstein, I., and Önyüksel, H. (2004). *In vitro* characterization of PEGylated phospholipid micelles for improved drug solubilization: Effects of PEG chain length and PC incorporation. *J. Pharm. Sci.* **93,** 2476–2487.

Attama, A. A., Reichl, S., and Muller-Goymann, C. C. (2008). Diclofenac sodium delivery to the eye: *In vitro* evaluation of novel solid lipid nanoparticle formulation using human cornea construct. *Int. J. Pharm.* **355,** 307–313.

Badawi, A., El-Laithy, H., Qidra, R., Mofty, H., and dally, M. (2008). Chitosan based nanocarriers for indomethacin ocular delivery. *Arch. Pharm. Res.* **31,** 1040–1049.

Cesur, H., Rubinstein, I., Pai, A., and Önyüksel, H. (2009). Self-associated indisulam in phospholipid-based nanomicelles: A potential nanomedicine for cancer. *Nanomedicine* **5,** 178–183.

Cho, K., Wang, X., Chen, Z., Shin, D. M., and Nie, S. (2008). Therapeutic nanoparticles for drug delivery in cancer. *Clin. Cancer Res.* **14,** 1310–1316.

Cotran, R. S., and Majno, G. (1964). The delayed and prolonged vascular leakage in inflammation. I. Topography of the leaking vessels after thermal injury. *Am. J. Pathol.* **45,** 261–281.

Dagar, S., Sekosan, M., Lee, B. S., Rubinstein, I., and Önyüksel, H. (2001). VIP receptors as molecular targets of breast cancer: Implications for targeted imaging and drug delivery. *J. Control. Release* **74,** 129–134.

Delgado, M., Abad, C., Martinez, C., Leceta, J., and Gomariz, R. P. (2001). Vasoactive intestinal peptide prevents experimental arthritis by downregulating both autoimmune and inflammatory components of the disease. *Nat. Med.* **7,** 563–568.

Diebold, Y., Jarrín, M., Sáez, V., Carvalho, E. L. S., Orea, M., Calonge, M., Seijo, B., and Alonso, M. J. (2007). Ocular drug delivery by liposome–chitosan nanoparticle complexes (LCS-NP). *Biomaterials* **28,** 1553–1564.

Draize, J. H., Woodard, G., and Calvery, H. O. (1944). Methods for the study of irritation and toxicity of substances applied topically to the skin and mucous membranes. *J. Pharmacol. Exp. Ther.* **82,** 377–390.

Fahrenkrug, J., Hannibal, J., Tams, J., and Georg, B. (2000). Immunohistochemical localization of the VIP1 receptor (VPAC1R) in Rat cerebral blood vessels: Relation to PACAP and VIP containing nerves. *J. Cereb. Blood Flow Metab.* **20,** 1205–1214.

Gao, Y., Liu, X. L., and Li, X. R. (2011). Research progress on siRNA delivery with nonviral carriers. *Int. J. Nanomedicine* **6,** 1017–1025.

Hegen, M., Keith, J. C., Jr., Collins, M., and Nickerson-Nutter, C. L. (2008). Utility of animal models for identification of potential therapeutics for rheumatoid arthritis. *Ann. Rheum. Dis.* **67,** 1505–1515.

Ishihara, T., Takahashi, M., Higaki, M., Mizushima, Y., and Mizushima, T. (2010). Preparation and characterization of a nanoparticulate formulation composed of PEG-PLA and PLA as anti-inflammatory agents. *Int. J. Pharm.* **385,** 170–175.

Koning, G. A., Schiffelers, R. M., Wauben, M. H. M., Kok, R. J., Mastrobattista, E., Molema, G., ten Hagen, T. L. M., and Storm, G. (2006). Targeting of angiogenic endothelial cells at sites of inflammation by dexamethasone phosphate-containing RGD peptide liposomes inhibits experimental arthritis. *Arthritis Rheum.* **54,** 1198–1208.

Koo, O. M., Rubinstein, I., and Önyüksel, H. (2005a). Camptothecin in sterically stabilized phospholipid micelles: A novel nanomedicine. *Nanomedicine* **1,** 77–84.

Koo, O. M., Rubinstein, I., and Önyüksel, H. (2005b). Role of nanotechnology in targeted drug delivery and imaging: A concise review. *Nanomedicine* **1,** 193–212.

Koo, O. M., Rubinstein, I., and Önyüksel, H. (2006). Camptothecin in sterically stabilized phospholipid nano-micelles: A novel solvent pH change solubilization method. *J. Nanosci. Nanotechnol.* **6,** 2996–3000.

Koo, O. M., Rubinstein, I., and Önyüksel, H. (2011). Actively targeted low-dose camptothecin as a safe, long-acting, disease-modifying nanomedicine for rheumatoid arthritis. *Pharm. Res.* **28,** 776–787.

Krawisz, J. E., Sharon, P., and Stenson, W. F. (1984). Quantitative assay for acute intestinal inflammation based on myeloperoxidase activity. Assessment of inflammation in Rat and hamster models. *Gastroenterology* **87,** 1344–1350.

Krishnadas, A., Rubinstein, I., and Önyüksel, H. (2003). Sterically stabilized phospholipid mixed micelles: *In vitro* evaluation as a novel carrier for water-insoluble drugs. *Pharm. Res.* **20,** 297–302.

Kumar, V., Robbins, S. L., Cotran, R. S., and Kumar, V. (2010). Robbins and Cotran's Pathologic Basis of Disease. Saunders, Philadelphia, PA.

Kuzmis, A., Lim, S. B., Desai, E., Jeon, E., Lee, B. S., Rubinstein, I., and Önyüksel, H. (2011). Micellar nanomedicine of human neuropeptide Y. *Nanomedicine* **7,** 464–471.

Lampugnani, M. G., and Dejana, E. (1997). Interendothelial junctions: Structure, signalling and functional roles. *Curr. Opin. Cell Biol.* **9,** 674–682.

Lee, I. A., Bae, E. A., Hyun, Y. J., and Kim, D. H. (2010). Dextran sulfate sodium and 2,4,6-trinitrobenzene sulfonic acid induce lipid peroxidation by the proliferation of intestinal gram-negative bacteria in mice. *J. Inflamm. (Lond)* **7,** 7.

Li, M., Al-Jamal, K. T., Kostarelos, K., and Reineke, J. (2010). Physiologically based pharmacokinetic modeling of nanoparticles. *ACS Nano* **4,** 6303–6317.

Lim, S. B., Rubinstein, I., and Önyüksel, H. (2008). Freeze drying of peptide drugs self-associated with long-circulating, biocompatible and biodegradable sterically stabilized phospholipid nanomicelles. *Int. J. Pharm.* **356,** 345–350.

Lim, S. B., Rubinstein, I., Sadikot, R. T., Artwohl, J. E., and Önyüksel, H. (2011). A novel peptide nanomedicine against acute lung injury: GLP-1 in phospholipid micelles. *Pharm. Res.* **28,** 662–672.

Maeda, H., Wu, J., Sawa, T., Matsumura, Y., and Hori, K. (2000). Tumor vascular permeability and the EPR effect in macromolecular therapeutics: A review. *J. Controlled Release* **65,** 271–284.

Meissner, Y., Pellequer, Y., and Lamprecht, A. (2006). Nanoparticles in inflammatory bowel disease: Particle targeting versus pH-sensitive delivery. *Int. J. Pharm.* **316,** 138.

Mizoguchi, A., and Mizoguchi, E. (2010). Animal models of IBD: Linkage to human disease. *Curr. Opin. Pharmacol.* **10,** 578–587.

Moghimi, S. M., Hunter, A. C., and Murray, J. C. (2001). Long-circulating and target-specific nanoparticles: Theory to practice. *Pharmacol. Rev.* **53,** 283–318.

Ostanin, D. V., Bao, J., Koboziev, I., Gray, L., Robinson-Jackson, S. A., Kosloski-Davidson, M., Price, V. H., and Grisham, M. B. (2009). T cell transfer model of chronic colitis: Concepts, considerations, and tricks of the trade. *Am. J. Physiol. Gastrointest. Liver Physiol.* **296,** G135–G146.

Plevy, S. E., and Targan, S. R. (2011). Future therapeutic approaches for inflammatory bowel diseases. *Gastroenterology* **140,** 1838–1846.

Rubinstein, I., Soos, I., and Önyüksel, H. (2008). Intracellular delivery of VIP-grafted sterically stabilized phospholipid mixed nanomicelles in human breast cancer cells. *Chem. Biol. Interact.* **171,** 190–194.

Serpe, L., Canaparo, R., Muntoni, E., Eandi, M., Zara, G. P., Daperno, M., Sostegni, R., Martinasso, G., Ippolito, L., Vivenza, N., Gasco, M. R., and Pera, A. (2010). Solid lipid nanoparticles as anti-inflammatory drug delivery system in a human inflammatory bowel disease whole-blood model. *Eur. J. Pharm. Sci.* **39,** 428–436.

Sethi, V., Önyüksel, H., and Rubinstein, I. (2003). Stabilization of a-helical vasoactive intestinal peptide in sterically stabilized micelles for potential treatment of rheumatoid arthritis. 30th Annual Meeting & Exposition of the Controlled Release Society, 691.

Seyfoddin, A., Shaw, J., and Al-Kassas, R. (2010). Solid lipid nanoparticles for ocular drug delivery. *Drug Deliv.* **17,** 467–489.

Ulbrich, W., and Lamprecht, A. (2010). Targeted drug-delivery approaches by nanoparticulate carriers in the therapy of inflammatory diseases. *J. R. Soc. Interface* **7,** S55–S66.

van den Hoven, J. M., Hofkens, W., Wauben, M. H., Wagenaar-Hilbers, J. P., Beijnen, J. H., Nuijen, B., Metselaar, J. M., and Storm, G. (2011). Optimizing the

therapeutic index of liposomal glucocorticoids in experimental arthritis. *Int. J. Pharm.* **416,** 471–477.

Vega, E., Egea, M. A., Valls, O., Espina, M., and García, M. L. (2006). Flurbiprofen loaded biodegradable nanoparticles for ophtalmic administration. *J. Pharm. Sci.* **95,** 2393–2405.

Vichai, V., and Kirtikara, K. (2006). Sulforhodamine B colorimetric assay for cytotoxicity screening. *Nat. Protoc.* **1,** 1112–1116.

Vukovic, L., Khatib, F. A., Drake, S. P., Madriaga, A., Brandenburg, K. S., Kral, P., and Önyüksel, H. (2011). Structure and dynamics of highly PEG-ylated sterically stabilized micelles in aqueous media. *J. Am. Chem. Soc.* **133,** 13481–13488.

Wen, Z. S., Xu, Y. L., Zou, X. T., and Xu, Z. R. (2011). Chitosan nanoparticles act as an adjuvant to promote both Th1 and Th2 immune responses induced by ovalbumin in mice. *Mar. Drugs* **9,** 1038–1055.

Yadav, V. R., Suresh, S., Devi, K., and Yadav, S. (2009). Novel formulation of solid lipid microparticles of curcumin for anti-angiogenic and anti-inflammatory activity for optimization of therapy of inflammatory bowel disease. *J. Pharm. Pharmacol.* **61,** 311–321.

Ye, J., Zhou, X., Zhang, N., and Wang, Q. (2008). Injectable actarit-loaded solid lipid nanoparticles as passive targeting therapeutic agents for rheumatoid arthritis. *Int. J. Pharm.* **352,** 273–279.

Zhang, L., Li, Y., Zhang, C., Wang, Y., and Song, C. (2009). Pharmacokinetics and tolerance study of intravitreal injection of dexamethasone-loaded nanoparticles in rabbits. *Int. J. Nanomedicine* **4,** 175–183.

CHAPTER NINETEEN

Polymeric Nanoparticles for the Selective Therapy of Inflammatory Bowel Disease

Philip Wachsmann* *and* Alf Lamprecht*,†

Contents

Abstract

The two main forms of inflammatory bowel disease (IBD) are Crohn's disease and ulcerative colitis. Both diseases are chronic relapsing inflammations of the gut. The challenge for drug carrier systems that are used for the therapy of IBD is the delivery of the active ingredient to the site of inflammation. A site-directed targeting should lead to higher local drug concentrations, less

* Laboratory of Pharmaceutical Technology and Biopharmaceutics, University of Bonn, Bonn, Germany
† Laboratory of Pharmaceutical Engineering, University of Franche-Comté, Besançon, France

Methods in Enzymology, Volume 508
ISSN 0076-6879, DOI: 10.1016/B978-0-12-391860-4.00019-7

systemic absorption, and therewith to less adverse effects. Because nanoparticulate drug carrier systems have the ability to accumulate in the inflamed regions, they offer a new targeting approach in IBD. We describe preparation techniques for polymeric nanoparticles and methods to characterize their physicochemical properties, their behavior in cell culture, and the therapeutic efficiency in murine experimental colitis models.

1. Introduction

1.1. Pathophysiology of inflammatory bowel disease

The two main forms of inflammatory bowel disease (IBD) are Crohn's disease (CD) and ulcerative colitis (UC). Both diseases are chronic relapsing inflammations of the gut. The highest incidence rates for both diseases are in northern Europe and North America, but the incidence rates in other countries are increasing (Loftus, 2004). The etiology is not completely understood yet. Contributing factors for the onset of IBD seem to be the genetic background, the environmental conditions, and luminal antigens in combination with a misregulated immune response (Sartor, 2006). Twin studies indicate a genetic background of IBD, which is stronger in CD than in UC (Halfvarson *et al.*, 2003). At least nine loci have been correlated with IBD (Newman and Siminovitch, 2005). Identified proteins that are affected by these mutations are, for example, the protein product of nucleotide-binding oligomerization domain 2 (NOD2; Ogura *et al.*, 2001), and the protein product of multidrug resistance 1 (MDR1) gene P-glycoprotein (P-gp; Brant *et al.*, 2003). NOD2 is an intracellular receptor that is involved in the recognition of bacterial cell wall constituents and participates not only in the immune response to bacterial infections but also in the regulation of immunity to commensal bacteria (Cario, 2005). P-gp is an efflux transporter that eliminates substances from the cytosol, and therewith helps mediate immunity against bacterial products (Ho *et al.*, 2005).

These findings are in compliance with the current theory of the pathophysiology of IBD as a multifactorial disease. Genetic predisposition, together with environmental conditions, for example, nutrition or gastrointestinal infections (Baumgart and Carding, 2007), leads to a dysregulated immune response to commensal bacteria (Chassaing and Darfeuille-Michaud, 2011). This can be shown by the presence of mucosal antibodies against commensal bacteria (Macpherson *et al.*, 1996) and the identification of bacterial flagellin as an antigen in CD (Lodes *et al.*, 2004).

IBD seems to be related to an altered barrier function of the enterocytes (Gassler *et al.*, 2001). This leads to an infiltration with and stimulation of immune-related cells, for example, macrophages and dendritic cells (Seldenrijk *et al.*, 1989), and subsequently to an excessive immune response.

Both diseases differ in the localization in the gut, the cytokine profile and the layers that are involved in the inflammatory processes. CD can be found in the whole intestine, but mostly the terminal ileum, caecum, and colon are affected. In contrast to UC, affected areas alternate with unaffected areas. UC starts generally from the rectum and ascends the colon (Bouma and Strober, 2003). CD shows a cytokine profile of T-helper (T_H)1 and T_H17 cells, whereas UC seems to be mainly T_H2 mediated. This results in different cytokine levels and susceptibility to different treatments (Strober and Fuss, 2011).

1.2. Standard treatment

The goal of IBD treatment is the induction and maintenance of remission. According to the location of the inflamed areas and the severity of disease, especially UC can be treated with rectal formulations, like suppositories or enemas. Therefore, formulations with 5-aminosalicylic acid (5-ASA) derivatives and corticosteroids like budesonide or fluticasone are currently in use (Gionchetti *et al.*, 2003).

5-Aminosalicylates are the most common oral treatment. Besides technological approaches to achieve colonic delivery of the active ingredient, which are discussed below, prodrugs like sulfasalazine or olsalazine are used. Depending on the clinical response, the medication can be adjusted including oral corticosteroids, tumor necrosis factor antibodies like Infliximab, and immunosuppressors like cyclosporine and azathioprine (Burger and Travis, 2011).

1.3. Nanoparticles in IBD

The challenge for drug carrier systems, which are used for the therapy of IBD, is the delivery of the active ingredient to the site of inflammation. A site-directed targeting should lead to higher local drug concentrations at the inflammation site, less unintended systemic absorption of the drug, and consequently less adverse effects.

Rectal delivery is limited to the rectum and the sigmoid colon (Williams *et al.*, 1987), thus inefficient in cases where inflammation is located in the upper areas of the gastrointestinal tract. In consequence, many cases require oral drug delivery to ensure a successful therapy.

The conventional strategies for oral colon-directed delivery are mainly time-, pH-, or microflora controlled (Asghar and Chandran, 2006). Time-controlled systems release the active ingredient after or during a defined time, so that the active ingredient reaches the colon, whereas pH-controlled systems rely on the pH change that occurs during the gastrointestinal passage. Microflora-controlled systems release the drug through degradation by the microflora of the colon.

The problems of these strategies are the altered conditions during an inflammation. The passage time through the colon is highly variable in IBD

patients (Hardy *et al.*, 1988), the pH is more acidic at the inflamed areas (Fallingborg *et al.*, 1993), and the composition of the gut flora of IBD patients differs from the one of healthy persons (Swidsinski *et al.*, 2007). Therefore, a delivery strategy where the accumulation of the active ingredient is related to pathophysiological alterations at the inflamed site, rather than on very general physiological parameters taken from healthy state of the gastrointestinal tract, is much more promising for a selective targeting (Lamprecht, 2010).

The adhesion of small particulate drug carriers at inflamed gut areas is size dependent. After oral application of different-sized polystyrene nanoparticles (NP) in an experimental rat colitis model, the 100 nm particles showed a significantly higher adhesion to the inflamed colon areas than the 10 μm particles, and a 6.5-fold higher accumulation compared to healthy controls (Lamprecht *et al.*, 2001). The increased adhesion at the inflamed areas might be explained by different alterations at the inflamed areas. The infiltration with immune-related cells leads to the presence of phagocytes. Especially, the interaction of NP with macrophages is well studied (Chellat *et al.*, 2005) and leads to the assumption that the NP might be taken up by these cells. Another possible reason is the increased mucus production at the inflamed regions, which might lead to a higher particle adhesion. Finally, the ulcerations might facilitate the adhesion and lead therewith to an increased particle accumulation.

A following study with tacrolimus-containing NP in a TNBS- and oxazolone rat model showed that the increased particle adhesion leads to a higher drug concentration at the inflamed sections of the colon, and thus to a higher therapeutic efficiency compared to a drug solution (Lamprecht *et al.*, 2005a).

However, the main drawback of nanoparticulate drug carrier systems remains the rapid release of encapsulated drugs because of their large surface area. Different approaches have been developed to realize a slower or delayed release of the active ingredient.

One idea is to combine the targeting strategies of pH-dependent delivery and NP targeting. The encapsulation of 6-Coumarin-containing nanoparticles into pH-sensitive microparticles composed of Eudragit P-4135F led to a decreased plasma concentration compared to free solution and nonencapsulated NP. The encapsulation of tacrolimus into the same delivery system led to a significantly reduced myeloperoxidase (MPO) activity and colon body weight index compared to the control group. Both results together indicate a more local delivery of the entrapped drug compared to free NP (Lamprecht *et al.*, 2005b).

Another strategy is the covalent binding of the drug to NP. Such particles containing methyl-5-ASA bound to the matrix polymer poly (ε-caprolactone) showed a slowdown of the drug release *in vitro*, which should allow efficient colon targeting. In a murine TNBS colitis model, these particles with a 5-ASA dose of 0.5 mg/kg showed a comparable efficiency to a 5-ASA solution at a dose of 30 mg/kg (Pertuit *et al.*, 2007).

2. Nanoparticle Classification and Preparation

The large majority of NP used in drug delivery are prepared from organic compounds, and among them, polymers are probably the most prominent materials. The requirements for such materials include biocompatibility and biodegradability to ensure the elimination of the excipients with time. For example, poly[D,L-lactide-*co*-glycolide] (PLGA) meets these requirements.

2.1. Preparation techniques for polymeric nanoparticles

There is a wide variety of preparation techniques for polymeric NP. The process can start either from monomers, which are polymerized during the preparation, or from preformed polymers; but, nowadays, mainly preformed polymers are given priority. According to the properties of the matrix materials, the preparation method needs to be adapted. Here, only the most relevant methods are addressed.

2.1.1. Emulsification–solvent evaporation

The emulsification–solvent evaporation technique is suitable for the encapsulation of lipophilic drugs (Bodmeier and Cheng, 1990). The technique is based on an oil–water emulsion. The lipophilic drug and the water-insoluble polymer are dissolved in an organic solvent, which has to be immiscible with water. Often used organic solvents are methylene chloride and ethyl acetate (Vauthier and Bouchemal, 2009). Although the latter is partly miscible with water, it is often preferred because of its less toxic properties. A typical composition contains approximately 100–200 mg of polymer, 5–20 mg of lipophilic drug, and 1–5 ml of organic solvent.

This organic solution is emulsified with an aqueous phase (≈20–50 ml) by an ultrasound probe. The aqueous phase mostly contains a surfactant to stabilize the emulsion. Polyvinyl alcohol and polysorbates are common surfactants and are commonly used in a concentration range between 0.1% and 10%. After the emulsification, the organic solvent is removed by continuous stirring, increase of temperature, or reduced pressure. The removal of the organic phase leads to the precipitation of the water-insoluble polymer as NP.

A modification of this technique that allows the encapsulation of hydrophilic drugs is the water-in-oil-in-water (W/O/W) method (Blanco and Alonso, 1997; Lamprecht *et al.*, 1999). The hydrophilic drug is dissolved in a water phase which is emulsified with an organic phase. For the first emulsion, a water-in-oil surfactant is needed. This first emulsion is again

emulsified with an aqueous phase to build a W/O/W emulsion. Afterward the organic solvent is removed as described above.

Size-determining parameters are the surfactant concentration and the viscosities of the outer and inner phases. Higher surfactant concentrations lead, in general, to smaller particle sizes, because of their interface stabilizing properties. By contrast, higher concentrations lead, especially with polymeric surfactants, to a higher viscosity of the outer phase and thus to increasing particle sizes. The viscosity of the inner phase can be adjusted by the concentration of the polymer, whereas lower polymer concentrations lead to lower viscosities, which leads generally to smaller particle sizes (Desgouilles *et al.*, 2003).

Both variants of the solvent evaporation method lead to an aqueous NP suspension. Especially when used in cell or *in vivo* experiments, this suspension has to be purified from excess surfactant and nonencapsulated drug. Adequate methods are repeated centrifugation steps or dialysis. The particles produced by this method normally range between 100 and 500 nm (Pinto Reis *et al.*, 2006).

2.1.2. Emulsification–solvent diffusion

The emulsification–solvent diffusion method is based on an oil–water emulsion system. An organic solvent, which is partly miscible with water, is employed. First, the aqueous phase and the organic phase are saturated with each other. Then, the polymer and the lipophilic drug are dissolved in the water-saturated organic phase and emulsified by ultrasound with the solvent-saturated aqueous phase. The emulsion is then diluted with aqueous media. Because of its water miscibility, the organic solvent diffuses into the aqueous phase and the polymer is precipitated as NP (Vauthier and Bouchemal, 2009).

Parameters influencing the size are the polymer concentration and the ratio of the internal and external phases. An increase of both parameters leads to an increasing particle size (Quintanar-Guerrero *et al.*, 1998). A higher miscibility with water of the organic solvent and an increased stirring rate lead to smaller particle sizes (Vauthier and Bouchemal, 2009).

2.1.3. Nanoprecipitation

Nanoprecipitation occurs when the polymer is dissolved in a solvent, and this solution is added to a nonsolvent of the polymer. Solvent and nonsolvent have to be miscible. The fast diffusion of the polymer solution into the nonsolvent leads to the precipitation of NP. Therefore, an organic solvent that is completely miscible with water is needed. For example, ethanol, acetone, or their mixtures can be used. Polymer and lipophilic drugs are dissolved in the solvent and added to the stirred aqueous phase that usually contains a surfactant (Vauthier and Bouchemal, 2009).

The fast diffusion of the solvent into the aqueous phase leads to the precipitation of the polymeric nanospheres. The remaining organic solvent has to be removed by reduced pressure or continuous stirring.

A typical composition consists of 1–10 mg lipophilic drug and 100–200 mg of polymer, which are dissolved in 10 ml of organic solvent and poured into 50–100 ml aqueous phase. The main size-influencing factors are the polymer concentration and the composition of the organic phase (Chorny *et al.*, 2002). The sizes range between 100 and 500 nm (Vauthier and Bouchemal, 2009).

3. Characterization of Nanoparticulate Drug Carrier Systems

The interactions of NP with their biological environment depend mainly on their physicochemical properties. In particular, the influence of size, surface properties, and morphology are important and therefore investigated. Methods for the size characterization are photon correlation spectroscopy (PCS), atomic force microscopy, and electron microscopy. The latter two also give information about the shape of the particles and surface morphology.

Modifications of the particle surface can be monitored by measuring the zeta-potential. The zeta-potential is defined as the electric potential at the slipping plane of a particle moving in an electrolyte solution. The value of the zeta-potential gives an indication of potential changes of the surface charge. The exact value can be used to predict the stability of disperse systems (Müller, 1996).

To monitor surface modifications of particles, the change of the zeta-potential is a more reliable parameter than its exact value, because the latter is influenced by various parameters, for example, the charge of the unmodified particles.

3.1. Photon correlation spectroscopy

PCS is used to determine the particle size. The measurement is based on the Brownian motion. Particles in suspension diffuse in the dispersion medium, and the speed of the particles' movement depends on their hydrodynamic diameter. This relationship is described by the Stokes–Einstein relation. A laser passes through the diluted sample and the scattered light is detected with a photomultiplier at a certain angle, normally 90°. The time-dependent fluctuation of intensity is recorded, and the size is calculated by comparison with an autocorrelation function.

For the measurement, the sample has to be diluted to an appropriate concentration, because multiscattering would influence the results. Besides

information on the mean diameter, polydispersity is also determined and describes the variation of the sizes given by a value between 0 and 1, where smaller values indicate narrow size distributions (Villari and Micali, 2008).

3.2. Zeta-potential

Modifications of the particle surface that lead to an altered surface charge can be quantified as a change of the zeta-potential. The exact value of the zeta-potential is converted from the electrokinetic mobility by measuring the velocity of the particles in an electric field by the help of a laser (Müller, 1996).

3.3. Dissolution test

The release profile of classical drug carrier systems can be examined by the dissolution test. Standard instruments are the paddle and the basket method, which are described in the United States Pharmacopeia (USP). The main problem for nanoscale drug carrier systems is the separation of the released drug from the NP suspension. Therefore, mainly two different approaches exist.

One methodology is based on the separation of NP from the drug solution after the sampling, for example, by centrifugation or filtration. The main drawback of this technique is to ensure that no further release of drug occurs during the separation procedure.

The second approach is to separate the release compartment from the sampling compartment by a dialysis membrane. This ensures that the released drug can equilibrate between the two compartments, whereas the NP are too large to cross the membrane (Panyam *et al.*, 2003). Therefore, the NP suspension is placed into a dialysis bag of defined length and width and put into a glass beaker, which contains the release medium. This release system is kept at 37 °C and shaken at a constant speed. At predefined time points, samples are withdrawn and analyzed for their drug content. The release rate is calculated as the percentage of the encapsulated drug.

A more standardized method has been described recently (Abdel-Mottaleb and Lamprecht, 2011). This method is a modification of the dissolution apparatus I of the USP, where a glass tube, which is closed at the lower side with a dialysis membrane, replaces the basket (Fig. 19.1). This allows the standardization of the dialysis area and the rotation speed. In this study was shown that this release method allows the differentiation of colloidal formulations for their release profiles, whereas this was not possible with the dialysis bag method.

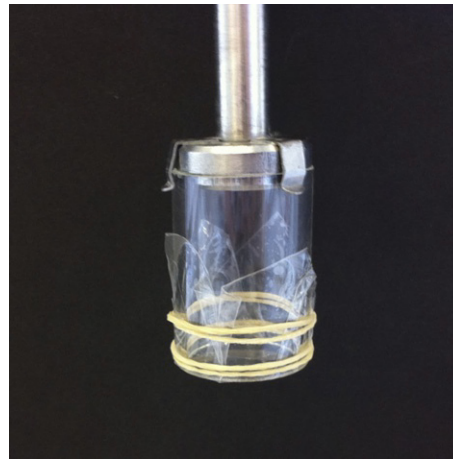

Figure 19.1 Modified dissolution apparatus as described by Abdel-Mottaleb and Lamprecht (2011). The conventional basket of the dissolution apparatus I as described in the USP is displaced by a glass tube, which is separated from the dissolution medium by a dialysis membrane. This ensures a constant surface area for the drug release and allows therewith the standardization of dissolutions test for colloidal drug carrier systems.

4. Cell Models

To determine the particles' toxicity and their ability to interact with their biological environment, cell culture experiments can be used. It should be kept in mind that cell culture models still nowadays hardly reflect the complex situation of an inflamed tissue and are usually useful just for the determination of single parameters. For example, general NP toxicity can be determined with standard procedures such as the MTT and lactate dehydrogenase (LDH) assays. Furthermore, the determination of cytokine levels gives valuable information about cellular stress.

The examination of the particle–cell interactions is focussed on the active internalization, which may allow the targeting of specific cell types and thereby influence the site-directed delivery of drugs. Additionally, the intracellular targeting of particles is of special interest, for example, offering the potential for nuclear localization for gene delivery applications. Other approaches require the cytosolic availability of the drugs, and, therefore, targeting involves different requirements for the NP properties (Panyam and Labhasetwar, 2003).

Commonly used cell lines in the research field of IBD are the human colorectal cancer cell line Caco-2 and the murine macrophage-like cell line

RAW 264.7 (Garrido-Mesa *et al.*, 2011). The main drawback of monoculture systems is the lack of complexity and, therefore, the inability to simulate inflammatory processes. Thus, existing models are very much simplified.

Tanoue *et al.* (2008) developed a model based on the coculture of RAW 264.7 cells and Caco-2 cells. In the model, the Caco-2 cells are seeded on Transwell inserts (4.67 cm^2) and grown until they reach confluency, and then transferred into 6-well plates, which are preloaded with RAW 264.7 cells. Tanoue *et al.* (2008) could show that the stimulation of the RAW 264.7 cells with lipopolysaccharides leads to an inflammatory response of the Caco-2 cells, which is measured by the interleukin-8 level. Furthermore, the transepithelial electric resistance of the Caco-2 monolayer was decreased.

Leonard *et al.* (2010) developed a three-dimensional coculture model. In this system, macrophages and dendritic cells, which are derived from peripheral blood monocytes, are seeded into a collagen matrix (80%) on a Transwell insert. Afterward, Caco-2 cells are seeded on top of the collagen matrix and further cultivated for 21 days with Caco-2 medium in the apical, and macrophage medium in the basolateral compartment. The inflammation model is induced by the addition of interleukin-1β to the apical side. Leonard *et al.* (2010) determined the localization of different-sized NP in the model and could show a higher colocalization with immune-competent cells under inflamed conditions.

4.1. Cytotoxicty

4.1.1. MTT-assay

The MTT-assay can be used to determine the viability of nanoparticle-treated cells. 3-(4,5-dimethylthiazol-2-yl)-2,5-diphenyl tetrazolium bromide (MTT) is a yellow dye, which is reduced by cellular enzymes to the blue product formazan. Because the transformation is only possible in viable cells, the amount of blue formazan is proportional to the number of these cells (Mosmann, 1983).

The cells are seeded in 96-well plates and are allowed to attach for 24 h. Thereafter, the medium is replaced by 200 µl of a NP suspension at different concentrations and incubated for 8–24 h. After the incubation period, 20 µl MTT (5 mg/ml in PBS) is added and further incubated for 2 h. Subsequently, the supernatant is removed, and the cells and MTT crystals are dissolved in a mixture of DMSO, acetic acid, and sodium dodecyl sulfate (99.4 ml:0.6 ml:10 g). The generated amount of blue formazan is determined spectrophotometrically at 570 nm. Wells without cells serve as a negative control, and their absorbance has to be subtracted from the other results. Untreated cells are the positive control (Lindl and Gstraunthaler, 2008). The results are calculated as the percentage of viability in relation to the untreated cells.

4.1.2. LDH-assay

LDH is an enzyme that is normally localized in the cytosol and released by damaged cells (Henderson *et al.*, 1985). Thus, the concentration of LDH in the cell supernatant is an indicator for cell damage.

The cells are seeded in microplates and after attachment they are incubated with the nanoparticle formulations. The released LDH can be determined with commercially available LDH-Kits (e.g., CytoTox 96 Kit, Promega; Anas *et al.*, 2009). To avoid false negative results, the ability of the particles to absorb LDH at their surface has to be determined (Clift *et al.*, 2008).

4.1.3. Cytokines

The MTT- and LDH-assay are used to determine the cell viability. The results of both assays are only affected by growth-inhibiting or direct cytotoxic reactions. The determination of cytokine levels allows the quantification of cell stress that does not lead directly to cell death.

The determined cytokine has to be chosen with respect to the profile of the cell line. For the murine monocyte–macrophage cell line, RAW 264.7, tumor necrosis factor-α is quantified (Palomäki *et al.*, 2010). For the human colorectal cancer cell line, Caco-2 interleukin-8 is often used as a marker cytokine (Leonard *et al.*, 2010). The incubation with blank nanoparticles leads normally to a concentration-dependent increase of the cytokine level (Clift *et al.*, 2010).

4.2. Nanoparticle–cell interaction

The interaction of NP with cells has been studied extensively. The main focus lies on the association with the cell surface, followed by active internalization routes into the different cell types.

The interaction of NP with cells is triggered by various particle properties. The main influencing parameters are the size (Gaumet *et al.*, 2009), the shape (Gratton *et al.*, 2008), and the surface properties (Hartmann *et al.*, 2000), which can be determined as described before.

Possible ways of internalization are, for example, phagocytosis, clathrin-mediated endocytosis, caveolae-mediated endocytosis, and macropinocytosis (Hillaireau and Couvreur, 2009). The mentioned pathways lead to different intracellular localizations of the internalized particles and show different size specificities. Phagocytosis and macropinocytosis exhibit minor size specificity, although a preference for larger particles for phagocytosis is reported (Schäfer *et al.*, 1992; Tabata and Ikada, 1988), whereas clathrin-mediated endocytosis and caveolae-mediated endocytosis have a size specificity for particles smaller than 200 and 500 nm, respectively (Rejman *et al.*, 2004; Wang *et al.*, 2009). Furthermore, it was shown that particles with

diameters below 42 nm are internalized by a nonclathrin and noncaveolae-dependent pathway (Lai *et al.*, 2007). These internalization routes differ in the intracellular fate of the internalized particles and in the rate of internalization.

Phagocytosis takes place mainly in specialized phagocytes. After adhesion to the cell surface and recognition by specific receptors, the particles are internalized into phagosomes, which mature and eventually fuse with lysosomes to generate the phagolysosome. In the latter, the particles are exposed to an acidic- and enzyme-rich environment, which can lead to their degradation. Clathrin-mediated endocytosis, which takes place in all mammalian cells, also leads to a lysosomal localization of the particles. By contrast, caveolae-mediated endocytosis ends up in cytosolic caveolar vesicles, which show a lack of degradative enzymes. The latter has a slower internalization rate than clathrin-mediated endocytosis (Hillaireau and Couvreur, 2009).

4.2.1. Quantitative determination of cell interaction

The quantitative determination of cell interaction is mainly determined with fluorescently labeled particles. They can be prepared easily by adding a lipophilic fluorescent dye to the organic phase during the standard preparation procedure. For example, Nile red and 6-coumarin are used (Davda and Labhasetwar, 2002).

The interaction can be determined by incubating the cells with a NP suspension. The concentration used in the experiments should be in the nontoxic range, which requires the previous determination of cell viability, usually performed by the MTT-assay. Furthermore, the incubation medium has a great influence on the internalization. Especially, the addition of serum proteins leads to opsonisation processes (Owens and Peppas, 2006), which strongly influence the adhesion and internalization. Thus, the adhesion medium has to be chosen with respect to the desired application.

After seeding and attachment of the cells, the medium is replaced by the NP suspension. After the incubation period, the supernatant is removed and the cells are washed with cold PBS to avoid further internalization or externalization processes. The amount of cell-associated particles can either be quantified by direct measurement of cell-associated fluorescence (Gaumet *et al.*, 2009), or the fluorescent dye can be extracted from the cells using an organic solvent, or cells are lysed with a lysis buffer. The amount of particles is determined by the fluorescence intensity after extraction.

To distinguish between active and passive internalization and adhesion, the incubation can be repeated at 4 °C. The low temperature leads to a slowdown of the cells' metabolism, and therewith to a nearly complete lack of ATP-dependent active transport processes.

Through the use of inhibitors, the elucidation of the underlying transport processes is possible. Commonly used inhibitors are chlorpromazine

(5–10 μg/ml; Sigma) for clathrin-mediated endocytosis, filipin (1–10 μg/ml; Sigma) or genistein (200 μ*M*; Sigma) for caveolae-mediated internalization, and cytochalasin B (1–5 μg/ml; Sigma) for phagocytosis (Rejman *et al.*, 2004).

Another method used frequently for the examination of internalization processes is flow cytometry. Adherent cells have to be detached and resuspended prior to the analysis. The fluorescence signals of the internalized particles are then detected from individual cells (Anas *et al.*, 2009).

4.2.2. Qualitative determination of cell interaction and NP localization

The location of NP inside the cells is of great interest and can be visualized by confocal laser scanning microscopy (CLSM). CLSM allows the acquisition of optical sections in the micrometer range, provides precise information on the intracellular localization of the fluorescence signals of the internalized NP, and enables the three-dimensional reconstruction of the cell structure.

For CLSM, the structural component of interest has to be fluorescently labeled. We describe a protocol to label the cell membrane and the nucleus, which is optimized for the RAW 264.7 cell line, but can be adjusted for other cell lines. This might be of interest to ensure that the particles are internalized and are not only adhering to the cell surface. For the labeling of the cell membrane, fluorescent dye-coupled lectins are frequently used. The choice of the right dye has to be done according to the color of particle labeling and the color of other labeled compartments.

The cells are seeded into wells containing previously cleaned coverslips and allowed to attach. Then the medium is removed and the cells are incubated with the particle suspension as described above. Afterward, they are washed with cold PBS and kept at 4 °C for 30 min. The PBS is removed and replaced with fluorescently labeled lectin concanavalin A (100 μg/ml; Molecular Probes) and incubated at 4 °C for 5 min to avoid the active entry of the lectin. Subsequently, the cells are washed with warm (37 °C) PBS and fixed with a 37 °C formaldehyde solution (4%) for 15 min. After another washing step with PBS, the cells are incubated with a 300 n*M* solution of DAPI (4′,6-diamidino-2-phenylindole) for 5 min to stain the nuclei. The cells are again washed with PBS, the supernatant is removed, and the coverslips are mounted on microscope slides with a standard mounting medium, for example, Prolong Gold (Molecular Probes).

A typical result is shown in Fig. 19.2. RAW 264.7 cells were incubated with Nile red-loaded ethylcellulose NP for 2 h. Thereafter, the above-mentioned staining protocol is applied with a concanavalin A Alexa Fluor 488 conjugate as lectin. The samples are examined using an inverted CLSM such as the Nikon Eclipse Ti (Nikon Corporation Inc., Tokyo, Japan).

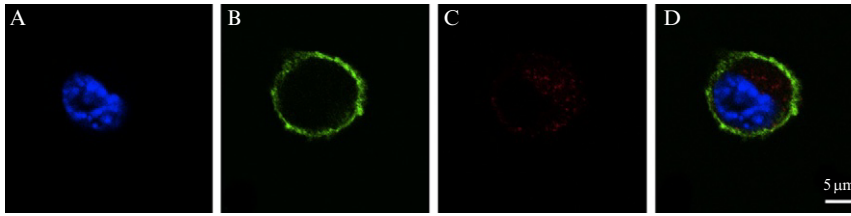

Figure 19.2 RAW 264.7 cells were incubated with Nile red-loaded ethylcellulose nanoparticles at 37 °C for 2 h. The nucleus was stained with DAPI (blue channel), the cell membrane with a concanavalin A Alexa Fluor 488 conjugate (green channel), and the nanoparticles were detected in the red channel. (A) Blue DAPI channel; (B) Green Alexa Fluor 488 channel; (C) Red channel; (D) Merge. The particles are internalized by the cells, as can be seen by their intracellular localization.

5. *In Vivo* Models

There is a wide variety of *in vivo* models for IBD. A detailed review can be found in Jurjus *et al.* (2004). According to this review, the models can be classified into gene knockout models, transgenic mouse and rat models, spontaneous colitis models, inducible colitis models, and adoptive transfer models. The most often used models in the research of nanoparticulate drug delivery are the chemical inducible models, in particular, TNBS-, Oxazolone-, and DSS colitis.

5.1. TNBS colitis

The TNBS colitis model uses the organic acid 2,4,6-trinitrobenzene sulfonic acid (TNBS) to induce inflammation. Often used animals are Sprague–Dawley rats or BALB/c mice. The inflammation is induced by intrarectal application of a TNBS solution in 50% ethanol.

First, the animals are lightly anesthetized with isoflurane to allow an exact location of the induction. Then, TNBS is administered via a syringe. A typical dose is 150 mg/kg body weight (Mladenovska *et al.*, 2007). After the TNBS application, the animals have to be kept in this position to ensure the right localization of the acid. For mice, the location is normally 4 cm (Pertuit *et al.*, 2007), and for rats, 8 cm (Mladenovska *et al.*, 2007) from the anus. After the induction of the colitis, the animals are housed for a period of 2 days. This allows the full development of the disease. Thereafter, the animals are treated with the test formulations, which can be administered either orally or rectally.

The advantage of this model is the exact location of the inflammation, which facilitates the identification and isolation of the inflamed areas.

The TNBS colitis model is closer related to CD, because its cytokine profile is T_H1 related (Neurath *et al.*, 1995).

5.2. Oxazolone colitis

The inflammation is induced by 4-ethoxymethylene-2-phenyl-2-oxazolin-5-one (Oxazolone). For colitis induction, male Wistar rats are first sensitized by dermal application of 12 mg Oxazolone dissolved in 300 µl of an ethanol/acetone (1:4) mixture. The colitis is induced 1 week later by the rectal application of 10 mg Oxazolone dissolved in 450 µl of an ethanol/water mixture. After 48 h, which allow the complete development of the disease, the animals are treated with the test formulations (Lamprecht *et al.*, 2005b). The oxazolone model is also reported for mice (Wirtz and Neurath, 2007).

In contrast to the TNBS model, the oxazolone model is T_H2-related. Therefore, it is more related to UC than to CD (Heller *et al.*, 2002).

5.3. DSS colitis

The dextran sulfate sodium (DSS) model can be applied in mice and rats (Hoffmann *et al.*, 2002). The inflammation is induced by the addition of 5% DSS to the drinking water for 7 days (Hartmann *et al.*, 2000). Thereafter, the animals can be treated with the test formulations and the disease severity can be assessed as described below.

5.4. Assessment of therapeutic effects

The severity of disease can be assessed using different parameters. The clinical activity score (CAS) and the body weight allow the assessment of the severity of the diseases in the living animal. After the resection of the colon, different inflammatory markers can be determined to evaluate the therapeutic efficiency. For example, the activity of MPO and alkaline phosphatase is used. A frequently used parameter that is easily accessible is the weight/length ratio of the colon.

5.4.1. Clinical activity score

The CAS, as described by Hartmann *et al.* (2000), is used to assess the severity of disease. With CAS, it is possible to evaluate the disease's course. Parameters like weight loss, stool consistency, and rectal bleeding are taken into account.

The body weight is scored according to the percentage of loss: no loss is scored as 0 points, 1–5% as 1 point, 5–10% as 2 points, 10–20% as 3 points, and more than 20% as 4 points.

Stool consistency is scored as follows: 0 points for well-formed pellets, 2 points for pasty and semiformed stools, and 4 points for liquid stools.

Rectal bleeding is scored by the hemoccult test: 0 points for no blood or negative hemoccult test, 2 points for positive hemoccult, and 4 points for gross bleeding.

The scores for three parameters are added and divided by three. The result evaluates the disease's severity on a scale from 0 to 4.

In Fig. 19.3, the CAS of a murine TNBS colitis model is shown. The mice were orally treated either with blank nanoparticles, methyl-5-ASA-bound poly(ε-caprolactone) nanoparticles (0.5 mg 5-ASA/kg), or 5-ASA solution (30 and 100 mg/kg; Pertuit *et al.*, 2007).

5.4.2. Myeloperoxidase

MPO is an enzyme that is found in mammalian granulocytes. The MPO activity is used to determine the infiltration of tissue sections with these cells.

The tissue specimen is weighed and minced in 1 ml of hexadecyltrimethylammonium bromide buffer (0.5% in 50 m*M* phosphate buffer, pH 6.0) on ice and homogenized. The homogenate is sonicated for 10 s, freeze-thawed three times, and centrifuged at 10,000 rpm for 3 min. MPO activity in the supernatant is determined spectrophotometrically. Phosphate buffer (2.9 ml, pH 6.0) containing 0.53 m*M* *o*-dianisidine hydrochloride solution

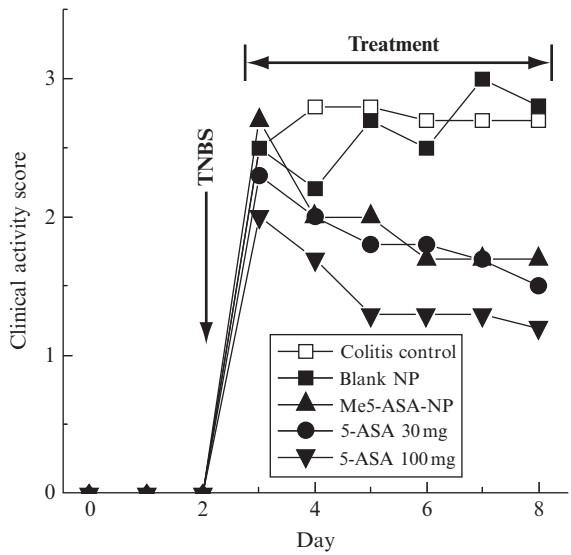

Figure 19.3 Clinical activity score in a TNBS mouse model (Mean $n = 6$). The animals were treated daily for six consecutive days with blank nanoparticles, methyl-5-ASA-bound poly(ε-caprolactone) nanoparticles (0.5 mg 5-ASA/kg), 5-ASA solution (30 mg/kg), or 5-ASA solution (100 mg/kg). Reprinted from Pertuit *et al.* (2007), Copyright (2007), with permission from Elsevier.

and 0.15 m*M* hydrogen peroxide are mixed with 0.1 ml of supernatant. The change in absorbance at 460 nm is measured for 5 min.

One unit of MPO activity is defined as the amount that degrades 1 μmol of peroxide per minute at 25 °C (Xia and Zweier, 1997). The results are calculated as MPO activity per wet tissue weight.

In Fig. 19.4, the MPO activity standardized to wet tissue weight of a murine TNBS colitis model is shown. The mice were treated either with blank NP, methyl-5-ASA-bound nanoparticles (0.5 mg/kg) or with 5-ASA solution (30 and 100 mg/kg; Pertuit *et al.*, 2007).

5.4.3. Cytokines

Inflammation can be assessed by measuring cytokine levels. For example, tumor necrosis factor-α, interleukin-8, and interleukin-1β are suitable (Lahat *et al.*, 2007). Therefore, either the cytokine concentration in the supernatant of tissue homogenates is determined with commercially available ELISA-Kits (Hartmann *et al.*, 2000). Alternatively, the expression level of the cytokines is determined after isolating the RNA from the tissue (TRIzol Reagent; Invitrogen) and employing the real-time reverse transcription polymerase chain reaction (Laroui *et al.*, 2010).

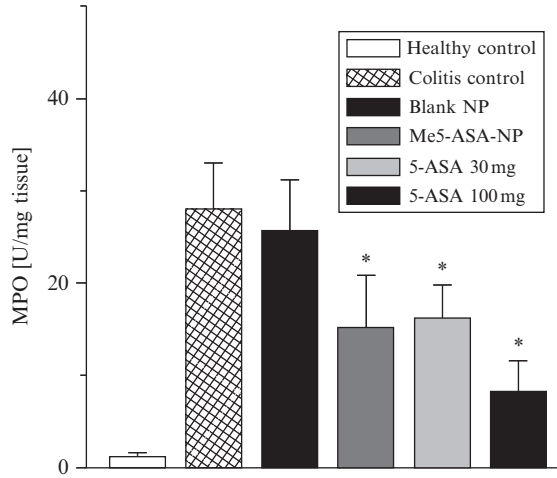

Figure 19.4 Myeloperoxidase (MPO) activity standardized to wet tissue weight in a TNBS mouse model after daily oral treatment for six consecutive days with blank nanoparticles, methyl-5-ASA-bound poly(ε-caprolactone) nanoparticles (0.5 mg 5-ASA/kg), 5-ASA solution (30 mg/kg), or 5-ASA solution (100 mg/kg; Mean ± SD; $n = 6$; $^{*}P < 0.05$ compared with colitis control). The nanoparticles show a comparable efficiency as the 5-ASA solution given at a dose of 30 mg/kg. Reprinted from Pertuit *et al.* (2007), Copyright (2007), with permission from Elsevier.

6. Concluding Remarks

Polymeric nanoparticles are able to accumulate at inflamed regions in IBD, and thus enhance the therapeutic efficiency of several drugs in murine and rat colitis models. Therefore, they might offer a new targeting approach for the treatment of IBD. Although the mechanisms of accumulation in humans and animals should be comparable, a remaining challenge is the clinical proof of the efficacy of this targeting approach.

REFERENCES

Abdel-Mottaleb, M. M. A., and Lamprecht, A. (2011). Standardized in vitro drug release test for colloidal drug carriers using modified USP dissolution apparatus I. *Drug Dev. Ind. Pharm.* **37,** 178–184.

Anas, A., Okuda, T., Kawashima, N., Nakayama, K., Itoh, T., Ishikawa, M., and Biju, V. (2009). Clathrin-mediated endocytosis of quantum dot-peptide conjugates in living cells. *ACS Nano* **3,** 2419–2429.

Asghar, L. F. A., and Chandran, S. (2006). Multiparticulate formulation approach to colon specific drug delivery: Current perspectives. *J. Pharm. Pharm. Sci.* **9,** 327–338.

Baumgart, D. C., and Carding, S. R. (2007). Inflammatory bowel disease: Cause and immunobiology. *Lancet* **369,** 1627–1640.

Blanco, M. D., and Alonso, M. J. (1997). Development and characterization of protein-loaded poly(lactide-co-glycolide) nanospheres. *Eur. J. Pharm. Biopharm.* **43,** 287–294.

Bodmeier, R., and Cheng, H. (1990). Indomethacin polymeric nanosuspensions prepared by microfluidization. *J. Control. Release* **12,** 223–233.

Bouma, G., and Strober, W. (2003). The immunological and genetic basis of inflammatory bowel disease. *Nat. Rev. Immunol.* **3,** 521–533.

Brant, S. R., Panhuysen, C. I., Nicolae, D., Reddy, D. M., Bonen, D. K., Karaliukas, R., Zhang, L., Swanson, E., Datta, L. W., Moran, T., Ravenhill, G., Duerr, R. H., *et al.* (2003). MDR1 Ala893 polymorphism is associated with inflammatory bowel disease. *Am. J. Hum. Genet.* **73,** 1282–1292.

Burger, D., and Travis, S. (2011). Conventional medical management of inflammatory bowel disease. *Gastroenterology* **140,** 1827.e2–1837.e2.

Cario, E. (2005). Bacterial interactions with cells of the intestinal mucosa: Toll-like receptors and NOD2. *Gut* **54,** 1182–1193.

Chassaing, B., and Darfeuille-Michaud, A. (2011). The commensal microbiota and enteropathogens in the pathogenesis of inflammatory bowel diseases. *Gastroenterology* **140,** 1720.e3–1728e3.

Chellat, F., Merhi, Y., Moreau, A., and Yahia, L. (2005). Therapeutic potential of nanoparticulate systems for macrophage targeting. *Biomaterials* **26,** 7260–7275.

Chorny, M., Fishbein, I., Danenberg, H. D., and Golomb, G. (2002). Lipophilic drug loaded nanospheres prepared by nanoprecipitation: Effect of formulation variables on size, drug recovery and release kinetics. *J. Control. Release* **83,** 389–400.

Clift, M. J. D., Rothen-Rutishauser, B., Brown, D. M., Duffin, R., Donaldson, K., Proudfoot, L., Guy, K., and Stone, V. (2008). The impact of different nanoparticle surface chemistry and size on uptake and toxicity in a murine macrophage cell line. *Toxicol. Appl. Pharmacol.* **232,** 418–427.

Clift, M. J. D., Bhattacharjee, S., Brown, D. M., and Stone, V. (2010). The effects of serum on the toxicity of manufactured nanoparticles. *Toxicol. Lett.* **198,** 358–365.

Davda, J., and Labhasetwar, V. (2002). Characterization of nanoparticle uptake by endothelial cells. *Int. J. Pharm.* **233,** 515–519.

Desgouilles, S., Vauthier, C., Bazile, D., Vacus, J., Grossiord, J., Veillard, M., and Couvreur, P. (2003). The design of nanoparticles obtained by solvent evaporation: A comprehensive study. *Langmuir* **19,** 9504–9510.

Fallingborg, J., Christensen, L. A., Jacobsen, B. A., and Rasmussen, S. N. (1993). Very low intraluminal colonic pH in patients with active ulcerative colitis. *Dig. Dis. Sci.* **38,** 1989–1993.

Garrido-Mesa, N., Camuesco, D., Arribas, B., Comalada, M., Bailón, E., Cueto-Sola, M., Utrilla, P., Nieto, A., Zarzuelo, A., Rodríguez-Cabezas, M. E., and Gálvez, J. (2011). The intestinal anti-inflammatory effect of minocycline in experimental colitis involves both its immunomodulatory and antimicrobial properties. *Pharmacol. Res.* **63,** 308–319.

Gassler, N., Rohr, C., Schneider, A., Kartenbeck, J., Bach, A., Obermüller, N., Otto, H. F., and Autschbach, F. (2001). Inflammatory bowel disease is associated with changes of enterocytic junctions. *Am. J. Physiol. Gastrointest. Liver Physiol.* **281,** G216–G228.

Gaumet, M., Gurny, R., and Delie, F. (2009). Localization and quantification of biodegradable particles in an intestinal cell model: The influence of particle size. *Eur. J. Pharm. Sci.* **36,** 465–473.

Gionchetti, P., Rizzello, F., Habal, F., Morselli, C., Amadini, C., Romagnoli, R., and Campieri, M. (2003). Standard treatment of ulcerative colitis. *Dig. Dis.* **21,** 157–167.

Gratton, S. E. A., Ropp, P. A., Pohlhaus, P. D., Luft, J. C., Madden, V. J., Napier, M. E., and DeSimone, J. M. (2008). The effect of particle design on cellular internalization pathways. *Proc. Natl. Acad. Sci. USA* **105,** 11613–11618.

Halfvarson, J., Bodin, L., Tysk, C., Lindberg, E., and Järnerot, G. (2003). Inflammatory bowel disease in a Swedish twin cohort: A long-term follow-up of concordance and clinical characteristics. *Gastroenterology* **124,** 1767–1773.

Hardy, J. G., Davis, S., Khosla, R., and Robertson, C. (1988). Gastrointestinal transit of small tablets in patients with ulcerative colitis. *Int. J. Pharm.* **48,** 79–82.

Hartmann, G., Bidlingmaier, C., Siegmund, B., Albrich, S., Schulze, J., Tschoep, K., Eigler, A., Lehr, H. A., and Endres, S. (2000). Specific type IV phosphodiesterase inhibitor rolipram mitigates experimental colitis in mice. *J. Pharmacol. Exp. Ther.* **292,** 22–30.

Heller, F., Fuss, I. J., Nieuwenhuis, E. E., Blumberg, R. S., and Strober, W. (2002). Oxazolone colitis, a Th2 colitis model resembling ulcerative colitis, is mediated by IL-13-producing NK-T cells. *Immunity* **17,** 629–638.

Henderson, R. F., Benson, J. M., Hahn, F. F., Hobbs, C. H., Jones, R. K., Mauderly, J. L., McClellan, R. O., and Pickrell, J. A. (1985). New approaches for the evaluation of pulmonary toxicity: Bronchoalveolar lavage fluid analysis. *Fundam. Appl. Toxicol.* **5,** 451–458.

Hillaireau, H., and Couvreur, P. (2009). Nanocarriers' entry into the cell: Relevance to drug delivery. *Cell. Mol. Life Sci.* **66,** 2873–2896.

Ho, G. T., Nimmo, E. R., Tenesa, A., Fennell, J., Drummond, H., Mowat, C., Arnott, I. D., and Satsangi, J. (2005). Allelic variations of the multidrug resistance gene determine susceptibility and disease behavior in ulcerative colitis. *Gastroenterology* **128,** 288–296.

Hoffmann, J. C., Pawlowski, N. N., Kühl, A. A., Höhne, W., and Zeitz, M. (2002). Animal models of inflammatory bowel disease: An overview. *Pathobiology* **70,** 121–130.

Jurjus, A. R., Khoury, N. N., and Reimund, J. M. (2004). Animal models of inflammatory bowel disease. *J. Pharmacol. Toxicol. Methods* **50,** 81–92.

Lahat, G., Halperin, D., Barazovsky, E., Shalit, I., Rabau, M., Klausner, J., and Fabian, I. (2007). Immunomodulatory effects of ciprofloxacin in TNBS-induced colitis in mice. *Inflamm. Bowel Dis.* **13,** 557–565.

Lai, S. K., Hida, K., Man, S. T., Chen, C., Machamer, C., Schroer, T. A., and Hanes, J. (2007). Privileged delivery of polymer nanoparticles to the perinuclear region of live cells via a non-clathrin, non-degradative pathway. *Biomaterials* **28,** 2876–2884.

Lamprecht, A. (2010). Selective nanoparticle adhesion can enhance colitis therapy. *Nat. Rev. Gastroenterol. Hepatol.* **7,** 311–312.

Lamprecht, A., Ubrich, N., Hombreiro Pérez, M., Lehr, C. M., Hoffman, M., and Maincent, P. (1999). Biodegradable monodispersed nanoparticles prepared by pressure homogenization-emulsification. *Int. J. Pharm.* **184,** 97–105.

Lamprecht, A., Schäfer, U., and Lehr, C. M. (2001). Size-dependent bioadhesion of micro-and nanoparticulate carriers to the inflamed colonic mucosa. *Pharm. Res.* **18,** 788–793.

Lamprecht, A., Yamamoto, H., Takeuchi, H., and Kawashima, Y. (2005a). Nanoparticles enhance therapeutic efficiency by selectively increased local drug dose in experimental colitis in rats. *J. Pharmacol. Exp. Ther.* **315,** 196–202.

Lamprecht, A., Yamamoto, H., Takeuchi, H., and Kawashima, Y. (2005b). A pH-sensitive microsphere system for the colon delivery of tacrolimus containing nanoparticles. *J. Control. Release* **104,** 337–346.

Laroui, H., Dalmasso, G., Nguyen, H. T., Yan, Y., Sitaraman, S. V., and Merlin, D. (2010). Drug-loaded nanoparticles targeted to the colon with polysaccharide hydrogel reduce colitis in a mouse model. *Gastroenterology* **138,** 843–853.

Leonard, F., Collnot, E. M., and Lehr, C. M. (2010). A 3-dimensional co-culture of enterocytes, macrophages and dendritic cells to model the inflamed intestinal mucosa in vitro. *Mol. Pharm.* **7,** 2103–2119.

Lindl, T., and Gstraunthaler, G. (2008). Zell- und Gewebekultur. 6th edn. Spektrum Akademischer Verlag, Heidelberg.

Lodes, M. J., Cong, Y., Elson, C. O., Mohamath, R., Landers, C. J., Targan, S. R., Fort, M., and Hershberg, R. M. (2004). Bacterial flagellin is a dominant antigen in Crohn disease. *J. Clin. Invest.* **113,** 1296–1306.

Loftus, E. V. (2004). Clinical epidemiology of inflammatory bowel disease: Incidence, prevalence, and environmental influences. *Gastroenterology* **126,** 1504–1517.

Macpherson, A., Khoo, U. Y., Forgacs, I., Philpott-Howard, J., and Bjarnason, I. (1996). Mucosal antibodies in inflammatory bowel disease are directed against intestinal bacteria. *Gut* **38,** 365–375.

Mladenovska, K., Raicki, R., Janevik, E., Ristoski, T., Pavlova, M., Kavrakovski, Z., Dodov, M., and Goracinova, K. (2007). Colon-specific delivery of 5-aminosalicylic acid from chitosan-Ca-alginate microparticles. *Int. J. Pharm.* **342,** 124–136.

Mosmann, T. (1983). Rapid colorimetric assay for cellular growth and survival: Application to proliferation and cytotoxicity assays. *J. Immunol. Methods* **65,** 55–63.

Müller, R. H. (1996). *Zetapotential und Partikelladung in der Laborpraxis*. Wissenschaftliche Verlagsgesellschaft mbH, Stuttgart.

Neurath, M. F., Fuss, I., Kelsall, B. L., Stüber, E., and Strober, W. (1995). Antibodies to interleukin 12 abrogate established experimental colitis in mice. *J. Exp. Med.* **182,** 1281–1290.

Newman, B., and Siminovitch, K. A. (2005). Recent advances in the genetics of inflammatory bowel disease. *Curr. Opin. Gastroenterol.* **21,** 401–407.

Ogura, Y., Bonen, D. K., Inohara, N., Nicolae, D. L., Chen, F. F., Ramos, R., Britton, H., Moran, T., Karaliuskas, R., Duerr, R. H., Achkar, J. P., Brant, S. R., *et al.* (2001). A frameshift mutation in NOD2 associated with susceptibility to Crohn's disease. *Nature* **411,** 603–606.

Owens, D. E., and Peppas, N. A. (2006). Opsonization, biodistribution, and pharmacokinetics of polymeric nanoparticles. *Int. J. Pharm.* **307,** 93–102.

Palomäki, J., Karisola, P., Pylkkänen, L., Savolainen, K., and Alenius, H. (2010). Engineered nanomaterials cause cytotoxicity and activation on mouse antigen presenting cells. *Toxicology* **267,** 125–131.

Panyam, J., and Labhasetwar, V. (2003). Biodegradable nanoparticles for drug and gene delivery to cells and tissue. *Adv. Drug Deliv. Rev.* **55,** 329–347.

Panyam, J., Sahoo, S. K., Prabha, S., Bargar, T., and Labhasetwar, V. (2003). Fluorescence and electron microscopy probes for cellular and tissue uptake of poly(D,L-lactide-co-glycolide) nanoparticles. *Int. J. Pharm.* **262,** 1–11.

Pertuit, D., Moulari, B., Betz, T., Nadaradjane, A., Neumann, D., Ismaïli, L., Refouvelet, B., Pellequer, Y., and Lamprecht, A. (2007). 5-Amino salicylic acid bound nanoparticles for the therapy of inflammatory bowel disease. *J. Control. Release* **123,** 211–218.

Pinto Reis, C., Neufeld, R. J., Ribeiro, A. J., and Veiga, F. (2006). Nanoencapsulation I. Methods for preparation of drug-loaded polymeric nanoparticles. *Nanomedicine* **2,** 8–21.

Quintanar-Guerrero, D., Allémann, E., Fessi, H., and Doelker, E. (1998). Preparation techniques and mechanisms of formation of biodegradable nanoparticles from preformed polymers. *Drug Dev. Ind. Pharm.* **24,** 1113–1128.

Rejman, J., Oberle, V., Zuhorn, I., and Hoekstra, D. (2004). Size-dependent internalization of particles via the pathways of clathrin- and caveolae-mediated endocytosis. *Biochem. J.* **377,** 159–169.

Sartor, R. B. (2006). Mechanisms of disease: Pathogenesis of Crohn's disease and ulcerative colitis. *Nat. Clin. Pract. Gastroenterol. Hepatol.* **3,** 390–407.

Schäfer, V., von Briesen, H., Andreesen, R., Steffan, A., Royer, C., Tröster, S., Kreuter, J., and Rübsamen-Waigmann, H. (1992). Phagocytosis of nanoparticles by human immunodeficiency virus (HlV)-infected macrophages: A possibility for antiviral drug targeting. *Pharm. Res.* **9,** 541–546.

Seldenrijk, C. A., Drexhage, H. A., Meuwissen, S. G., Pals, S. T., and Meijer, C. J. (1989). Dendritic cells and scavenger macrophages in chronic inflammatory bowel disease. *Gut* **30,** 484–491.

Strober, W., and Fuss, I. J. (2011). Proinflammatory cytokines in the pathogenesis of inflammatory bowel diseases. *Gastroenterology* **140,** 1756.e1–1767.e1.

Swidsinski, A., Loening-Baucke, V., Theissig, F., Engelhardt, H., Bengmark, S., Koch, S., Lochs, H., and Dörffel, Y. (2007). Comparative study of the intestinal mucus barrier in normal and inflamed colon. *Gut* **56,** 343–350.

Tabata, Y., and Ikada, Y. (1988). Effect of the size and surface charge of polymer microspheres on their phagocytosis by macrophage. *Biomaterials* **9,** 356–362.

Tanoue, T., Nishitani, Y., Kanazawa, K., Hashimoto, T., and Mizuno, M. (2008). In vitro model to estimate gut inflammation using co-cultured Caco-2 and RAW264.7 cells. *Biochem. Biophys. Res. Commun.* **374,** 565–569.

Vauthier, C., and Bouchemal, K. (2009). Methods for the preparation and manufacture of polymeric nanoparticles. *Pharm. Res.* **26,** 1025–1058.

Villari, V., and Micali, N. (2008). Light scattering as spectroscopic tool for the study of disperse systems useful in pharmaceutical sciences. *J. Pharm. Sci.* **97,** 1703–1730.

Wang, Z., Tiruppathi, C., Minshall, R. D., and Malik, A. B. (2009). Size and dynamics of caveolae studied using nanoparticles in living endothelial cells. *ACS Nano* **3,** 4110–4116.

Williams, C. N., Haber, G., and Aquino, J. A. (1987). Double-blind, placebo-controlled evaluation of 5-ASA suppositories in active distal proctitis and measurement of extent of spread using 99mTc-labeled 5-ASA suppositories. *Dig. Dis. Sci.* **32,** 71S–75S.

Wirtz, S., and Neurath, M. F. (2007). Mouse models of inflammatory bowel disease. *Adv. Drug Deliv. Rev.* **59,** 1073–1083.

Xia, Y., and Zweier, J. L. (1997). Measurement of myeloperoxidase in leukocyte-containing tissues. *Anal. Biochem.* **245,** 93–96.

Author Index

Note: Page numbers followed by "*f*" indicate figures, and "*t*" indicate tables.

B

D

E

H

I

J

K

M

N

Q

R

S

T

X

Y

Z

Subject Index

Note: Page numbers followed by "*f*" indicate figures, and "*t*" indicate tables.

L

Q

R

S